R. C. Hansen

(1)

Proceedings of the

1980

ANTENNA APPLICATIONS

SYMPOSIUM

Sponsored by

DEPUTY FOR ELECTRONIC TECHNOLOGY

ROME AIR DEVELOPMENT CENTER

ELECTRONIC SYSTEMS DIVISION

AIR FORCE SYSTEMS COMMAND

AND

ELECTROMAGNETICS LABORATORY

UNIVERSITY OF ILLINOIS

URBANA - CHAMPAIGN, ILLINOIS 61801

September 24, 25, 26, 1980

Robert Allerton Park

University of Illinois

"The views and conclusions contained in this document are those of the authors and should not be interpreted as necessarily representing the official policies or endorsements, either expressed or implied, of the Electromagnetic Sciences Division, Rome Air Development Center, USAF Systems Command."

PROCEEDINGS OF THE

1980

ANTENNA APPLICATIONS

SYMPOSIUM

Sponsored by

DEPUTY FOR ELECTRONIC TECHNOLOGY

ROME AIR DEVELOPMENT CENTER

ELECTRONIC SYSTEMS DIVISION

AIR FORCE SYSTEMS COMMAND

and

ELECTROMAGNETICS LABORATORY

UNIVERSITY OF ILLINOIS

URBANA-CHAMPAIGN, ILLINOIS 61801

September 24, 25, 26, 1980

Robert Allerton Park

University of Illinois

PROGRAM FOR 1980 ANTENNA APPLICATIONS SYMPOSIUM

WEDNESDAY, SEPTEMBER 24, 1980

ARRAYS

Welcome

† "Antenna Technology for Satellite Communications Systems," Leon Ricardi, MIT Lincoln Laboratory, Lexington, MA.

† "Tent Shaped Phased Array Antenna for Satellite Communications," Tony Chuang, Harris Corporation, Melbourne, FL.

"An SHF Microstrip Phased Array Antenna for Satellite Communication," Frank W. Cipolla and Ken Kudrna, Ball Aerospace Systems Division, Boulder, CO.

† "The Next Generation of Phased Array Transmit/Receive Modules," R. Hunter Chilton, RADC, Griffis AFB, NY.

"S-Band, Polarization Diverse, Low-Sidelobe Array," Gary E. Evans and William F. Hoover, Jr., Westinghouse Electric Corp., Baltimore, MD.

"Low Sidelobe Electronically Agile Cylindrical Array," John C. Herper*, John J. Stangel*, and Donald A. Hildebrand**, Sperry Gyroscope, Great Neck, NY*, and Rome Air Development Center, Griffis AFB, NY**. removed

ANTENNA DESIGN

"Design of a Broadband Impedance Matching Section for Peripherally Fed Helical Antennas, " Dirk E. Baker, National Institute for Aeronautics and Systems Technology Council for Scientific and Industrial Research, Pretoria, South Africa.

"Swept-Frequency Radiation Pattern Anomalies on Helical Antennas," J. M. Tranquilla, G. B. Graham, and S. Y. Jee, University of New Brunswick, Fredericton, N.B., Canada.

"Corporate-Tuner Short Monopole Antennas," G. Morin and K. G. Balmain, University of Toronto, Toronto, Canada.

† "Survivable UHF Dual Mode Antennas for Minuteman and Titan," V. J. Zanella, Boeing, Seattle, WA.

"Global Positioning System Monitor Station Antenna," Lenrod Goldstone, IEM, Owego, NY.

† "An Optimization of a Solar Power Satellite Antenna," R. A. Gilbert and Y. T. Lo, University of Illinois, Urbana, IL.

"Design of Transverse Slot Arrays Fed by Boxed Stripline," P. K. Park* and R. S. Elliott**, Hughes Missiles System Division, Canoga Park, CA*, and University of California, Los Angeles, CA**.

---

†Not included in this volume

"Application of Impedance Boundary Conditions to Numerical Solution of Corrugated and Receiver Horns with Rotational Symmetry," K. A. Iskander* and L. Shafai**, Spar Aerospace Limited*, and The University of Manitoba, Winnipeg, Manitoba, Canada**.

THURSDAY, SEPTEMBER 25, 1980

LOW-PROFILE ANTENNAS

"The Wire Grid Microstrip Antenna," Richard Conti and John Toth, Raytheon, Bedford, MA.

"A Simple Experimental Method For Separating Loss Parameters of a Microstrip Antenna," W. F. Richards*, Y. T. Lo** and J. Brewer**, University of Houston, Houston, TX*, and University of Illinois, Urbana, IL**.

"Dual-Polarized, Enhanced Bandwidth Microstrip Antennas," M. M. Millar and K. R. Carver, New Mexico State University, Las Cruces, NM.

† "Frequency Agile, Polarization Diverse, Multimode Microstrip Antennas," Fred Farrar, Harry Diamond Laboratories, Adelphi, MD.

"The Hybrid Slot, a Versatile Low-Profile Radiator with Small Reflection Coefficient," Paul E. Mayes and T. Cwik, University of Illinois, Urbana, IL.

† "Wide Bandwidth Printed Circuit Antenna Systems," K. D. Arkind, Sanders Associates, Nashua, NH.

† "Microstrip Phased Array Technology," Ron Stockton, Ball Aerospace Corporation, Boulder, CO.

ANTENNA SYSTEMS AND RADOMES

"Adaptive Antenna/Receiver-Processor System," G. G. Chadwick, J. G. Charitat, W. Gee, C. C. Hung and J. L. McFarland, Lockheed Missiles and Space Co., Inc., Sunnyvale, CA.

"WESTAR IV Antenna System," R. D. Ward, P. S. Bains, F. A. Taormina, Hughes Aircraft Company, El Segundo, CA.

"Completely-Overlapped-Subarray Fed Antenna for Broadband, Wide Scan Angle, Low Sidelobe Radar Applications," Hugh L. Southal, RADC/EEA, Hanscom AFB, MA.

"A Fast Versatile Waveguide Branch-Line Coupler Design Method," C. C. Hung, Lockheed, Sunnyvale, CA.

† "Wideband Microwave Lens Antenna for Tactical Radar Applications," Peter Franchi, Nicholas P. Kernweis and Walter Rotman, RADC, Hanscom AFB, MA.

"Investigation of Metal-Grid Angular Filters," P. W. Hannan and J. F. Pedersen, Hazeltine Corporation, Greenlawn, NY.

† "Vector Diffraction Analysis of Antenna/Radome Systems," G. E. Miller, Boeing, Seattle, WA.

"Lens Effect in Dielectric Radomes," M. S. Sheshadri, S. W. Lee and R. Mittra, University of Illinois, Urbana, IL.

FRIDAY, SEPTEMBER 26, 1980

ANALYSIS AND MEASUREMENTS

"A Hybrid Method of Moments - GTD Technique for Computing Electromagnetic Coupling Between Two Monopole Antennas on a Large Cylindrical Surface," Steven A. Davidson* and Gary A. Thiele**, Wright-Patterson AFB, OH*, and University of Dayton, Dayton, OH**.

† "Mutual Admittance Computation for Slot Antennas with Baffles in Between," P. J. Contoyannis, G. Franceschetti and N. G. Alexopoulos, University of California, Los Angeles, CA.

"Broadband Conical Spiral Antenna RCS Prediction Using Thin-Wire Approximation," M. S. Sohel, General Dynamics, Fort Worth, TX.

"A Low Sidelobe Shaped Beam Synthesis Procedure," K. G. Ramsey, Westinghouse Electric Corporation, Baltimore, MD.

"Development of a 150-Watt Pulsed S-Band Tripler Source," H. K. Hom and R. I. Wolfson, ITT Gilfillan, Van Nuys, CA.

"Range Distance Requirements for Measuring Low and Ultralow Sidelobe Antenna Patterns," P. S. Hacker and H. E. Schrank, Westinghouse Electric Corporation, Baltimore, MD.

† "Measurements of Antenna Pulse Response," Paul R. Caron, Southeastern Massachusetts University, MA.

"An Interface Between Anechoic Chamber and Computer," R. Willers, Eagle Signal, Davenport, IA.

"Experimental Results of a Commutating Feed for Circular Arrays," R. I. Wolfson, C. F. Cho and G. G. Charlton, ITT Gilfillan, Van Nuys, CA.

An SHF Microstrip Phased Array Antenna For Satellite Communication

Frank W. Cipolla and Ken Kudrna
Ball Aerospace Systems Division
Boulder, Colorado 80306

ABSTRACT

The demand for conformal, low profile, low cost phased arrays has increased dramatically during the past few years. Both airborne and ground based applications have placed stringent requirements on phased arrays. Ball Aerospace Systems Division has designed and built microstrip phased arrays which meet these requirements.

1.0 INTRODUCTION

The SHF Satellite Communication Band requires user antennas in a number of configurations and environments. All user antennas must meet the following operating requirements:

Frequency:	7250 - 7750 MHz - Receive
	7900 - 8400 MHz - Transmit
Polarization:	Left Hand Circular - Receive
	Right Hand Circular - Transmit
Gain:	30dBic Minimum
Steering Coverage:	Full Upper Hemisphere

This work was sponsored by the Air Force Systems Command, Rome Air Development Center, Griffiss Air Force Base, New York, 13441.

2.0 ARRAY CONFIGURATION

The Airborne Array has been configured from numerous subarrays as shown in Figure 1. The subarrays are microstrip multi-layer modules consisting of 64 microstrip disk radiators in a triangular lattice, 64 quadrature branch line hybrids to excite circular polarization, 64 3-bit digital phase shifters, a 64 way equal power corporate feed, and the decoder/driver electronics to control the phase shifters. In Figure 2, an expanded view of a single element of a subarry is depicted. It shows the integrated approach of the multi-layer design.

Each subarray is identical to any other and can be placed in any location in the larger array. The subarrays are excited at the center by a waveguide corporate feed which is mounted externally to the aircraft skin. As a subarray is mounted in the large array, it is connected to the waveguide via a waveguide to coax adapter. It is also connected to the D.C. power supplies and the digital data bus at the same time. This simplifies the installation of the array and makes repairs easier.

Penetrations through the aircraft skin are required for one waveguide flange and two electrical connectors only. The total thickness of the array is 1.5 inches and weighs 230 pounds. The array consists of 64 subarrays and has a theoretical directivity of 41dBi.

The ground configurations are essentially the same as the airborne system described above.

3.0 ENVIRONMENTAL CONSIDERATION

In aircraft applications, the array must withstand wide temperature variations as well as pressure differentials. The all microstrip subarray module is extremely rugged and can withstand these variations.

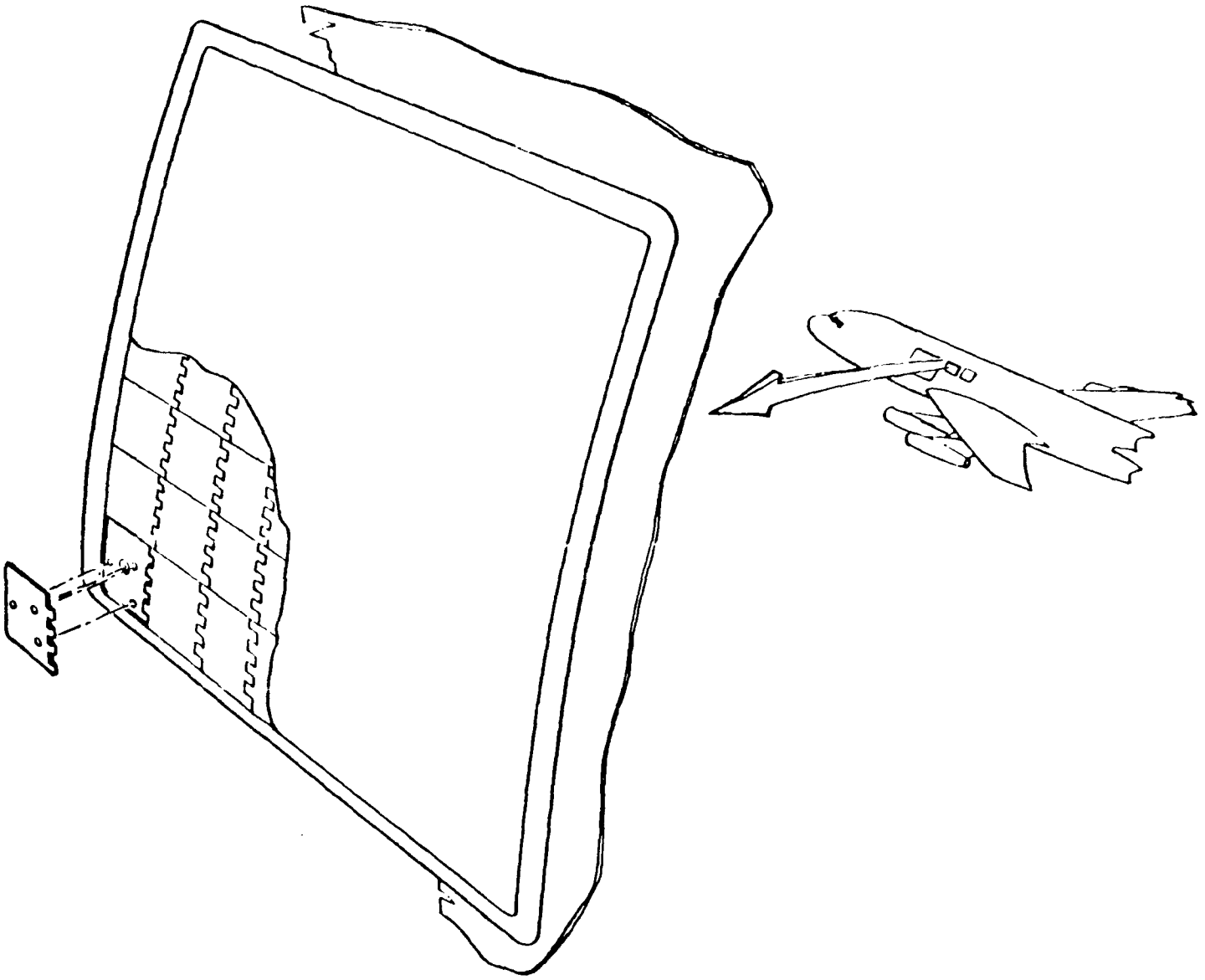

Figure 1. SHF Microstrip Phased Array
For Airborne Applications

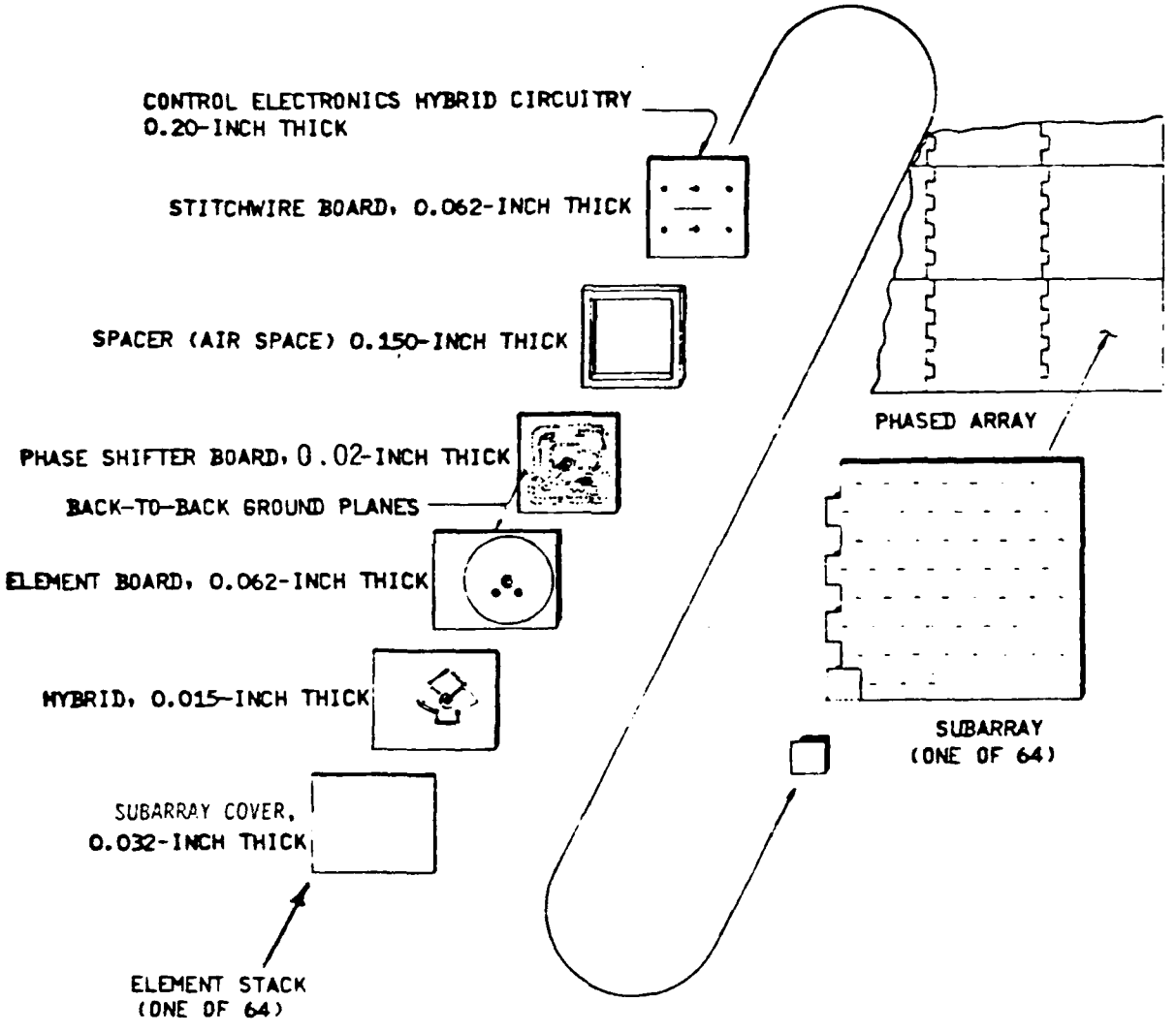

Figure 2. Multi-layer Microstrip Subarray Design

The array is also extremely resistant to nuclear EMP and lightning.

The installation can be accomplished without requiring recertification of the aircraft. This is due to the fact that the structural members of the fuselage are not distrubed during the installation.

4.0 CONCLUSION

The modular subarray approach is a highly flexible design which easily adapts itself to many different applications. The basic building block (the subarray module) is identical for both airborne and ground based applications. The waveguide feed would change in order for it to conform to the surface of the host vehicle.

S-BAND, POLARIZATION DIVERSE, LOW-SIDELOBE ARRAY *

Gary E. Evans
William F. Hoover, Jr.

Westinghouse Electric Corporation
Command and Control Division
Baltimore, Maryland

Abstract

The design of a low sidelobe, wideband, planar array is discussed which is applicable to a high-power, polarization diverse, S-band tactical radar. The specific design, fabrication, and test of a line source has been used to demonstrate the critical unit in such an array.

Design details are discussed, including development of wideband, high-isolation couplers; development of a crossed-dipole radiator for linear and circular polarizations; and the use of air-dielectric stripline in the corporate feed. Mutual coupling, grating lobe, and bandwidth considerations as well as size, weight, and tactical constraints are discussed. An extensive error analysis as it applies to antenna sidelobe levels has been conducted. Sources of both correlated and uncorrelated errors are identified. This error information is used to calculate the azimuth patterns of the line source and of an array of N line sources. Radiation pattern measurements of the single line source agree favorably with predicted patterns and demonstrate low-sidelobe performance for vertical, horizontal, and circular polarizations.

Background

The increasingly complex ECM environment in which tactical radars are called on to operate has placed continually more stringent requirements on the antenna. Low and ultra-low sidelobe antennas are required; adaptive arrays, polarization diversity, and frequency agility are sought; and wide instantaneous bandwidths, etc. are needed as well.

A tactical radar which scans in elevation, rotates in azimuth, and demonstrates several of the above characteristics has been the topic of this study. Such a radar could conceptually look like that of figure 1 and, specifically, we will discuss the design of an array antenna whose characteristics are given in table 1. A block diagram of the array is shown in figure 2 and is discussed below.

Array Design

The specified elevation coverage of -0.5 to $+20$ deg is small enough that the exact tilt of the array is not critical. Splitting the coverage minimizes the number of rows, but the long range, lowest angles should be favored for gain and for minimum effect on sidelobes. A tilt of 7 deg was selected, with elevation scanning from -7.5 to $+13$ deg.

For uniformity of rows and for realization of low sidelobes off the principal plane, a rectangular grid of radiators was chosen. For a rectangular grid, the maximum row spacing is

$$S = \frac{\lambda_{min}}{1 + \sin 13 \text{ deg} + \sin 2 \text{ deg}}$$

to avoid skirts of the grating lobe. This requires 64.6 rows. However, past mutual coupling experience has shown that long-range coupling (coupling between nonadjacent radiators) is a critical factor in determining

*This work was supported by the Rome Air Development Center, Electromagnetic Sciences Division, Hanscom AFB, Mass. under contract no. F19628-78-C-0151.

bandwidth and that coupling increases markedly near grating lobe boundaries. To a first order, elevation changes do not affect azimuth patterns, but with edge effects, the change is only negligible to the extent that the coupling is moderate. A modest margin around the grating lobes is adequate and is ensured by the use of perhaps 10 percent more rows. Thus, 72 rows was chosen that, with an aperture size of 14 feet, results in a row spacing of 2.333 in. Similar considerations result in a minimum number of columns of 56, but a safe number of 64. In this case, long-range mutual coupling increases directly as the grating lobe is approached. If coupling changes with frequency, a fixed divider will produce changing patterns. Thus, 64 elements spaced 2.625 inches apart represents a margin of safety.

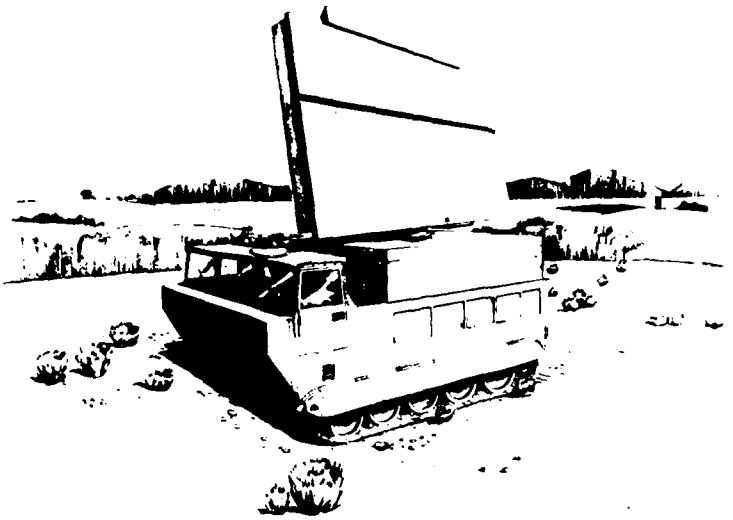

Figure 1. Tactical Array Comprised of Low Sidelobe Line Sources

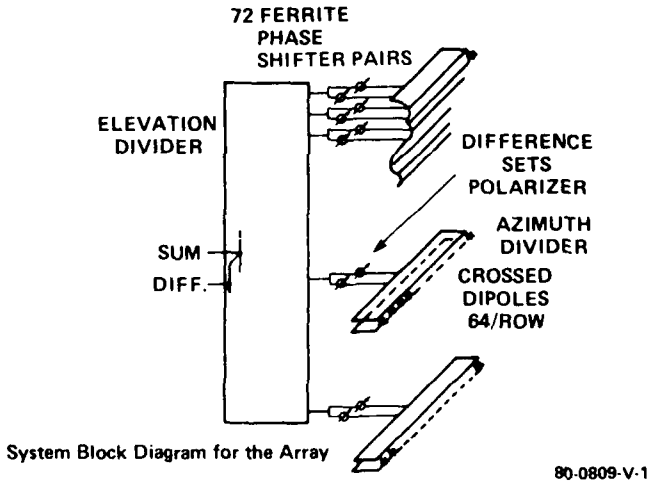

Figure 2. Block Diagram of Array in Figure 1

Beam scanning is called for in elevation from − 0.5 to + 20 deg. At boresight, beamwidth provided by the 14-ft. aperture size is about 1.5 deg wide. Over the scanning range, it was calculated that the beamwidth changes less than 3 percent. In fact, it could become desirable, and is entirely feasible, that the beam could be broadened deliberately to save scan time at higher elevation angles. The steering commands are corrected for frequency to the center of the instantaneous band. Only slight degradation of the beam shape occurs across the instantaneous bandwidth.

Table 1. Specifications for an Array Comprised of Low Sidelobe Line Sources

General	Tactical, lightweight, mobile
Size	14' x 14' max.
Weight	6000 lbs. max.
Peak Power	2 kw/row
Duty	6%
Frequency	3.1 to 3.6 GHz
Instantaneous Bandwidth	200 MHz
Polarization (Switchable)	LHC, RHC, V, H
Gain	40 dBi min.
Azimuth-rotating	
Resolution	1.5 degrees max.
Sidelobes 1st	-35 dB
2nd	-38 dB
3rd	-41 dB
Wide Angle	-50 dB
Elevation	
Scanning	-.5 degrees to 20 degrees
Sidelobes	-25 dB

A waveguide assembly provides low-loss and high-power handling capability for the elevation power divider. A monopulse network that utilizes a shared aperture for sum and difference beams was designed to yield low-sidelobe (– 25 dB or below) performance for both beams.

Switching between polarizations (V, H, RHC, and LHC) can most logically be done at three places: at the radiating element, on the row level, or at the system input. Intermediate points within the rows are not desirable since the switch tolerances contribute greatly to the azimuth error sidelobes, placing severe limitations on the devices. If switching is done at the radiators, a single power divider can be used, but this has several disadvantages: a large number of polarizers are needed, more stringent tolerances on each polarizer are needed, and there are limitations in having a single polarization channel. If switching is done at the input, a single polarizer feeds two complete divider assemblies and thus makes available the two polarization components for weather mapping, ECM analysis, target enhancement, etc. If, however, switching is done at the row level, only 72 polarizers are required and their tolerances only affect the elevation pattern. Two separate but identical dividers for each row are then required, though, so that the orthogonal components of each radiator can be fed. Also, the orthogonal polarization is unavailable except by rows. An advantage in tolerances is realized, however, since differences between dividers affect polarization purity to a minor extent, considering the precision already required for low sidelobes. Cost and tolerance considerations thus favor switching at the row level. The same phase shifters used for polarization diversity can also be used for elevation beam steering, as shown in figure 3.

The specified 40 dBi gain requires close attention to minimizing loss. The phase shifters discussed above for polarization switching and beam steering would be most likely a ferrite configuration. Other losses in the system could be minimized by the use of air-dielectric stripline in the power divider, etc. A loss budget is shown in table 2. It is obvious that the full 14 × 14 ft. allowable array size must be utilized in order to meet the gain specification.

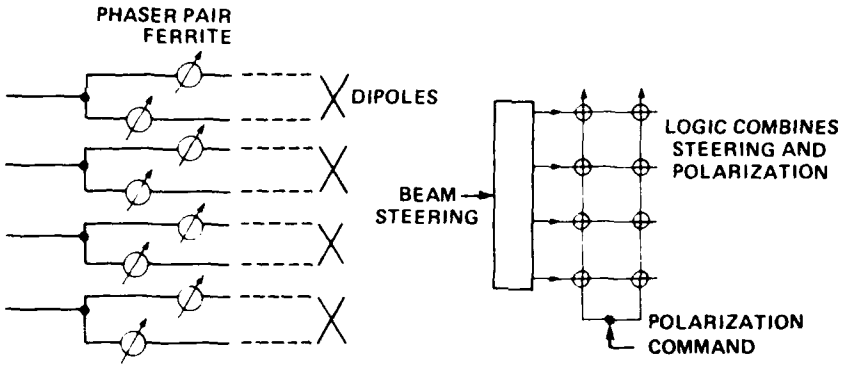

Location of Ferrite Phase Shifters for Elevation Scanning and Polarization Diversity

80-0809-V-2

Figure 3. Location of Ferrite Phase Shifters for Elevation Scanning and Polarization Diversity

Table 2. Loss Budget

Aperture Gain	44.56 dB
Azimuth Pattern Efficiency	-1.70 dB
Elevation Pattern Efficiency	- .70 dB
Steering (Horizon)	- .03 dB
Ideal Gain	42.13 dB
Losses	
Radome	- .10 dB
VSWR	- .11 dB
Errors	- .12 dB
Azimuth Divider	
Cables	-. 17 dB
Air Dielectric Stripline	- .46 dB
Polarizer and Ferrite Phase Shifter	- .60 dB
72:1 Divider - Waveguide	- .55 dB
Total Loss	-2.11 dB
Net Gain	40.00 dB

Design of the Row

The critical unit in the above described tactical array is the horizontal line source. As mentioned, 72 of these rows spaced 2.333 inches apart would comprise the full size 14 × 14 ft. array. Such a line source was fabricated and tested and is discussed below.

The row is shown schematically in figure 4. Sixty-four crossed dipoles are spaced 2.625 inches apart along the 14-ft. length. The upper and lower power dividers feed identical distributions to the two orthogonal polarization components of the crossed dipoles.

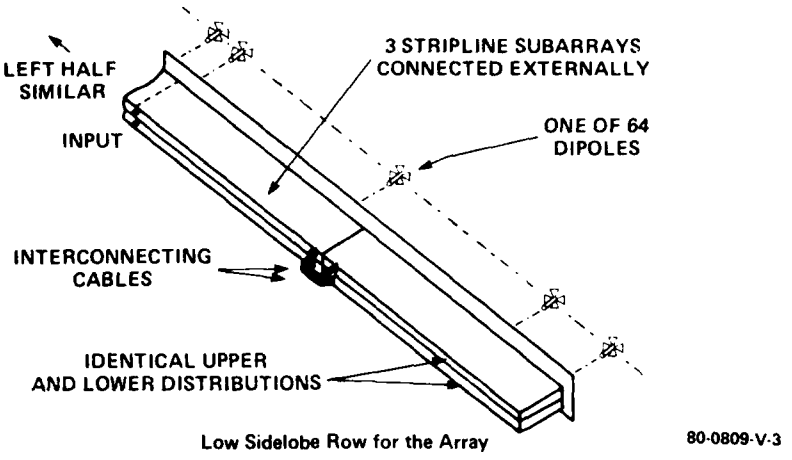

Figure 4. Low Sidelobe Row for the Array of Figure 1

The row sidelobe requirements are not as stringent as those of the full size array because of the randomization of errors from row to row that occurs when 72 rows are used in the array. This is not to minimize the importance of achieving a low sidelobe row, however, and to do this requires that precisely located radiators be driven with precisely the correct power and phase for that frequency. This requires, first, that we know what the correct phase and amplitude values are in the presence of mutual coupling and that the coupling can be accounted for in the divider; second, that coupling be reasonably constant with frequency and elevation scan; and third, that the power divider be frequency insensitive and that it be fabricated using precise, repeatable techniques.

Mutual coupling between radiators has two effects; it influences the radiator impedance, and it influences the current distribution across the array. The former affects all radiators, while the latter affects only those elements near the edge of the array. Both effects are a function of frequency, elevation scan angle, and polarization. The synthesis of the theoretical azimuth distribution is interrelated with the error calculations since varying errors are allowed at different azimuth angles. Error sidelobes are largest near the main beam, since all errors that affect large areas are enhanced by the forward gain of the area. Certain systematic errors affect particular sectors. This is so long-range mutual coupling (which occurs when grating lobes enter real space) tends to make sidelobe levels rise at certain azimuth angles as a result of scanning in elevation. In an infinite array, azimuth is independent of elevation except for an impedance change that is constant along the row. For a finite tapered array, the effect is very small except at the array corners or except when long-range coupling exists. For mutual coupling between close neighbors, the amplitudes are relatively constant except at the edge. Thus, by symmetry the coupling from the row above tends to vary oppositeiy from the row below. At large distances (long range mutual coupling), however, the magnitudes can be different and not cancel, with the result that the current distribution and pattern are altered. Figure 5, for example, shows the computed sidelobe degradation for a 0.75λ element spacing at 10 deg elevation steering in a waveguide array. Fortunately, minor alterations to the distributions can eliminate the energy at these angles, as long as the element spacing has been chosen to keep them well away from the main beam. Figure 6 shows the modifications made o the row's theoretical azimuth distribution.

The choice of azimuth distribution, then, is a compromise. For this application, 15 dB higher errors were allowed near the main beam than at wide angles. Even higher allowances would be useful, but the loss in efficiency and resolution that would occur with ultra-low first sidelobes cannot be tolerated.

The modifications to the azimuth distribution assume a corporate-fed power divider of isolated couplers and also assume suppression of spurious radiator modes (discussed later). Because the differences in calculated mutual coupling were not large for vertical and horizontal polarizations, a compromise distribution was used so that identical power dividers could be fabricated to feed the two polarizations. Using this compromise distribution, pattern deterioration due to scan and frequency change was determined for both polarizations. It was found that sidelobes rose most rapidly at low frequencies and did so equally for positive and negative scan angles. Consequently, the distribution was optimized at 3249.5 MHz and at + 7 deg elevation scan angle.

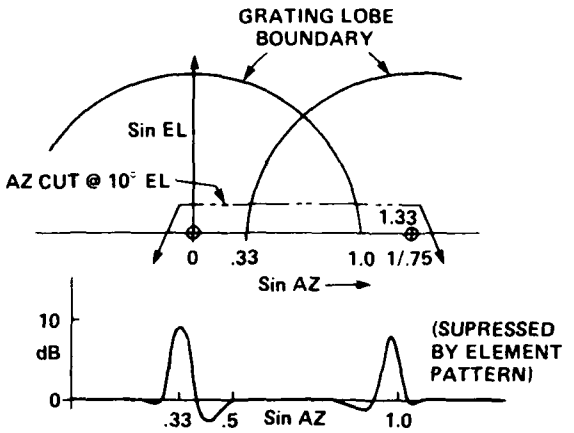

Sidelobe Enhancement at Grating Lobe Boundaries Computed for -50dB Basic Level
(.75λ Spacing in Width, .7λ Spacing in Height, 10 degrees Elevation Steering, Waveguide Array)

80-0809-V-4

Figure 5. Sidelobe Degradation at Grating Lobe Boundaries Computed for −50 dB Basic Level

- o Designed at +7°
- o Vertical polarization
- o Use of isolated couplers & suppression of dipole post mode assumed

With Mutual Coupling / Without Mutual Coupling

-6.82 / 26.03

ELEM	AMPLITUDE	PHASE	POWER	DB		ELEM	AMPLITUDE	PHASE	POWER	DB
1	.058544	1.10	.003427	-24.65	28.22	33	1.201521	-6.82	1.443654	1.59
2	.033331	-11.25	.001111	-29.54	25.49	34	1.194796	-6.82	1.427537	1.55
3	.055008	-9.00	.003026	-25.19	23.05	35	1.181433	-6.82	1.395784	1.45
4	.071191	-5.99	.005068	-22.95	20.84	36	1.161664	-6.81	1.349464	1.30
5	.089872	-6.83	.008077	-20.93		37	1.135754	-6.82	1.289936	1.11
6	.114431	-7.35	.013094	-18.83		38	1.104011	-6.83	1.218840	.86
7	.142106	-6.92	.020194	-16.95		39	1.066955	-6.82	1.138394	.56
8	.172049	-6.79	.029601	-15.29		40	1.025155	-6.82	1.050942	.22
9	.206128	-6.98	.042489	-13.72		41	.979052	-6.83	.958542	-.18
10	.244402	-6.96	.059732	-12.24		42	.929263	-6.83	.863529	-.64
11	.285570	-6.85	.081550	-10.89		43	.876620	-6.82	.768463	-1.14
12	.329808	-6.87	.108773	-9.63		44	.821720	-6.84	.675223	-1.71
13	.377645	-6.91	.142616	-8.46		45	.765053	-6.85	.585305	-2.33
14	.428298	-6.87	.183440	-7.37		46	.707491	-6.84	.500543	-3.01
15	.481010	-6.84	.231371	-6.36		47	.649855	-6.84	.422312	-3.74
16	.535855	-6.87	.287140	-5.42		48	.592464	-6.86	.351013	-4.55
17	.592464	-6.86	.351013	-4.55		49	.535855	-6.87	.287140	-5.42
18	.649855	-6.84	.422312	-3.74		50	.481010	-6.84	.231371	-6.36
19	.707491	-6.84	.500543	-3.01		51	.428298	-6.87	.183440	-7.37
20	.765053	-6.85	.585305	-2.33		52	.377645	-6.91	.142616	-8.46
21	.821720	-6.84	.675223	-1.71		53	.329808	-6.87	.108773	-9.63
22	.876620	-6.82	.768463	-1.14		54	.285570	-6.85	.081550	-10.89
23	.929263	-6.83	.863529	-.64		55	.244402	-6.96	.059732	-12.24
24	.979052	-6.83	.958542	-.18		56	.206128	-6.98	.042489	-13.72
25	1.025155	-6.82	1.050942	.22		57	.172049	-6.79	.029601	-15.29
26	1.066955	-6.82	1.138394	.56		58	.142106	-6.92	.020194	-16.95
27	1.104011	-6.83	1.218840	.86		59	.114431	-7.35	.013094	-18.83
28	1.135754	-6.82	1.289936	1.11		60	.089872	-6.83	.008077	-20.93
29	1.161664	-6.81	1.349464	1.30		61	.071191	-5.99	.005068	-22.95
30	1.181433	-6.82	1.395784	1.45	1.55	62	.055008	-9.00	.003026	-25.19
31	1.194796	-6.82	1.427537	1.55	1.59	63	.033331	-11.25	.001111	-29.54
32	1.201521	-6.82	1.443654	1.59		64	.058544	1.10	.003427	-24.65

-6.82

EFF= 1.6870 DB.

EFF= .0000 DB.

Figure 6. Mutual Coupling Analysis - Vertical Polarization

Corporate power dividers, where line lengths to all radiators are kept within 0.5λ of each other, are necessary for the specified bandwidth. The tolerances necessary for achieving low sidelobes require the divider to be precise and repeatably manufacturable. Further, the 40 dBi gain spec requires that the divider be low loss. Air dielectric stripline meets these requirements. The absence of a dielectric-filled stripline lowers RF loss and eliminates a source of phase error. The fact that the circuitry is stamped on numerically-controlled machinery to ±0.005-in. tolerances makes it cheap to fabricate, precise, and repeatable. For applications where even tighter tolerances are called for or where high-power capability is needed (160 kW peak or more), a computer-controlled milled circuit is used.

A further consideration was the type of coupler to be used in the power divider. Impedance dividers (with no isolation) work well when looking into perfectly matched loads, and they work in slotted waveguides if the slot impedance is known precisely. However, they are extremely sensitive to load impedance. A 1.1:1 VSWR changes output power ±0.4 dB, more than the total allowable amplitude error. The fact that the dipole radiator impedance varies with frequency and scan compounds the problem. Clearly, an isolated coupler must be used. Frequency dispersion is another consideration. Coupling ratio and phase must remain constant across the band in order to achieve low sidelobe performance. Several coupler types that exhibit flat amplitude response exhibit quadrature or other non-zero phase differences at their outputs which would have to be compensated for. The Wilkinson-type "split-T" coupler is therefore a logical choice, since its outputs are isolated from each other and are always in phase.

The circuit layout for the low sidelobe row is shown schematically in figure 7. The 64-element row is symmetric about its center; figure 7 shows half of the complete row. This particular layout has allowed all coupling values to fall within the range of 3 dB to 5 dB.

A fabricated divider package is shown in figure 8 without dipoles or top ground plane attached. The 14-ft. row is fabricated in three subarrays; figure 8 shows one of the outer packages of 16 elements. The center package is 7-ft. long and contains 32 elements. Figure 9 shows a closeup of the stripline circuitry.

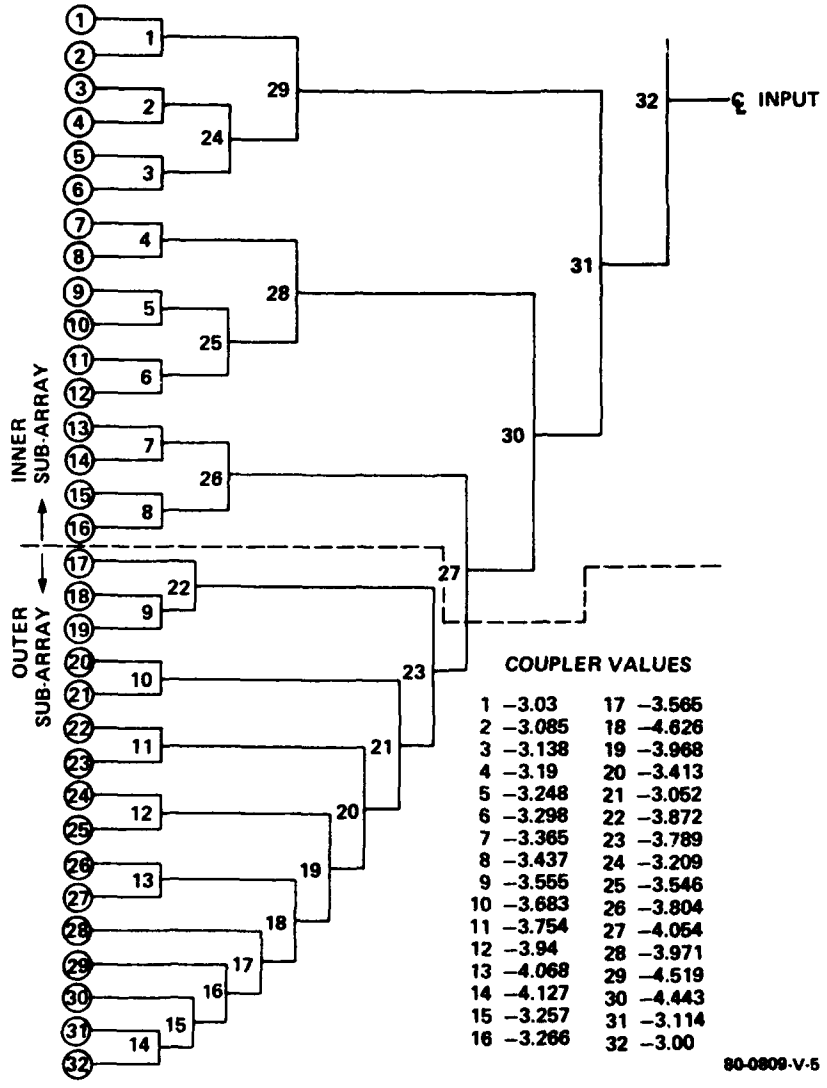

Figure 7. Power Divider Layout for the Row

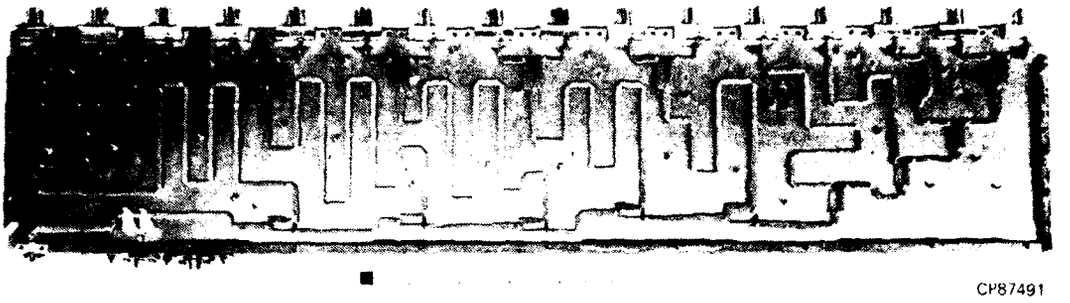

Figure 8. Air-Dielectric Stripline Power Divider - Outboard Section of 16 Elements. Underneath Is Another Identical Divider for the Orthogonal Polarization.

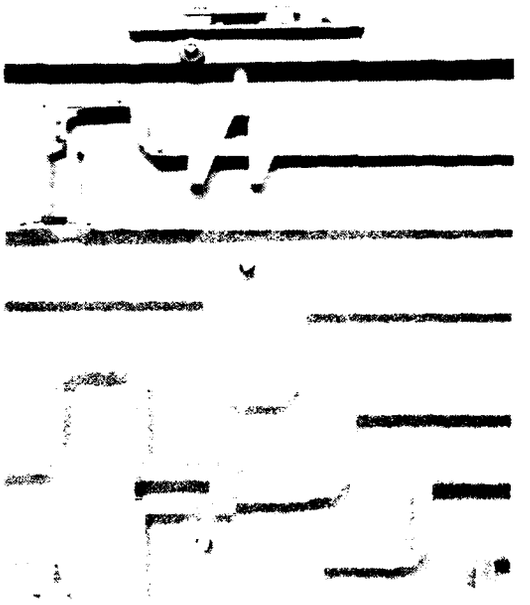

Figure 9. Close-Up of Divider Package

As mentioned, the stripline divider packages, both center conductors and ground planes, were stamped on N/C machinery. Figure 10 shows the circuitry of figure 8 as it is stamped from a 0.063-in.-thick sheet of aluminum. The frequency response of individual couplers and the accuracy to which coupling values can be predicted is demonstrated in figures 11 and 12. Figure 11 shows the response of a 3-dB coupler. Amplitude response across a 15-percent band is flat to within ± 0.025 dB, phase difference between output ports is zero across the band to within measurement accuracy, and isolation is 25 dB or greater. Figure 12 shows the response of a 4.7-dB coupler. This coupler is at the extreme end of the range of coupling values in the row divider and, thus, represents the most sensitive frequency response. Its response is, however, very well behaved.

Since the row is a mirror image about its centerline, it was necessary to breadboard only half of the 14-ft. row to substantiate that the distribution was satisfactory. Thus, a computer-aided design (CAD) program was used to lay out and dimension the circuitry, with the output being a computer tape for control of the stamping machinery. Table 3 compares the design values of the 31 couplers in the half row to the values as measured on a network analyzer. Deviation from design did not exceed 0.26 dB for any coupler in this "first-cut" breadboard. Of course, accuracy on the first iteration is not really the issue since the computer tape can easily be

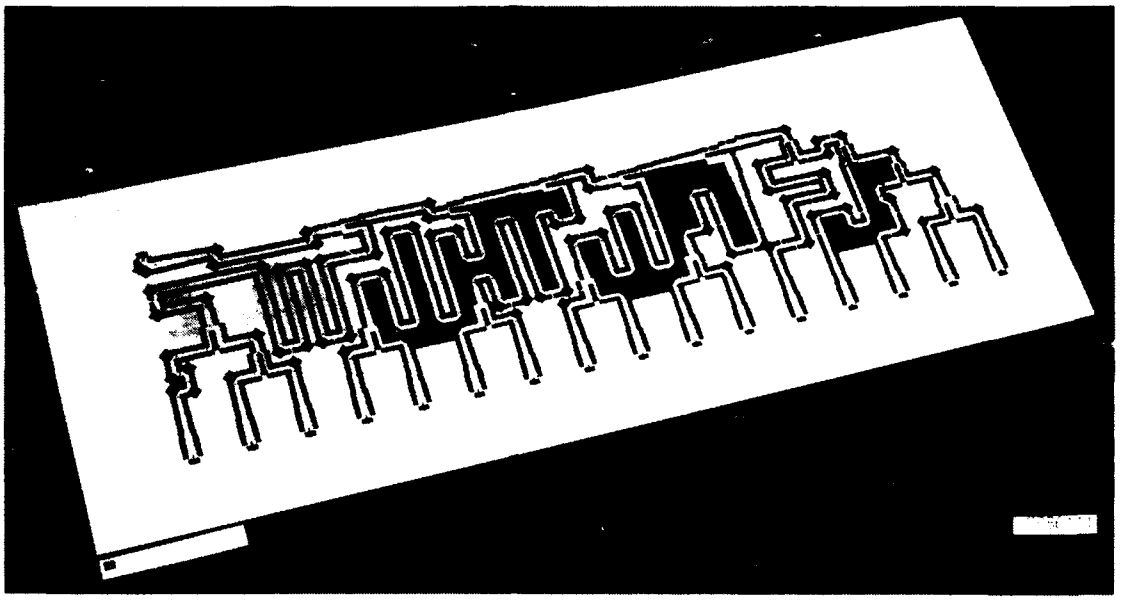

Figure 10. The Stamped Stripline Center Conductor of Figure 8 Before it Is Released From its Frame. Material Is 0.063-in. Thick Aluminum Sheet.

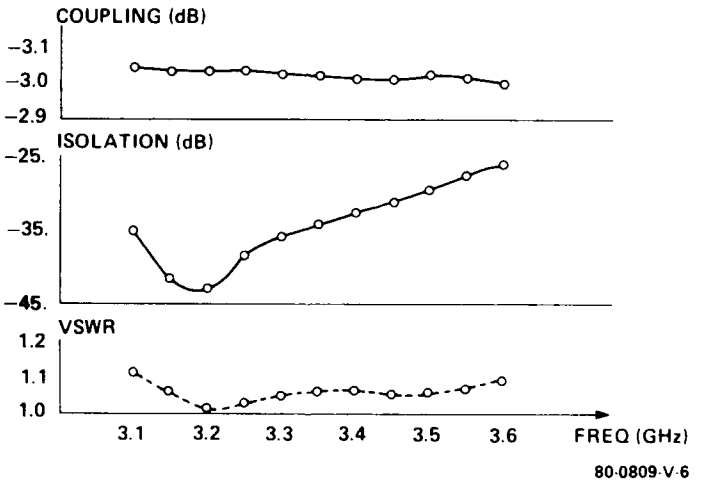

Figure 11. Response of a 3-dB Coupler

modified to account for deviations between design values and measured values. Repeatability from stamping to stamping is crucial, however, and once the final computer tape is obtained, accuracy from circuit to circuit is several times better than the accuracy of the first iteration. Figure 13 shows network analyzer data of the response measured for the divider package of figure 8. Note that even for output ports that are – 32 dB down from the input, amplitude is flat across the band to within 0.25 dB typically.

Aside from the corporate-fed power divider, the other major component in the row design is the radiating element that is capable of linear and circular polarizations. Both a crossed dipole and an annular slot radiator were investigated. Although the slot is inherently a better radiator for circular polarization since its E and H plane patterns are the same, nevertheless its bandwidth was found to be considerably less than that of the dipole. Also, figure 14 shows that over the + 13 deg, – 7.5 deg scan angles we are interested in, the difference in E and H plane patterns of the dipole is not a limit in achieving the required bandwidth.

We have found that the differences in radiator impedance can be considerable when the element is either isolated, in a one-dimensional array, or in a two-dimensional array. For this reason, the dipole is impedance matched in a fixture such as that shown in figure 15. The flared plates above and below the dipole serve as

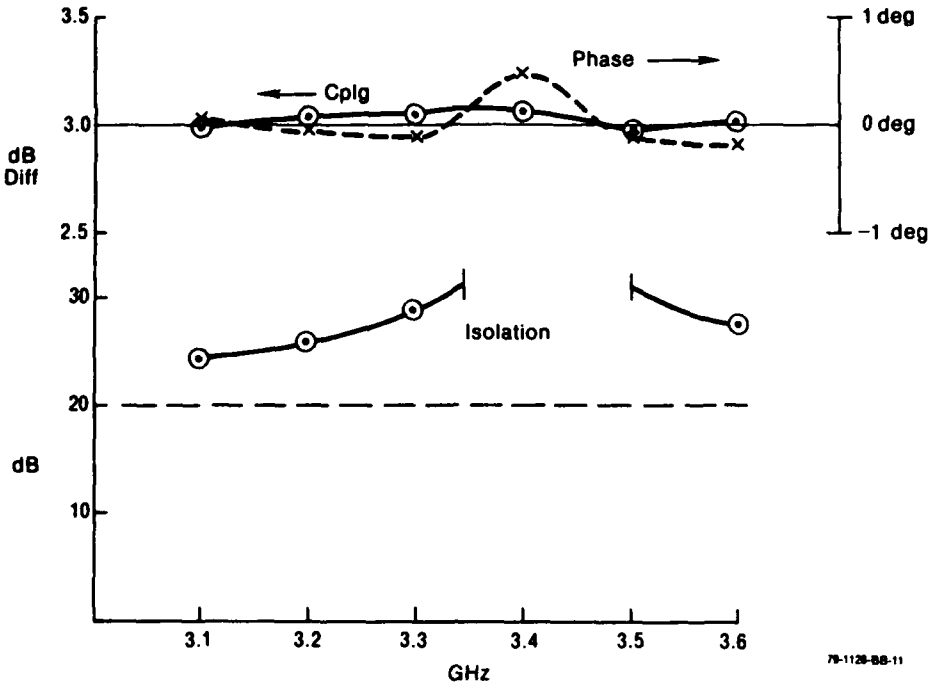

Figure 12. Response of a 4.7-dB Coupler

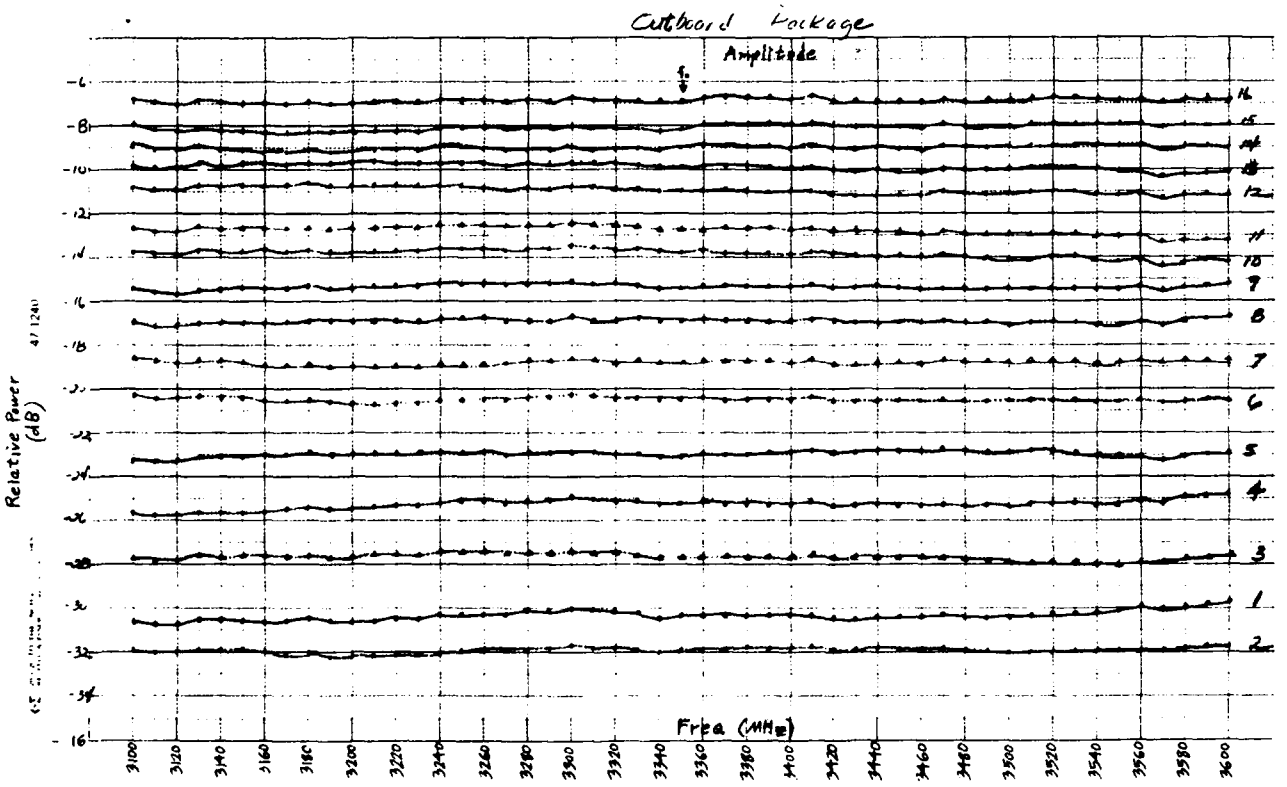

Figure 13. Network Analyzer Response of the Outboard Package of Figure 8

Table 3. Comparison of Coupler Design Values vs Actual Measured Values on First Iteration

Coupler No.	Design Value (dB)	Measured Value (dB)	Error (dB)
1	-3.08	-3.09	-.01
2	-3.14	-3.18	-.04
3	-3.19	-3.11	.08
4	-3.24	-3.20	.04
5	-3.29	-3.40	-.11
6	-3.35	-3.29	.06
7	-3.41	-3.55	-.14
8	-3.48	-3.40	.08
9	-3.60	-3.57	.03
10	-3.67	-3.67	.01
11	-3.80	-3.66	.14
12	-3.99	-3.95	.04
13	-4.09	-4.05	.04
14	-4.17	-3.93	.24
15	-3.27	-3.33	-.06
16	-3.37	-3.18	.19
17	-3.67	-3.69	.02
18	-4.62	-4.77	-.15
19	-3.98	-3.98	0
20	-3.42	-3.37	.05
21	-3.15	-3.03	.12
22	-3.95	-3.79	.16
23	-3.80	-3.73	.0
24	-3.26	-3.18	.08
25	-3.60	-3.59	.01
26	-3.86	-3.78	.08
27	-4.01	-4.27	-.26
28	-4.05	-3.88	.17
29	-4.60	-4.40	.2
30	-4.44	-4.70	-.26
31	-3.20	-3.19	.01

image plates that present an infinite 1-D array to the dipoles in the E plane. To simulate conditions in the H plane, a computer program is used in combination with measurements on a network analyzer to measure and account for the coupling between H-plane neighbors. The net result is the capability of matching the radiator in a simulated environment that approximates the environment presented to a typical radiator in the two-dimensional array.

A further consideration in design of the dipole is the possible presence of a second (spurious) mode that can affect the radiation pattern while going undetected at the feed input. Figure 16 shows the source of such currents on the vertical dipole support post. The input drives only the horizontal dipole "arms," but the

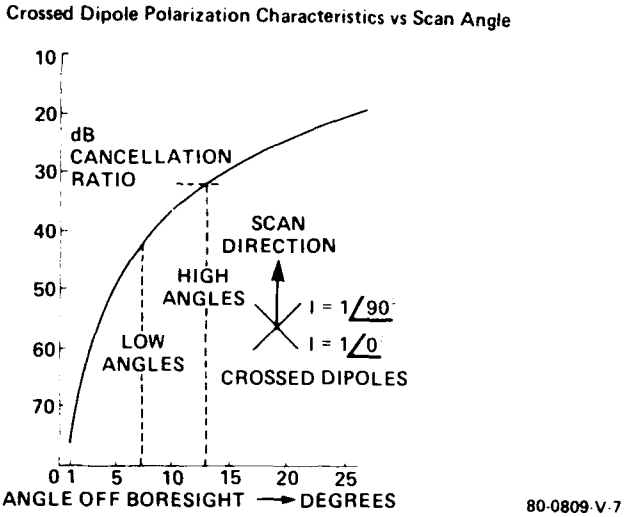

Figure 14. Crossed Dipole Polarization Characteristics vs Scan Angle

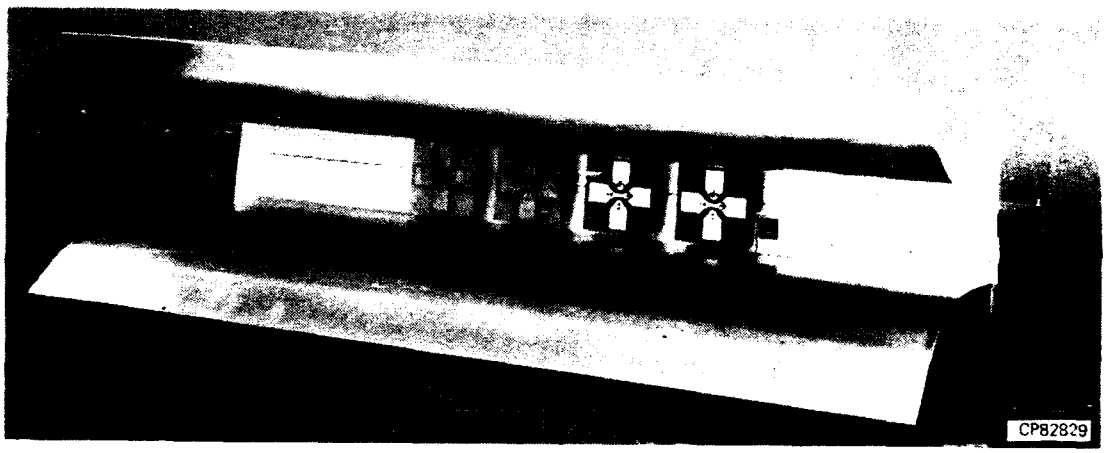

Figure 15. Fixture Used To Match the Dipole in a Simulated 2-D Environment

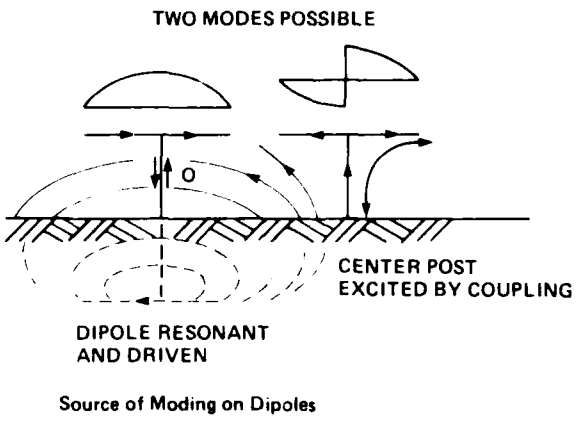

Figure 16. Source of Moding on Dipole Support Post

vertical component of the radiation from nearby dipoles induces currents in the vertical support post. These currents have been shown by anechoic chamber tests to radiate a monopole pattern. Since these induced currents are symmetric on both conductors of the dipole post, they produce a zero potential across the dipole terminals and thus are undetected there. Further, whereas normal radiation decays rapidly along the ground plane, the post constitutes a top-loaded monopole that radiates freely over the ground plane. For these reasons, the dipole is designed to suppress this mode by presenting a high-impedance, nonresonant condition to the vertical radiation that is coupled from neighboring radiators.

Figure 17 shows the row with dipoles attached and with the top plane cover removed. Figure 18 shows the components of the crossed dipole. The block with four protruding posts is machined on N/C machinery. Two of these posts are coaxial feeds for the two polarization components. The other two posts form a mechanical support and also comprise part of the balun for each polarization component. The block itself forms the transition from the stripline divider network to the coaxial dipole feed. The post and balun impedance has been optimized to suppress the spurious post mode. Other components shown are the small dielectric pellets used for impedance matching and the two printed circuit boards that form the dipole radiating "arms."

Figure 17. Row During Assembly; Opposite Side Has an Identical Stripline Network to Feed the Other Polarization

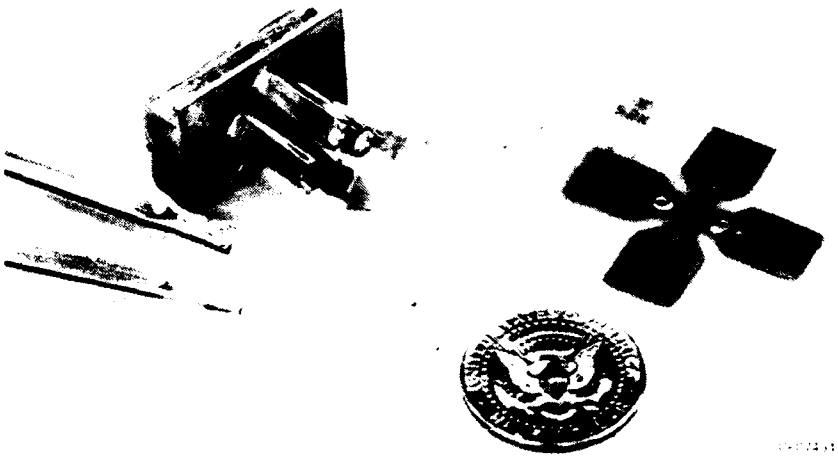

Figure 18. Components of the Crossed Dipole for Linear and Circular Polarizations

Corporate-Fed Array Error Analysis

A goal of the program was to determine the nature and magnitude of the errors involved, to allocate an error budget that delineates acceptable tolerances during fabrication, and to determine the relationship between sidelobe levels and error levels for both a single line source and for an array of N line sources.

Many error analyses in the past have assumed a random distribution of errors across the antenna. The antenna pattern consequences of errors are, in fact, strongly dependent on the nature of the error and its location. In particular, systematic errors cause large localized sidelobes, and gradual errors cause large sidelobes masked by the main beam. Corporate dividers tend to cause errors grouped into subarrays, as opposed to slotted waveguides which tend to have gradually changing errors. Three types of errors are significant:

- Errors with predetermined distributions that can be described by known equations. One such error is the phase curvature due to a finite pattern range length.
- Systematic errors. One such type is the frequency variation of couplers. Every row of a multiple row antenna has the same variation, and the errors are thereby magnified.
- Random errors. These usually result from manufacturing or material variations. They have progressively less peak effect as the number of rows (N) is increased.

Corporate-fed arrays typically have a number of "identical" rows tied together by a column divider. Considering random errors, the effect on a single row is approximately N times as significant as the same errors distributed over an array of N rows. If the error of each row is a statistical variable having an rms value of δ times the applied voltage and if we let each row have a gain G_{row} and an error gain of $G_{e_{row}}$, then the ratio of array peak gain to array error gain is:

$$\frac{G_p}{G_e} = (\eta_v N/\delta^2)\,(G_{row}/G_{e_{row}}) \tag{1}$$

where η_v is the vertical aperture efficiency (i.e., the ratio of peak gain to the gain of a uniformly illuminated array). Thus, the effect of these statistically independent errors is reduced by the "effective" number of rows $\eta_v N$.

The error δ^2 is a composite of phase (ϵ^2) and amplitude (α^2), which are normally independent, so that $\delta^2 = \alpha^2 + \epsilon^2$, where ϵ is in radians and α is a fractional voltage. To illustrate the magnitude of the errors involved, we find that either 0.1 radians or a ratio of 0.1 volts (0.9 dB) has a minor effect on gain independent of the error distribution:

$$G_p = 10 \log (1 - \delta^2) = -0.05 \text{ dB}$$

whereas the level of error sidelobes depends entirely on the number of independent samples or the size of the correlated region. For the above cited errors, the sidelobe contribution $G_e/G_p = -10 \log (N_{eff}/\delta^2)$ varies from

-37 dB for $N_{eff} = 50$ (systematic row to row) to

-54 dB for $N_{eff} = 2500$ (random).

Equation (1) gives the magnitude of the error sidelobe envelope. The shape of the envelope can also be determined. Given a Gaussian distribution of the error magnitudes with standard deviation δ, the loss in gain is fixed, and with it, the total power in the sidelobes. The angular distribution of the sidelobes depends, of course, on the spatial distribution of the errors. For the known errors such as curvature, the distribution is exactly calculable. For the others we can relate the spatial and angular distributions in a statistical fashion. If the single radiator is the smallest correlated region, the error pattern in one plane is:

$$F_e(\theta) = F_d(\theta) \sum_{n=1}^{N} \alpha V_n e^{j2\pi(\epsilon + X_n \sin\theta)/\lambda}$$

where $F_d(\theta)$ is the dipole (or other radiator) pattern in the array and V_n is the ideal distribution at dipole n.

If the errors are correlated over a certain repeated region, the summation can be reordered to first add over the region:

$$F_e(\theta) = F_d(\theta) \sum_{N\ regions} \alpha e^{j2\pi \epsilon \lambda} \sum V_n e^{j2\pi X_n \sin \theta / \lambda}$$

To the extent that the regions are identical (such as a row or subarray) they can be factored into a region pattern $F_r(\theta)$:

$$F_e(\theta) = F_d(\theta) F_r(\theta) \sum_{N\ regions} \alpha V_n e^{j2\pi \epsilon \lambda}$$

This means that the various sources of error contribute a random error pattern multiplied by a region pattern. The location errors of the physical subarrays making up the array are treated this way, using $F_r(\theta) = W(\sin x)/x$ as the region pattern.

The corporate divider tends to have a particular distribution of regions as illustrated in figure 19. For NE = 64 radiators, it is typical to have $\log_2(64) = 6$ levels of couplers with the higher levels being progressively more important over a smaller angular region. The first level of coupler errors causes individual radiator errors with an envelope of the radiator pattern. The next four levels affect groups of 2, 4, 8, and 16 radiators. We can approximate these as a stepped group of uniformly illuminated regions. The last coupler (the input coupler) is special in that it feeds two halves, and we are only interested in a symmetry. Errors common to the halves have no effect on pattern shape, so there is only one error distribution of interest. For low sidelobe distributions, this pattern has been calculated to be approximately:

$$V_6 = (1 - \cos y)/y + y(1 + \cos y)/(y^2 + \pi^2)$$

where $y = (\pi W/\lambda) \sin \theta$

Thus, the total error power pattern, including the radiator pattern, is of the form:

$$\text{Error power} = P_{in}\left[X^{-2} \sum_{m=1}^{5} \frac{(\delta m^2 \sin mx)^2}{m} + kV_6^2\right] \tag{2}$$

where $x = y/NE$

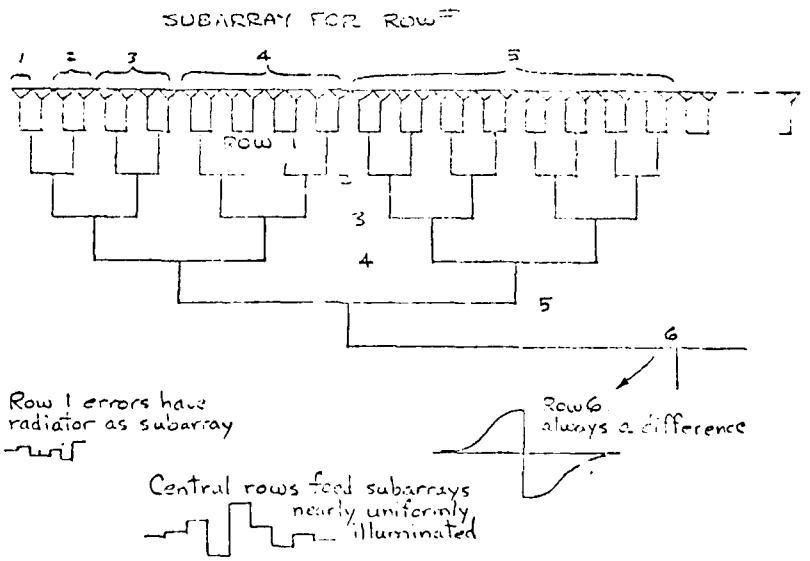

Figure 19. Errors in 1:64 Corporate Divider

If the errors are randomly distributed in space, the error sidelobes far off boresight are a vector sum of randomly phased voltages and, therefore, follow a Rayleigh distribution, even if the errors were not normally distributed to start with. The magnitude of the sidelobe voltage level V_s has a probability density:

$$p(V_s) = \frac{V_s}{\sigma^2} e^{-V_s^2/\sigma^2}$$

where σ^2 is equal to the error power level spread over 4π steradians:

$$\sigma^2 = \sigma^2/4\pi$$

Taking into account their correlation, the sidelobe rms level relative to the pattern peak has a statistical characteristic as in equation (2) or, more generally for any particular region, it varies with the dipole and region envelopes as:

$$\sigma^2 = F_d^2(\theta)F_r^2(\theta)\frac{\alpha^2 + \epsilon^2}{4\pi \quad \eta N} \tag{3}$$

Ordinarily, this error is added to existing theoretical sidelobes of level V_o. When a random vector is added to such a known vector, the distribution of the sum has been shown* to have a probability density of:

$$p(V_s) = \frac{2V_s}{\sigma^2}\left[e^{-\frac{(V_s^2 + V_o^2)}{\sigma^2}}\right]\left[I_o\left(\frac{V_s V_o}{\sigma^2}\right)\right] \tag{4}$$

where I_o is the Bessel function with imaginary argument.

This equation gives the probability that the sidelobe level will be between V_s and $V_s + dV_s$. Integrating this from O to V would give the more useful total probability that sidelobes will be below V. Unfortunately, the solution is very difficult. For error $\sigma^2 = 20$ dB below V_o^2 and V_s^2, we have the term:

$$e^{-\frac{(V_s^2 + V_o^2)}{\sigma^2}} = e^{-200}$$

while $I_o\left(\frac{V_s V_o}{\sigma^2}\right) = \sum_{m=0}^{\infty} \frac{100^{m/2}}{m!}$ is enormous and requires several hundred terms to converge. Fortunately, numerical solutions exist for the related problem of detecting signals in noise**. We can use these to obtain approximate formulas for the levels, say V_5 and V_9, which will not be exceeded 50 and 90 percent of the time, respectively. If S^2 is the ratio of theoretical to error power, then:

$$V_5 = (1.2 + 1.6356S - 1.0073\sqrt{s})V_{err}$$

$$V_9 = (2.1 + 0.75S + 0.12S^2)V_{err}$$

which are accurate enough until $S^2 = 50$, beyond which the theoretical and total voltages are nearly identical.

The above statistical analyses was used to compute predicted radiation patterns for the line source and for the full size array (N = 72). Table 4 shows the error budget for various design, fabrication, and test phases encountered during the manufacturing process. This error budget represents errors and tolerances that are

*ITT Handbook, "Reference Data for Radio Engineers", Stratford Press, Inc., New York, N.Y.; p. 992.

**D.K. Barton, "Radar System Analysis", Prentice Hall, Inc., Englewood Cliffs, New Jersey; pp. 13-16.

Table 4. Error Summary

ERROR SOURCE	MAGNITUDE	SIDELOBE LEVEL (dB)	REMARKS
Radome	– –	–64.0	Element Envelope
Array Flatness	0.005"	– –	–50 dB beyond real space
Array Contour	0.035"	–50.0 –70.0	@ first sidelobe @ fourth sidelobe
Dipole Misalignment	1.0°	–70.3	Near 90°
Mutual Coupling	1.0°/0.1 dB	–70.5	Row Gain *
Divider			
Design Error	1.0°/0.1 dB	–62	Row Gain
Center Conductor Manufacture	0.15 dB 2.25°	–64.4	Element Envelope
Center Conductor Support Post	0.25°	–63.2	Element Envelope
Multiple Reflections	0.50°	–76.3	Element Envelope
Main Divider Manufacture	0.15 dB	– –	Subarray Envelope –55.3 dB Adjusted Out
	2.00°	– –	Subarray Envelope –55.3 dB Adjusted Out
Multiple Relfections	0.50°	–67.1	Subarray Envelope
Network Analyzer Residual Error	0.5 dB/0.5°	–62.9	Subarray Envelope
Network Analyzer Residual Error	0.5 dB/0.5°	–71.9	Element Envelope
Temperature	1.4°	– –	Beam Shape

*Those with the row gain are concentrated in the azimuth principal plane.

80-0809-T-9

physically achievable, and the calculated patterns shown in figure 20 show that this error budget ensures that the array sidelobe levels will be within the specified levels of table 1. The patterns shown here are calculated for a 90-percent probability that the indicated sidelobe level will not be exceeded. Figure 21 shows the calculated pattern for a single line source under the same conditions as figure 20. In a later section, these calculated patterns are compared to measured patterns of a line source.

Test Procedure for the Line Source

Fabrication and test of a single row is an economical way to demonstrate the critical unit in the full size array. A test of this nature does, however, have serious impact on the quality of the radiation pattern. Part of the degradation is due to the statistical averaging of errors over fewer samples. A significant part of the degradation is due to the pattern range limitations imposed by the broad fan beam of the line source. This problem is demonstrated by figure 22 which shows the measured patterns of a single waveguide stick and a full array under the same test conditions.

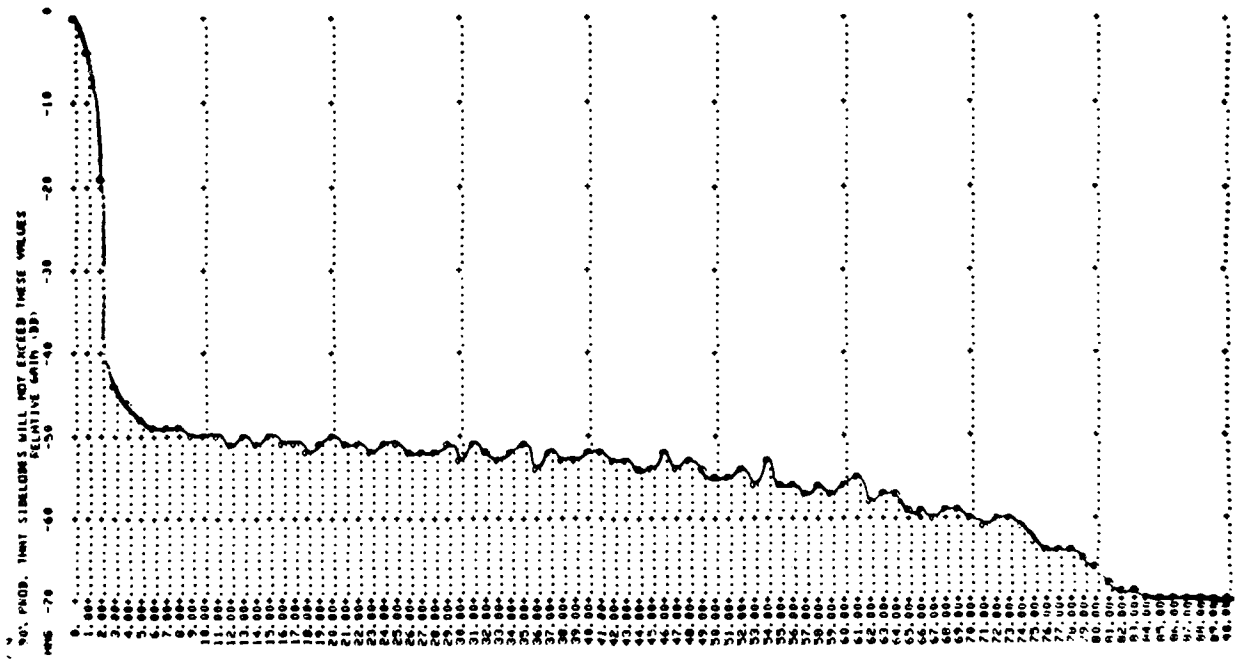

Azimuth Angle (Degrees)

Figure 20. Full Size Array (N = 72); Probability = 90%

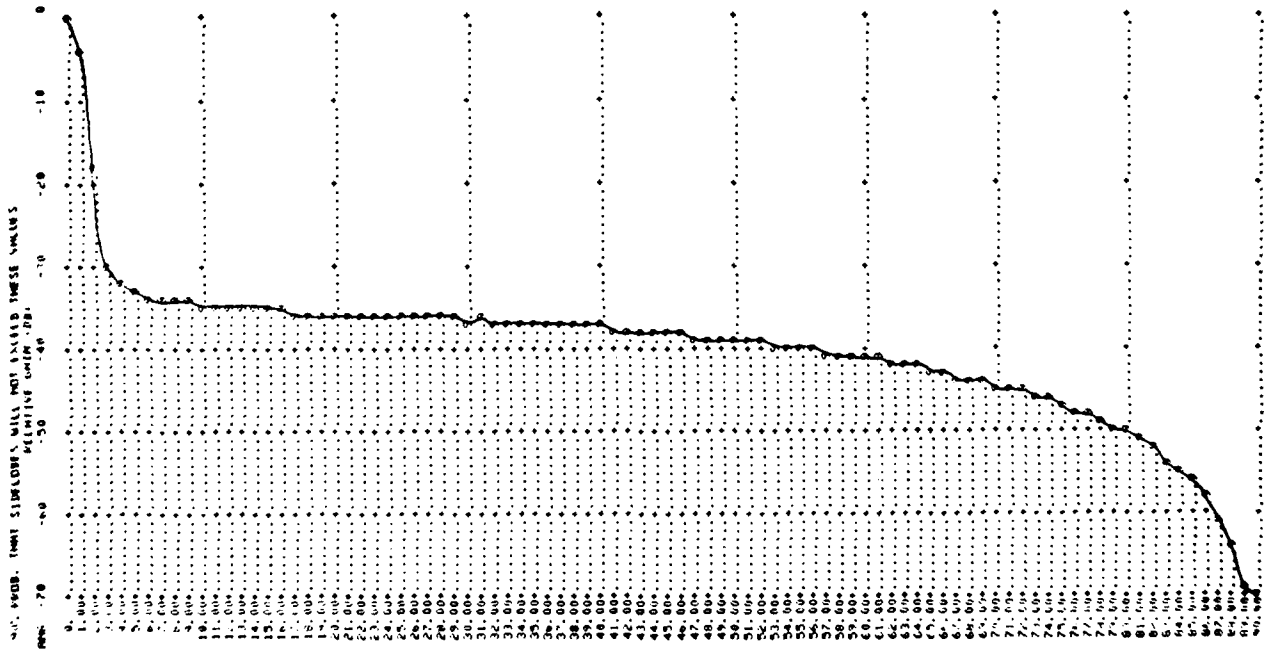

Azimuth Angle (Degrees)

Figure 21. A Single Row (N = 1); Probability = 90%

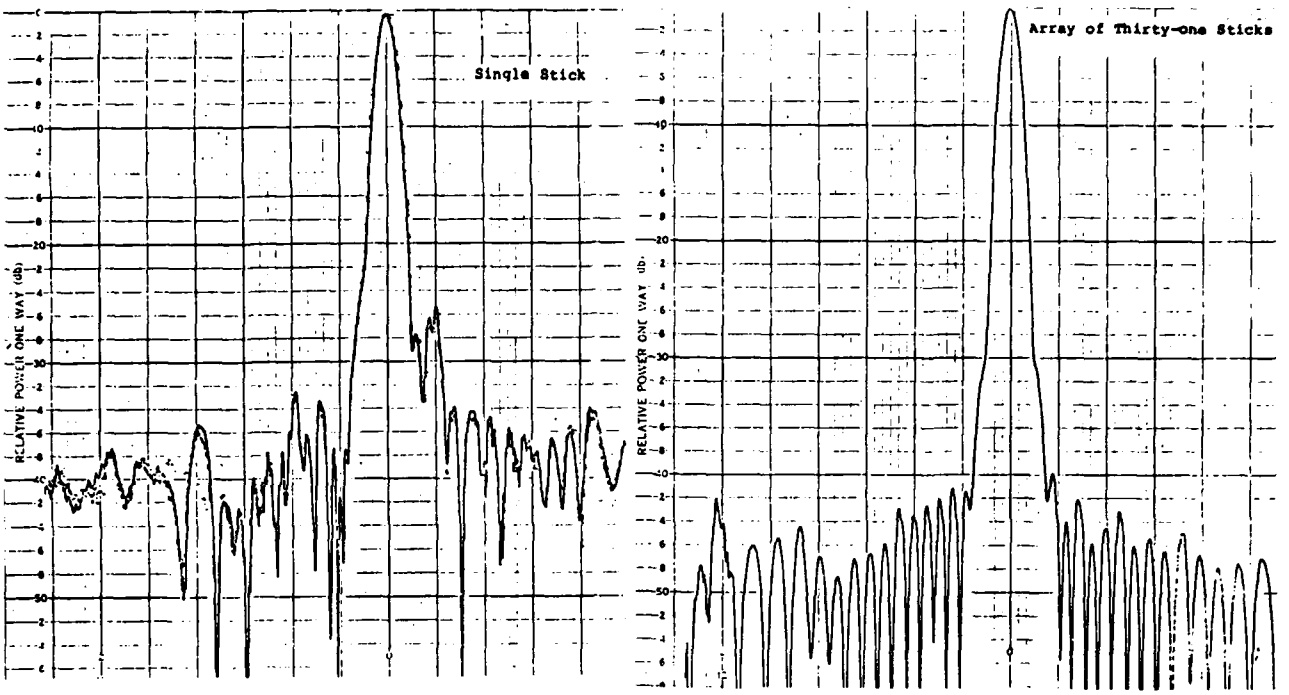

Figure 22. Single Stick Waveguide Pattern vs Full Array Pattern Under the Same Conditions

If a reflector is added to the line source, the statistical averaging of errors is not enhanced, but at least the directivity of the pattern has been increased such that some of the range pattern problems associated with a broad fan beam are lessened. This was the approach taken for testing of the line source in this program. Figures 23 through 27 show the test setup. For the linear polarization perpendicular to the long axis of the row (called "H-plane" polarization for our purposes here), a horn reflector 24 inches in length with an aperture width of 12 inches was used. For the linear polarization parallel to the long axis of the row ("E-plane polarization"), a much broader horn was used to avoid being in cut-off. For circular polarization, no horn was used so that the two linear components would have similar gains. Also, in order to further minimize the effects of a broad beamwidth, the patterns were taken with the row held vertically on the mount, and "half-patterns" were recorded by rotating the antenna skyward.

Figures 25 and 27 show the patterns formed by these horns. The 15.5 deg and 55 deg beamwidths that were obtained in the H-plane horn and E-plane horn, respectively, are a considerable improvement for test purposes over the element patterns that would have existed in that plane.

Test Results

The measured H-plane linear polarization pattern for the row at center frequency (3.35 GHz) is shown in figure 28. Again, this is the linear polarization component that is perpendicular to the long axis of the row. The pattern was taken with the row held vertically and rotated skyward as in figure 24. The calculated sidelobe levels for the single line source and for the full array that were obtained using the statistical analysis previously discussed (figures 20 and 21) are drawn in for comparison. The agreement between the measured line source pattern and the calculated pattern is fairly good. We do feel, however, that it could be improved significantly. Most of the degradation in the measured sidelobe levels of the single stick, it is felt, were due to random errors associated with assembly tolerances. The accuracy of the N/C stampings is quite acceptable; the tolerances associated with hand assembly of the row piece parts probably comprised the bulk of the tolerance build-up. For fabrication of the full array in a production situation, proper fixturing to maintain assembly tolerances would be justifiable since costs are amortized over many rows.

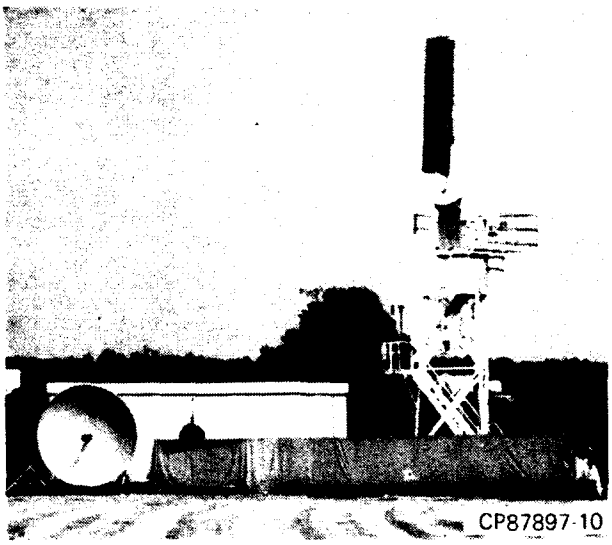

Figure 23. The Line Source During Pattern Tests on the Ground Range

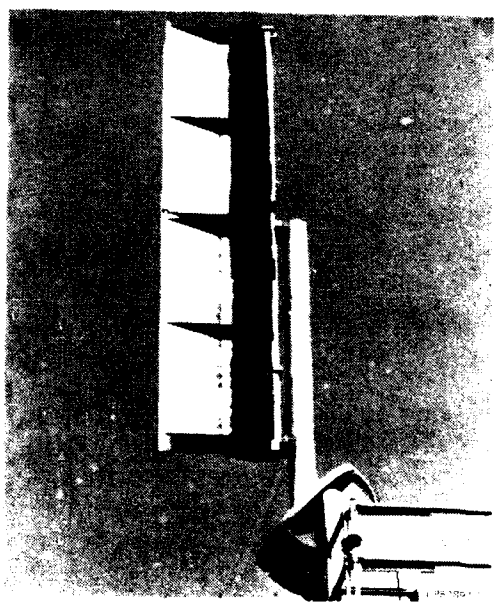

Figure 24. Horn Used to Test the H-Plane Linear Polarization

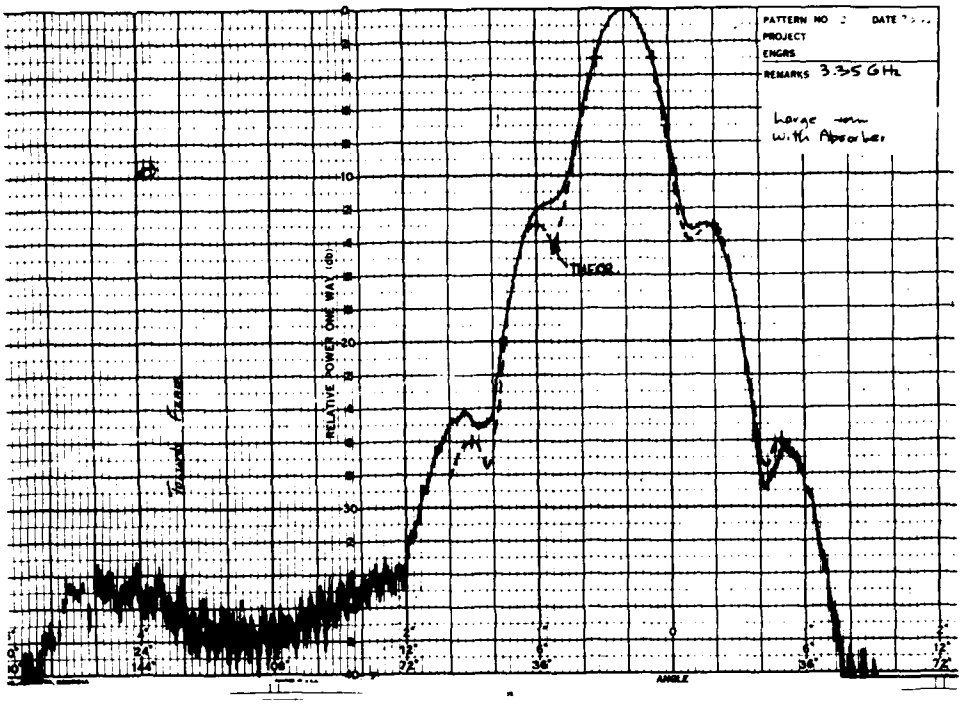

Figure 25. Pattern of the Horn in Figure 24

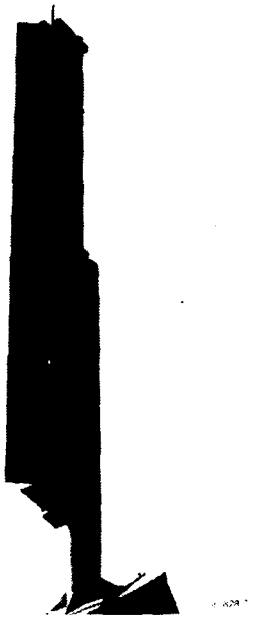

Figure 26. Broad Horn Used to Test the E-Plane Linear Polarization

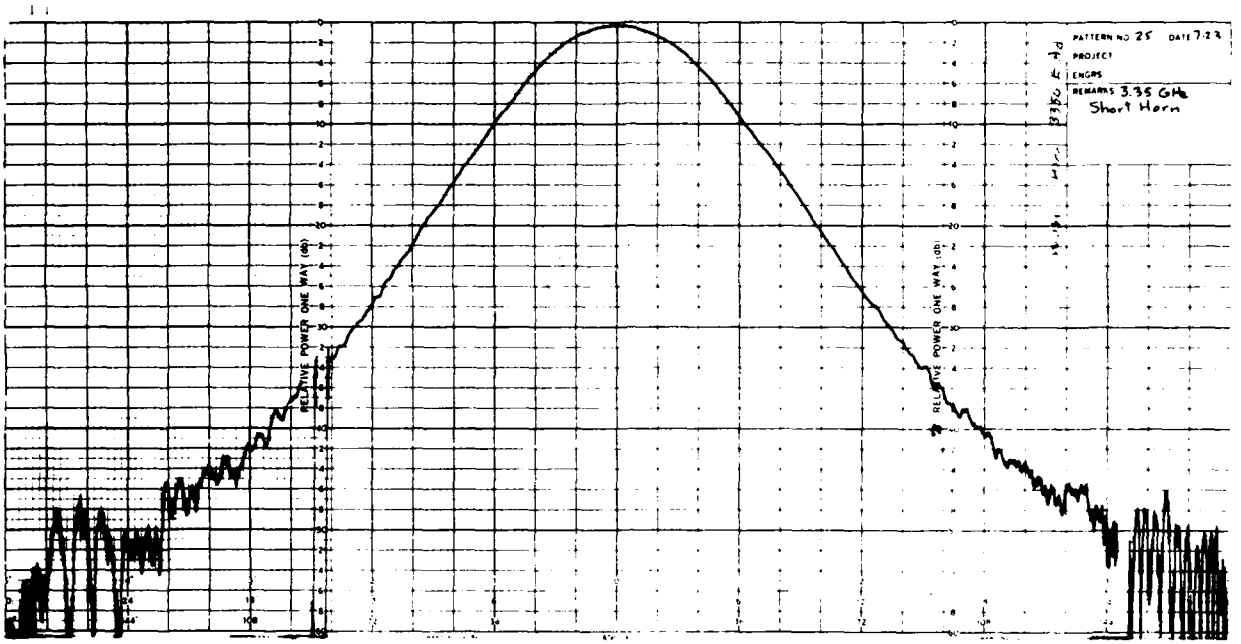

Figure 27. Pattern of the Horn in Figure 26

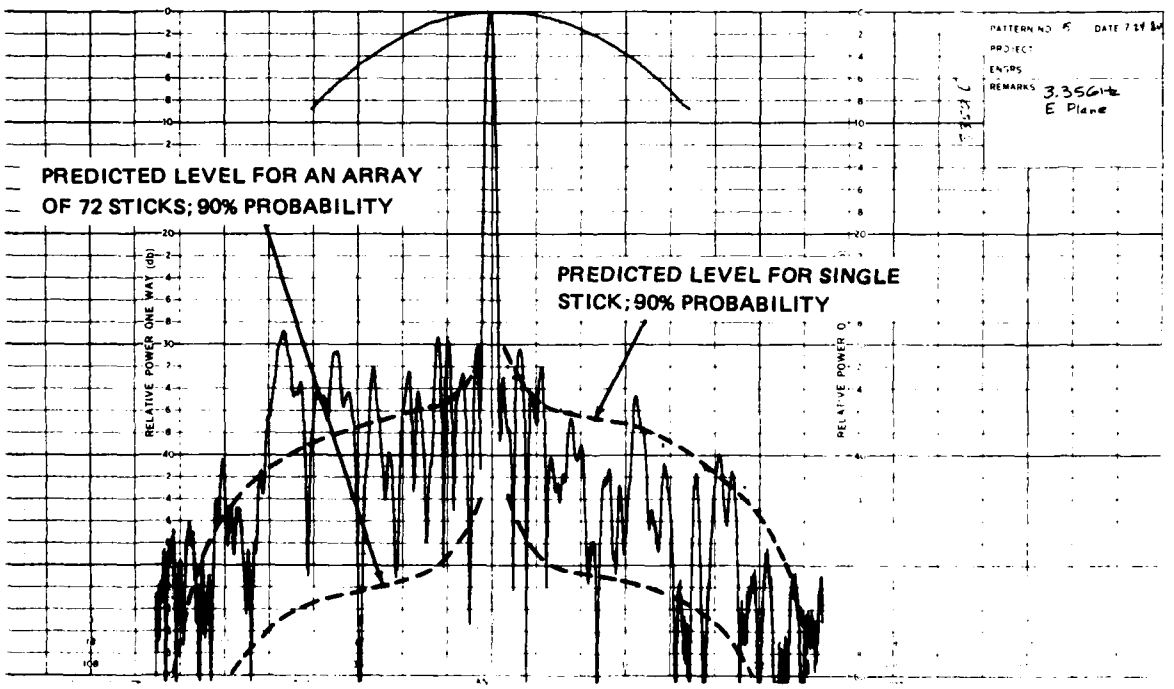

Figure 28. E-Plane Linear Polarization at 3.35 GHz for the Single Row

Figure 29 shows the H-plane linear polarization pattern at center frequency. Agreement between the theoretical and measured pattern of the single row indicates that a full size array of 72 such rows would closely approach the sidelobe specifications of table 1.

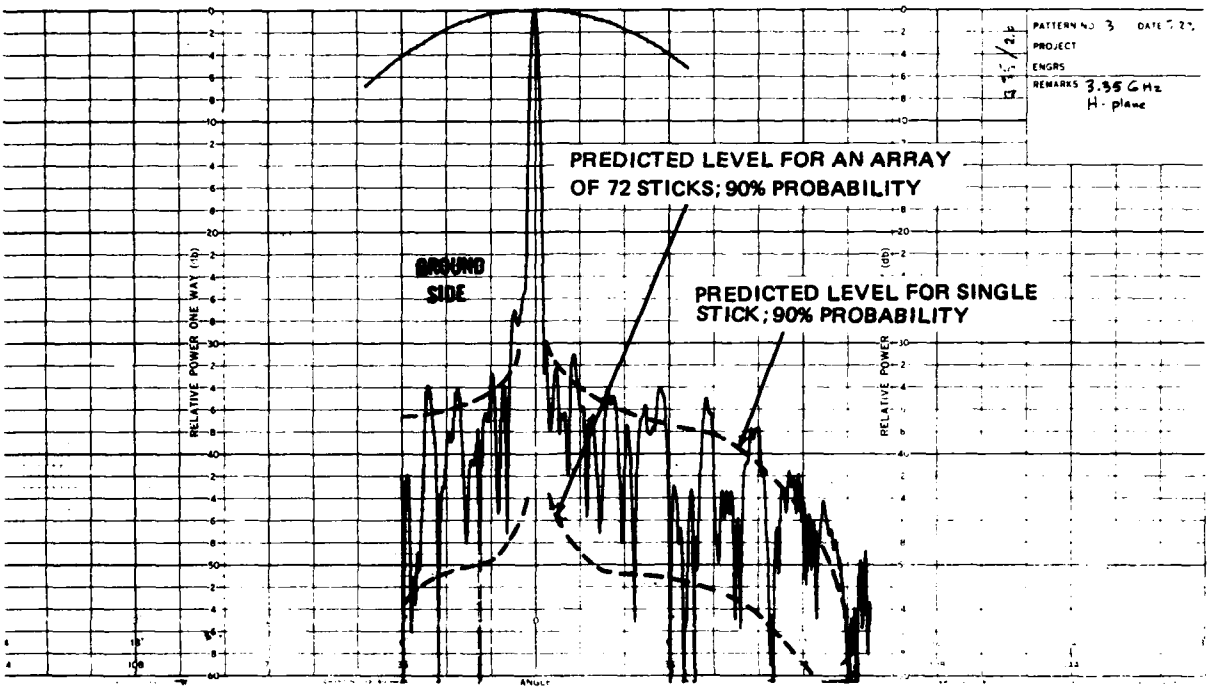

Figure 29. H-Plane Linear Polarization at 3.35 GHz for the Single Row

Figure 30 shows both polarizations across the 3.1 to 3.6 GHz band, and table 5 shows VSWR. It is interesting to note the changes occurring in the calculated patterns of the line source and the array of 72 line sources. The calculated line source sidelobe levels are somewhat worse at the band edges due to the frequency response of the power divider and dipoles. The calculated sidelobe levels of the full size array, however, are considerably more degraded at the band edges than at center frequency because the power divider errors are now correlated from row to row and very little statistical averaging takes place.

Because of limitations in time and money, several aspects of the program unfortunately remained unresolved to some degree. We were not able, for example, to completely examine the circular polarization capabilities of the line source. As discussed in the first section, polarization switching and beam steering in the full array would be accomplished using the same set of ferrite phase shifters. For the purposes of demonstrating circular polarization of the single line source, it was our intent to use simple mechanical switching. It became evident during tests that the switching set-up was introducing its own frequency variations that could not be resolved in the time frame allotted. Figure 31 shows the circular polarization pattern of the line source taken at center frequency. Certainly the potential demonstrated here needs to be pursued.

Also, although the intended frequency band of operation was 3.1 to 3.6 GHz, patterns that were taken below and above that band showed that the potential for a 50 percent bandwidth exists. Figure 32 shows representative patterns.

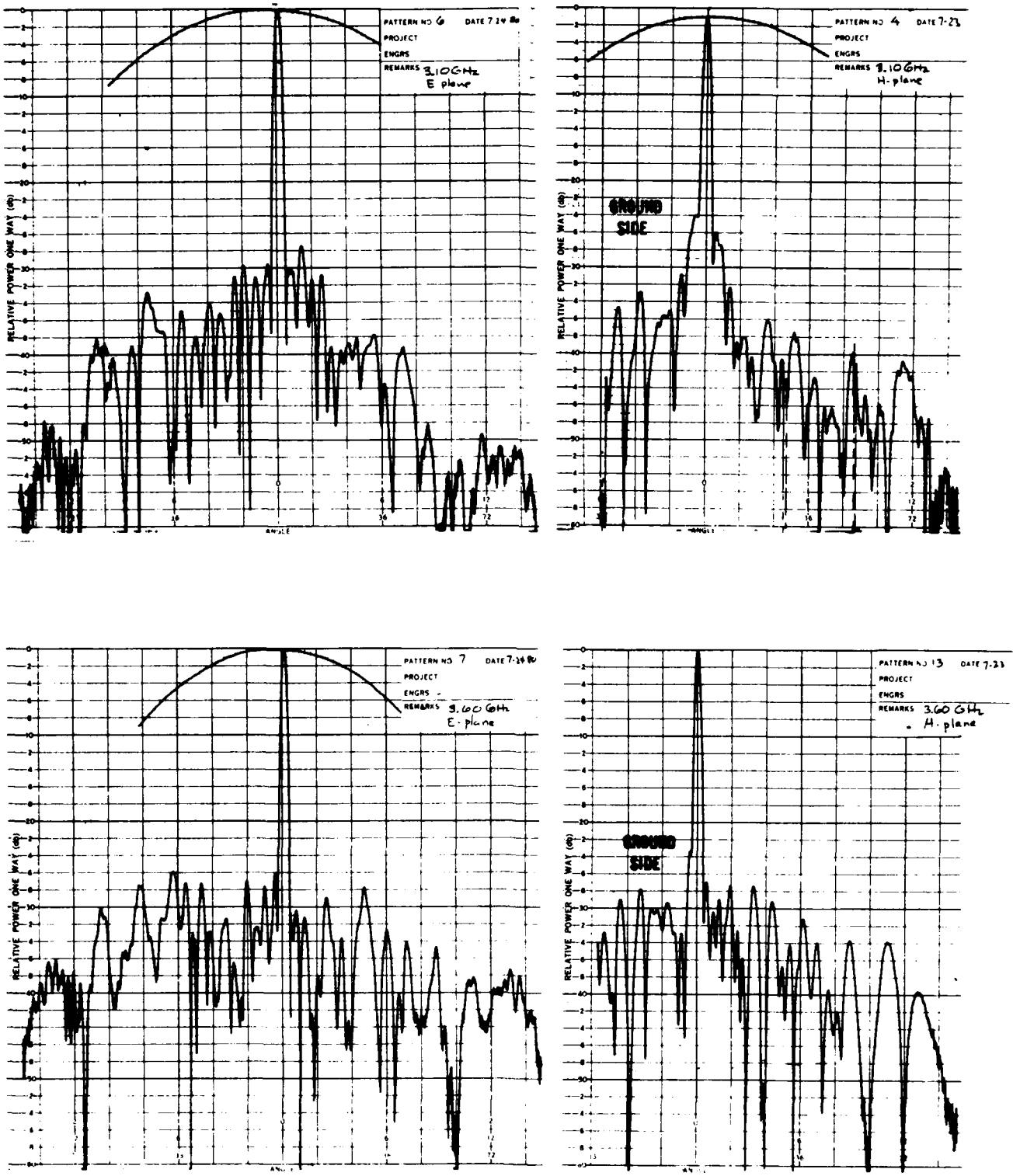

Figure 30. Single Row Patterns for Both Linear Polarizations at the Edges of the Band

Table 5. VSWR of the Line Source

Frequency (GHz)	E-Plane Polarization	H-Plane Polarization
3.1	1.6:1	1.58:1
3.2	1.38	2.40
3.3	1.32	2.15
3.4	1.20	1.67
3.5	1.15	1.54
3.6	1.40	1.28

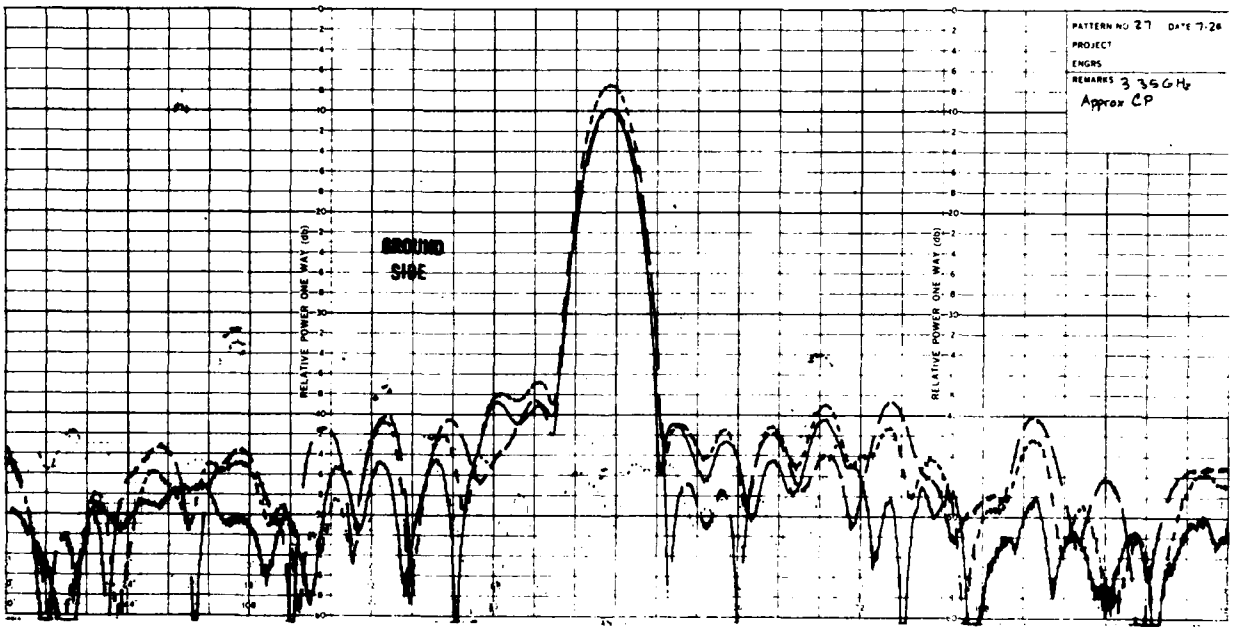

Figure 31. Circular Polarization of the Line Source at 3.35 GHz

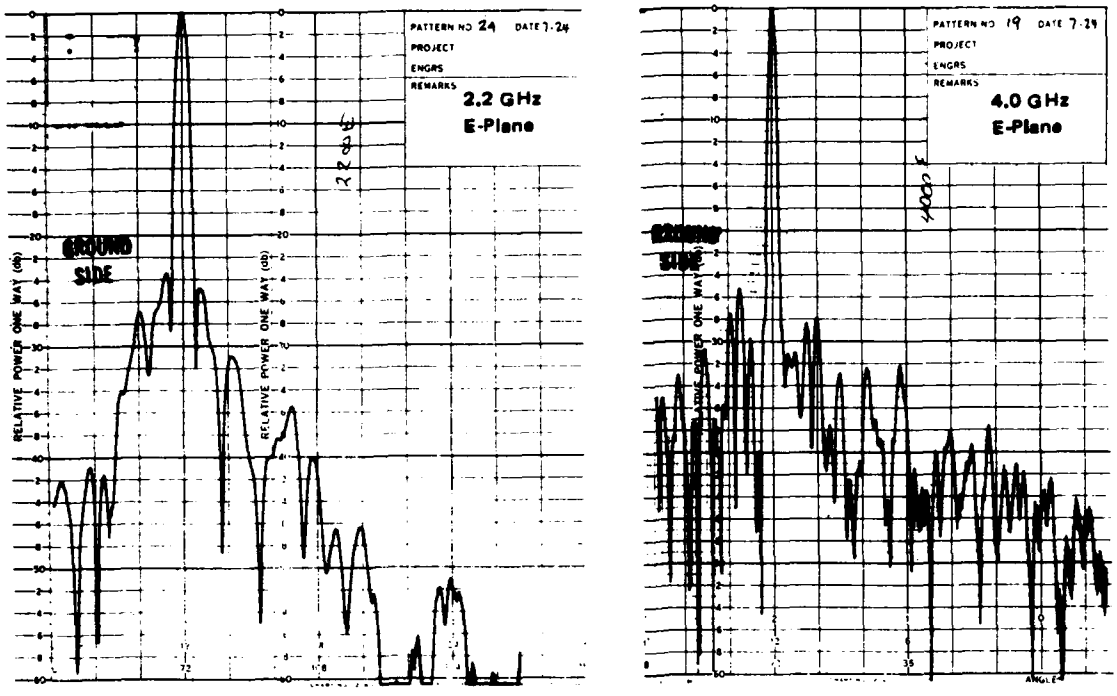

Figure 32. Patterns Taken Above and Below the Design Band Show Potential for a Much Wider Bandwidth

Summary

The design of an array for a high-performance S-band tactical radar has been described that rotates in azimuth and scans in elevation. An error analysis for such a corporate-fed array has been presented that calculates the effect of both correlated and uncorrelated errors on the sidelobe performance of a line source and of an array of N line sources. A line source of 64 elements has been built that demonstrates sidelobe performance in agreement with the above error analysis. An array of 72 such line sources would be expected to exhibit sidelobes approaching the specified -35, -38, -41, and -50 dB levels (first, second, third, and wide-angle lobes, respectively). The line source has demonstrated a usable bandwidth in excess of 500 Hz and has demonstrated both linear and circular polarizations.

DESIGN OF A BROADBAND IMPEDANCE MATCHING SECTION FOR PERIPHERALLY FED HELICAL ANTENNAS

by

Dirk E. Baker

NATIONAL INSTITUTE FOR AERONAUTICS AND

SYSTEMS TECHNOLOGY

COUNCIL FOR SCIENTIFIC AND INDUSTRIAL RESEARCH

P.O. BOX 395, PRETORIA

SOUTH AFRICA

Presented at

THE 1980 ANTENNA APPLICATIONS SYMPOSIUM

UNIVERSITY OF ILLINOIS

ALLERTON PARK

MONTICELLO, ILLINOIS

SEPTEMBER 1980

DESIGN OF A BROADBAND IMPEDANCE MATCHING SECTION FOR PERIPHERALLY FED HELICAL ANTENNAS

Dirk E. Baker

(Abstract)

For applications requiring circular polarization and moderate gain over frequency bands of up to about an octave, the helical beam antenna remains an attractive solution. Commercially available helical antennas generally specify a VSWR of 1.8 over only about a 20% bandwidth. It is sometimes necessary to have low VSWR ($\leq$1.2, say) over near octave bandwidths.

This paper describes a frequency-insensitive means of feeding the helical antenna. Detailed measurements show that the impedance of the peripherally fed helix differs significantly from that of its more usual axially fed counterpart. A precise design procedure is given for an impedance matching section which is incorporated directly into the first turn of the peripherally fed helical antenna to convert the input impedance to 50 Ω. Measured data in good agreement with design predictions are presented to show that a VSWR $\leq$1.2 can be readily achieved over octave bandwidths.

The downward shift in operating frequency for helices supported on dielectric cylinders is predicted by means of the effective filling factor. Mechanical details suitable for mass production of these antennas are given. Using this frequency-insensitive feed design, helical antennas with low VSWR over octave bandwidths within the frequency range from 500 MHz to 4 GHz have been manufactured.

I. INTRODUCTION

The impedance characteristics of axially fed helical antennas have been treated extensively [1] - [5] and the terminal resistance, R, of the axially fed helix is given by the empirical relation $R = 140\ C/\lambda\ \Omega$, where C/λ is the helix circumference in wavelengths [4], [5]. For many applications a 50 Ω input impedance is desired and this is commonly achieved by the use of coaxial quarter-wave transformers between the 50 Ω line and the input to the helical antenna [2], [3]. Kraus [6] has described a method for achieving a 50 Ω input impedance for the helical antenna by increasing the conductor size close to the feed point at the ground plane. This lowers the characteristic impedance of the transmission line formed by the conductor-ground plane combination and transforms the helix impedance to a lower value. However, the method in [6] does not give the geometry of the impedance matching section and the conductor-to-ground plane spacing is adjusted experimentally to achieve the desired performance.

There has recently been renewed interest in improving the performance of helical antennas [7] - [9]. A quasi-taper helix (consisting of uniform and tapered sections) was shown to have improved gain, pattern and axial ratio characteristics over those of the conventional uniform diameter helix [7]. Experimental parametric studies of 1 to 8 wavelength uniform helical antennas have been used to establish empirical expressions for the antenna peak gain and bandwidth as a function of the helix parameters [8]. In both these studies printed circuit microstrip transformers were used to match the helix impedance (≈140 Ω) to the 50 Ω coaxial input. The VSWR measured at the input to the matching transformer was <1.9 : 1 over the 650 to 1 100 MHz frequency range used in the studies and was typically ≤1.5 : 1. A new helical antenna incorporating a cone-shaped fully tapered helical section at the free end provides significant improvement in the on- and off-boresight axial ratio over that of the conventional uniform diameter helix [9]. The helical antennas were matched using impedance transformers; the measured VSWR was better than 1.4 : 1 over a 20% band.

From the most recent investigations of the helical antenna [7] - [9], it is clear that a simple means of feeding the helix to achieve low VSWR (≤1.2, say) over its entire usable bandwidth is one of the few aspects of helical antenna design which has not been satisfactorily resolved. This investigation describes a frequency-insensitive means of feeding the helical antenna. Measurements show that the impedance characteristics of peripherally fed helical antennas differ significantly from those of their more usual axially fed counterparts. A quantitative design procedure is given for an impedance matching section incorporated into the first turn of the peripherally fed helical antenna to convert the input impedance to 50 Ω. Measured reflection coefficient data are presented for helical antennas incorporating the matching section and it is shown how a simple termination at the free end of the helix extends the high-frequency

range of the antenna. The design is also applied to a helix supported on a dielectric tube and measured results are given to illustrate the downward shift of the lower cut-off frequency relative to that of a similar antenna supported on a styrofoam cylinder. The effective filling factor is introduced as an aid to predicting the amount of frequency shift.

II. DESIGN OF THE MATCHING SECTION

The method described by Hecken [10] for the design of broadband matching sections forms the basis of the present discussion and for convenience his notation is retained. Fig. 1 shows a schematic diagram of a peripherally fed helix and illustrates the coordinates used for the impedance matching section of length ℓ. The impedance matching section is a continuous transmission line (formed by the conductor-ground plane combination) of variable impedance which transforms the helix impedance, Z_2, to the line impedance, Z_1. At any point along the tapered line, the desired impedance at that point, $Z_c(s)$, is specified by (Eq. (29) of [10]):

$$\log_e Z_c(s) = \frac{1}{2}\log_e(Z_2 Z_1) + \frac{1}{2}\log_e\left(\frac{Z_2}{Z_1}\right) G(B,s) \qquad (1)$$

where $s = 2x/\ell$. The function $G(B,s)$ is tabulated in [10] for specified values of B or it may be rapidly computed [11].

The impedance change along the tapered line remains gradual and at any point along the line the impedance may be approximated by the characteristic impedance of a circular wire above a ground plane [12]

$$Z_c(s) = \frac{60}{\sqrt{\varepsilon_r}} \cosh^{-1}\frac{2h}{d}$$

$$= \frac{60}{\sqrt{\varepsilon_r}} \log_e\left\{\frac{2h}{d} + \sqrt{\left(\frac{2h}{d}\right)^2 - 1}\right\} \qquad (2)$$

where ε_r is the relative dielectric constant, d is the diameter of the circular conductor and $h = h(s)$ is the spacing between the ground plane and the centre of the circular conductor (see inset in Fig. 1).

Equations (1) and (2) define the shape of the impedance matching section. For peripherally fed helical antennas, the helix impedance, Z_2, is the only unknown.

A. Helix impedance

Extensive measurements were made to determine the terminal impedance characteristics of peripherally fed helical antennas with pitch angles of 12° and 14°. The experimental helices were all wound using copper conductors of circular cross section. The conductor diameters used were 1.8 mm and 5.0 mm corresponding to 0.0064 and 0.017 wavelengths at the centre frequency (i.e., the frequency at which the helix circumference is equal to a free-space wavelength). For all antenna models, the helix conductor was supported on a styrofoam cylinder glued to the ground plane. Apart from strips of masking tape, no other mechanical supports such as metallic centre tubes were used during the measurements. For all measurements a conventional circular ground plane with a diameter equal to the helix circumference was used to back the helix.

Figs. 2 and 3 show the magnitude and phase of the reflection coefficient on a 50 Ω line for a 12° pitch angle and conductor diameters of 5.0 mm and 1.8 mm, respectively. For the 5.0 mm conductor a carefully designed feed finger similar to that proposed in [3] must be used to connect the helix to the transmission line. The length and cone angle of the feed finger were selected to maintain a nearly constant impedance [140 Ω as computed with Eq. (2)] from the input connector to the point where the feed finger joins the helix conductor. If a feed finger is not used and the 5.0 mm conductor is joined directly to the input connector (ground plane spacing = 4.7 mm), the initial section of the helix acts as an impedance transformer which tends to lower the measured impedance and to increase its frequency variation (see Fig. 2). Without the feed finger the phase (not shown) has an average value of about -15° compared to the case with feed finger where the phase varies around 0°. A feed finger is not required for the 1.8 mm conductor since it can be connected directly to the input and still maintain a 140 Ω impedance between the helix conductor and the ground plane at the input. For the thinner conductor the magnitude of the reflection coefficient is somewhat larger than that for the thicker conductor and the phase varies around -5° rather than around 0° (see Fig. 3). From Fig. 3 it is clear that the magnitude of the reflection coefficient decreases by only about 1 dB over the range of circumferences C/λ between 0.8 and 1.2. The magnitude and phase reference lines for a short circuit plane on the upper surface of the ground plane were established using the HP8750A storage-normaliser.

The helix conductor and feed finger maintain a constant pitch angle over the entire length of the helix. At the free end, the helix is terminated by the addition of two or more turns in the form of a planar Archimedes spiral lying in the plane perpendicular to the helix axis (see Fig. 1). This simple termination removes the resonant region ($C/\lambda > 1.1$) found in the completely uniform helix and decreases the frequency dependence of the helix impedance for $C/\lambda > 1.1$ (see Section III for a more detailed discussion of the effects of the spiral end taper on helical antenna performance).

The real and imaginary parts of the helix impedance are readily computed from the measured magnitude and phase data for the reflection coefficient ($\rho = |A|e^{j\phi}$). These calculations show that:

(a) the terminal impedance is nearly a pure resistance, but the resistance for the 0.0064 wavelength diameter conductor is higher by a factor of about 1.2 than that for the 0.017 wavelength diameter conductor,

(b) the resistance variation as a function of frequency is not nearly as large as that for axially fed helices and the resistance decreases with increasing frequency,

(c) for the same conductor diameter, the resistance of helices with a pitch angle of 14° is about 5% higher than the resistance for a pitch angle of 12°.

From impedance measurements on a large number of peripherally fed helical antennas with the feed arrangements of Figs. 2 and 3, it was found that in the frequency range corresponding to helix circumferences between 0.8 and 1.2 wavelengths the terminal resistance, R, was within ±10% when the following empirical expression was used:

$$R = \frac{150}{\sqrt{\frac{C}{\lambda}}} \text{ ohms} \qquad (3)$$

This applies to peripherally fed helices with $12° \leq \alpha \leq 14°$, $0.8 \leq C/\lambda \leq 1.2$, and $n > 4$. Equation (3) applies particularly to conductors of cylindrical cross section with diameters, d, between about 0.006 and 0.02 wavelengths at the centre frequency. For thinner conductors the resistance will be somewhat higher than predicted by Eq. (3) and for thicker conductors the resistance will be lower. This formula (3) contrasts with that for axially fed helices ($R = 140\ C/\lambda$) where the resistance is directly proportional to frequency and increases with frequency.

B. Matching section profile

For the matching section design, the impedance of the peripherally fed helix (Z_2 in Eq. (2)), was taken as 150 Ω (when thin conductors of the order of 0.006 wavelength are used a value of Z_2 about 10% higher than this can give improved matching at the low-frequency end). The function G(B,s) in Eq. (1) was selected for a design which requires a maximum reflection coefficient of -21 dB at the 50 Ω input connector to the helix (this corresponds to the first column of values in Table 1 of [10]). The desired values of the impedance $Z_c(s)$ along the matching section (the "Hecken taper") and the corresponding values of h(s) are given in Table 1 below. From Eq. (2) we have

$$h(s) = \frac{d}{2} \cosh\left(\frac{\sqrt{\varepsilon_r}\, Z_c(s)}{60}\right) \qquad (4)$$

The values of h in Table 1 are computed for $\varepsilon_r = 1$ and d = 1.8 mm. Since h is directly proportional to d, the appropriate values of h for other conductor diameters can be scaled directly from this table. For $\varepsilon_r \neq 1$, i.e. matching taper embedded in dielectric, the values of h in Table 1 must be calculated from Eq. (4) with the appropriate value of ε_r.

This design requires that the minimum length of the impedance taper be 0.44 λ at the lowest operating frequency [10]. The low frequency cut-off characteristics of helical antennas have been defined [13], [14] and a value of $C/\lambda = 0.7$ may be taken as being representative of helices with $12° \leq \alpha \leq 14°$. This means that the taper must be about 0.63 wavelengths long at the centre frequency, i.e. the matching section extends from the feed point to a little beyond half the helix circumference. From Table 1 it is clear that the conductor of the matching section lies quite close to the ground plane over the first half of the taper. Note also that the impedance at the midpoint of the matching section, $|s| = 0$, is the geometric mean of Z_1 and Z_2, i.e., $Z_c(0) = \sqrt{Z_1 Z_2} = \sqrt{50 \times 150} = 86.6$ Ω. This means that the shape of the first half of the matching section does not change too rapidly with a change in Z_2 and there is some leeway in the choice of the helix impedance Z_2. The match at the high-frequency end is very sensitive to deviations from the desired matching section profile over the first half of the matching section, at the low-frequency end the match is comparatively insensitive to Z_2 provided the value selected is high enough. NOTE: The Hecken taper described here represents the shortest taper to achieve a -21 dB reflection coefficient. Longer tapers [10] can be used in an attempt to achieve still better performance; with the matching section incorporated into the first turn the maximum taper length is equal to the helix circumference.

III. EXPERIMENTAL RESULTS

Experimental results showing the reflection coefficient achieved on a 50 Ω line will be presented for two types of peripherally fed helical antennas, these being: (a) helix supported on a styrofoam cylinder with the matching section in air and (b) helix supported on a dielectric tube with the matching section embedded in dielectric.

A. Helix on styrofoam

The impedance matching section in Table 1 was incorporated into the first turn of a peripherally fed helical antenna of standard design with centre frequency 1.364 GHz, pitch angle 13.8° and helix conductor diameter 1.8 mm. Fig. 4 shows the measured reflection coefficient.

The solid curve is for a uniform helix incorporating the matching section at the input. The term "uniform" here refers to a helix of constant pitch and diameter from the output of the matching section to the tip of the free end of the helix. Above $C/\lambda \approx 1.25$ the reflection coefficient is greater than -20 dB. The dashed curve shows the reflection coefficient when the free end of the helix is truncated with a two turn planar Archimedes spiral of the form $r = D/2 - k\phi$ where r is the distance from the helix axis, D is the helix diameter, k is a constant and ϕ the azimuth angle. The precise shape of the truncation is not critical for achieving improved reflection coefficient at the high-frequency end but for the sake of definiteness the Archimedes spiral was used. With this truncation the reflection coefficient is <-22 dB (VSWR <1.2) from 0.98 to 1.97 GHz. This 2 : 1 frequency band covers the entire usable bandwidth of the helical antenna as specified by gain and pattern [8]. The addition of the spiral end taper has very little effect on the reflection coefficient below $C/\lambda = 1.0$ and the low-frequency limit of the antenna on the basis of reflection coefficient is extremely well defined.

The idea of truncating the free end of the helix is not new, in fact Kraus [15] suggested changing the spacing of the last turn as a method for improving the axial ratio. The most commonly used method of truncating the helix to achieve improved axial ratio is by the addition of a cone-shaped helical section at the free end of the helix [7], [9], [16]. The planar Archimedes spiral end section proposed here gives significant improvement in axial ratio over the uniform helix provided there are more than two turns and the minimum radius of the spiral is less than about D/6. The number of turns will depend on the helix diameter and the conductor diameter. For example, a four turn planar end taper maintains an on-boresight axial ratio <0.8 dB over a wide band from $C/\lambda = 0.8$ to 1.2 for a helix with $\alpha = 12°$. Without the end taper the axial ratio is

greater than 1 dB above $C/\lambda = 1.05$ (cf. the results in [9]). Although the planar spiral end section is not quite as effective as the fully tapered conical section [9], it does have the significant advantage that it does not increase the overall length of the helical antenna. The antenna with the fully tapered conical section is 37.5% longer than a similar antenna with a planar spiral end section [9].

B. Helix on dielectric tube

A helical antenna supported on a styrofoam cylinder is an extremely flimsy structure; for mechanical rigidity the helix is often supported on a dielectric tube. The presence of the dielectric can significantly alter the operating band of the helix relative to the free-space centre frequency.

The data in Table 1 were used for the matching section of a helical antenna of standard design with centre frequency 1.073 GHz, pitch angle 12° and helix conductor diameter 1.8 mm. The dashed curve in Fig. 5 shows the measured reflection coefficient when the helix is supported on a styrofoam cylinder. The reflection coefficient is <-20 dB and the well defined low-frequency cut off is again evident. An antenna similar to the one above was manufactured except that the helix conductor and impedance matching section were embedded in dielectric as shown in Fig. 6.

The groove for the helix conductor and the impedance matching section is machined in a single operation with the aid of a numerically controlled lathe (NC lathe). The dielectric used for the antenna was polyvinyl chloride (PVC) with a measured dielectric constant $\varepsilon_r = 2.70$ and a loss tangent of 0.01. The matching section data in Table 1 cannot be used and the impedance taper was recalculated with $\varepsilon_r = 2.70$ and a helix impedance Z_2 of 130 Ω. The presence of the dielectric lowers the helix impedance from the nominal 150 Ω free-space value. The antenna is assembled in a single operation, the central PVC cylinder is screwed to the ground plane by means of stainless steel screws parallel to the helix axis, the PVC tube carrying the helix conductor slips over this cylinder and the outer PVC ring slips over the cylinder once the conductor has been soldered to the input connector. Radial screws at locations where they do not influence the matching section complete the assembly (see Fig. 6 for details, screws not shown). The conductor-to-ground plane spacing, h, achieved using the NC lathe had a maximum deviation of +2% from the design goal. Essentially identical antennas can be produced by this procedure which automatically solves the problem of holding the matching section in place.

The solid curve in Fig. 5 shows the reflection coefficient for the helical antenna supported on PVC. The reflection coefficient is <-20 dB over the band of interest and there has been a downward shift in the cut-off frequency of about 100 MHz. This represents a significant shift in centre frequency and there will also be a shift in the frequency at which the peak gain occurs.

To predict the downward shift in frequency, it is necessary to determine the effective dielectric constant, ε_{eff}, and the effective filling factor, F, for the air-dielectric medium surrounding the helix. These quantities are related as follows

$$\varepsilon_{eff} = (1 + F(\varepsilon_r - 1)) \tag{5}$$

From Fig. 5 we can obtain ε_{eff} from the frequency shift and hence F for the helix-air-dielectric configuration of Fig. 6. Thus

$$\varepsilon_{eff} = \left(\frac{f_{c\,a}}{f_{c\,d}}\right)^2 \tag{6}$$

where $f_{c\,a}$ = low-frequency cut off for helix in air and $f_{c\,d}$ = low-frequency cut off for helix on dielectric. From Fig. 5, taking the low-frequency cut off arbitrarily as that frequency where the reflection coefficient first reaches -20 dB,

$$\varepsilon_{eff} = \left(\frac{0.792}{0.691}\right)^2 = 1.314$$

Therefore, with $\varepsilon_r = 2.70$ we have F = 0.185 for the configuration shown in Fig. 6. The downward frequency shift for an arbitrary antenna is then calculated as follows: with F = 0.185 and a knowledge of ε_r for the supporting structure use Eq. (5) to obtain ε_{eff}, then $f_{c\,d} = f_{c\,a}/\sqrt{\varepsilon_{eff}}$. The cut-off frequency for air is related to the centre frequency, f_o, by $f_{c\,a} = \beta f_o$ where β has a value 0.74 for $\alpha = 12°$ and 0.71 for $\alpha = 14°$ (see Figs. 4 and 5). The validity of this procedure has been checked for several antennas supported on plexiglass ($\varepsilon_r = 2.60$). For example, an antenna on plexiglass with D = 133 mm and $\alpha = 12°$ has a predicted cut-off frequency of 467 MHz using this procedure; the measured cut-off frequency was 473 MHz. Although the filling factor, F, was 0.185 for the helix conductor fully recessed in the dielectric tube (see Fig. 6), this value has been found to give good results for helix conductors which are only partially recessed. This design procedure has been applied successfully to antennas in the 500 MHz to 4 GHz frequency range.

As stated above, the value of Z_2 chosen for matching the PVC helix was 130 Ω. This value corresponds to a reduction of the 150 Ω in Eq. (3) by a factor $1/\sqrt{\varepsilon_{eff}}$. For a helix with ten turns supported on styrofoam and a pitch angle of 12.5° the peak gain occurs at a circumference $C/\lambda \simeq 1.135$ and the peak gain is 13.8 dB referred to a circularly polarised illuminating source [8]. For the 12°, ten turn helix on PVC of Figs. 5 and 6 the peak gain occurs at a frequency of 1.06 GHz and has a value of 13.6 dB (see Fig. 7). For the helix on PVC the free-space centre frequency $f_o = 1.073$ GHz is reduced by a factor $1/\sqrt{\varepsilon_{eff}}$ to $f_{o\,d} = 0.936$ GHz which may be regarded as the centre frequency for the PVC helix. The peak gain should occur at a frequency where $(C/\lambda)_d = 1.135$, i.e. at 1.062 GHz which is in excellent agreement with the actual value of 1.06 GHz. The performance of helical antennas supported on dielectric materials can be predicted from the design data of antennas supported on styrofoam forms (as given in [8], for example) provided the centre frequency and cut-off frequency of the antennas supported on dielectric are appropriately adjusted by the effective dielectric constant which may be deduced from the effective filling factor and the dielectric constant of the supporting material.

IV. CONCLUSIONS

The terminal resistance of peripherally fed helical antennas decreases with increasing frequency and is given to within ±10% by the empirical expression $R = 150/\sqrt{C/\lambda}$ ohms for $12° \leq \alpha \leq 14°$, $0.8 \leq C/\lambda \leq 1.2$ and $n > 4$. By using the appropriate helix impedance, a table was constructed to define the impedance values and conductor-to-ground plane spacings for the Hecken taper which constitutes the broadband impedance matching section. Measured data was presented to show how the addition of a planar Archimedes spiral of a few turns to the free end of the helix improves the impedance match for $C/\lambda > 1.1$ and decreases the axial ratio. The impedance matching section incorporated into the first turn of a peripherally fed helix achieved VSWR ≤ 1.2 over the entire usable bandwidth of the helical antenna. The downward shift in the low-frequency cut off of helices supported on dielectric rather than styrofoam forms was used to deduce the effective filling factor. By appropriate use of the effective dielectric constant, the performance of helical antennas supported on dielectric forms can be predicted from the design data of helices supported on styrofoam forms. Mechanical details were presented for a ruggedised antenna where the helix is supported on dielectric and the impedance matching section is captivated in the dielectric.

ACKNOWLEDGMENT

The author wishes to thank Prof. John D. Kraus of the Ohio State University Radio Observatory for helpful discussions and the CSIR for permission to publish this work.

TABLE 1 : Characteristic impedance, $Z_c(s)$, and conductor spacing, h(s), as a function of distance, s, along the impedance matching section (helix conductor diameter d = 1.8 mm)

|s|	G(B,s)	$Z_c(+\|s\|)$ Ω	h(+|s|) mm	$Z_c(-\|s\|)$ Ω	h(-|s|) mm
0.00	0.00000	86.60	2.01	86.60	2.01
0.05	0.05473	89.25	2.09	84.04	1.94
0.10	0.10939	91.97	2.18	81.55	1.87
0.15	0.16390	94.76	2.28	79.15	1.80
0.20	0.21819	97.63	2.38	76.82	1.74
0.25	0.27218	100.57	2.49	74.58	1.69
0.30	0.32580	103.57	2.61	72.41	1.64
0.35	0.37899	106.65	2.74	70.33	1.59
0.40	0.43166	109.78	2.88	68.32	1.55
0.45	0.48375	112.96	3.03	66.39	1.51
0.50	0.53519	116.20	3.19	64.54	1.47
0.55	0.58591	119.48	3.36	62.77	1.44
0.60	0.63586	122.81	3.54	61.07	1.41
0.65	0.68495	126.16	3.74	59.45	1.39
0.70	0.73314	129.55	3.95	57.89	1.35
0.75	0.78036	132.95	4.18	56.41	1.33
0.80	0.82655	136.37	4.41	55.00	1.31
0.85	0.87166	139.79	4.67	53.65	1.29
0.90	0.91564	143.21	4.94	52.37	1.27
0.95	0.95844	146.61	5.22	51.15	1.25
1.00	1.00000	150.00	5.52	50.00	1.23

NOTES:
1. $s = 2x/\ell$, where ℓ is the length of the taper
2. $G(B,-s) = -G(B,s)$
3. $\varepsilon_r = 1.0$

REFERENCES

[1] O.J. Glasser and J.D. Kraus, "Measured impedances of helical beam antennas", J. Applied Phys., vol. 19, pp. 193 - 197, February 1948.

[2] J.D. Kraus, "Helical beam antennas for wideband applications", Proc. IRE, vol. 36, pp. 1236 - 1242, October 1948.

[3] R.J. Stegun, "Impedance matching of helical antennas", IEEE Trans. Antennas Propagat., vol. AP - 12, pp. 125 - 126, January 1964.

[4] J.D. Kraus, Antennas. New York : McGraw-Hill, 1950, Ch. 7.

[5] E.F. Harris, "Helical antennas", in Antenna Engineering Handbook, H. Jasik, Ed. New York : McGraw-Hill, 1961, Ch. 7.

[6] J.D. Kraus, "A 50-ohm input impedance for helical beam antennas", IEEE Trans. Antennas Propagat., vol. AP - 25, p. 913, November 1977.

[7] J.L. Wong and H.E. King, "Broadband quasi-taper helical antennas", IEEE Trans. Antennas Propagat., vol. AP - 27, pp. 72 - 78, January 1979.

[8] H.E. King and J.L. Wong, "Characteristics of 1 to 8 wavelength uniform helical antennas", IEEE Trans. Antennas Propagat., vol. AP - 28, pp. 291 - 296, March 1980.

[9] C. Donn, "A new helical antenna design for better on- and off-boresight axial ratio performance", IEEE Trans. Antennas Propagat., vol. AP - 28, pp. 264 - 267, March 1980.

[10] R.P. Hecken, "A near-optimum matching section without discontinuities", IEEE Trans. Microwave Theory and Tech., vol. MTT-20, pp. 734 - 739, November 1972.

[11] J.H. Cloete, "Computation of the Hecken impedance function", IEEE Trans. Microwave Theory and Tech., vol. MTT - 25, p. 440, May 1977.

[12] M.A.R. Gunston, Microwave transmission-line impedance data. London : Van Nostrand Reinhold, 1972, Ch. 2.

[13] T.S.M. Maclean and W.E.J. Farvis, "The sheath-helix approach to the helical aerial", Proc. IEE, vol. 109, Part C, no. 16, pp. 548 - 555, May 1962.

[14] T.S.M. Maclean, "An engineering study of the helical aerial", Proc. IEE, vol. 110, no. 1, pp. 112 - 116, January 1963.

[15] J.D. Kraus, "Helical beam antenna", Electronics, vol. 20, pp. 109 - 111, April 1947.

[16] D.J. Angelakos and D. Kajfez, "Modifications on the axial-mode helical antenna", in Proc. IEEE, vol. 55, no. 4, pp. 558 - 559, April 1967.

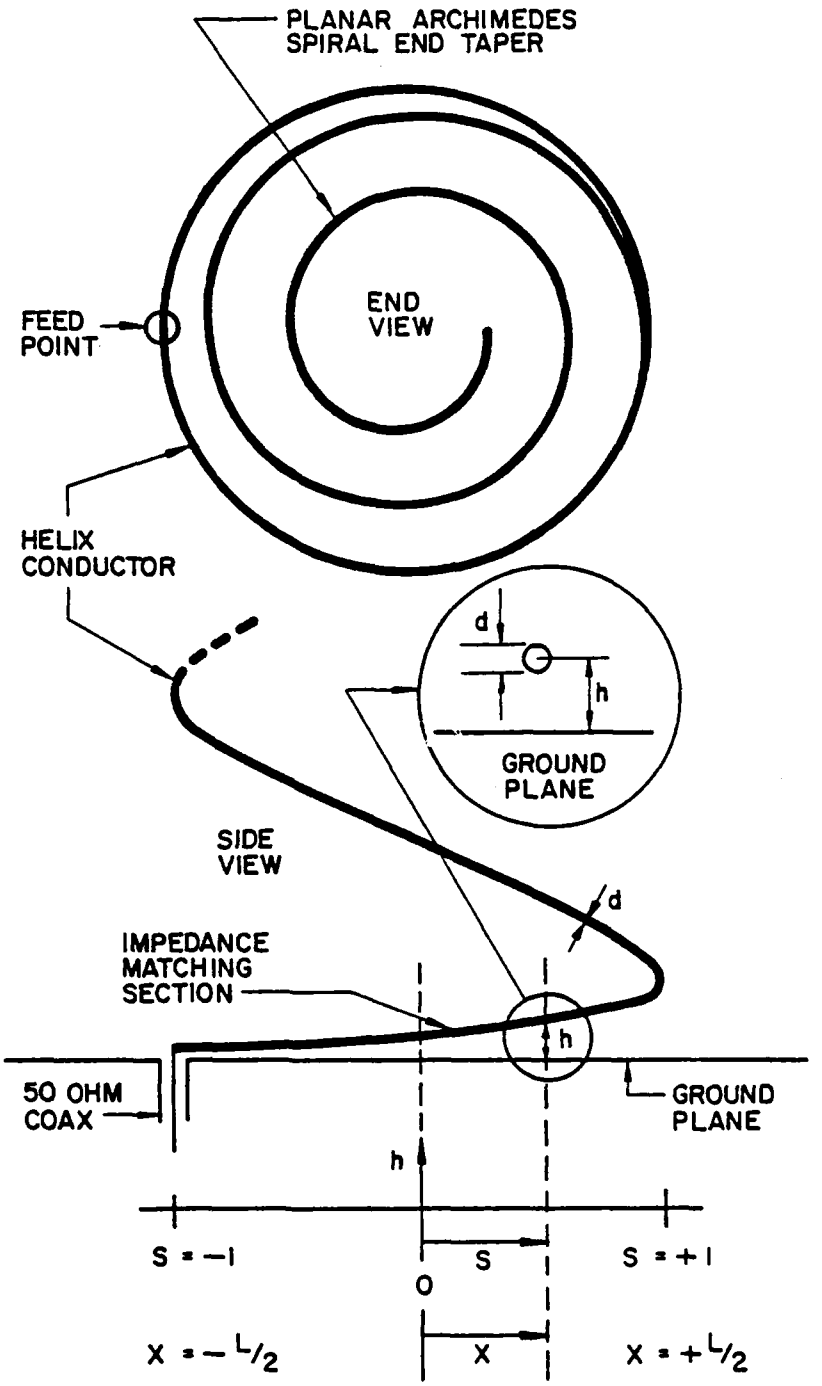

FIGURE 1 : Schematic diagram of a peripherally fed helical antenna illustrating the matching section coordinates and the termination of the helix at the free end.

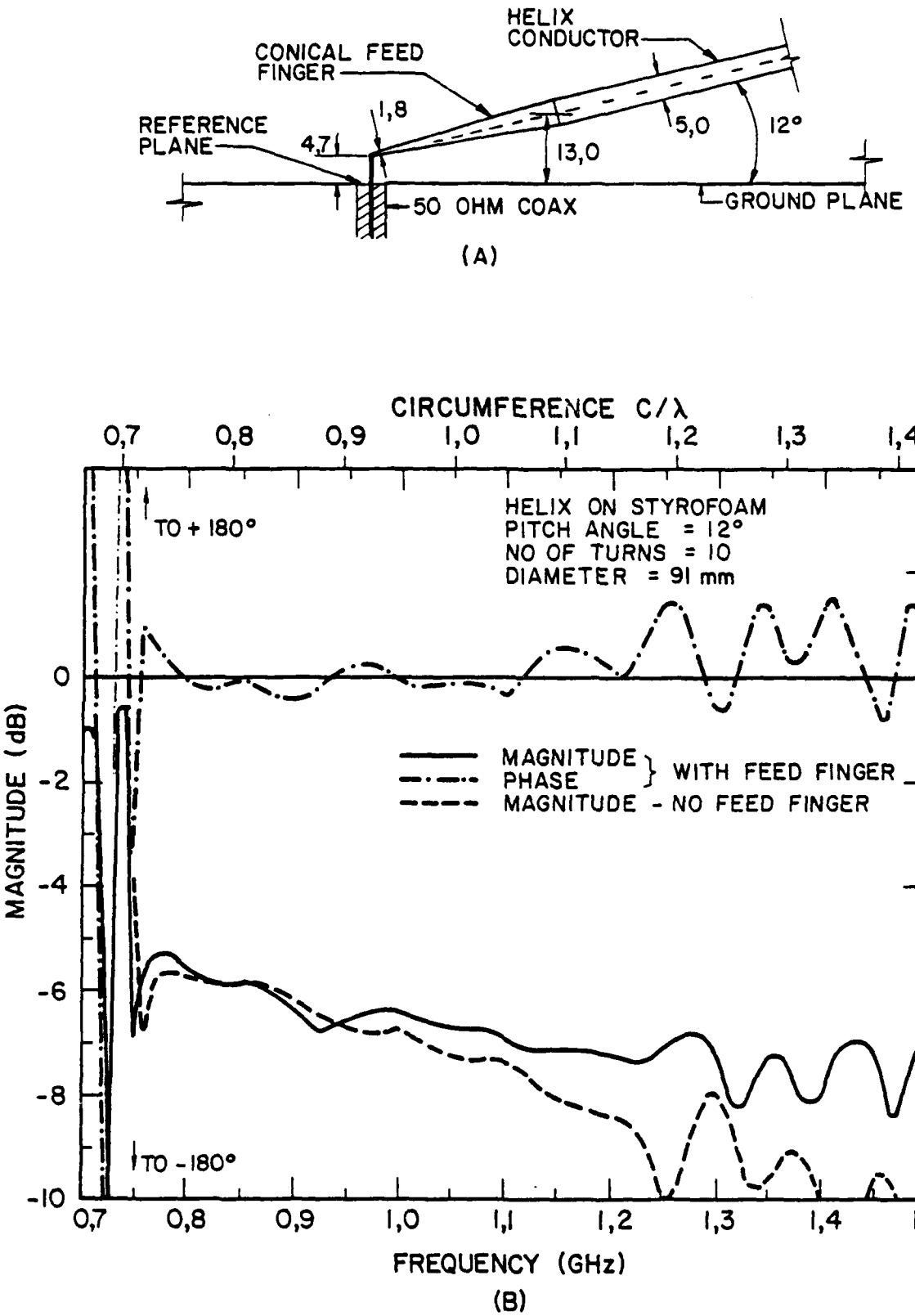

FIGURE 2 : Feed configuration (a) and magnitude and phase of the reflection coefficient (b) of a peripherally fed helix with 12° pitch angle and 5.0 mm conductor diameter.

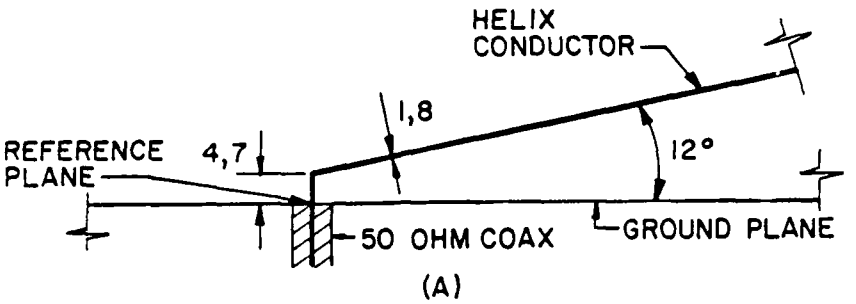

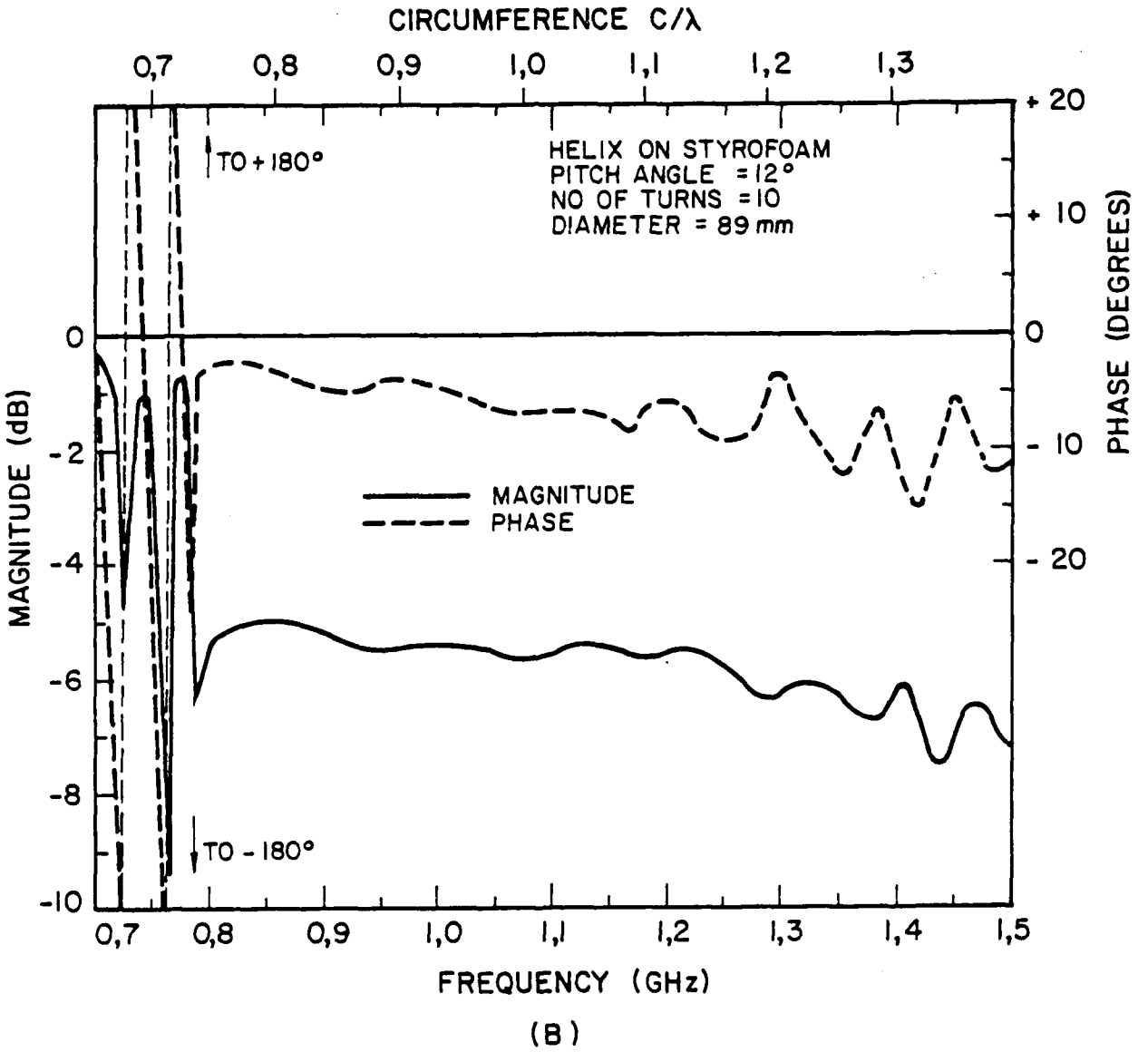

FIGURE 3 : Feed configuration (a) and magnitude and phase of the reflection coefficient (b) of a peripherally fed helix with 12° pitch angle and 1.8 mm conductor diameter.

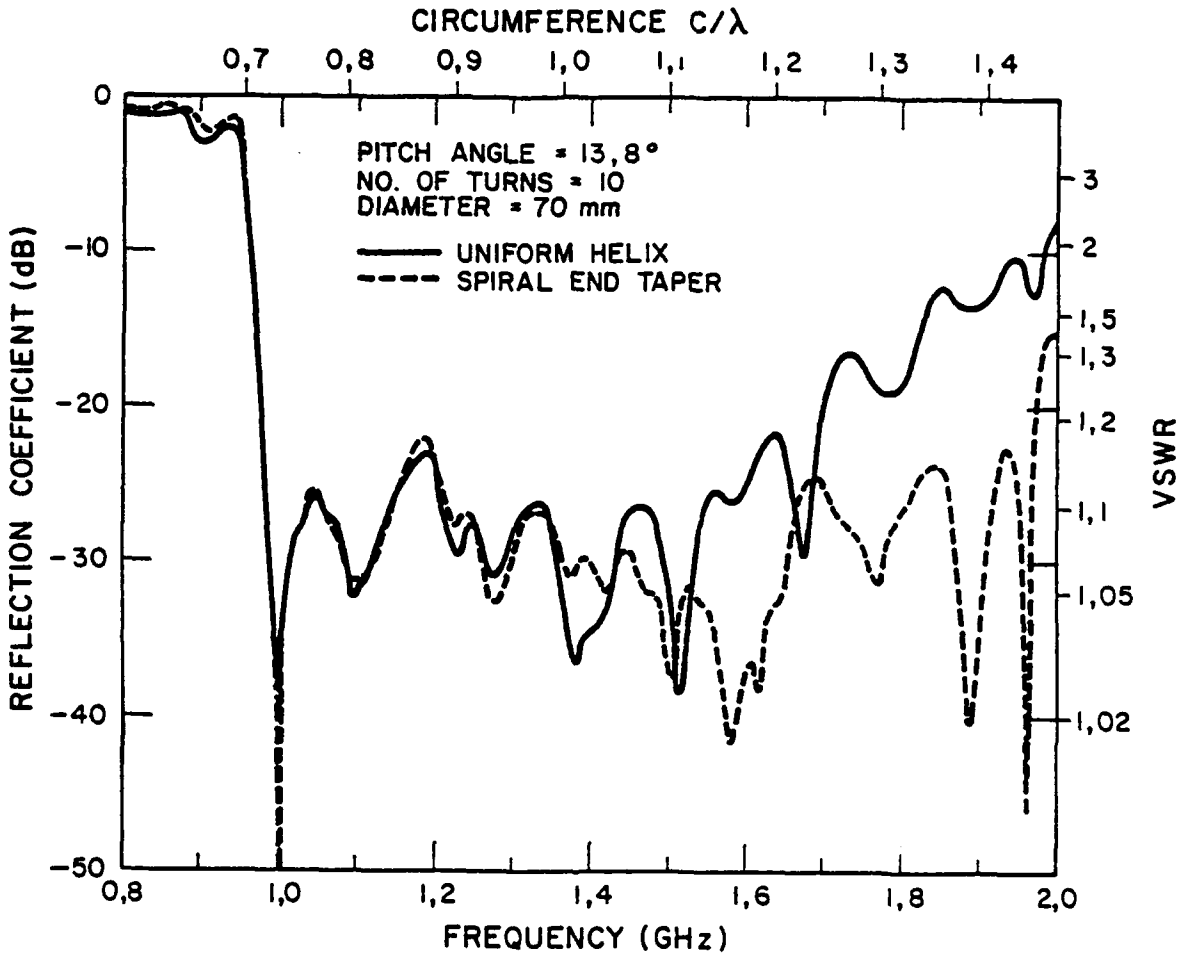

FIGURE 4 : Reflection coefficient of a 70 mm diameter helical antenna with pitch angle of 13.8° and conductor diameter of 1.8 mm showing the effect of the Archimedes spiral end taper.

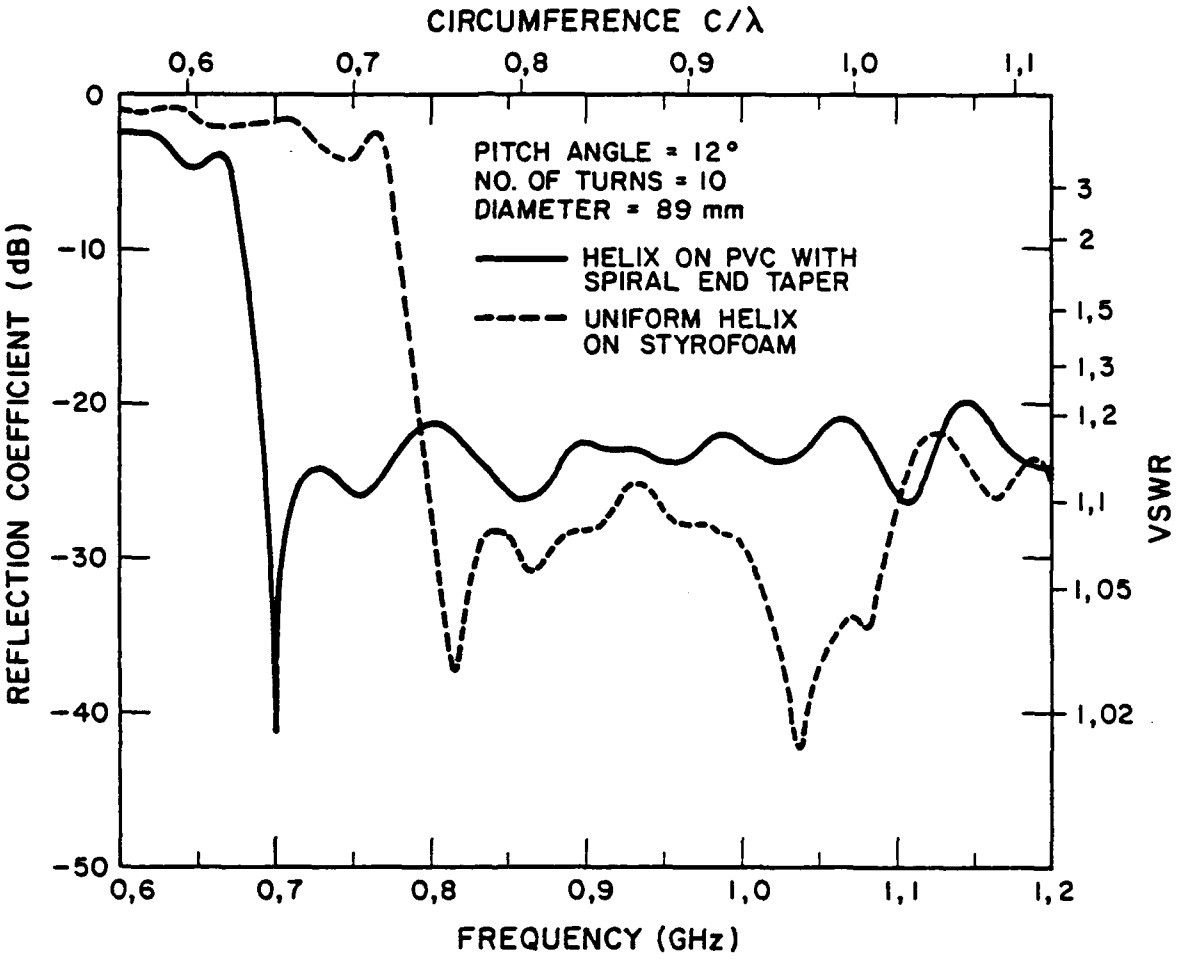

FIGURE 5 : Reflection coefficient of a 89 mm diameter helical antenna with pitch angle of 12° and conductor diameter of 1.8 mm showing the downward shift in cut-off frequency for a helix supported on a PVC rather than a styrofoam former.

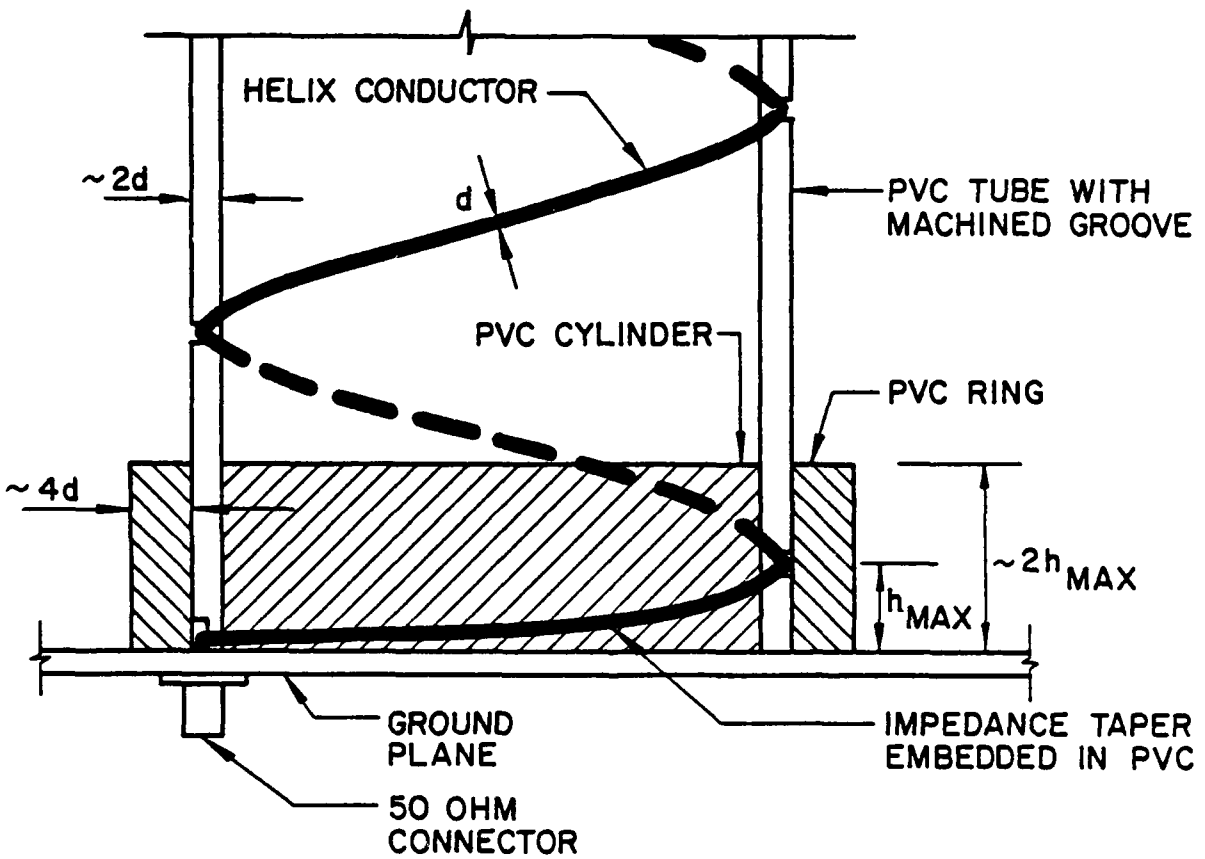

FIGURE 6 : Section through a peripherally fed helical antenna with the matching section embedded in dielectric. The impedance taper and helix conductor are shown schematically.

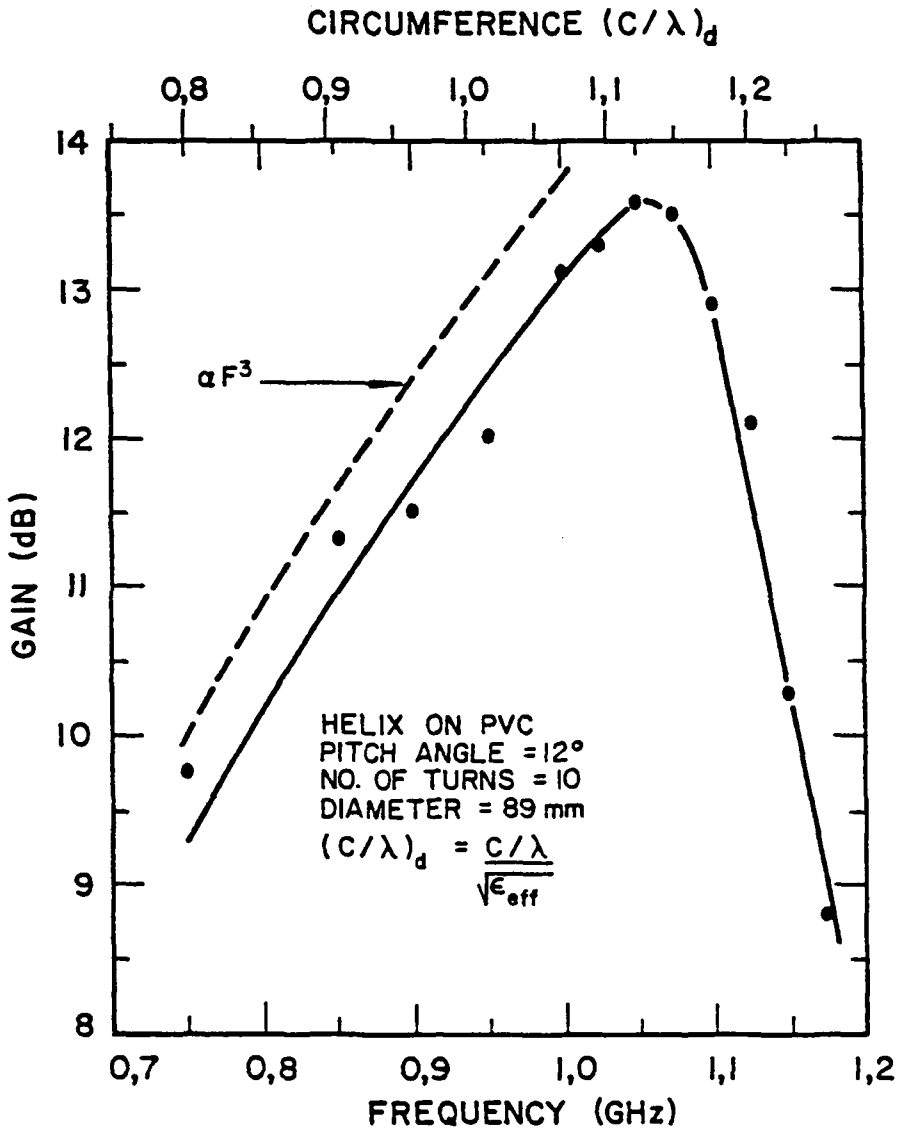

FIGURE 7 : Gain of a 10 turn, 89 mm diameter helical antenna for a pitch angle of 12° and helix conductor supported on PVC (ε_r = 2.70).

SWEPT-FREQUENCY RADIATION PATTERN ANOMALIES ON HELICAL ANTENNAS

J.M. Tranquilla
Department of Electrical Engineering
University of New Brunswick
Fredericton, N.B., Canada

G.B. Graham
Department of Electrical Engineering
University of New Brunswick
Fredericton, N.B., Canada

S.Y. Jee
Department of Electrical Engineering
University of New Brunswick
Fredericton, N.B., Canada

ABSTRACT

Measurements of the swept-frequency radiation patterns for several helical antennas indicate that the low-frequency edge of the passband (and extending below the bandedge) is marked by the occurrence of a class of anomalous responses which are characterized by very narrowband fluctuations in the swept-frequency gain and axial ratio plots. Several tapering schemes have been tested and it is shown that, in general, all these anomalies cannot be controlled by tapering. A separate class of anomalous responses occurs above the upper passband edge of the uniform helical antenna. These responses are similar to those which occur at the lower bandedge except that they can be controlled by end-tapering.

INTRODUCTION

Several papers are available in the literature presenting the solution of the determinantal equations which describe the infinite sheath and tape helix antennas.[1,2,3] Recently researchers[4] have shown that a class of anomalous responses (characterized in the swept-frequency input VSWR plot of the uniform helix as a series of narrowband oscillations at the upper bandedge) occurs and that they can be eliminated by tapering the helix, resulting in improved bandwidth and VSWR. Kraus[5] has explained that in the so-called "normal mode" ($C_\lambda < 3/4$, corresponding to $f < 580$ MHz for the uniform helix used in this study) the current distribution on the helix is sinusoidal due to a standing wave caused by an outward-travelling and reflected T_0 wave. In the "beam or axial mode" ($3/4 < C_\lambda < 4/3$, corresponding to 580 MHz $< f <$ 1020 MHz) the T_0 mode is attenuated and the unattenuated T_1 mode causes a nearly uniform current distribution along the helix. At frequencies above the beam mode ($C_\lambda > 4/3$) the occurrence of higher order modes again results in a current standing wave along the helix. However the connection between the responses reported in [4] and those reported here and Kraus' explanation is not immediately clear nor is it clear how end-tapering reported in [4] can be applied systematically to control anomalous responses.

In this work we examine the measured broadband radiation characteristics of several helical antennas (similar to those described in [4] above) which are used in addition to theoretical dispersion curves to show the general characteristics of narrowband anomalous responses on the uniform helical antenna. Figure 1 illustrates the antennas considered in this study.

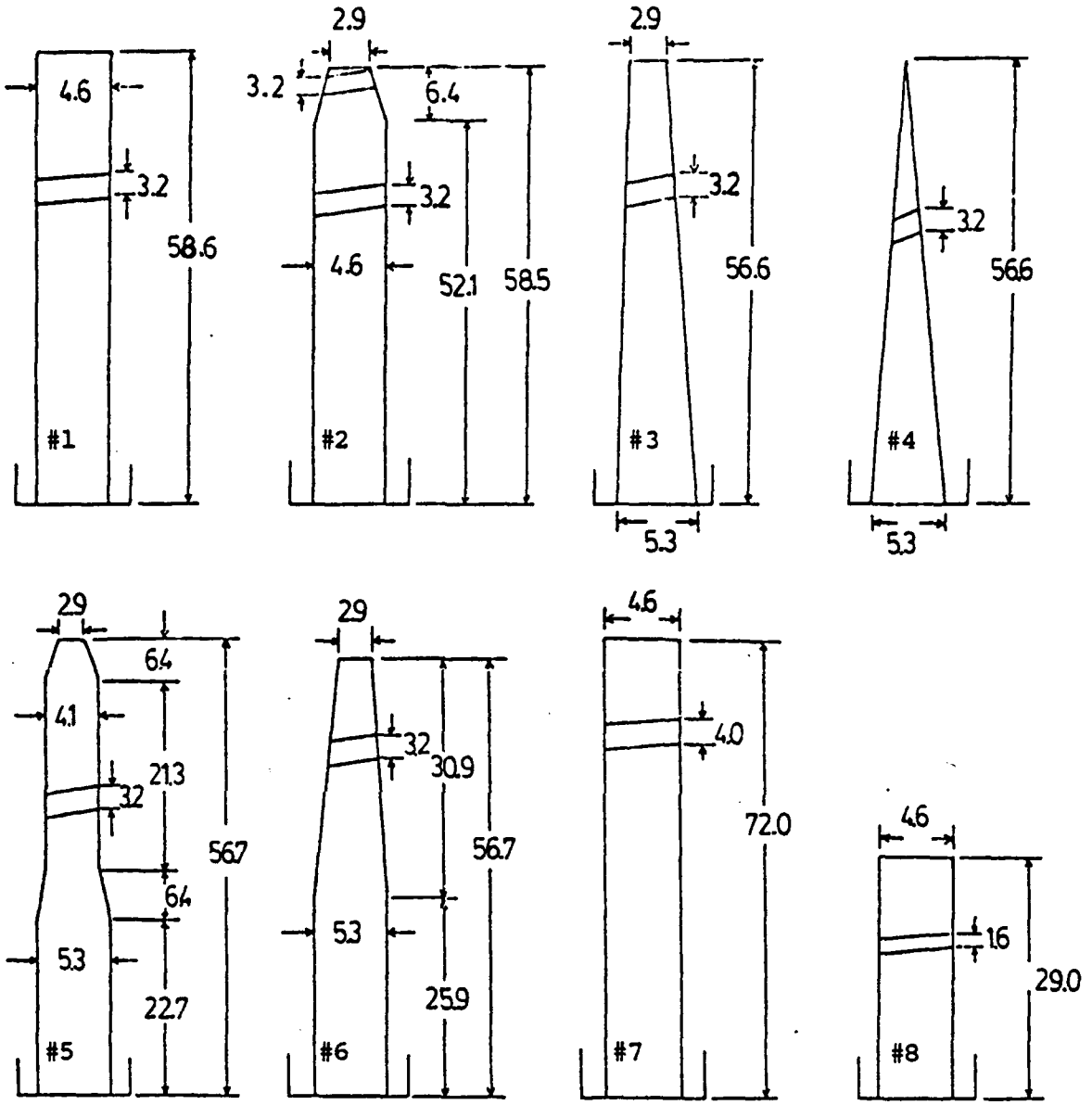

Fig. 1 Dimensions of 18-turn helical antennas. All conductors are 2mm diameter circular copper stock. Dimensions shown are in inches. Each antenna is mounted on a cylindrical reflector cavity, 11.25" D x 3.75" H.

RADIATION PATTERNS

Figure 2 shows the measured gain-frequency patterns for eight 18-turn helical antennas. For the uniform helix two groups of anomalous responses are visible as very narrowband gain fluctuations. One group occurs near the high frequency bandedge and, as will be shown later, is related to the VSWR anomalies reported in [4]. This group of anomalous responses is present on the uniform helix but does not appear on the gain-frequency plots for the tapered-end helices. Another group of anomalous responses occurs near the low-frequency bandedge and occupies a relatively wider band than the first group mentioned earlier. The use of various tapering schemes produces some change in these anomalies but, in general, all the anomalies cannot be suppressed by end-tapering. This suggests that there is some distinction between these two groups of anomalous responses and so we consider each to be a distinct class which will be designated as class A anomalies (near the low frequency bandedge) and class B anomalies (near the high frequency bandedge).

Axial ratio measurements were made for each of the antennas and are presented in Figure 3. In the bands containing the class A and B anomalies the axial ratio plots show very large, narrowband fluctuations. When end-tapering is used the class B responses are suppressed, however the class A responses are not controlled and, in fact, become more severe.

INPUT REFLECTION COEFFICIENT

Figure 4 shows the measured swept-frequency input voltage reflection coefficient characteristics for several of the antennas. For the uniform helix the class B anomalies are evident and may be controlled by end-tapering as reported in [4]. In addition, the class A anomalies, which

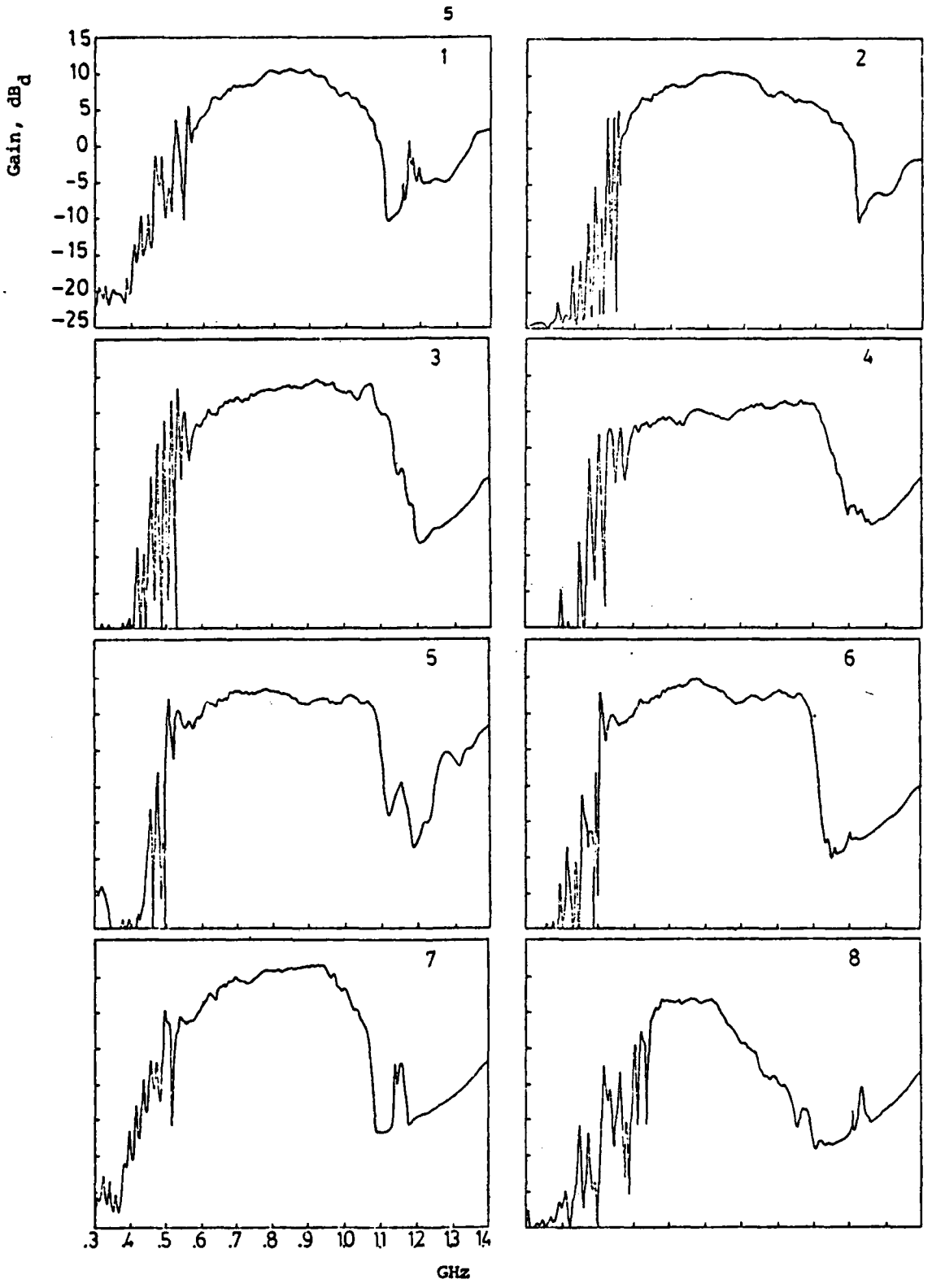

Fig. 2 Measured gain-frequency plots for eight experimental helical antennas. Gain is measured in dB with respect to a linear half-wave dipole.

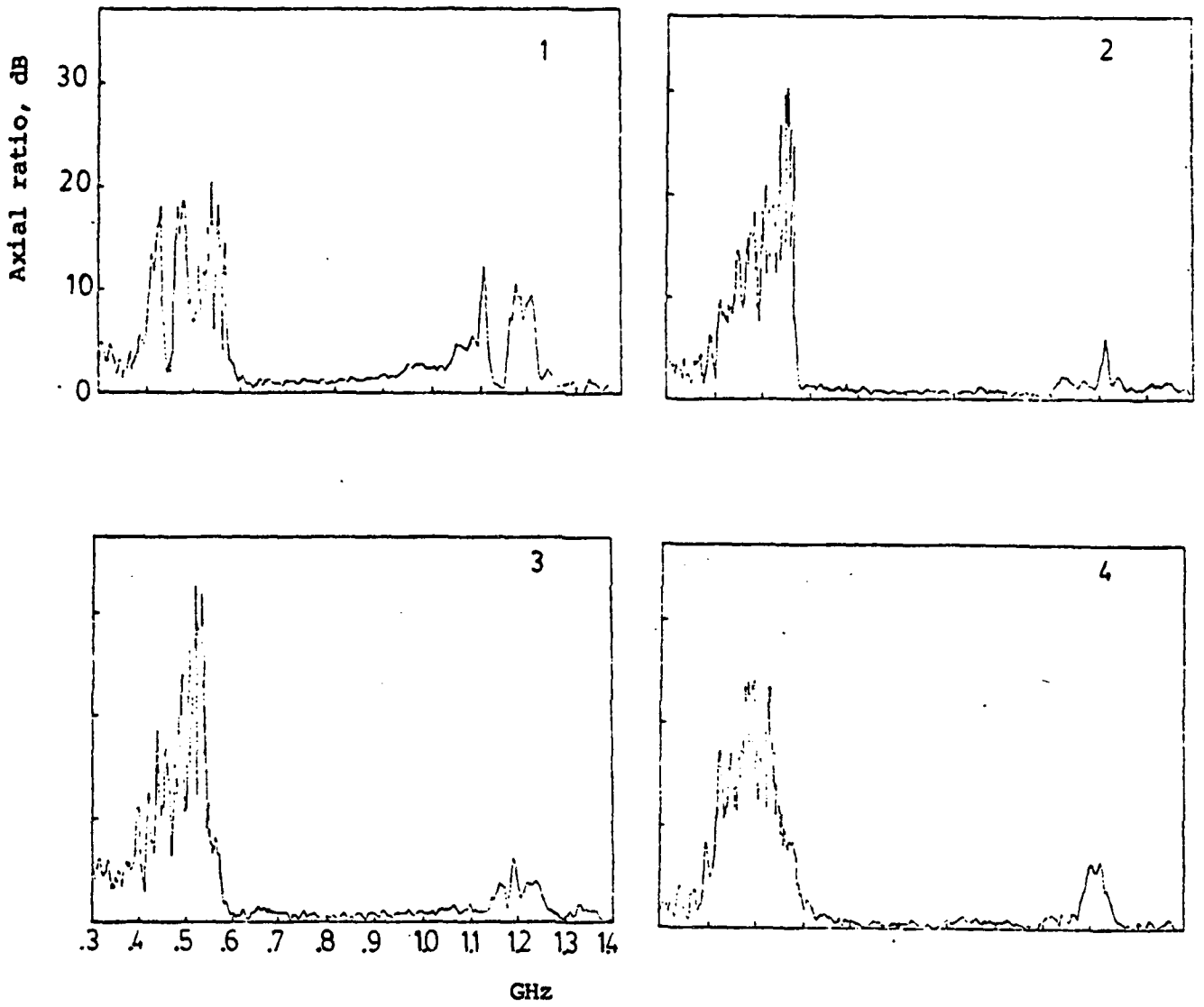

Fig. 3 Measured axial ratio for experimental helical antennas.

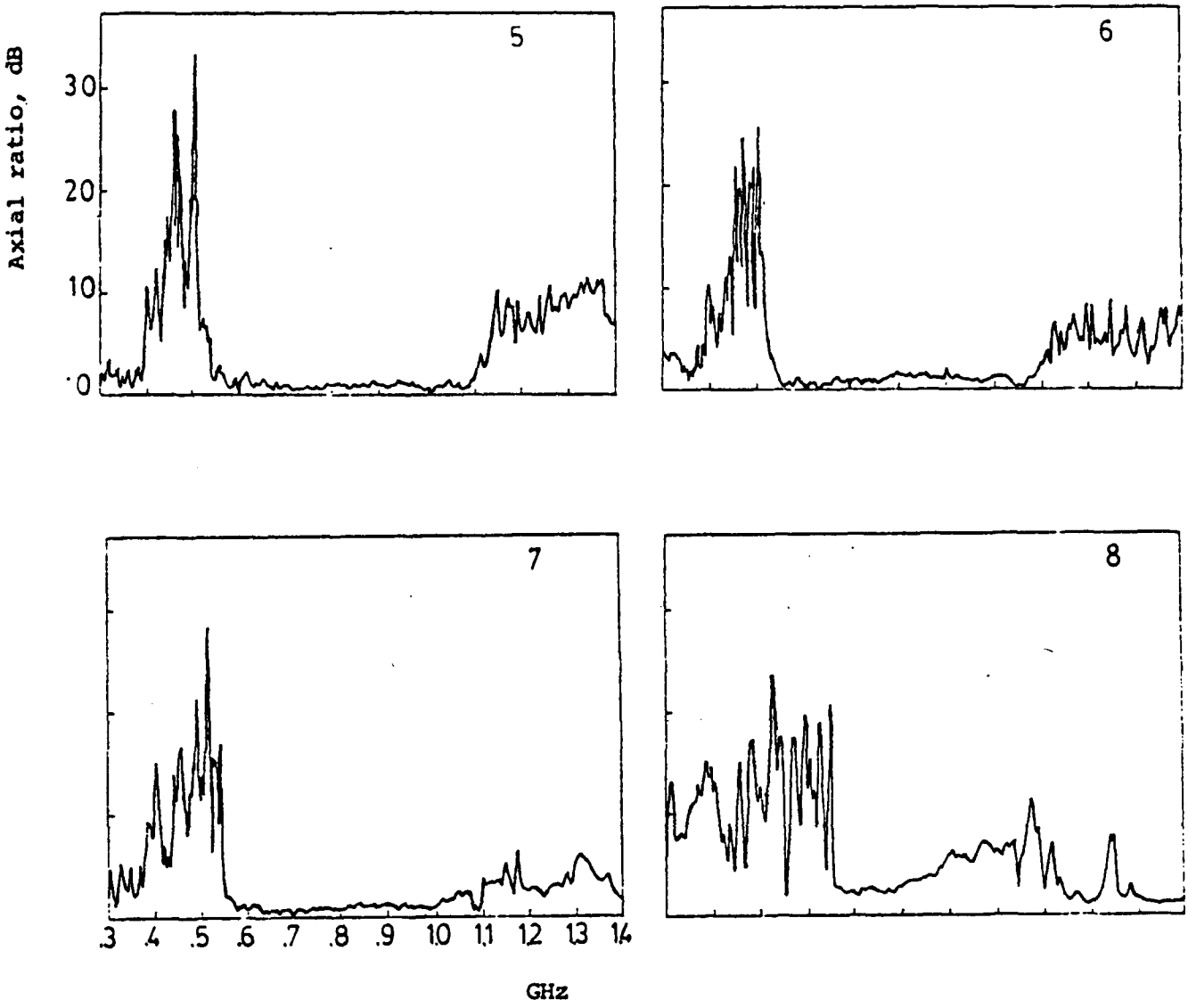

Fig. 3 (cont'd) Measured axial ratio for experimental helical antennas.

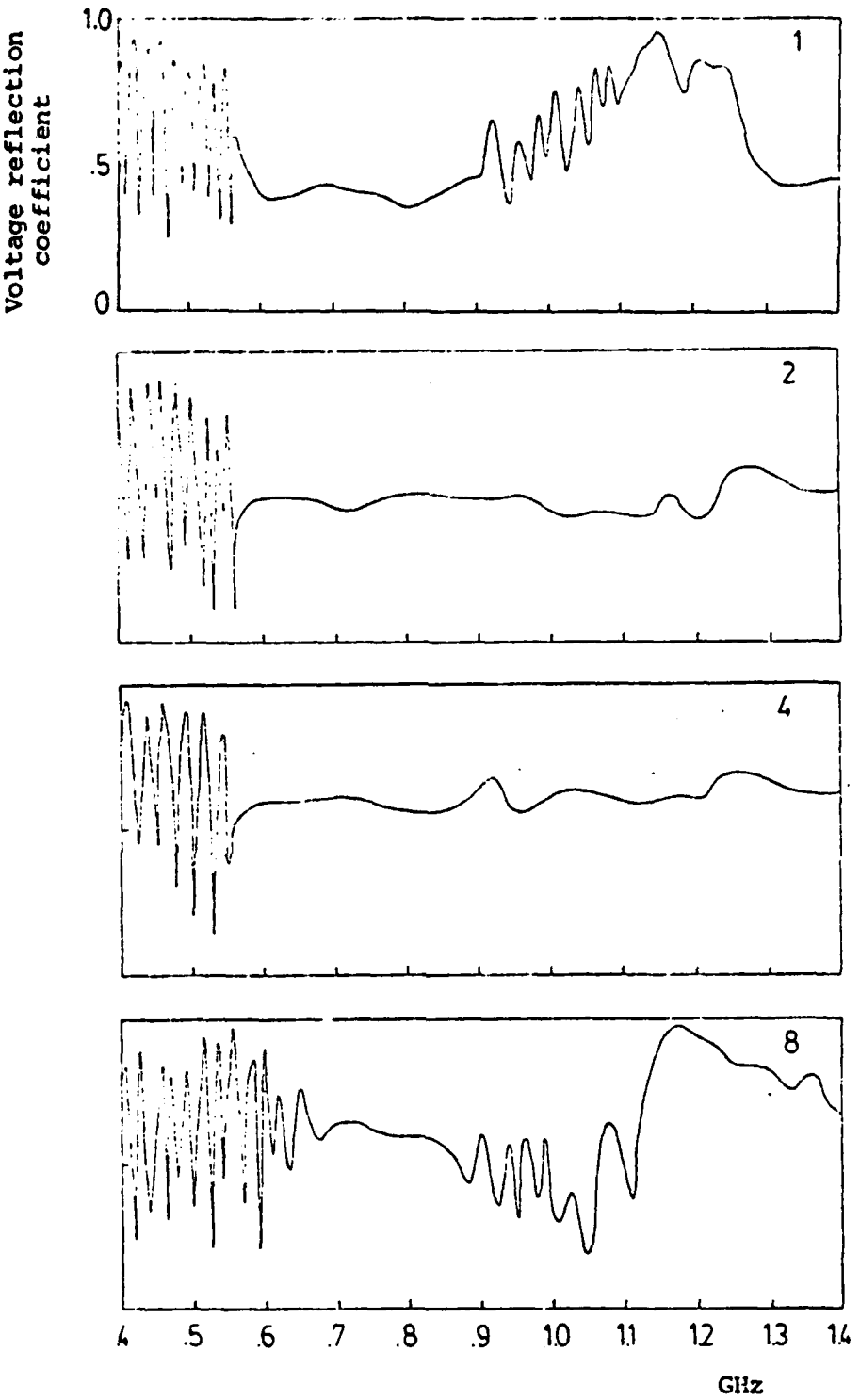

Fig. 4 Measured voltage reflection coefficient for several of the helical antennas. Antennas are fed directly from 50Ω coaxial cable. Nominal computed antenna input impedance is 130Ω for the uniform helix (#1).

were not reported in [4], are marked by very large reflection coefficients and are not suppressed by end-tapering.

DISPERSION CHARACTERISTICS

The solution of the infinite tape helix determinantal equation for both real and complex propagation coefficients has been carried out by other researchers as cited earlier and is repeated in this work (for complex propagation coefficients) using the dimensions of the uniform helical antenna being studied. Figure 5 shows the dispersion diagram for an infinite uniform helix having a diameter and pitch as in the experimental antenna. Also included in this Figure are the frequencies at which the A- and B-type anomalies were observed in the radiation patterns. We note that the A-type anomalies are associated with the region of the dispersion curve near the upper edge of the first passband and the B-type anomalies occur near the mid to upper edge of the second passband. In each case the anomalies occur in a region of the dispersion diagram where the phase shift per cell is approximately π radians, i.e. corresponding points on successive loops in the helix carry currents which are almost 180° out of phase.

ANTENNA TAPERING

Wong and King[4] have shown that various tapering schemes may be used to effectively reduce or eliminate high frequency (B-type) anomalies in the impedance and axial ratio characteristics. If we consider again the dispersion curve for the infinite uniform helix we note that the B-type anomalies occur in a region where two modes exist: an unwanted attenuated wave whose phase velocity approaches the speed of free space

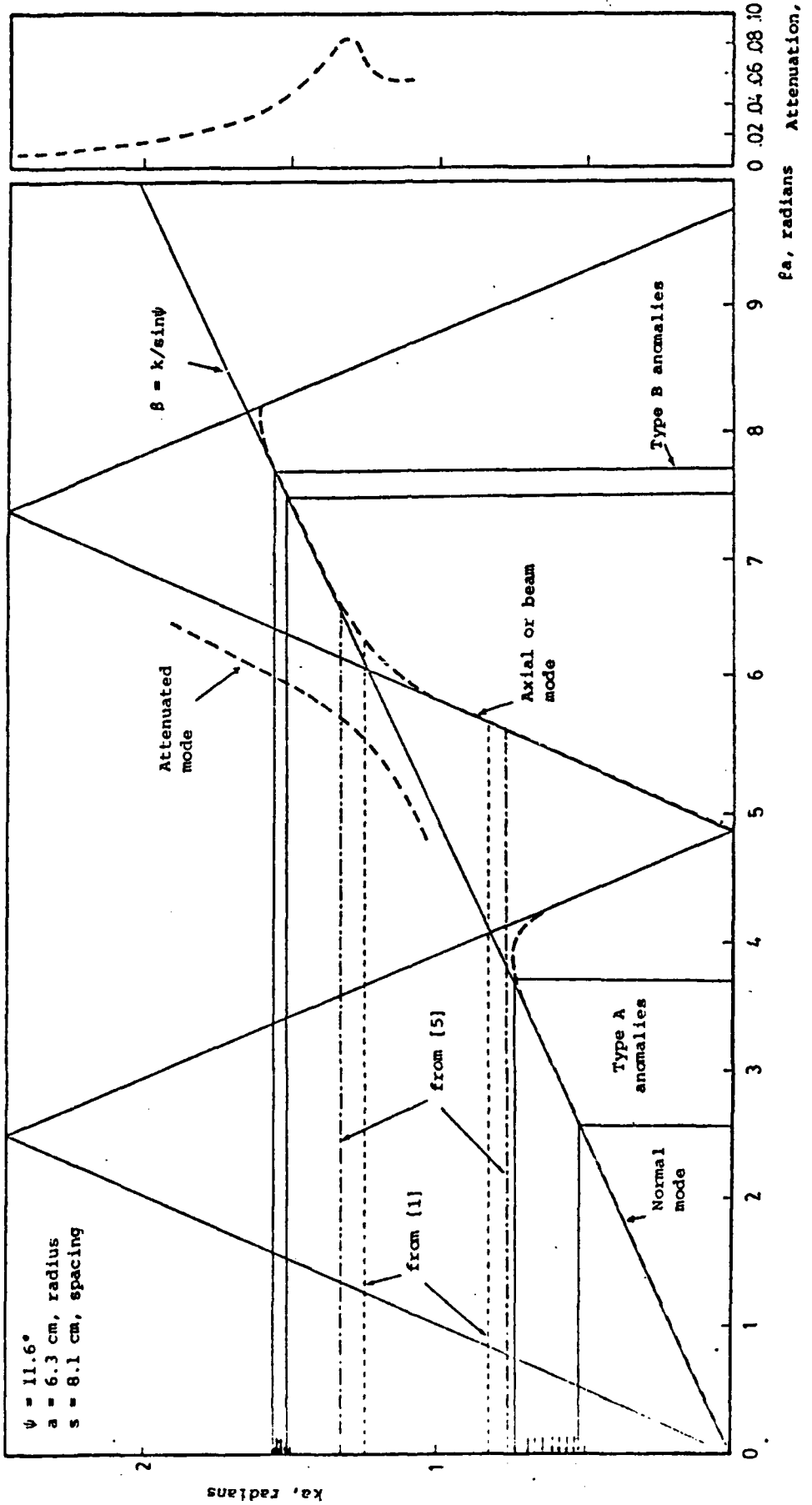

Fig. 5 Dispersion diagram for infinite uniform helix. Bandlimits for axial mode are indicated from references [1] and [5]. Attenuation curve is for the attenuated mode indicated. Arrows in the anomaly bands indicate frequencies at which anomalies were observed in radiation patterns.

propagation and a slow wave whose phase velocity is asymptotic to the line $\beta = k/\sin\psi$. The occurrence of both modes in this region and the discontinuity of the phase velocity at the end of the antenna will result in a reflection of energy from the end as has been observed on several classes of periodic dipole antennas.[6-10] In these cases tapering the antenna (or using a quasi-tapering scheme as reported by Wong and King[4]) causes the wave travelling along the helix to encounter a region of reduced radius or, referring to the dispersion curve, causes the operating point to effectively move downward along the dispersion curve (to a smaller ka value) away from the anomaly band. In so moving the operating point the attenuation of the unwanted wave increases and the phase velocity of the axial mode wave approaches that of free space, thus reducing end reflection and eliminating the anomalies. A further result of tapering would be to extend the bandwidth upward in much the same way as with the Yagi.[9]

Considering now the A-type anomalies we note that these anomalies occur immediately below the cutoff region of the normal mode. Tapering the antenna has the effect of moving the operating point downward along the curve away from the cutoff region, but in so moving the phase velocity does not approach the free space value. Instead it approaches the $\beta = k/\sin\psi$ value, thus end reflection cannot be eliminated. Measured radiation and input reflection coefficient patterns presented earlier confirm that tapering does not control these anomalies.

RELATION TO SIMILAR ANOMALOUS RESPONSES ON PERIODIC DIPOLE ARRAYS

Recent research[6-10] on the occurrence of anomalous responses in the broadband radiation characteristics of several classes of periodic

dipole arrays has shown that these anomalies are resonances which are characterized by very large out-of-phase currents on adjacent dipoles (or sets of dipoles) in the array. The phase distribution curves of these periodic dipole arrays have proven to be helpful in showing that resonances usually occur in a band immediately below the dipole array cutoff frequency where the cell phase separation is almost exactly 180°. Element tapering schemes have been successful in eliminating resonances and extending the bandwidth of Yagi arrays[10] and the use of electrically lossy material either in the transmission feedline termination or along the feedline itself on log-periodic dipole arrays has proven effective in suppressing many of the resonances on these antennas.[6,8,11]

The anomalous responses which have been observed for the helical antenna are similar to the resonances on periodic dipole arrays in several important respects:

i) they are extremely narrowband;

ii) at least several of them are dependent upon the antenna termination in that end-tapering reduces or eliminates the anomalies;

iii) the dispersion curves indicate that the anomalies occur in bands where the cell phase separation is nearly 180°.

The similarity between the anomalous responses on the helical antenna and those on periodic dipole arrays leads one to suspect that the responses on the helical antenna are also resonances which are characterized by a large standing wave due to end reflection or cutoff. In order to show conclusively that such is the case one must model the finite length helix and examine the computed current distribution as well as the

computed radiation patterns to compare with experimental results. This model is presently being developed and it is expected to be a valuable aid in the analysis and design of uniform as well as tapered helical antennas.

CONCLUSIONS

Measurements of the broadband gain-frequency plots of several helical antennas have indicated the occurrence of several anomalous responses which are characterized by very narrowband variations in gain, axial ratio and input impedance. The dispersion characteristics of the infinite uniform tape helix are obtained by solving the helix determinantal equation and are used to show that the observed anomalies occur when the loop (cell) phase separation is nearly 180°. It has been shown that end-tapering may be used to eliminate anomalies at the upper bandedge of the antenna, however the anomalies near the lower bandedge are not generally controlled by tapering. Similarities between the anomalies on the helical antenna and the resonant behaviour of periodic dipole arrays have been pointed out.

REFERENCES

1. T.S.M. MacLean and R.G. Kouyoumjian, "The Bandwidth of Helical Antennas", IRE Transactions on Antennas and Propagation, AP-7, Special Supplement, pp s379-s386, December 1959.

2. T.S.M. MacLean and W.E.J. Farvis, "The Sheath-Helix Approach to the Helical Aerial", Proceedings of IEE, Vol. 109, Part C, No. 16, pp 548-555, May 1962.

3. A.R. Neureuther, P.W. Klock and R. Mittra, "A Study of the Sheath Helix with a Conducting Core and its Application to the Helical Antenna", IEEE Transactions on Antennas and Propagation, Vol. AP-15, No. 2, pp 203-210, March 1967.

4. J.L. Wong and H.E. King, "Broadband Quasi-Taper Helical Antennas", IEEE Transactions on Antennas and Propagation, Vol. AP-27, No. 1, pp 72-78, January 1979.

5. J.D. Kraus, Antennas, New York, McGraw-Hill, 1950, pp 173-216.

6. J.M. Tranquilla and K.G. Balmain, "A Study of TEM Resonances on a Class of Parallel Dipole Arrays", Proceedings of the 1977 Antenna Applications Symposium, Urbana, Illinois, April 1977.

7. J.M. Tranquilla and K.G. Balmain, "Resonance Phenomena on Yagi Arrays", Proceedings of National Radio Science Meeting, University of Washington, Seattle, Washington, June 1979.

8. J.M. Tranquilla and K.G. Balmain, "Analysis of the Loop-Coupled Log-Periodic Dipole Array", Proceedings of National Radio Science Meeting, University of Washington, Seattle, Washington, June 1979.

9. J.M. Tranquilla and G.B. Graham, "Resonance Phenomena on Multiple-Yagi Arrays", Proceedings of 1979 Antenna Applications Symposium, Urbana, Illinois, September 1979.

10. J.M. Tranquilla and G.B. Graham, "The Development of Certain Anomalous Responses on Single Yagi Antennas as a Function of Antenna Length", Conference Digest, International Electrical, Electronics Conference and Exposition, pp 206-207, October 1979.

11. K.G. Balmain and J.N. Nkeng, "Asymmetry Phenomenon of Log-Periodic Dipole Antennas", IEEE Transactions on Antennas and Propagation, Vol. AP-24, No. 4, pp 402-410, July 1976.

CORPORATE-TUNER SHORT MONOPOLE ANTENNAS

G. Morin and K.G. Balmain
Department of Electrical Engineering
University of Toronto
Toronto, Canada M5S 1A4

INTRODUCTION

A short monopole over a highly-conducting ground has a capacitive input impedance with a small real part. In general, a great deal of tuning is necessary for this type of antenna, in the form of reactance cancellation and resistance transformation.

However, the short monopole can be made self-resonant by adding a horizontal wire at its top, making the so-called "inverted-L antenna". At resonance, its input resistance is about four times higher than the real part of the input impedance of the monopole itself at the same frequency. Still, it is far from the 50 ohms of a standard cable and a tuner is necessary to match the antenna to the transmission line.

It is shown in this paper that by adding one or two more wires to the inverted-L antenna, one can increase significantly the input resistance at resonance without degradation of the efficiency. Moreover, in some cases, an increase in the bandwidth of the antenna can be obtained.

This work was supported by the National Sciences and Engineering Research Council of Canada, under Grant A-4140.

REVIEW OF THE INVERTED-L ANTENNA

The widely used inverted-L antenna has been thoroughly described by King and Harrison [1969]. It consists of a quarter-wavelength monopole bent at 90° at some distance H from the ground, as in Fig. 1.

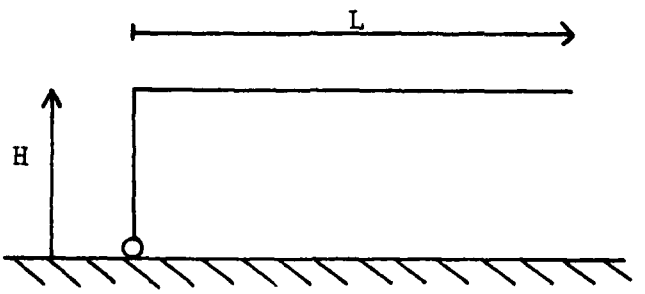

Fig. 1 Inverted-L antenna

The first resonance occurs when

$$L + H \approx \lambda/4 \tag{1}$$

The radiation resistance, when H<<L, is given by King and Harrison [1969] as

$$R = \frac{60\,\beta^2 H^2}{\sin^2 \beta L}\left(1 - \frac{\sin 2\beta L}{2\beta L}\right) \tag{2}$$

where $\beta = 2\pi/\lambda$.

Using a thin-wire program from Richmond [1974], one can compute the input impedance and the power gain. In Fig. 2c, the input impedance, as computed, is plotted on a Smith chart for the antenna in Fig. 2a. The wire is made of copper and its diameter is 0.81 mm. The antenna is fed with a 50-ohm transmission line. Fig. 2b shows G_z versus frequency where G_z is the power gain in the horizontal plane minus the mismatch loss in the 50-ohm transmission line. One notices that the resonance occurs approximately at 500 MHz as predicted by (1). The resistance at resonance is about 12 ohms. The ef-

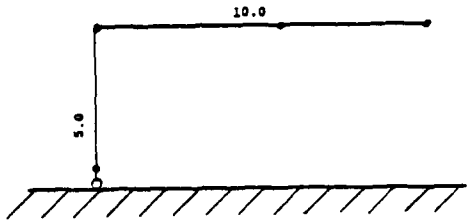

(a)

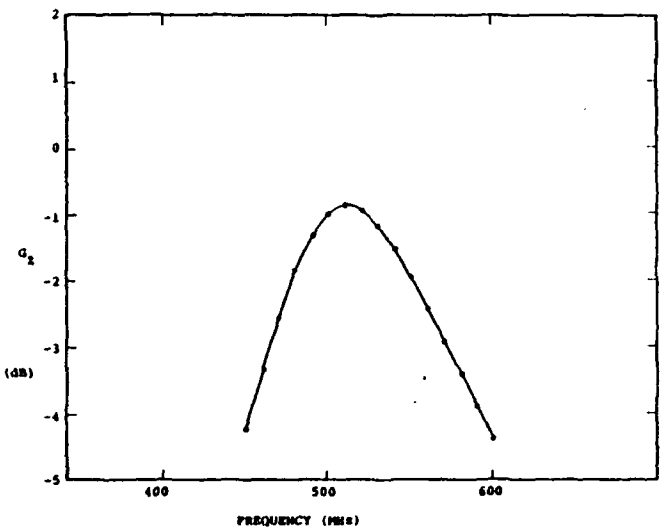

(b)

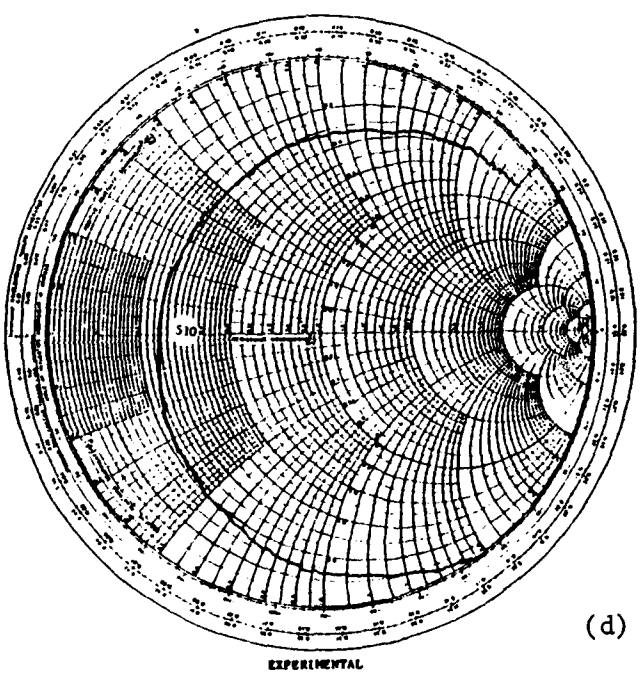

(d)

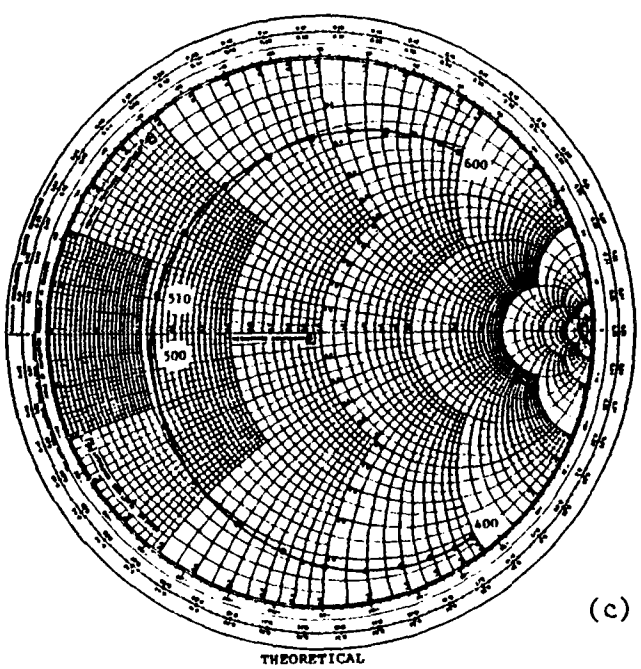

(c)

Fig. 2 Inverted-L antenna

ficiency at 500 MHz is 98.5% as computed by the program. Figure 2d shows measurements of the impedance; the agreement with the computed impedance is within 15% while the resonant frequency is predicted to within 2%.

A simplified circuit model for the inverted-L antenna is the series RLC circuit in Fig. 3,

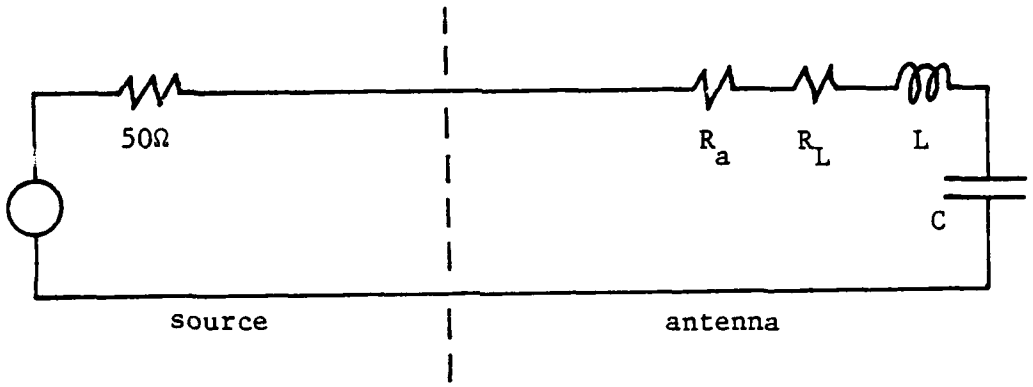

Fig. 3 Simplified model of an inverted-L antenna

where R_a is the radiation resistance and R_L is the loss resistance in the wire.

THE F ANTENNA

The working principle of an F antenna is the same as tapping into a parallel-resonant circuit or a half-wave transmission-line resonator.

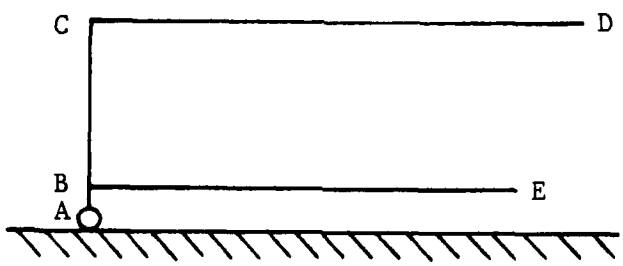

Fig. 4 F antenna

In Fig. 4, the segment DCBE will resonate when its length is about $\lambda/2$. The generator is connected by AB somewhere close to the center of DCBE. When the resonance occurs, a strong current flows in CB which produces the desired radiation. However a smaller current flows in AB and the generator sees a larger resistance than it would see without BE.

In Fig. 5, the computed input impedance and gain G_z are plotted for one particular case, along with the impedance measured in the laboratory. One notices that the impedance curve is characteristic of coupled resonators. The input resistance at 540 MHz is about 50 ohms as desired. G_z has increased by almost 2 dB at its maximum but the bandwidth is smaller. The computed efficiency at the maximum gain frequency is 97.2%, a decrease of 1.3% compared to the inverted-L antenna.

Fig. 6 shows a comparison of G_z for an F antenna with G_z for an inverted-L antenna using a perfect transformer to match it to the transmission line. It can be seen that the gain and bandwidth are almost the same but the F-antenna curve shows some asymmetry.

The thin-wire computer program gives the currents in the wires. It is found that, at resonance, all currents are in phase in the directions indicated in Fig. 7 below.

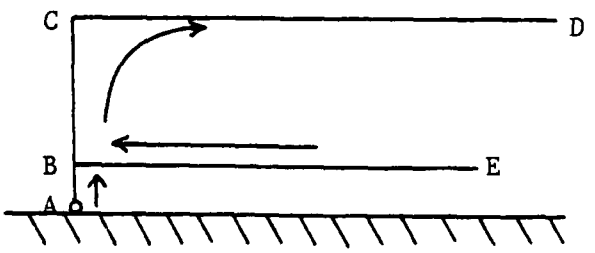

Fig. 7 Currents in F antenna

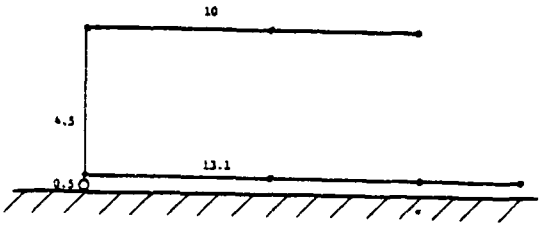

(a)

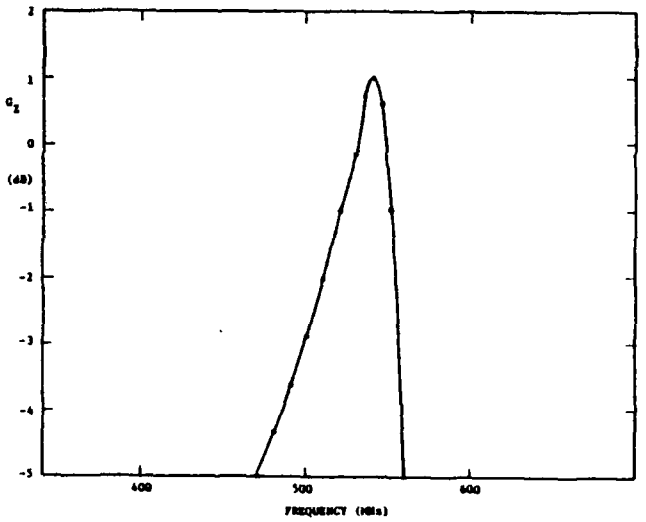

(b)

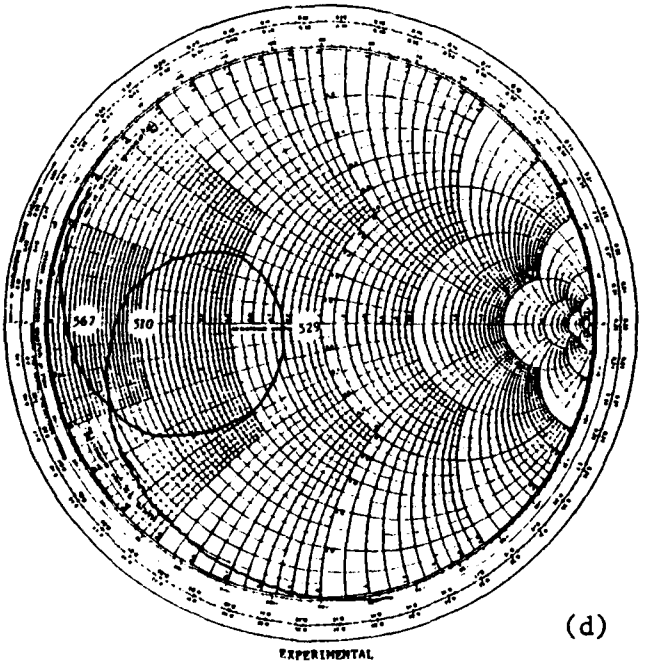

(d)

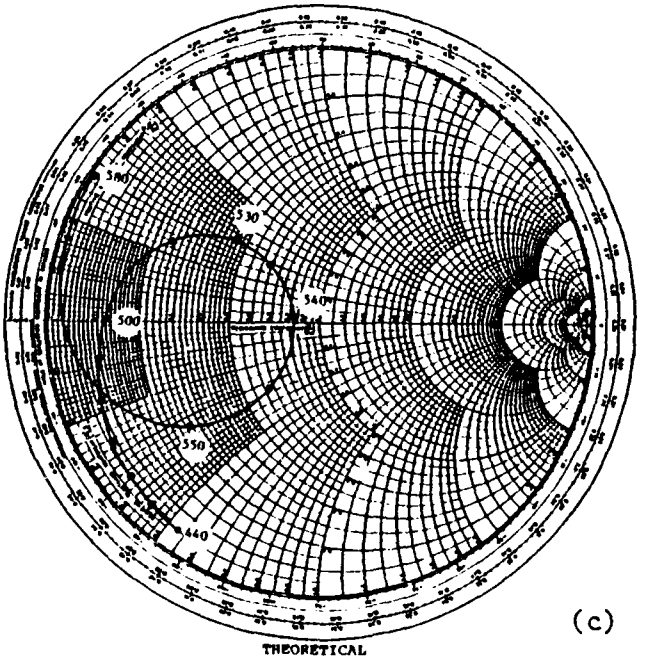

(c)

Fig. 5 F antenna

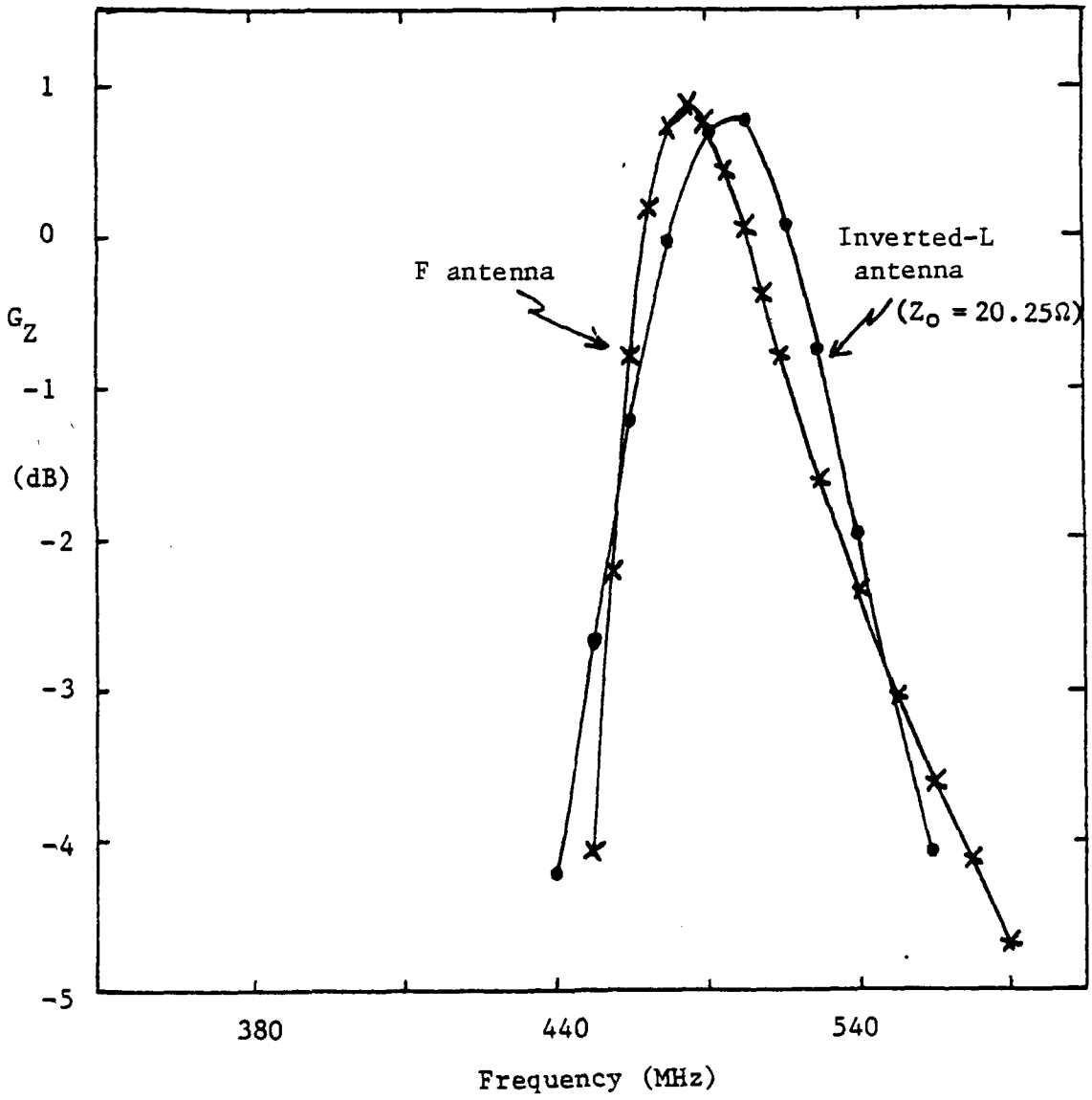

Fig. 6 Comparison of F antenna with inverted-L matched with perfect transformer (Z_o is transmission line impedance seen through the transformer).

The current in the generator is smaller than the current in BC as expected.

A simplified circuit model of the antenna is given in Fig. 8.

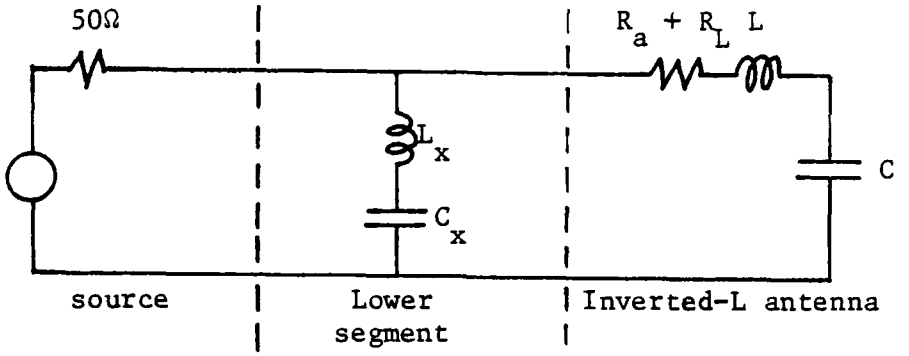

Fig. 8 Circuit model of F antenna.

The bottom wire is represented by the two components $L_x C_x$ in parallel with the inverted-L antenna. The radiation and loss in the lower segment are neglected. One can show easily that $L_x C_x$ shift the natural resonant frequency of the inverted-L antenna up or down depending on their values. The larger the shift, the larger the input resistance will be.

It is found experimentally and theoretically that any input resistance can be obtained by adjusting the length of the bottom wire but this is at the expense of the bandwidth.

THE DOUBLE-F ANTENNA

An extra wire can still be added to the F antenna in order to obtain even better performance. This is what we called a "Double-F antenna" as illustrated in Fig. 9.

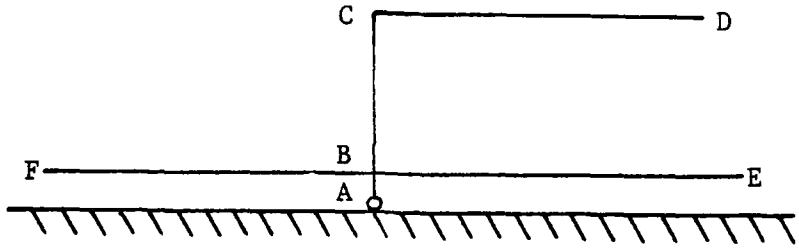

Fig. 9 Double-F antenna

In Fig. 10, an example is given where it is attempted to obtain a constant VSWR throughout the passband. Compared to the inverted-L antenna, the Double-F antenna has a high gain G_z and larger bandwidth. Compared to the F antenna it has larger bandwidth but smaller gain.

The analysis of the currents in the antenna explains how the increased bandwidth is obtained. Let us assume that FB is larger than BE. The first resonance occurs when FBCD is about half a wavelength long. The next resonance occurs when ABCD is about a quarter of a wavelength long and the last one, when EBCD is about half a wavelength long. These three resonances combined together yield the exceptional bandwidth obtained. It is noticed that two of the resonances are similar to the one in the F antenna and that the second resonance is similar to the inverted-L antenna. Therefore, both F-antenna-type resonances have an adjustable input resistance but not the other one.

A simplified circuit model of the Double-F antenna is the following:

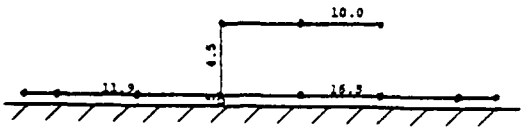

(a)

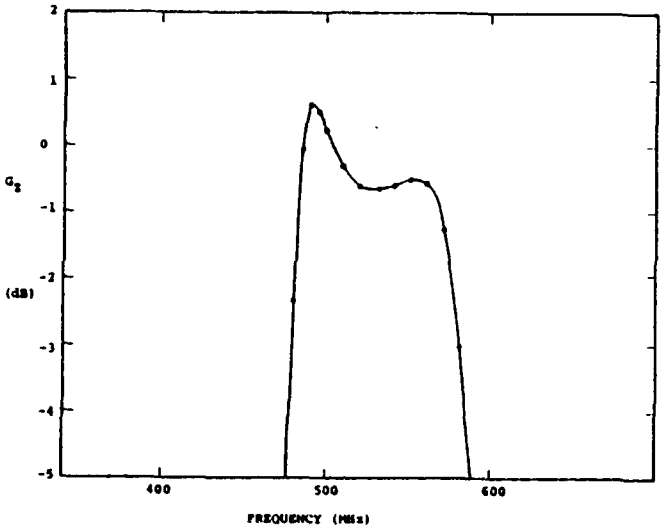

(b)

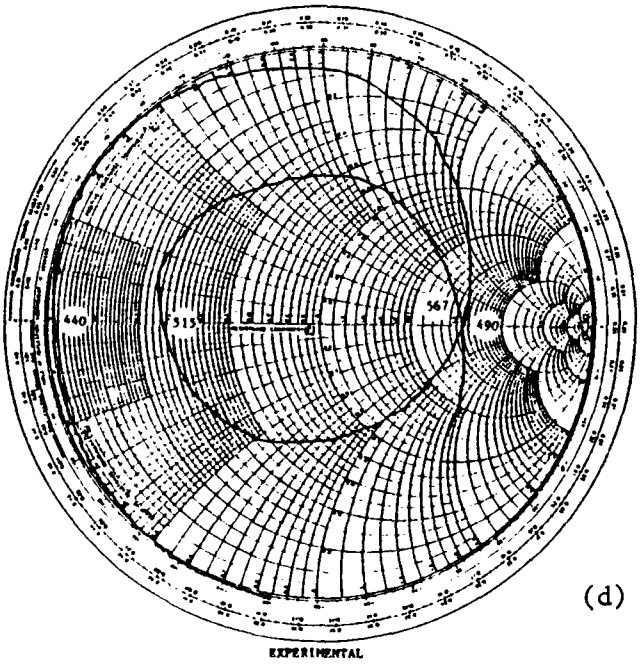

(d)

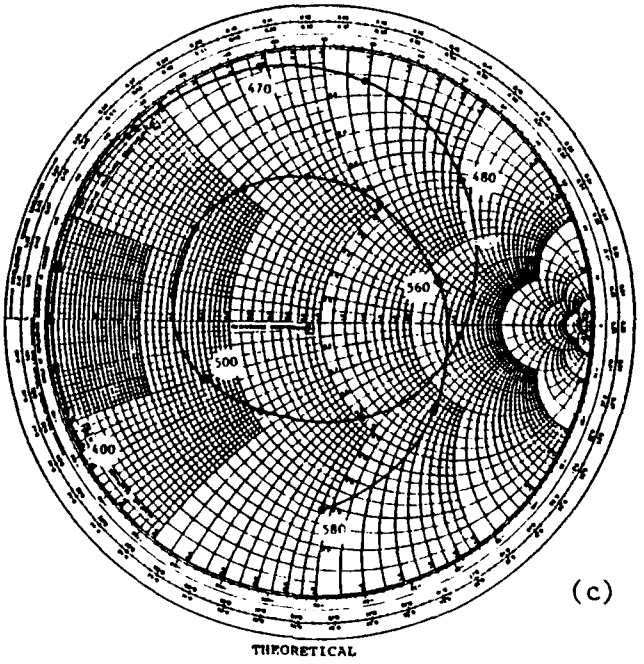

(c)

Fig. 10 Double-F antenna

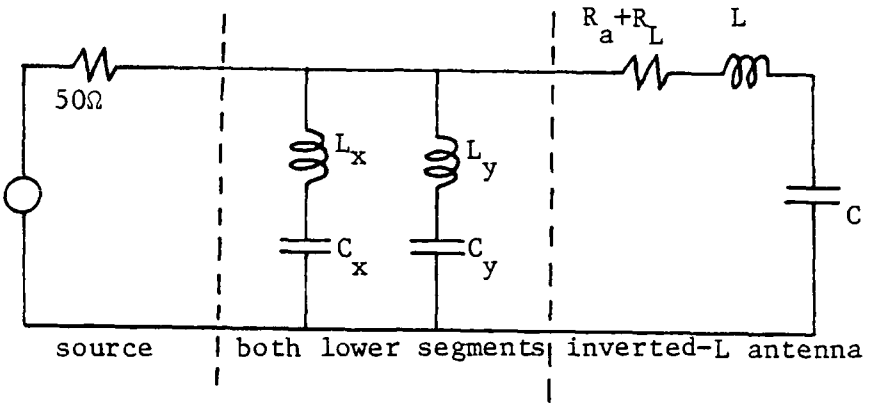

Fig. 11 Double-F antenna

This is equivalent to a double-tuning of the antenna. It can be easily seen that L_xC_x and L_yC_y short the generator at their own resonant frequencies and thus they impose limits on the bandwidth of the system. The resonance of $L_xC_xL_yC_y$ combined is equivalent to the resonance with FBE$\approx\lambda/2$. However, it does not appear on the graphs because it has a very high impedance which is in parallel with the comparatively low impedance of the inverted-L section.

Fig. 12 shows a higher Double-F antenna. The power gain and the bandwidth are increased compared to the previous antenna in Fig. 10. The bottom wires must be close to the ground if the antenna is to function properly. However, these wires do not have to be tied together. By changing their heights above the ground it is possible to get a better match of the antenna to the transmission line. Fig. 13 shows an example where a smaller VSWR

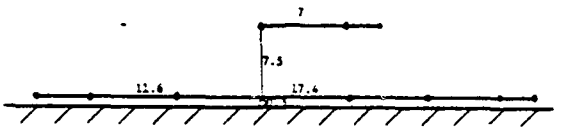

(a)

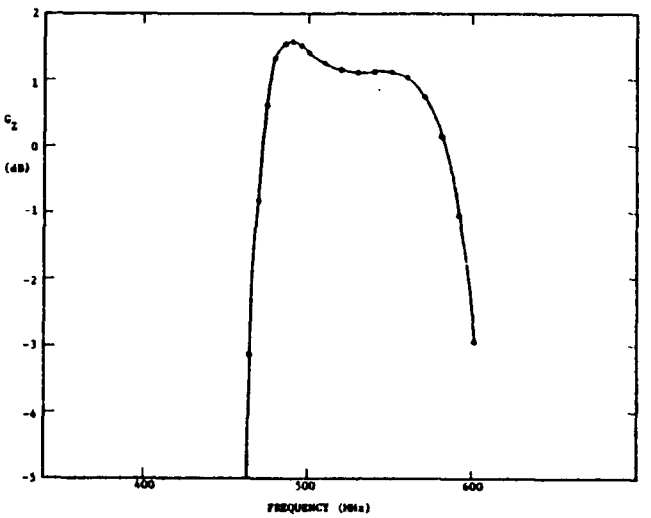

(b)

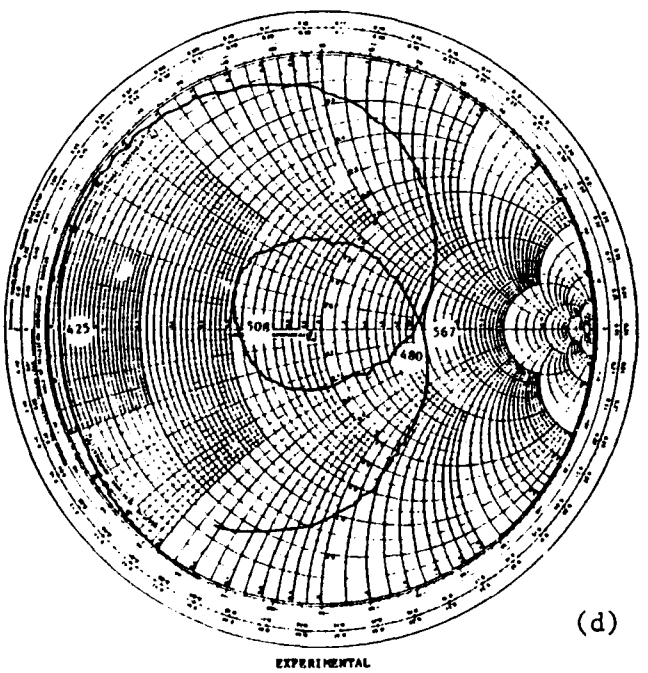

(d)

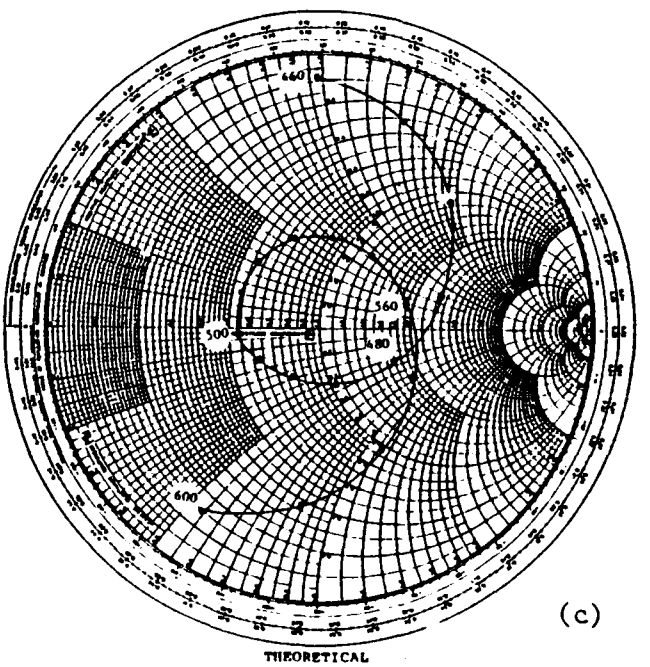

(c)

Fig. 12 Double-F antenna

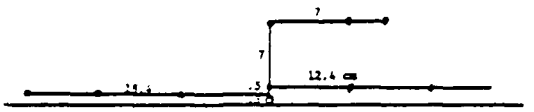

(a)

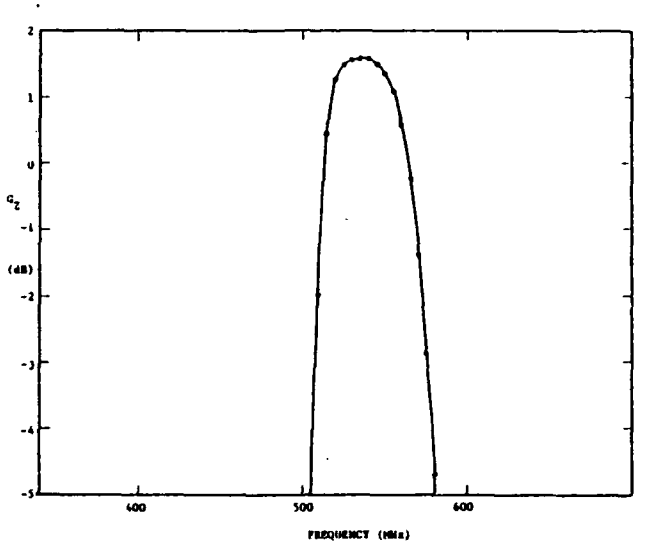

(b)

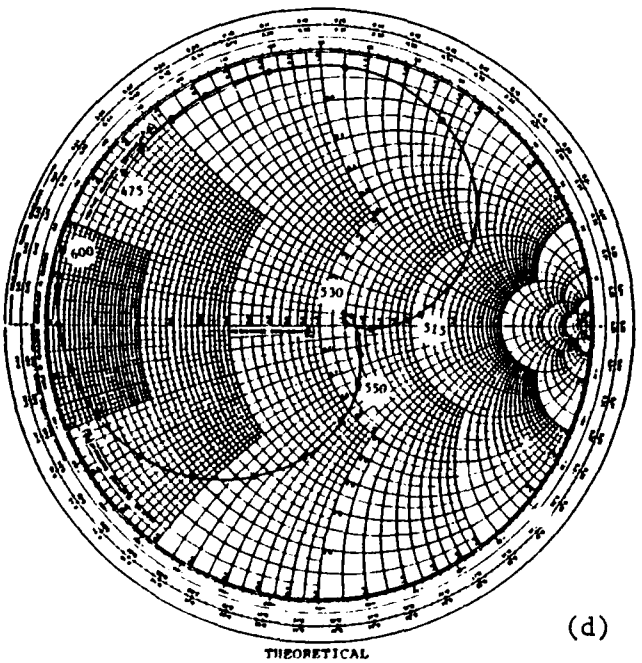

(d)

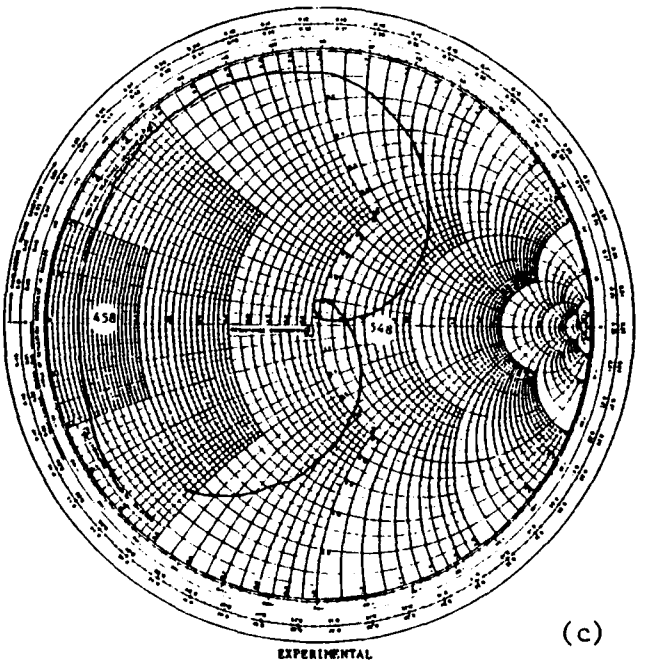

(c)

Fig. 13 Modified Double-F antenna

than before is obtained. The gain is as good as an F antenna but the bandwidth is larger.

The F and Double-F antenna can have their horizontal segments wrapped in their respective horizontal planes without affecting greatly their frequency response. A loose wrapping decreases the bandwidth and increases slightly the gain G_z due to less radiation in unwanted directions by these segments. However, a tighter wrapping will decrease G_z due to a decrease in the efficiency caused by the proximity of the wires.

CONCLUSIONS

In this paper, it is shown that the F-antenna can replace advantageously the inverted-L antenna because of its higher input resistance. The Double-F antenna is shown to have a larger bandwidth than either the F or the inverted-L antenna and a higher impedance than the inverted-L antenna.

REFERENCES

King, R.W.P., Harrison, C.W. (1969), Antennas and waves: a modern approach, MIT Press, Cambridge, Mass.

Richmond, J.H. (1974), Computer program for thin-wire structures in homogeneous conducting medium, NASA CR-2399, June 1974.

GLOBAL POSITIONING SYSTEM MONITOR STATION ANTENNA

Lenrod Goldstone
IBM
Owego, N.Y.

INTRODUCTION

A ground station antenna has been designed to enable the hemispheric recep- of Space Vehicle generated signals in the L-Band region (1.227 and 1.575 GHz) while simultaneously rejecting multipath signals arriving from below the horizon. The antenna type, a modified turnstile antenna, was selected for development from among various candidate antennas because of its simplicity in electrical design and mechanical construction, its ease of development, and its low initial and production costs.

The objectives of the Monitor Station Antenna can be summarized as follows: The antenna element is to be contained within a volume 5' in diameter and 3' in height and weigh less than 50 pounds. The antenna is to remain in operation worldwide in an ambient temperature range of -42° to +52°C with wind velocities of up to 60 meters per second and precipitation rates of up to 10cm per hour. The antenna can be protected by a radome and use up to 3KW of heating elements to keep the radome, radiating elements, and ground plane clear of snow and ice.

The antenna performance is to fall within the limits of gain shown in Figure 1 when illuminated by a right circular polarized signal of 2dB maximum axial ratio at 1227 ± 20MHz and 1575 ± 20 MHz, and its phase center is to remain within ±2cm over 15° to 90° in elevation and for any azimuth.

DESIGN ALTERNATIVES

Many candidate antennas were considered among which were: Combinations of monopole and turnstiles, crossed cavity backed slots, microstrip patch antennas, quadrifilar and conical helics, volute antennas, hybrid spirals, and the horizontal turnstile.

From the list of candidates, a modification of the horizontal turnstile was selected because of its extreme simplicity and because it had the best overall marks in a parameter study performed by the author and summarized in figure 2.

DESIGN PROCEDURE

The basic radiating element is a dipole constructed from two equal lengths of .141 diameter semi-rigid cable with the outer conductor stripped from the end of the cable and the cables bent to form a sleeve dipole as shown in figure 3. The two transmission lines are soldered together and brought behind the ground plane where they are connected to a 180° hybrid to provide the balun for the dipole.

A dipole placed 1/4 λ above the ground plane does not provide sufficient coverage to satisfy the "hemispherical" coverage requirement of the objectives, nor is the E and H plane patterns close enough to being equal to satisfy the eliptical polarization requirements of the objectives.

The first step in broadening the E plane pattern was to bend the arms toward the ground place to simulate more of a loop effect. This was not sufficient to obtain the desired result so the element was raised above the ground plane

to almost 1/2 wavelength to flatten the E plane pattern and direct the energy more toward the horizon. The results are shown in figure 4.

The circular ground plane size was selected at 56" to give maximum multipath rejection from below the horizon and represents a compromise between back lobe suppression and wind and de-icing surface area.

After the single dipole was developed for pattern, impedance match was examined in order to produce the lowest insertion loss. Since the dipole is to be fed by a hybrid, any reflected energy would end up in the termination and the input VSWR would appear to be that of the hybrid. If the antenna element itself had a large VSWR, the resulting gain loss would be equal to the transmission loss associated with that VSWR. Thus, the VSWR of the antenna element must be less than 1.5.1 to keep the VSWR loss less than 0.2 dB.

The impedance of each half of the sleeve dipole was measured by using two identical slotted lines between the 180° hybrid and the dipole as shown in figure 5. The length of the sleeve dipoles were adjusted slightly to match the low end of the band and the resulting impedance at a reference plane below the ground plane as shown in figure 6.

Examination of the curve shows that the two frequencies of interest 1227 and 1575 MHz can be impedance matched by a low impedance transformer that is approximately 1/2 long at 1227 and almost 3/4 long at 1575 unaffecting the VSWR at 1227 while matching 1575. A 25 ohm transformer was selected because it was the closest commercially available transmission line that would accomplish the desired results. The impedance after matching is shown in figure 7.

The design procedure is now almost complete, only requiring the addition of the second dipole. This is a simple matter and the complete turnstile can now be constructed using 4 equal lengths of transmission line with the outer conductors stripped off and the ends all bent downward in an identical manner as was done for the single dipole. The 4 outer jackets are then soldered together and brought below the ground plane. There, the four 25 ohm transformers are connected in place and the outputs are connected to two 90° hybrids which in turn are connected to one 180° hybrid. The output of the 180° hybrid is brought out through the pipe support which houses the hybrid and matching network and supports the ground plane. The complete schematic is shown in figure 8 and the antenna is shown in figure 9.

The patterns of each band recorded using a RHCP transmitter is shown in figure 10 and 13 and the final VSWR is shown in figure 14. The phase center patterns are shown in figure 15 and 16.

Besides the simplicity of the electrical design and ease of construction, an additional advantage of this design is that it does not require a radome and the whole antenna can be de-iced by heating the ground plane and the dipole outer conductors. The tight fit of the outer jacket of the cable to the teflon and the teflon to the center conductor provides a water tight seal preventing moisture from entering the dipole.

CONCLUSION

A simple, inexpensive, easily manufacturable antenna has been constructed from four pieces of .141 semi-rigid cable, 3 hybrids, a piece of pipe and a handful of connectors. This antenna satisfies the requirements of the global positioning system monitor station antenna. This antenna prototype has been in operation in Sunnyvale, California and in Gaithersburg, Md. since February 1980 and has provided a steady multipath free signal from satellites from rising to setting from about 5° above the horizon.

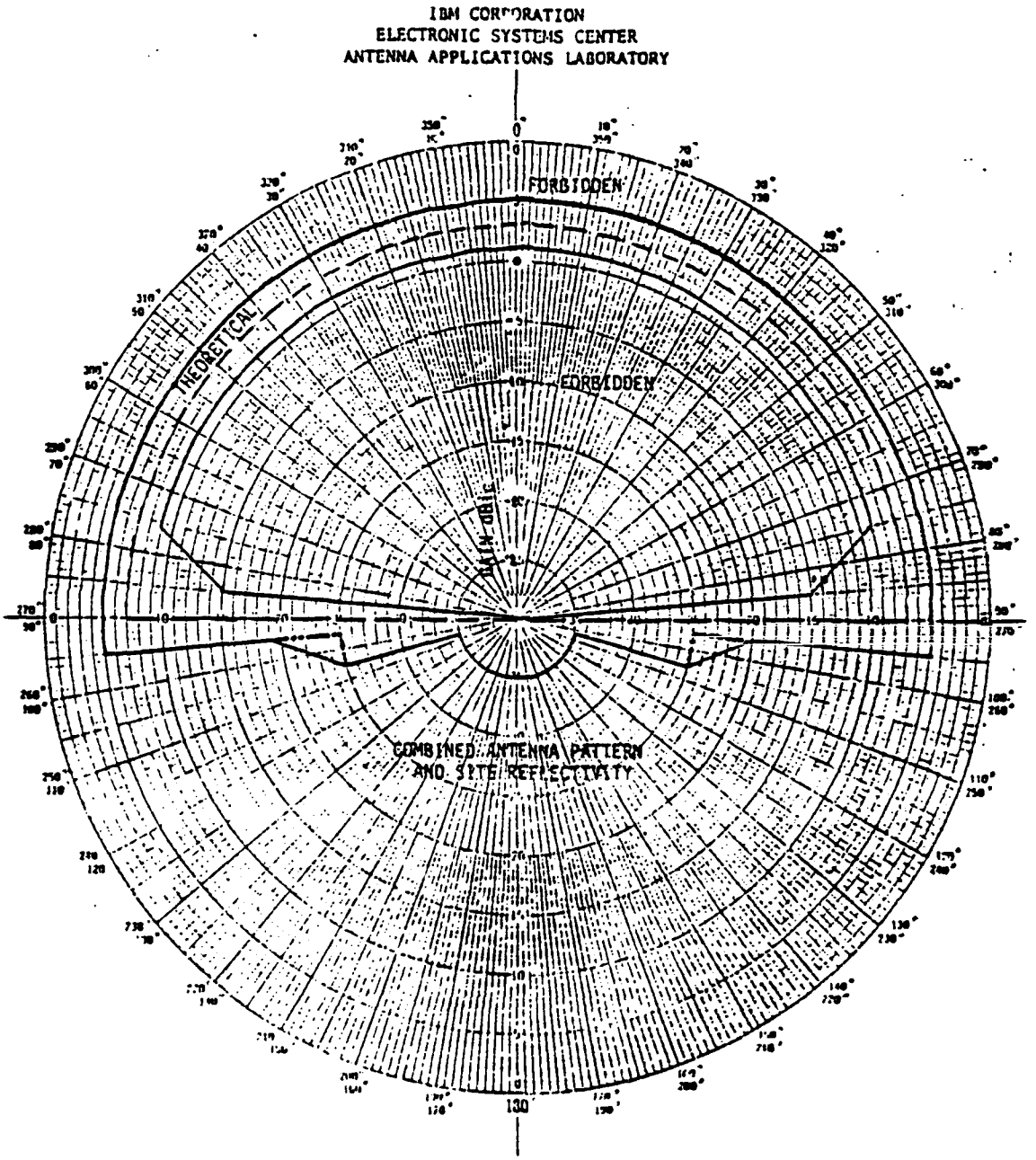

Figure 1. Antenna Gain Objectives.

GPS Monitor Station Antenna Trade-Off

	Parameters							
Candidates	Coverage	Rejection	Phase Stability	Single Antenna	Ground Plane	Ease of De-icing	Reliability	Cost
Vert Array/Turn	Good	Fair	Fair	No	No	Fair	Medium	High
Monopole-Turnstyle	Good	Fair	Good	No	Yes	Fair	Medium	Medium
Crossed Slot	Fair	Fair	Excellent	Yes	Yes	Fair	High	Low
Microstrip "Patch"	Fair	Fair	Excellent	No	Yes	Fair	Medium	Low
Quadrifilar Helix	Good	Fair	Unknown	No	No	Good	" Medium	Medium-Low
Conical Spiral	Fair	Fair	Poor	Yes	No	Good	High	Low
Horn	Fair	Fair	Excellent	Yes	No	Fair	High	Medium
Horizontal Turnstyle	Good	Fair	Good	Yes	Yes	Good	High	Low
Volute	Fair	Poor	Unknown	Yes	No	Good	High	Low
Hybrid Spiral	Good	Fair	Unknown	Yes	Yes	Fair	High	Low

Figure 2. Parameter Study Summary.

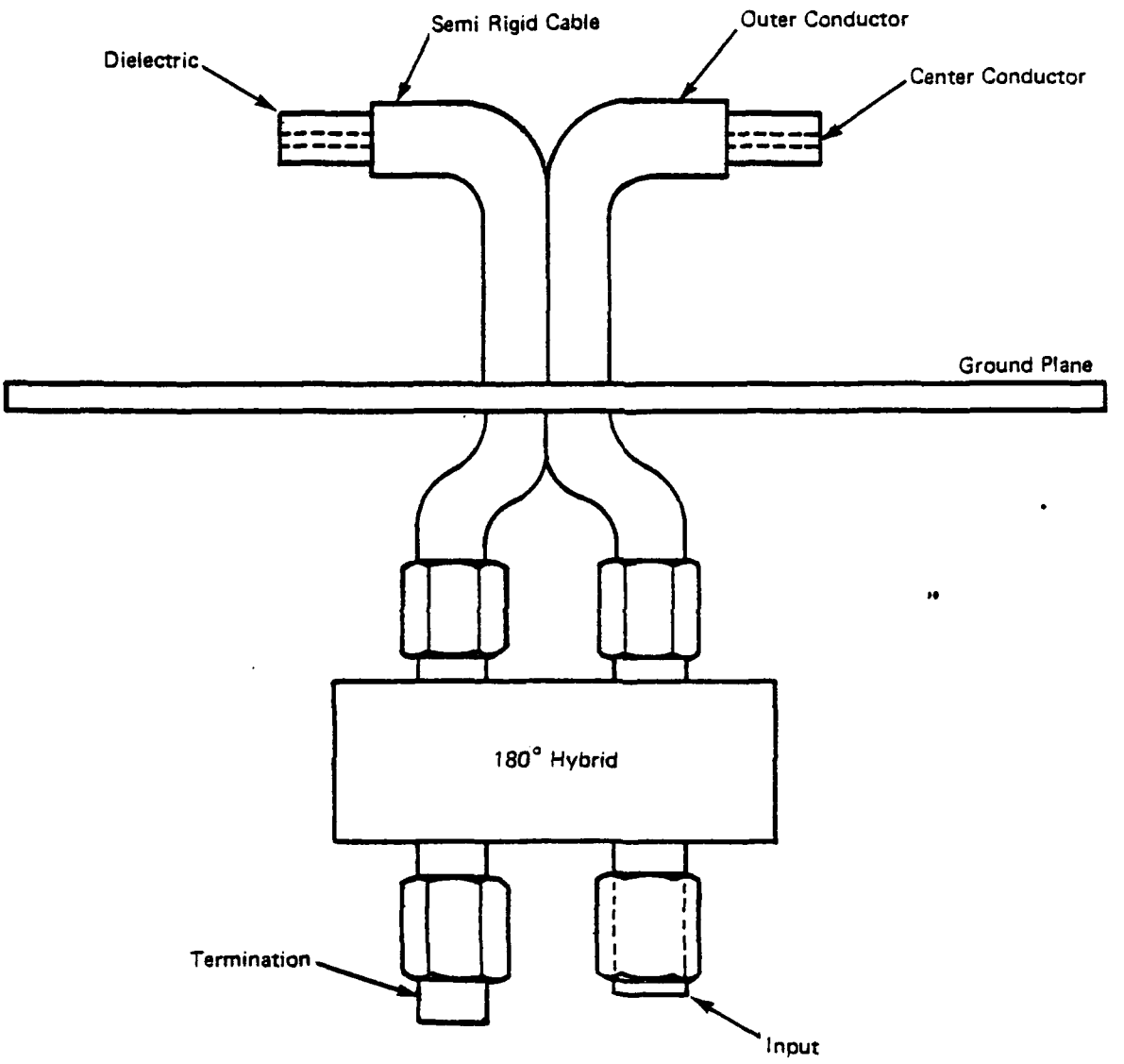

Figure 3. Basic Sleeve Dipole.

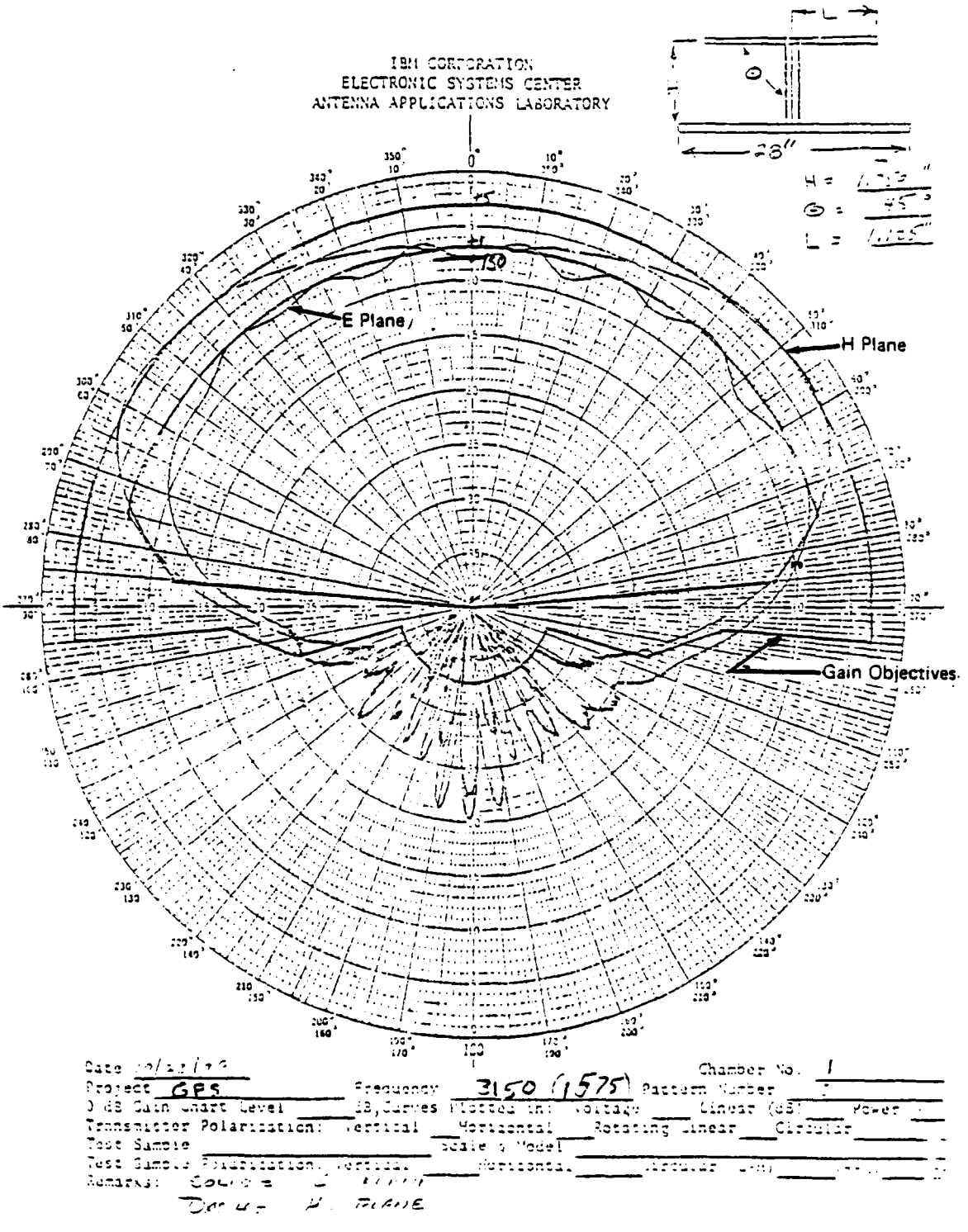

Figure 4. Pattern of Single Bent Dipole.

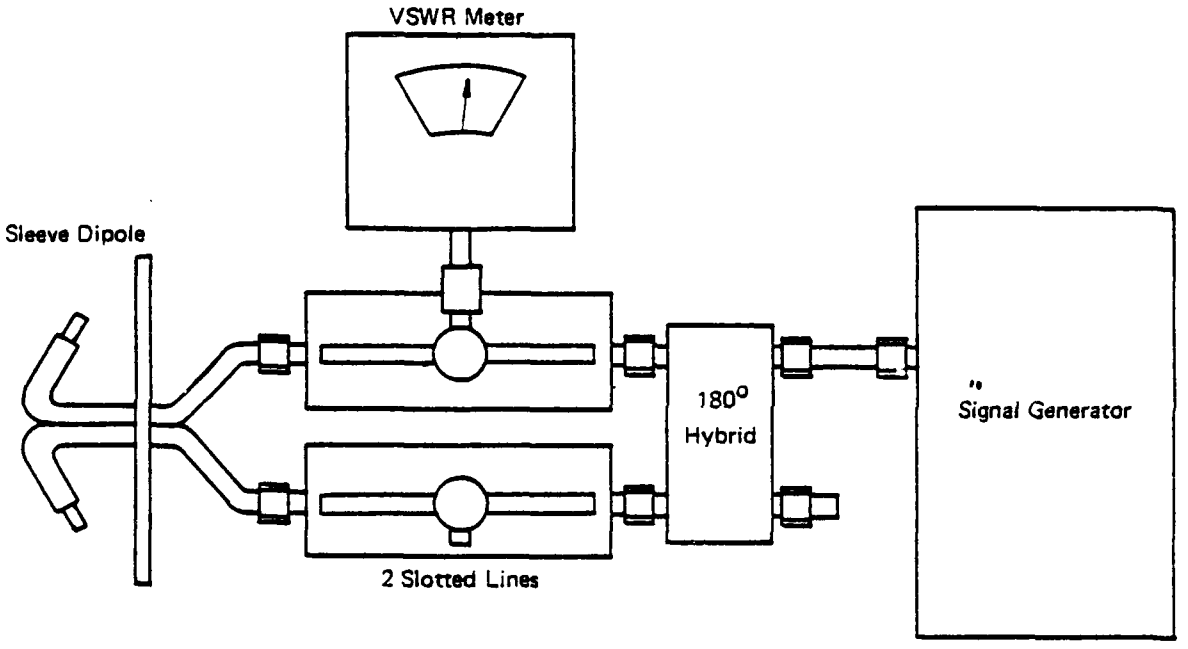

Figure 5. Two Slotted Line Impedance Measurement.

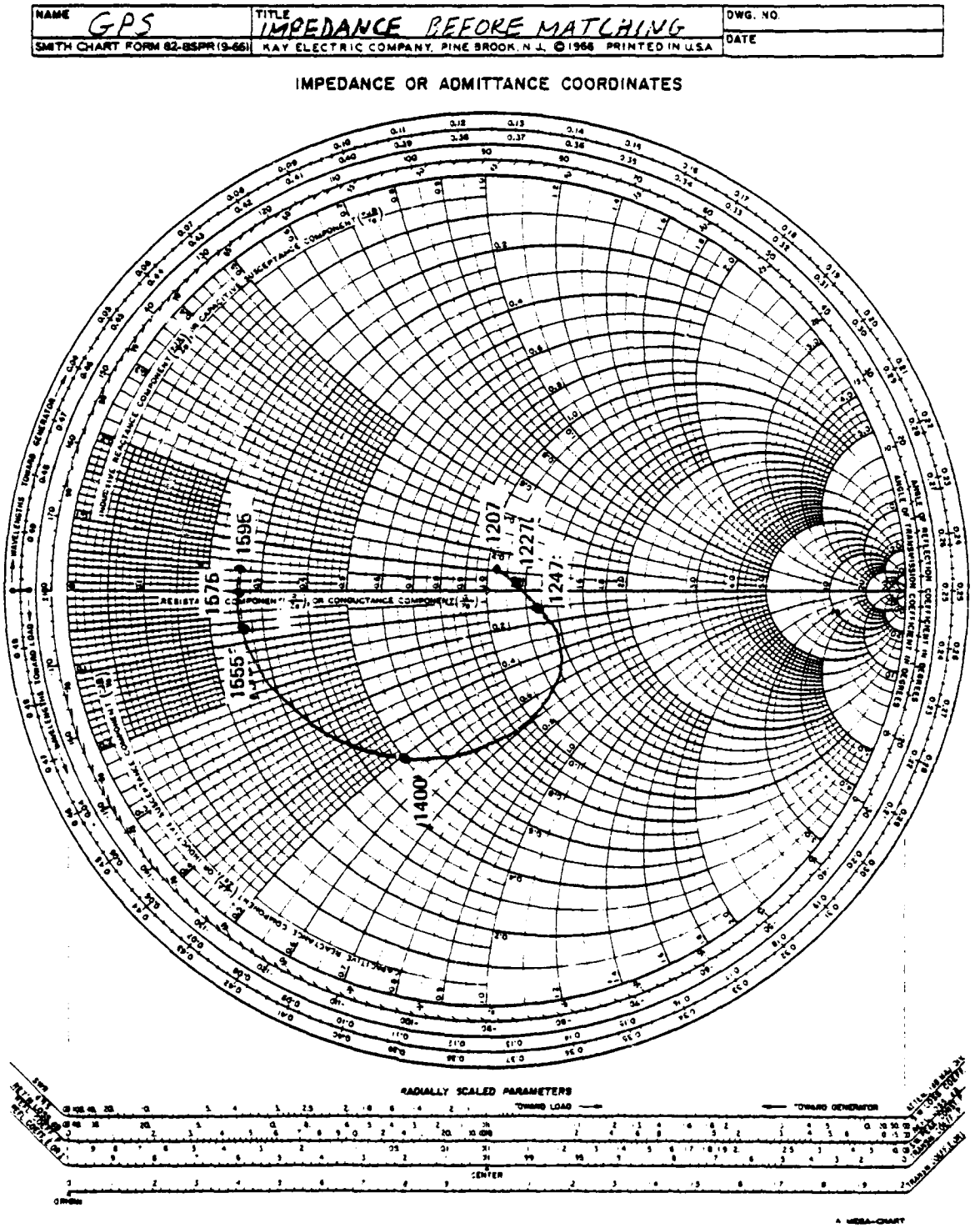

Figure 6. Impedance of Dipole Half before Matching.

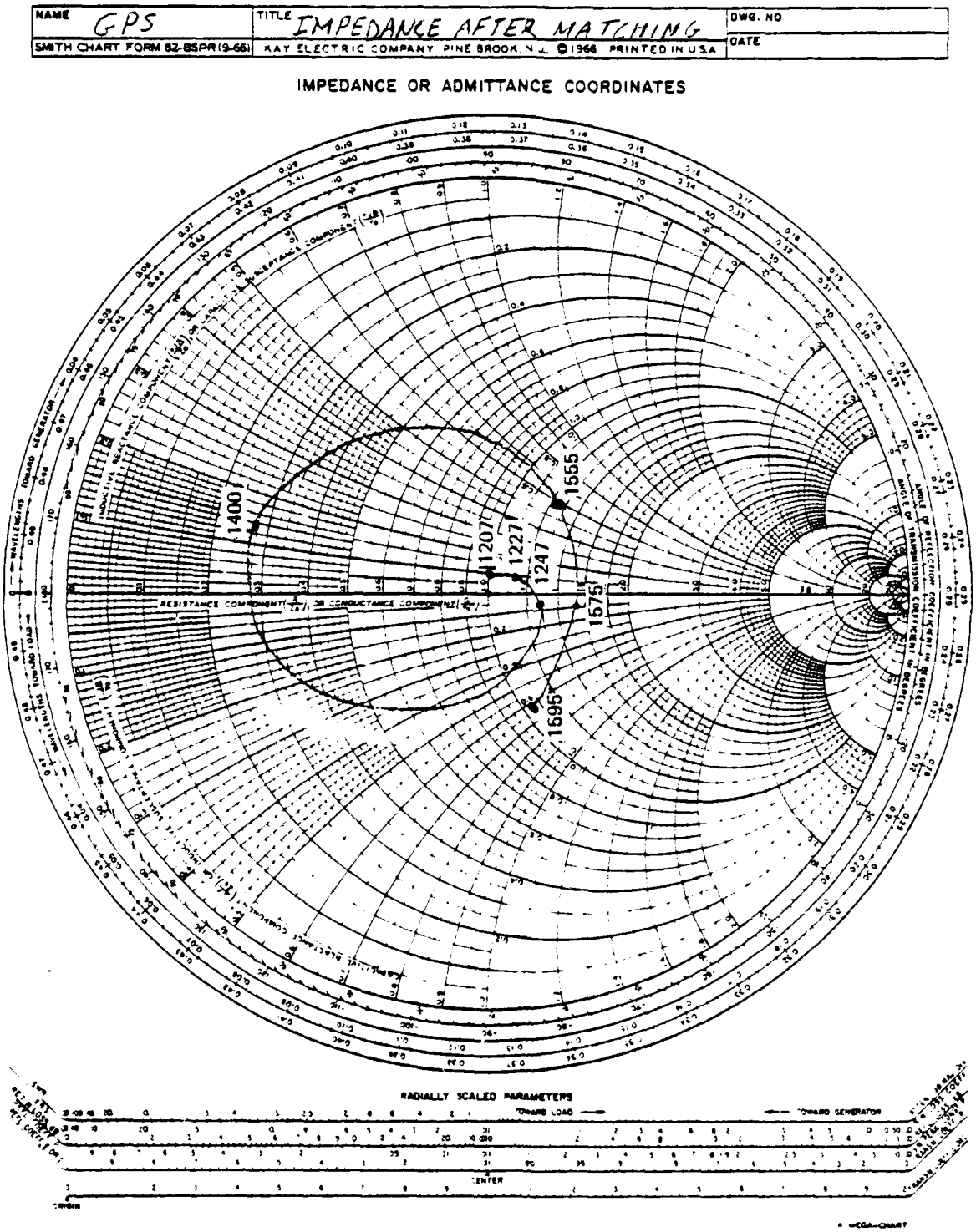

Figure 7. Impedance of Dipole Half after Matching.

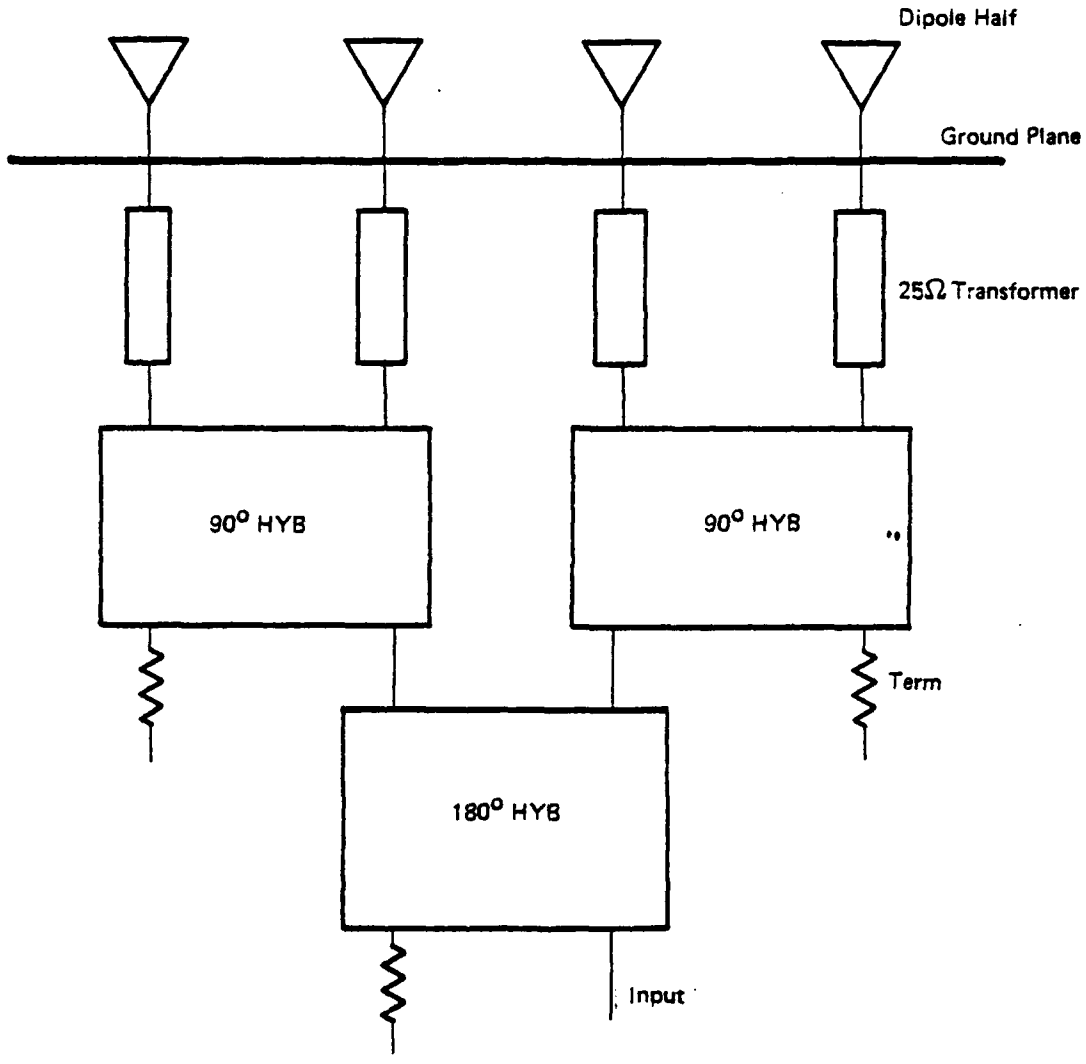

Figure 8. Antenna Schematic.

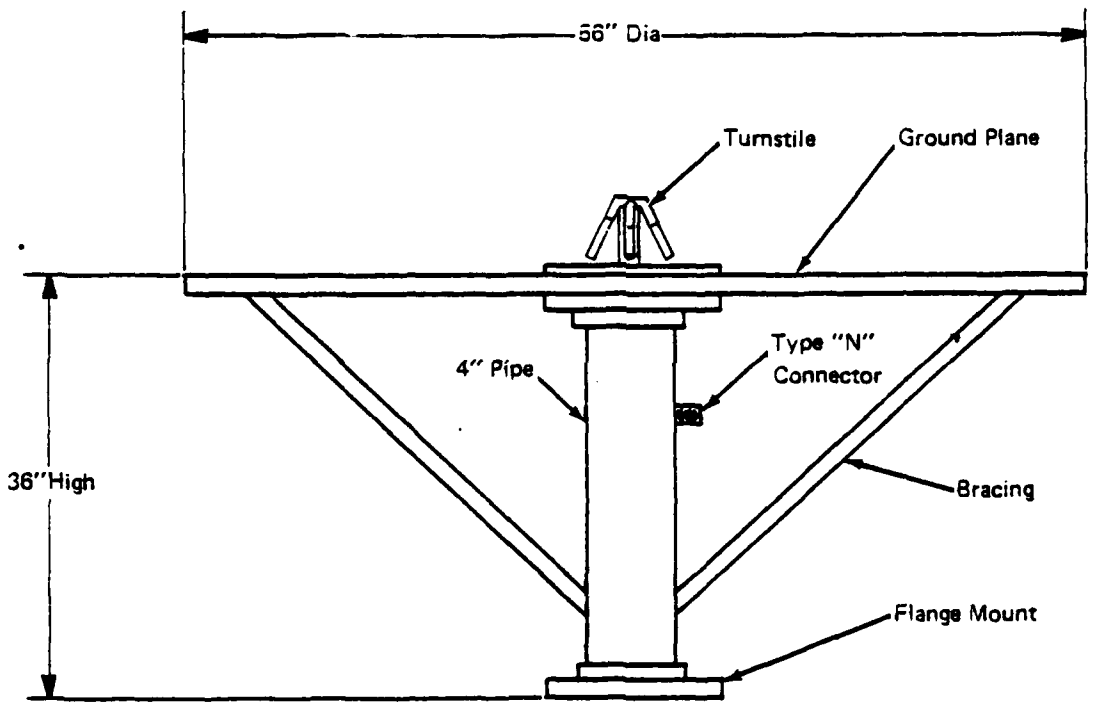

Figure 9. Complete Antenna.

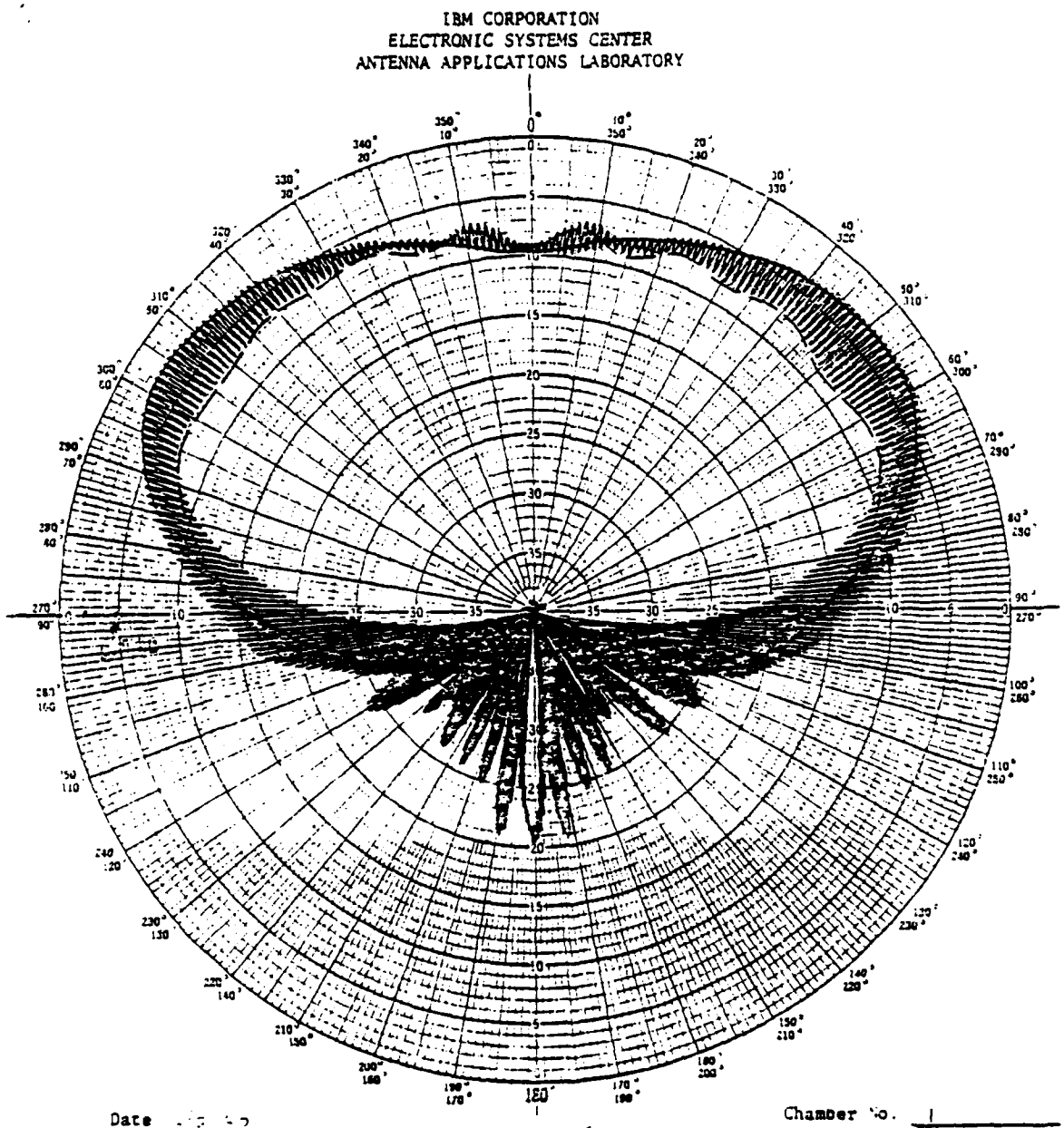

Figure 10. Antenna Patterns.

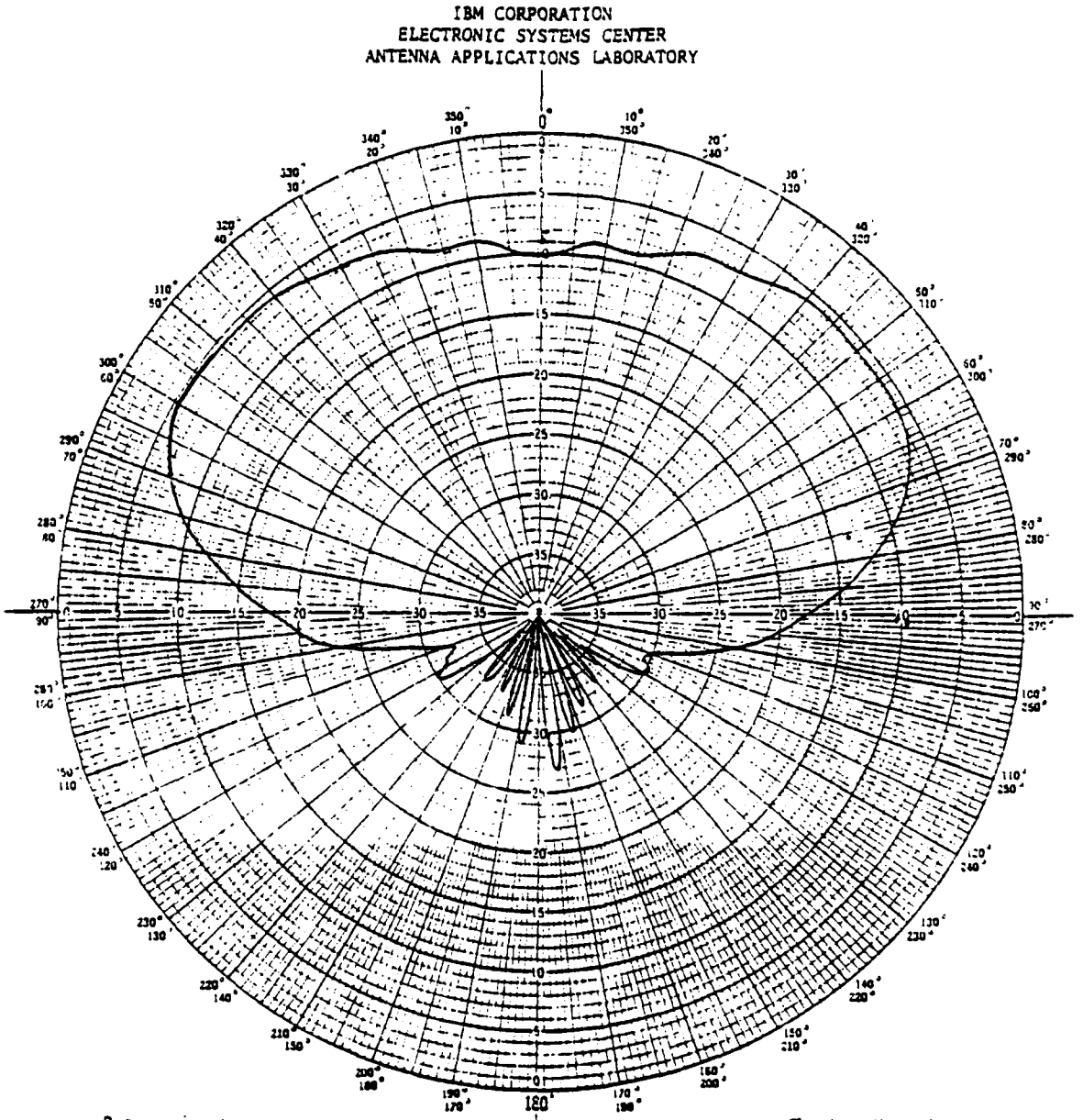

Figure 11. Antenna Patterns.

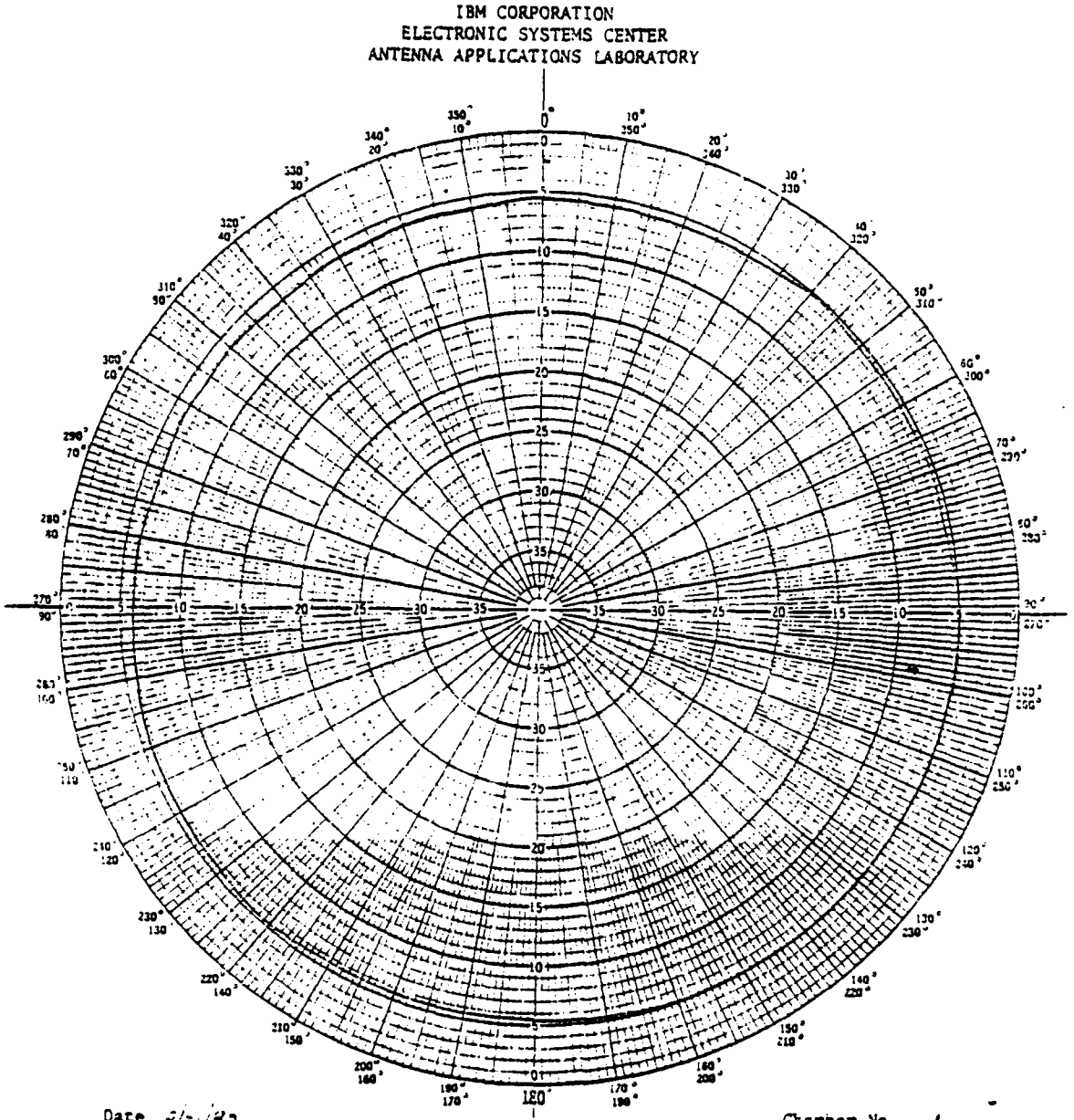

Figure 12. Antenna Patterns.

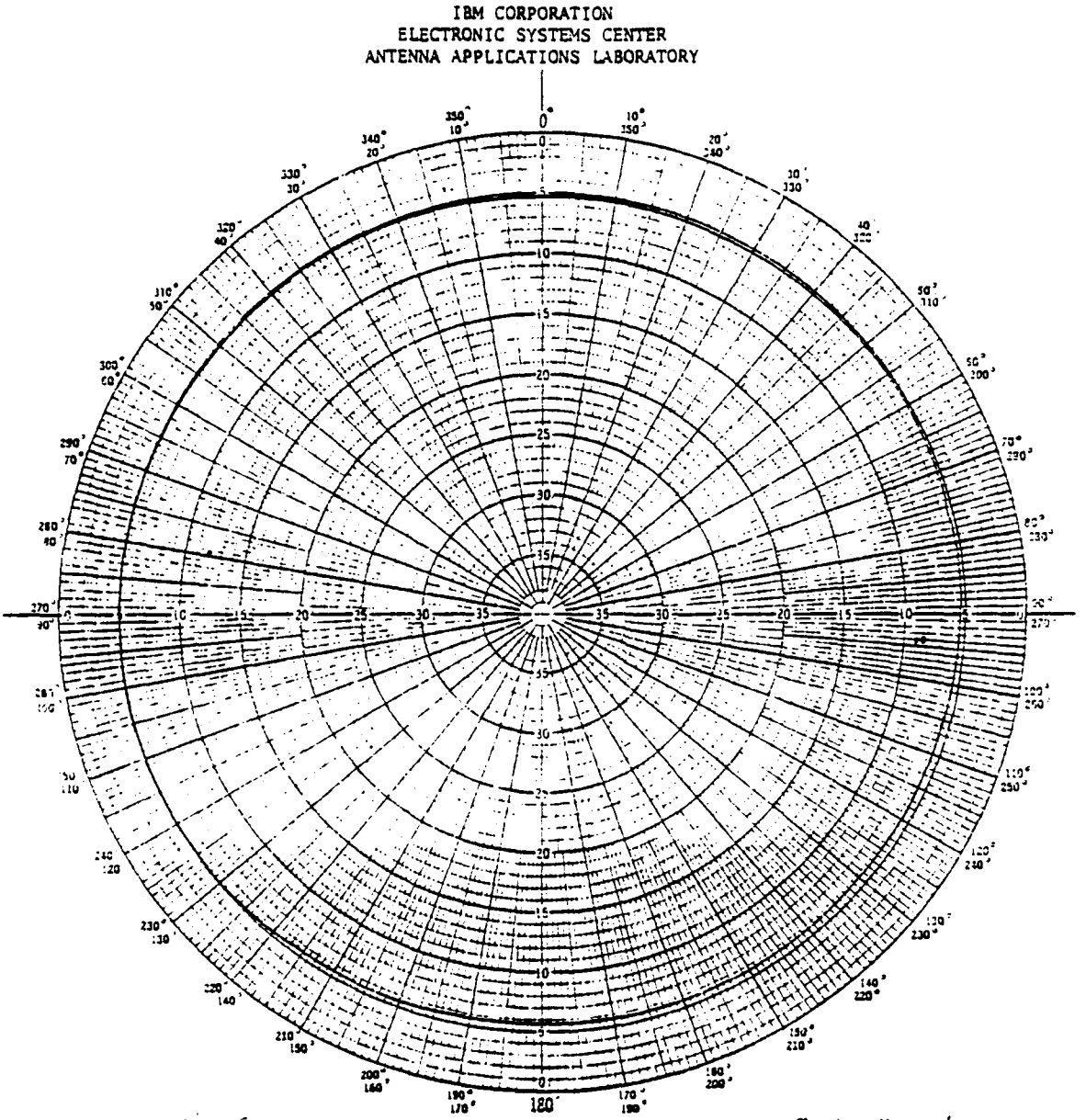

Figure 13. Antenna Patterns.

	Final Data With Hybrid And Cable 2/23/80								
Freq	VSWR								
1207	1.15								
1227	1.11								
1247	1.15								
1555	1.19								
1575	1.09								
1595	1.05								

Figure 14. Final VSWR.

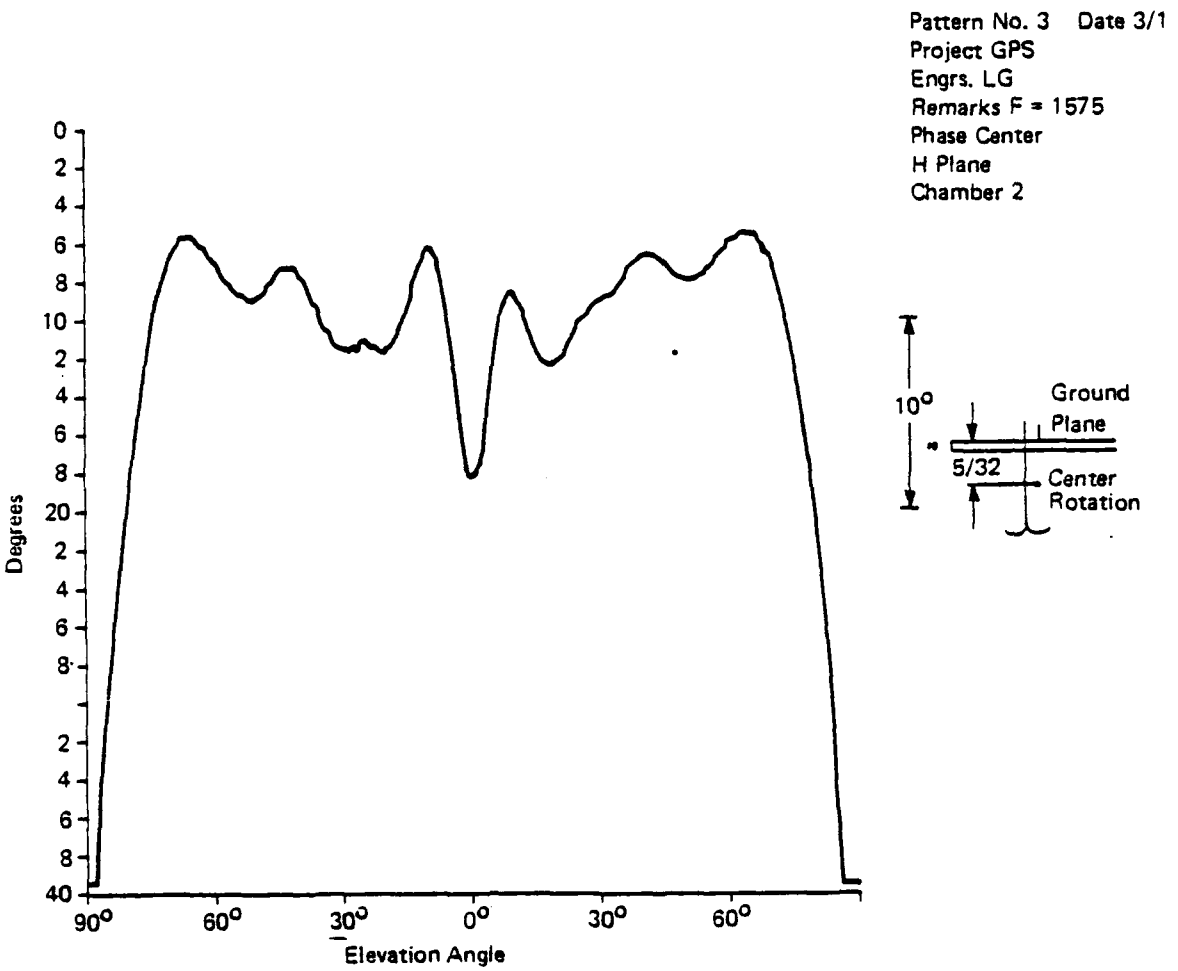

Figure 15. Phase Center Patterns.

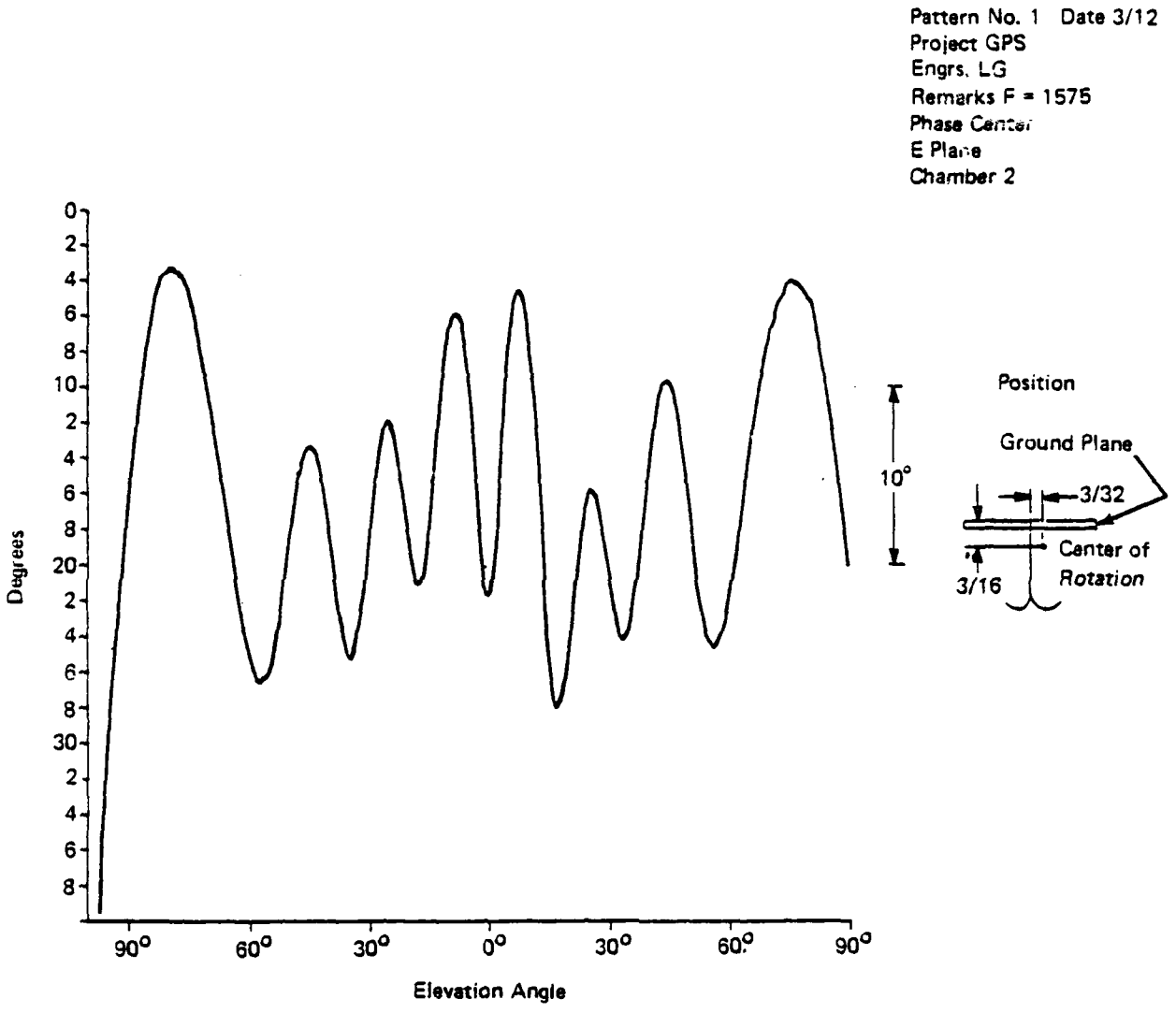

Figure 16. Phase Center Patterns.

DESIGN OF TRANSVERSE SLOT ARRAYS FED BY BOXED STRIPLINE *

P.K. Park† and R.S. Elliott††

Abstract - A design procedure is presented whereby the lengths and offsets of an array of transverse slots can be determined, in the presence of mutual coupling, when the slots are excited by a boxed stripline and when pattern and input impedance are specified. The design is based on two sets of simultaneous equations. One set relates the TEM scattering off each slot to the field distribution in the slot, in the manner of Stevenson. The other set relates the stripline-fed slot array to an equivalent, properly loaded slot array, center-fed by two-wire lines, whose mutual impedance terms are easily calculated. The procedure is illustrated by the design of an eight element linear array. Experimental data in support of the theory is offered.

Introduction - An earlier paper [1] described the design procedure for determining the dimensions of a longitudinal slot array fed by boxed stripline when pattern and input impedance are specified. A slot module for that configuration is shown in Figure 1. The slot is on the centerline of the broad wall and thus cannot scatter a TE_{10} mode. This permits the transverse dimension of the box to be larger, as a consequence of which the slot is enough shorter to allow modules to be placed in tandem to form a linear array. Slot excitation is governed by the tilt of the strip as it passes under the slot. The phase of excitation is governed by slot length. These two parameters, slot length and strip tilt, are used to excite each element of the

*This work was sponsored by the U.S. Air Force.

†Senior Staff Scientist, Hughes Missile Systems Division, Canoga Park, CA 91304. Post-Doctoral Research Engineer at UCLA.

††Professor of Electrical Science, University of California, Los Angeles, CA 90024. Consultant to Hughes.

array with the proper amplitude and phase needed to produce the desired pattern, and with the sum of the back-scattered waves off the individual slots corresponding to the desired input impedance. Mutual coupling must be considered if good performance is expected, particularly when boxed striplines are placed side by side to form planar arrays. The design procedure takes this effect into account. A ten element linear array has been designed, built, and tested using this approach, and gave good agreement with the theory [1].

The module for a transverse slot fed by a boxed stripline is considerably different in appearance and is shown in Figure 2. The strip is seen to be offset, but parallel to a side wall, and passes underneath the slot near the slot's extremity. This is to make the coupling light enough to be in the dynamic range normally needed for array applications. The excitation of the slot in amplitude and phase is governed by the length of the slot and the offset of the slot relative to the strip. The design problem is to determine these two parameters for each slot in an array in order to achieve, in the presence of mutual coupling, the desired pattern and input impedance.

A sequence of plate-through holes is seen to be placed near the exit and entry ports of the module, which is normally dielectric-filled. The resulting curtains of metal pins effectively isolate adjacent modules from each other internally, except for the TEM mode. Thus only external mutual coupling needs to be considered.

The next section of this paper is concerned with the establishment of a theory which explains the behavior of families of these transverse slot modules. This is followed by the presentation of experimental data on a single module and then by a description of the design of an eight element linear array of transverse slots fed by boxed stripline.

Theory - The analysis for the transverse slot case parallels to a considerable extent what has already been presented for the longitudinal slot case [1]. The basic module, shown in Figure 3, is a two-port device, the ports being at $z = \pm\lambda_{TEM}/2$, with λ_{TEM} the wavelength of the TEM mode. No loss in generality occurs if the ports are taken at the positions $z = \pm\lambda_{TEM}$, shown dotted in Figure 3, because relations between the two sets of ports involve simple, known linear transformations. With this convention adopted, the equivalent circuit for the n^{th} module is shown in Figure 4. The slot is modeled by a series impedance because scattering off the slot is asymmetrical.

This equivalent circuit is based on the assumption that all higher order modes are negligible at $z = \pm\lambda_{TEM}/2$, partly due to the box size, and partly due to the two curtains of metal pins. To the extent that this is true, the fields at $z = \pm\lambda_{TEM}/2$ are TEM, consisting generally of waves traveling in both directions. These TEM fields will be represented by the voltage/current pair (V_n, I_n) at the input port $z = -\lambda_{TEM}$. A load impedance Z_n^L is placed at the output port $z = +\lambda_{TEM}$. This impedance can represent what the n^{th} module "sees" looking down its branch line at all the slots beyond, or could be an appropriate termination, such as a short circuit.

The active impedance Z_n^A, which represents the n^{th} slot in the equivalent circuit of Figure 4, is an important parameter in this analysis. Its meaning can be appreciated by considering the inter-relations among all the slots. To account for mutual coupling, one can write

$$V_n = \sum_{m=1}^{N} I_m Z_{nm} \qquad (1)$$

in which Z_{nm} is the mutual impedance between the ports n and m. Z_{nn} is the self impedance seen at port n, that is, the input impedance when all other input ports are open circuited. Thus

$$Z_{nn} = Z_n + Z_n^L \tag{2}$$

with Z_n the value that Z_n^A assumes when all other input ports are open circuited. Z_n is commonly called the self impedance of the n^{th} slot.

Generally, the input impedance at the n^{th} port is given by

$$Z_n^{in} = \frac{V_n}{I_n} = \sum_{m=1}^{N} \frac{I_m}{I_n} Z_{nm} = Z_{nn} + \sum_{m=1}^{N}{}' \frac{I_m}{I_n} Z_{nm} = Z_n + Z_n^L + \sum_{m=1}^{N}{}' \frac{I_m}{I_n} Z_{nm} \tag{3}$$

in which the prime on the summation sign means that the term m=n has been excluded. It follows that

$$Z_n^A = Z_n + \sum_{m=1}^{N}{}' \frac{I_m}{I_n} Z_{nm} = Z_n + Z_n^B \tag{4}$$

In words, equation (4) states that the active impedance at the terminals of the n^{th} module equals the self impedance of the n^{th} slot plus a term Z_n^B which accounts for mutual coupling. This latter term is a summation that involves not only the mutual impedances between ports, but also the relative currents at the different ports. As the analysis develops further, it will be seen that Z_n^A is decisive in determining the amplitude and phase of the electric field in the n^{th} slot. Since the latter is dictated by the desired radiation pattern, Z_n^A is a key parameter in array design.

A justification for the equivalent circuit of Figure 4 lies in the assumption that the electric field distribution in each slot is entirely

Z-directed. In this case, the back-scattered wave B and the forward scattered wave C are related by the expression [2]

$$B = -C = \frac{\int_{slot} E_z^{slot} H_{TEM,x} dS}{2 \int_0^a \int_0^b \vec{E}_{TEM} \times \vec{H}_{TEM} \cdot \vec{1}_z \, dS} \tag{5}$$

with a and b the transverse box dimensions. $\vec{E}_{TEM}$ and $\vec{H}_{TEM}$ are the fields associated with a TEM mode of unit amplitude traveling along the boxed stripline.

The slot voltage distribution can be connected to the electric field distribution in the slot by the defining relation

$$V(\xi) = \int_{-w/2}^{w/2} E_z(\xi, z) dz \tag{6}$$

with w the width of the slot and ξ an x-directed variable measured from the center of the slot. It will be assumed that $V(\xi)$ is expressible in the form

$$V(\xi) = V^s \sin[k_s(\ell - |\xi|)] \tag{7}$$

In(7) V^s is the peak slot voltage and k_s is a wave number determined by experiment ($k_s \ell_{res} = \pi/2$, with $2\ell_{res}$ the resonant length of the slot).

The field distribution $H_{TEM,x}(x,y)$ has been found [3] for the case of a strip which is $\bar{x}$-centered in the box but at an arbitrary height in the y-direction. That solution has been used to approximate $H_{TEM,x}(x,y)$ for a strip which is neither x-centered nor y-centered in the box. This has been done by assuming that the field to the left of the strip is the same as though the right side wall were moved so as to be the same distance from the strip as the actual distance between the strip and the left side wall. A similar artifice was used to approximate the field to the right of the strip.

With E_z^{slot} and $H_{TEM,x}$ represented as just described, equation (5) can be evaluated numerically. The back scattering coefficient B will clearly depend on s, the offset of the slot edge from the strip centerline, and 2ℓ, the slot length. Expressly,

$$B(s,\ell) = V^s \frac{\int_{-\ell}^{\ell} \sin[k_s(\ell-|\xi|)]\, H_{TEM,x}\,(\xi+s+a'-\ell,b)}{2\int_o^a \int_o^b \vec{E}_{TEM} \times \vec{H}_{TEM} \cdot \vec{1}_z dS} \tag{8}$$

$$= V^s f(s,\ell)$$

Anti-symmetric scattering typified by (5) is consistent with the equivalent circuit of Figure 4 and can also be expressed in the form

$$B = -C = \frac{1}{2} Z_n^A I_n \tag{9}$$

with I_n the mode current at $z=0$, and thus also at $z= -\lambda_{TEM}$. When (8) and (9) are combined, the relation between the mode current I_n and the peak slot voltage V_n^s is established, viz.,

$$I_n = \frac{2f_n(s_n,\ell)}{Z_n^A} V_n^s \tag{10}$$

In slot array design problems of this type, V_n^s is governed by pattern requirements. For a standing wave array, I_n will be common to all slots in any branch line. Equation (10) is the first of two basic design equations needed to determine the slot length $2\ell_n$ and the slot offset s_n for each slot in the array.

The second basic equation arises from a consideration of external mutual coupling. To initiate this development, it is desirable to link the stripline-fed slot array to an equivalent array of slots fed by two wires. To accomplish this linkage, assume first that the stripline-fed slot array is imbedded in an infinite planar ground plane. Next, imagine an identical array of slots in an

infinite ground plane, but center-fed by two-wire lines, and radiating into a half-space. If the same slot voltages V_n^s are established in both arrays, since the field distribution in the n^{th} slot is essentially the same for the two methods of feeding, the half-space radiation patterns will be the same. (Small element pattern differences will have negligible effect for large arrays.) However, the impedance characteristics of the two arrays will not be the same. The reason for this is that the stripline-fed slots cause higher order mode internal scattering which contributes to the reactive component of Z_n, and which is dependent on slot offset s_n. A similar effect does not exist in the equivalent array. To model this effect, one can place a load admittance $Y_n^{2W,L}$ across the terminals of the corresponding two-wire center-fed slot. When this is done, the circuit equations for the two-wire slot array are given by

$$I_n^{2W} = \sum_{m=1}^{N} V_m^s \, \text{sink}_{s_m \ell_m} \, Y_{nm}^{2W} \tag{11}$$

in which the superscript 2W stands for two-wire. In (11), Y_{nm}^{2W} (with $m \neq n$) has its customary meaning, being the mutual admittance between slots m and n when they are center-fed by two wires. This is a quantity which can be computed readily from well-established formulas.†

†Use of Booker's extension of Babinet's principle [4] yields the result that $Y_{nm}^{2W} = (2/\eta^2) Z_{nm}^{2W}$ with η the impedance of free space, and Z_{nm}^{2W} the mutual impedance between equivalent two-wire center-fed strip dipoles which are radiating into a full space. Z_{nm}^{2W} is calculable from fairly simple integrals [5].

The term Y_{nn}^{2W} which appears in (11) stands for the loaded self admittance of the n^{th} two-wire center-fed slot, i.e.,

$$Y_{nn}^{2W} = Y_n^{2W} + Y_n^{2W,L} \tag{12}$$

in which Y_n^{2W} is the conventional (unloaded) self admittance.

The load $Y_n^{2W,L}$ must be selected so that the complex power flows in the two arrays are properly related. This means that the equation

$$\frac{1}{2} I_n (I_n Z_n^A)^* = \frac{1}{2} V_n^s \sin k_s \ell_n \, I_n^{2W*} \tag{13}$$

needs to be satisfied for every n, for otherwise the impedance characteristics of the two arrays will not be the same.

In (13), the left side refers to the complex power flow at the cross section $z=0$ in the stripline-fed slot array. (It is important to remember that I_n is the mode current.) The right side refers to the two-wire center-fed slot array.

Multiplication of (10) by its complex conjugate gives

$$I_n I_n^* Z_n^{A*} Z_n^A = 4 f_n f_n^* V_n^s V_n^{s*} \tag{14}$$

From (13),

$$I_n I_n^* Z_n^{A*} = V_n^s V_n^{s*} \sin^2 k_s \ell_n \frac{I_n^{2W*}}{V_n^{s*} \sin k_s \ell_n} = V_n^s V_n^{s*} \sin^2 k_s \ell_n \, Y_n^{2W,A*} \tag{15}$$

in which $Y_n^{2W,A}$ is the active input admittance of the n^{th} two-wire center-fed slot.

If (14) and (15) are combined, one obtains

$$Z_n^A = \frac{4|f_n|^2}{\sin^2 k_s \ell_n \, Y_n^{2W,A*}} = \frac{4|f_n / \sin k_s \ell_n|^2}{Y_{nn}^{2W*} + \sum_{m=1}^{N}{}' \frac{V_m^{s*} \sin k_s \ell_m}{V_n^{s*} \sin k_s \ell_n} Y_{nm}^{2W*}} \tag{16}$$

For the case of a single isolated slot, (16) reduces to

$$Z_n = \frac{4|f_n/\text{sink}_s \ell_n|^2}{2W^*} \quad \text{or} \quad Y_{nn}^{2W^*} = \frac{4|f_n/\text{sink}_s \ell_n|^2}{Z_n} \tag{17}$$

with Z_n the self impedance of the stripline-fed slot. Substitution of (17) in (16) gives

$$Z_n^A = \frac{4|f_n/\text{sink}_s \ell_n|^2}{\frac{4|f_n/\text{sink}_s \ell_n|^2}{Z_n} + \sum_{m=1}^{N}{}' \frac{V_m^{s*}}{V_n^{s*}} \frac{\text{sink}_s \ell_m}{\text{sink}_s \ell_n} Y_{nm}^*} \tag{18}$$

Equation (18) is the second basic design equation. Used in conjunction with (10), it permits determination of the slot dimensions needed to obtain a specified pattern and input impedance.

The Design Procedure - The foregoing theory can be used to design one and two dimensional arrays of stripline-fed transverse slots, with either resonant or non-resonant slot spacings. For simplicity, the procedure will be described for the case of a linear array with resonant spacing.

Assume that the self impedance function $Z_n(s_n, \ell_n)$ is known either through theory or experiment. (This subject will be treated in the next section.) Recall that the function $f_n(s_n, \ell_n)$ is known from (8), and that Y_{nm}^* is calculable if ℓ_n, ℓ_m, and the relative positions of the two slots are known.

The design process can be launched by assuming a starting set of slot dimensions (s_n, ℓ_n) for every slot in the array. (This could be the set that would apply in the absence of mutual coupling, or it could simply be the set which places the center of each slot on the centerline of the broad wall, with each slot of resonant length. The starting dimensions are not critically important, because the process must be iterated and its convergence is

insensitive to initial conditions.) With the starting slot dimensions known, the relative positions of all slots are also known, so Y^*_{nm} can be computed for all n and m ($n \neq m$). With the pattern specified, V^s_n is known for all n, and thus a starting value can be computed for the series.

$$\mathcal{Y}_n = \sum_{m=1}^{N}{}' \frac{V^{s*}_m \, \text{sink}_{s_m \ell_m}}{V^{s*}_n \, \text{sink}_{s_n \ell_n}} Y^*_{nm} \tag{19}$$

A study of (18) reveals that, if Z^A_n is to be pure real

$$\mathcal{I}_m \frac{4|f_n/\text{sink}_{s_n \ell_n}|^2}{Z_n} = -\mathcal{I}_m \mathcal{Y}_n \tag{20}$$

Since $f_n(s_n,\ell_n)$ and $Z_n(s_n,\ell_n)$ are known functions, a computer search can be undertaken for the couplet (s_n,ℓ_n) which satisfies (20). One finds that the solution is a <u>continuum</u> of couplets. Similarly, there is a continuum of couplets which satisfies (20) for the m^{th} slot, etc.

For a <u>given</u> couplet (s_n,ℓ_n) which satisfies (20), there is a unique couplet (s_m,ℓ_m) which not only satisfies (20) but, in conjunction with the given couplet (s_n,ℓ_n), also satisfies

$$\frac{f_n(s_n,\ell_n)}{Z^A_n} V^s_n = \frac{f_m(s_m,\ell_m)}{Z^A_m} V^s_m \tag{21}$$

Equation (21) has been derived from the other basic design equation, (10), on the assumption that $I_n = I_m$, since this is to be a resonantly spaced linear array.

Equation (21) can be used to "pair-up" compatible couplets, thus creating famities of slot dimensions which simultaneously satisfy (18) and (21). If an input match is desired, one must choose the famity for which

$$\sum_{n=1}^{N} Z_n^A = Z_o \tag{22}$$

with Z_o the characteristic impedance of the stripline.

The procedure must be iterated because the new slot dimensions provide the opportunity to refine the calculation of $\mathcal{Y}_n$. The process usually converges rapidly, with two or three iterations sufficing.

The Self Impedance Function $Z_n(s_n,\ell_n)$ - The self impedance as a function of slot length and offset can be determined theoretically (e.g., using the method of moments), or it can be determined experimentally. We chose the latter course and constructed a test module. The boxed stripline dimensions (cf. Figure 3) were a = 3.45", b = 0.25", a' = 2.60", b' = 0.125". The strip was 0.1764" wide and the box was filled with teflon/glass for which $\epsilon_r = 2.5$. The characteristic impedance of a stripline of these dimensions is 50 ohms.

The radiating slot had a width of 0.25" and a variable length. A curtain of plate-through holes was placed 2" on each side of the slot. The holes were 0.25" in centers with the holes nearest a side wall 0.35" from the side wall. Three holes were eliminated to permit passage of the strip.

$Z(s,\ell)$ was measured at a sequence of frequencies using an automatic network analyzer. Typical results are shown in Figure 5, for a frequency of 1.75 GHz. One can observe that for a given offset the impedance passes smoothly through resonance as the slot length is varied. It is a simple matter to polyfit this data to provide a functional representation of the self impedance.

It was hoped that $Z(s,\ell)$ would be a well-behaved function at the frequency which places the two curtains of plate-through holes exactly one quide

wavelength apart, since this would halve the number of curtains needed in an array. For our test module, this would occur at 1.87 GHz. However, the data at that frequency was poorly-behaved, as can be seen from Figure 6. Apparently the higher order mode resonances which can occur at that cavity size introduce effects which are undesirable, and we concluded that this situation should be avoided.

An Eight Element Linear Array - The experimental data shown in Figure 5 has been used to design an eight element, resonantly spaced array, for operation at 1.75 GHz. A 20 dB Dolph-Chebyshev pattern was prescribed, together with an input match. Feeding is to be via a coaxial Tee at the center of the array.

The design procedure described earlier in this paper has been employed and yielded the slot dimensions shown in Table 1. The active and self impedance of each slot is depicted in Figure 7 and provides graphic evidence of the effect of mutual coupling.

At this writing, an array is being fabricated to the dimensions shown in Table I. It is hoped that experimental data on the performance of this array will be available at the time of the symposium.

Conclusions - A design procedure has been established which is applicable to arrays of transverse slots fed by a dielectric-filled boxed stripline. Experimental data giving the self impedance of a single module as a function of slot dimensions has been obtained. This has been used to design an eight element linear array.

Acknowledgments - The authors wish to express their appreciation to the Hughes Missile Systems Division for use of their fabrication and test facilities during the course of this project, and particularly to George Stern for his help and counsel.

References

[1] P.K. Park and R.S. Elliott, "Design of Collinear Longitudinal Slot Arrays Fed by Boxed Stripline." Presented at IEEE AP/URSI Symposium, Quebec, June, 1980. Full paper to appear in IEEE AP Transactions, January, 1981.

[2] S. Silver, "Microwave Antenna Theory and Design," MIT Rad. Lab. Series, vol. 12, pp. 286-295, Dover Publications, Inc., New York; 1965.

[3] P.K. Park, "Theory Analysis, and Design of a New Type of Strip-Fed Slot Array," Ph.D. Dissertation at UCLA, 1979.

[4] H.G. Booker, "Slot Aerials and Their Relation to Complementary Wire Aerials," JIEE (London), Part IIIA, vol. 93, pp. 620-626; 1946.

[5] H.C. Baker and A.H. LaGrone, "Digital Computation of the Mutual Impedance Between Thin Dipoles," IEEE Trans. Antennas and Propagat., vol. AP-10, pp. 172-178; 1962.

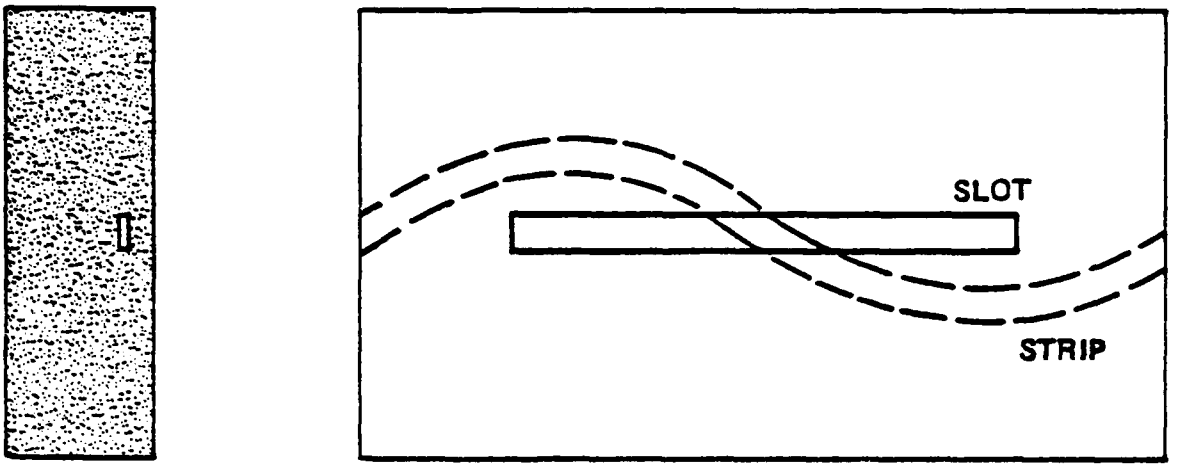

Figure 1. Boxed-Stripline/Longitudinal-Slot Module

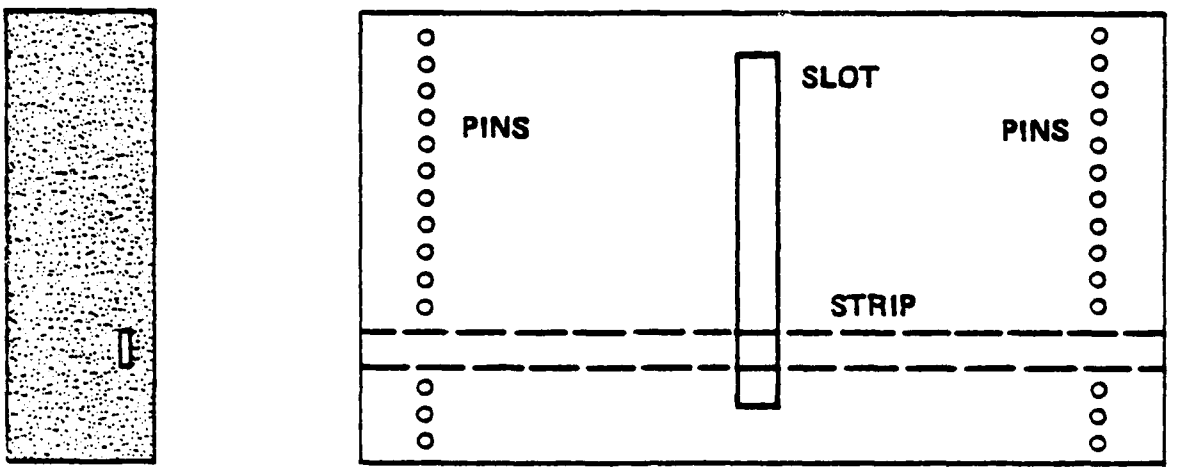

Figure 2. Boxed-Stripline/Transverse-Slot Module

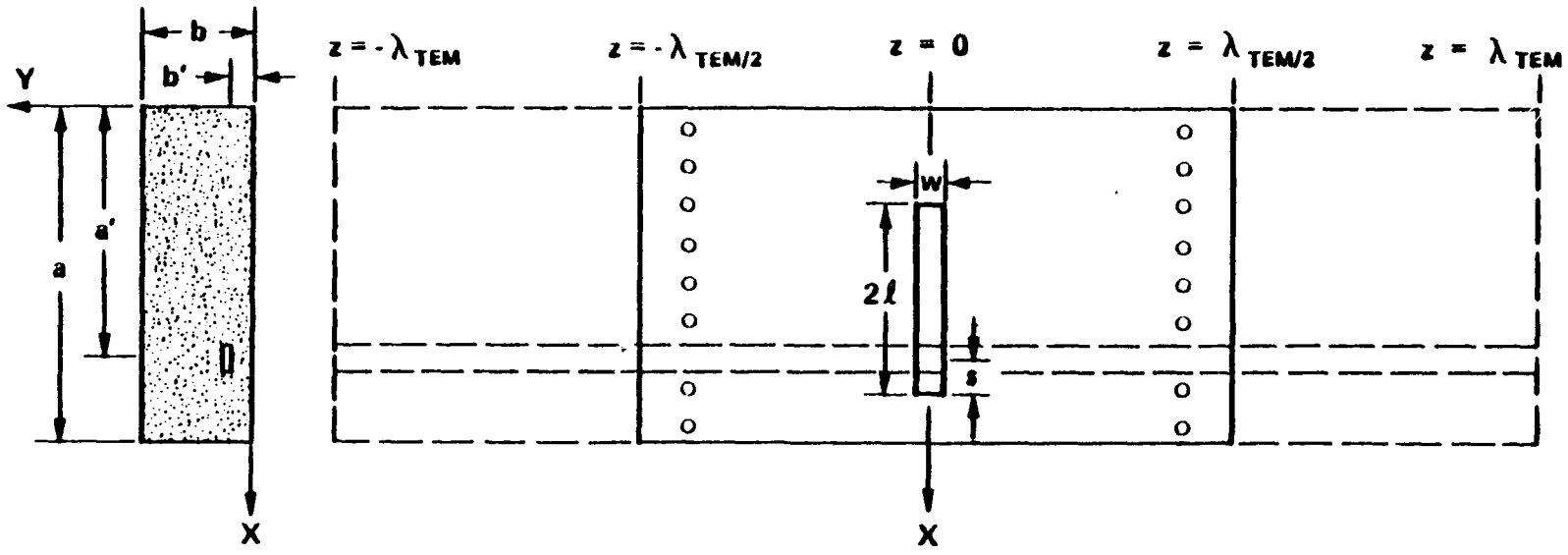

Figure 3. Extended Transverse Slot Module

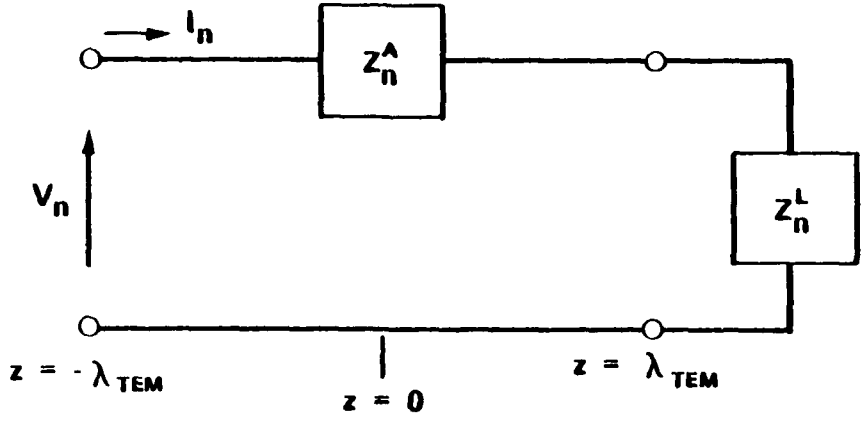

Figure 4. Equivalent Circuit of n^{th} Module

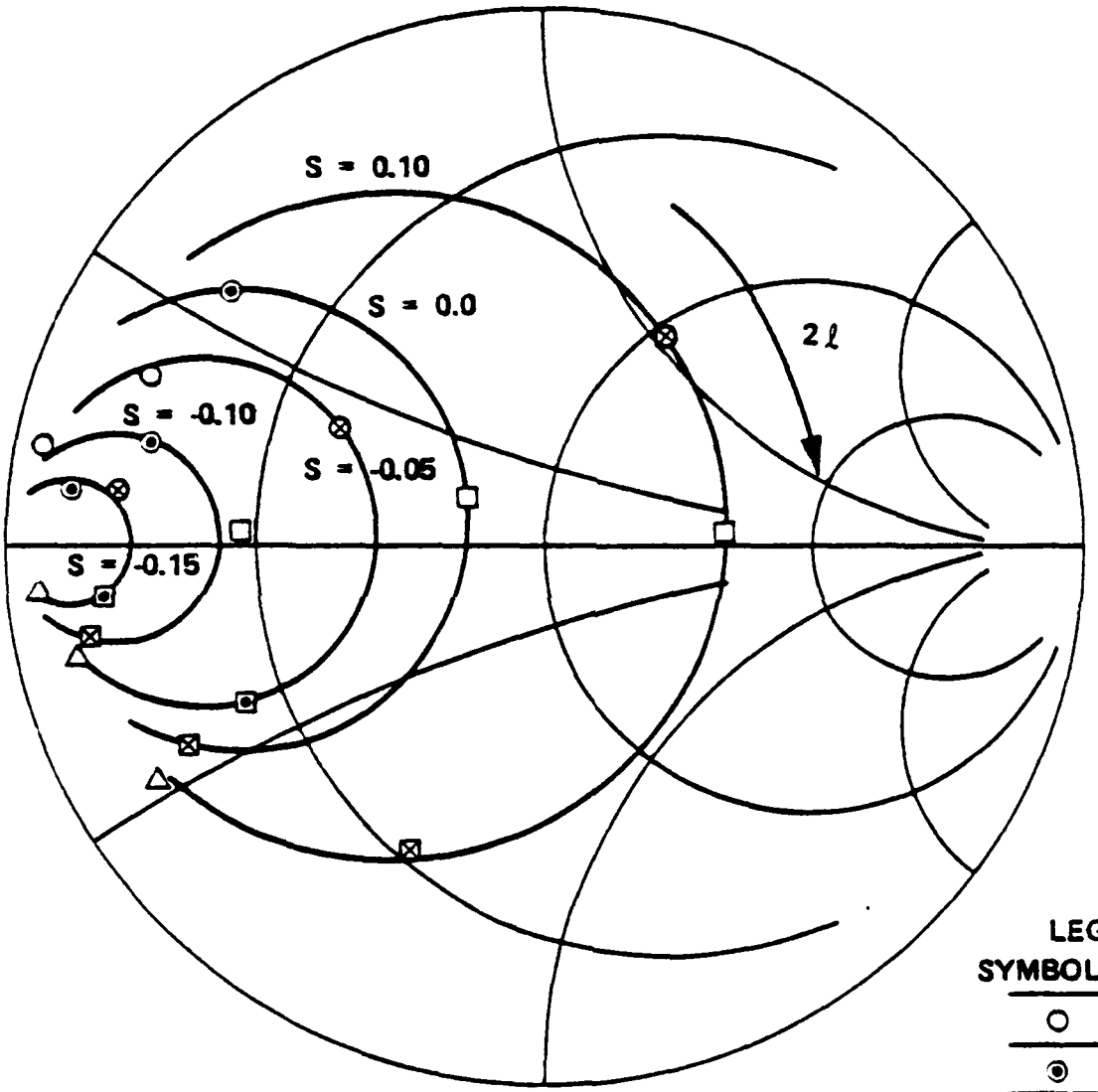

LEGEND SYMBOL	2ℓ
○	1.85"
⊙	1.9"
⊗	1.95"
□	2"
⊡	2.05"
⊠	2.1"
△	2.15"

Figure 5. Self Impedance Data for Single Module. f=1.75 GHz.

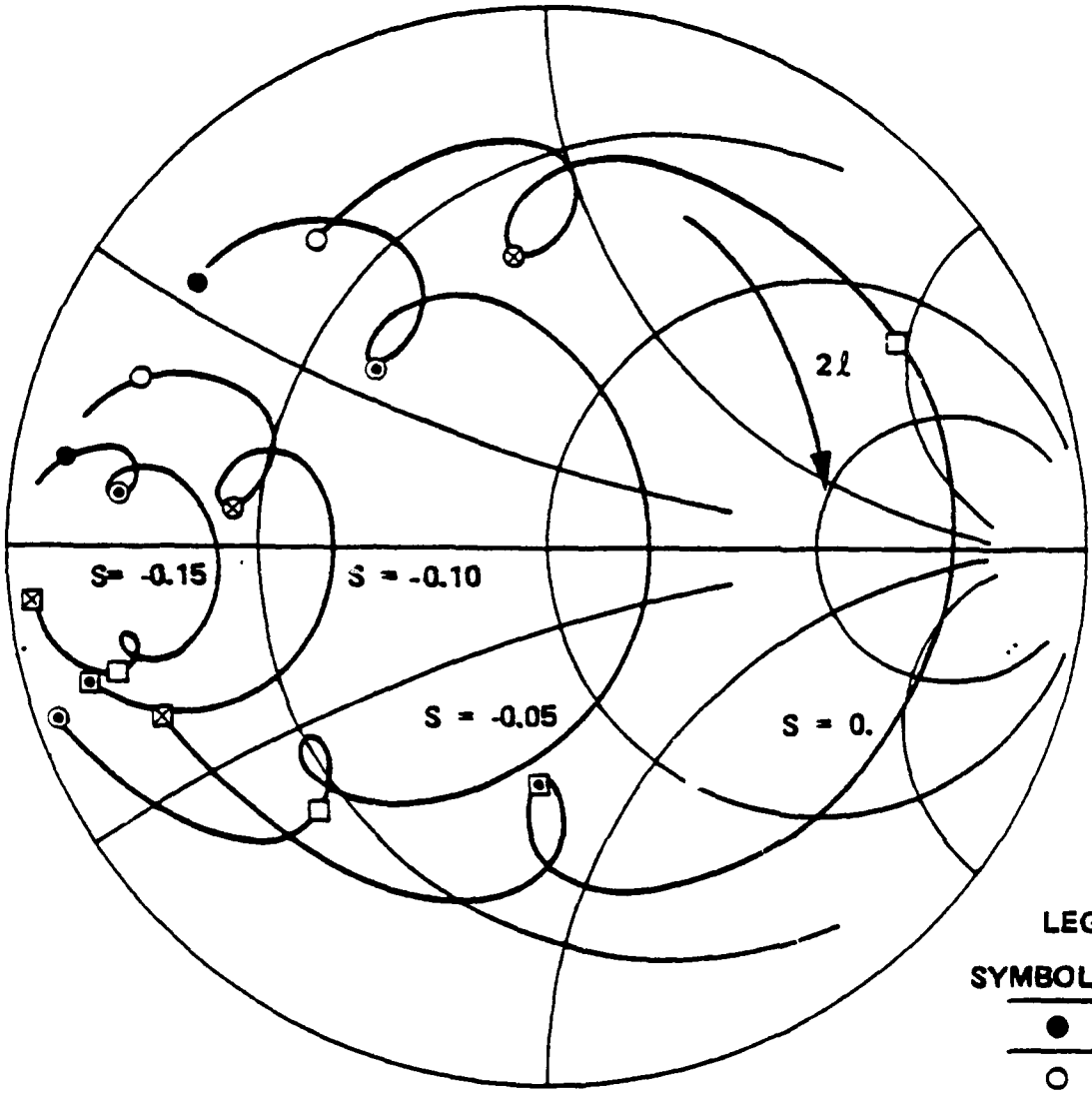

LEGEND

SYMBOL	2ℓ
●	1.56
○	1.60
◉	1.65
⊗	1.90
□	1.75
⊡	1.80
⊠	1.85

Figure 6. Self Impedance Data for Single Module. f=1.87 GHz.

APPLICATION OF IMPEDANCE BOUNDARY CONDITIONS TO NUMERICAL SOLUTION OF CORRUGATED AND RECEIVER HORNS WITH ROTATIONAL SYMMETRY

K. A. ISKANDER

SPAR AEROSPACE LIMITED, ELECTRONICS GROUP

STE. ANNE-DE-BELLEVUE, QUEBEC, CANADA H9X 3R2

AND

L. SHAFAI

DEPARTMENT OF ELECTRICAL ENGINEERING, UNIVERSITY OF MANITOBA, WINNIPEG, MANITOBA, CANADA R3T 2N2

ABSTRACT: An integral equation is used to study the scattering properties of corrugated surfaces utilized in corrugated horn designs. Scalar and vector potentials are used to obtain the desired integral equations and the symmetry of bodies of revolution is utilized to obtain the formulation for rotationally symmetric corrugated horns. Radiation patterns of these horns are obtained by replacing the corrugations with an anisotropic surface impedance. The Waveguide excitation is simulated by the field of a Hertzian dipole situated near the end wall of the Waveguide. The same formulation is used to study the scattering properties of horns in the receiving mode. In this case the Waveguide termination is an isotropic surface impedance and the exciting dipole is placed at a far distance from the scattering horn.

Recently, the problem of radiation from corrugated horns has been studied extensively in relation with the design of scalar feeds for reflector antennas. Generally, two main approaches have been utilized. The most elaborate approach is based on the model expansion and aperture integration methods [1] where many approximating assumptions related to outer wall currents, slot depths, horn wall lengths, etc. deemed necessary. The second method, which has not found widespread application, is based on the numerical solution of the corrugated horn problems [2].

In the present study we use an integral equation formulation to the problem of corrugated and rotationally symmetric horn antennas. To overcome the problem of extensive storage and computer time, we represent the corrugation by an anisotropic surface impedance. With this representation, the boundary conditions are applied on a smooth surface counterpart, and consequently, the large corrugated surface is reduced to a small one. The required surface impendancies determined approximately as the ratio of electric to magnetic components of electromagnetic field which can propagate inside the grooves of the corrugations.

The required integral equation is obtained from the expression of the scattered field E^S from a surface supporting non-vanishing electric and magnetic current densities, J and M. Hence:

$$\bar{E}^S = - J\omega\bar{A} - \nabla V - \nabla X \bar{F} \qquad (1)$$

where $\bar{A}$ and $\bar{F}$ are the electric and magnetic vector potentials defined as:

$$\bar{A} = \mu \int_s \bar{J}\phi ds'; \quad \bar{J} = \hat{n} \times \bar{H} \qquad (2)$$

$$\bar{F} = \int_s \bar{M}\ \phi ds'; \quad \bar{M} = \bar{E} \times \hat{n} \qquad (3)$$

and V is the electric scalar potential given by

$$V = 1/\epsilon \int_s \sigma\phi\ ds' \qquad (4)$$

σ is the surface electric charge density; μ and ϵ are the permeability and permitivity of free space; s is the scattering surface, and ϕ is the free space Green's function.

The surface electric charge density is related to $\bar{J}$ through the equation of continuity; while $\bar{M}$ can be expressed in terms of $\bar{J}$ as

$$\bar{M} = \bar{\bar{Z}} \cdot (n \times \bar{J}) \qquad (5)$$

$\bar{\bar{Z}}$ is a dyadic representing the anisotropic surface impedance and n is an outward unit normal to the scattering surface. From here, and also from the fact that the total tangential electric field is zero at a point approaching the scattering surface from the inside, one can write

$$\bar{E}^{inc} = j\omega\mu \int_s \bar{J}\phi ds' + 1/j\omega\epsilon\ \nabla \int_s (\nabla_s . \bar{J})\phi ds' + \nabla \times \int_s \bar{\bar{Z}} . (n \times \bar{J})\phi\ ds' \qquad (6)$$

where ∇_s is the surface divergence operator. Equation (6) is the desired integral equation for the current J and can be solved using the method of moments [3].

Corrugated horns:

By placing a Hertzian dipole at a short distance ($\sim\lambda_g/4$) from the inner waverguide termination, the radiated field from the horn can be obtained as the sum of the fields due to $\bar{J}$ and $\bar{M}$ on the scattering surface, plus the field directly incident from the dipole. The corrugations are substituted by the anisotropic surface impedance $\bar{\bar{Z}}$ whose components are [4,5].

$$z^{\phi} = 0 \quad \text{and} \quad z^{t} = \frac{-jg}{g+\delta}\eta \tan k\, d \qquad (7)$$

where g, δ and d are the corrugation parameters defined in Figure 1. The superscripts ϕ and t denote the two perpendicular directions, tangential to the body of revolution.

Figure 2 shows the close agreement in the copolar radiation patterns obtained through experiment [6] and numerical solutions.

Figure 3 shows the cross-polar patterns for different corrugation parameters.

Receiver Horns

In many practical cases, it is desirable to study the scattering properties of receiver horns under loaded conditions. This problem has been investigated recently by Frandsen [7] who simulated the matched load by movable short circuits in the waveguide section of the horn. In the present work, we simulate the effect of load impendance by an impedance boundary condition on the inner surface of the horn end wall. In particular, for a dominant mode matched horn, the impedance on the inner surface of the waveguide

termination may be assumed to be equal to the characteristic impendance of the TE_{11} circular waveguide mode. In this case, the components of the anisotropic surface impedance become

$$z^t = -\frac{\omega\mu}{k_z} = z^\phi \qquad (8)$$

where k_z is the axial propagation constant in the waveguide. Here E^{inc} is obtained by placing the exciting dipole at a far distance.

Results from the present method are compared with those of Frandsen in Figure (5) for a radiating open ended waveguide Figure (4) (equivalent to a horn with zero flare angle). Good agreement is seen to be reached when a sufficient number of triangle functions is used in the expansion of current for the moment method of solution. Figures 6 and 7 show the behaviour of the surface currents when the waveguide termination is changed from zero to the characteristic impendance of the TE_{11} mode. Standing and travelling wave characters for the respective cases can be clearly seen. This behaviour can be used to check the convergence of the solution.

References

[1] Clarricoats, P.J.B., and Saha, P.K., "Propagation and Radiation Behaviour of Corrugated Feeds", Parts I and II, Proc. IEE, 1971, 118A, pp. 1167-1186.

[2] Mentzer, C.A. and Peters, L., "Properties of Cutoff Corrugated Surfaces for Corrugated Horn Design", IEEE Trans., 1974, AP-22, pp. 191-196.

[3] Harrington, R.F., "Field Computation by Moment Methods", The MacMillan Co., NY, 1968.

[4] Shafai, L., and Hansen J.E., "Matrix Formulation of Corrugated Feeds by using Impedance Boundary Conditions", Elect. letters, 1977, Vol. 13, No. 11, pp. 310-311.

[5] _____: "Correction to Matrix Formulation of Corrugated Feeds by Using Impedance Boundary Conditions", Elect. letters, 1977, Vol. 13, pp. 491.

[6] Shafai, L. "A High Performance Feed for a Low Cost Earth Terminal", Communications Research Centre, Tech. Memorandum, No. 59/77, February 1977.

[7] Frandsen, A., "Computation of Scattering and Radiation from Open Ended Waveguides and Small Horns", IEEE International Symposium on Antennas and Propagat, University of Washington, pp. 360-363, June 1979.

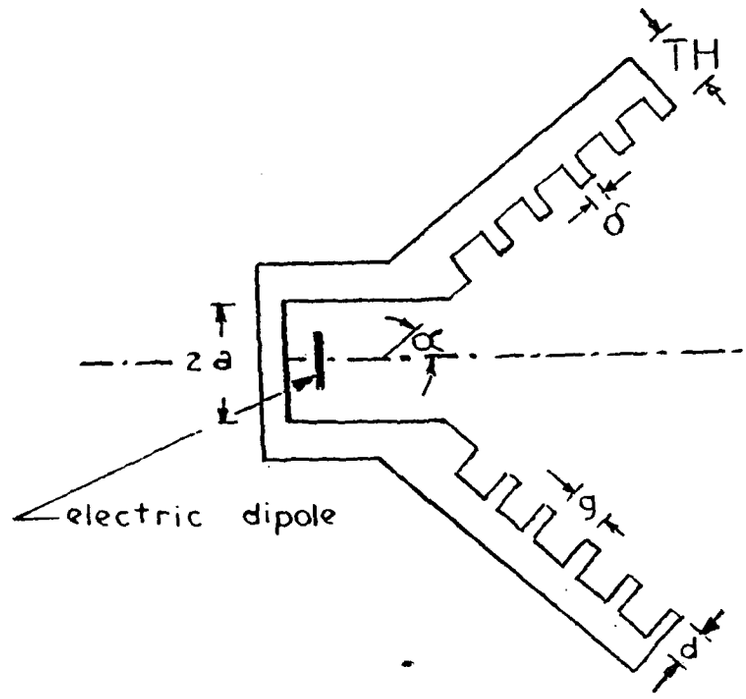

Fig.1 Rotationally Symmetric Corrugated Horn with excitation for TE_{11} Circular Waveguide Mode.

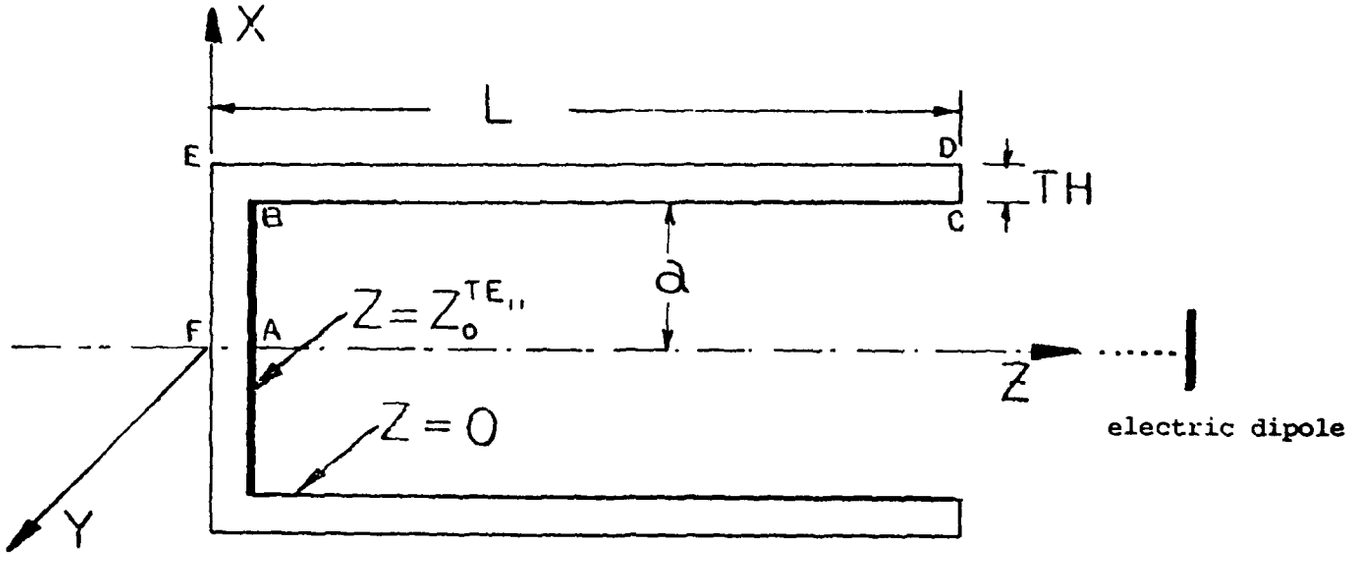

Fig. 4. Scattering Model using impedance boundaries.

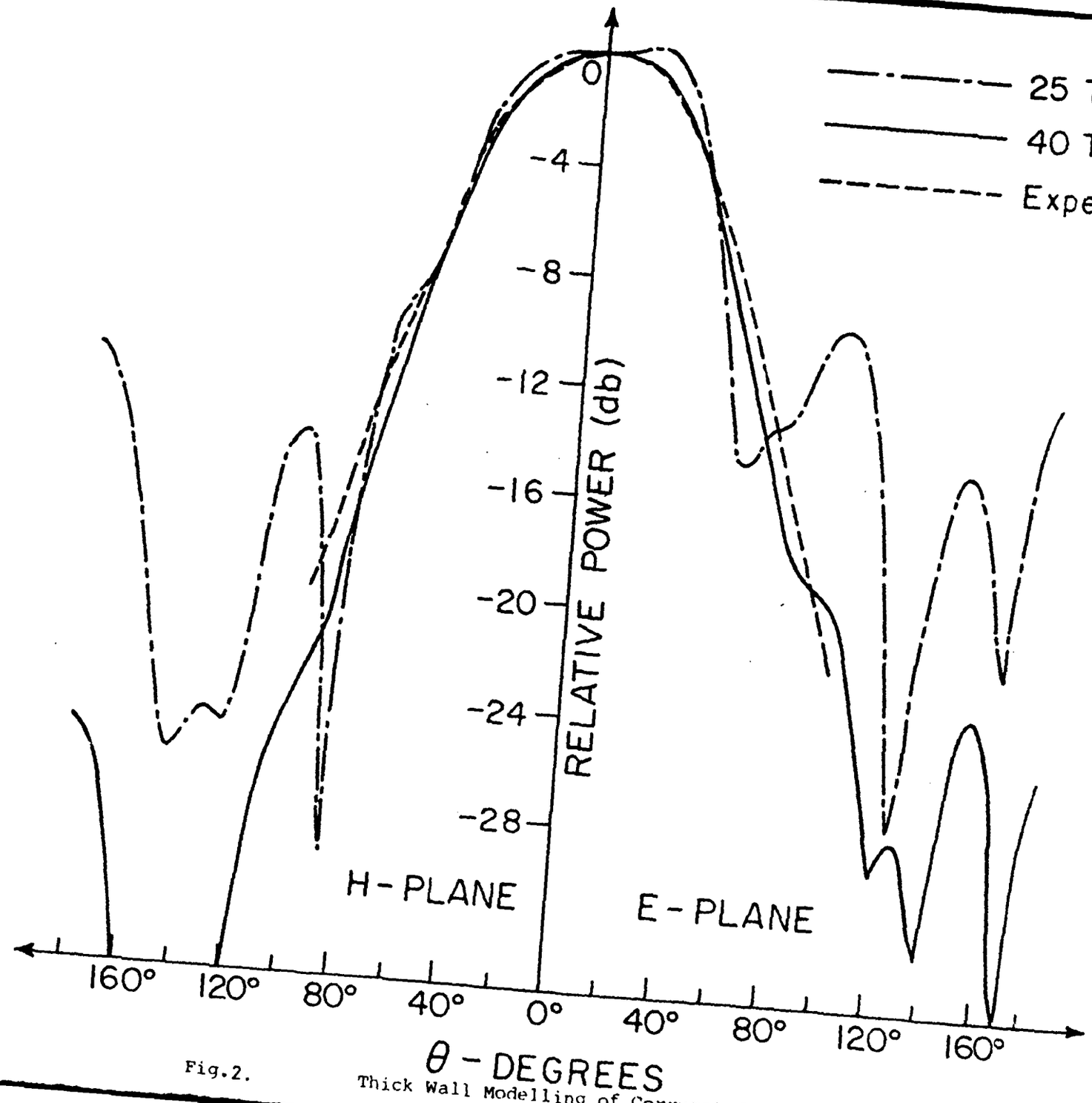

Fig.2. Thick Wall Modelling of Corrugated Horn. (Radiation Patterns).

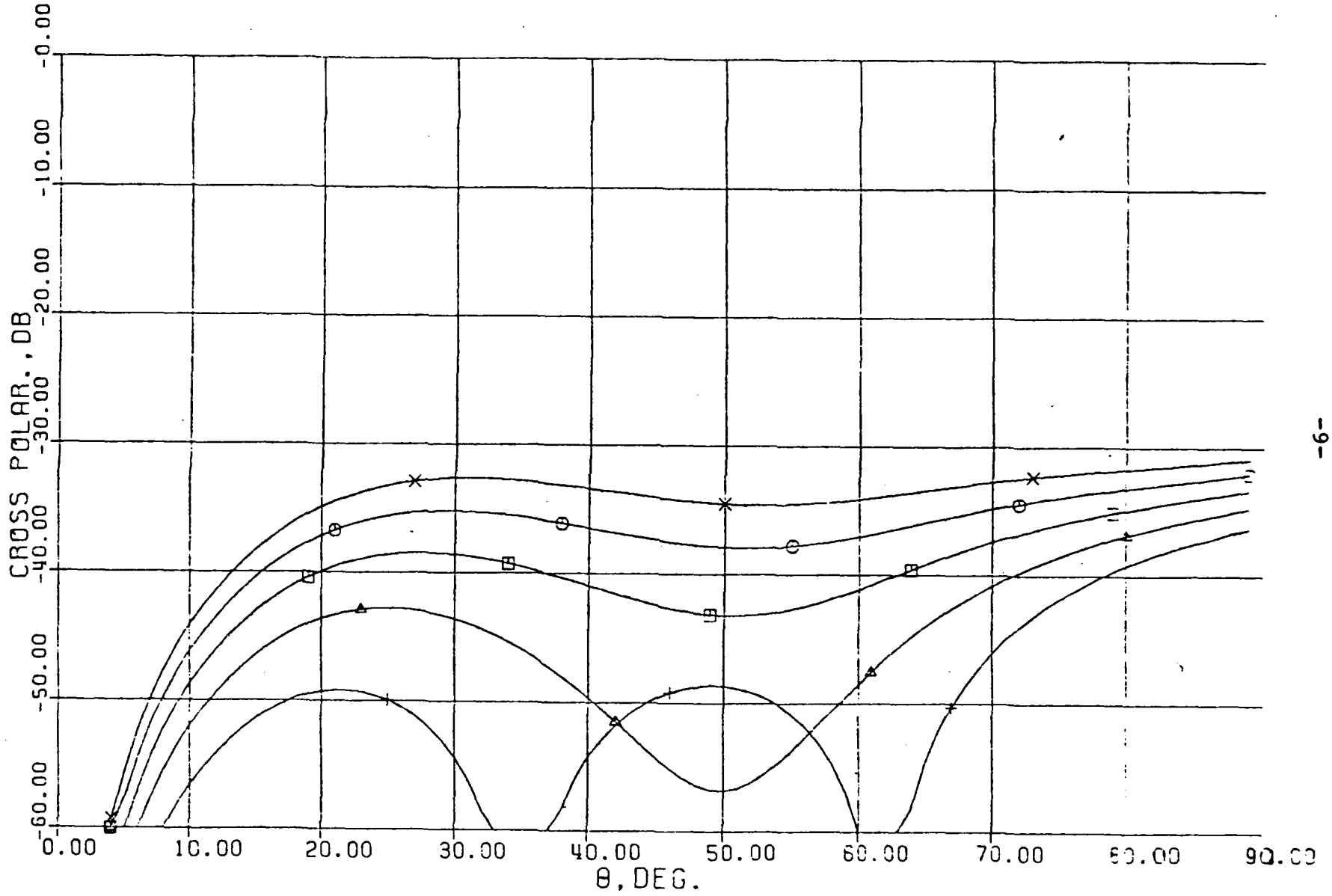

Fig. 3. Cross-Polar radiation patterns for optimum corrugated horn with $a/\lambda = 0.32$; $\alpha = 30^{\circ}$.

x $d/\lambda = 0.13$ Δ $d/\lambda = 0.16$

○ $= 0.14$

□ $= 0.15$ + $= 0.17$

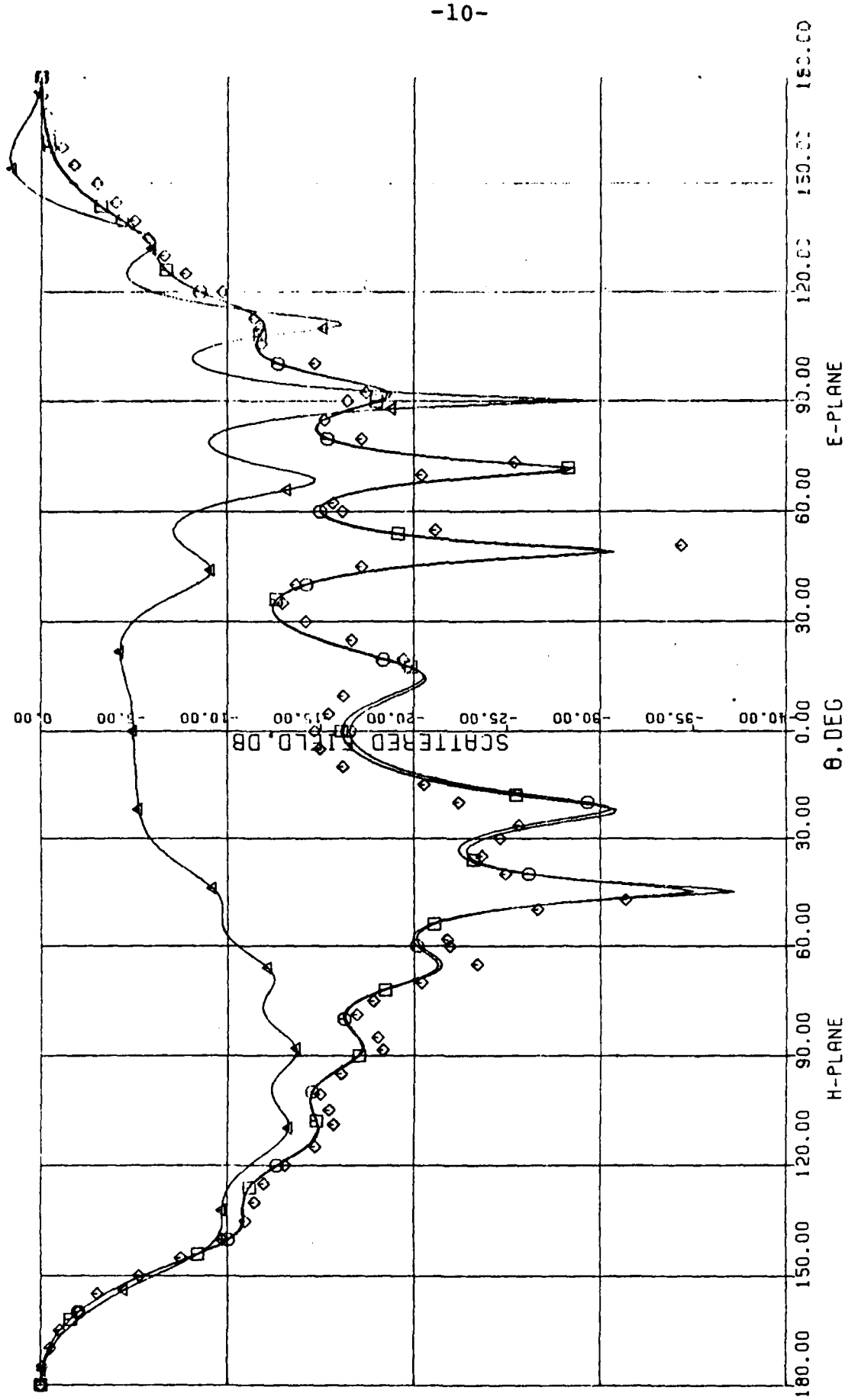

Fig. 5. Scattering patterns from a waveguide section with $L/\lambda = 2.5$; $\lambda = 0.35$; TE/TM = 0.1 .

◇ Frandsen's Solution [7] .

△ Present Solution with NP = 40 .

□ Present Solution with NP = 60 .

○ Present Solution with NP = 120 .

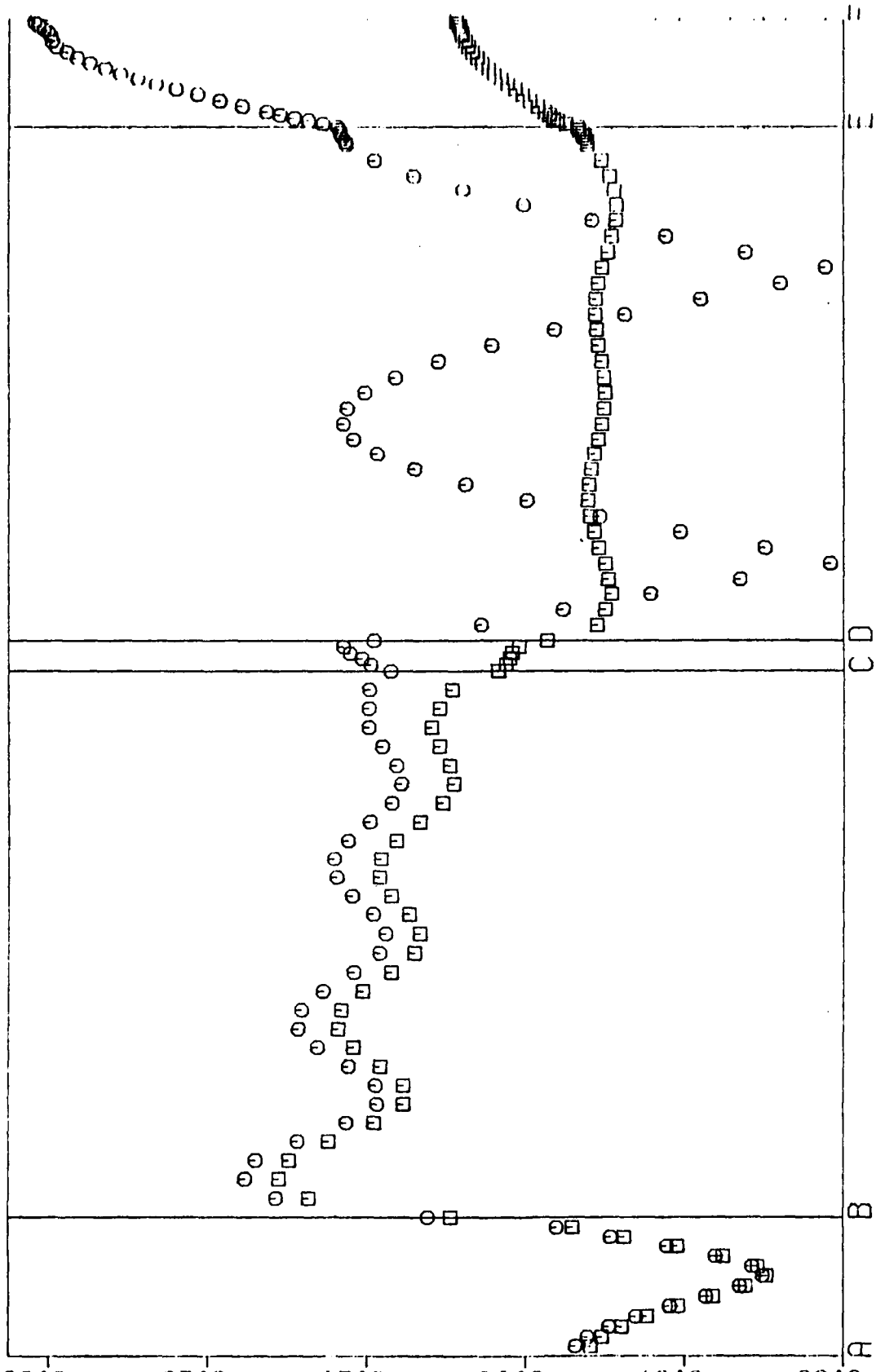

Fig. 6. Induced current I_t on a waveguide section with

$L/\lambda = 1.75$; $a/\lambda = 0.35$; $TH/\lambda = 0.1$;

○ $Z_t = Z_\phi = 0.0$; □ $Z_t = Z_\phi = Z_0^{TE_{11}}$.

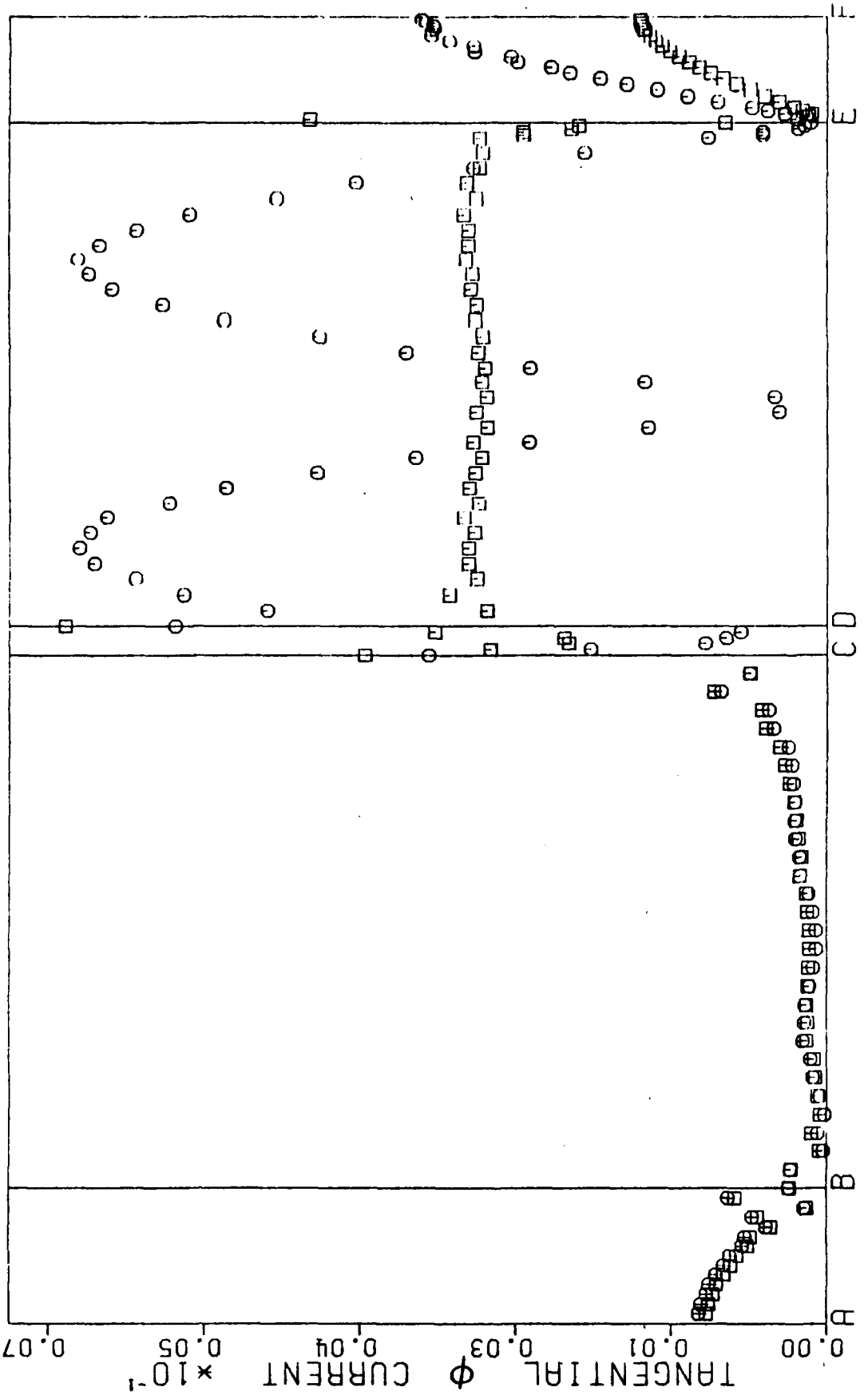

Fig. 7. Induced Current I_ϕ on a Waveguide Section with
$L/\lambda = 1.75$; $a/\lambda = 0.35$; $TH/\lambda = 0.1$;
□ $Z_t = Z_\phi = 0.0$; ☐ $Z_t = Z_\phi = Z_0^{TE_{11}}$.

THE WIRE GRID MICROSTRIP ANTENNA

Richard Conti
John Toth

of
Raytheon Company
Missile Systems Division
Bedford, Massachusetts

ABSTRACT

A description is given of an antenna consisting of an interconnected wire grid formed by etching metallic lines on a dielectric sheet backed by a metallic ground plane. The theory of operation, analytical model and experimental findings for this novel approach to a printed array are described. The device is low cost, light weight and has sufficient bandwidth to be of use in a variety of applications. An analytical model is used to establish transmission line equivalent circuits for the wire grid elements. Current distributions determined from the model are shown to predict accurately the measured pattern performance of a typical implementation. The bandwidth as established by various pattern parameters is quantitatively assessed. Particular emphasis is given to methods of amplitude control through control of line impedances. A particular design implementation is presented for a five wavelength circular array with independent quadrant control. Measured results from this configuration are compared to theory.

1. INTRODUCTION

During the past ten years microstrip antenna technology has made significant advances in both theory of operation and application. However, conventional microstrip patch-type radiators exhibit undesirable bandwidth and cross-polarization limitations. A microstrip printed circuit grid antenna which combines all the usual benefits of conventional patch-type radiators with good bandwidth (typically 6 - 12 percent) and adequate cross-polarization control has been developed. This microstrip configuration features an integrated microwave feed as well as aperture illumination control necessary for providing low sidelobe performance. This class of microstrip antenna is more appropriately referred to as a wire grid antenna.

Microstrip wire grid antenna configurations are composed of staggered interconnected rectangular loops as shown in Figure 1. The basic wire loop dimensions are approximately one wavelength by a half wavelength in the dielectric. These rectangular elements can be arrayed vertically, horizontally or in planar aperture configurations. The multiple loop grid conductor pattern is most conveniently formed by etching metallic lines on a dielectric sheet backed by a metallic ground plane.

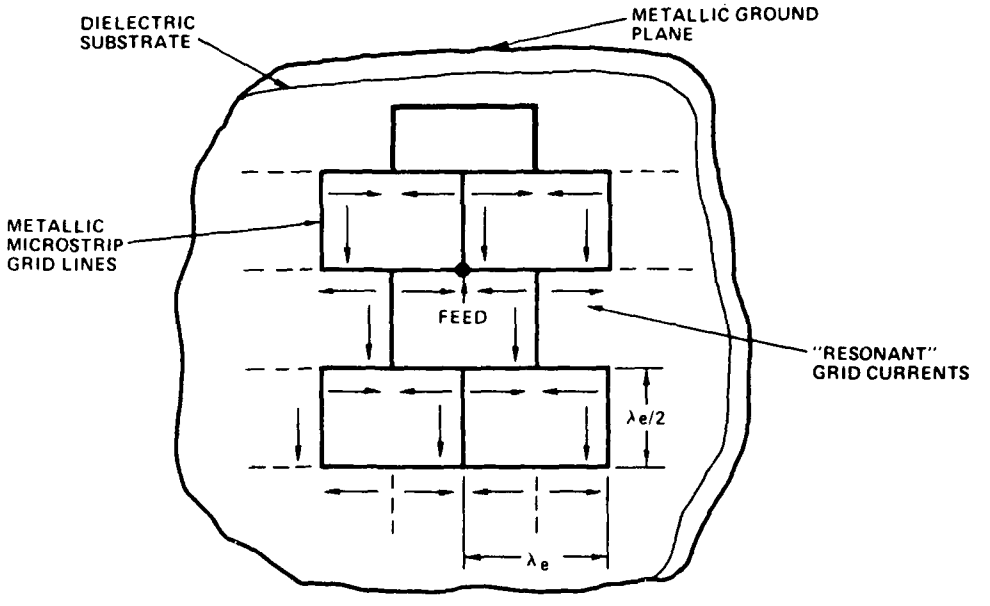

Figure 1 - Microstrip Wire Grid Configuration

2. THEORY OF OPERATION

The wire grid structure in air was first presented by Kraus[1] for frequency scanning applications. As pointed out by Kraus, the loop conductors function as both wire radiators and as transmission lines. For the design frequency of interest, the loops are sized such that the current directions on the array at any instant are approximately as shown in Figure 1. The current on each vertical ($\lambda/2$) loop side is essentially in phase while each horizontal loop segment supports a full wavelength current element. Thus, for example, along an axis normal to the surface, the vertically polarized field components can be phase adjusted to add while the horizontally polarized field components cancel. Proper choice of frequency, feed point and loop parameters permit the grid structure

to be used as a traveling wave device (frequency scanning) as proposed by Kraus and Tiuri et al,[2] and as a resonant (broadside) radiating structure. This paper discusses the latter use of a resonant radiating structure.

The basic principles of operation have been established through careful analysis of measured data on a multiplicity of single and multiple loop wire grid configurations, some of which are shown in Figure 2. The radiation properties of the structure are determined by loop geometry and by the current distribution implemented at each radiator. A specific geometry establishes an array factor which can be used to predict near-in pattern parameters about the resonant frequency. Incorporating each vertical and horizontal line segment in the calculation will provide proper accounting of any amplitude taper that is inherently due to the placement of radiators. However, accurate prediction of frequency and angle behavior require inclusion of the current distribution for each radiator in order to establish the element factor contribution. To obtain the currents an analytical model of the circuit has been developed using a microwave computer aided design (MCAD) program. The MCAD program uses a multiport analysis and is capable of accounting for the dual functions of transmission and radiation that each element in the grid is required to perform. The output allows a complete pattern calculation.

The typical wire grid configuration shown in Figure 1 is approximately three inches in diameter with detailed data at two frequencies presented in Figures 3 and 4. At the center of the design band, data in Figure 3 indicates reasonably close agreement of measured data with predicted patterns utilizing element current distributions. These distributions assumed a propagation constant (β) close to that of the microstrip configuration of a conductor on a dielectric. Simple array factor calculations can be seen to be inadequate in predicting elevation (E-plane) performance. Figure 4 shows measured and simulated far field radiation patterns at about six percent below center frequency where the current distribution creates a totally irregular pattern. The agreement of the model and measured data is quite good which confirms the models validity. It can be noted that the array factor pattern for this frequency is substantially the same as in Figure 3.

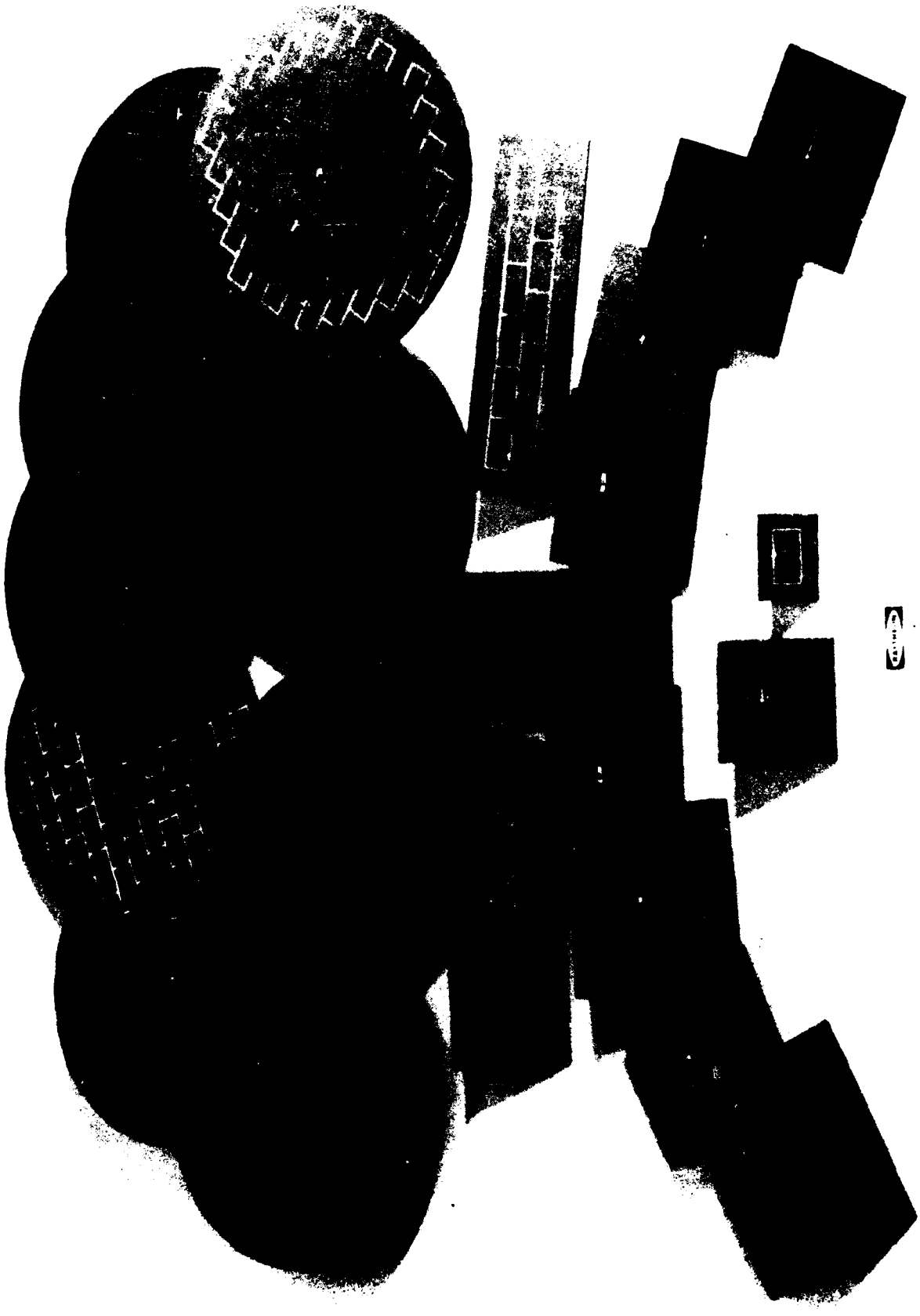

Figure 2 - Printed Circuit Wire Grid Apertures

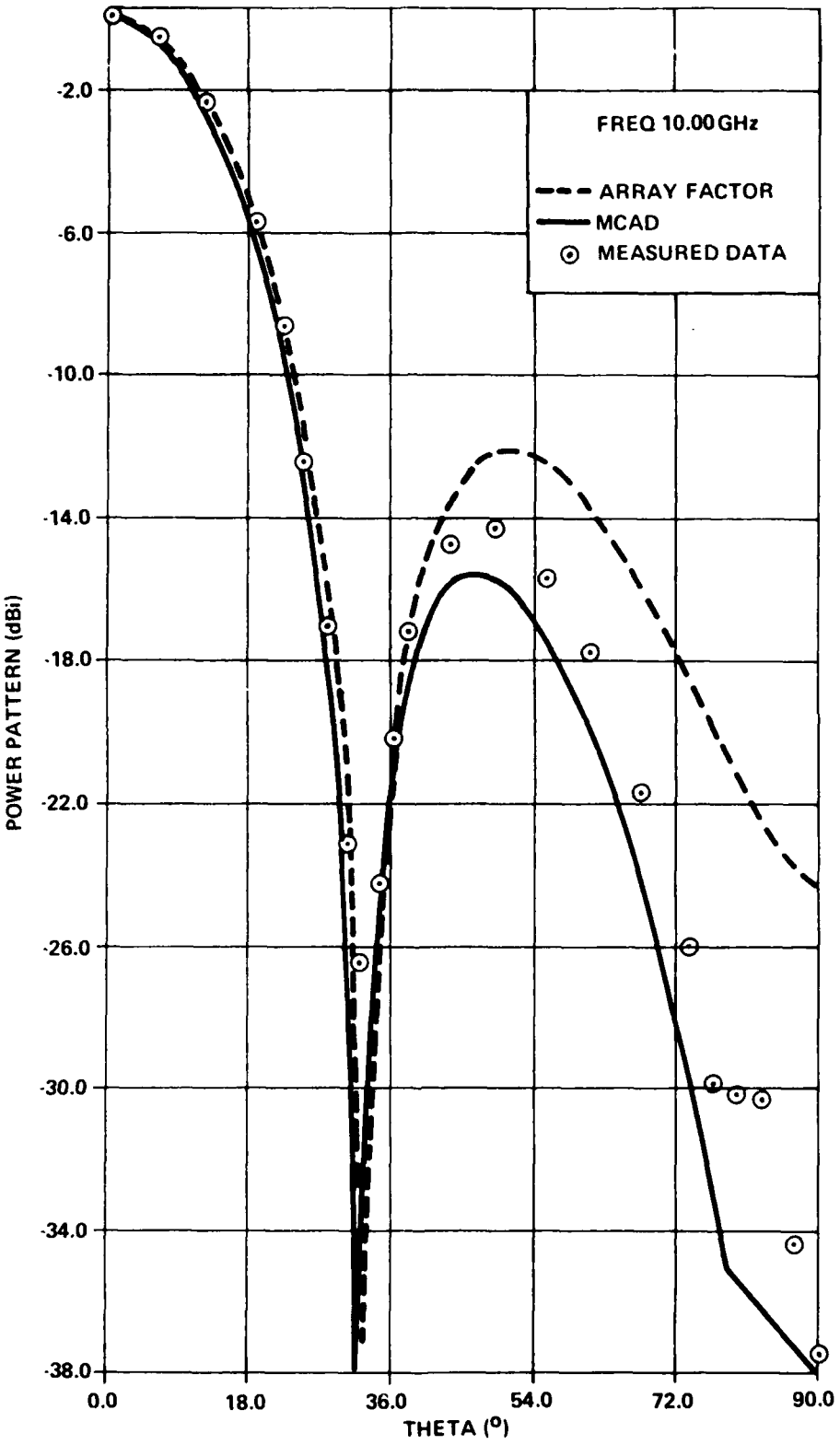

Figure 3a - Measured and Simulated Azimuth Plane Radiation Patterns for Configuration Shown in Figure 1

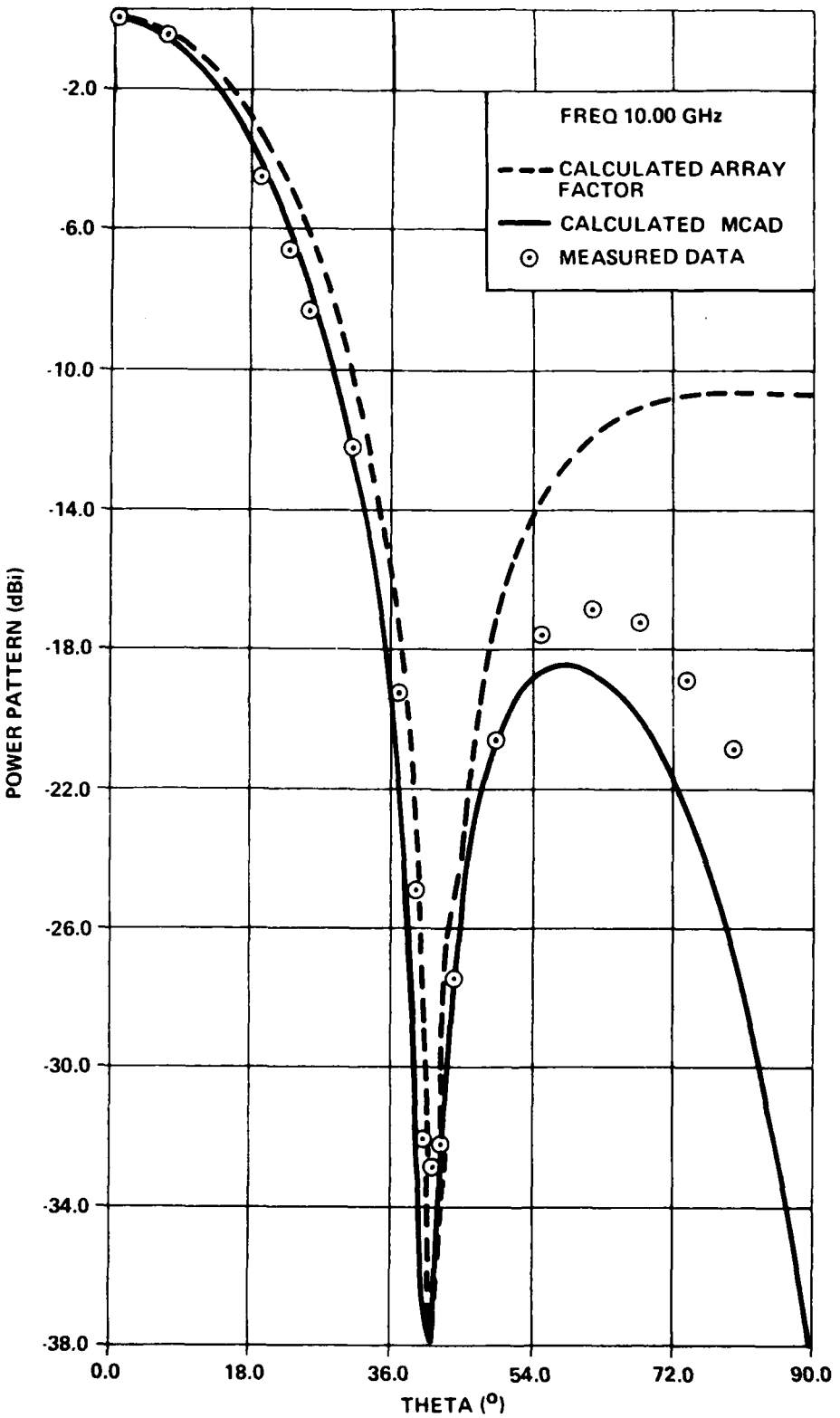

Figure 3b - Measured and Simulated Elevation Plane Far Field Radiation Patterns for Configuration Shown in Figure 1

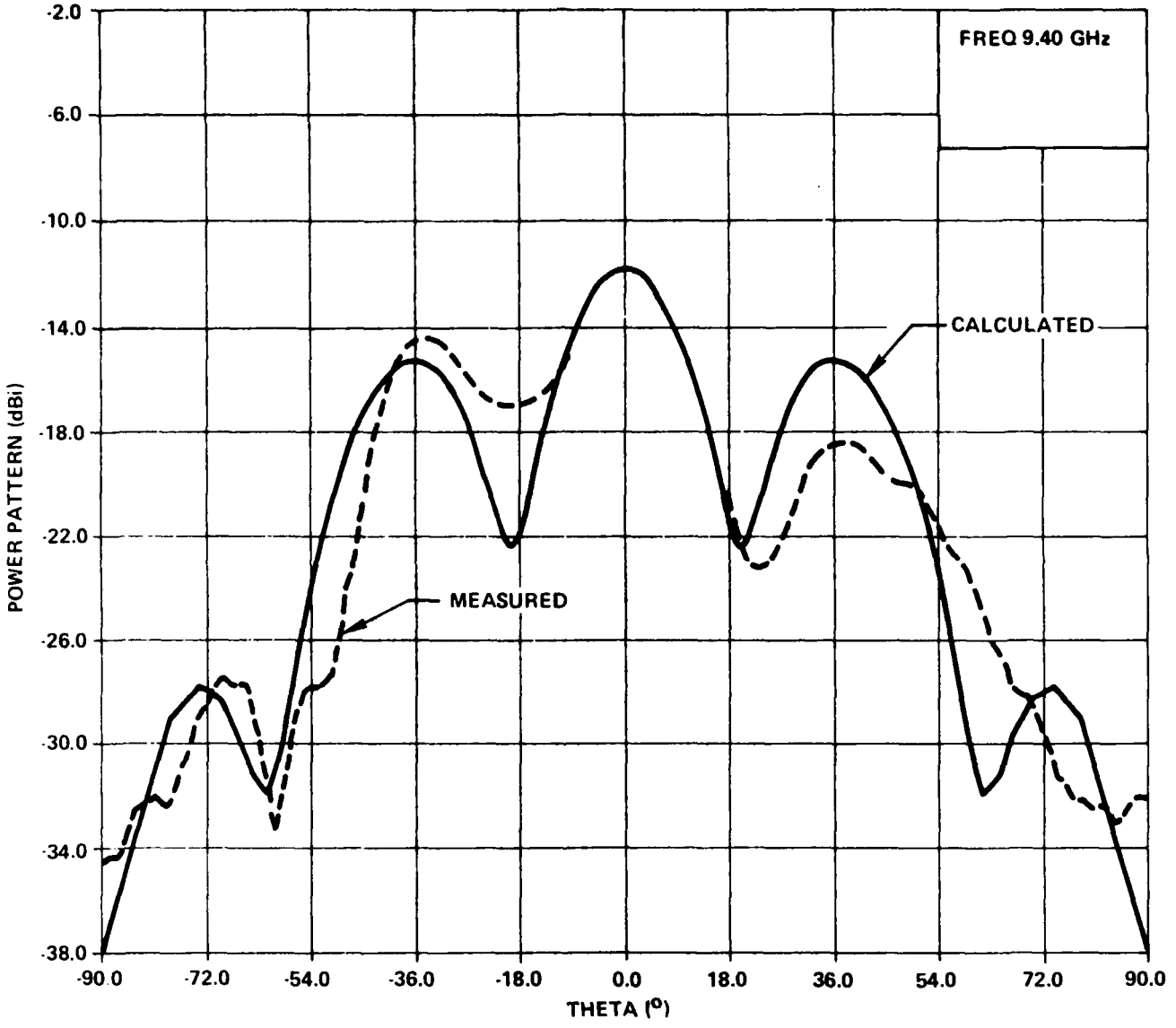

Figure 4a - Measured and Simulated Azimuth Plane Far Field Radiation Patterns for Configuration Shown in Figure 1

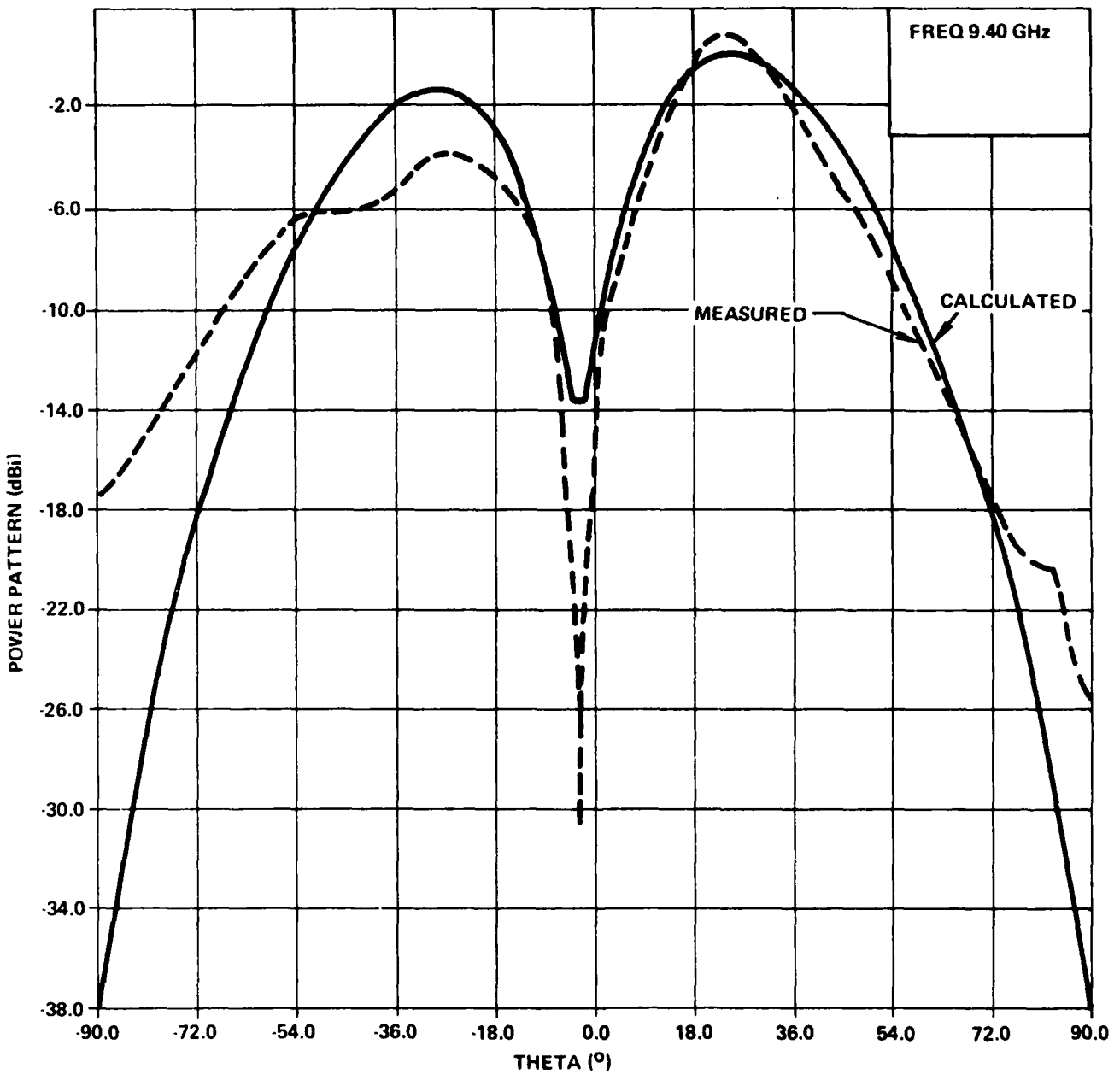

Figure 4b - Measured and Simulated Elevation Plane Far Field Radiation Patterns for Configuration Shown in Figure 1

3. BANDWIDTH AND CROSS POLARIZATION

Bandwidth and cross polarization characteristics vary with the array size (in particular with the number of array loops per feed point) and configuration. Consequently, a single loop radiates both senses of linear polarization with peak levels of similar magnitude and maintains its pattern performance over a relatively large bandwidth. Addition of more loops, works to reduce the magnitude of the cross-polarized peaks and shrink the available bandwidth over which the vertical radiators remain in phase. The useful bandwidth can be defined under any one of several sets of criteria depending on the relative importance of changes in the various radiation pattern characteristics. Available empirical bandwidth data associated with several of the prominent radiation pattern parameters are graphed in Figure 5. The data utilized to generate these bandwidth curves was compiled from measurements of principal plane radiation pattern plots for several different planar array configurations. Figure 5 provides a first cut evaluation of parameter bandwidth versus array size. The criteria used for determining individual parameter bandwidths is defined in Table I.

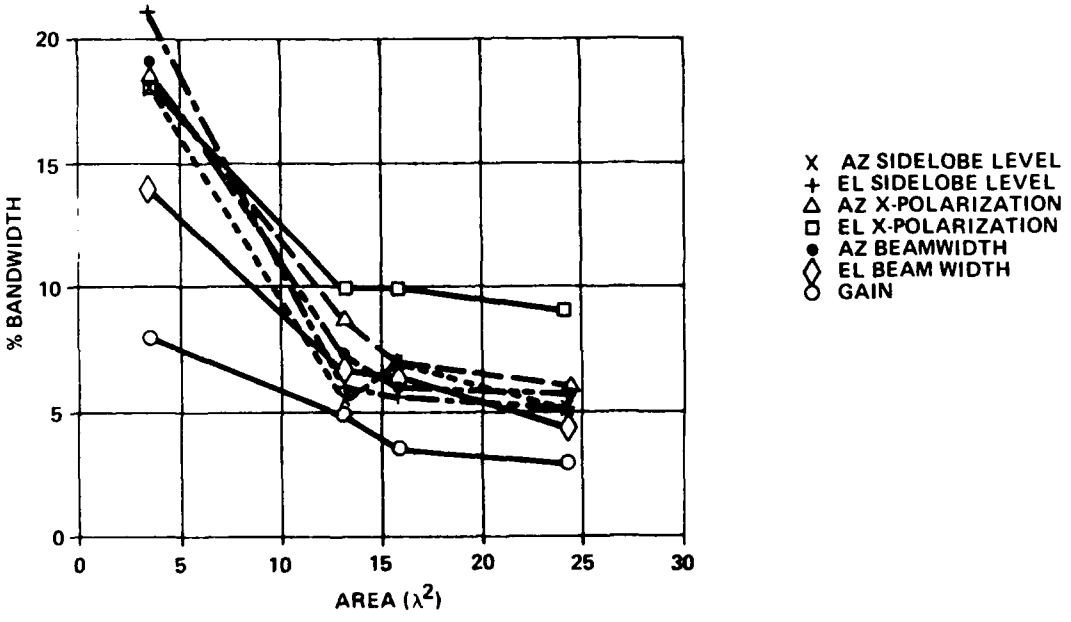

Figure 5 - Radiation Pattern Parameter Frequency Bandwidth

TABLE I BANDWIDTH CRITERIA

PATTERN PARAMETER	CRITERION
Sidelobe Level	+2dB Above Nominal
X-Polarization Level	$\geq$ 20dB Below Beam Peak
Half Power Beamwidth	$\pm$ 1° From Nominal
Gain	$\geq$ 2dB Below Peak Gain

4. AMPLITUDE TAPERING

The microstrip wire grid structure permits an on-aperture illumination control integrated into the grid configuration. This aperture illumination control technique provides individual (vertical halfwave) element amplitude control. By varying the width (and hence the impedance, transmission and radiation properties) of selected grid radiating elements, a relatively complete degree of aperture amplitude control is achieved which is necessary for obtaining low sidelobe aperture distributions. Appropriate radiator line widths can be calculated using a modified reactive power divider type analysis. Figure 6 shows a linear array for which a one dimensional amplitude taper has been applied by increasing selected radiator widths (vertical elements) appropriately. Measured radiation pattern and calculated array factors for the linear array configurations of Figure 6 are shown in Figure 7. A 5 dB lowering of the first sidelobe is achieved without any significant degradation in operating bandwidth or overall radiation pattern characteristics as is predicted by analysis.

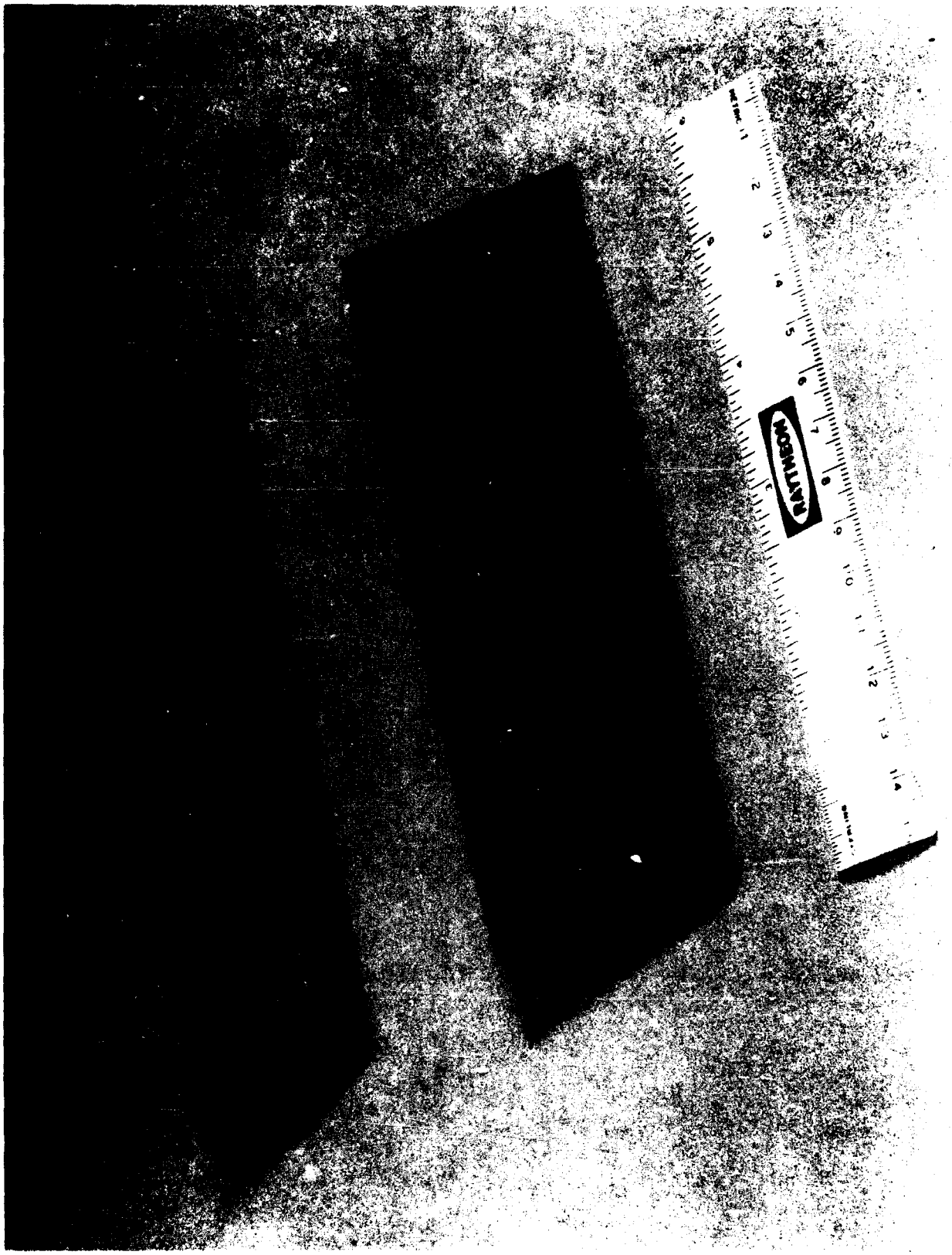

Figure 6 - Wire Grid Linear Array 2E (With and Without Amplitude Tapering)

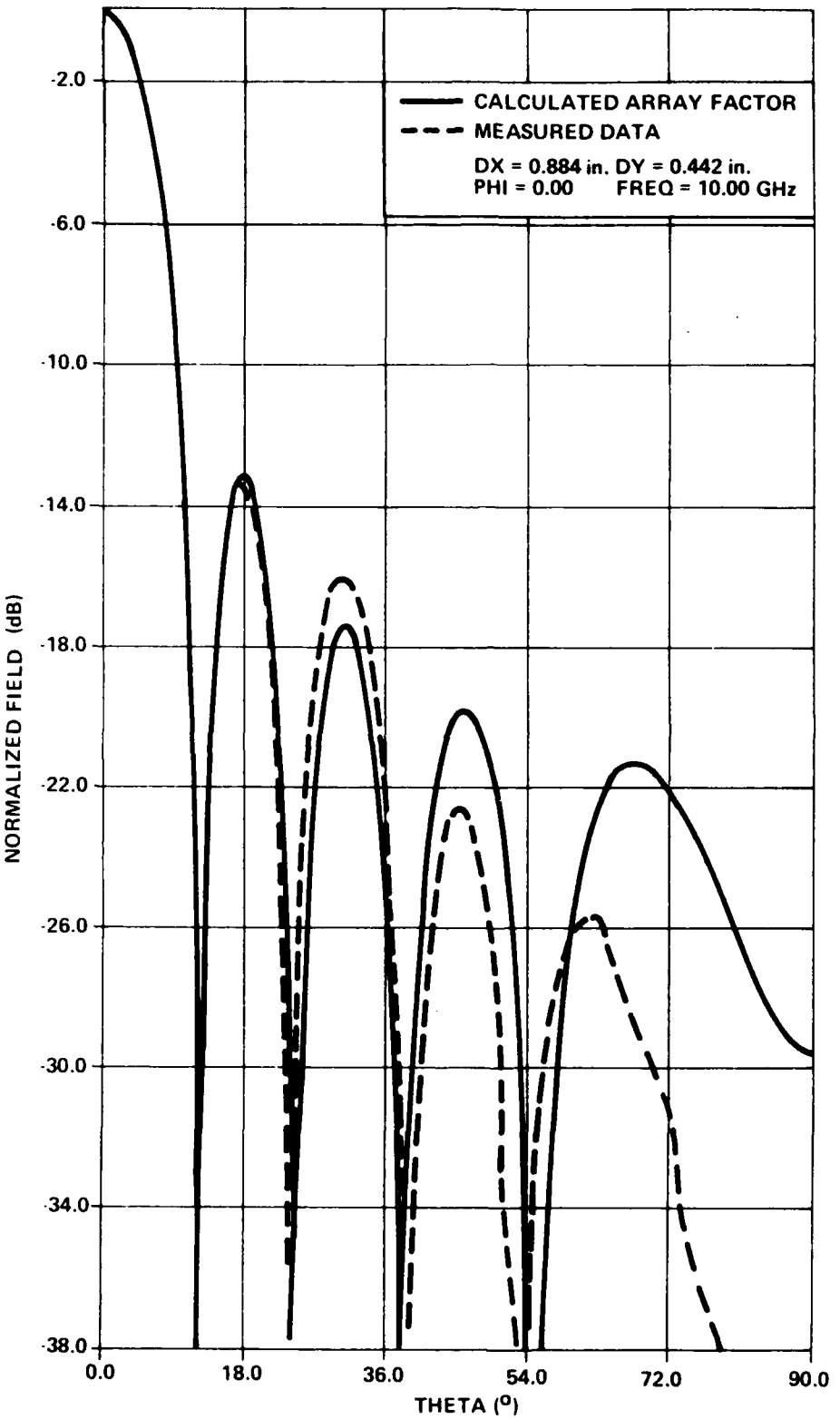

Figure 7a - 2E Array (No Amplitude Tapering)

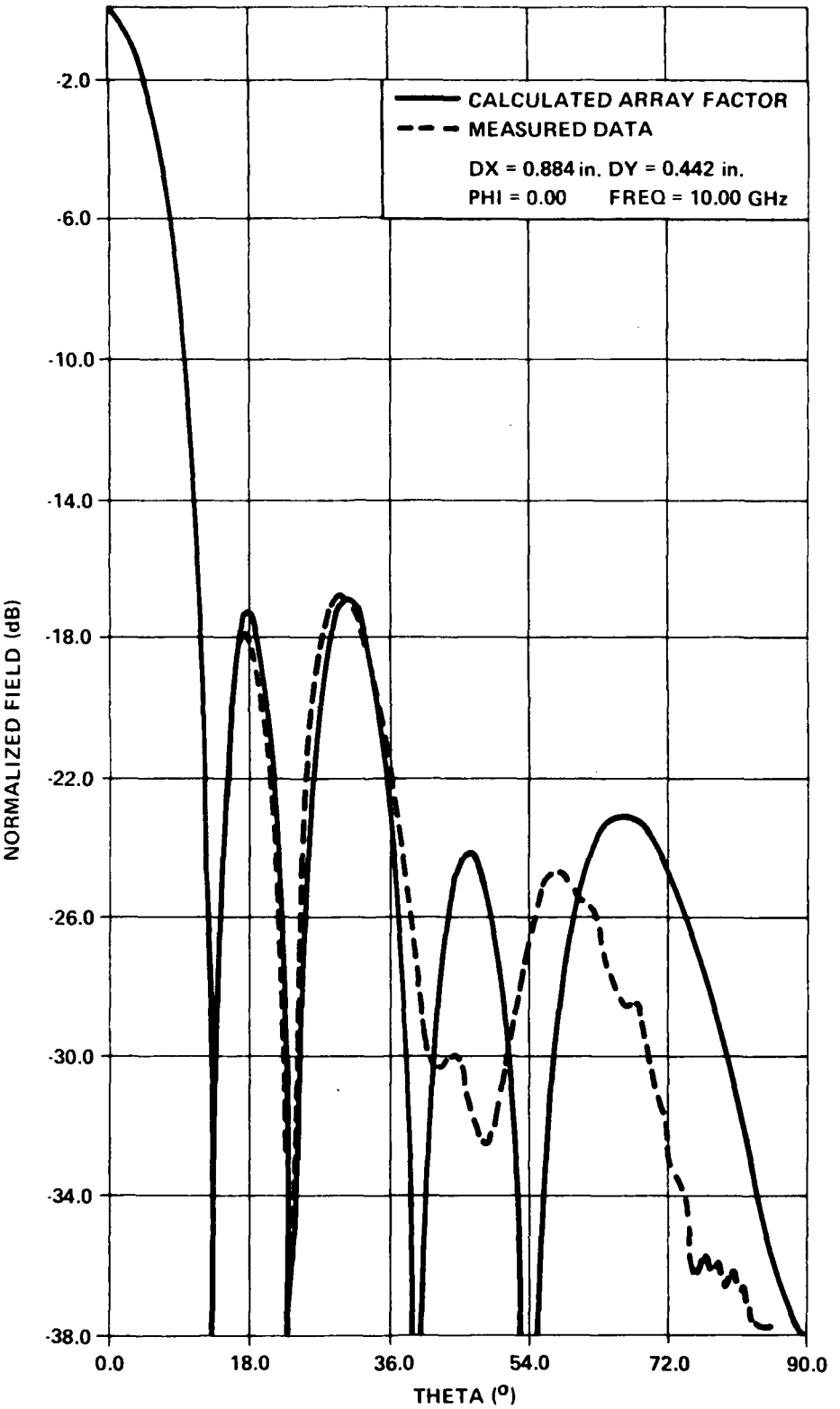

Figure 7b - 2E Array (With Amplitude Tapering)

5. WIRE GRID MICROSTRIP ANTENNA DESIGN

The basic multiple loop design methods needed for a particular application have been defined in the previous section. Although more accurate techniques have been presented, conventional array factor analysis provides satisfactory predictions of array performance over the functional bandwidth of each configuration. Therefore, this method will be utilized as both a design tool and as a check on measured data. As an example of the wire grid design procedure, the effort involved in configuration of an approximately 5λ diameter quadrant monopulse antenna aperture will be discussed. The required performance criteria for this antenna were selected to be consistent with a comparably sized waveguide flat plate slot array antenna with sum sidelobes of 18-10 dB, difference sidelobes > 12 dB down and across polarized levels down more than 20 dB over a 3-6 percent frequency bandwidth. All levels are relative to the sum beam peak.

As is the case in all planar array design, it is important for the Wire Grid Microstrip configuration to effectively utilize the entire available circular area. For a 5 λ diameter array on a Teflon type material ($\varepsilon = 2.2$), the quadrant loop configuration shown in Figure 8 provides the lowest sidelobes. The final quadrant separation was chosen for the best compromise between Σ and Δ channel radiation pattern performance. Measured principal plane pattern cuts for this configuration are consistent with the predicted uniformly illuminated array factor performance. It is evident that the near broadside sum elevation sidelobe levels ($\approx$13 dB) do not meet the above mentioned performance criteria and an aperture taper will be required.

Several amplitude tapers were applied to the vertical radiators of the monopulse grid configuration shown in Figure 8 in order to lower the sum sidelobes. A $\bar{n}$=3 (sidelobe level = -25 dB) circular Taylor distribution was selected to provide low first sidelobe levels (< -20 dB) while maintaining a tolerable taper loss (-0.5 dB). The appropriate quadrant voltage distribution of this taper is shown in the lower left quadrant of Figure 9. The calculated sum channel array factor predicts that near broadside sidelobes are >20 dB below the sum peak.

The circular Taylor taper can be implemented using the impedance amplitude tapering technique presented previously. Utilizing the impedance of a 0.010 inch line width (a convenient width for etching) as the reference value for the lowest voltage level, all impedance levels and line widths required to

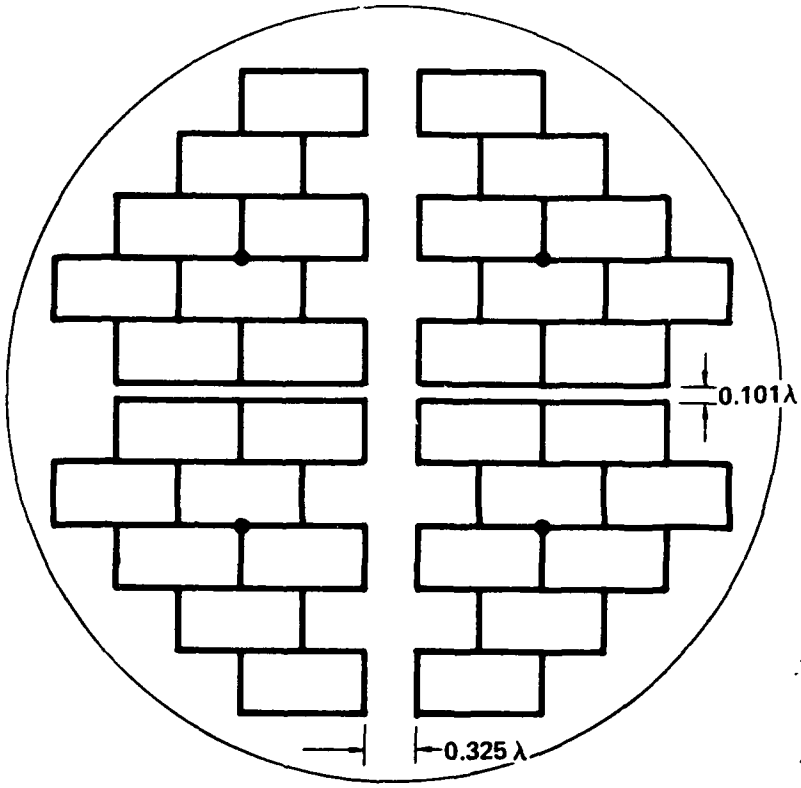

Figure 8 - 5 Diameter Uniformly Illuminated Quadrant Monopulse

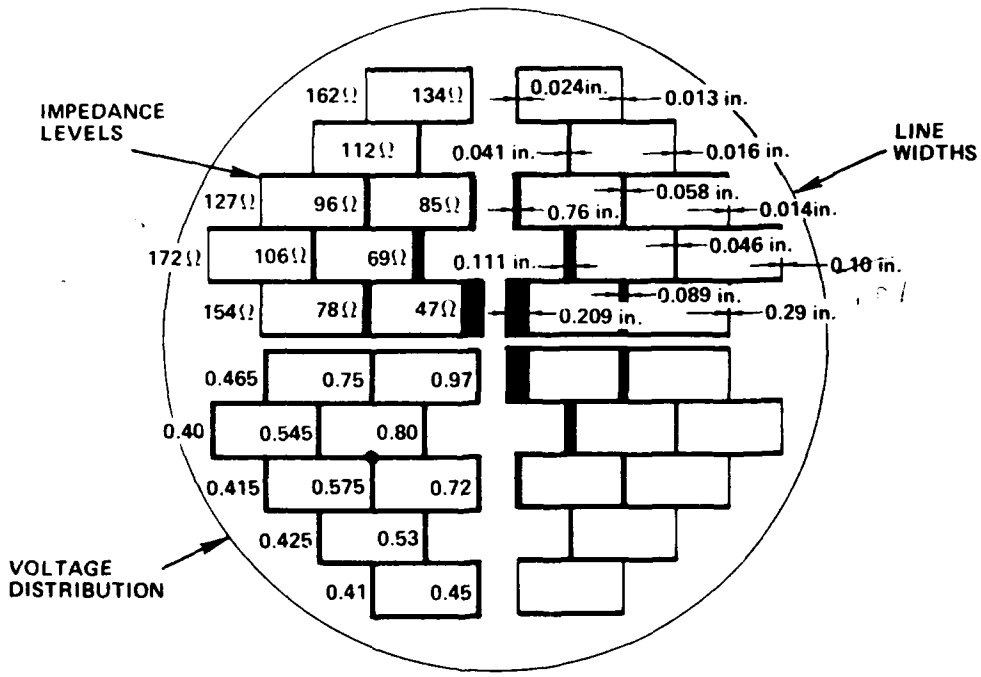

Figure 9 - Quadrant Vertical Radiator Microstrip Voltage Distribution, Line Impedance Levels and Line Widths Required for $\bar{N}$=3 Circular Taylor Tapered Aperture Distribution

describe the aperture taper can be calculated. The resulting values are indicated in the upper two quadrants of the tapered monopulse aperture shown in Figure 9. This configuration was fabricated on 0.05λ Duroid 5880 substrate material and measured with a phase balanced laboratory monopulse network. The sum and elevation difference monopulse channel principal plane far field radiation patterns (co- and cross-polarization) measured at center band are presented in Figures 10 to 12 along with calculated array factor patterns. As can be seen, excellent agreement has been achieved between measurement and theory. The gain of this monopulse grid configuration was also measured at center band and found to be 22.8 dB when the monopulse and interconnecting cable losses are separately measured and subtracted. A summary of the measured center band principal plane pattern performance is tabulated in Table II.

6. CONCLUSIONS

The Wire Grid Microstrip antenna presented in this paper provides a low cost lightweight structure with sufficient design flexibility to be useful in a variety of applications. Adequate gain, bandwidth, cross polarization quality and sidelobe performance can be achieved for planar as well as linear type arrays. This microstrip configuration easily incorporates illumination control into the grid as well as partially or totally incorporating the array feed into the radiating structure.

Grid performance in terms of pattern parameters is adequately predicted by either array factor analysis (near-in performance) or a more rigorous analysis utilizing transmission line equivalent circuits for the wire grid element.

The printed circuit wire grid antenna configuration offers a simple microwave media on a single dielectric board. This construction inherently allows the use of simple, accurate, low cost microstrip etching fabrication techniques and height comparable to typical waveguide or stripline antenna. The wire grid configuration can provide comparable bandwidths to these conventional type antennas, thus providing a low cost alternative for many applications.

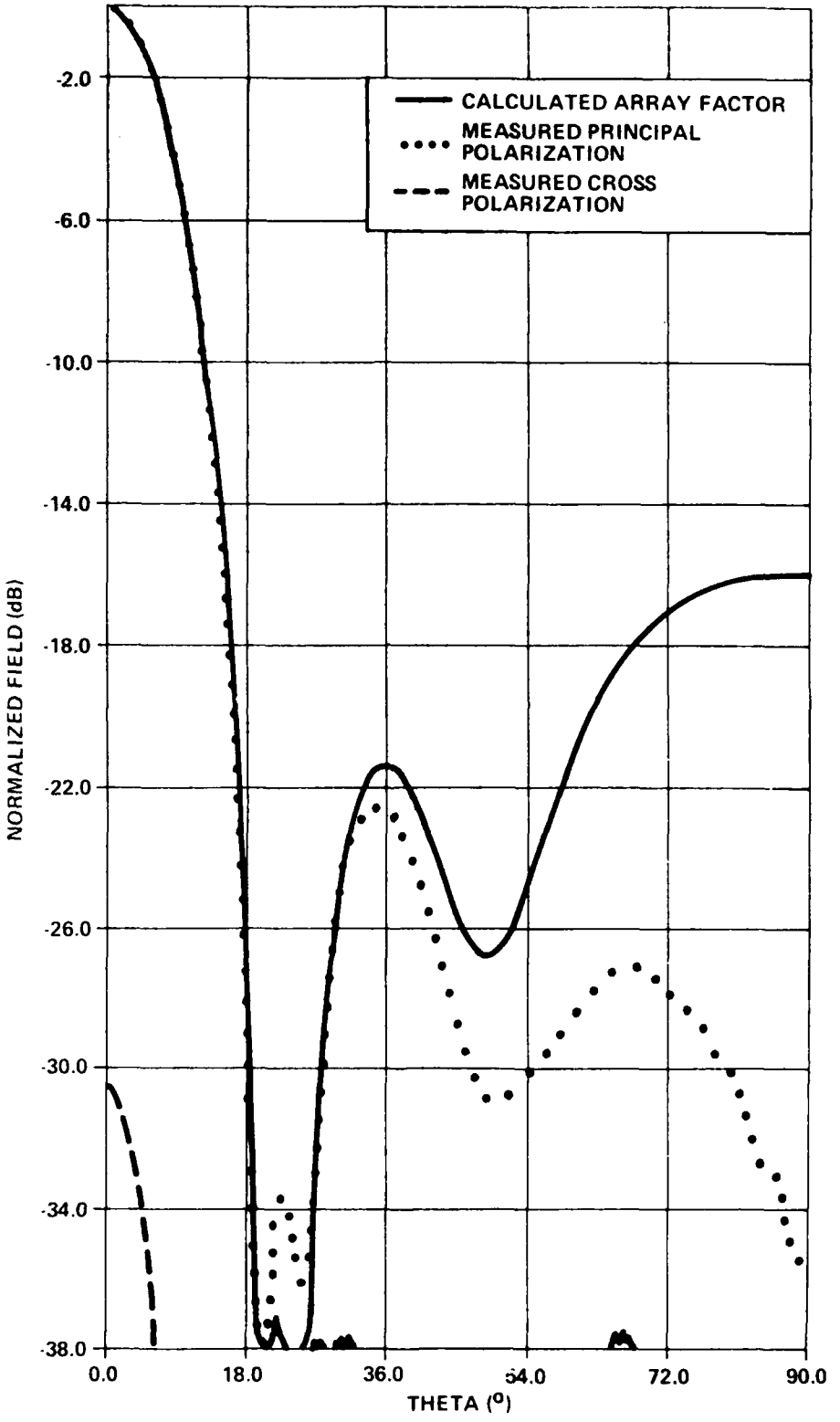

Figure 10 - Monopulse Σ Channel Center Band Azimuth Plane Far Field Radiation Pattern, PHI = 0°

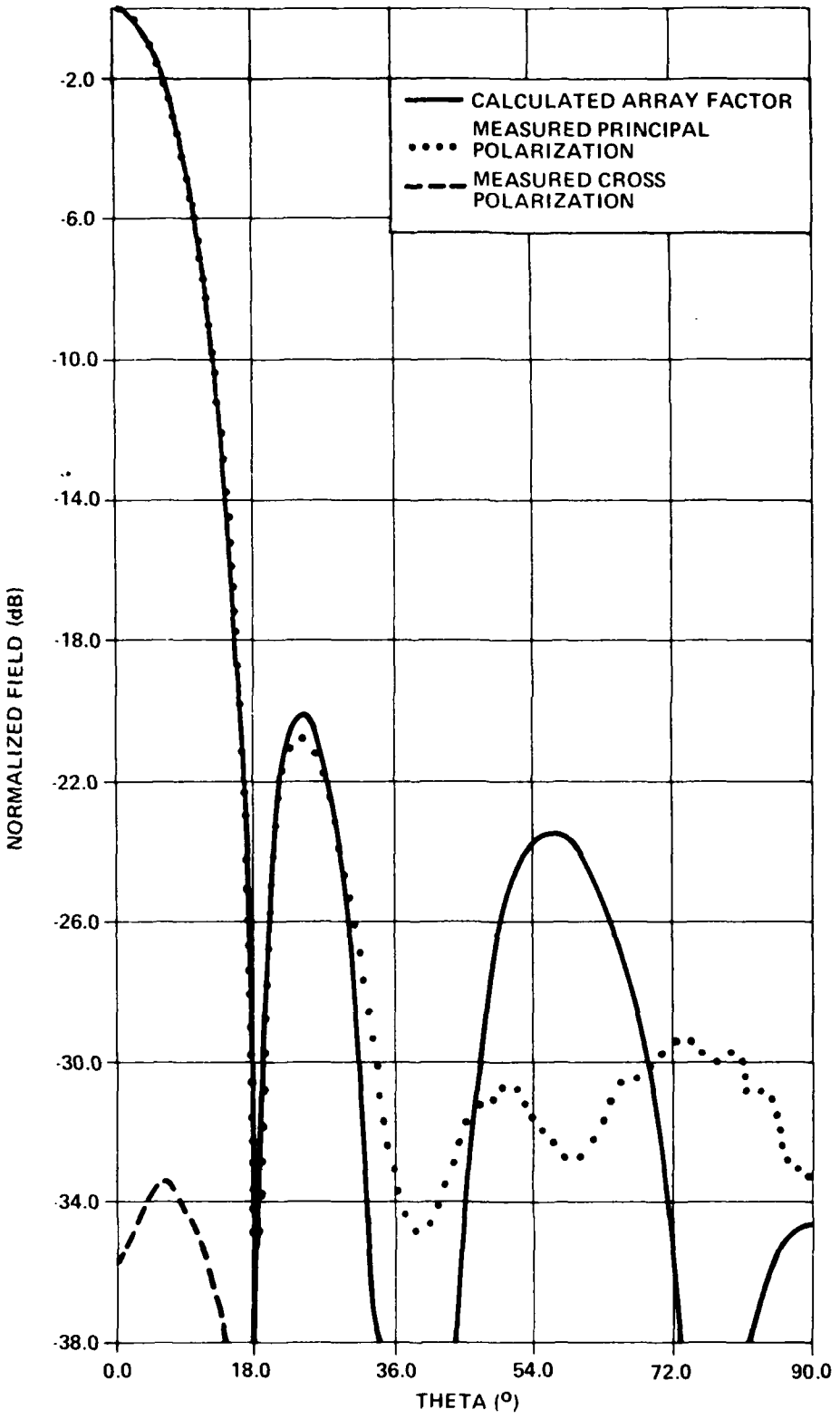

Figure 11 - Monopulse Σ Channel Center Band Elevation Plane Far Field Radiation Pattern, PHI = 90°

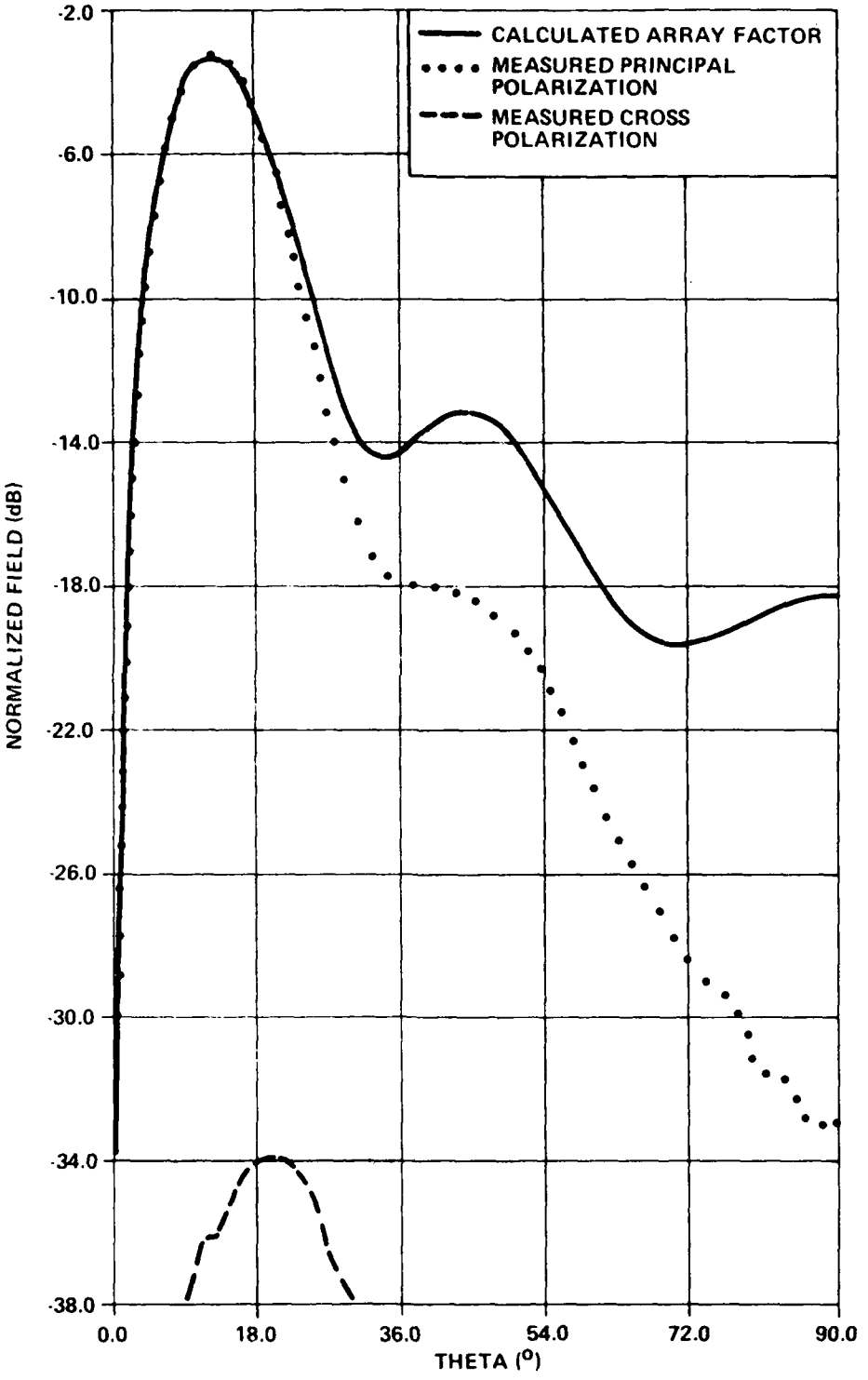

Figure 12 - Monopulse Δ EL Channel Center Band Elevation Plane Far Field Radiation Pattern, PHI = 90°

TABLE II MONOPULSE WIRE GRID ARRAY PERFORMANCE

Gain	22.8 dB
Σ Sidelobes	> 20dB Below Σ Peak
Δ Sidelobes	> 17dB Below Σ Peak
Null Depth	30dB Below Σ Peak
X-Polarization	> 25dB Below Σ Peak

REFERENCES

[1]Kraus, J.D., "A Backward Angle End Fire Antenna," IEEE Transactions on Antennas and Propagation, Volume AP-12, pp. 48-50; January 1964. See also J.D. Kraus and K.R. Carver, "Electromagnetics," McGraw Hill Co., N.Y., N.Y., Section 14-16, 1973.

[2]Tiuri, M., Tallqvist, S., Urpo, S., "Chain Antennas," 1974 International IEEE/AP-S Symposium and Digest, Georgia Institute of Technology, Atlanta, Georgia, pp. 274-277, 1974.

A SIMPLE EXPERIMENTAL METHOD FOR SEPARATING LOSS PARAMETERS OF A MICROSTRIP ANTENNA

W. F. RICHARDS, Y. T. LO, J. BREWER

***abstract*- This note presents a simple method for the computation of both the dielectric loss tangent and the conductivity of the metal cladding of printed circuit boards at microwave frequencies. Since the treatment of the cladding in the lamination process affects its conductivity, losses in the dielectric and the metal cannot be measured separately. Thus, an analytical means for separating these losses must be employed. The method described in this note accomplishes this by utilizing the different dependence of the two losses on dielectric thickness in thin cavities.**

I. INTRODUCTION

Manufacturers of printed circuit boards (PCB) commonly supply data on the relative dielectric constant and loss tangent of the substrate with no mention of the loss in the metallic cladding. A *naive* user might automatically refer to a table for the published value of conductivity of the cladding, unaware that the treatment of the surface in the cladding process can decrease the effective conductivity of the metal significantly. A knowledge of these losses is important in computations of characteristics of microstrip antennas [1], [2] as well as circuit elements using the PCB. Of course, it is necessary to be able to *separate* these two types of losses *without altering the surface conditio.. between the metal and the substrate.* This note describes a simple method for experimentally determining both the dielectric loss tangent and the conductivity. The procedure involves the construction of two or more thin cavities from the PCB of equal dimensions except for thickness. The "Q's" of these cavities are measured and the loss tangent and skin depth are computed from these.

II. THEORY

Within a cavity, the time-averaged power lost within the dielectric of loss tangent, δ, is

$$P_d = \delta\omega\epsilon \iiint_V \mathbf{E}\cdot\mathbf{E}^* dv \qquad (1)$$

$$= 2\delta\omega W_E$$

where ω is the angular frequency, ϵ is the relative dielectric constant of the PCB, $\mathbf{E}$ is the electric field, and W_E is the time-averaged electric stored energy within the cavity. If the cavity is thin, the fields will essentially be z-independent and $\mathbf{E}$ will be directed along the z-axis. Assuming that the metal cladding is several skin depths thick and *can be considered* uniform, then the power absorbed within the walls of the thin cavity is

$$P_{Cu} = \frac{2}{\sigma\Delta}\int\int_S \mathbf{H}\cdot\mathbf{H}^* ds = \frac{4}{\sigma\Delta\mu_0 t}\frac{1}{2}\mu_0\int\int\int_V \mathbf{H}\cdot\mathbf{H}^* dv \tag{2}$$

$$= 2\frac{\Delta}{t}\omega W_M$$

where σ is the conductivity of the cladding, Δ is the corresponding "skin depth," $\mu_0 = 4\pi 10^{-7}$ H/m, t is the thickness of the cavity, S is the surface of the cladding on both sides of the dielectric, and W_M is the magnetic stored energy. In obtaining (2), the power lost in the narrow side walls of the cavity was neglected since for thin cavities this contribution is not significant. However, when this loss is not negligible, a correction can easily be found except that the final result is not as simple and elegant as that given below [3]. From (1) and (2), at resonance (where $W_E = W_M$), the reciprocal of the quality factor of the cavity is

$$\frac{1}{Q} = \frac{P_{Cu} + P_d}{2\omega W_E} = \delta + \frac{\Delta}{t}\,. \tag{3}$$

For a fixed t and a measured Q, (3) describes a straight line in the $\delta-\Delta$ plane whose slope is $1/t$. If the material is assumed to be uniform, it is then possible to determine δ and Δ by measuring Q's of several cavities of various thicknesses, t.

III. PROCEDURE

The experimental procedure consists of cutting a sample of doubly-clad PCB to some rather arbitrary shape which, when fashioned into a cavity, supports modes resonant at frequencies for which the parameters δ and σ are desired. A cavity is formed by joining the two conducting surfaces of the PCB of thickness, t, along the side walls with good conducting material. For example, copper foil may be soldered to the two sides of the PCB. A feed point is chosen that will allow the excitation of the desired resonant modes. The feed is formed by connecting

the sheath of a coaxial cable to one surface while its center conductor is connected through the dielectric to the other surface. The Q's of this cavity are measured at the desired resonant frequencies.

A second cavity is constructed, preferably using material from the same board from which the first cavity was cut, of twice the thickness of the first cavity. This is done by cutting *two* sections of PCB with the same dimensions as those for the first cavity. The cladding on one side of each of the two sections is removed. The two are then clamped together dielectric-to-dielectric to form a "sandwich" of thickness, $2t$. Finally, this sandwich is made into a cavity and a feed added as in the first cavity. The Q is measured for this cavity and a second line in the $\delta-\Delta$ plane is drawn from equation (3) with t replaced by $2t$. The intersection of this line with that corresponding to the first cavity yields the dielectric loss tangent, δ_0, and the skin depth, Δ_0, of the cladding. From the latter, the conductivity is immediately deduced. Of course, for more accurate results, measurements for cavities of more than two thicknesses should be made.

IV. RESULTS

This procedure was carried out for *many* samples of Rexolite 2200 [3]. Figure 1 shows a typical example of measurements performed at 680 MHz. Since the Q's of the cavities are quite high and difficult to measure accurately, a range of Q's was obtained for any given sample when the measurements were repeated. The measurements were made at various times since the Q might also vary with physical conditions such as moisture. Also, different clamping pressures were applied in measurements of the same samples to determine if small air gaps in the "sandwich" affected the measured Q. Our results seemed to indicate that clamping pressure had no significant effect on the results. Thus the lines represented by equation (3) becomes the "bands" shown in fig. 1. In this case, *three* cavities were constructed of nominal thicknesses $\frac{1}{16}$, $\frac{1}{8}$, and $\frac{3}{16}$ inch. The solid black region in the figure represents the overlap of all three bands and most probably contains the *true point* (δ_0, Δ_0). The centroid of this region is a reasonable point to take for (δ_0, Δ_0). If this is done, one concludes that the loss tangent of this

sample of material is $1.1 \cdot 10^{-3}$ and the conductivity of the cladding is 364 K /cm. This conductivity is about $\frac{5}{8}$ the value of pure copper. Thus, it is apparent that the surface finish can have a *significant* effect on the conductivity. Inclusion of the estimated loss in the side walls of the cavity is found to have an insignificant effect on the computed values of δ_0 and Δ_0.

It would be highly desirable to have an independent check of the validity of this method with an entirely different technique. To the knowledge of the authors, none seems to be available which separates the two types of losses without altering the actual surface condition of the cladding (although there have been investigations on the *effect* of surface roughness of the copper itself, *ie.*, in the absence of bonding agent and substrate). However, using the loss parameters determined by this procedure, the authors computed the input impedances of a number of microstrip antennas. The agreement between these computed results and the corresponding measured input impedances was very close [2]. This indirect test suggests that the method discussed in this paper indeed gives useful results.

V. CONCLUSIONS

A very simple method for determining the loss parameters of printed circuit boards is presented which can be employed without the necessity of sophisticated equipment and the use of complicated formulas. The accuracy of the final results depends mainly upon the accuracy to which the quality factor of a cavity can be measured. Even a rough estimate of the conductivity obtained by this method can be useful and is more than what is provided by manufacturers.

REFERENCES

1 Y. T. Lo, D. Solomon, and W. F. Richards, "Theory and experiment on microstrip antennas," *IEEE Trans. Antennas Propagat.*, vol. 27, pp. 137-145, Mar. 1979.

2 W. F. Richards, Y. T. Lo, "An Improved Theory for Microstrip Antennas and Applications," *IEEE Trans. Antennas Propagat.*, (to be published)

3 Y. T. Lo, W. F. Richards, J. E. Brewer, "Evaluation of Losses in Microstrip Antenna Materials," *RADC Interim report* under contract No. F19628-78-C-0025, November, 1979.

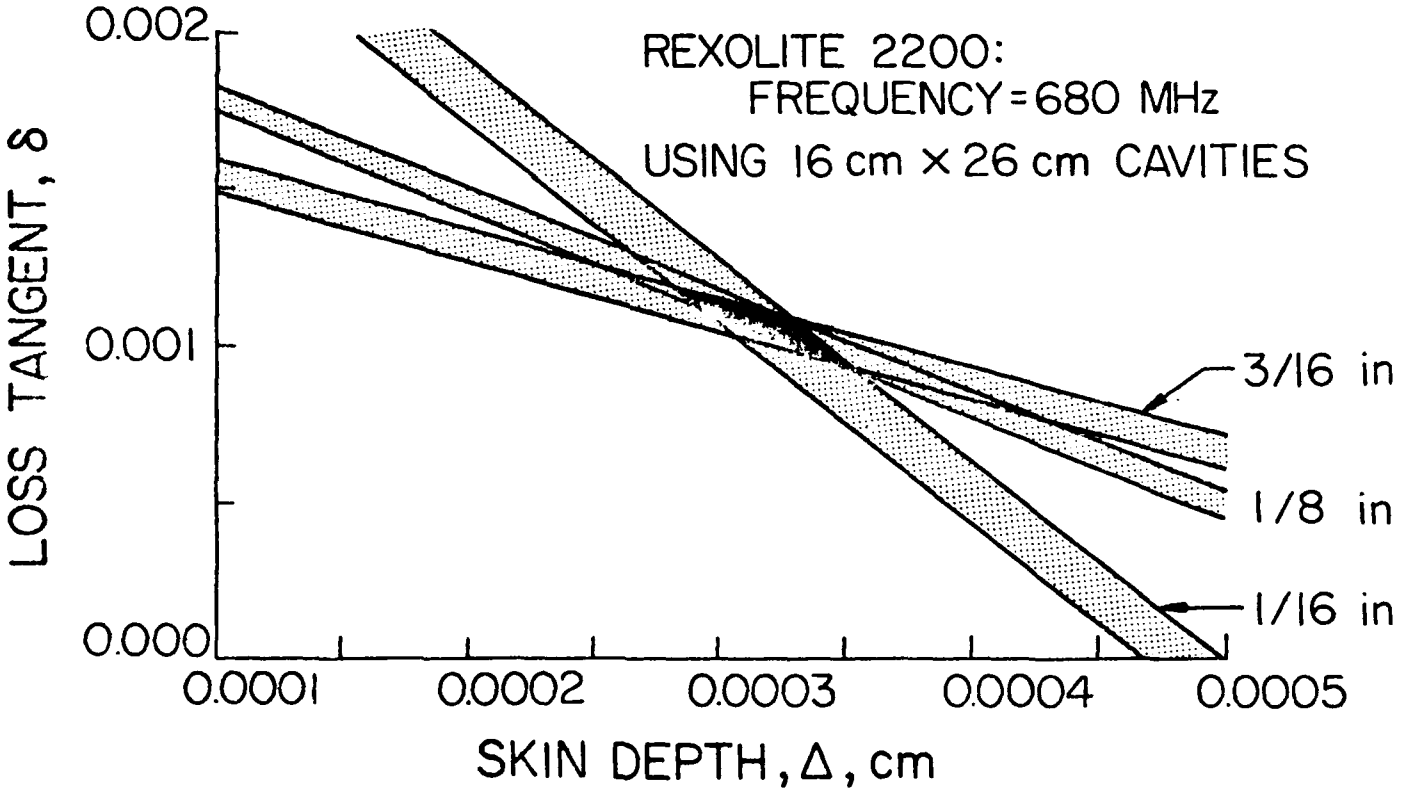

Figure 1. Loss tangent versus skin depth for Rexolite 2200 for dielectric thicknesses of 1/16, 1/8, and 3/16 inch.

DUAL-POLARIZED, ENHANCED BANDWIDTH MICROSTRIP ANTENNAS

M. M. Millar and K. R. Carver
Physical Science Laboratory
New Mexico State University
Las Cruces, N. M. 88003

INTRODUCTION

Dual-polarized microstrip antennas with moderate bandwidths are useful in a variety of applications ranging from polarization-diverse communication systems to dual-polarized microwave radiometers. The microstrip antennas described in this paper were developed in response to a need for light-weight planar arrays to be used with an airborne 1415 MHz dual-polarized microwave radiometer. The design goal for the VSWR = 2:1 bandwidth was 70 MHz, i.e. 5%.

This paper summarizes measurements of impedance, polarization purity and pattern shape for both individual isolated dual-polarized microstrip elements as well as arrays of these elements. Techniques for incorporating an integrated stripline feed system for the arrays are also described.

ELEMENT DESIGN

The basic element used in this study is a square microstrip patch of side dimension A, fed by two orthogonally-oriented coaxial probes, each at inset distance B from the patch edge, as shown in Fig. 1. The patch is etched on one side of a .0065" PTFE board, with the copper removed on the opposite side. This thin board is then adhesively bonded to a 0.25" thick Hexcell sheet, with a ground plane formed by a copper-coated .0065" PTFE board bonded to the lower side of the Hexcell sheet. The Hexcell material has been successfully used in large microstrip antennas such as the SAR antennas used on both SEASAT and SIR-A [1,2]. It was selected for this application because a thicker substrate was needed to achieve the required bandwidth than the 1/16" to 1/8" thickness commercially-available PTFE laminates. At 1415 MHz, this Hexcell composite corresponds to an electrical thickness of $.03\lambda_0$ and an expected Q of about 20, i.e., a bandwidth of 3.5% [3].

Bartley and Huebner [4] have described a linear array of 16 dual-polarized square or circular microstrip elements using Duroid 5870 p.c. board which was $0.014\lambda_0$ thick. This corresponds to a VSWR = 2.0 bandwidth of about 1.4%, which is insufficient for the present application.

The first objective was to optimize the isolated element performance by adjusting dimensions A and B to achieve the best overall return loss and insertion loss combination over the bandwidth. The element was designed to have a nominal input impedance of 50 ohms at 1415 MHz. The following paragraphs describe the technique for measuring element performance.

CROSS-POLARIZATION MEASUREMENT TECHNIQUES

An ideal horizontally-polarized antenna will receive only horizontally-polarized radiation and will reject all vertically-polarized radiation. Thus, one method for measuring the cross-polarization level is to orient the test microstrip patch for horizontally-polarized reception and illuminate it first with a horizontally-polarized incident wave (with the received power adjusted to 0 dB) and then illuminate it with a vertically-polarized incident wave and note the dB reduction in received power. This requires the use of a polarization-clean antenna range and is time-consuming.

An alternative approach is to make a transmitting insertion loss measurement in which the input power to the horizontal (H) port is adjusted to 0 dB and the output power from the vertical (V) port is measured by a network analyzer, i.e. 20 log $|S_{12}|$. This measurement describes the ratio of the incident voltage on port H to the emerging voltage from port V when port V is properly terminated. Since each of these voltages is proportional to the interior microstrip cavity field of the respective modes associated with each port [5], the insertion loss measurement is actually a measure of coupling between the two spatially-orthogonal dominant modes of the square cavity. This coupling occurs because of the perturbation of the cavity dominant mode field by the feed probes.

Fig. 2 illustrates an S-parameter test set configuration for measurement of S_{11}, S_{22}, S_{12} and S_{21} where 1 refers to port H and 2 refers to port V. In the switch configuration shown, input rf power is fed to the H port of the microstrip patch through the main arm of directional coupler B. A small portion of the input signal is coupled through a -20 dB arm via switch S_2 and a line stretcher to provide a reference output signal. The V port of the antenna is coupled to a 50 ohm load via the main arm of directional coupler A, which also provides a -20 dB coupled signal (proportional to $|S_{12}|^2$) which routes through switch S_1 to the test channel output. By use of the switches, the remaining S parameters can be conveniently measured, including the input impedance to either port when a polar display device is used with the network analyzer. It should be noted that the accuracy of the $|S_{12}|$ measurement with this technique depends on both antenna ports being well matched to 50 ohms, since both 50 ohm sources and detectors are being used. Although this is a disadvantage for frequencies or patch dimensions presenting a poor match, nonetheless this laboratory technique can lead quickly to estimates of the optimum patch dimensions A and feed inset distances B. Measurements were made on six separate square patches whose side dimensions A were 7.8, 8.3, 8.9, 9.0, 9.1 and 9.6 cm respectively. For each of these patches, measurements were made for feed inset distances B of 0.5, 1.0, 2.0, 2.5, 3.0 and 3.5 cm so that 36 separate antenna configurations resulted.

A better, although more time-consuming, measure of the cross-polarization level is to operate the antenna as it is used in practice, i.e. as a receiver, as described earlier. These measurements were made on the NMSU/PSL 100' model antenna range using a 6' diameter dish with disk-dipole feed as a source; this arrangement produces a very polarization-pure incident signal whose intrinsic cross-polarization level is greater than 40 dB below the desired polarization signal level.

MEASURED RESULTS FOR SINGLE ELEMENTS

For each of the 36 separate single-element antennas, measurements of insertion loss and return loss were made at 1400, 1415 and 1430 MHz. Fig. 3 is a graph of the insertion loss vs. patch dimension A with inset distance B

as a parameter, at 1415 MHz. It can be seen that the best insertion loss is obtained at A = 8.3 cm, B = 2.5 cm, i.e. A = $0.391\lambda_0$ and B = $.118\lambda_0$. This gives a ratio of B/A = .30 for a thickness of $.03\lambda_0$ as compared to the Bartley and Huebner value of B/A = .35 for a thickness of $.014\lambda_0$. Fig. 4 is a graph of insertion loss vs. patch dimension A with B = 2.5 cm, at 1400, 1415 and 1430 MHz, which demonstrates that with A = 8.3 cm, the optimum insertion loss frequency is above 1415 MHz.

Unfortunately, the optimum parameters for best insertion loss are not in general optimum in the sense of best return loss. Fig. 5 shows the return loss vs. patch dimension A for several values of B, all at 1415 MHz. It is seen that the best return loss is obtained for A = 8.9 cm, B = 2.5 cm. Fig. 6 shows the dependence of the return loss on patch dimension A for B = 2.5 cm, at 1400, 1415 and 1430 MHz. This shows that the best return loss is obtained at 1415 MHz.

With this in mind, A is now set to 8.9 cm (for best return loss), and a measurement is made of the insertion loss vs. frequency for several values of B as shown in Fig. 7. For this case, the best insertion loss (regardless of return loss) is obtained at 1400 MHz for B = 3.0 cm. However, at the 1415 MHz center frequency, the best <u>combination</u> of insertion loss and return loss is obtained for B = 2.5 cm, (B/A = .28) where the return loss is below 30 dB and the insertion loss is about 28 dB. Fig. 8 illustrates the measured input impedance vs. frequency for both ports of the optimum patch with A = 8.9 cm, B = 2.5 cm, showing a center frequency VSWR = 1.15 and a 75 MHz bandwidth (5.3%) at VSWR = 2.0. This enhanced bandwidth is due to the relatively large substrate thickness.

Cross-polarization levels are conventionally measured on an antenna range by first recording a pattern cut with the incident wave of like polarization to the test antenna, e.g. horizontal. The source antenna is then rotated 90° so that an orthogonally-polarized wave (e.g. vertical) is incident on the test antenna and a second pattern cut is recorded. The difference between the recorded levels on the beam peak of the principal component and the corresponding cross component is usually referred to as the cross-polarization level.

A polarization pattern may also be recorded on the beam peak, from which the axial ratio and tilt angle may be noted. Unless the polarization ellipse major axes are lined up with the microstrip patch principal axes, the cross-polarization level will be less than the axial ratio. For some of the antennas tested, the axial ratio was 7 dB greater than the measured cross-polarization.

The antenna range-measured value of the cross-polarization levels for both ports (A = 8.9 cm, B = 2.0 cm) are also shown in Fig. 7 and are seen to be close to the measured insertion loss. In general, the cross-polarization level for a single isolated dual-polarized element ranges from -25 to -30 dB, depending on frequency and geometry.

FOUR-ELEMENT IN-LINE ARRAY

An in-line array of four dual-polarized square microstrip patches was constructed, with A = 8.9 cm, B = 2.5 cm and an inter-element spacing of 13.8 cm ($0.65\lambda_0$ at 1415 MHz). Two separate feed networks were used, the first a corporate coaxial cable harness and the second a corporate stripline network (see Fig. 9) plated on a .0065" PTFE board separated from two copper ground planes by two 1/4"-thick Hexcell layers. This 1/2"-thick stripline network was juxtaposed to the bottom of the microstrip array with connections from elements to the network made by short vertical wires soldered on both sides. The Hexcell is bonded to the PTFE using Hexcelite HP-326 adhesive.

The input impedance to both vertical and horizontal ports is shown in Fig. 10 for the integrated stripline feed network. The center frequency VSWR is 1.6 and 1.4 for the vertical and horizontal ports and the VSWR = 2.0 bandwidth is 160 MHz (11.4%) and 150 MHz (10.7%) for the V and H ports respectively.

It was discovered after initial tests that the Hexcell-to-PTFE bond was loose near two of the array elements and that the substrate thickness was uneven in these areas. This was due to insufficient bonding pressure and time during array sandwich assembly. This bonding time should be a minimum of 48 hours.

This condition was partly corrected by periodically mechanically clamping the board together with nylon bolts through the board. The measured patterns along the array axis, using the stripline feed network, and before clamping are shown in Fig. 11 for both vertical and horizontal ports. The principal component pattern, which has peak gains of 12 dBi and 13 dBi for V and H ports, shows skewed sidelobes and filled-in nulls as a result of the aperture phase asymmetry caused by the uneven substrate thickness. The on-axis cross-polarization levels range from 13 to 17 dB. The measured insertion loss vs. frequency for this array (before clamping) is shown in Fig. 12 for both stripline and coaxial feed networks. The insertion loss curves are similar for both feed systems and show that the insertion loss improves at the lower frequencies.

Fig. 13 shows the 4-element in-line array patterns after substituting a coaxial harness for the stripline feed network and substrate clamping to produce more uniform thickness. The gain of both ports is now 14 dBi and the principal component pattern shape is much improved. The on-axis cross-polarization levels are now 23 dB and 25 dB for V and H ports respectively. The axial ratio levels are 24 dB and 25 dB for the V and H ports respectively. The input impedance to both vertical and horizontal ports through this harness is shown in Fig. 14. The center frequency VSWR is 1.15 and 1.25 for the V and H ports and the VSWR = 2.0 bandwidth is 79 MHz (5.6%) and 72 MHz (5.1%) for the V and H ports respectively.

Table 1 lists the measured input impedances at 1415 MHz to each port with all other ports terminated in 50 Ω loads, before and after clamping. After clamping, the individual impedances cluster more closely to 50 Ω.

The results of these "before" and "after" experiments have been included to illustrate the importance of uniformity in adhesion, bonding and electrical thickness of the Hexcell substrate composites.

Table 1

Measured Input Impedances at 1415 MHz

Element	Before Clamping	After Clamping
1-V	47 - j5 Ω	43 + j1 Ω
1-H	45 - j4 Ω	41 + j6 Ω
2-V	45 - j0 Ω	35 + j8 Ω
2-H	50 - j2 Ω	45 + j8 Ω
3-V	63 + j2 Ω	48 + j4 Ω
3-H	76 + j8 Ω	68 + j9 Ω
4-V	62 + j0 Ω	60 + j3 Ω
4-H	62 + j5 Ω	51 + j6 Ω

FOUR-ELEMENT STAGGERED ARRAY

In order to determine the effect of array geometry on both pattern shape and cross-polarization level, a coaxial harness-fed 4-element staggered (echelon) array was constructed as shown in Fig. 15. Such an array geometry can be extended to diamond lattice configurations with reduced mutual coupling between elements.

The PTFE/Hexcell sandwich for this array was adhesively bonded under greater pressure and for twice as long (48 hours) as for the 4-element in-line array so that the thickness was much more uniform. Table 2 summarizes the input impedance at 1415 MHz to each port with all other ports terminated in 50 Ω loads.

Table 2

Input Impedance to Staggered Array
at 1415 MHz

Element	Input Impedance
1-V	49 + j1 Ω
1-H	51 + j6 Ω
2-V	47 + j5 Ω
2-H	47 + j3 Ω
3-V	50 + j0 Ω
3-H	54 + j1 Ω
4-V	49 + j4 Ω
4-H	41 + j7 Ω

It is seen that the input impedances are tightly clustered about the design value of 50 Ω. The array was excited from below with a coaxial harness as depicted in Fig. 15. The input impedance to both V and H ports through this harness is shown in Fig. 16. The center frequency VSWR is 1.00 and 1.12 for the V and H ports and the VSWR = 2.0 bandwidth is 69 MHz (4.9%) and 86 MHz (6.1%) for the V and H ports respectively.

The measured insertion loss vs. frequency for the staggered array is shown in Fig. 17 where a -27 dB level is found at 1415 MHz. The array patterns are shown in Fig. 18 and are similar to those of Fig. 13 for the in-line array. The on-axis cross-polarization levels are 22 dB and 25 dB for the V and H ports respectively. The axial ratio measurements are 28 dB and 32 dB for the V and H ports respectively.

CONCLUSIONS

It has been found that the best insertion loss and the best return loss of an element are obtained with different patch dimensions and feed point locations. For the Hexcell substrate used, a good compromise is found with a patch side length A of $0.42\lambda_0$ and an inset feed point distance of $0.12\lambda_0$.

The performance of elements, arrays and stripline feeds discussed in this report is sensitive to variations in their substrate thicknesses. Therefore, air gaps in the substrate will deteriorate impedance, cross-polarization level and pattern shape, as demonstrated with the 4-element in-line array. This problem can be avoided if adequate, uniform pressure is applied in assembly of substrate sandwich over a minimum of 48 hours, i.e., exceeding the 12-16 hour manufacturer's specifications.

It should be noted that the pattern and impedance performance of the in-line and staggered arrays when fed by coaxial harness are quite similar and both arrays meet the design goals. Due to topological considerations and mutual coupling between feed lines a stripline feed network would perform more successfully in the staggered array case than for the in-line case.

ACKNOWLEDGEMENT

This work was supported in part by NASA Johnson Space Center and the U. S. Army Research Office.

REFERENCES

1. Sanford, G. G., A. G. Brejcha and L. G. Keeler, "The SEASAT-A SAR Antenna," Proc. of the SAR Technology Conference, New Mexico State University, Las Cruces, p. IV-1-1, March 8-10, 1978.

2. Murphy, L. R., "SEASAT and SIR-A Microstrip Antennas," Proc. of the Printed Circuit Antenna Technology Workshop, New Mexico State Univeristy, Las Cruces, pp. 18-1 - 18-20, Oct. 17-19, 1979.

3. Carver, K. R. and J. W. Mink, "Microstrip Antenna Technology," IEEE Trans. Antennas and Prop., AP-28, No. 6, November 1980.

4. Bartley, S. W. and D. A. Huebner, "A Dual Beam Low Sidelobe Microstrip Array," Digest 1979 IEEE AP-S International Symposium, Seattle, Vol. I, pp. 130-133, June 18-22, 1979.

5. Carver, K. R., "A Modal Expansion Theory for the Microstrip Antenna," Digest 1979 IEEE AP-S International Symposium, Seattle, Vol. I, pp. 101-104, June 18-22, 1979.

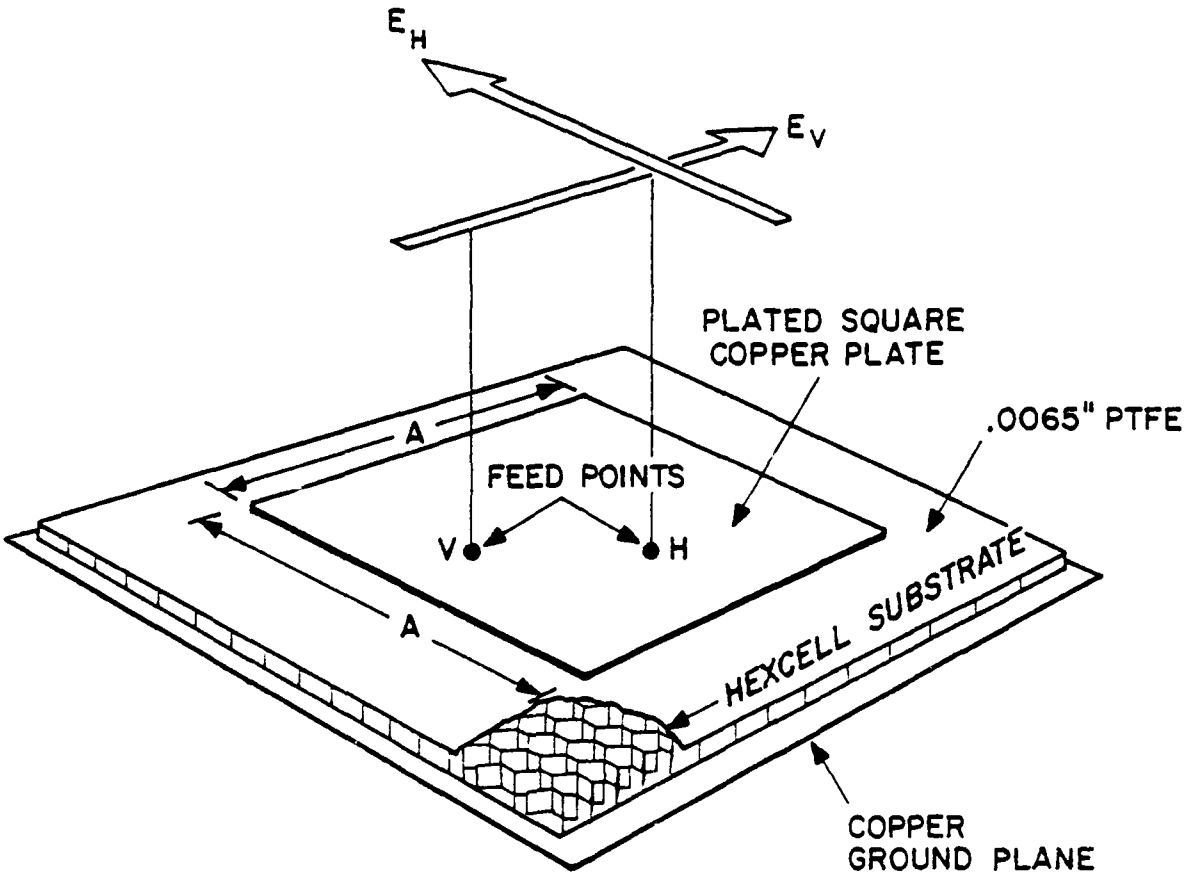

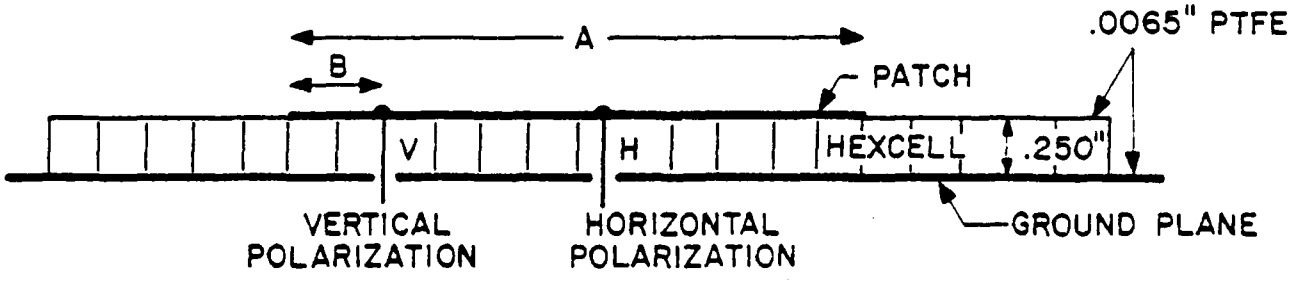

Fig. 1 Perspective and cross-sectional views of dual-polarized microstrip square antenna element

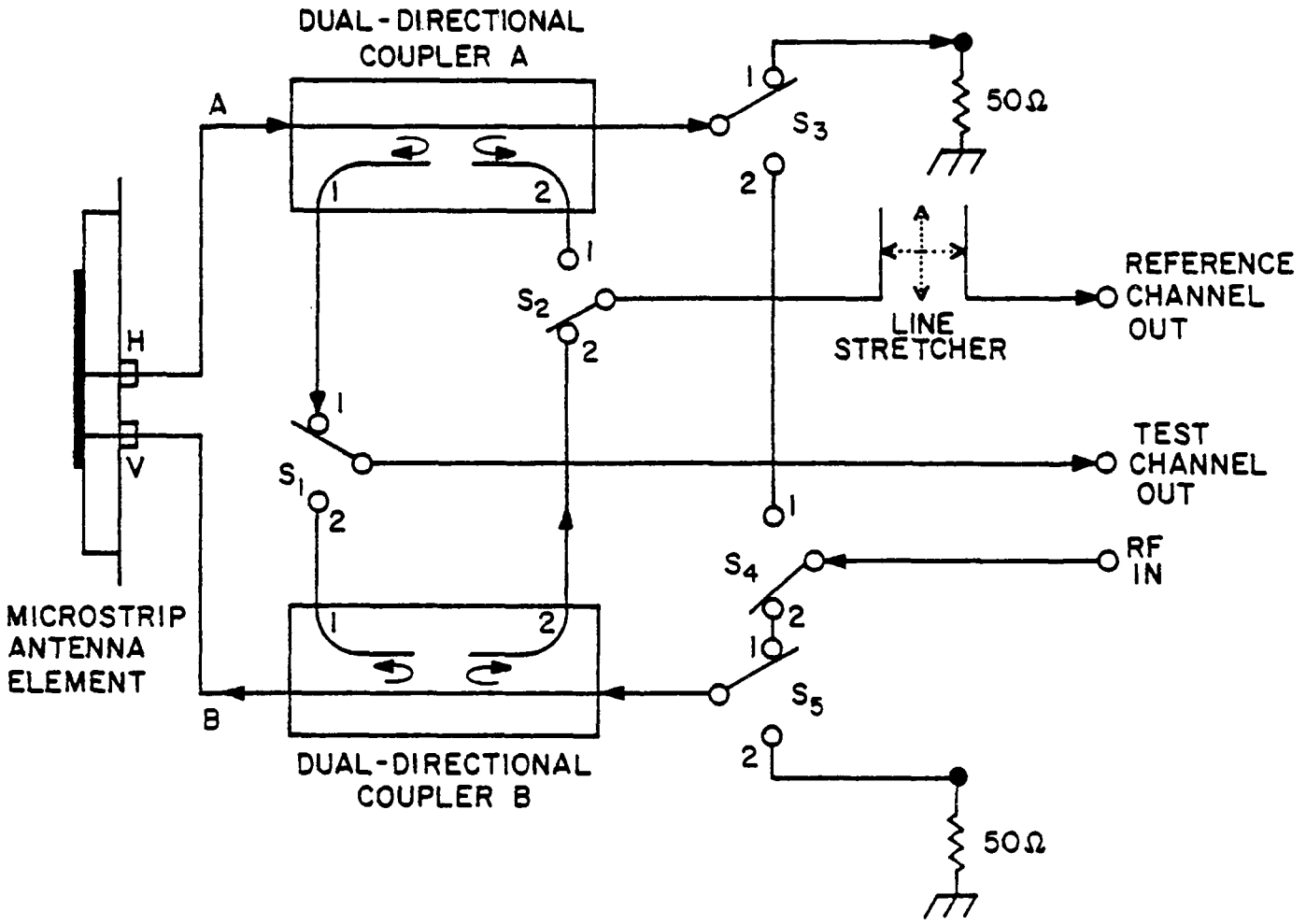

Fig. 2 Simplified signal flow diagram of S-Parameter Test Set for the S_{12} mode (after Operating and Service Manual for the HP8745A, Hewlett Packard Co., p.3-4, 1969)

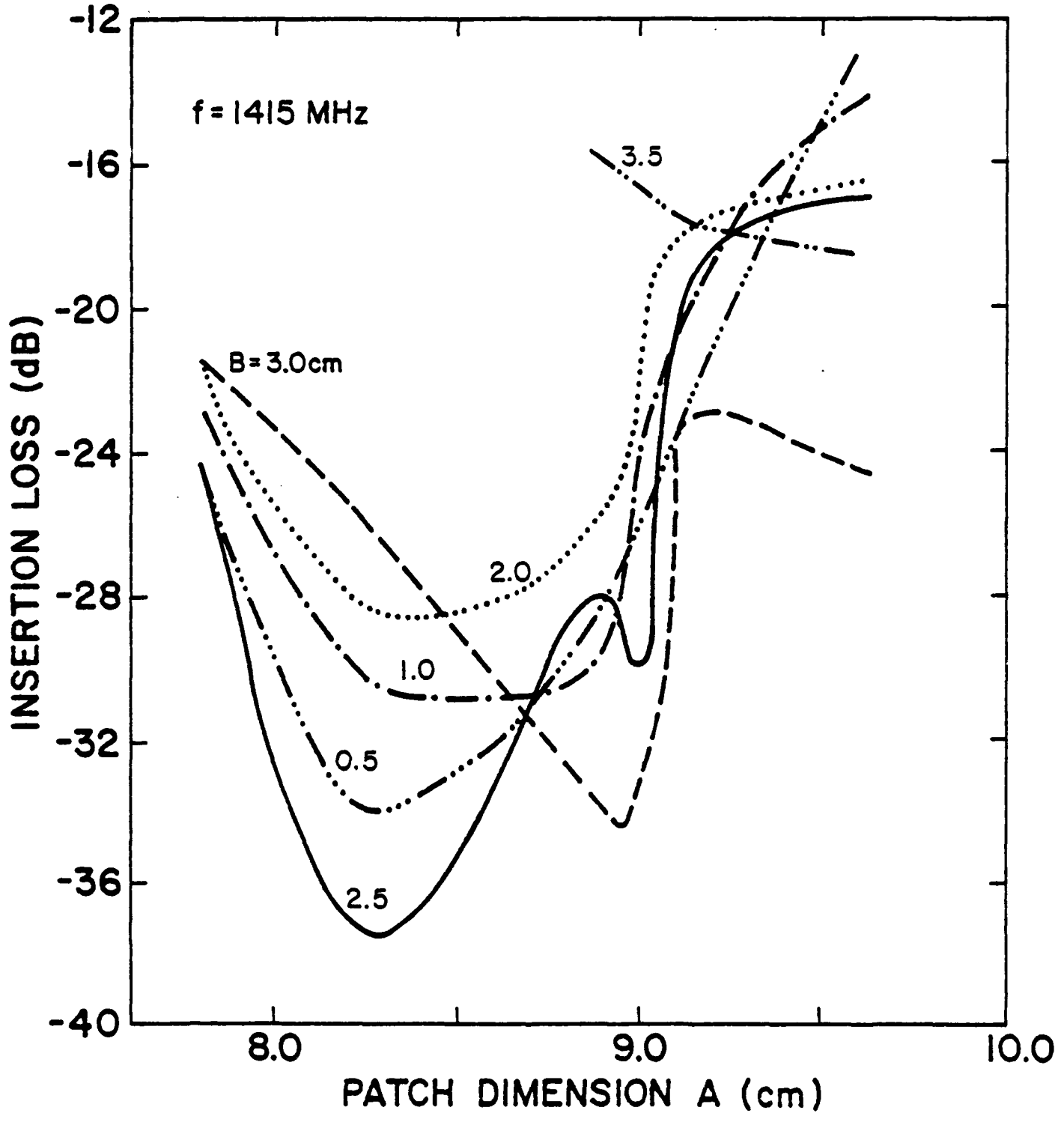

Fig. 3 Measured insertion loss vs. patch dimension A with inset distance B as a parameter, at 1415 MHz

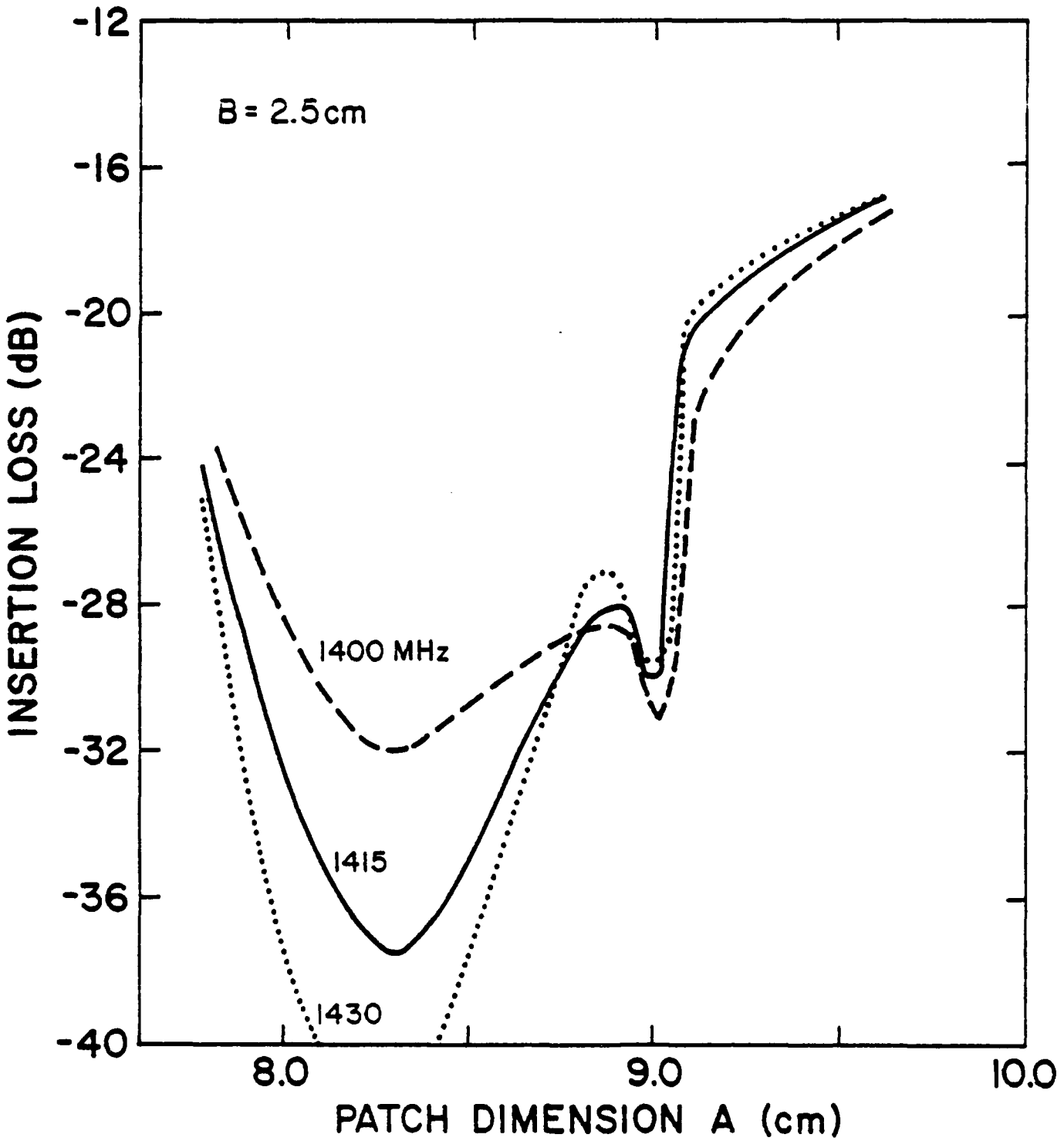

Fig. 4 Measured insertion loss vs. patch dimension A with frequency as a parameter, using B=2.5 cm.

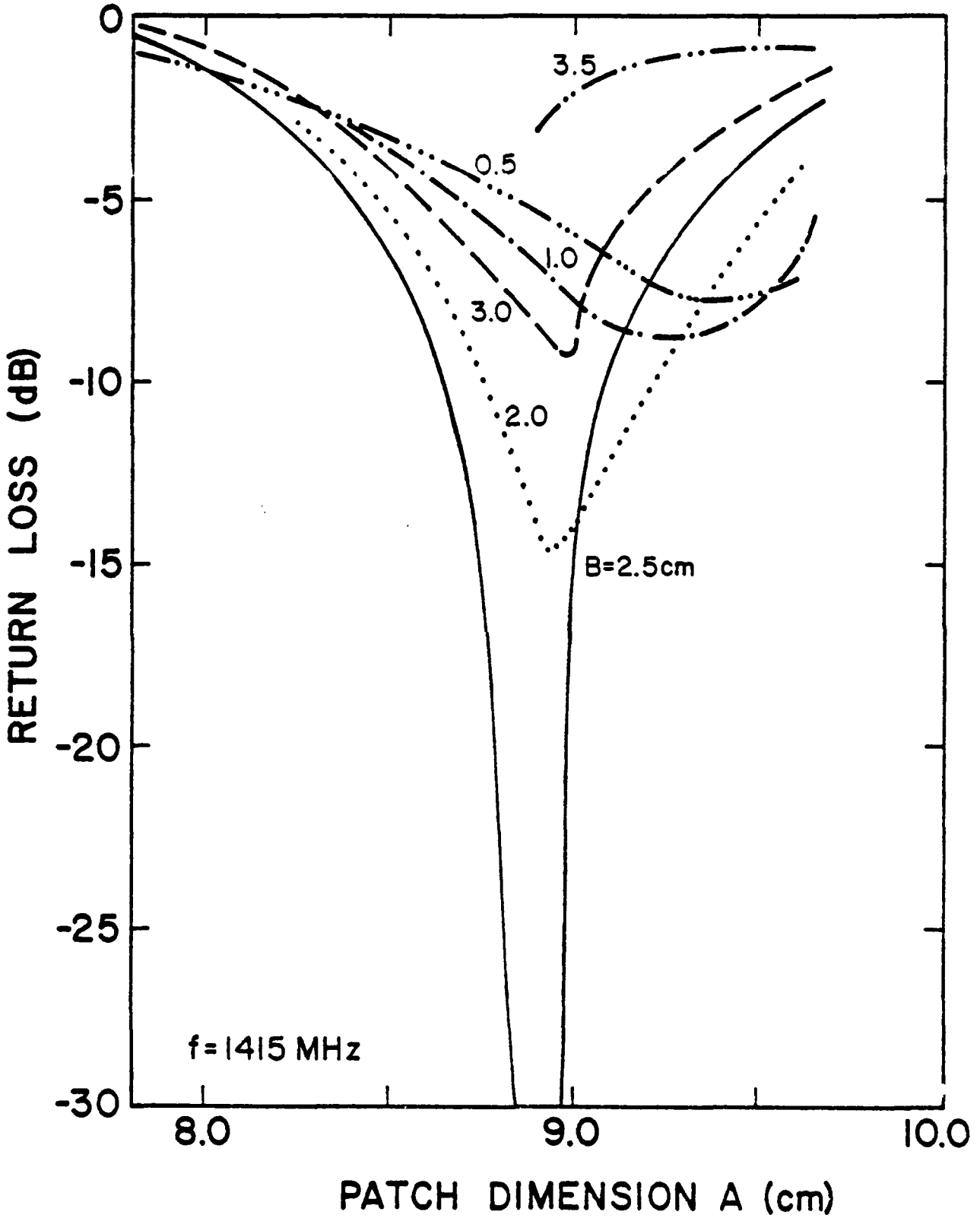

Fig. 5 Measured retrun loss vs. patch dimension A with inset distance B as a parameter, at 1415 MHz

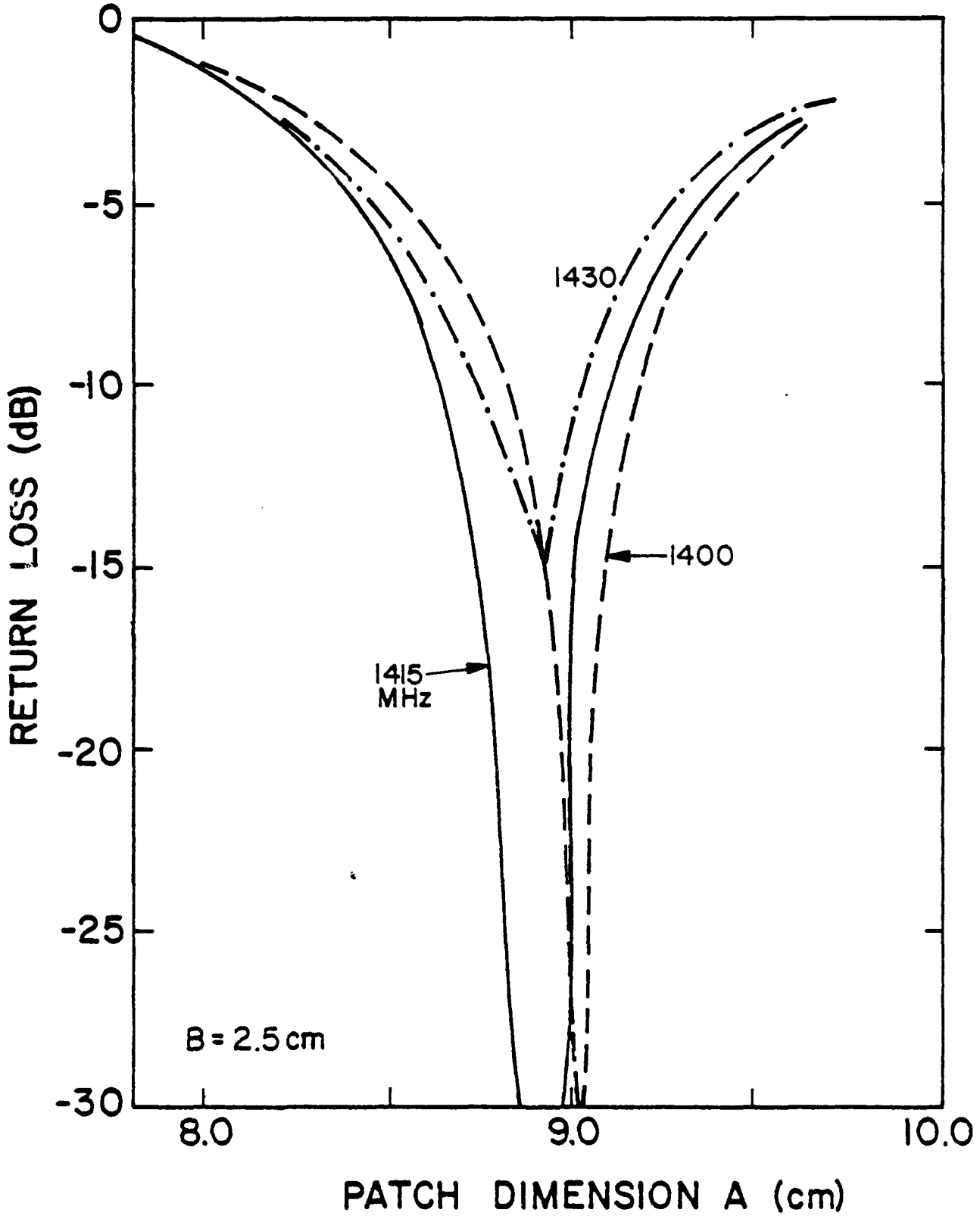

Fig. 6 Measured return loss vs. patch dimension A with frequency as a parameter, using B=2.5 cm.

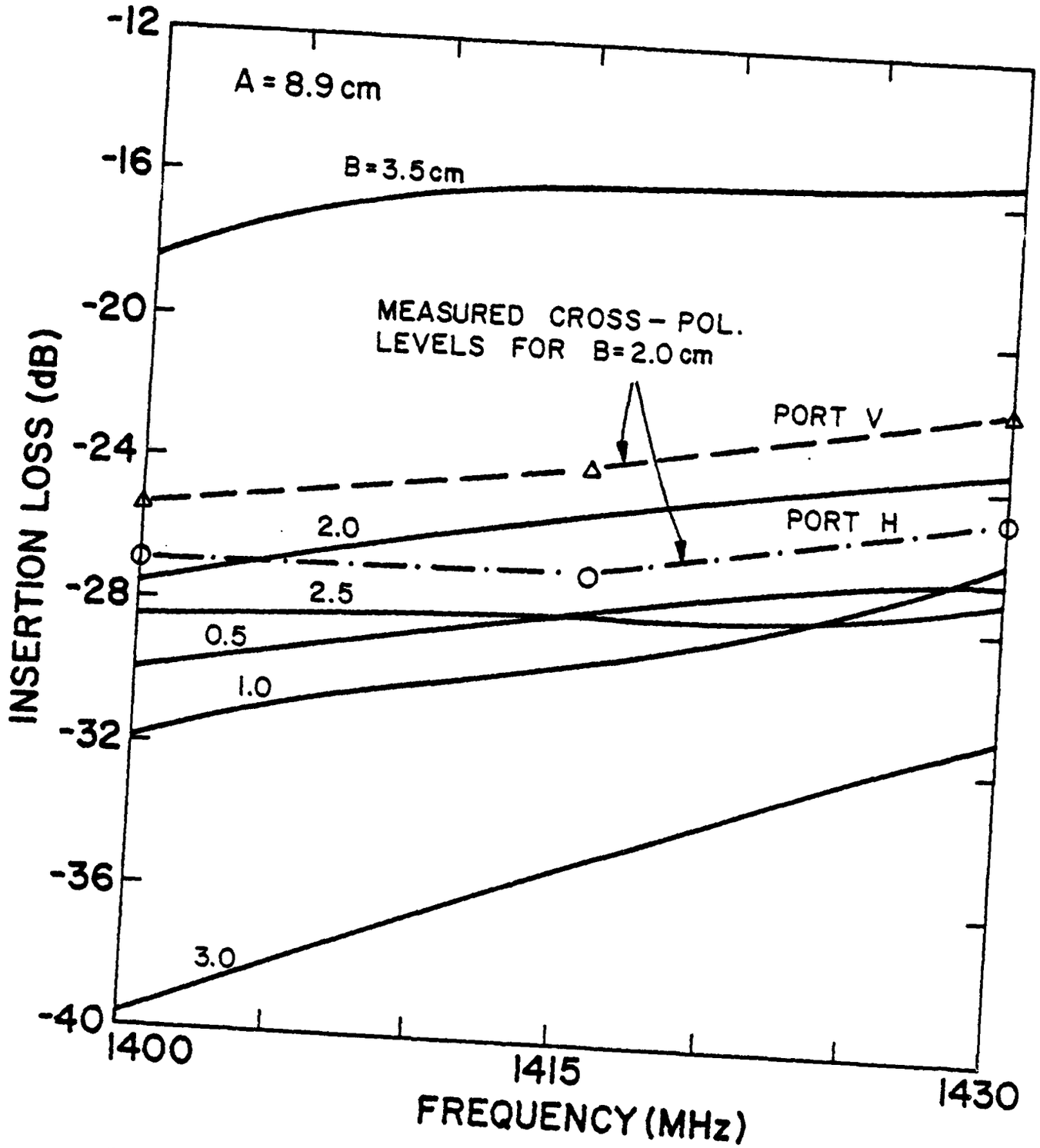

Fig. 7 Measured insertion loss vs. frequency with inset distance B as parameter, for A=8.9 cm.

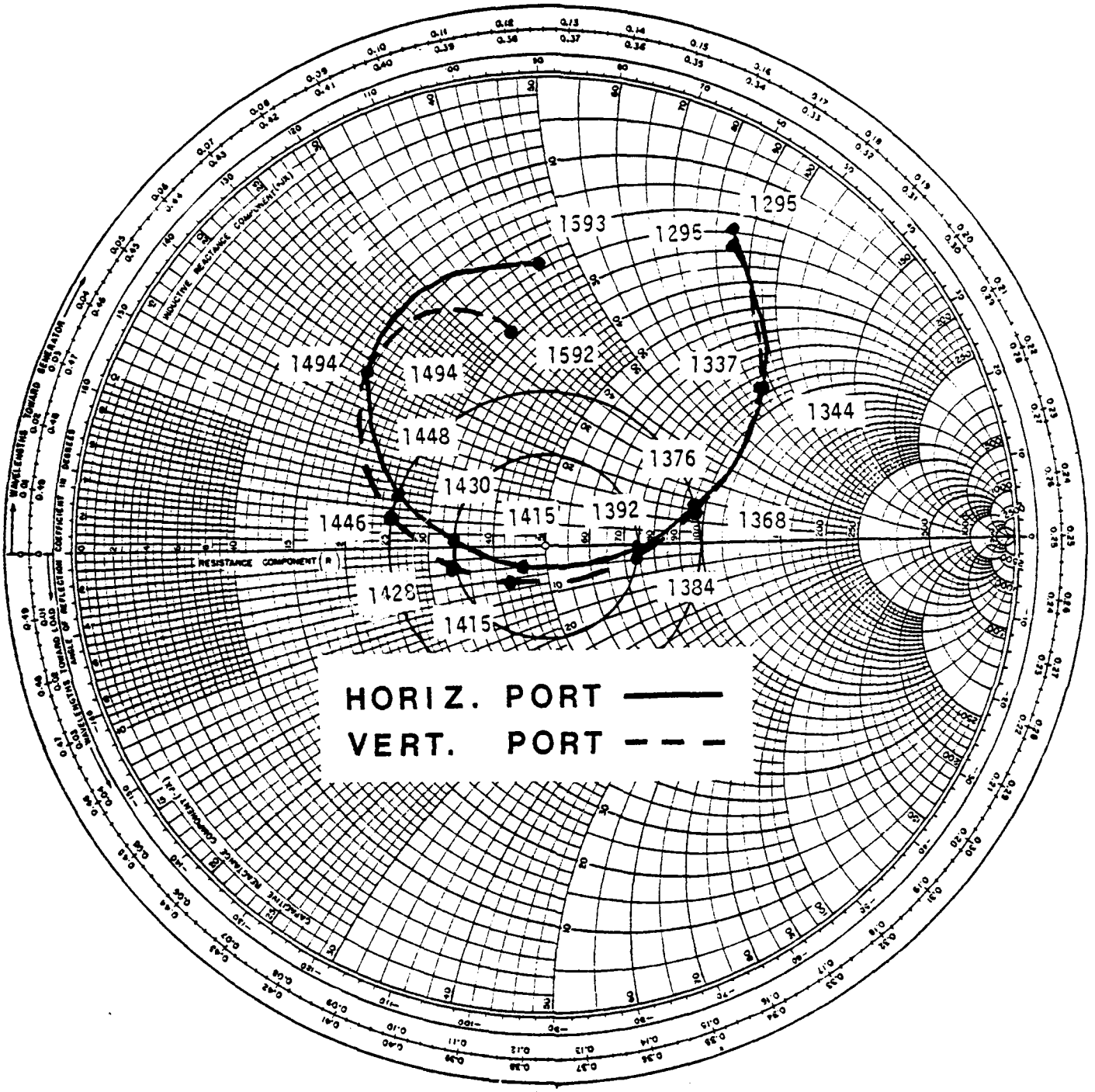

Fig. 8 Measured impedance vs. frequency for V and H ports of single microstrip antenna element with A=8.9 cm. and B=2.5 cm.

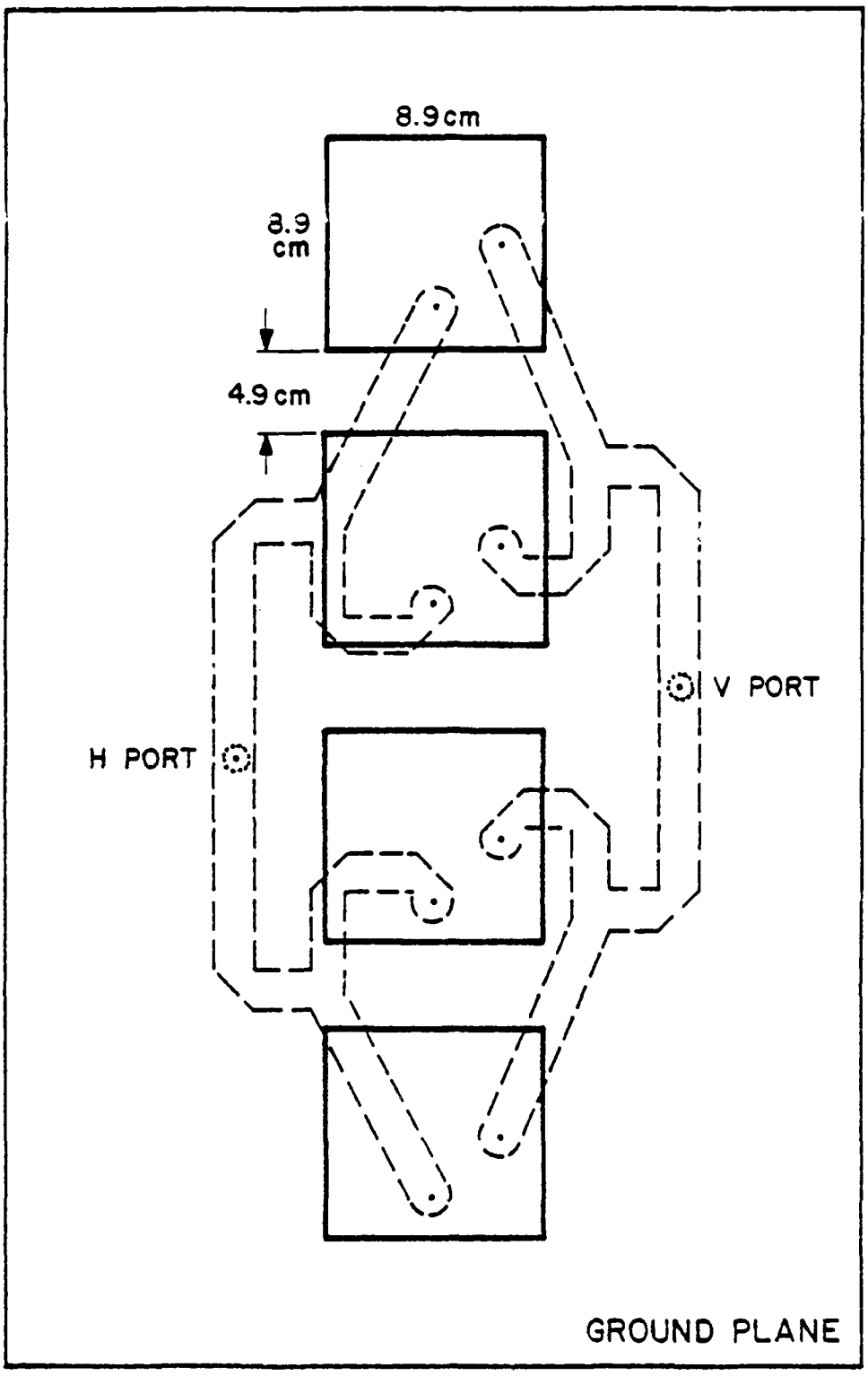

Fig. 9 Top view of 4-element in-line array of dual-polarized elements, showing stripline feed system on separate Hexcell substrate under the array

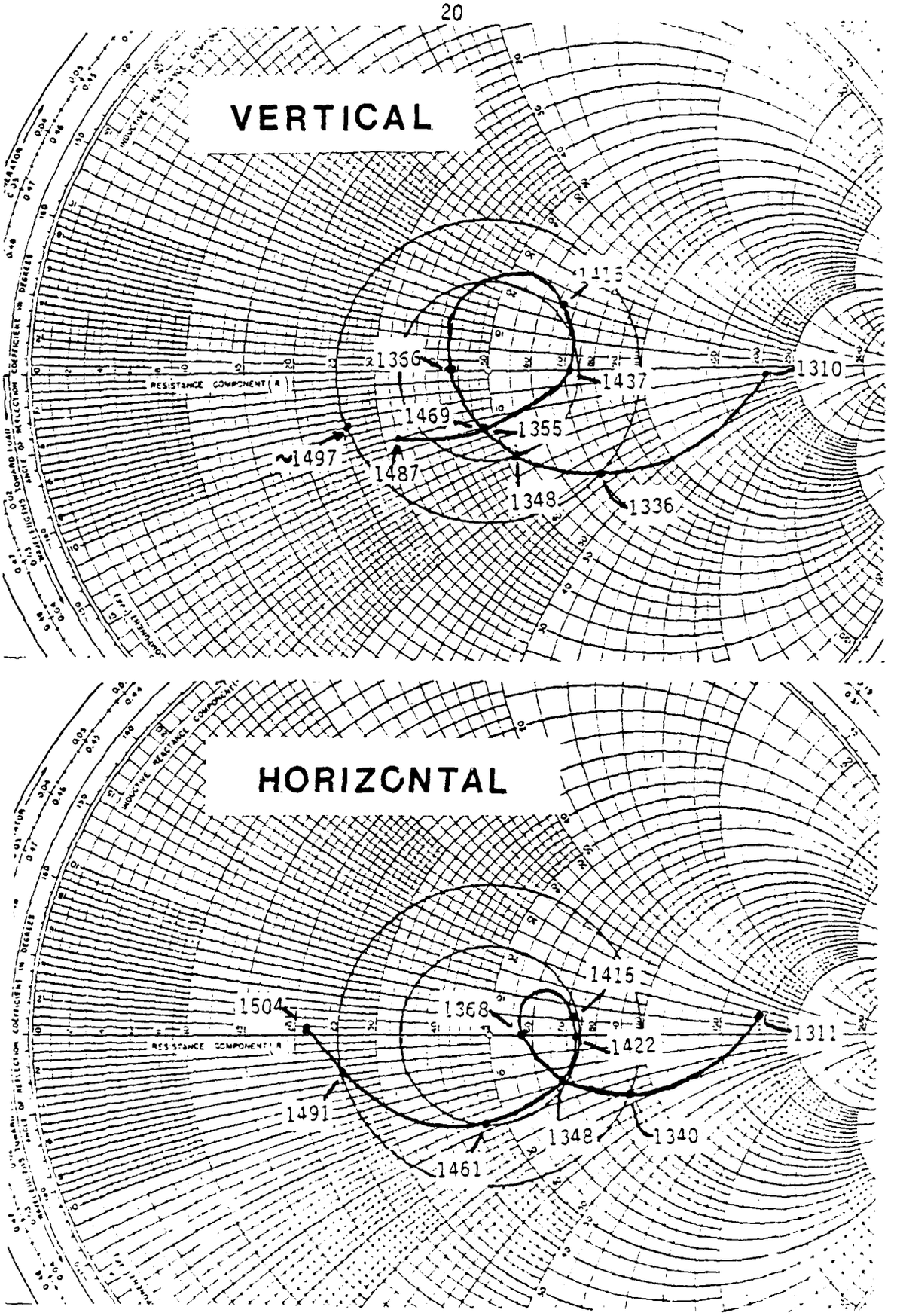

Fig. 10 Measured impedance vs. frequency for V and H ports of 4-element in-line array with integrated stripline feed network

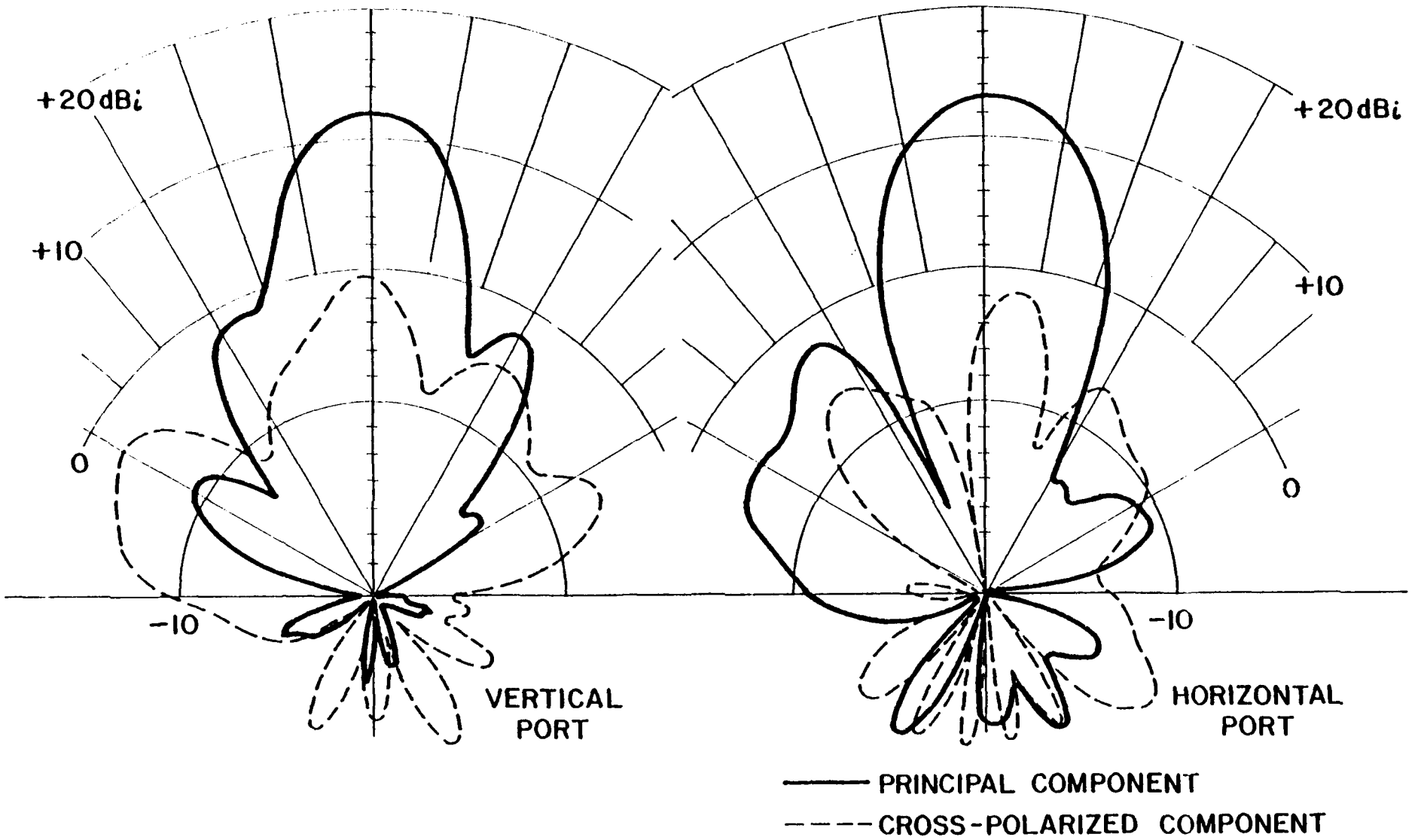

Fig. 11 Measured patterns along the array axis for the 4-element in-line array with integrated stripline feed network

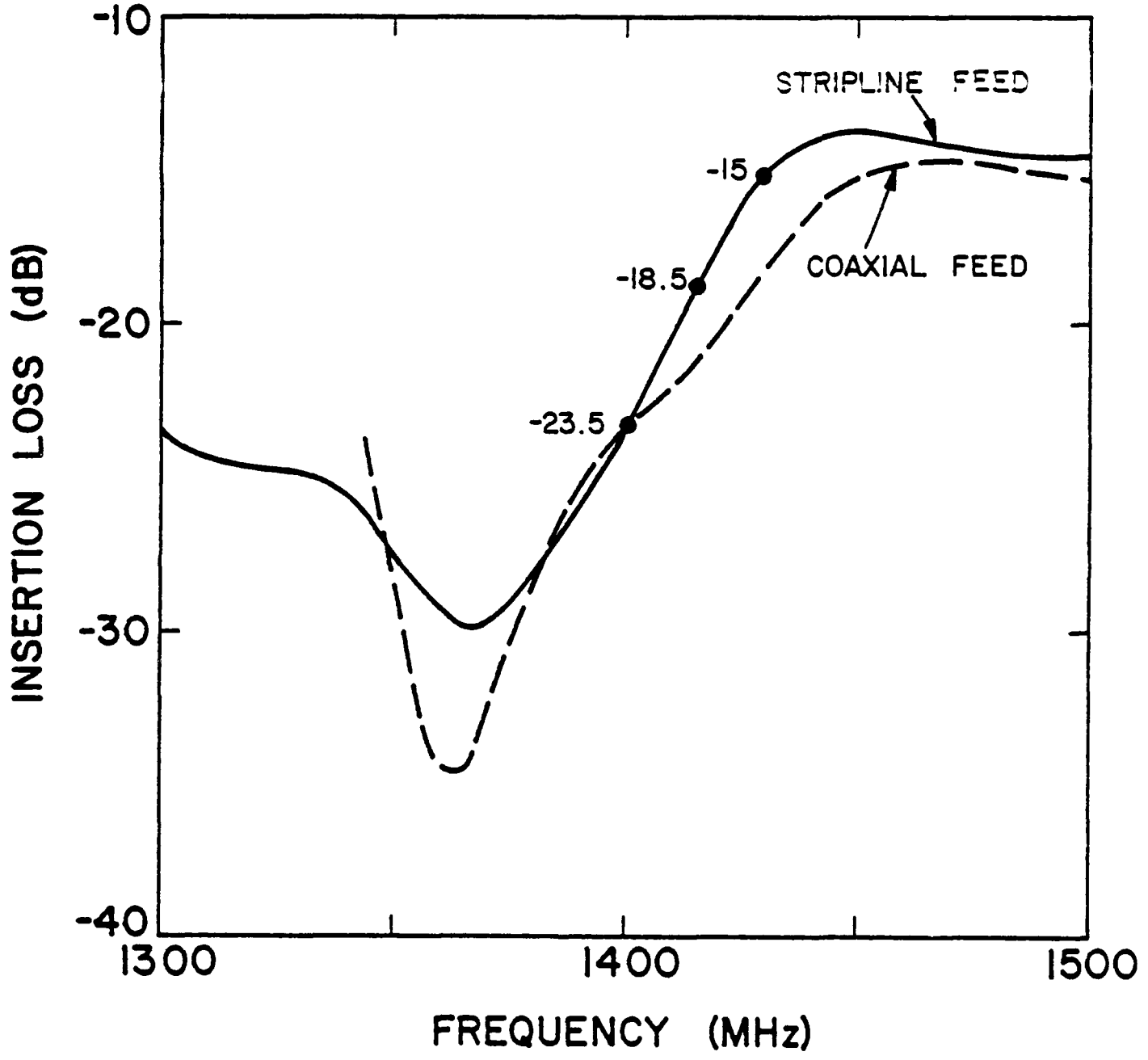

Fig. 12 Measured insertion loss vs. frequency for 4-element in-line array before clamping

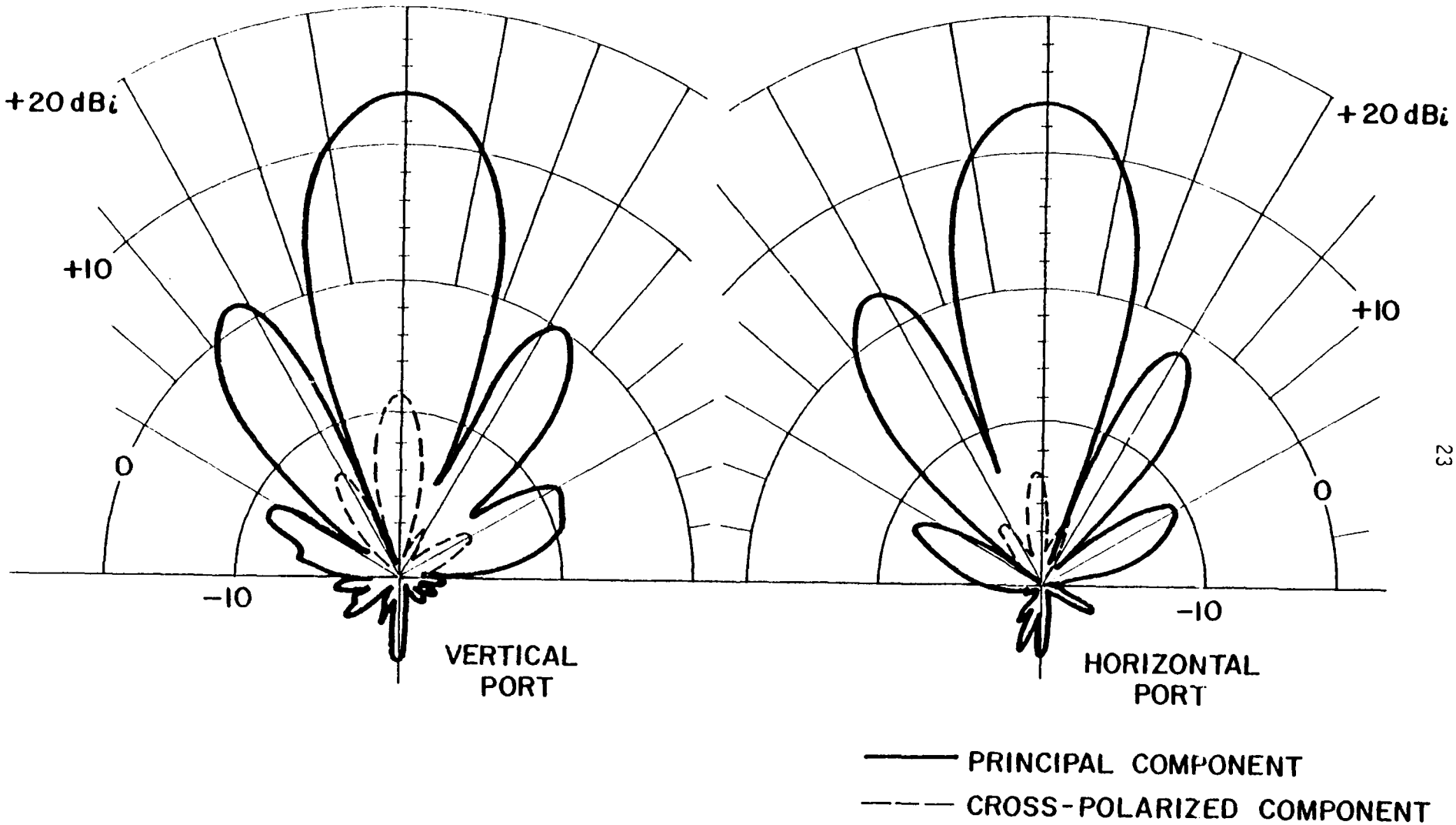

Fig. 13 Measured patterns along the array axis for the 4-element in-line array with coaxial feed harness

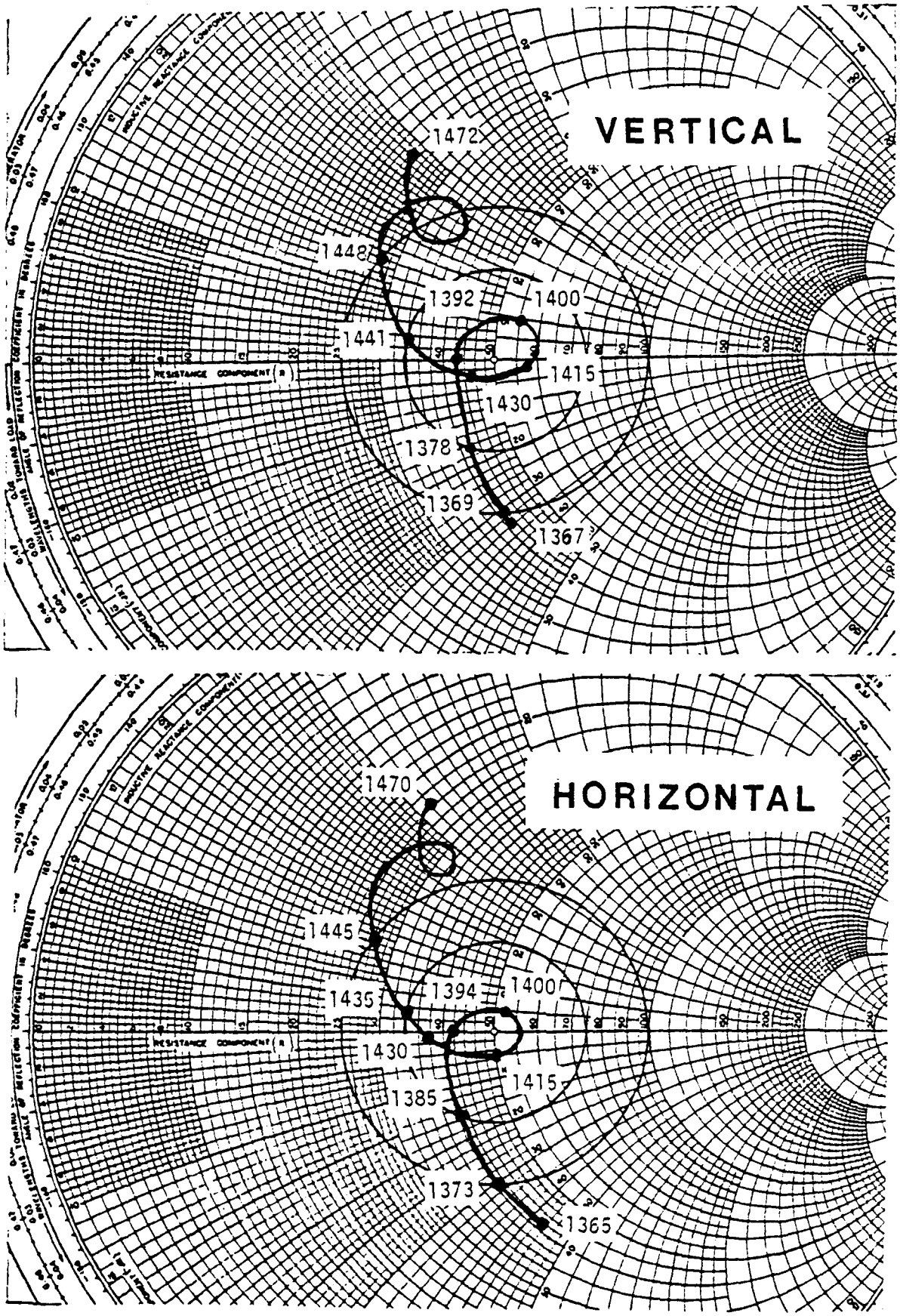

Fig. 14 Measured impedance vs. frequency for V and H ports of 4-element in-line array with coaxial feed harness

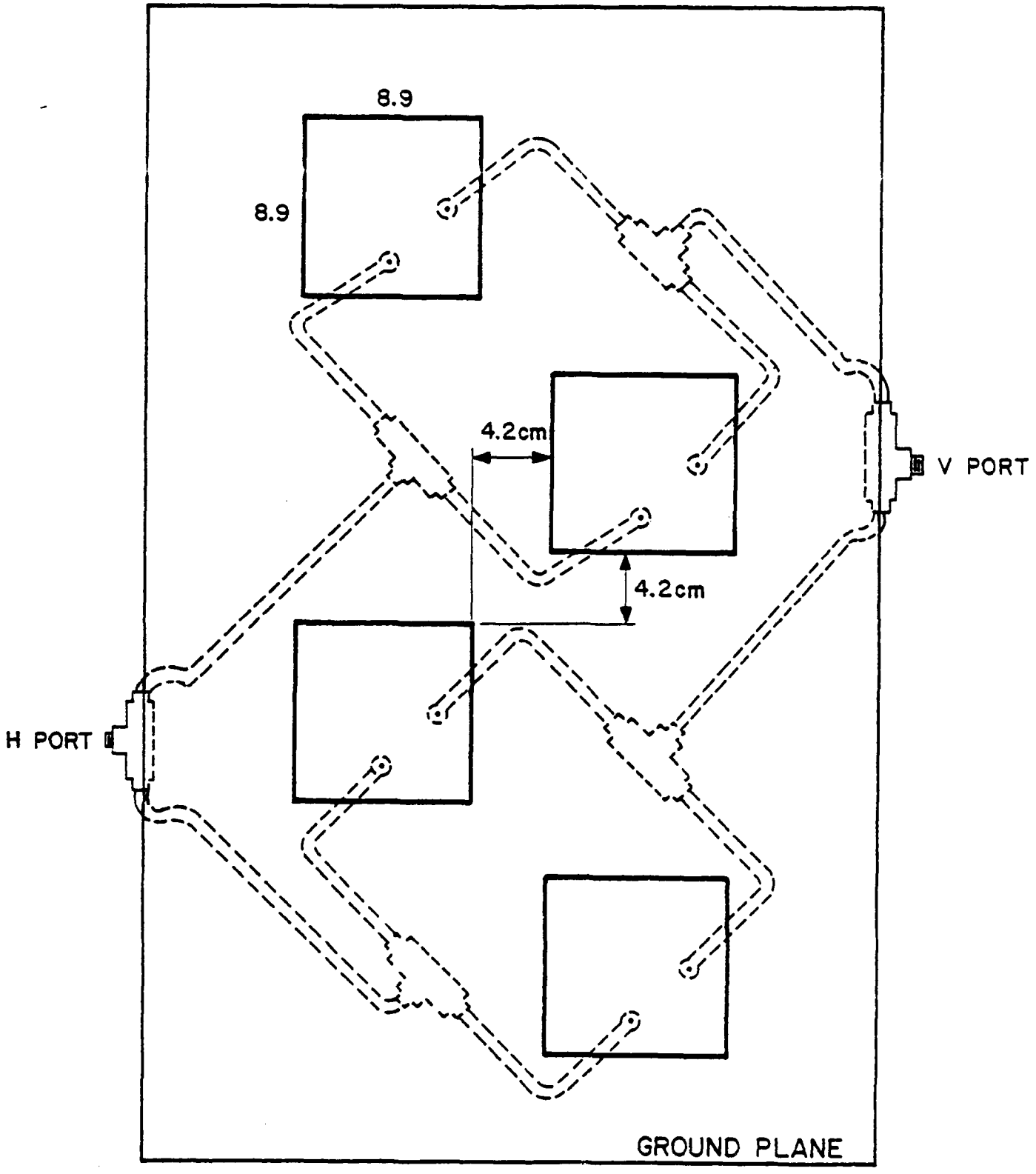

Fig. 15 Top view of 4-element staggered array of dual-polarized elements, showing coaxial feed harness under the array

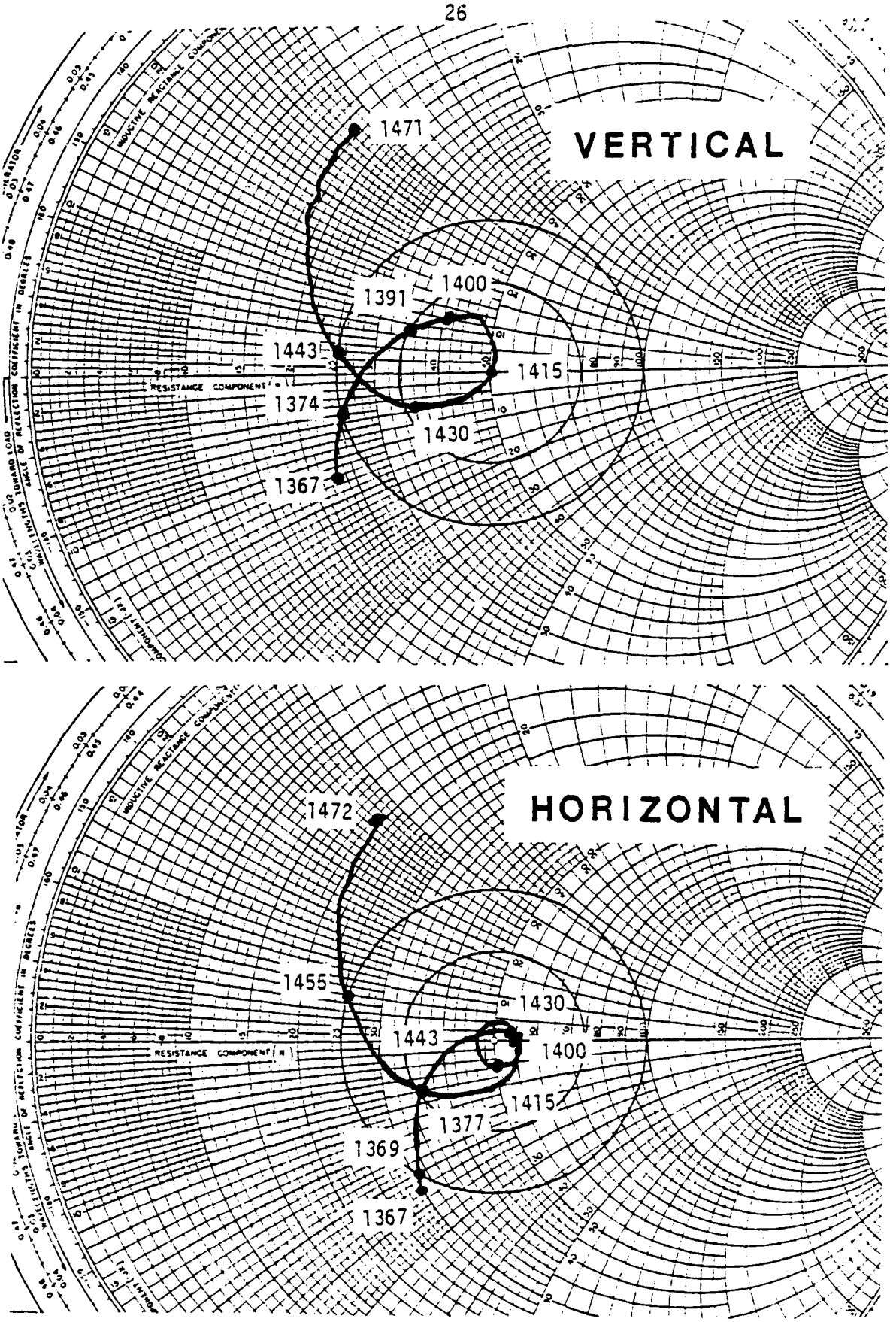

Fig. 16 Measured impedance vs. frequency for V and H ports of 4-element staggered array

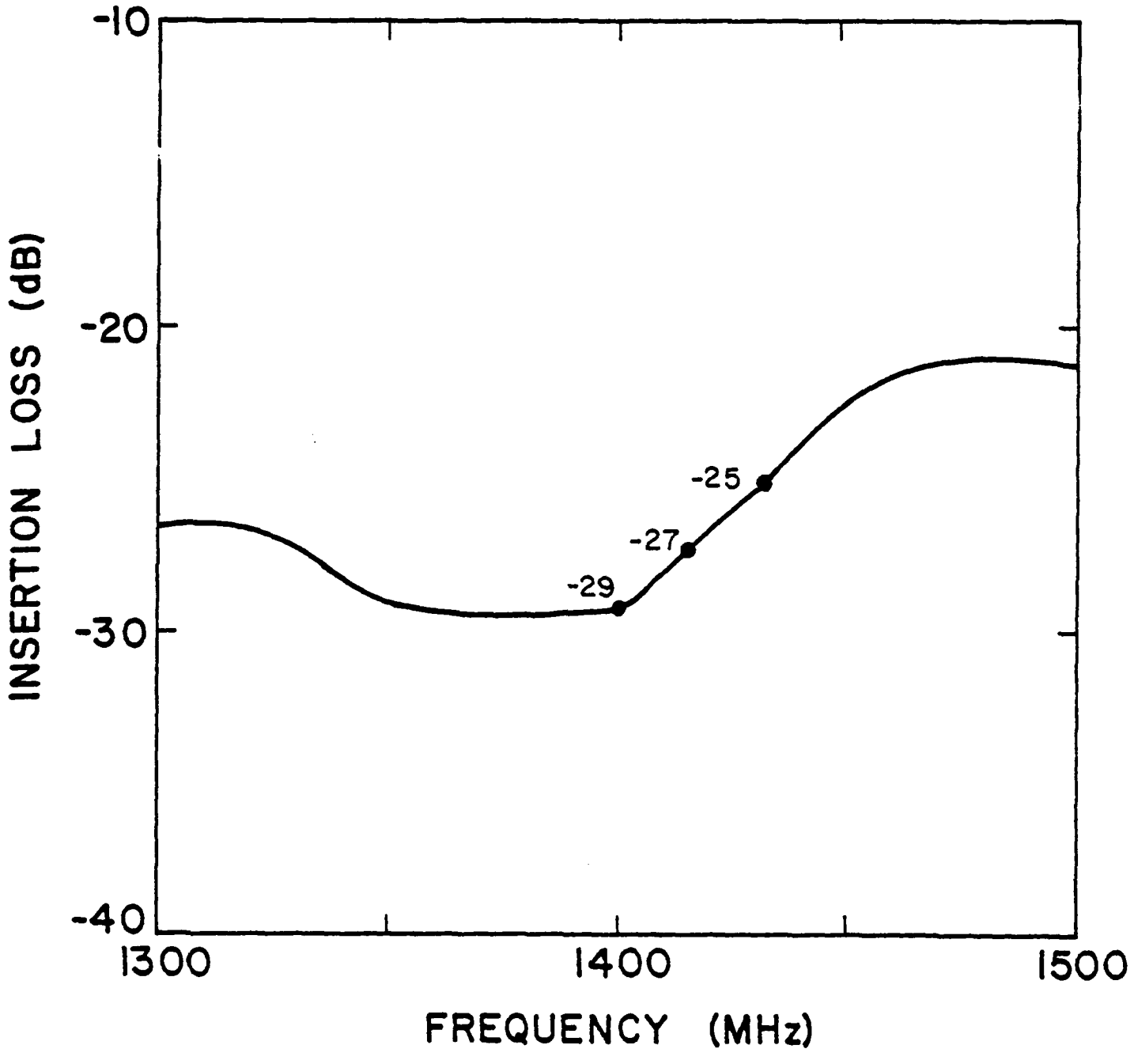

Fig. 17 Measured insertion loss vs. frequency for 4-element staggered array

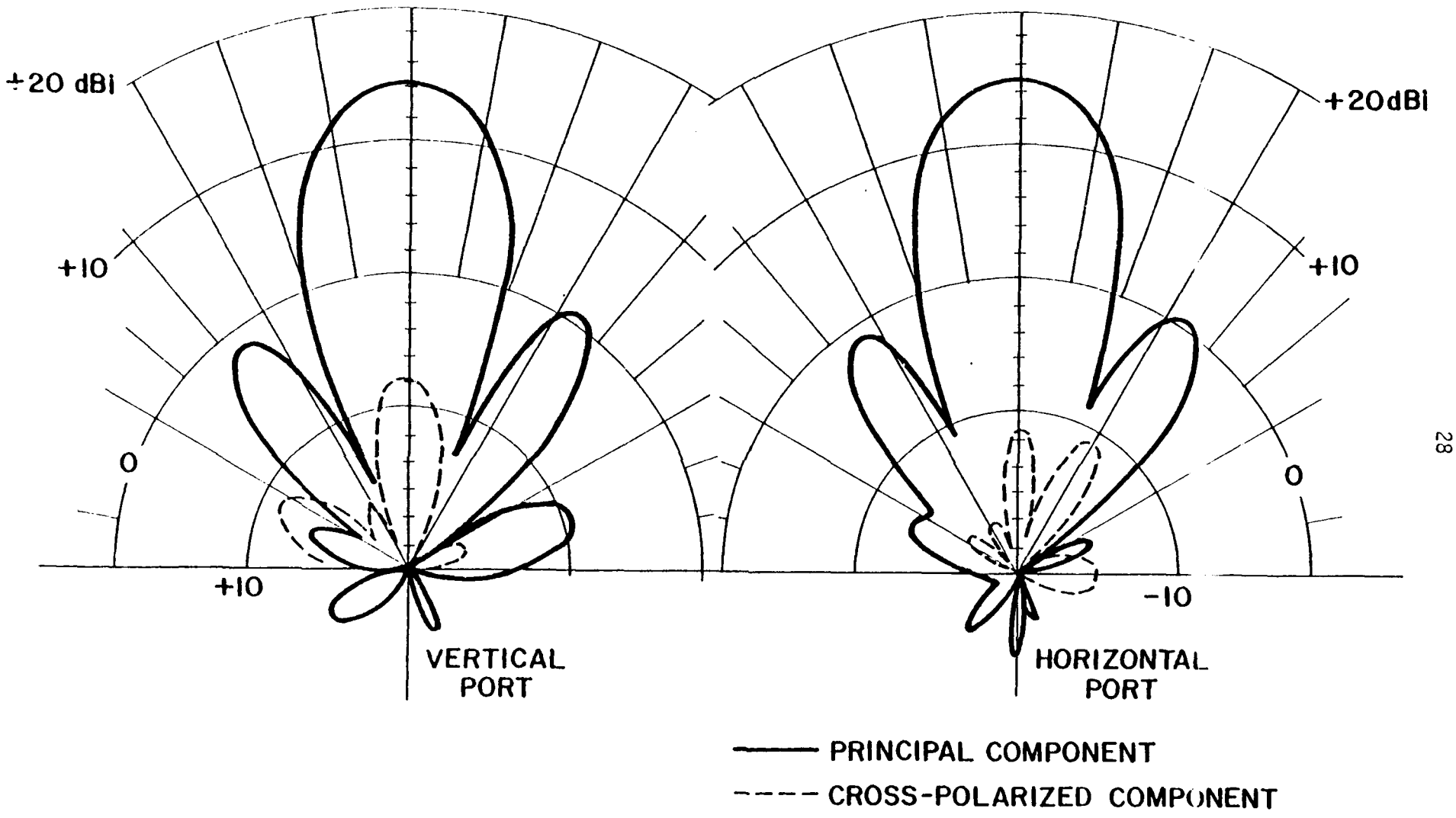

Fig. 18 Measured patterns along the array axis for the 4-element staggered array

THE HYBRID SLOT, A VERSATILE LOW-PROFILE RADIATOR WITH SMALL REFLECTION COEFFICIENT

P. E. Mayes and T. Cwik
Electrical Engineering Department
University of Illinois
Urbana, IL 61801

This paper describes a two-port, stripline-fed; cavity-backed slot antenna which has several unique features: (1) the reflection coefficient is small over a wide frequency band, (2) omnidirectional or one of several directive patterns can be selected, (3) the antenna responds to both the electric and magnetic fields to combat fading in a standing wave field, (4) coupling to the feedline can be controlled by simply changing the size of the slot.

Several applications exist for a radiating element which causes small reflections over a wide range of coupling. In frequency-scanning slot arrays, an impedance anomaly at broadside is produced by scattering in the feed network [Fritz, 1973]. A similar problem occurs in certain log-periodic antennas where a stop-region may occur between the feedpoint and active region [Ingerson and Mayes, 1968]. The synthesis of prescribed patterns from slot arrays is simplified when internal scattering is negligible.

DEVELOPMENT OF THE HYBRID SLOT

Figure 1 shows a conventional stripline-fed, narrow, rectangular slot. The two parallel ground planes are separated by a distance, b. The region between the ground planes is filled with low-loss dielectric of relative permittivity, ε_r, except for the thin conducting strip of width, w, which

is parallel to the ground planes and midway between them. The rectangular slot of length a, and width, b', is cut into the upper ground plane only. To prevent the excitation of propagating modes in the parallel plate waveguide formed by the ground planes, the slot is surrounded by metal posts which form the cavity walls.

The stripline-fed slot is a two-port antenna. It can be fed by means of a coax-to-stripline transducer on either side of the slot. It is convenient to express the electrical performance of the slot in terms of the scattering parameters of this two-port. A reference plane for measurement of the S-parameters was established in the center of the narrow dimension of the slot. Figure 2 shows a typical plot of S11 versus frequency for a slot 5-in. by 0.156-in. fed by a 50-ohm stripline with b = 0.375-in. and ϵ_r = 2.6. At frequencies below .7 GHz the magnitude of S11 is low, since the slot is small in terms of the wavelength and consequently does not appreciably load the stripline. From .7 to 1.252 GHz the magnitude of S11 increases and the phase decreases. At 1.252 GHz the first resonance occurs (S11 real), but the impedance is high compared to 50-ohms so that there is a sizeable reflection. This type of behavior is typical of a resonant element, inductive at low frequencies, in series with the line.

Figure 3 shows computed S11 versus electrical length, θ, for the parallel combination a short-circuited transmission line stub (characteristic conductance Gos) and a lumped conductance Gs. This model can be made to represent the slot more accurately by making Gs a function of frequency.

A slot radiator which produces S11 of small magnitude over a wide band could be used in the frequency-scanning and log-periodic arrays

mentioned above and in other non-conventional ways. It is well-known that two-ports with complementary series and shunt arms have image impedances that are slowly varying over wide frequency bands. The element which is complementary to the shorted stub is an open stub. Figure 4 shows a symmetric T-network in which shorted stubs form the series elements and an open stub forms the shunt element. Losses are included in the conductance, Gs, and resistance, Rs, in parallel and series with the shorted and open stubs, respectively. When GsRs >> 1, the image impedance changes very little with frequency.

A monopole antenna has impedance behavior similar to that of the open stub. A monopole could be connected to a stripline through a small hole in the upper ground plane. To reduce the vertical dimension required, the monopole can be top-loaded as illustrated in Figure 5 in which the monopole extends a distance, h, above the ground plane and is top loaded by a conducting disc of radius, r. The measured S11 for a monopole with h = 1.0-in. and r = 0.3-in. is shown in Figure 6. To be exactly complementary it woul be necessary for S11 (monopole) = -S11 (slot) at each frequency. Comparison of Figures 2 and 6 shows that this condition has been approximately satisfied in the neighborhood of resonance for the two antennas.

Once established that the top-loaded monopole has approximately the desired characteristics, the vertical height can be minimized by allowing h to go to zero and maintaining the resonant frequency by increasing the radius of the disc. This procedure results in the slot shown in Figure 7. The top-load disc is now a conducting patch in the same plane as the upper ground plane. It is surrounded by an annular slot. But since the diameter

of the annular slot, R, is less than the length, a, of the original linear slot, the two slot geometries are combined; hence the name, hybrid slot. The hybrid slot preserves desirable features of previously developed monopole-slot antennas [Mayes et al., 1972], but has a smaller height.

TEST RESULTS

Figure 8 shows the measured S11 for a hybrid slot with R = 0.7-in., r = 0.65-in. and a = 5.2-in. The VSWR is less than 2 over most of the band from .7 GHz to 1.36 GHz. To complete the description of the electrical performance of this particular hybrid slot, measured S21 versus frequency is shown in Figure 9. Note that the operating band of the hybrid slot as a single radiator is more likely to be determined by gain (efficiency) rather than impedance match. In the band between 1.325 and 1.345 GHz less than 10% of the incident power is dissipated in the matched load on the unfed port.

The horizontal plane pattern of the annular slot is omnidirectional, like that of an electric dipole perpendicular to the ground plane. However, the pattern of the linear slot in the same plane has a figure-eight shape with 180-degree phase difference between the two lobes. When these two patterns are combined with the appropriate amplitude and phase relationship, the resulting pattern will be a cardioid. Figure 10 shows measured patterns of a hybrid slot with R = 0.8-in., r = 0.7-in., a = 5.2-in. at 1.362 GHz showing that the above conditions have been approximately satisfied. The pattern bandwidth depends upon how well these excitation conditions can be maintained as frequency changes. By feeding Port 1, the cardioid maximum occurs in the direction of that port. Hence,

feeding Port 2 will reverse the direction of the beam. By feeding both ports in phase, the linear slot fields cancel and the annular slot pattern alone is obtained. By feeding both ports 180-degrees out-of-phase, the annular slot fields cancel and the linear slot pattern alone is obtained.

The variation in response in a standing-wave field was evaluated by observing the received signal as a function of the displacement of a large vertical ground plane located in the direction opposite the transmitting antenna. As the ground plane was moved back and forth a distance of 2 wavelengths, the maximum deviation of the received signal was 4.3 dB. This contrasts with a variation of about 13 dB observed with the annular slot alone.

CONCLUSIONS

The hybrid slot provides some unique features that are advantageous for several antenna and array applications. Stable impedance over a wide frequency band is inherent in its design. Omnidirectional, figure-eight and cardioid patterns are selectively available. In the cardioid pattern mode, the antenna responds to both electric and magnetic field, thus providing the possibility of reducing fades in a multipath field [Lee, 1967], [Itoh et al., 1979]. At a particular frequency, coupling to the hybrid slot can be adjusted by varying the size of the slot. Since the hybrid slot is well-matched over a wide frequency band, the reflection remains small regardless of the slot size over a wide range of sizes.

ACKNOWLEDGEMENT

This work was supported in part by a grant from the Eileen S. Andrew Foundation.

REFERENCES

Fritz, W. A., "A frequency-scanning, stripline-fed periodic slot array," M. S. Thesis, Electrical Engineering Department, University of Illinois, Urbana, Illinois, 1973.

Ingerson, P. G. and P. E. Mayes, "Log-periodic antennas with modulated-impedance feeders," IEEE Trans., AP-16, No. 6, pp. 633-642, November, 1968.

Itoh, K., R. Watanabe and T. Matsumoto, "Slot-monopole antenna system for energy-density reception at UHF," IEEE Trans., AP-27, No. 4, pp. 485-489, July 1979.

Lee, W. C. Y., "Statistical analysis of level crossing and duration of fades of the signal from an energy density mobile radio antenna," Bell Syst. Tech. Jour., vol. 46, pp. 417-448, Feb. 1967.

Mayes, P. E., W. T. Warren and F. M. Wiesenmeyer, "The monopole-slot: a small broadband unidirectional antenna," IEEE Trans., AP-20, No. 4, pp. 489-493, July 1972.

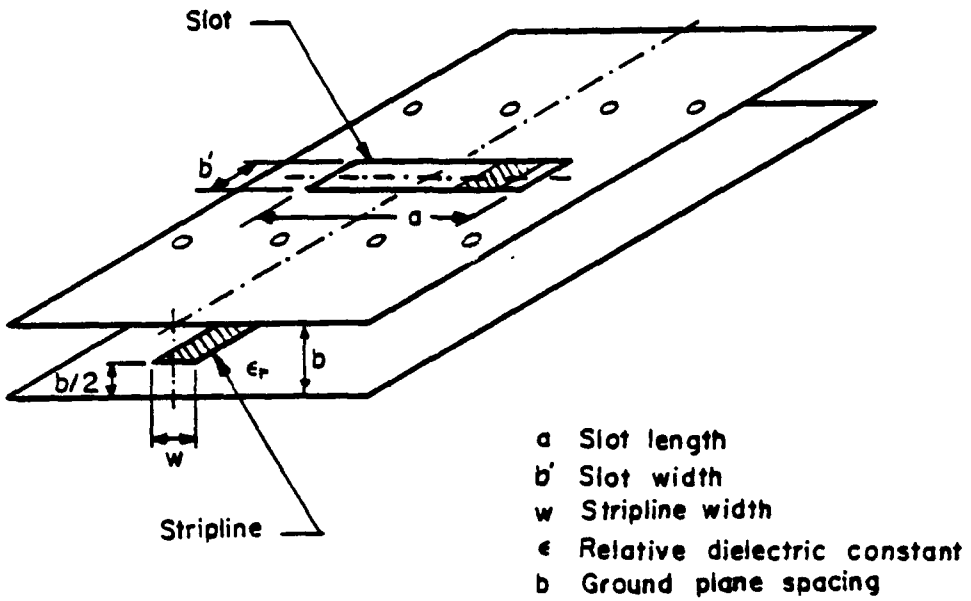

Figure 1. Stripline and slot configuration.

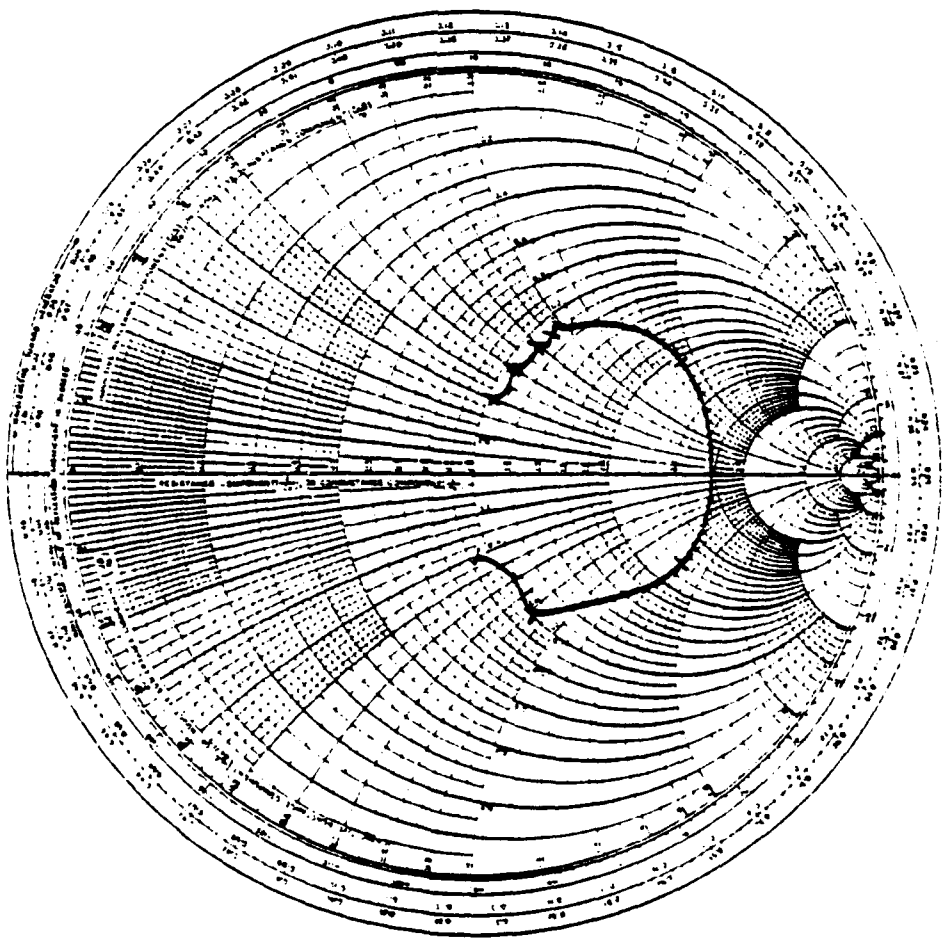

Figure 2. S_{11} versus frequency for stripline-fed slot. (a=5.0 in.)
Frequency (GHz) ticks, 0.7, 0.8, 0.9, 1.0, 1.2, 1.252, 1.30, 1.40, 1.50.

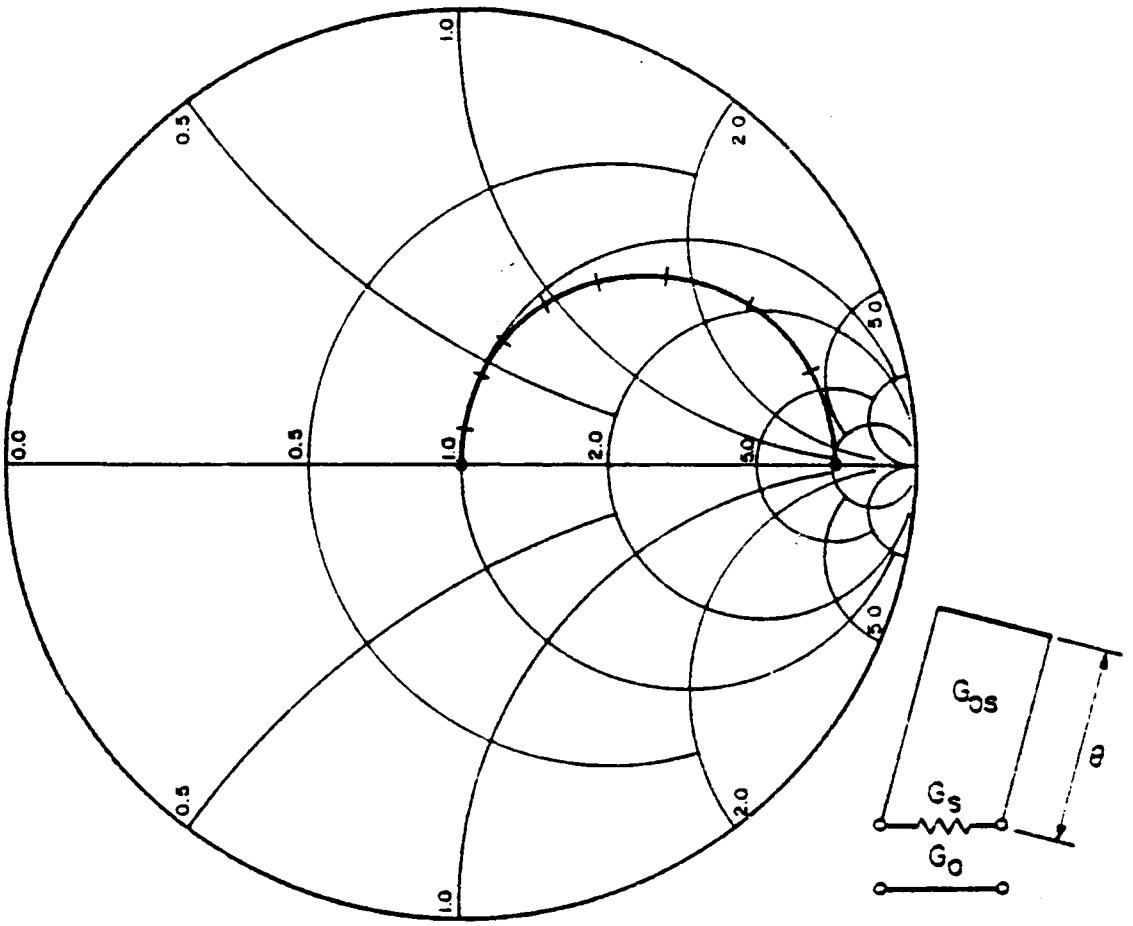

Figure 3. Computed S_{11} versus electrical length, θ, for shorted stub circuit shown. Frequency ticks spaced 10 degrees. (G_{os} = 18.5 mmhos, G_o = 20 mmhos, G_s = 2 mmhos)

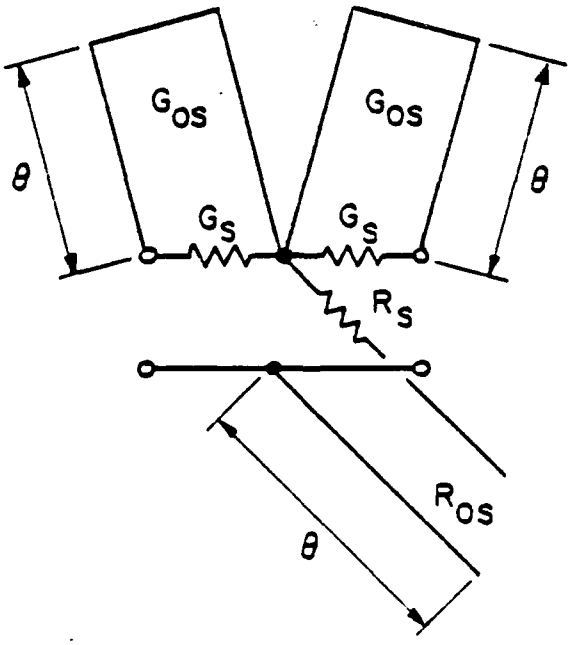

Figure 4. Lossy two-port T network.

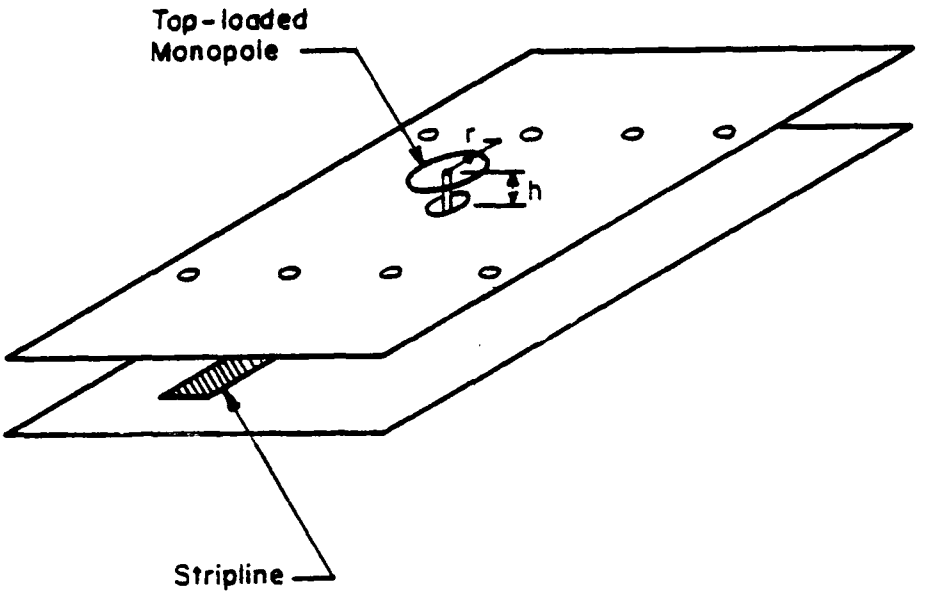

Figure 5. Stripline-fed top-loaded monopole.

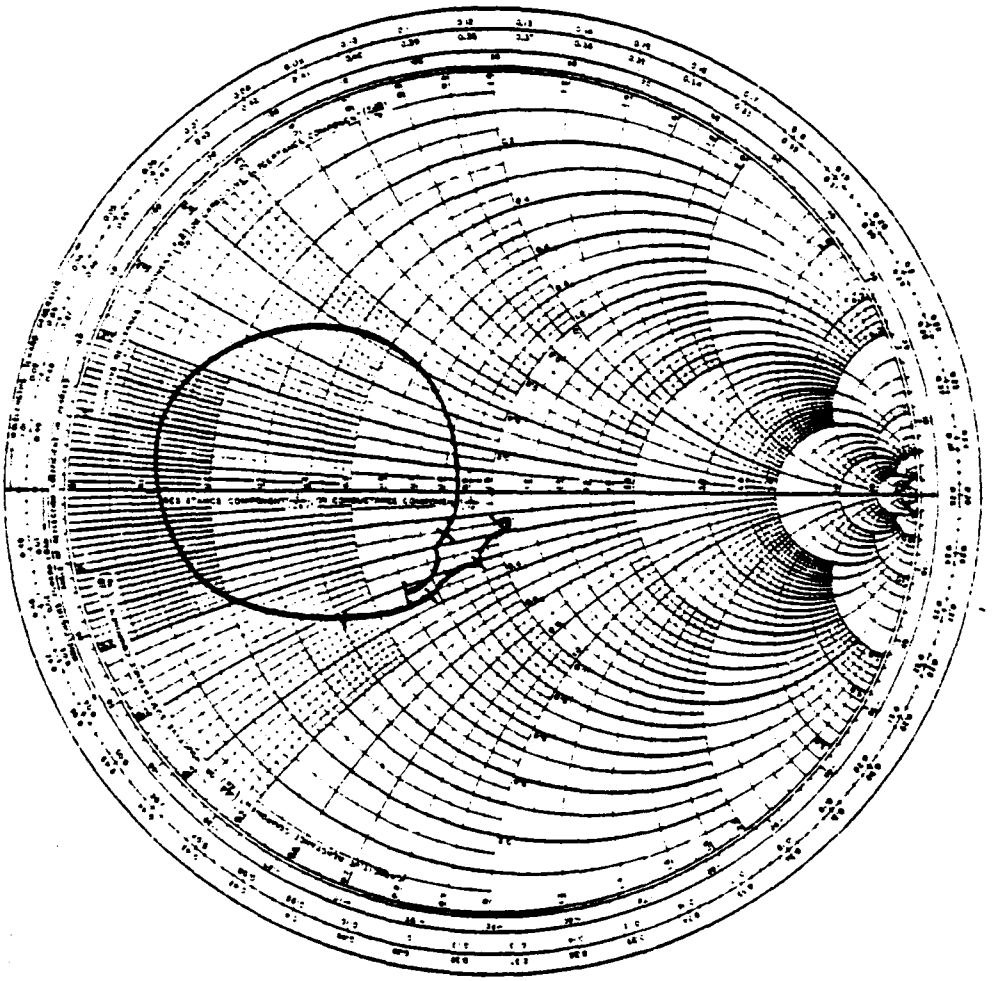

Figure 6. S_{11} versus frequency for stripline-fed top-loaded monopole. Frequency (GHz) ticks, 0.7, 1.0, 1.1, 1.2, 1.257, 1.3, 1.35. (h = 1.0 in., r = 0.3 in.)

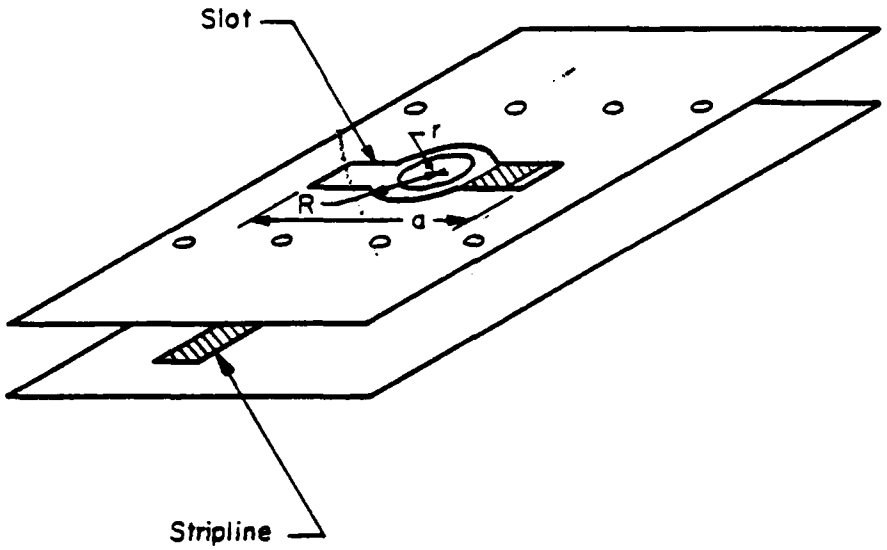

Figure 7. Stripline-fed hybrid slot.

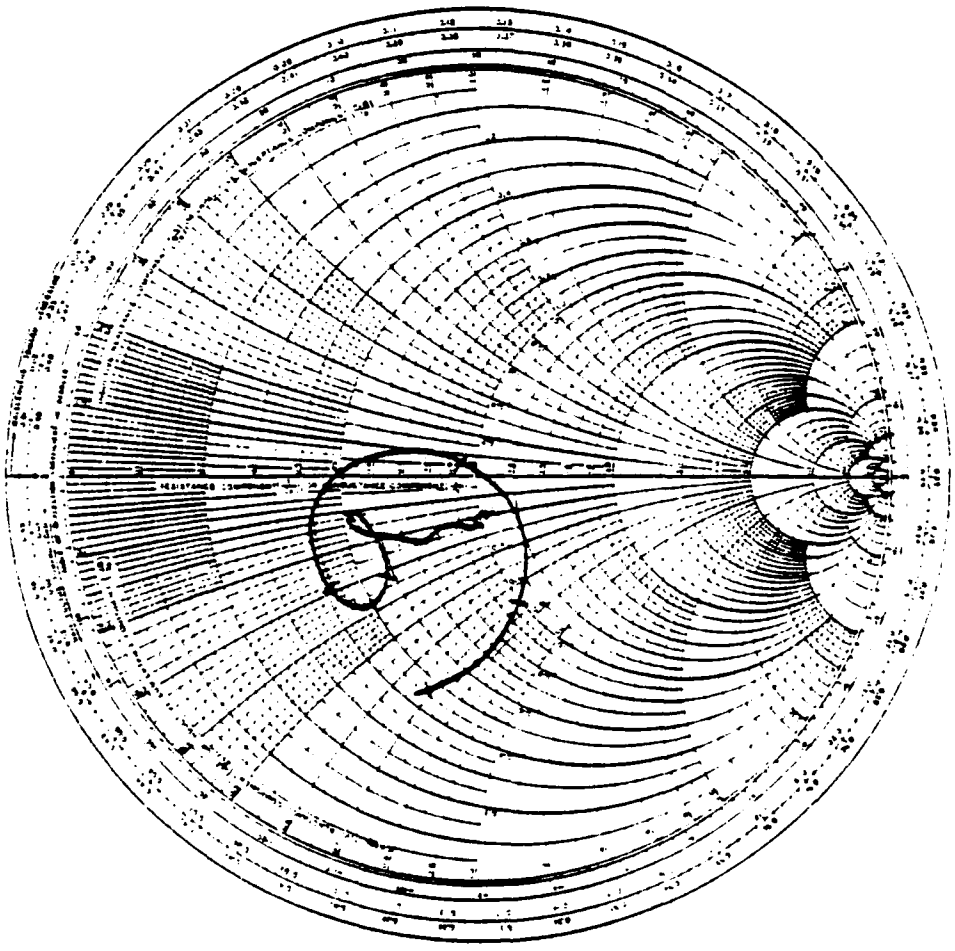

Figure 8. S_{11} versus frequency for stripline-fed hybrid slot. Frequency (GHz) ticks, 0.7, 0.8, 0.9, 1.0, 1.282, 1.3, 1.32, 1.334, 1.340, 1.348, 1.36. (R = 0.7 in., r = 0.65 in., a = 5.2 in.)

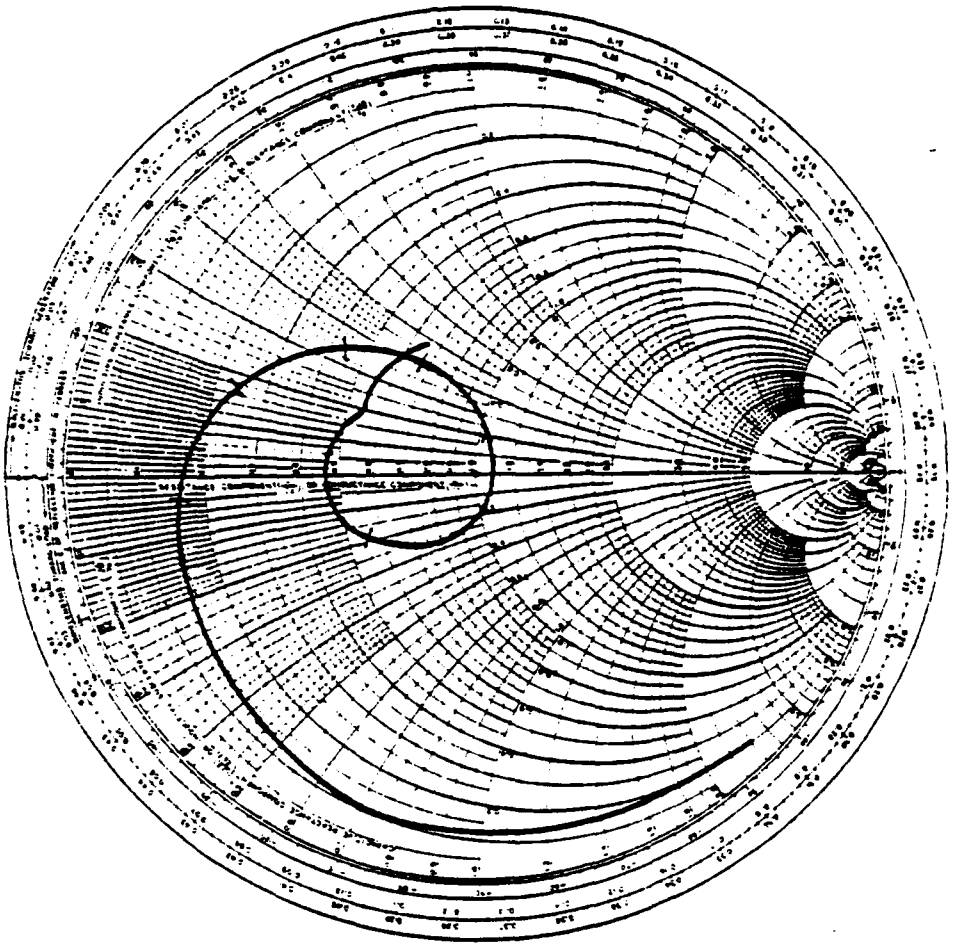

Figure 9. S_{21} verusu frequency for stripline-fed hybrid slot. Frequency (GHz) ticks, 1.25, 1.28, 1.31, 1.325, 1.345. (R = 0.7 in., r = 0.65 in., a = 5.2 in.)

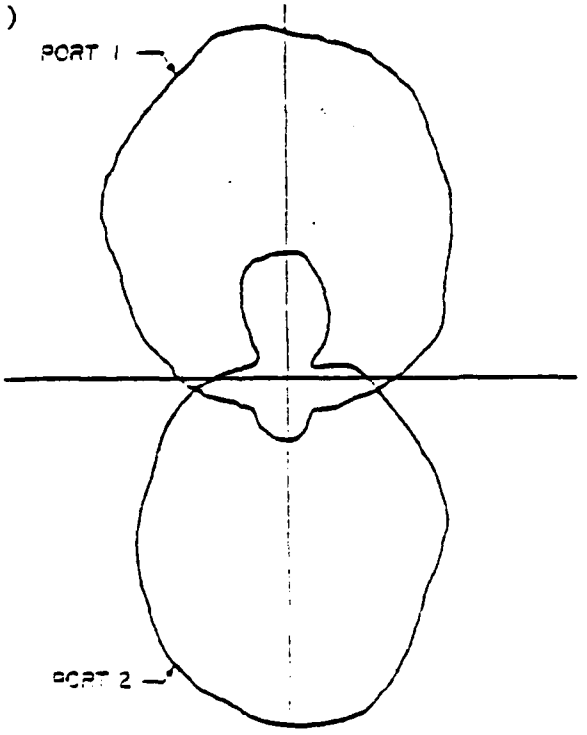

Figure 10. Azimuthal pattern hybrid slot fed at Port 1 and Port 2. (R = 0.8 in., r = 0.7 in., a = 5.2 in.)

ADAPTIVE ANTENNA/RECEIVER-PROCESSOR SYSTEM

G. G. Chadwick, J. G. Charitat, W. Gee
C. C. Hung and J. L. McFarland

Lockheed Missiles and Space Co., Inc.
Sunnyvale, CA 94086

1. INTRODUCTION

Lockheed Missiles and Space Company (LMSC) has developed an adaptive reflector antenna system capable of nulling a large number of very broadband jammers located anywhere in space with arbitrary polarization. The technique utilizes an adaptive array feed located in the focal plane of a Cassegrain or prime focus fed reflector.

A computer simulation program was written to predict the performance of this approach. The results of this program indicate outstanding performance.

Last year field tests were performed using a slow sequential correlation scheme to prove these predictions. The measured data agreed with the predictions of the computer program: the jammers were driven more than 12 dB below the noise level. Unfortunately, broad instantaneous bandwidth could not be demonstrated because, in the interest of economy and expediency, the system mechanization would not allow it.

This year, a 19 element fast parallel correlation scheme is being fabricated and is to be tested this fall. It is expected that these results will also agree with the computer predictions: at least 45 to 50 dB of jammer cancellation with only a few dB gain loss for four 400 MHz bandwidth jammers at 3.2 GHz.

Antenna design concept is discussed in Section 2. Adaptive algorithm used in the adaptive system and the improvement ratio which is useful for the system designers are presented in Section 3 and 4 respectively. Section 5 describes the computer simulation. The rest of a 12-channel narrow band, sequential adaptive system is then presented in Section 6. In this section, the computed results are shown in agreement with the measured results and hence proved the design concept. A 19-channel, wide bandwidth parallel adaptive system, which is under development, is discussed briefly in Section 7.

2. ANTENNA DESIGN CONCEPT

The fundamental antenna design approach taken by LMSC is to eliminate the need for auxiliary antennas used as an adjunct to the main antenna for adaptive purposes. To achieve this, an array of radiating elements, which is much smaller in size than the reflector, is placed in the focal plane of a prime fed or Cassegrain fed antenna. The array is typically an equilaterally spaced array similar to that depicted in Figure 1. Thus, the same array of elements is used for both the formation of the main beam and the

formation of adaptive signals. In general, each of the radiating element ports contains an adaptive complex weight, followed by a summing network. The output of the summing network forms the main beam output. Least-mean-square (LMS) adaptive algorithm is used to set the complex weights, as depicted in Figure 2. Beam scanning can be accomplished by varying the output of the power divider.

Using the LMSC feed array approach, a number of improvements over the more conventional peripheral element approach is realized. The time dispersion across the small array aperture is much less than across the dish periphery; hence, a vast improvement in bandwidth capability is realized. Moreover, the response of each feed is a very high gain beam scanned slightly off axis. This configuration is capable of effectively nulling out a multitude of simultaneous broadband randomly polarized jammers located anywhere in space, including the main beam skirt up to about the -3dB points. Furthermore, there is no associated enormous loss in gain after adaptation, even for jammers located in the skirt of the main beam. This capability is beyond that which is realizable using a peripheral array of elements around the dish edge since the gain of the peripheral element array is much less, typically, than than of the main beam.

Only singly polarized elements are typically used in the LMSC approach, since each of the feeds tend to respond to any polarization approximately equally on the average, although each feeds' pattern is scanned to a different space angle.

To gain physical insight into the performance capability of the LMSC approach, a computer program was written, covered in Section 6, for a Cassegrain configuration.

Table 1 summarizes the cases covered. Numerous cases were run so that the final results could be presented statistically.

The first antenna system analyzed, was the 46' dish that used a subreflector design such that θ_r, the included half angle of the equivalent paraboloid was 19.2°. A 19 element hexagonally spaced array was chosen as the feed configuration. Initially, the radiators were spaced .85 $\bar{\lambda}$ apart at 2.25 GHz. The system was allowed to adapt against noise only, yielding the optimum weights for the feed distribution given in Figure 3. The element spacing was decreased to .6 $\bar{\lambda}$ yielding for θ_r = 28.3° the results of Figure 4.

Then 4 jammers, whose spatial positions were generated randomly with equal likelihood in the sidelobe region (anywhere outside the main beam) was postulated to have power densities at the receive position of 40, 50, 60, and 55 dB above that which an isotropic antenna would receive. (These power levels were held fixed throughout this study.) Figures 5, 6 and 7 show the reference signal-to-noise ratio and the jammer-to-noise ratio both before and after adaptation for θ_r = 28.3°.

Figures 8 and 9 show plots of the cancellation ratio (or improvement ratio as defined in Section 4) and gain after adaptation parametric on bandwidth based on the previous results.

Figures 10 and 11 show the same results as Figures 8 and 9 but in a statistical format.

The same feed array was then used (in conjunction with the appropriate subreflector) to feed the same main dish but using a smaller magnification ratio. Figures 12 and 13 show the optimum weights, adapting against noise only, for $\Theta_r = 35^\circ$ and 50°, respectively. Data was taken to $\Theta_r = 60^\circ$. Figure 13 shows the results of varying Θ_r: $\Theta_r = 50^\circ$ is the best solution.

To illustrate the gross improvement in performance as Θ_r approached the optimum solution (for a given feed array design) Figures 14 and 15 apply to the case of $\Theta_r = 19.2^\circ$ while Figures 16 and 17 apply to $\Theta_r = 50^\circ$. The $\Theta_r = 50^\circ$ solution is far superior in terms of both the cancellation ratio and gain after adaptation.

In an effort to explain what is happening as Θ_r varies, a <u>single</u> jammer was postulated to produce a jammer-to-noise ratio much greater than unity. Under these conditions, it can be shown that

$$M = \frac{\text{Gain After Adaptation}}{\text{Gain Max Achievable}} = 1 - \frac{\langle V_S\ V_J \rangle^2}{\langle V_S\ V_S \rangle \langle V_J\ V_J \rangle}$$

where $[V_S]$ and $[V_J]$ are column vectors for the antenna pattern response in the 19 pipes for the signal of interest (SOI) and jammer, respectively, and where the inner product $\langle AB \rangle$ is defined as $[A]^{*T}\,[B]$, where $[A]^{*T}$ is the complex conjugate transpose.

M will maximize for $[V_S]^T$ of the form

$$[V_S]^T = [1,\ 0,\ 0,\ \ldots\ 0]$$

That is to say that all feeds, except for the center feed, are placed in the naturally occurring nulls of the local plane distribution.

Under this condition

$$M = 1 - \frac{V_{J_1}^2}{\sum_{i=1}^{19} V_{J_i}^2} = \frac{\sum_{j=2}^{19} V_{J_i}^2}{\sum_{i=1}^{19} V_{J_i}^2} = \frac{P\,\Big|_2^{19}}{P\,\Big|_1^{19}}$$

or

$$M = \frac{\text{Jam Power in all but center pipe}}{\text{Total Jam Power}}$$

Using the results of the single jammer case, one concludes that the best design would be one in which the center element alone achieves most of the gain while the remaining elements are placed on naturally occurring nulls of the focal plane distribution (or receive), thereby rendering them mathematically orthogonal to the center element. The only loss sufferred would then be the fractional amount of total power furnished to the elements surrounding the center element. An attempt was made to cover the case of multiple jammers by use of the Woodbury identity; however, it became very cumbersome and was discarded. On the other hand, the results of this study indicates that the best performance, in terms of both cancellation ratio and loss in gain after adaptation seem to indicate that the optimum design is the same as for the single jammer case. A heuristic argument could be made to the effect that the number of degrees of freedom is less than the number of adaptive feeds unless the patterns produced by the feeds are disjoint. It is apparent that such a case is reached when the feeds fall on naturally occurring nulls of the focal plane distribution (except for center element).

A very limited amount of data was taken at X-band, using a 37 element feed array and varying θ_r from 12^o to 29^o (not the optimum). Figures 18 through 21 are the results. The same type of trends are evident.

Although this data was derived for a Cassegrain configuration, there is reason to believe that the same or very similar results could be achieved using a prime focus feed array.

3. ADAPTIVE ALGORITHM

An adaptive antenna system is presently being assembled on the Lockheed antenna test range to demonstrate the concepts described in this paper. A 19 channel receiver system and a hybrid digital/analog control system has been fabricated to support these tests. Which algorithm for the control system was chosen to support this effort was unimportant in this series of tests because the advances in system technology being demonstrated are mostly in the antenna design and analysis. Any of many algorithms could have been chosen, but the Least-Mean-Square (LMS) algorithm with a main-beam maintenance (1)(2)(3)(7) was used for expediency, economy, and certain desirable traits in demonstrating system performance. Analysis of this algorithm performance has been described in the literature (2)(3). A simulation of the system in digital computer software predicts excellent, wide bandwidth adaptation for this system.

Figure 22 is a block diagram of the adaptive receiver.

The optimal weights of an adaptive antenna are determined by minimizing the squared error between the received signal and the desired response. Let

$$\overline{X}(t) = \left[X_1(t),\ X_2(t),\ldots\ldots,X_m(t)\right]^T$$

be the input signals to the adaptive system in the m receive channels and

$$W = \left[W_1, W_2, \ldots\ldots, W_m\right]^T$$

be the weight vector. The output is the weighted sum of input signals

$$y(t) = \overline{X}^T(t) \cdot \overline{W} = \overline{W}^T \cdot \overline{X}(t)$$

Supposed d(t) is the desired response. The difference between d(t) and y(t) is given by

$$\varepsilon(t) = d(t) - y(t) = d(t) - \overline{W}^T \cdot \overline{X}(t)$$

The quantity to be minimized is therefore

$$E\left[\varepsilon^2(t)\right] = E\left[d(t) - \overline{W} \cdot \overline{X}(t)\right]^2$$

where E denotes the ensemble average. The optimal weights are then obtained by setting the gradient of $E\left[\varepsilon^2(t)\right]$ equal to zero and is readily found to be

$$\overline{W}_{opt} = \overline{\overline{R}}^{-1} \cdot \overline{P}$$

where $\overline{W}_{opt}$ is the matrix of optimum weights, and

$$\overline{P} \triangleq E\left[d(t)X(t)\right]^T = E\left[d(t)X_1(t), d(t)X_2(t), .., d(t)X_m(t)\right]^T$$

$$\overline{\overline{R}} \triangleq E\left[\overline{X}(t)\overline{X}^T(t)\right]$$

$$E\begin{bmatrix} X_1(t)X_1(t) & X_1(t)X_2(t) & \ldots\ldots & X_1(t)X_m(t) \\ X_2(t)X_1(t) & X_2(t)X_2(t) & \ldots\ldots & X_2(t)X_m(t) \\ \vdots & \vdots & & \vdots \\ X_m(t)X_1(t) & X_m(t)X_2(t) & \ldots\ldots & X_m(t)X_m(t) \end{bmatrix}$$

$\overline{P}$ is the cross correlation between the desired response and the input signal X(t). $\overline{\overline{R}}$ is the auto-correlation matrix of the input signal X(t). $\overline{\overline{R}}$ is real, symmetric and positive definite (in rare cases positive semi-definite). The minimum error is

$$E\left[\varepsilon^2_{min}\right] = E\left[d^2(t)\right] - \overline{W}^T_{opt} \cdot \overline{P}$$

Since $\bar{\bar{R}}$ is positive definite, it is always possible to find a transformation, such that after the transformation, $\bar{\bar{R}}$ is a diagonal matrix. In this transformed space, it can be shown that the eigenvalue of $\bar{\bar{R}}$ are inversely proportional to the time constant of the adaptive system. The larger the eigenvalues of $\bar{\bar{R}}$ are, the faster the system will adapt.

4. IMPROVEMENT RATIO

Two parameters are required to describe the performance of an adaptive antenna system. One, obviously, is the suppression of the jammer below the unadapted system response. The other is some measure of the antenna performance in receiving the signal of interest (SOI) which was in the unadapted main beam. There is always some change in the antenna main beam response due to the adaptive system. Adaptation creates nulls in the direction of the jammer by altering the power distribution and phase of the antenna array (or the array of the main antenna and auxiliary antennae). Any perturbation in the array illumination from optimum will alter the antenna for field response with a likely decrease in main beam gain.

A description of the adaptive antenna response is complicated by two characteristics of an adaptive antenna system. Simple statements about the suppression of jammer power and on-axis gain of the adapted antenna system are insufficient. The jammer average power level is normally reduced below the average receiver noise level by the relatively long averaging times in the adaptive processor. Thus, only that difference between the unadapted system jammer power and the adapted receiver noise power is of interest to the system designer - - not the total reduction in the jammer. The other system consideration is the preamplifiers normally placed between the antenna elements and the adaptive system weights. Together, these comprise a variable gain (or loss) in the antenna array before the antenna beam is formed in the beam forming matrix. The addition of a variable noise to the "antenna output" (from the beam forming matrix) complicates the description of antenna system performance because, in this antenna system beam forming matrix output, the received SOI level is constant but the receiver noise level is continuously variable. Therefore, speaking of jammer suppression or antenna signal gain can be grossly misleading.

These problems in semantics can be circumvented easily by focusing on the measures of system performance which are of interest to system designers. The meaningful measure of adaptive system performance is the signal to noise-plus-jam ratio improvement provided by the adaptive system. This easily computed measure includes both the effects of signal losses due to the fact that the antenna array (including peripheral auxiliary antennae elements, if used) illumination has been perturbed from optimum to create nulls in the direction of the jammer and the effects of reducing the jammer power. Also, this easily computed measure is a valid indicator of the increase in system effectiveness obtained by inclusion of the adaptive system.

A good definition of the other main system performance measure is slightly more elusive. The system design engineer must size the transmitter to provide minimum signal to noise ratio in the receiver, before and after

adaptation, with or without jammers present, for a minimum utilization ratio. Antenna gain is not relevent until after the beam forming matrix, after a variable amount of amplifier noise has been added.

Again, the problem of defining gain can be easily overcome by specifying the change in system signal-to-noise ratio relative to the maximum signal-to-noise ratio obtainable with an antenna system with the closest to optimum array illumination obtainable. It will be shown that these are easily computed quantities and, in fact, the variation of the signal to noise ratio from optimum is an output of the previous system modeling computation.

The figure of merit and the gain change described above are easily computed. The figures of merit will be referred to as the improvement ratio, (IR) is

$$IR = \frac{S/(N + J)}{S'/(N'+J')} = \frac{\text{sig-to-interference after}}{\text{sig-to-interference before}}$$

where IR is the improvement ratio, S' is the beam forming matrix signal power output before adaptation, and S the signal output after adaptation; N' and N are the noise power output before and after adaptation; and J' and J the jammer power output before and after adaptation. Rearranging terms yields:

$$IR = \left(\frac{S/N}{S'/N'}\right)\left(\frac{1 + \frac{J'}{N'}}{1 + \frac{J}{N}}\right)$$

In words, this measure of performance is approximately the magnitude of the reduction in interference, in dB, less the reduction in signal-to-noise in dB, which is the result of adaptation. Reduction in signal-to-noise due to adaptation is simply the first factor of this relation

$$GC = \frac{S/N}{S'/N'}$$

which is referred to simply as the gain change. Thus, the system designer can obtain the after adaptation system performance from the gain change and the unadapted, ideal, antenna performance.

5. COMPUTER SIMULATION

A general digital computer program has been developed to simulate the adaptive Cassegrain antenna performance. This computer program not only verifies the adaptive Cassegrain antenna design concept analytically but also provides performance predictions.

The complete program computes the antenna for field pattern before adaptation and then with given power levels and directions of interferences (jammers), computes the optimal weights of the feed array. These optimal weights minimize the interference received and maximize the desired signal received.

Having obtained these optimal weights, the computer program computes the far field pattern after adaptation and the jammer cancellation ratio. The computer program can also be used to synthesize the maximum antenna gain pattern by using the internal interference (receiver noise) only in the adaptation process.

A closed-form expression of the Cassegrain antenna far field pattern is used in the program. Blockage effect and spillover field are also considered in the program. Details of mathematical formulation used in the computer program are given in (9) .

The inputs and outputs of the computer program are summarized in Table 2 and 3.

6. DEMONSTRATION MODEL AND TEST RESULTS

The LMSC adaptive antenna approach raised several questions which could not be conclusively answered by only an analytical approach. No reasonable mathematical model can include all the response characteristics, cable leakage, conducted interference and edge diffraction effects which plague all hardware systems. These small subtle anomalies in the response of the antenna are normally not of any significance when the sidelobe response level and main beam gain of the antenna are the important considerations. However, these normally inconsequential effects become of great importance when attempting to generate nulls in the antenna response which are far down from the main beam peak. Therefore, a demonstration model was designed, fabricated and tested to prove the design concept.

The adaptive system is a twelve channel sequential system to work with a narrow bandwidth planar array. Figure 23 shows the Cassegrain antenna on the range. The main reflector is of 30 ft. diameter and the center operating frequency is 6 GHz. Three jammers are available as shown in Figure 24 as locked in the second sidelobe at 0.95 degrees off center of the main beam, another one is the intermediate sidelobe region 23 degrees off boresight and the third one is the far sidelobe region at 66 degrees off boresight where the mode of propagation is mostly by direct propagation to the feed, reflection from spars and multipath. The system was tested with one, two and three jammers and the system suppressed the jammers in all cases.

Figures 25 and 26 are unretouched Polaroid photographs of a spectrum analyzer display showing suppression of the jammer and enhancement of the signal of interest in both photographs. Two jammers were used - one in the second sidelobe and one in the intermediate sidelobe at 23 degrees from boresight. The spectrum analyzer bandwidth was 10 kilohertz - the approximate effective noise bandwidth of the control processor system. Therefore, the signal-to-noise ratio read from the spectrum analyzer was the signal-to-noise ratio with which the adaptive processor was working.

In Figures 25 and 26 there are two jammers, a signal of interest in the main beam, and the beam steering reference. The two jammers are in the center with unadapted signal-to-noise ratios of +37 dB and +34dB. The signal-of-interest is to the right of the trace (higher in frequency) with a signal-to-noise of +12 dB. The reference signal is to the left (lowest frequency).

The before adaption signal magnitudes are shown in the top traces; and after adaption, in the lower traces. The jammers were suppressed to below noise in all trials. Changing the spectrum analyzer from 10 kilohertz to 1 kilohertz (and slowing the sweep speed) indicated that the jammer level was more than 12 dB below the 10 kilohertz bandwidth noise level. The jammer residual barely evident in the lower trace of Figure 25 is due to the change in range conditions discussed earlier in the time elapsed between the time the computer stopped after suppressing the jammer to the time the photograph was taken. The jammers had been suppressed more than 10 dB into the noise at the end of the adaptation sequence.

The computed jammer suppression was 48.23 dB. This compares almost exactly (within instrumentation limits) with a measured cancellation ratio of 47.7 dB (+34 dB plus 37 dB J/N before adaptation to two -12 dB ratios after adaptation. Note that these ratios must be changed to power ratios before addition).

The jammer was suppressed below the noise level because of averaging in the signal processor. The number of samples of the input which are averaged is increased as the adaptation progresses. This is done to increase the accuracy of the sampled input after each perturbation of the adaptive weights. The number of samples are increased from eight at the beginning of adaptation to a maximum of 256 samples. This reduces the ambiguity of the measure of correlation in the signal processor by the square root of 256, or 16. Due to the square-law characteristic of the correlation detector, this is a reduction in the correlation power measurement by 16, or 12 dB - the level to which the jammer signals can be suppressed below the noise in this processor system with this averaging.

The computed before and after adaptation antenna responses are shown in Figure 27. Note that after adaptation, deep nuuls formed in the direction of jammers and the main beam is not effected. As reported by Mayhan (6) multiple nulls also formed.

7. ADAPTIVE RECEIVER SYSTEM

A 19 channel adaptive reciever using parallel system and wide bandwidth components to demonstrate the full capabilities of the LMSC design is under development.

A number of improvements were incorporated in the design of the adaptive receiver to achieve wide bandwidth cancellation. Cancellation is accomplished at RF (3.2$\pm$0.2 GHz) rather than at IF to avoid accumulating

the phase dispersions of the mixers, filters and amplifiers. Furthermore, the RF microstrip networks and components are designed to hold the amplitude and phase imbalances to 0.1 dB and 0.6° respectively over the 400 MHz bandwidth to insure a maximum (>45 dB) null depth. Hence, post RF perturbations are less critical.

A single high level mixer followed by a soft limiting IF (800 MHz) amplifier and bandpass filter in the feedback loop provide a constant amplitude to the local oscillator port of the correlators, thus reducing the dependence of the jammer signal level. Operating in the feedback loop improves the dynamic range and ability to handle low level jammers.

Another important attribute inherent in the adaptive algorithm is the injection of a reference signal at the output of each antenna element and a difference (180°) signal back into the summing network. This feature enables the adaptive system to maximize the gain in the direction of the reference signal. The heart of the adaptive receiver is the complex weights. The complex weight provide 0 to 60 dB of attenuation or amplitude control and 360° phase rotation for each channel (antenna element).

The entire adaptive system, designed to operate between 3.0 and 3.4 GHz, was based on engineering conveniency because of readily available test equipment, RF devices and components. Microstrip networks were designed with low dielectric substrate merely for ease in fabrication and testing. No attempts were made to miniaturize the adaptive system during this phase of development. However, a parallel effort was initiated to microminiaturize the exact system with MIC technology. At this writing, an RF amplifier and constant impedance PIN attenuator for the complex weights have been successfully implemented on high dielectric alumina substrate and are currently undergoing engineering test and evaluation.

CONCLUSIONS

Lockheed Missiles and Space Company has successfully developed an adaptive antenna system which has the ability of nulling a multitude of simultaneous jammers of arbitrary positions and polarizations over a very wide instantaneous bandwidth.

A computer simulation of the LMSC approach indicates that the performance is far superior to that of the more conventional peripheral element approach.

Range tests have validated the computer simulation predictions.

System modeling on a digital computer, limited bandwidth testing, and small scale testing with a four channel brassplate adaptive system predict greater than 45 dB improvement (ratio) is attainable against a 400 MHz bandwidth jammer with a center frequency of 3.2 GHz.

At this writing, the 19 element adaptive receiver system is in final phase of the system integration and checkout. Full comprehensive testing and demonstration against a multiple jamming environment is scheduled this Fall.

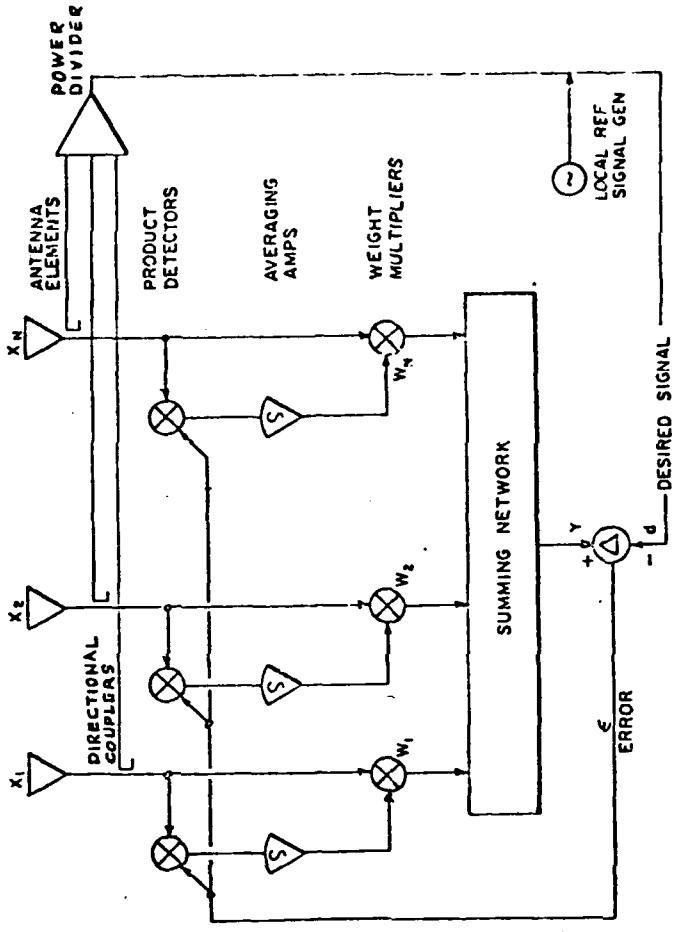

Figure 2 LMS Adaptive Algorithm

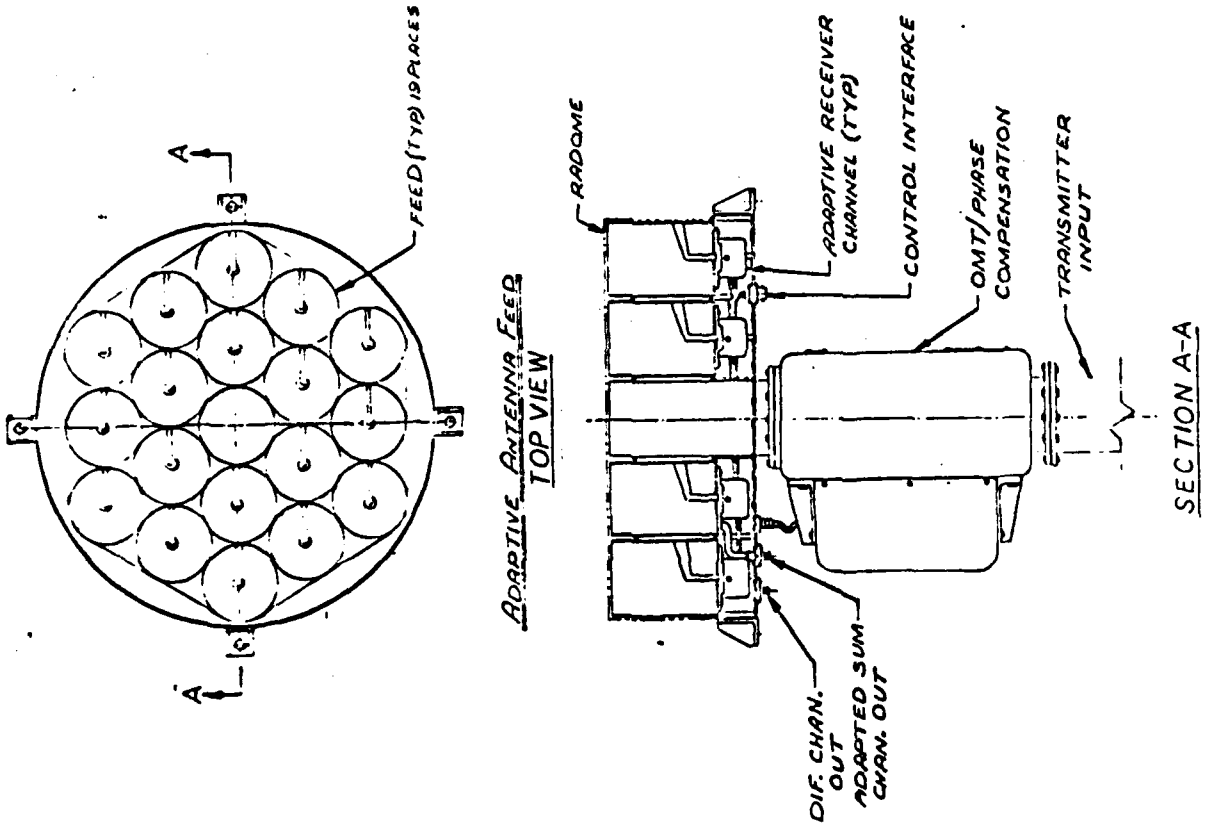

Figure 1 Equilaterally Spaced Array

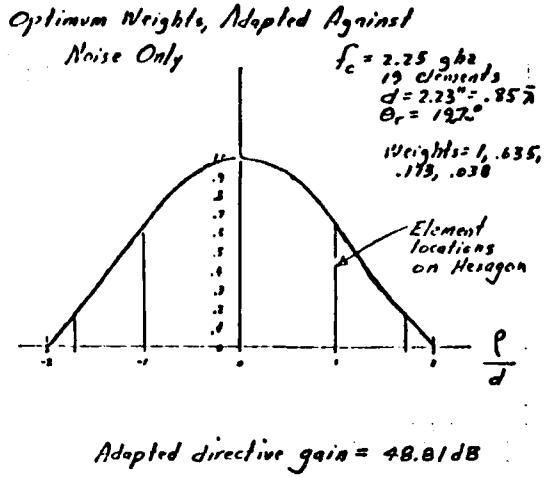

Figure 3 Adapted at d=.85

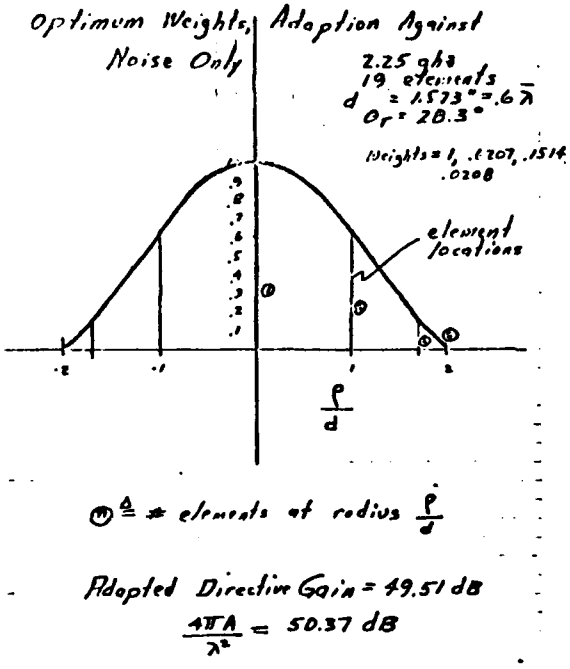

Figure 4 Adapted at d=.6

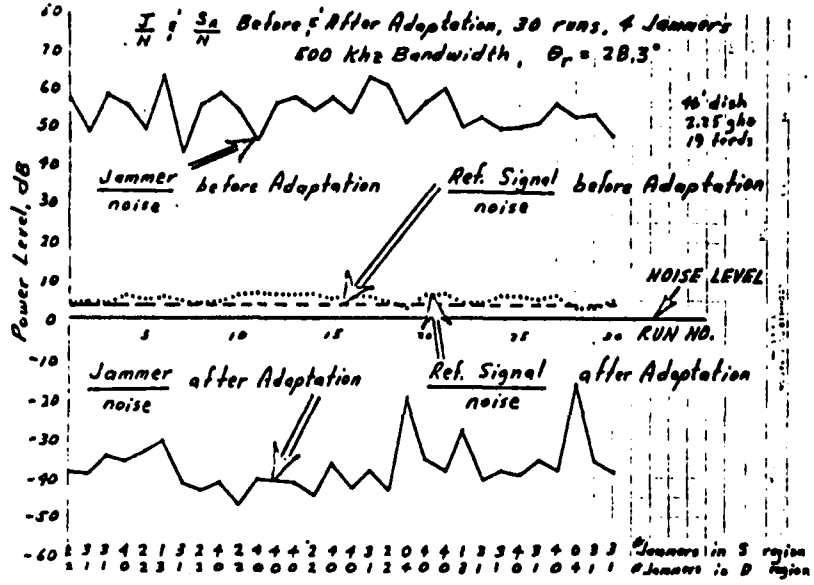

Figure 5 S/N and J/N Before and After Adaptation

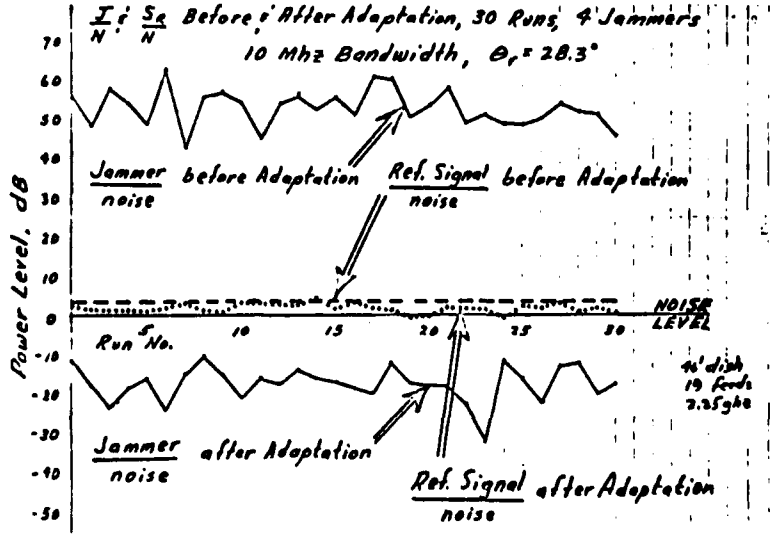

Figure 6 S/N and J/N Before and After Adaptation

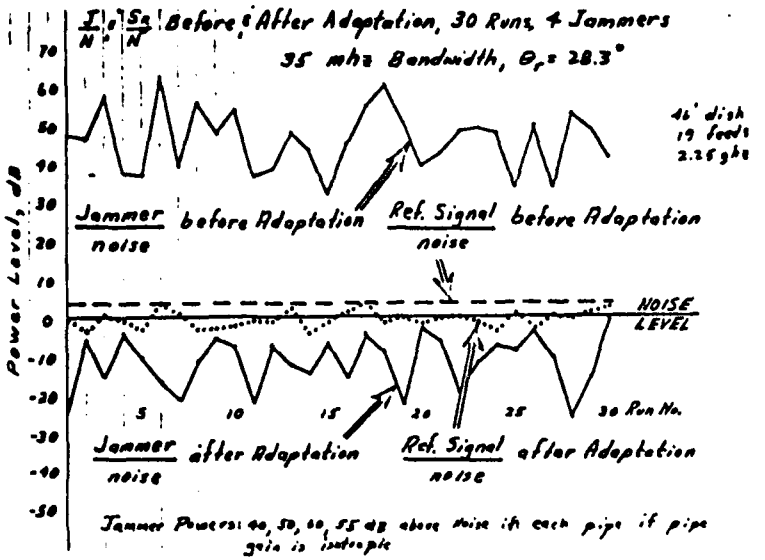

Figure 7 S/N and J/N Before and After Adaptation (35 Mhz)

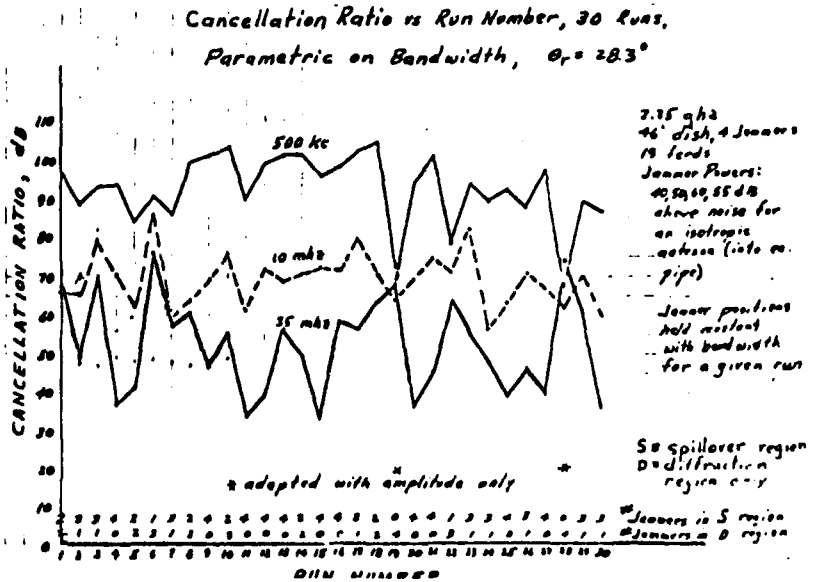

Figure 8 Cancellation (Improvement) Ratio After Adaptation

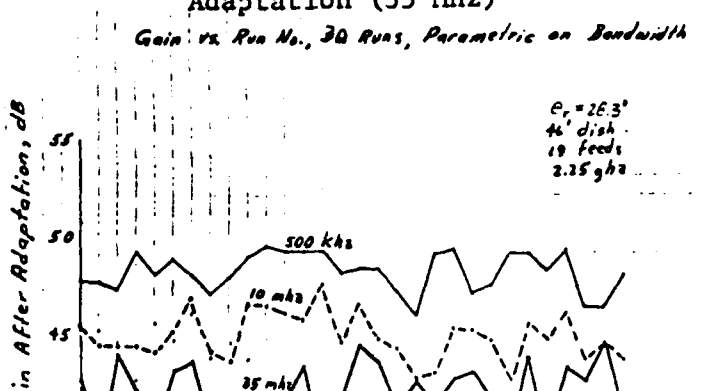

Figure 9 Gain (dB) After Adaptation

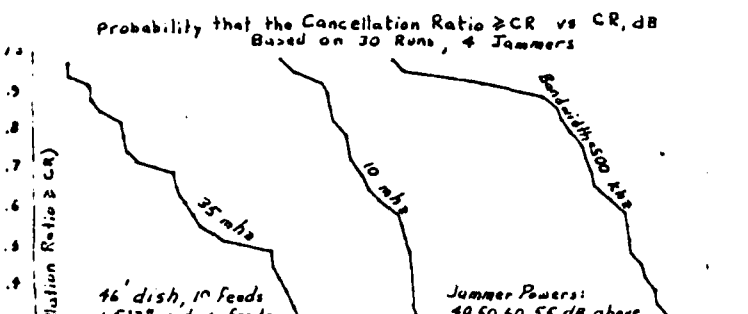

Figure 10 Probability of Cancellation Ratio

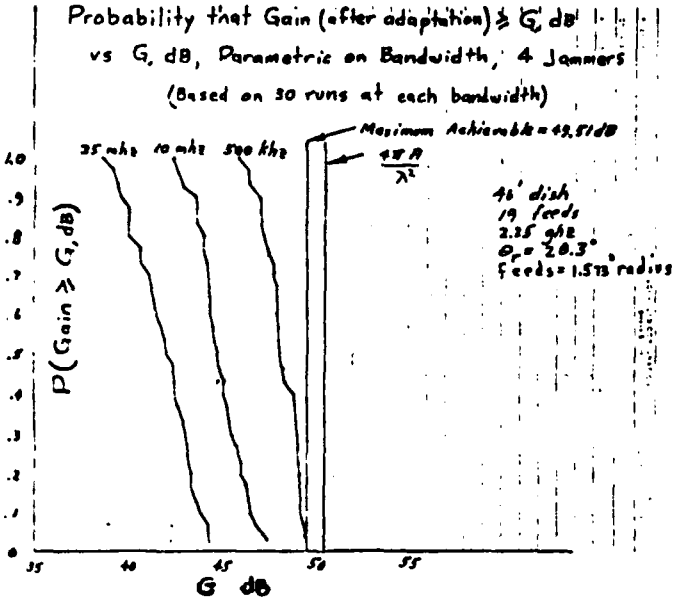

Figure 11 Probability of Gain After Adaptation

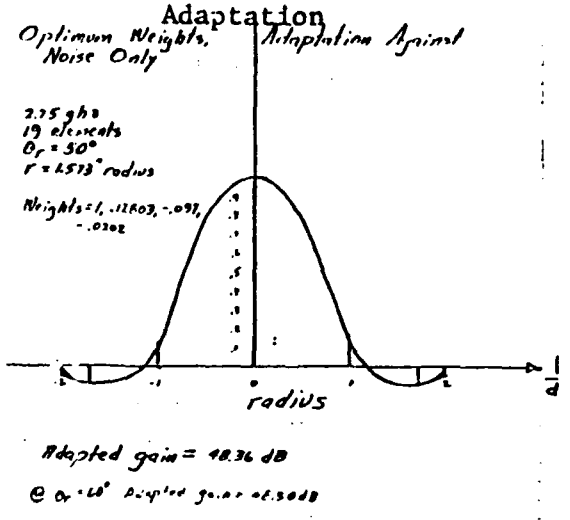

Figure 13 Optimum Weights (50 deg.)

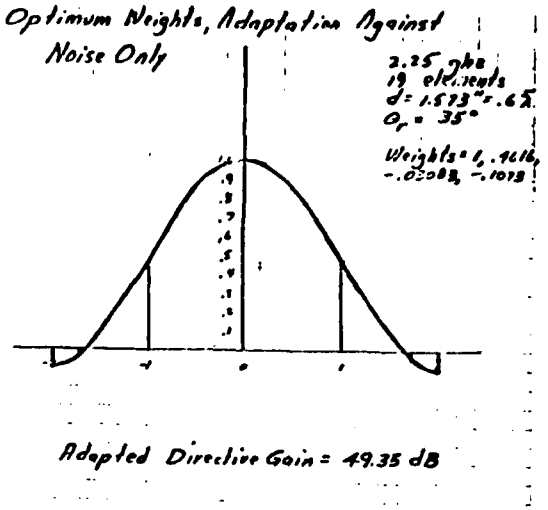

Figure 12 Optimum Weights (35 deg.)

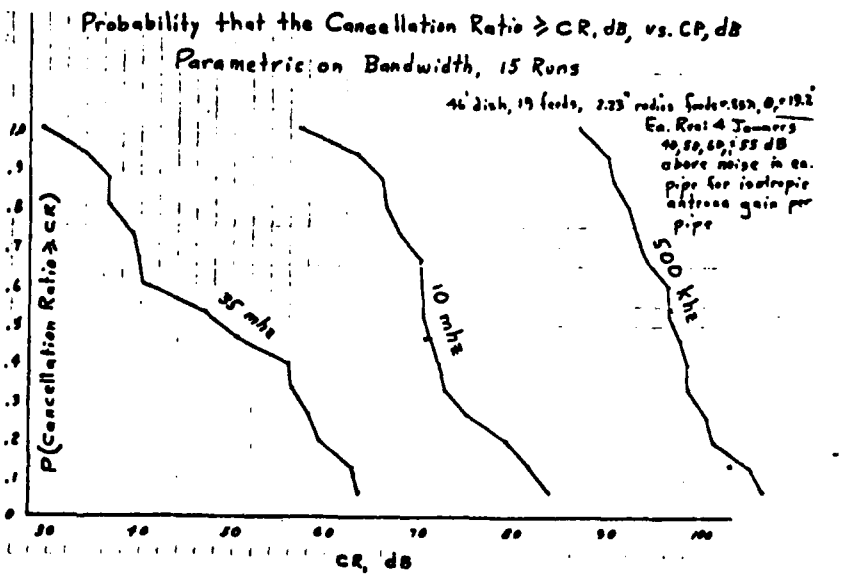

Figure 14 Probability of Cancellation Ratio (19.2 deg.)

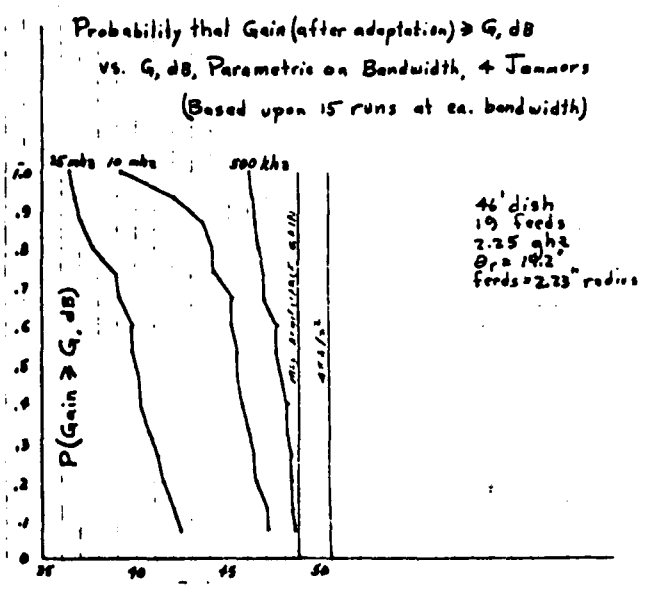

Figure 15 Probability of Gain (19.2 deg.)

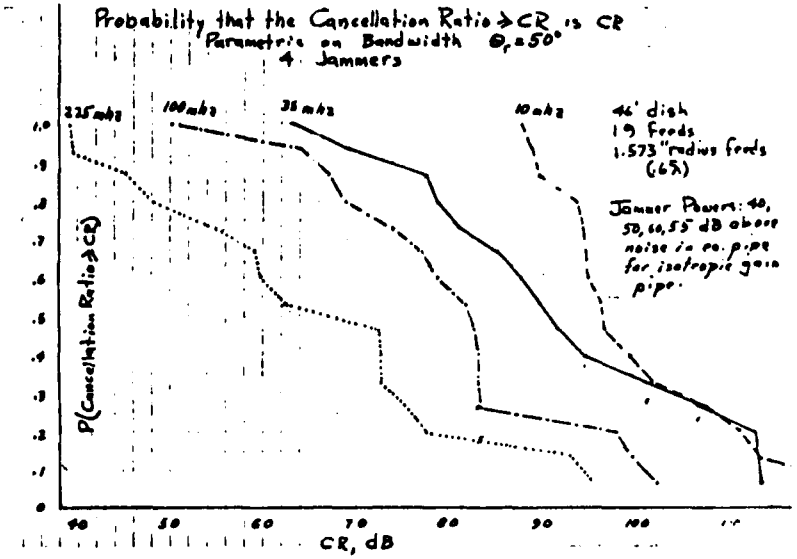

Figure 16 Probability of Cancellation Ratio (50 deg.)

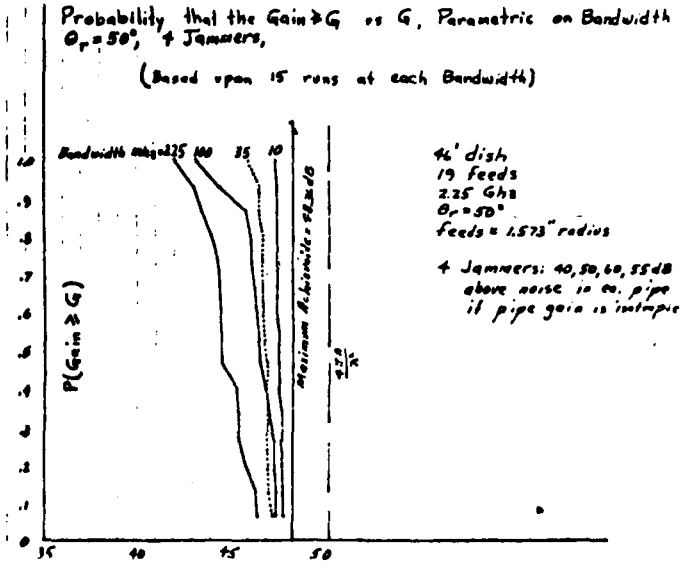

Figure 17 Probability of Gain (50 deg.)

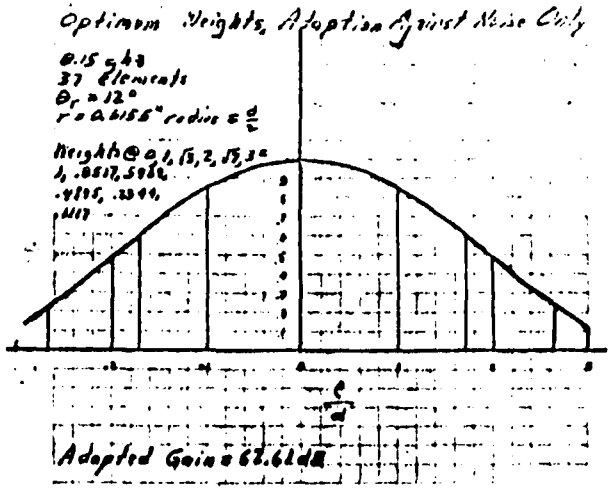

Figure 18 Optimum Weights (12 deg.)

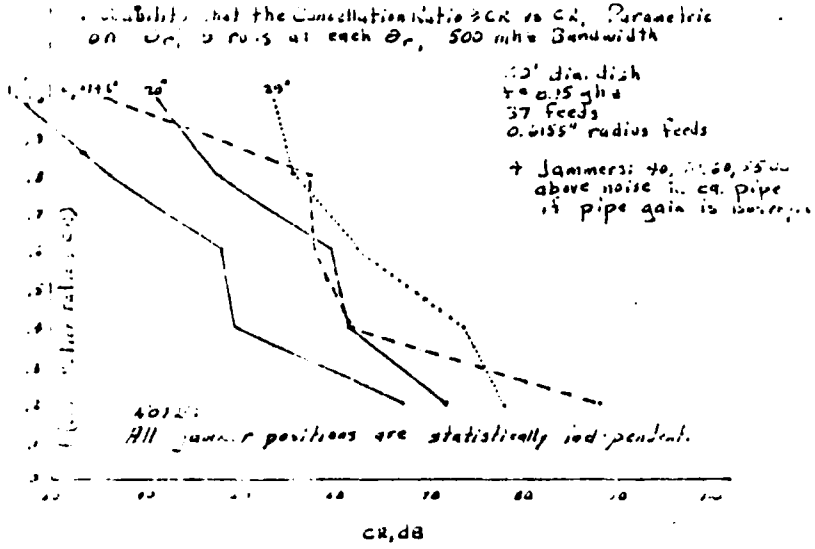

Figure 19 Probability of Cancellation Ratio (500 MHz Bandwidth)

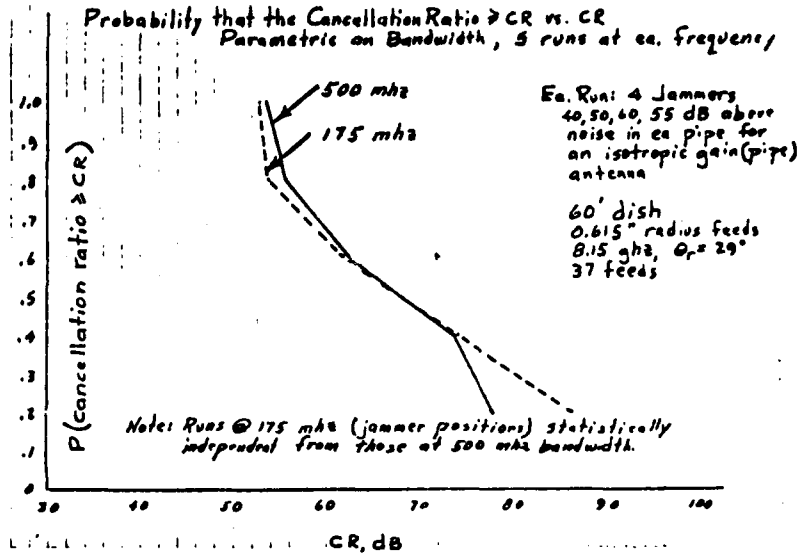

Figure 20 Probability of Cancellation Ratio (175 & 500 MHz)

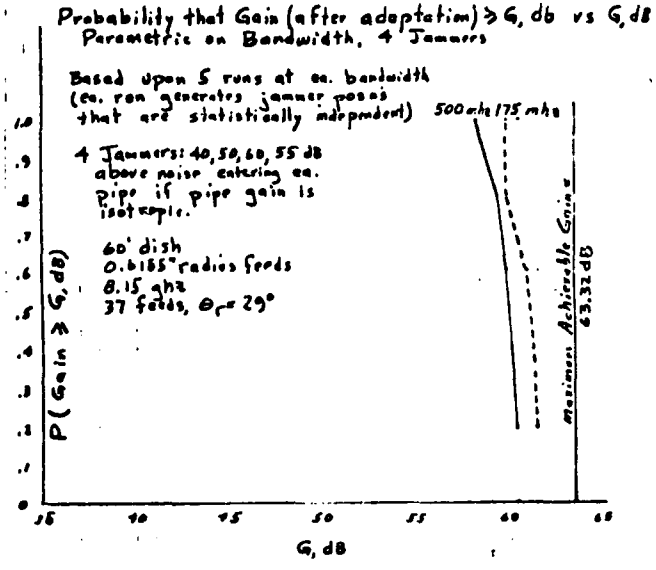

Figure 21 Probability of Gain (175 & 500 MHz)

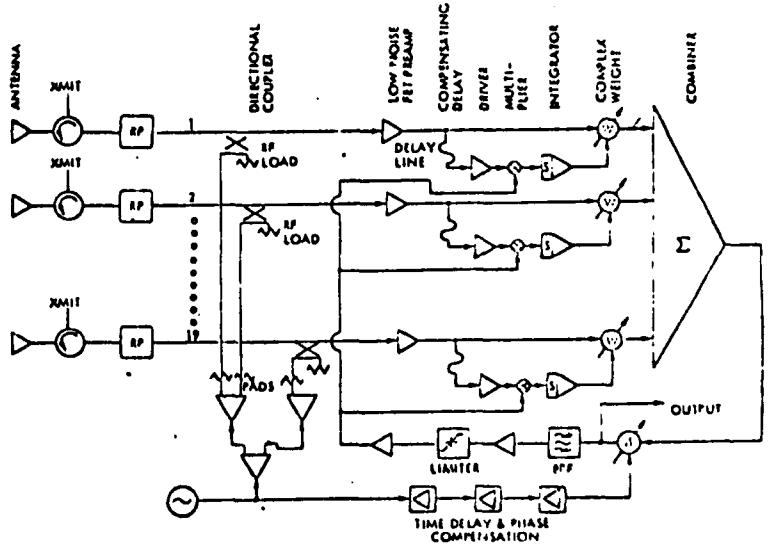

Figure 22 Adaptive Receiver System Block Diagram

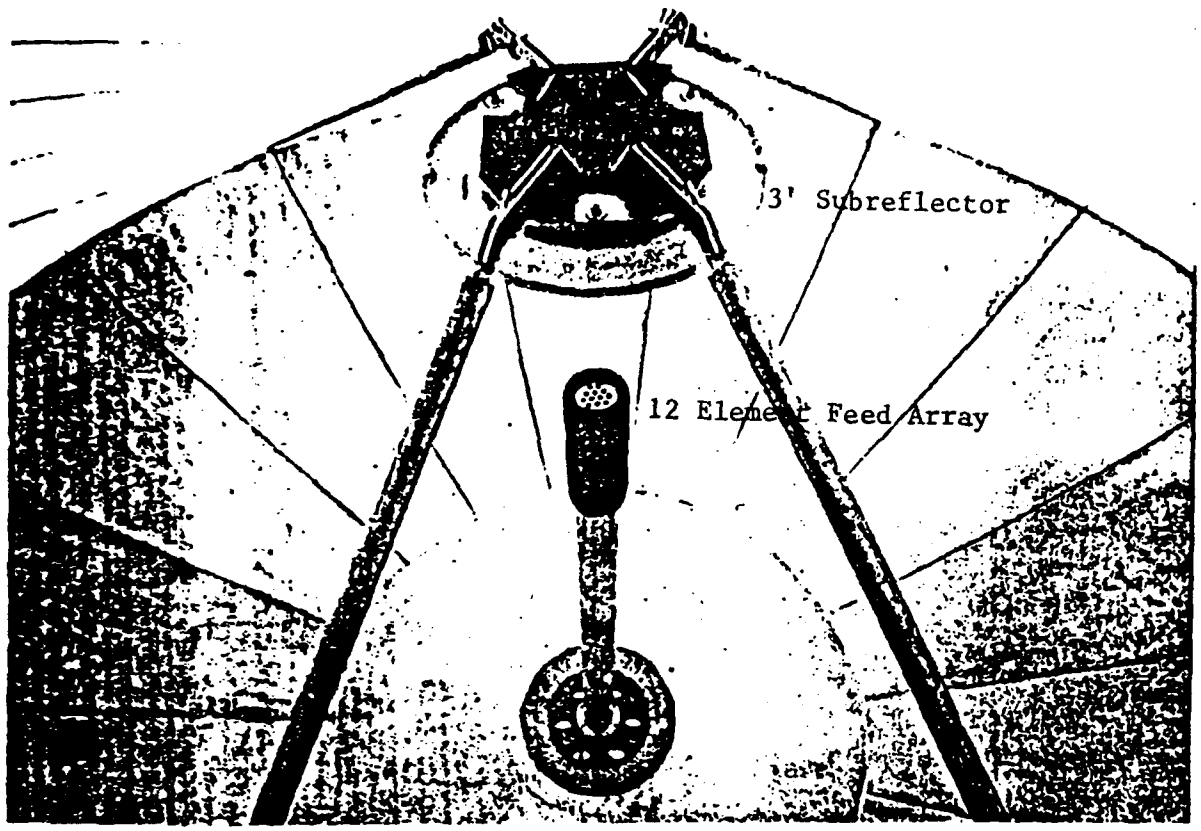

Figure 23 Cassegrain Reflector Adaptive System

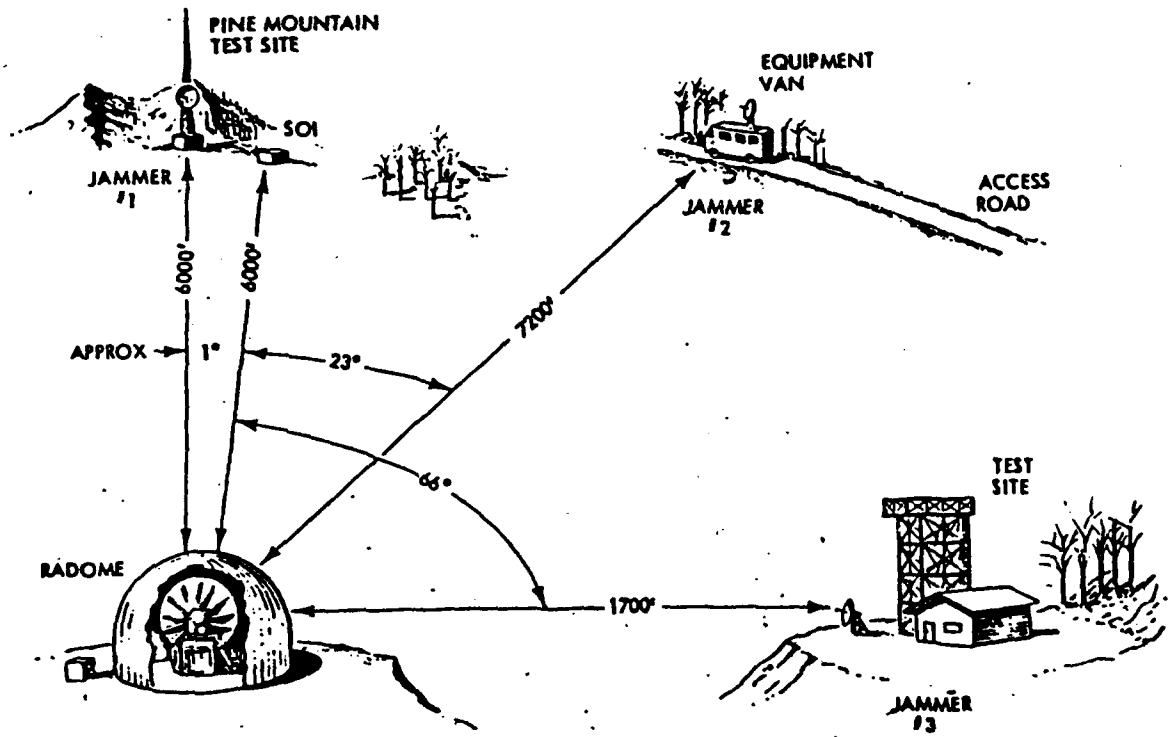

Figure 24 LMSC Santa Cruz Test Range

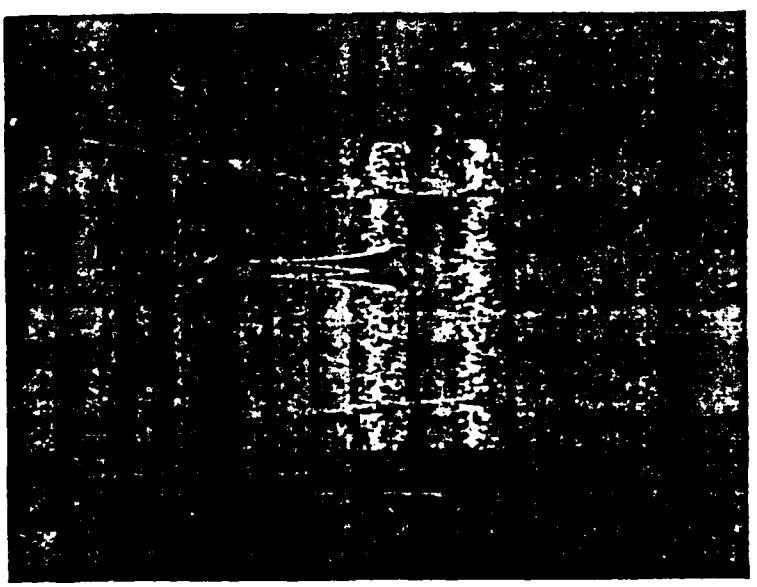

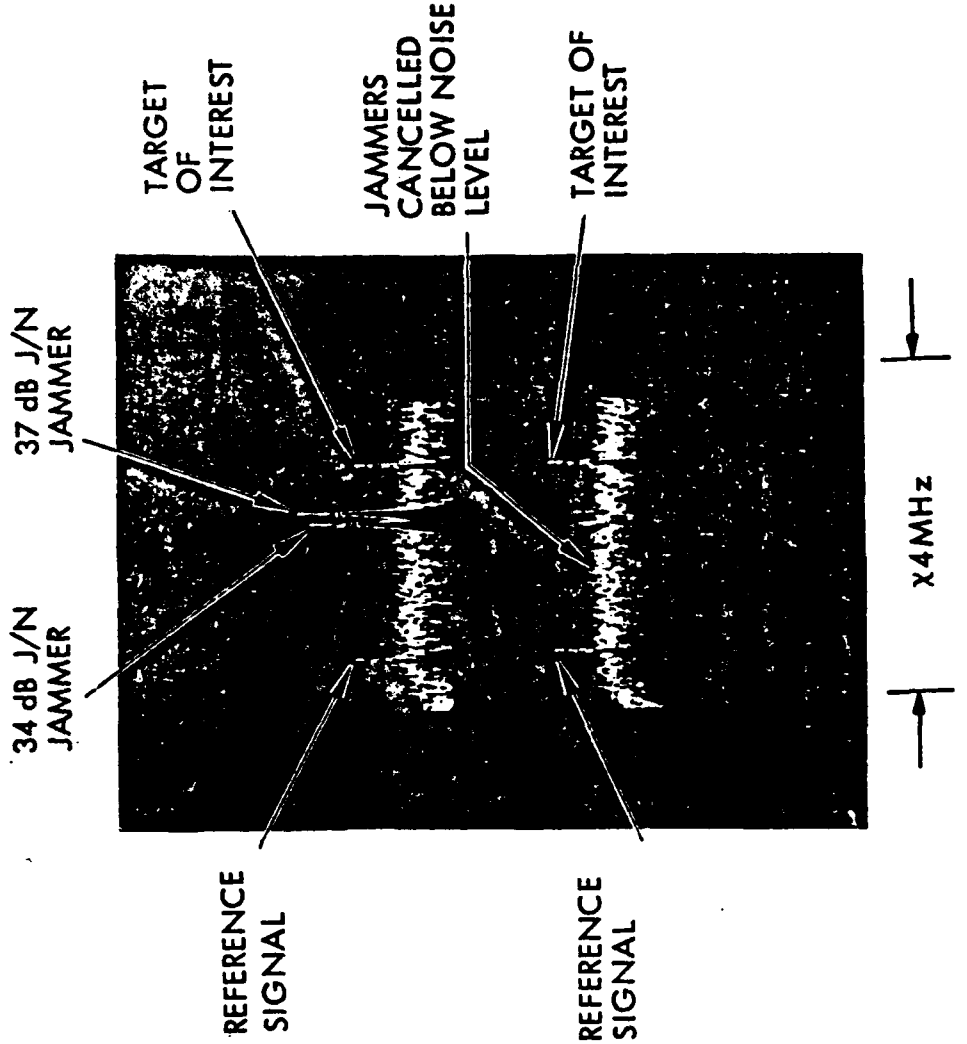

Figure 25 Adaptation Before and After. One Jammer at First Sidelobe (J/N=+37 dB). One Jammer 23 Degrees Off-Axis (-1 Degree in Elevation) (J/N =35 db). S/N Ratio Before and After 16 dB. Both Jammers Driven 15 dB Below Noise.

Figure 26 Spectrum Analyzer Display of Receiver IF Output Before and After Adaptation

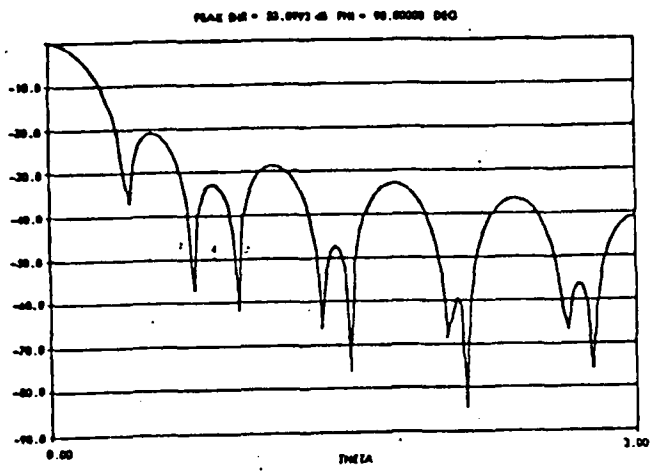

Before Adaptation

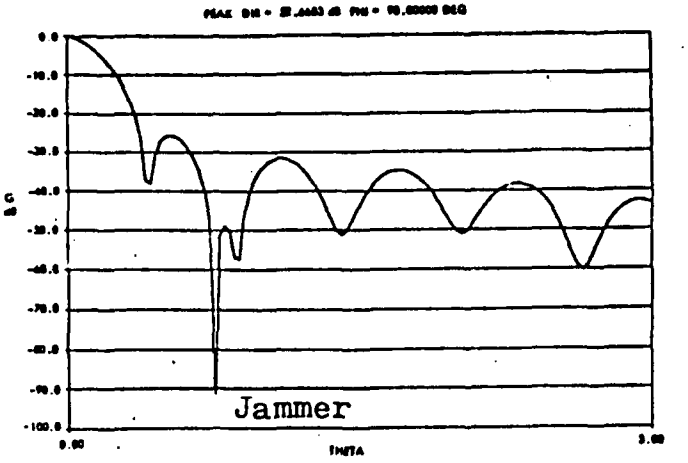

After Adaptation

Near Sidelobe Region

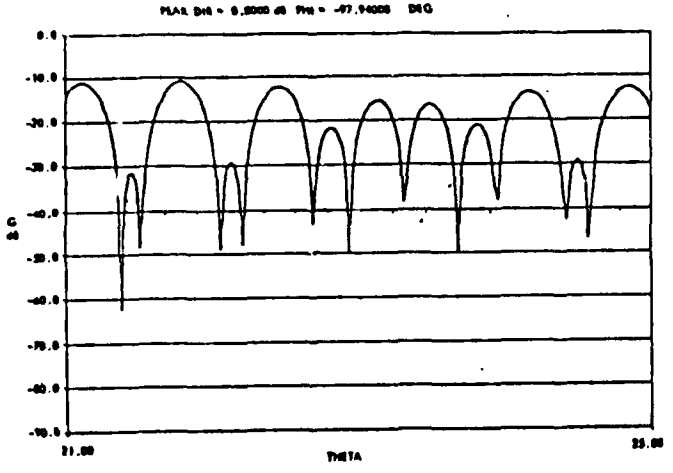

Before Adaptation

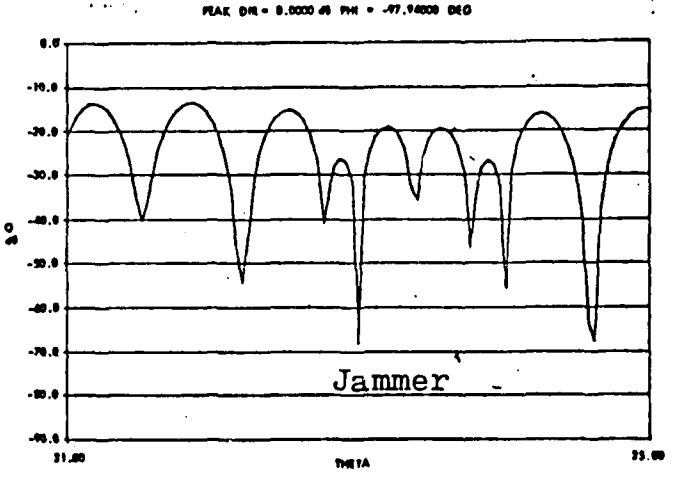

After Adaptation

Intermediate Sidelobe Region

Figure 27 Computed Adaptive Responses

Table 1 Computer Simulation Cases

- THREAT MODEL USED
  - FOUR JAMMERS
  - RANDOMLY PLACED IN SIDELOBES
  - JAMMER POWER = 40, 50, 60, 55 dB ABOVE RECEIVER NOISE FOR ISOTROPIC GAIN ANTENNA
  - VARIOUS BANDWIDTHS
- SYSTEMS ANALYZED
  - 46 FT. DIA DISH, F/D = 0.4
  - CENTER FREQUENCY = 2.25 Ghz
  - BANDWIDTHS: 500 Kc, 10 mhz, 35 mhz
  - 60 FT DIA DISH, F/D = 0.34
  - CENTER FREQUENCY 8.15 Ghz
  - BANDWIDTHS: 175 mhz, 500 mhz
- VARIED CASSEGRAIN PARAMETERS
  - FEED ELEMENT SIZE AND SPACING
  - NUMBER OF FEED ELEMENTS
  - MAGNIFICATION
- NUMEROUS CASES RUN
- FINAL DATA PRESENTED STATISTICALLY
  - P (CANCELLATION RATIO $\geq$ CR)
  - P (GAIN AFTER ADAPTION $\geq$ G)

Table 2 Computer Input Capabilities

1. ANY CASSEGRAIN GEOMETRY
   - a) ANY DISH SIZE
   - b) ANY SUBREFLECTOR GEOMETRY
   - c) ANY BEAM DEVIATION FACTOR
   - d) ANY f/D
2. ANY FREQUENCY
3. ANY NUMBER OF FEED ELEMENTS WITH ANY DISTRIBUTION
4. ANY NUMBER OF JAMMERS AT ANY LOCATION WITH ANY POWER (LIMITED ONLY BY ITEM 3)
5. ANY BEAM SHAPE
6. ANY NUMBER OF CONTROLS ON BEAM SHAPE CONSISTENT WITH (3) AND (4)
7. ANY BANDWIDTH

Table 3 Computer Outputs

- PROGRAM SYNTHESIZES DESIRED PATTERN WITHIN LIMITS IMPOSED BY GEOMETRY
- PROVIDES ADAPTIVE TIME BY PROVIDING EIGENVALUE SOLUTIONS
- PROVIDE BEFORE AND AFTER PATTERN SHAPE IN ANY PLACE BEFORE AND AFTER
- PROVIDES ANTENNA DIRECTIVITY BEFORE AND AFTER
- PROVIDES CANCELLATION RATIO AND J/N AND S/N AFTER

BIBLIOGRAPHY

(1) IEEE Transaction Antennas and Propagation (Special Issue on Active and Adaptive Antennas), Vol. AP-12, March 1964

(2) IEEE Transaction Antennas and Propagation (Special Issue on Adaptive Antennas), Vol. AP-24, No. 5, September 1976

(3) B. Widrow, P. E. Mantey, L. J. Griffiths, and B. B. Goode, Adaptive Antenna Systems, Proceedings of the IEEE, Vol. 55, No. 12, December 1967

(4) W. F. Gabriel, Adaptive Arrays - An Introduction, Proceedings of the IEEE, Vol. 64, No. 2, February 1976

(5) K. L. Reinhard, Adaptive Antenna Array for Coded Communications Systems, Ohio State University Research Foundation, Technical Report No. RADC-R-74-102, May 1974, AD-782395

(6) J. T. Mayhan, Adaptive Nulling with Multiple-Beam-Antennas, Lincoln Laboratory Technical Note 1976-18, 30 September 1976. ESD-TR-76-304

(7) B. Widrow, et al., Adaptive Noise Cancelling: Principles and Applications, Proceeding of the IEEE, Vol. 63, No. 12, December 1975

(8) C. Zahm, Application of Adaptive Arrays to Suppress Strong Jammers in the Presence of Weak Signals, IEEE Transactions on Aerospace and Electronic System, Vol. AES-9, No. 2, March 1973

(9) J. G. Charitat, C. C. Hung, and J. L. McFarland, Adaptive Sidelobe Canceller Antenna System, Lockheed Missiles and Space Co., Interim Report LMSC-D522572, 30 June 1978

ACKNOWLEDGMENT

The authors are grateful to Dr. R. W. Haight for his continued management support and personal interest in the advancement of adaptive system technology and all the engineers and technicians who enthusiastically supported this ID program. And B. Suliteanu for deciphering and typing this paper.

G.G.C.
J.G.C.
W.G
C.C.H.
J.L.M.

LMSC
Synnyvale, CA

WESTAR IV Antenna System

R.D. Ward/P.S. Bains/F.A. Taormina

Hughes Aircraft Company
Space and Communications Group
Technology Division
El Segundo, California

Introduction

The WESTAR IV communications satellite (HS 376G), scheduled for launch in 1982, is a 24 channel active repeater system. It is a successor to the original WESTAR domestic communications satellite (HS 333A) built by Hughes Aircraft Company for Western Union and has a twofold increase in communications capacity. High gain shaped antenna beams provide C band (6 GHz receive/4 GHz transmit) coverage for the continental United States (CONUS), Alaska, Hawaii, Puerto Rico, and the Virgin Islands, as shown in Figure 1. The range of geosynchronous orbital locations for which coverage is provided is 79°W longitude to 140°W longitude. Frequency reuse is achieved by means of orthogonally polarized beams, requiring the antenna subsystem to receive and transmit in both vertical and horizontal polarizations. Two reflector surfaces (one for each polarization) are employed in a unique design which embodies the surface in a single physical structure. This structure consists of two gridded paraboloids placed one in front of the other. In this way the reflectors share a common aperture space with low transmission loss for orthogonal polarization.

Reflector Design

Figure 2 shows the geometry of the two reflectors. Their different offsets allow the vertically and horizontally polarized reflectors to be fed by two independent feed horn arrays which do not interfere with each other either physically or electrically. Polarization selectivity of each reflector is achieved through thin conductive strips which are parallel to the desired polarization and bonded to a dielectric substrate molded to the shape of the desired paraboloid. Tests have shown that insertion loss of the front reflector is less than 0.1 dB. The crosspolarization performance of the antenna is enhanced due to the suppression of currents which are orthogonal to the thin strips. As noted from Figure 2, the front grid reflects horizontal polarization, the rear grid, vertical. Figure 3 shows a breadboard reflector with horizontally and vertically polarized feeds.

Feed Network Design

The front reflector is fed by a seven horn array of horizontally polarized feed horns. Six of the horns are diplexed for transmit and receive use. Transmit and receive networks are optimized independently for best coverage. A block diagram of the horizontal transmit and receive networks is shown in Figure 4. The network consists of three parts: the transmit dual mode power divider, the receive power divider, and the combiner (diplexer) network. The transmit dual mode power divider distributes the output power and phase, as shown in Table 1. The two modes are electrically orthogonal as required for isolation at the inputs. Figures 5 and 6 show the beams produced by exciting the odd and even input ports of the horizontal transmit dual mode power divider. As indicated by the beam contours, there is some mode shift (relative beam scanning) produced by the two excitations, but the design is optimized for minimum difference. The horizontal receive network is a conventional hybrid power divider network. Figure 7 shows the minimum gain contours for the horizontal receive. Hawaiian coverage is not required for horizontal receive. The achievable antenna gains are expected to be approximately 0.6 dB less for transmit and 0.9 dB less for receive based on past performance. The losses include those of the network, feed horn, and reflector.

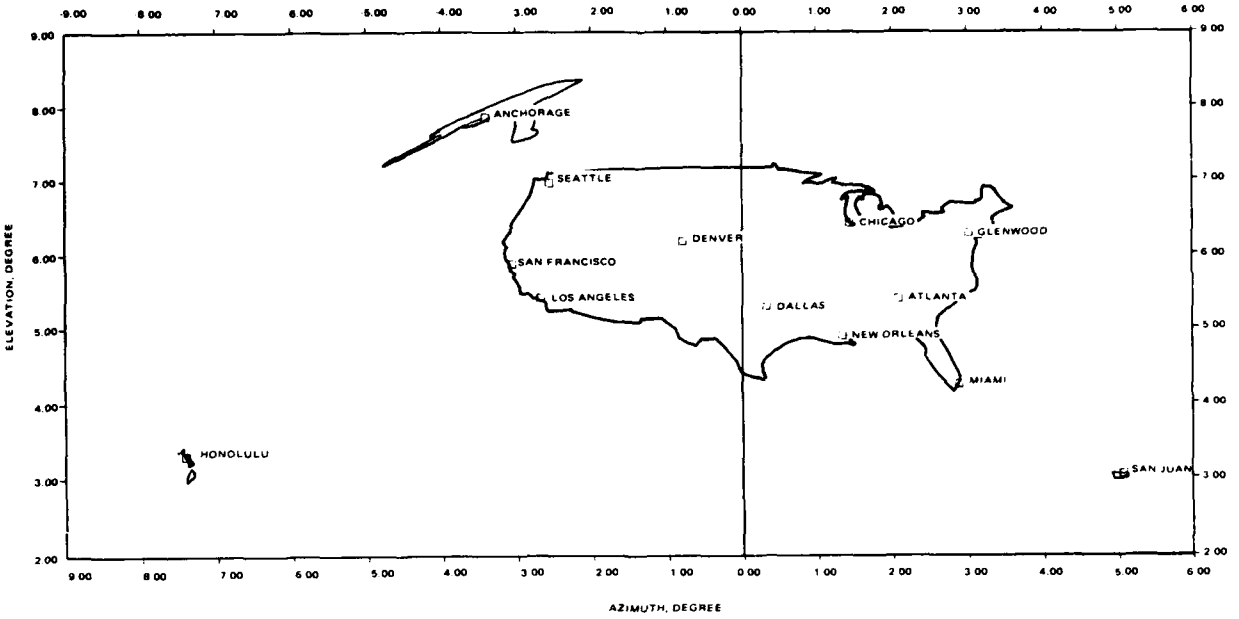

FIGURE 1. WESTAR IV COVERAGE

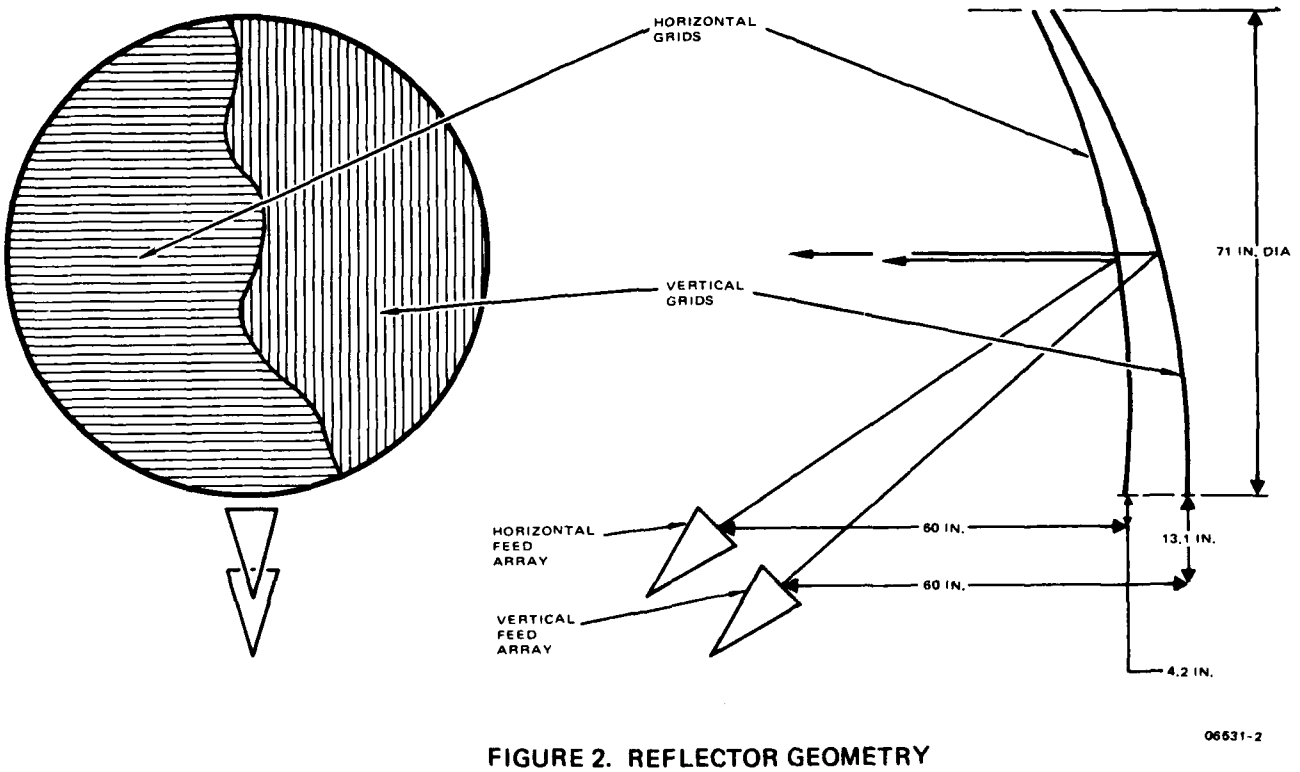

FIGURE 2. REFLECTOR GEOMETRY

06531-3

FIGURE 3. BREADBOARD REFLECTOR

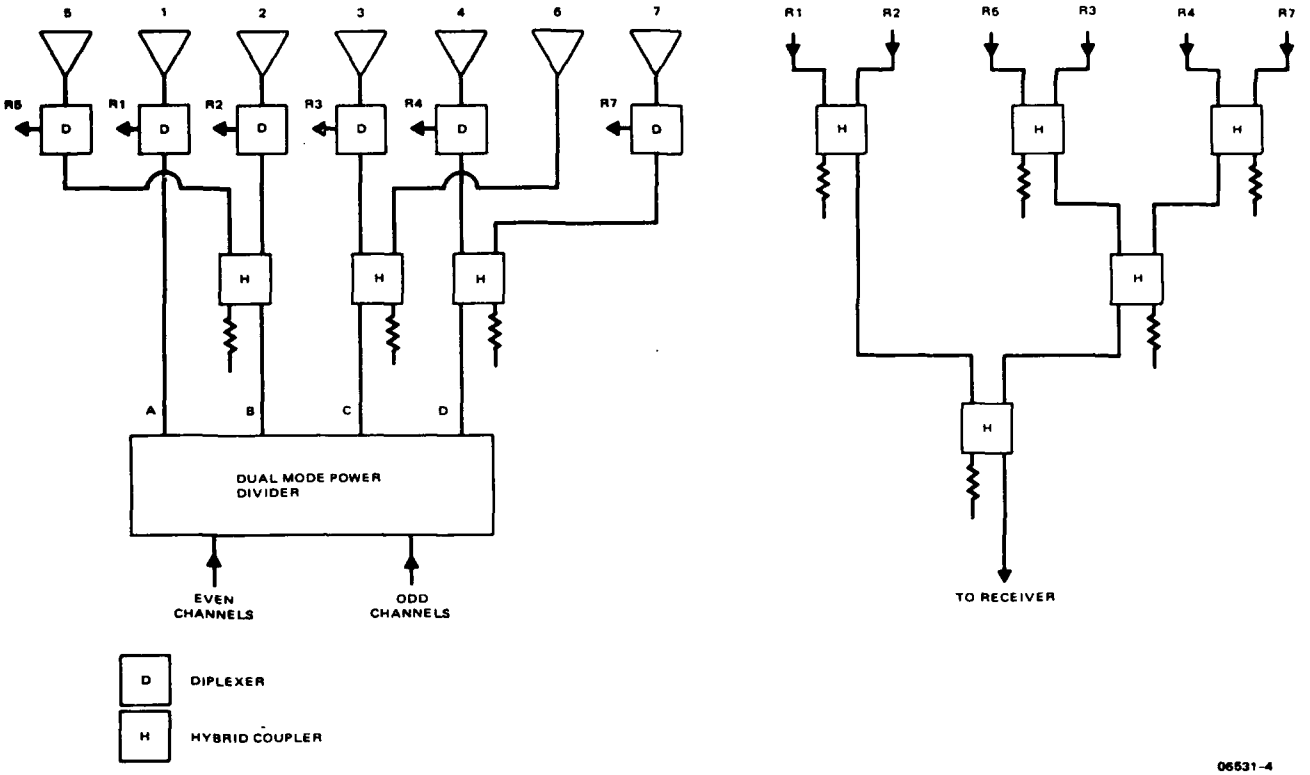

FIGURE 4. HORIZONTAL TRANSMIT AND RECEIVE NETWORKS

TABLE 1. DUAL MODE POWER DIVIDER OUTPUT DISTRIBUTION

Output Port	Odd Mode		Even Mode	
	Power	Phase	Power	Phase
A	0.25	0.0	0.25	0.0
B	0.25	45.0	0.25	−45.0
C	0.25	90.0	0.25	−90.0
D	0.25	135.0	0.25	−135.0

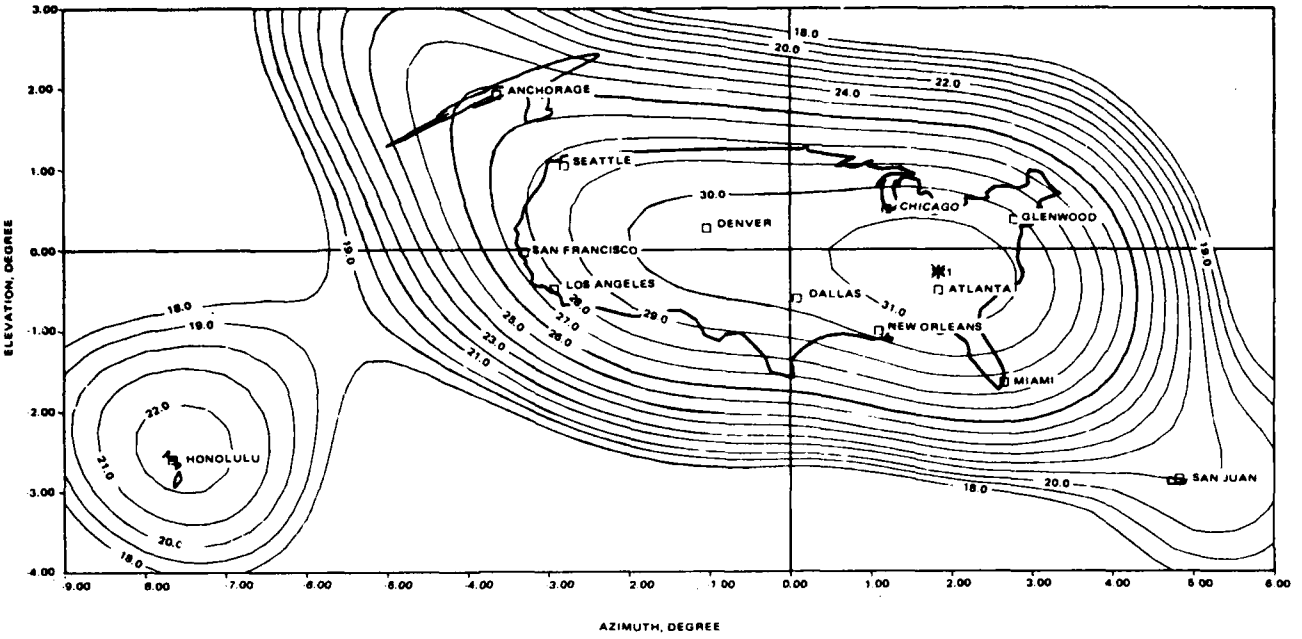

FIGURE 5. HORIZONTAL TRANSMIT ODD MODE

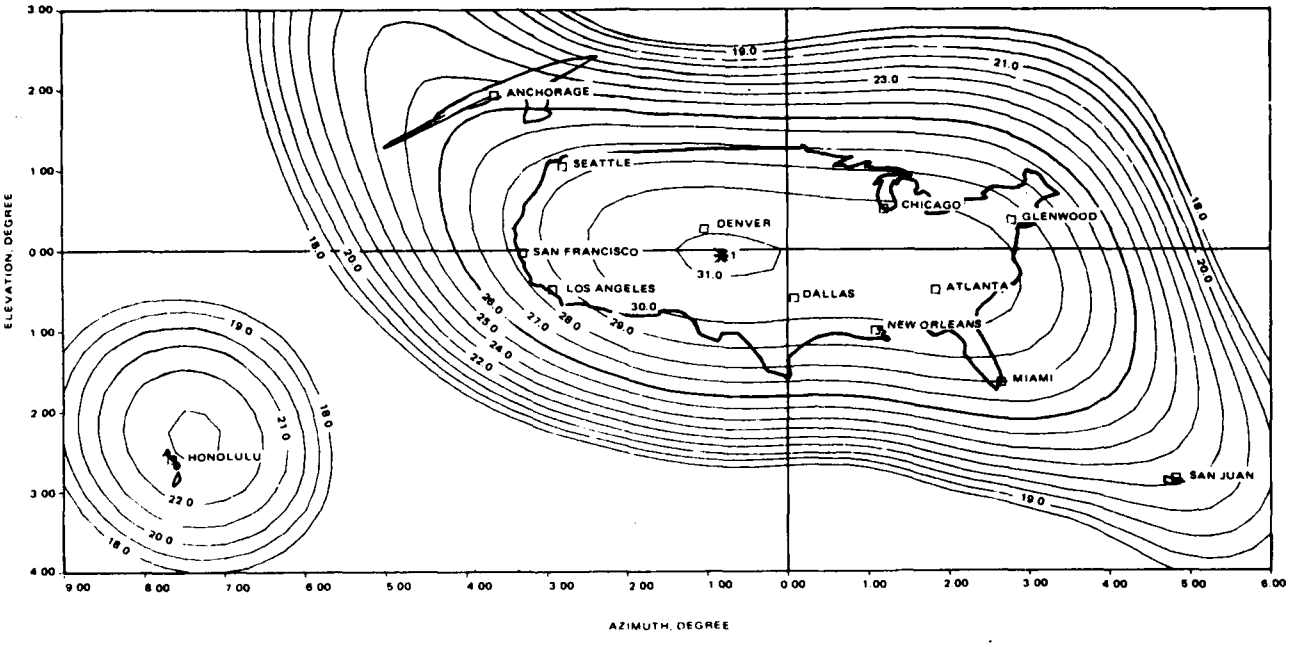

FIGURE 6. HORIZONTAL TRANSMIT EVEN MODE

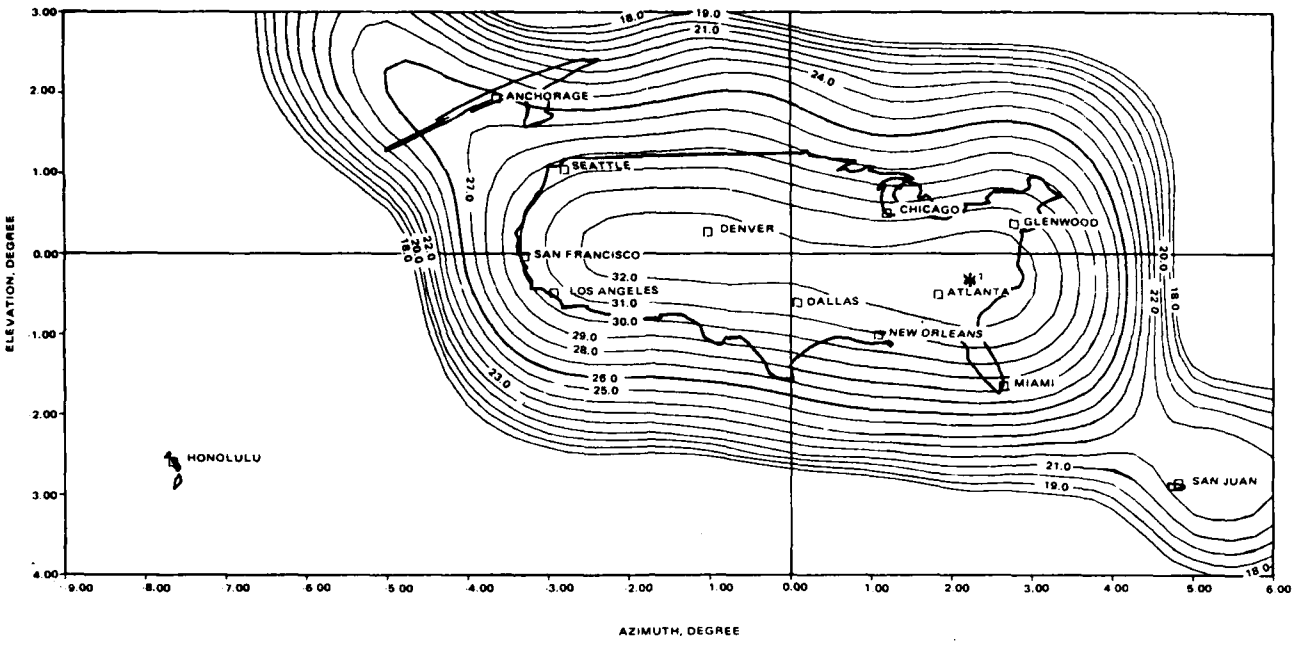

FIGURE 7. HORIZONTAL RECEIVE

The rear reflector is fed by an array of 16 vertically polarized feed horns. Fourteen of the horns are diplexed for both the transmit and receive bands. The coverage is slightly different than that of horizontal polarization, since Hawaii is included for receive but excluded for transmit. The block diagram for the vertical transmit and receive networks is shown in Figure 8. As in the case of horizontal transmit, a dual mode power divider is used for the vertical transmit network. For CONUS coverage, four subarrays of three horns each are used. The three horn subarray has the horns stacked vertically. Power is distributed to the subarray to produce the required secondary vertical beamwidth, but without the significant spillover loss produced by the high first sidelobe of an E-plane sectorial horn. To reduce the number of diplexers and hybrids required for the CONUS feed array, a broadband power divider was developed for the three horn subarray. The divider works for both the transmit and receive bands and allows for the use of a single diplexer for each subarray. Figures 9 and 10 show the minimum gain contours predicted for the vertical transmit and receive networks, respectively. As noted from Figure 8, the vertical receive network incorporates a monopulse tracking function. This network, designed to produce nulls in both azimuth and elevation from a ground transmitted beacon, provides for antenna pointing control to within $\pm 0.05°$ in both coordinates. This is especially important for reducing edge of beam (coverage) gain degradation associated with antenna pointing error.

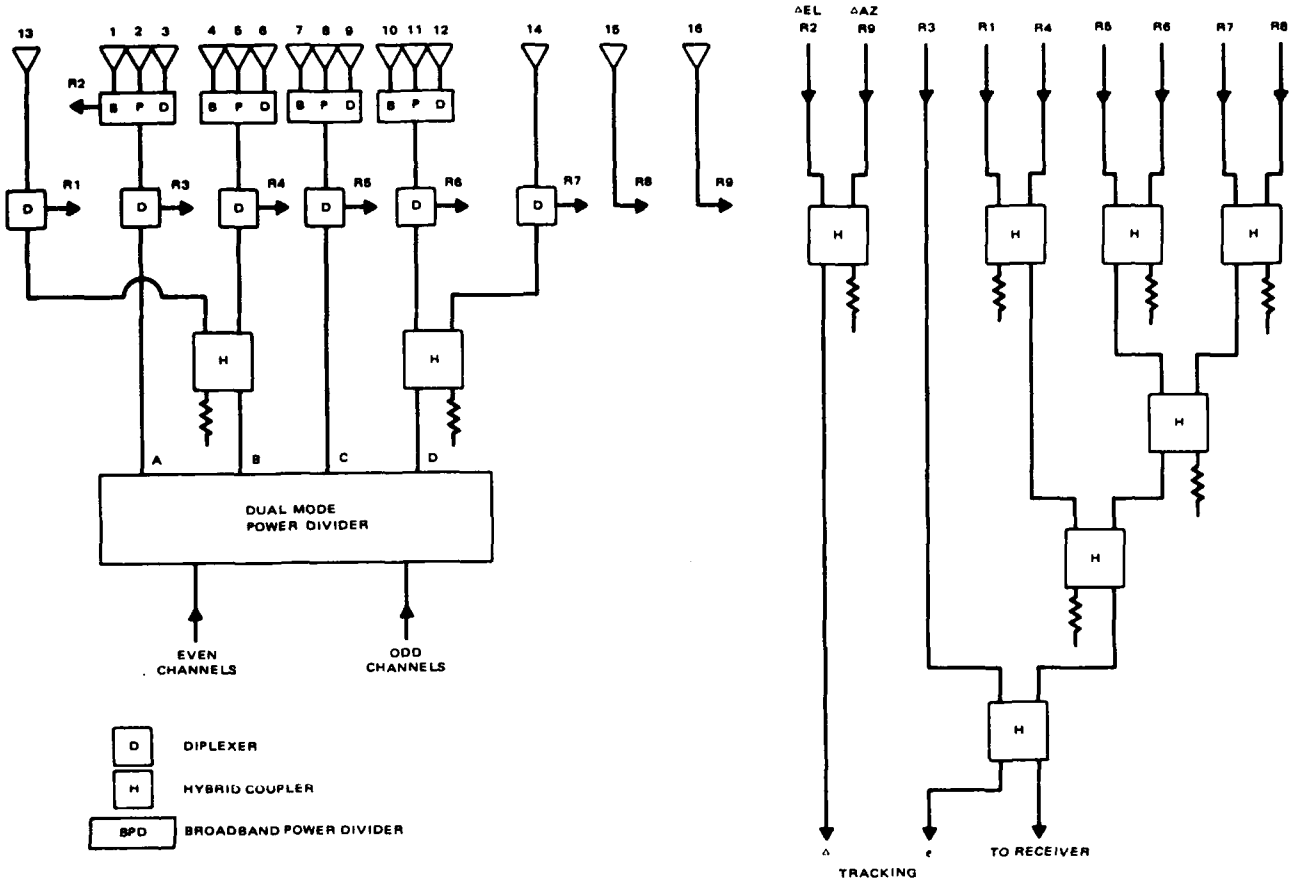

FIGURE 8. VERTICAL TRANSMIT AND RECEIVE NETWORKS

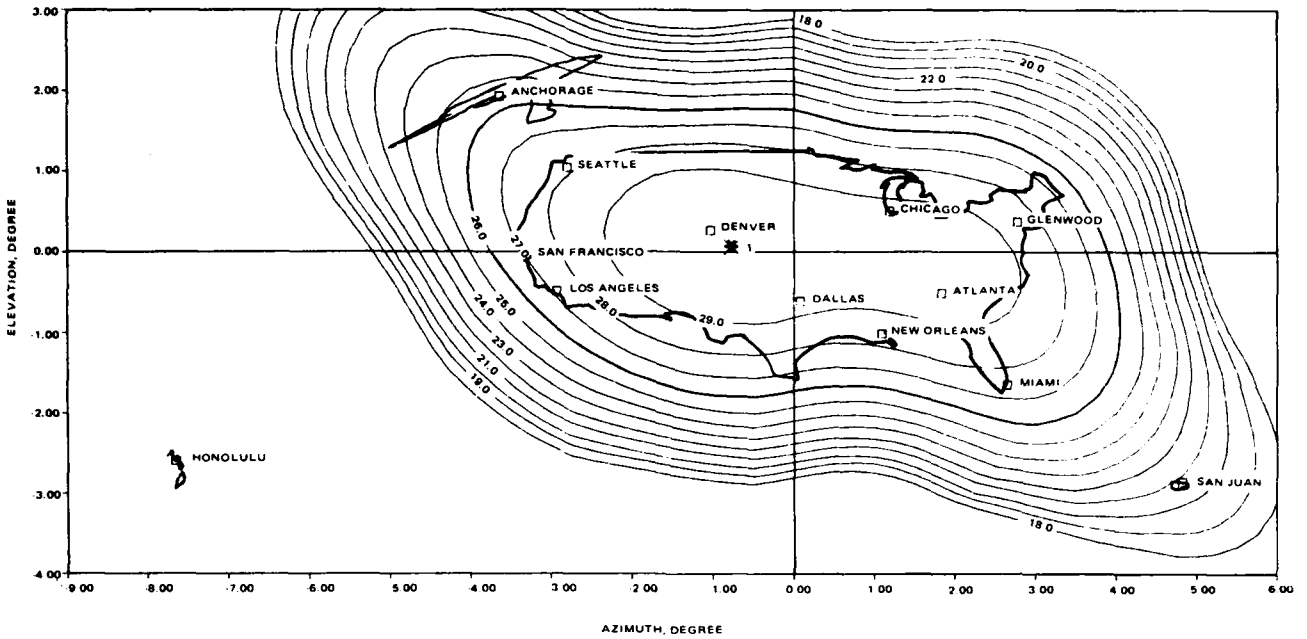

FIGURE 9. VERTICAL TRANSMIT

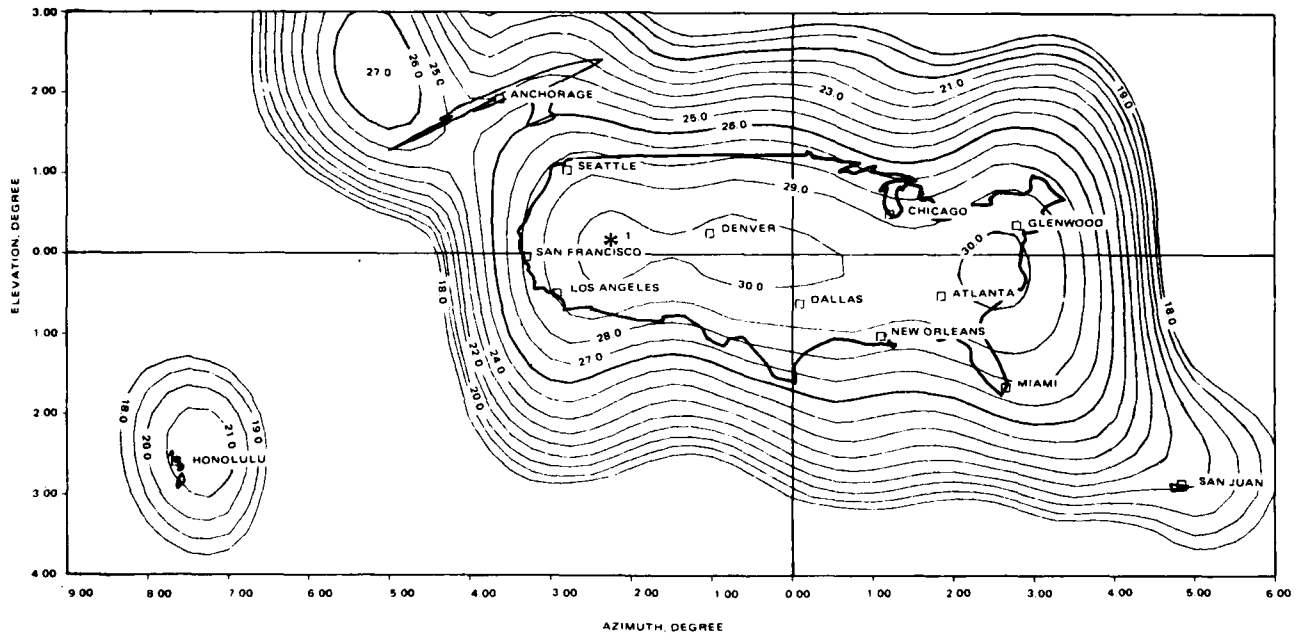

FIGURE 10. VERTICAL RECEIVE

COMPLETELY-OVERLAPPED-SUBARRAY FED ANTENNA FOR BROADBAND, WIDE SCAN ANGLE, LOW SIDELOBE RADAR APPLICATIONS

Hugh L. Southall, RADC/EEA, Hanscom AFB, MA

INTRODUCTION

To provide the large instantaneous bandwidth and large scan angle requirements of future radar systems, time delay must be employed for antenna weights. Tang[1] has surveyed time delay steering techniques and concluded that the completely overlapped subarray approach offers the widest bandwidth at the lowest cost since expensive time delay elements are included only at the subarray level. Borgiotti[2] provided a detailed analysis of such an antenna; however, only limited scanning was considered ($\pm$ 4.6° from array broadside).

The present paper describes an experimental completely-overlapped-subarray antenna with wide angle scanning, low sidelobe capability and other design goals listed in Table 1. Theory of operation and predicted performance are described in Section 1, the hardware is described in Section 2, in Section 3 error analyses are presented and in Section 4 preliminary test results on the feed subsystem are outlined.

TABLE 1

Antenna Design Parameters/Goals

Center Frequency (X-Band)	9 GHz
3 dB Beamwidth	2.5° @ θ_o = 0° and 5.0° @ θ_o = 55°
Scan Angles	0° and 55°
Gain (Net One-Way)	~ 37 dB @ θ_o = 0° and ~ 32 dB @ θ_o = 55°
Bandwidth	$\pm$ 10%
Sidelobe Levels	-35 dB near-in -40 dB far-out

SECTION 1 THEORY OF OPERATION

Fante[3,4] has presented the design equations and basic design parameters for the antenna. A simplified, "idealized," theory is presented here to describe fundamental operational characteristics. In Fig. 1, a functional diagram of the antenna is shown. For $e^{-j\omega t}$ time dependence, the field on Face C due to an incoming plane wave is given by

$$E_i(x) = e^{-j\frac{2\pi}{\lambda} x \sin\theta} \tag{1}$$

where λ is the free space wavelength at signal frequency f. After applying a beam steering phase tilt, the field is given by

$$E_i(x) = e^{-j\frac{2\pi}{\lambda} x \sin\theta + j\frac{2\pi}{\lambda_o} x \sin\theta_o} \tag{2}$$

where θ_o is the steering angle and λ_o is the center frequency wavelength. After propagating to the face of the feed, Face B, the field is given by

$$E_f(y) \cong e^{j\frac{2\pi}{\lambda} y^2/2F} \int_{-L/2}^{+L/2} E_\ell(x)\, e^{-j\frac{2\pi}{\lambda F} xy}\, dx \tag{3}$$

where the quadratic phase term is a near field effect which can be removed by quadratic time delay at Face B. If the quadratic term is removed, $E_\ell(x)$ is substituted into (3), and an "idealized" infinitely large array ($L \to \infty$) is assumed, then

$$E_{f\ell}(y) \cong \delta\left\{ y + \left[F\sin\theta - \frac{F\sin\theta_o}{R} \right] \right\} \tag{4}$$

where $R = \lambda_o/\lambda = f/f_o$ and δ is the delta function. Therefore, the field appears as a spot on Face B. For a microwave lens beam former (see Fig. 2 for an example), the p^{th} beam is directed at an angle ϕ_p from Face B, where

$$\sin\phi_p = \frac{D}{F}(p-1/2) \tag{5}$$

Note that the subarray beam patterns are $(\sin x)/x$ distributions and completely overlap one another on the array, hence the term "completely overlapped" subarray antenna. The voltage at the p^{th} beam port is

$$V_p = \int_{-b}^{+b} E_{f\ell}(y)\, e^{+j\frac{2\pi}{\lambda}\sin\phi_p\, y}\, dy \tag{6}$$

Using Eqs (4) and (5) in Eq (6) gives

$$V_p \cong e^{-j2\pi q(RS - S_o)} \tag{7}$$

where $q = p - 1/2$, and the scanning parameters are $S = (D/\lambda_o)\sin\theta$ and $S_o = (D/\lambda_o)\sin\theta_o$. After phase shift and time delay in each beam channel, the variable power divider performs a weighted summing which results in an output voltage

$$V = \sum_p \hat{I}_p \left\{ e^{+j2\pi qRS_c} \; (\text{time delay}) \quad - j2\pi qS_o \; (\text{phase advance}) \right\} V_p \tag{8}$$

Substituting Eq (7) into Eq (8) and recalling that the spot defined by Eq (4) must fall within $|y| \le b$ for our "idealized" system, the output signal as a function of far field angle is given by

$$V = (\lambda F)\, rect\left\{ \frac{\lambda F}{2bD}(RS - S_c) \right\} \sum_p \hat{I}_p\, e^{-j2\pi qR(S - S_c)} \tag{9}$$

where

$$rect\{\xi\} = \begin{cases} 1 & |\xi| \le 1/2 \\ 0 & \text{otherwise} \end{cases} \tag{10}$$

The antenna pattern is the product of a "window" (or rectangle function) and a pattern whose main beam does not shift in angle as the frequency varies, and whose sidelobe structure is determined by the subarray amplitude taper $\hat{I}_p$. These pattern properties are illustrated in Fig. 3.

The broadband performance of the completely overlapped subarray antenna is a direct result of these properties. For example, if the limiting frequencies

are defined as those frequencies where either (a) a grating lobe appears or (b) the window slides past the main beam (see Fig. 3) and defining $f = f_o + \delta f$, then the maximum frequency deviations from the center frequency are given in Table 2. For this analysis, $\gamma = bD/(\lambda_o F) \approx 0.4$, must be less than one.

TABLE 2

Maximum Frequency Deviations for $S_o > \gamma$*

	Main Lobe Condition	Grating Lobe Condition
$f > f_o$	$\delta f < \left(\frac{\gamma}{S_c - \gamma}\right) f_o$	$\delta f < \left(\frac{1-\gamma}{S_o+\gamma}\right) f_o$
$f < f_o$	$\delta f > \left(\frac{-\gamma}{S_o+\gamma}\right) f_o$	$\delta f > \left(\frac{\gamma-1}{S_o-\gamma}\right) f_o$

Ideal bandwidth (defined as the difference between the lower of the two upper frequency limits and the higher of the two lower frequency limits normalized by the center frequency) is plotted in Fig. 4 for the design parameters of the experimental antenna.

To account for the finite width of the array and the fact that discrete radiators are used on Faces B and C, the following equation is used to calculate the radiation pattern

$$F(\theta,\theta_o) = \sum_{k=-K+1}^{K} \sum_{n=-N+1}^{N} \sum_{p=-M+1}^{M} \hat{I}_p a_n e^{+j2\pi q(R-1)S_c} \times e^{-j2\pi \frac{\Delta\delta}{\lambda F}(n-1/2)(k-1/2)} e^{+j2\pi R\gamma_o q(n-1/2)} e^{-j2\pi \frac{\delta}{D}(RS-S_c)(k-1/2)} \qquad (11)$$

where

$$\gamma_c = \frac{\Delta D}{\lambda_o F} = .0524\,, \quad D = 1.833\lambda_o \text{ and } F = 19.77\lambda_o .$$

The a_n are the relative amplitude weights on Face B and for the experiment $a_n \approx 1$. There are 2K array elements located at positions $\delta(k-\frac{1}{2})$ on Face C and 2N feed elements located at positions $\Delta(n-\frac{1}{2})$ on Face B. For the experiment, 2K=60, 2N=16, 2M=16, $\delta = \lambda_o/2$ and $\Delta = 0.556\lambda_o$. An isotropic element pattern has been assumed for Eq. (11).

Radiation patterns are shown in Fig. 5. The first sidelobes are at -35 dB as a result of the subarray taper function

$$\hat{I}_{p'} = 1 + \left[\frac{\cos(\pi/M)}{\cos(\pi/2M)}\right] \cos\left\{\frac{\pi}{M}(p-1/2)\right\} \qquad (12)$$

Also, the "window" drastically reduces sidelobe levels at angles outside of $S = S_o - \gamma$ to $S = S_o + \gamma$. This is evident in Figure 5(C) where $S_o - \gamma$ corresponds to 37°.

*Note: For $S_o < \gamma$ there are no frequency limits.

To illustrate the effect of frequency variation on the pattern, the scan angle of 55^o was held fixed and patterns for $f = f_o$, $1.1f_o$ and $1.3f_o$ are plotted in Fig. 6. Note that the patterns are plotted versus the scanning parameter. In Fig. 6(a) the subarray window cuts off the far-out sidelobes at $S_o - \gamma = 1.1$; however, the cut-off is not abrupt (as it would be for a perfect window) due to the finite aperture of the main array. In order to understand the patterns for the two higher frequencies note that there are two sets of grating lobes. One set is due to the discrete placement of radiators on Face C and is determined by (see Eq. 11).

$$R(S-S_o)\,\delta/D = \pm n \tag{13}$$

where n = 1 for the two grating lobes closest to the main beam. The other set is due to the subarrays and repeats the main beam pattern when (see Eq. 9)

$$R(S-S_o) = \pm n. \tag{14}$$

For operation at the center frequency, Fig. 6(a), there are no grating lobes due to the discrete radiators on Face C; however, at S = 0.50, there is a subarray grating lobe which is suppressed by the window function whose edge is at S = 1.10. At a frequency 10% higher than the center frequency, Fig. 6(b), the subarray grating lobe is still suppressed since its location is now at S = 0.59 and the lower edge of the window has shifted down to only S = 0.96. Note, however, that a discrete radiator grating lobe appears at S = -1.827 (approximately -90^o). The window function fails to suppress this spurious lobe since its presence was neglected in the pattern analysis discussed earlier in conjunction with Figure 3. This grating lobe is present because of the chosen radiator spacing of $\lambda_o/2$ and the large scan angle (55^o) of the experiment and will not affect the main objectives of the program. In fact, the lobe will be reduced by the element pattern. For a 30% higher signal frequency, two spurious lobes appear, Fig. 6(c). The discrete grating lobe at the far left occurs at S = -1.315. A subarray grating lobe occurs at S = 0.73 and appears because the lower edge of the window has shifted down to S = 0.75 and the edge is sufficiently smeared out to pick up part of the grating lobe. This corresponds to the condition shown in Fig. 3(b).

In addition to a microwave lens beam former, a Butler matrix beam forming network was considered for the feed. An antenna pattern for an 8 beam/8 element Butler matrix feed is shown in Figure 7. Near-in sidelobes are below -30 dB and far-out sidelobes are quite low; however, the far-out sidelobes are considerably higher than those in Figure 5(c) for a 16 beam/16 element lens. The subarray taper for the Butler matrix feed is 0, -3, -10 and -28 dB (power) for B1R (beam one right, ie the first beam to the right of feed broadside), B2R, B3R and B4R (the right-most beam). The four left beams are tapered symmetrically. The beam pointing angles are determined by

$$\sin\phi_p = \frac{\lambda_o}{\Delta}\left(\frac{f_o}{f}\right)\left[\frac{(p-1/2)}{8}\right] \tag{15}$$

Thus the subarray beam pointing directions change with frequency, unlike the subarray beams of a microwave lens, (see Eq. (5)), and this causes an angular shift of the main lobe.

SECTION 2 HARDWARE DESCRIPTION

An experimental antenna is being fabricated to determine the operational performance of the completely overlapped subarray concept. In Fig. 8, the main parts of the antenna are shown to be: (1) the variable power divider, (2) the Rotman lens feed, and (3) the array lens including the 60 element linear array. Each subsystem is discussed in detail below, where operation is described in terms of the transmission mode with power entering the single port at the right in Fig. 8.

Variable Power Divider

The variable power divider provides 16 way power division with appropriate amplitude taper for each of the 16 beam ports of the Rotman lens. The 2-way and two 8-way X-band power dividers provide the one to 16 power division. The 16 miniature coaxial attenuators provide the amplitude taper given by Eq. (12) to a good approximation. Starting from the beam port nearest the center, the symmetrical power taper for both the 8 right and 8 left beam ports is: 0, -.5, -2.0, -4.0, -7.5, -12.0, -19.0 and -28 dB. Coaxial line stretchers provide phase adjustment in each beam port channel to phase match the outputs of the variable power divider and for any phase compensation required by the feed or connecting cable assemblies. Phase adjustment can be made over a range of 0 to 140° (or $\pm 70^{\circ}$) at 9 GHz and is accomplished by the adjustment mechanism illustrated in Fig. 8 which provides a screw type control for precise phase adjustment and a solid, cradle-type support to reduce accidental phase changes due to mechanical movement. The 16 semi-rigid, coaxial cables connecting the variable power divider to the 16 beam ports of the Rotman lens are used to introduce the correct time delay and phase advance (See Eq. (8)) into each beam channel. Phase advance is incorporated "modulo-2π" for the center frequency of 9 GHz. Since the phase shift through the cable is a function of the length ($\phi = \frac{360}{\lambda} \ell$, where ℓ is the cable electrical length), the phase will change as the frequency changes. This results in random phase errors for frequencies off center frequency as discussed in the next section.

Rotman Lens

As shown in Fig. 8, the feed subsystem is a 16 beam/16 element Rotman lens. The mechanical structure is a two dimensional "pill box" with flat aluminum plates separated by 0.40 inches. Element radiators are monopole probes which are connected to the semi-rigid cables by SMA connectors and extend into the waveguide region as shown in Fig. 8. There is one dummy element terminated with a 50 Ω load on each end of the input and pickup probe arrays to reduce edge effects. Since the beams are coherently combined, correcting time delays were applied in each beam channel using the 16 coaxial cables connecting the lens with the variable power divider. This correction is required since the lens was designed for g = 1.14 rather than 1.0, where g is the ratio of on-axis to off-axis focal length.[5] The set of 16 semi-rigid coaxial cables connecting the Rotman lens pick-up probes to the linear array on Face B also contain additional path length corrections which are determined by the lens design.[5] These cables also incorporate fixed time delays which compensate for the quadratic term in Eq. (3). The lens is designed such that each beam port provides approximately uniform illumination of the pick-up probes, therefore, the feed linear array will illuminate the array lens with orthogonal beams with approximate (sinx)/x distributions. The outermost beams point at 45° on either side of the normal to Face B.

Array Lens and 60 Element Linear Array

A large lens with a radius of 25.54 inches connects directly to the Rotman lens feed. The radiating aperture size of the linear array is 30 λ_o. Note that the mechanical structure is the same as the parallel plate Rotman lens construction; however, because of the large size, honeycomb stiffening material is placed over the plates to hold the strict tolerances required. There are five dummy radiating elements on each end of both the array lens pick-up probes and the 60 element linear array. Semi-rigid coaxial cables are used to connect the probes on the circular face of the lens to the linear array. These cables are used to introduce the beam steering phase tilt. For discrete probe positions, the coordinate x in Eq (2) becomes $\delta(k-1/2)$ for k= -K+1, -K+2,..., K-1, K, and the phase shift is $(360/\lambda)\delta(k-1/2)\sin\theta_o$. Again, the phase tilt will be correct only for $\lambda = \lambda_o$. Finally, there are two, 35° flare angles on the radiating aperture.

SECTION 3 ERROR ANALYSIS AND RF LOSS BUDGET

Sidelobe levels due to random phase errors in the antenna can be calculated using the results of Fante.[3] There are two distinct sidelobe regions: near-in sidelobes defined here to be within the subarray window enclosing the main beam and far-out sidelobes outside this region. For random phase errors, with variances σ_A^2, σ_B^2 and σ_C^2 (square radians) on Faces A, B, and C of the antenna, expressions for sidelobe levels (relative to the main beam peak power) are:

Near-In Sidelobe Level

$$SL = 0.1\ \sigma_A^2 + 0.002\ \sigma_B^2 + 0.077\ \sigma_C^2 \tag{16}$$

Far-Out Sidelobe Level

$$SL = 0.00012\ \sigma_A^2 + 0.00068\ \sigma_B^2 + 0.077\ \sigma_C^2 \tag{17}$$

and the sidelobe level in dB is 10 $\log_{10}$ SL. The phase errors at Face A are due to the variable power divider, line length and probe position uncertainties and at Faces B and C to probe position errors at both pick-up and radiating probes and to line length errors. Probe position tolerance is assumed to be 0.002 inches RMS. Calculated sidelobe levels are shown in Table 3 for different phase errors due to the variable power divider and coaxial lines. Note that the variable power divider phase error affects only the near-in sidelobe level; it is primarily line length phase errors which influence the far-out sidelobe levels. Near-in error sidelobes of -33 dB and far-out error sidelobes of -36 dB are predicted using the tolerances for the experimental antenna and the analysis described above.

TABLE 3

Side Lobe Levels for Various Random Phase Error Conditions

Random Phase Errors (degrees RMS)

Power Divider	Line Length	Near-In Error Sidelobe Level (dB)	Far-Out Error Sidelobe Level (dB)
3	3	-31	-36
5	3	-29	-36
7	3	-27	-36
3	2	-33	-40
2	2	-34	-40
1	1	-40	-44

The pattern in Fig. 9 was calculated for an assumed random phase error of 3 degrees RMS on Face C and perfect phases in the rest of the antenna. Using the error analysis gives -38 dB for both near-in and far-out error sidelobe levels, which is a few dB higher than the levels from Fig. 9, therefore, the equations yield slightly conservative (higher) sidelobe level estimates. The effect of random phase errors in the feed is illustrated in Fig. 10 for the Butler matrix. Measured phases at the 8 radiating elements were used for the calculation and all other phases were assumed to be perfect. The measured RMS phase error for any beam is~15 degrees, therefore, the sidelobes are increased greatly within the subarray window. The window still cuts off the far-out sidelobes to some degree; however, comparing Fig. 10 with Fig. 7 (where zero phase error was assumed) it is obvious that the far-out sidelobe level has been raised.

As mentioned earlier, since coaxial lines are being used to obtain phase shift, phase errors are introduced with changing frequency. This effect is shown in Figure 11.

A power budget considers the following losses: (1) at probe elements on Faces A, B and C, mismatch losses of 0.1 dB (VSWR $\simeq$ 1.4) five times for a total of 0.5 dB, (2) average losses of 1.0, 0.5 and 0.75 dB for the coaxial cables on Faces A, B and C respectively, (3) 0.50 and 0.75 dB for the Rotman lens and array lens respectively for the receive mode, (4) 0.5 dB insertion loss for the line stretchers, (5) 1.6 dB taper loss and (6) 1.2 dB insertion loss for the three power dividers. Total receive mode losses are 7.3 dB giving an antenna efficiency of about 20%. The calculated directivity assuming an azimuth pattern like Fig. 5(c) and an elevation pattern which is constant within the $\pm 35^{o}$ extent of the flare angles is 39.3 dB, therefore the gain is approximately 32 dB.

SECTION 4 FEED TEST RESULTS

Testing has been limited to the Butler matrix feed since the other components are still being fabricated. A test program for the complete antenna is scheduled for 1981. The Butler matrix was connected to an 8 element linear array (similar to the pill box structure of Fig. 8) and the composite 8 beam patterns shown in Fig. 12 were obtained on a Scientific-Atlanta 2020 Antenna Analyzer. Sidelobe levels are higher than the -13 dB for a $(\sin x)/x$ beam due to large random phase errors in the Butler matrix ($\approx 15^{o}$RMS) and the element pattern of the probes which was distorted by mutual coupling effects and by the edge effects of the relatively small aperture size of the linear array. In Fig. 13, mutual coupling between probes is illustrated by plotting the relative power coupled to the remaining 9 probes when power flows into either probe 1, 6 or 8. The power coupled to probes on either side of the excited probe is only 12 dB down from the input power level. For a linear array of open-ended waveguide radiators, this power level is more than 20 dB down. Therefore, mutual coupling will play an important role in the probe type radiator array.

CONCLUSION

An antenna utilizing time delay at the subarray level has been shown to have the potential of wide bandwidth, low sidelobes and wide angle scanning. Antenna pattern computer simulations were used to illustrate principal features and the effects of phase errors. Measurements made on the Butler matrix feed array simulator indicate that Butler matrix phase errors and mutual coupling between probe radiating elements adversely affect the pattern for this feed subsystem. Near-in sidelobes are raised above -20 dB; however, far-out sidelobes remain low, about -40 dB, due to the subarray window effect. The Rotman lens feed is expected to have better performance.

REFERENCES

1. Tang, R., "Survey of Time-Delay Beam Steering Techniques," Phased Array Antennas, Artech House Inc., 1970, p. 254.

2. Borgiotti, G.V., "An Antenna for Limited Scan in One Plane: Design Criteria and Numerical Simulation," IEEE Transactions on Antennas and Propagation, Vol. AP-25, No. 2, Mar. 1977, p. 232.

3. Fante, R.L., "Systems Study of Overlapped, Subarrayed Scanning Antennas," 1979 Symposium on Antenna Applications, Monticello, IL.

4. Fante, R.L., "Study of the Radiation Properties of Overlapped, Subarrayed Scanning Antennas," RADC-TR-79-293, In-House Report, Nov. 1979.

5. Rotman, W. and Turner, R.F., "Wide-Angle Microwave Lens for Line Source Applications," IEEE Transactions on Antennas and Propagation, Nov. 1963, p. 623.

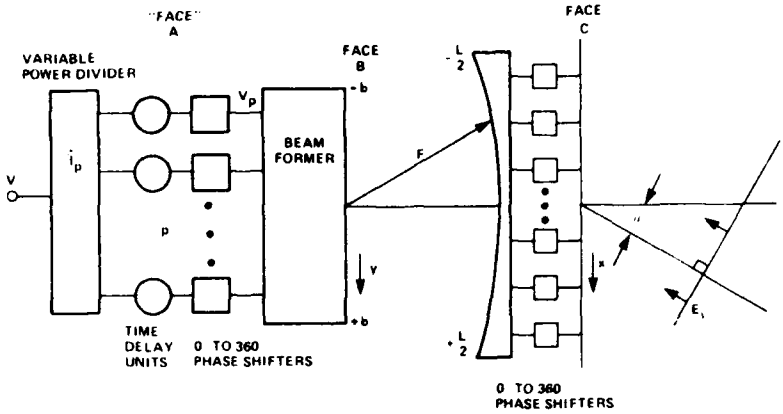

Figure 1. Functional diagram of the completely overlapped subarray antenna.

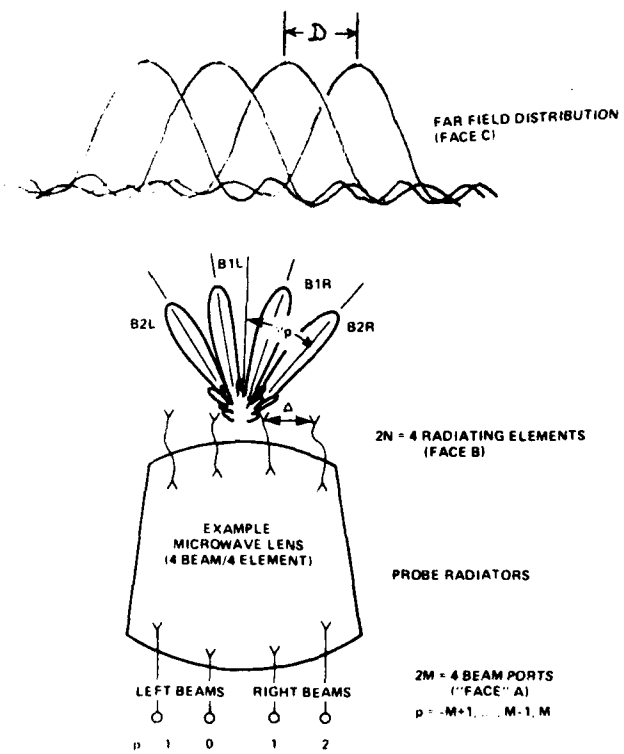

Figure 2. Nomenclature for a microwave lens (Example shown is a 4 beam/4 element lens).

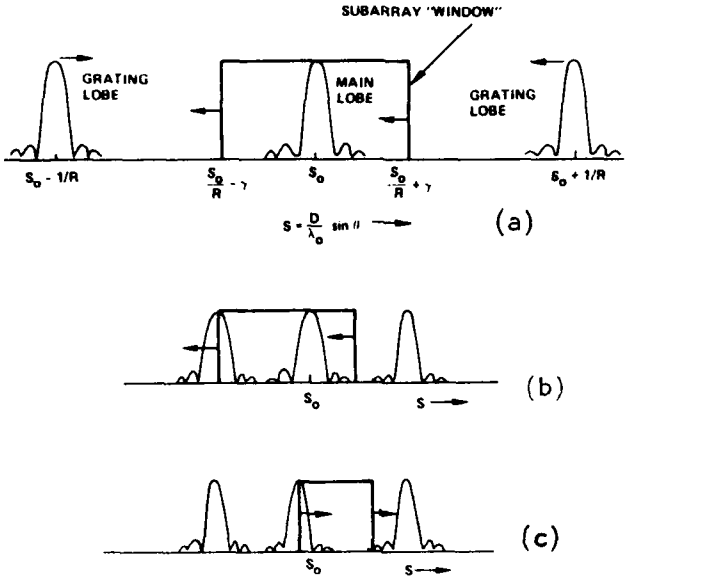

Figure 3. (a) Array lobes and subarray "window". Note that $R=f/f_o=1+(\delta f)/f_o$ and the arrows indicate the direction of shift for $f > f_o$, i.e. $\delta f > 0$. Just reverse the arrows to get the direction of shift for $f < f_o$. Also, note that the main lobe does not shift with frequency. (b) The subarray window shifts far enough to hit a grating lobe. (c) The subarray window hits the main lobe before reaching a grating lobe.

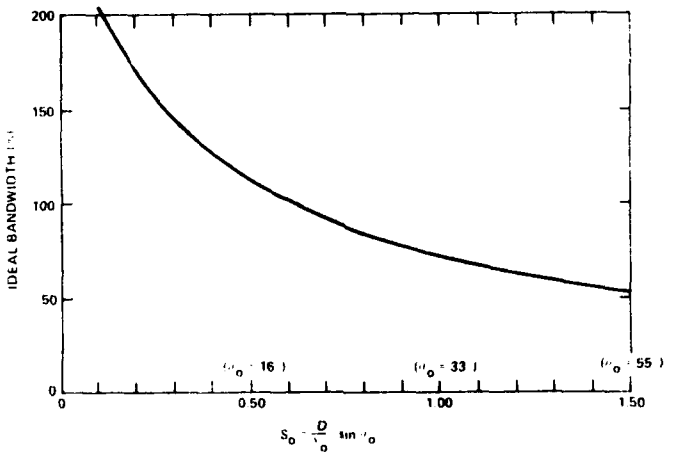

Figure 4. Ideal bandwidth versus scanning parameter.

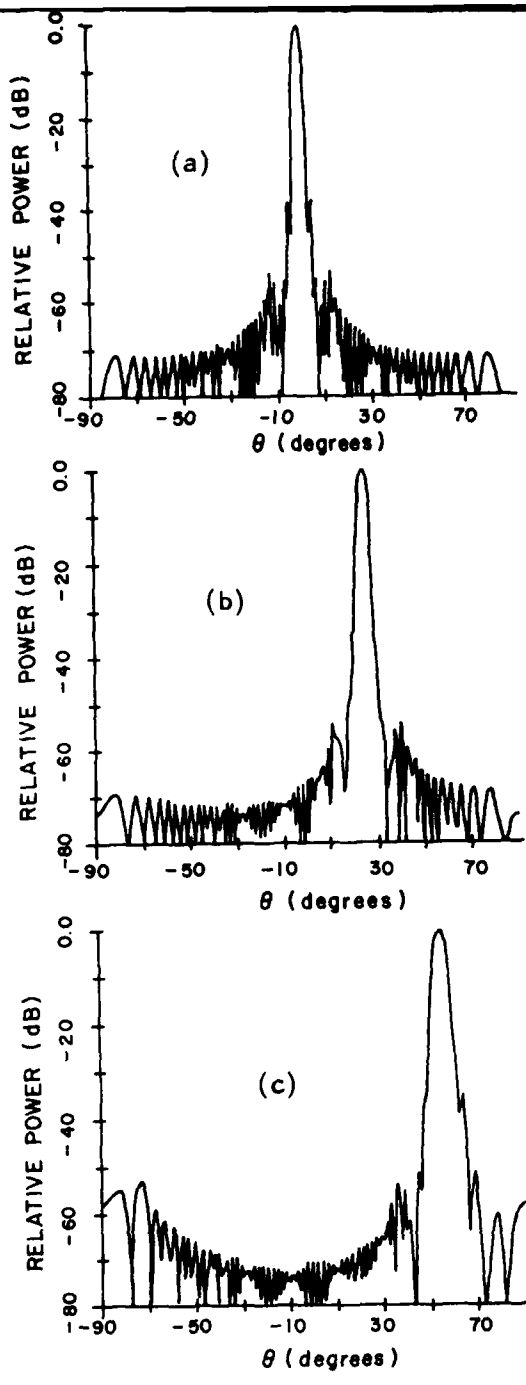

Figure 5. Theoretical antenna patterns for $f=f_o$. (a) $\theta_o=0^o$, (b) $\theta_o=25^o$, (c) $\theta_o=55^o$.

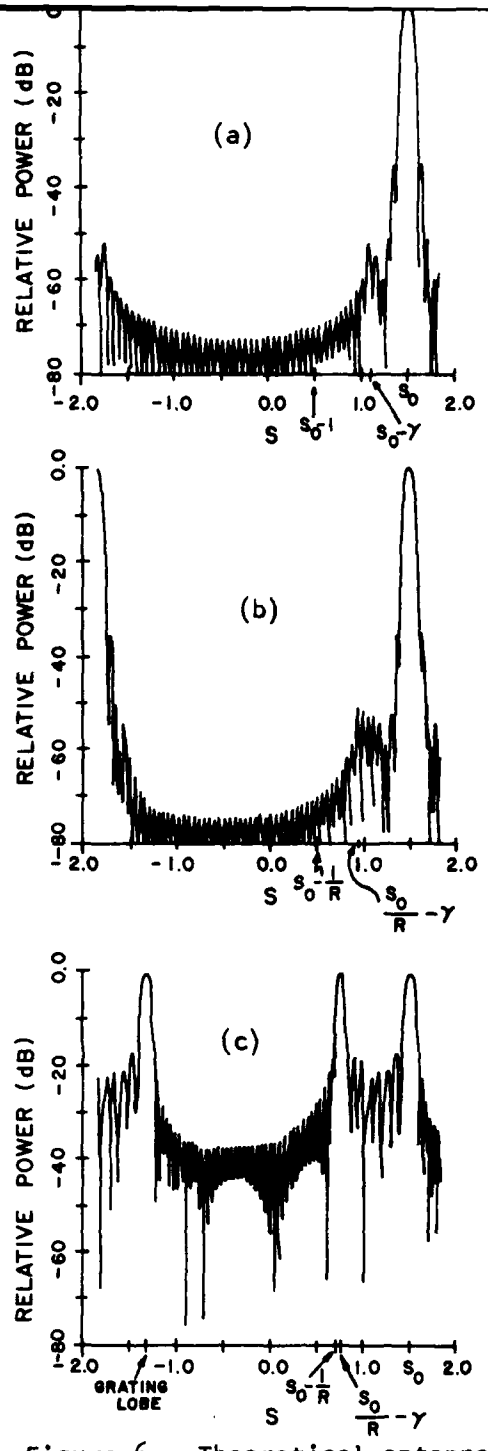

Figure 6. Theoretical antenna patterns for $\theta_o=55^o$ ($S_o=1.5$). (a) $f=f_o$, (b) $f=1.1f_o$, (c) $f=1.3f_o$.

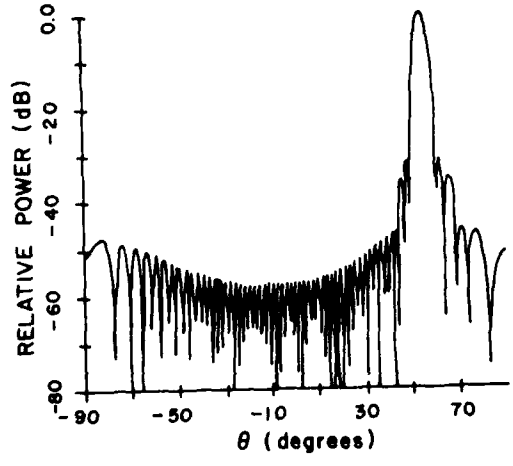

Figure 7. Theoretical antenna pattern using the Butler matrix as the feed ($f=f_o$, $\theta_o=55^o$ and perfect beam phases, i.e. no phase errors assumed).

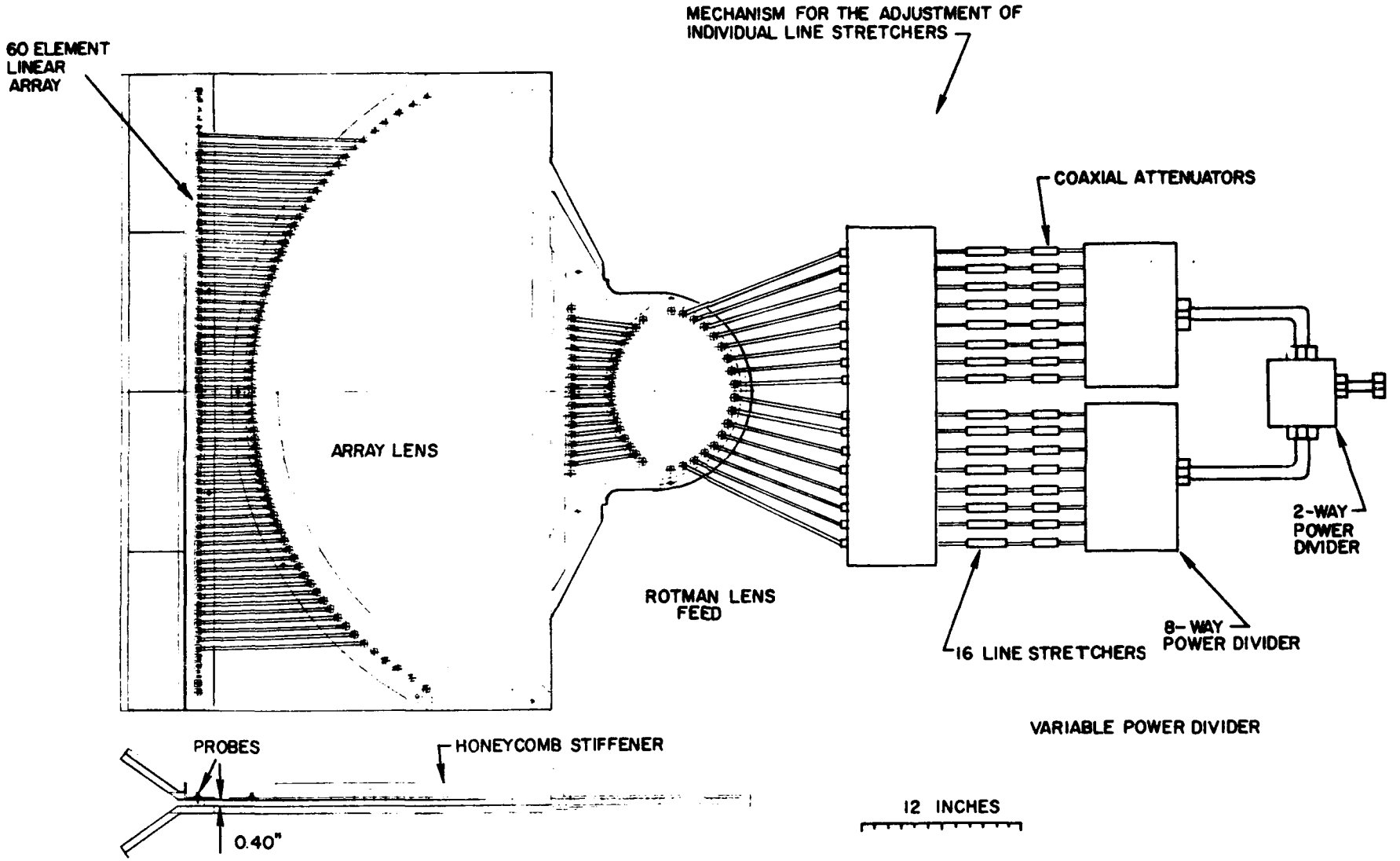

Figure 8. Hardware layout of the experimental completely overlapped subarray antenna.

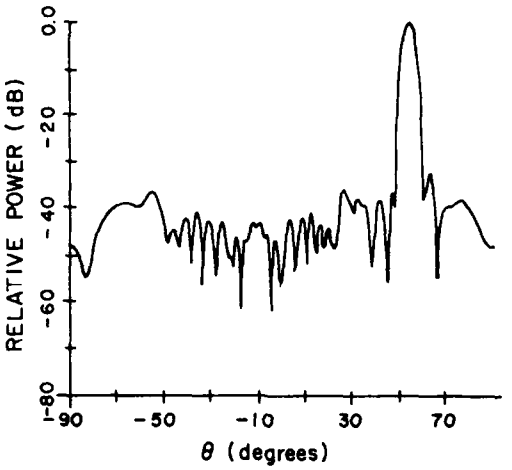

Figure 9. Theoretical antenna pattern for a random phase error of 3 degrees RMS on Face C ($f=f_o$ and $\theta_o=55^o$).

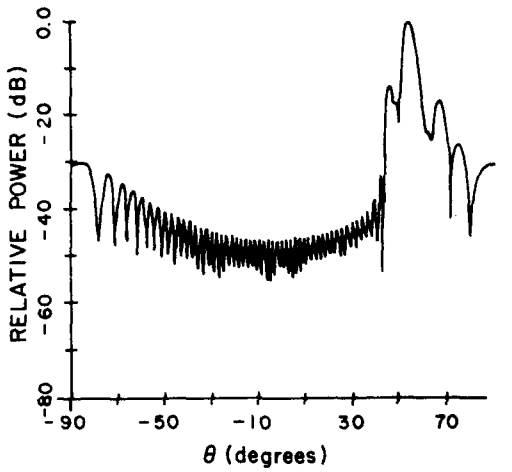

Figure 10. Theoretical antenna pattern using the Butler matrix as the feed ($f=f_o$, $\theta_o=55^o$ and measured beam phases and amplitudes on Face B were used in the simulation).

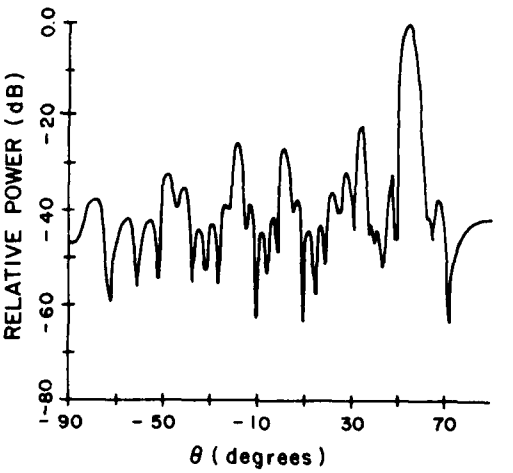

Figure 11. Theoreticai antenna pattern using "line length", i.e. modulo - 2π, phase shift at Faces A and C ($f=1.05f_o$ and $\theta_o=55^o$).

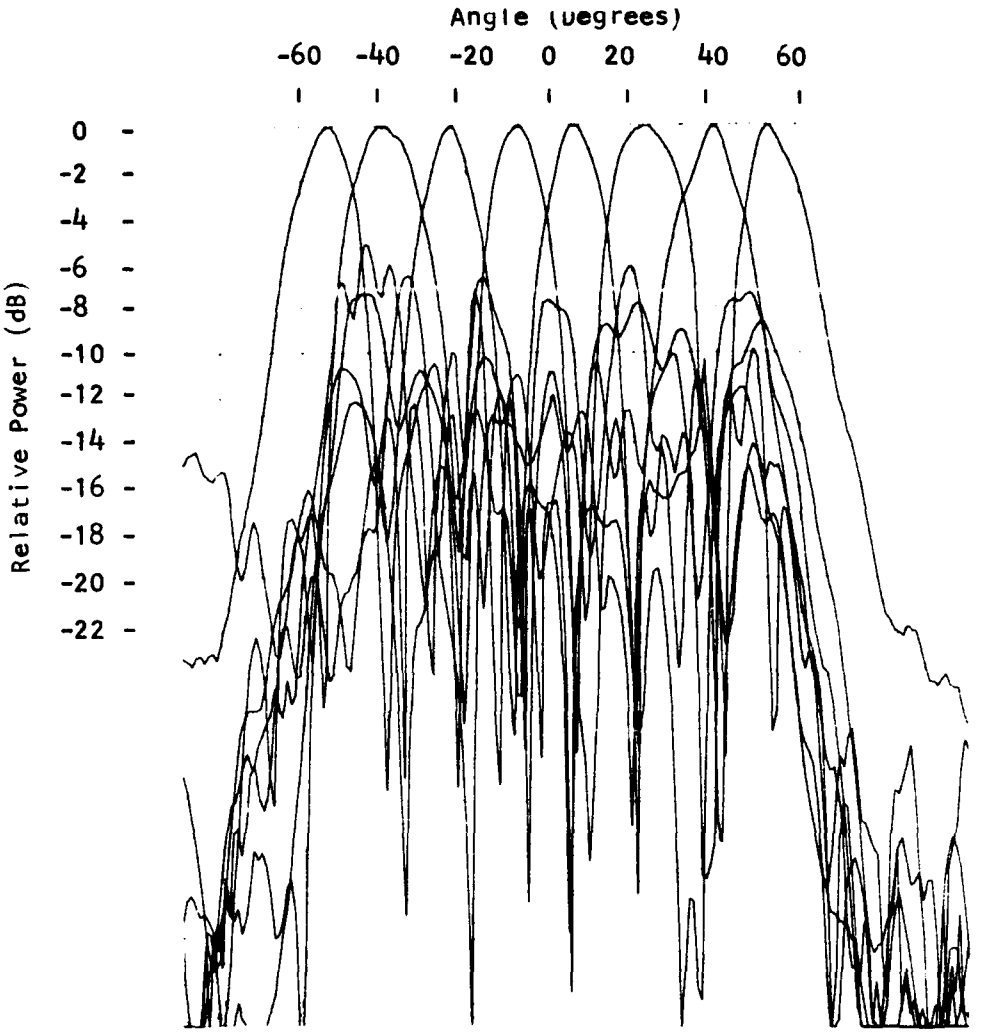

Figure 12. Composite of the 8 measured Butler matrix beam patterns.

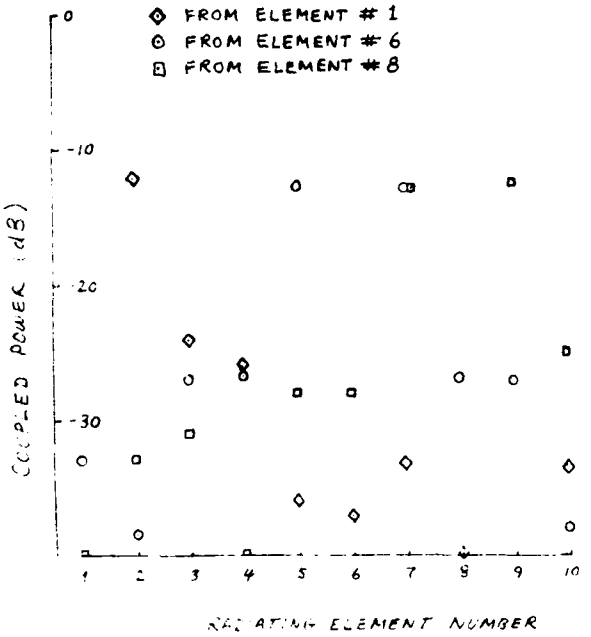

Figure 13. Measured power coupled between probe radiators for the 8 element Butler matrix linear array (simulation of Face B). Note: there are ten probes since the two end probes are dummies while only the center 8 elements are normally connected to the Butler matrix antenna ports.

A FAST VERSATILE WAVEGUIDE BRANCH-LINE COUPLER DESIGN METHOD

C. C. Hung

Lockheed Missiles and Space Co., Inc.

Sunnyvale, CA 94086

1. Introduction:

Antenna array designers are now often faced with extremely low sidelobe requirements (>35 dB). This extremely low sidelobe requirement mandates that the amplitude and phase of each array element be maintained very accurately. The feed network for low sidelobe and high power antenna arrays usually are formed in waveguide and employ precision couplers as the critical component. It is therefore essential to have a fast, versatile and very accurate design method for waveguide couplers to avoid any emirical adjustment.

The analysis and synthesis of waveguide branch-line couplers has been studied by Reed and Wheeler [1], Reed [2], Patterson [3], Young [4], Levy and Lind [5], and Levy [6, 7, 8, 9]. Levy's papers contain detailed information on the design of waveguide branch-line couplers, However Levy used Zolotarev functions to find the internal impedance levels within the coupler. These functions are cumbersome and corrections for the waveguide discontinuities must still be made.

A simple, fast, versatile and accurate computer-aided design method, which does not use any complicated mathematical functions, is presented here. The analysis of a waveguide branch-line coupler is first briefly reveiwed in Section 2. The design method is then discussed in Section 3. Some design examples are presented in Section 4. Section 5 contains a comparison between the measured and computed performance of a 3 dB coupler.

2. Analysis:

The performance of a symmetrical branch-line coupler can be computed using even/odd mode analysis [1] and the equivalent circuit of a waveguide T-junction. If the in-coming wave amplitude at port #1 in Figure 1 is of unity value and the out-going wave amplitudes at the four ports are A_1, A_2, A_3, and A_4, then the VSWR, coupling and directivity of this coupler are given by the following relationships:

$$VSWR = \frac{1 + |A_1|}{1 - |A_1|}$$

$$C = 20 \log |A_3| \text{ dB}$$

$$D = 20 \log \left| \frac{A_3}{A_4} \right| \text{ dB}$$

The out-going wave amplitudes at four ports can be obtained from the reflection coefficient (Γ) and transmission coefficient (T) of an even and mode analysis.

$$A_1 = 1/2 \ (\Gamma e + \Gamma o)$$
$$A_2 = 1/2 \ (Te + To)$$
$$A_3 = 1/2 \ (Te - To)$$
$$A_4 = 1/2 \ (\Gamma e - \Gamma o)$$

The equivalent circuit of a waveguide T-junction is given by Marcuvitz [10] and is shown in Figure 2, where B_a, B_b, B_c, and B_d are the discontinuity susceptances of the T-junction. Since, in a branch-line coupler, the T-junctions are separated by a length of waveguide (transmission line), the equivalent circuit transforms to that shown in Figure 3. The ABCD matrix of the equivalent circuit for both even and odd mode can now be computed readily. The reflection and transmission coefficients are related to the ABCD matrix as follows:

$$\Gamma e = \frac{(Ae + De) + (Be - Ce)}{Ae + Be + Ce + De}$$

$$Te = \frac{2}{Ae + Be + Ce + De}$$

$$\Gamma o = \frac{(Ao + Do) + (Bo - Co)}{Ao + Bc + Co + Dc}$$

$$To = \frac{2}{Ao + Bc + Co + Do}$$

For any given physical dimensions of a waveguide branch-line coupler, its performance can now be computed readily.

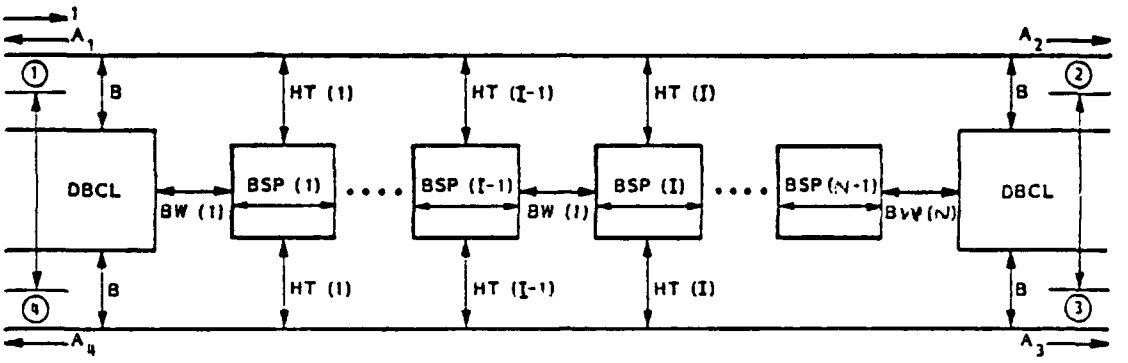

B – INPUT/OUTPUT WAVEGUIDE HEIGHT

A – INPUT/OUTPUT WAVEGUIDE WIDTH

DBCL – DISTANCE BETWEEN CENTER LINES OF INPUT/OUTPUT PORTS

Fig. 1 Branch-Line Waveguide Coupler

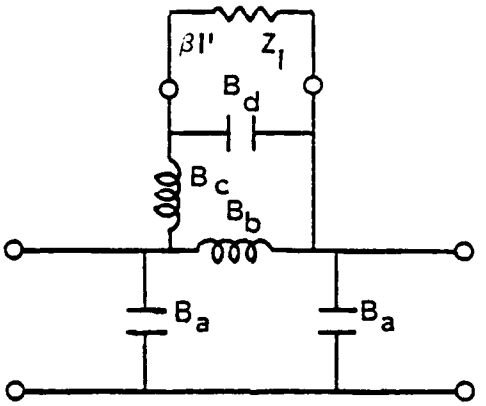

Z_1 = 0 FOR EVEN MODE

Z_1 = ∞ FOR ODD MODE

Fig. 2 Equivalent Circuit of a Waveguide T-Junction

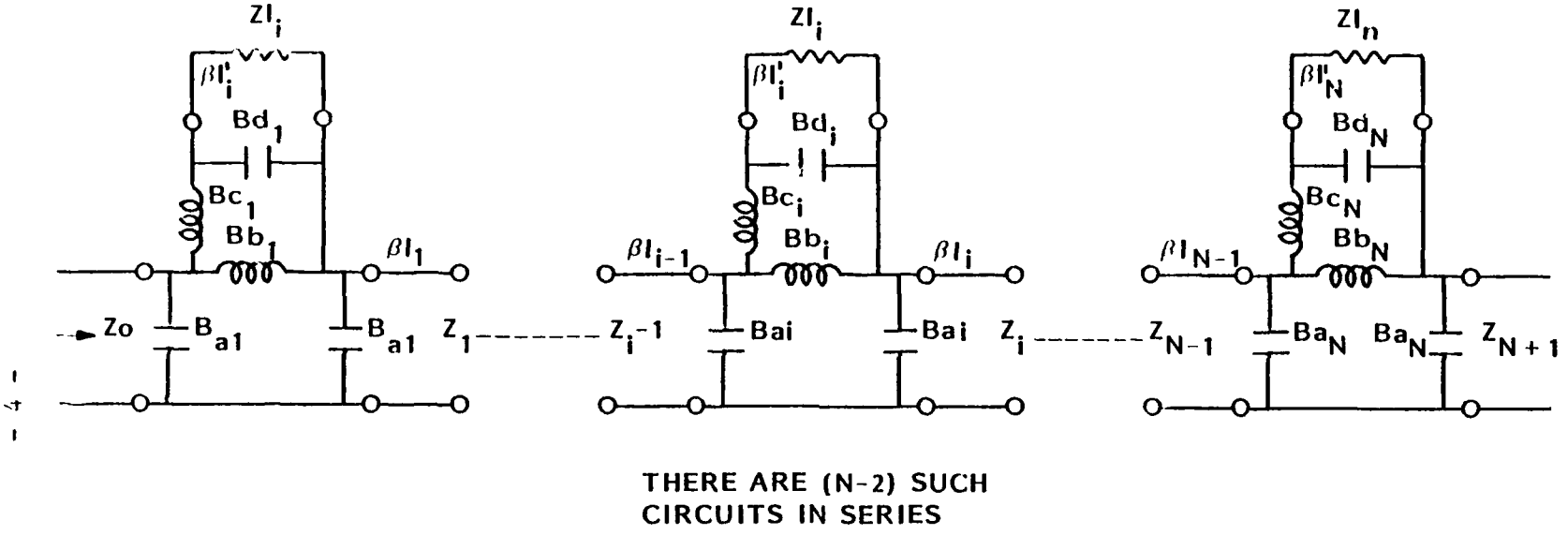

Fig. 3 Equivalent Circuit of a Branch-Line Coupler

3. Design Method:

Suppose the desired coupler performance, as a function of frequency, is described by the out-going waves at the four ports as A_{10} (f), A_{20} (f), A_{30} (f), and A_{40} (f) and also suppose that for a given set of physical dimensions, the coupler performance is described $A_1(f,\overline{x})$, $A_2(f,\overline{x})$, $A_3(f,\overline{x})$, and $A_4(f,\overline{x})$ where $\overline{x} = [x_1, x_2, \ldots\ldots, x_n]$ and represents the physical dimensions of the coupler. A figure of merit can be defined as follows:

$$F = F(\overline{x}) = \sum_{i=1}^{4} \int \left| A_i(f,\overline{x}) - A_{io}(f) \right|^2 df$$

This figure of merit is the measure of the difference in performance between the given coupler and the desired coupler. The objective now is to adjust the physical dimensions of the coupler such that this figure of merit becomes zero, i.e., until the actual performance approaches the desired performance as an asymptote.

The figure of merit, F , is a non-negative function of many variables with each variable being controlled by one physical parameter of the coupler. The objective is now to find the minimum of a non-negative function of many variables. The method of minimization has been studied by many researchers and a general subroutine is available [11]. The method used in this subroutine is basically the steepest descent method to find a local minimum. Starting with an initial design of the coupler, the minimization of the figure of merit will lead to the design of the coupler with the desired performance.

In this computer-aided design method, the desired coupler performance can be a maximally flat response, a Tchebyscheff response or any other synthesized response. No complicated mathematics are involved. Practical considerations dictate that certain physical dimensions, such as waveguide width and height, be kept constant. Mechanical or assembly considerations may also require certain physical dimensions to be fixed. Therefore, the number of variables in the minimization process is generally less than the number of physical parameters which can control the performance of the coupler.

The integration in the definition of figure of merit is converted to a finite sum in the actual computation. The derivatives required in the minimization process can be obtained numerically.

It has been found that the design for periodic branch-line couplers given in [12] is very useful as the initial design point for the present method.

Since the waveguide discontinuity is considered in the equivalent circuit, the corrections for the discontinuities are not necessary, and hance, no empirical adjustment is necessary.

4. Design Examples:

Three design examples will now be discussed. In all three examples, it takes only a few seconds on a Univac 1110/43 computer to converge to the final design. Constant coupling within the frequency band is the desired performance in the following examples.

(1) 3dB, 4-branch coupler

The waveguide is chosen to have a width of 1.072 inch and a height of 0.200 inch. The initial performance, or starting point, is as follows:

INITIAL PERFORMANCE

A = 1.0720

HEIGHT	BRANCH WIDTH	BRANCH SPACING
.2000	.0470	.3000
.2000	.1080	.3000
.2000	.1080	.3000
	.0470	

COUPLER LENGTH = 1.2100

DISTANCE BETWEEN CENTER LINES OF TWO WAVEGUIDES = .5180

FREQ	VSWR	COUPLED PORT		DIRECT PORT		DIRECTIVITY
		DB	DEG	DB	DEG	DB
9.4000	1.0689	3.2248	- 1.5805	2.8251	88.3754	25.95
9.5000	1.0682	3.2373	- 7.2478	2.8134	82.7126	26.00
9.6000	1.0669	3.2424	-12.8860	2.8082	77.0845	26.13
9.7000	1.0657	3.2401	-18.5006	2.8096	71.4853	26.28
9.8000	1.0651	3.2309	-24.0965	2.8176	65.9094	26.39
9.9000	1.0658	3.2148	-29.6790	2.8326	60.3519	26.35
10.0000	1.0685	3.1920	-35.2534	2.8549	54.8083	26.11

By keeping waveguide width and height fixed and also keeping the distance between center lines of two waveguides fixed, the minimization of the figure of merit gives following design and performance:

DESIRED COUPLING VALUE = 3.0100 (DB)

A = 1.0720 B = .2000

HEIGHT	BRANCH WIDTH	BRANCH SPACING
.2000	.0478	.2883
.2000	.1122	.2518
.2000	.1122	.2883
	.0478	

COUPLER LENGTH = 1.1483
DISTANCE BETWEEN CENTER LINES OF TWO WAVEGUIDES = .5180

FREQ	VSWR	COUPLED PORT		DIRECT PORT		DIRECTIVITY
		DB	DEG	DB	DEG	DB
9.4000	1.0071	2.9729	13.8528	3.0482	103.8522	45.98
9.5000	1.0024	2.9955	8.3604	3.0252	98.3605	55.30
9.6000	1.0009	3.0104	2.9096	3.0102	92.9096	63.64
9.7000	1.0021	3.0179	- 2.5062	3.0027	87.4937	56.51
9.8000	1.0021	3.0182	- 7.8930	3.0025	82.1070	56.79
9.9000	1.0008	3.0113	-13.2560	3.0093	76.7440	64.45
10.0000	1.0023	2.9975	-18.6005	3.0231	71.3994	55.80

Thus, a total unbalance of 0.43 dB is reduced to 0.04 dB and the minimum directivity is increased by 20 dB.

(2) 5dB, 5-branch coupler

The waveguide is of 1.072 x 0.200 cross section. The initial performance is as follows:

A = 1.0720 B = .2000

HEIGHT	BRANCH WIDTH	BRANCH SPACING
.2000	.0420	.3200
.2000	.0790	.3200
.2000	.0790	.3200
.2000	.0790	.3200
	.0420	

COUPLER LENGTH = 1.6010
DISTANCE BETWEEN CENTER LINES OF TWO WAVEGUIDES = .5180

FREQ	VSWR	COUPLED PORTS		DIRECT PORT		DIRECTIVITY
		DB	DEG	DB	DEG	DB
9.4000	1.0137	2.9617	- 92.5699	3.0603	- 2.5749	40.34
9.5000	1.0031	2.9761	- 99.7160	3.0448	- 9.7162	53.32
9.6000	1.0082	2.9845	-106.8160	3.0365	-16.8161	44.73
9.7000	1.0173	2.9868	-113.8757	3.0352	-23.8773	38.32
9.8000	1.0255	2.9831	-120.9008	3.0404	-30.9028	34.96
9.9000	1.0329	2.9735	-127.8965	3.0521	-37.8956	32.76
10.0000	1.0396	2.9580	-134.8675	3.0700	-44.8595	31.18

The initial design now gives only 3 dB coupling instead of the 5 dB desired. Again, by keeping the waveguide size fixed and also keeping the distance between center lines of the two waveguides fixed, the minimization gives following design and performance:

DESIRED COUPLING VALUE = 5.0000 (DB)

A = 1.0720 B = .2000

HEIGHT	BRANCH WIDTH	BRANCH SPACING
.2000	.0208	.3338
.2000	.0610	.3131
.2000	.0789	.3131
.2000	.0610	.3338
	.0208	

COUPLER LENGTH = 1.5362
DISTANCE BETWEEN CENTER LINES OF TWO WAVEGUIDES = .5180

		COUPLED PORT		DIRECT PORT		DIRECTIVITY
FREQ	VSWR	DB	DEG	DB	DEG	DB
9.4000	1.0032	4.9716	- 79.6972	1.6641	10.3026	47.88
9.5000	1.0019	4.9895	- 86.3000	1.6558	3.6999	52.39
9.6000	1.0008	5.0010	- 92.8638	1.6504	- 2.8638	59.74
9.7000	1.0008	5.0062	- 99.3922	1.6480	- 9.3922	66.31
9.8000	1.0012	5.0052	-105.8886	1.6485	-15.8887	58.45
9.9000	1.0015	4.9980	-112.3562	1.6518	-22.3563	54.77
10.0000	1.0018	4.9847	-118.7983	1.6580	-28.7983	52.62

The above performance is very good showing that the initial design is not critical.

(3) 2 dB, 5-branch coupler

A = 1.0720 B = .2000

HEIGHT	BRANCH WIDTH	BRANCH SPACING
.2000	.0400	.3200
.2000	.0800	.3200
.2000	.0800	.3200
.2000	.0800	.3200
	.0400	

COUPLER LENGTH = 1.6000
DISTANCE BETWEEN CENTER LINES OF TWO WAVEGUIDES = .5180

		COUPLED PORT		DIRECT PORT		DIRECTIVITY
FREQ	VSWR	DB	DEG	DB	DEG	DB
9.4000	1.0239	2.9837	- 92.3444	3.0395	- 2.3586	35.59
9.5000	1.0158	2.9976	- 99.4865	3.0241	- 9.4894	39.15

FREQ	VSWR	COUPLED PORT DB	COUPLED PORT DEG	DIRECT PORT DB	DIRECT PORT DEG	DIRECTIVITY DB
9.6000	1.0131	3.0057	-106.5831	3.0157	-16.5795	40.70
9.7000	1.0167	3.0078	-113.6394	3.0140	-23.6318	38.61
9.8000	1.0228	3.0041	-120.6608	3.0187	-30.6495	35.96
9.9000	1.0290	2.9944	-127.6520	3.0298	-37.6359	33.87
10.0000	1.0348	2.9789	-134.6176	3.0471	-44.5948	32.30

The final design and its performance as as follows:

DESIRED COUPLING VALUE = 2.0000 (DB)

A = 1.0720 B = .2000

HEIGHT	BRANCH WIDTH	BRANCH SPACING
.2000	.0250	.3326
.2000	.0965	.2763
.2000	.1314	.2763
.2000	.0965	.3326
	.0250	

COUPLER LENGTH = 1.5920

DISTANCE BETWEEN CENTER LINES OF TWO WAVEGUIDES = .5180

FREQ	VSWR	COUPLED PORT DB	COUPLED PORT DEG	DIRECT PORT DB	DIRECT PORT DEG	DIRECTIVITY DB
9.4000	1.0194	1.9794	- 87.8575	4.3676	2.1421	35.96
9.5000	1.0144	1.9940	- 95.2210	4.3411	- 5.2198	38.63
9.6000	1.0093	2.0017	-102.5383	4.3270	-12.5371	42.54
9.7000	1.0039	2.0025	-109.8171	4.3251	-19.8167	50.50
9.8000	1.0025	1.9965	-117.0651	4.3353	-27.0651	53.79
9.9000	1.0095	1.9838	-124.2900	4.3578	-34.2885	42.34
10.0000	1.0180	1.9644	-131.4997	4.3932	-41.4928	37.01

5. Measured Performance:

A 3 dB, 3-branch coupler designed using the equivalent circuit and method of minimization was fabricated. The coupler then was tested without any adjustment. The measured and computed performance are listed in Table 1. The measured couplings are within 0.1 dB of the computed value.

Since the accuracy of equizalent circuit deteriorates as the branch width becomes larger (compared with the waveguide height), the accuracy of the computed result of this 3 dB 3-branch coupler is not as good as that of a coupler with more than three branches or with less coupling. Therefore, the comparison between the measured and computed performance shown here are believed to represent a worst case.

6. Conclusion:

A computer-aided design method for waveguide branch-line coupler has been developed. This design method is fast, not limited to any particular desired coupler performance, and can include all the mechanical restrictions imposed on the coupler. The design method has been used to design over one hundred couplers, with coupling values ranging from 1.5 dB to 14 dB, in less than one day's time with excellent results.

WAVEGUIDE WIDTH = 1.072 HEIGHT = 0.200

COUPLER HEIGHT = 0.200, 0.200

BRANCH WIDTH = 0.084, 0.146, 0.084

BRANCH SPACING = 0.260, 0.260

FREQ	VSWR		COUPLED PORT (dB)	
	MEASURED	COMPUTED	MEASURED	COMPUTED
9.4	1.07	1.064	2.96	2.972
9.5	1.06	1.040	3.02	2.998
9.6	1.02	1.018	3.02	3.016
9.7	1.05	1.003	3.04	3.026
9.8	1.08	1.023	3.07	3.026
9.9	1.07	1.043	3.01	3.017
10.0	1.07	1.064	3.02	2.999

FREQ	DIRECT PORT (dB)		DIRECTIVITY (dB)	
	MEASURED	COMPUTED	MEASURED	COMPUTED
9.4	2.97	3.035	27.45	27.16
9.5	2.95	2.999	31.62	31.18
9.6	2.93	2.977	38.84	38.09
9.7	2.91	2.968	47.67	53.95
9.8	2.93	2.972	35.18	36.05
9.9	2.89	2.988	30.09	30.60
10.0	2.95	3.016	26.72	27.21

TABLE 1. MEASURED AND COMPUTED COUPLER PERFORMANCE

REFERENCES

1. J. Reed and G. J. Wheeler "A Method of Analysis of Symmetrical Four Port Networks" IRE Trans. Microwave Theory Tech, Vol. MTT-4, pp 246-252, Oct. 1956.

2. J. Reed "The Multiple Branch Waveguide Coupler" IRE Trans. Microwave Theory Tech, Vol. MT-6, pp 398-403. Oct. 1958.

3. K. G. Patterson "A Method for Accurate Design of a Broad-Band Multibranch Waveguide Coupler" IRE Trans. Microwave Theory Tech, Vol. MTT-7, pp466-473, Oct. 1959.

4. L. Young "Synchronous Branch Guide Directional Couplers for Low and High Power Applications" IRE Trans. Microwave Theory Tech, Vol. MTT-10, pp 459-475, Nov. 1962.

5. R. Levy and L. F. Lind "Synthesis of Symmetrical Branch-Guide Directional Couplers" IEEE Trans. Microwave Theory Tech, Vol. MTT-16, No. 2, pp80-89, Feb. 1968.

6. R. Levy "Analysis of Practical Branch-Guide Directionsl Couplers" IEEE Trans. Microwave Theory Tech, Vol. MTT-17, No. 5, pp 289-290, May 1969.

7. R. Levy "Generalized Rational Function Approximation in Finite Intervals Using Zolotarev Functions" IEEE Trans. Microwave Theory Tech, Vol. MTT-18, No. 12, pp 1052-1062, Dec. 1970.

8. R. Levy "A New Class of Distributed Prototype Filters with Application to Mixed Lumped/Distributed Component Design" IEEE Trans. Microwave Theory Tech, Vol. MTT-18, No. 12, pp 1064-1071, Dec. 1970.

9. R. Levy "Zolotarev Branch-Guide Couplers" IEEE Trans Microwave Theory Tech, Vol. MTT-21, No. 2, pp 95-99, Feb. 1973.

10. N. Marcuvitz, Waveguide Handbook, McGraw-Hill, 1951.

11. D. F. Shanno and K. H. Phua "Minimization of Unconstrained Multivariate Functions" ACM Trans. Mathematical Software, Vol. 2, No. 1, pp 87-94, March 1976.

12. G. L. Matthaei, L. Young and E. M. T. Jones "Microwave Filters, Impedance-Matching Networks and Coupling Structures", McGraw-Hill, 1964, pp 815-819.

WIDEBAND MICROWAVE LENS ANTENNA FOR TACTICAL RADAR APPLICATIONS

Peter Franchi
Nicholas Kernweis
Walter Rotman

Rome Air Development Center
Electromagnetic Sciences Division
Antennas & RF Components Branch
Hanscom AFB, MA 01731

Summary: A space-fed phased array antenna is being developed for tactical radar applications where large instantaneous bandwidths and low sidelobes are required. The limitation on bandwidth in a normal phased array system, caused by the use of phase shifters rather than time delay units, is overcome in this antenna by providing course beam steering through multiple switched feeds and fine beam steering by phase shifters.

The phased array antenna consists of a stack of identical constrained 2D microwave lenses with printed circuit dipoles interconnected between their inner and outer surfaces and with line source feeds spaced uniformly along the focal surface of the cylindrical structure. Each of the line source feeds is constructed as a parallel plate pillbox, operating in the TE_{01} mode and with a hybrid waveguide input to provide a monopulse capability in the elevation plane. A C-Band model of this lens, with a two degree beamwidth, ten percent bandwidth and scan range of ninety degrees in azimuth and fifty degrees in elevation, is under construction. Although this model does not contain, at present, the phase shifters required for fine beam steering, it will be capable of demonstrating the course beam steering in azimuth by switching between the four line source feeds. The principles of operation of this antenna design, as well as its potential extension to wider bandwidths and scan angles, will be discussed.

Introduction: An increasing number of low sidelobe antennas for military applications require phased array antennas with large instantaneous bandwidths for the reduction of interference and increased range resolution. The use of conventional phase shifters in large phase arrays severely limits the scan angle over which the bandwidth can be maintained. The use of a space-fed microwave lens with a small number of feeds that provide beams with wideband behavior overcomes this problem. Conventional low cost phase shifters can be used to provide wideband scanning at small angles close to the beam position defined by one of the feeds. Therefore, switching between feeds provides the wide-angle coarse scan and the phase shifters provide the small-angle fine scan. The complete antenna system, then, is a set of feeds feeding a microwave lens with phase shifters in the lens aperture. We are presently fabricating a lens antenna with the feeds, but without the phase shifters in order to reduce costs.

Design Principles: Before going into the lens design, a review of the bandwidth limitations is helpful. In Figure 1, the percentage bandwidth of a lens antenna is defined in terms of the maximum scan angle and the antenna diameter in wavelengths. For example, a sixty wavelength antenna with four feed points would give a seven percent bandwidth to cover a total angle of 90°. Likewise, a fifty wavelength antenna would have a nine percent bandwidth. Figure 2 demonstrates how the combination of wideband lens with a small number of feeds (in this example, four) can be used with the aperture phase shifters to give wideband, wide angle, phased array performance. Consider horn #4 as an example. With all the phase shifters at their zero settings, the angle that beam #4 makes with the array normal is equal to that of horn #4. Small scan perturbations away from this beam position is possible by the use of the phase shifters, without reducing the bandwidth below the amount given by the equation in Figure 2. In other words the use of a wideband, wide angle lens enables the maximum scan angle times the bandwidth product to be increased in proportion to the number of feeds used for the array.

Systems that require wide angle scan in both azimuth and elevation with wideband performance often use stacks of bootlace lenses feeding an orthogonal set of similar lenses. For moderate to high gain antennas this arrangement can be very bulky, expensive, complex, unreliable and heavy. A simpler antenna can be derived by replacing the point source horn feeds of a 2D bootlace lens with line source feeds in a 3D lens (see Figure 3). If the line source feeds are phased to radiate at zero elevation angle, the lens characteristics (defined by parameters such as size, shape, and optical path lengths) are exactly those of the 2D lens. Scanning in elevation, for this case, would restrict the beams to the same bandwidth limitations of Figure 1. If a cylindrical lens is designed to be fed by a line source phased to radiate at an elevation angle β (measured from the normal to the aperture), by symmetry it must equally well collimate the beam for a line source feed radiating at an angle of $-\beta$. In effect, the line source feed and lens combination has six perfect focal points (see Figure 4), consisting of three sets of focal points in azimuth at elevation angles of $\pm\beta$. This cylindrical lens design, together with aperture phase shifters, would give a large angular region, over which the phase aberations are small, for which wideband operation is possible.

The equations for the 3D cylindrical lens are derived from Figure 5 where F_2 represents the line source feed radiating at an angle β. A general ray from the line source to an arbitrary point on a wave front is set equal to the central ray. The solutions from the resulting set of equations (one for each focal point) completely specify the lens. It is interesting to note that the equations for the 3D cylindrical lens are identical to the 2D equations, defining the Rotman-Turner lens, when the path length w of the 2D lens is multiplied by $\cos\beta$. (In this transformation w is replaced everywhere by w' sec β). As a result, in the design of a 3D cylindrical lens, only the transmission line lengths in the 2D lens prototype need be changed since the lens contours remain unchanged.

Antenna Configuration:
A major task of this development effort is to obtain low sidelobes which can be adversely affected by improper choice of a large number of design parameters. For example, the mutual coupling, which changes both the

VSWR and the active element pattern, or line source spillover could raise sidelobes above acceptable levels. In addition, multiple internal reflections, edge effects and the several sources of phase and amplitude error (systematic lens errors, feed errors and random errors) are also expected to increase the sidelobe levels. All of these problems are being examined to ascertain the best approach for reducing their contribution. Our goal is to set all azimuth sidelobes, except for three symmetrical pairs closest to the main beam, to be below 50 dB, with the largest of these below 35 dB. For example, line source feed spillover will be eliminated by enclosing the feed lens combination in an absorbing shroud. Low feed spillover and good shroud design should keep the resulting new source of error (internal reflection) to sufficiently low levels. Resistive attenuation is added to the edge elements of the lens in the azimuth plane to provide better control of the amplitude taper. Since the line source feed radiates only a relatively small amount of power into this edge region, little additional loss is contributed. Resistive tapering also reduces mutual coupling effects at the edges and can help to reduce the variation of aperture taper with frequency if it can be well matched and designed so that its phase shift with frequency is identical to that of the lossless transmission line.

A microwave antenna which incorporates these principles is presently being designed, with initial testing and fabrication expected by the late fall. This lens will have elevation focal points at ±15° and azimuth focal points at 0° and ±30°. The lens, operating at C band, will be 42 inches wide and 39 inches high, with a total of 896 radiating elements. A parabolic pillbox antenna with monopulse feed, operating in the TE_{01} mode, serves as the line source feed and will be physically moved to obtain the various azimuth focal positions. The focal length of the lens is 40 inches.

A theoretical analysis was undertaken to determine the aperture and flare angle of the feed, the resistive tapering of the lens and the effect of these parameters on the far-field pattern. This analysis has not included mutual coupling random errors or mismatch effects, but models the azimuth behavior in most other critical aspects. Figure 6 represents the line source feed's far field radiation pattern while Figure 7 is the far field power pattern of the lens. These patterns are sufficiently within our specifications so that the actual model can be expected to have acceptable performance when manufacturing errors are included.

BANDWIDTH LIMITATIONS OF A SPACE-FED PHASED ARRAY

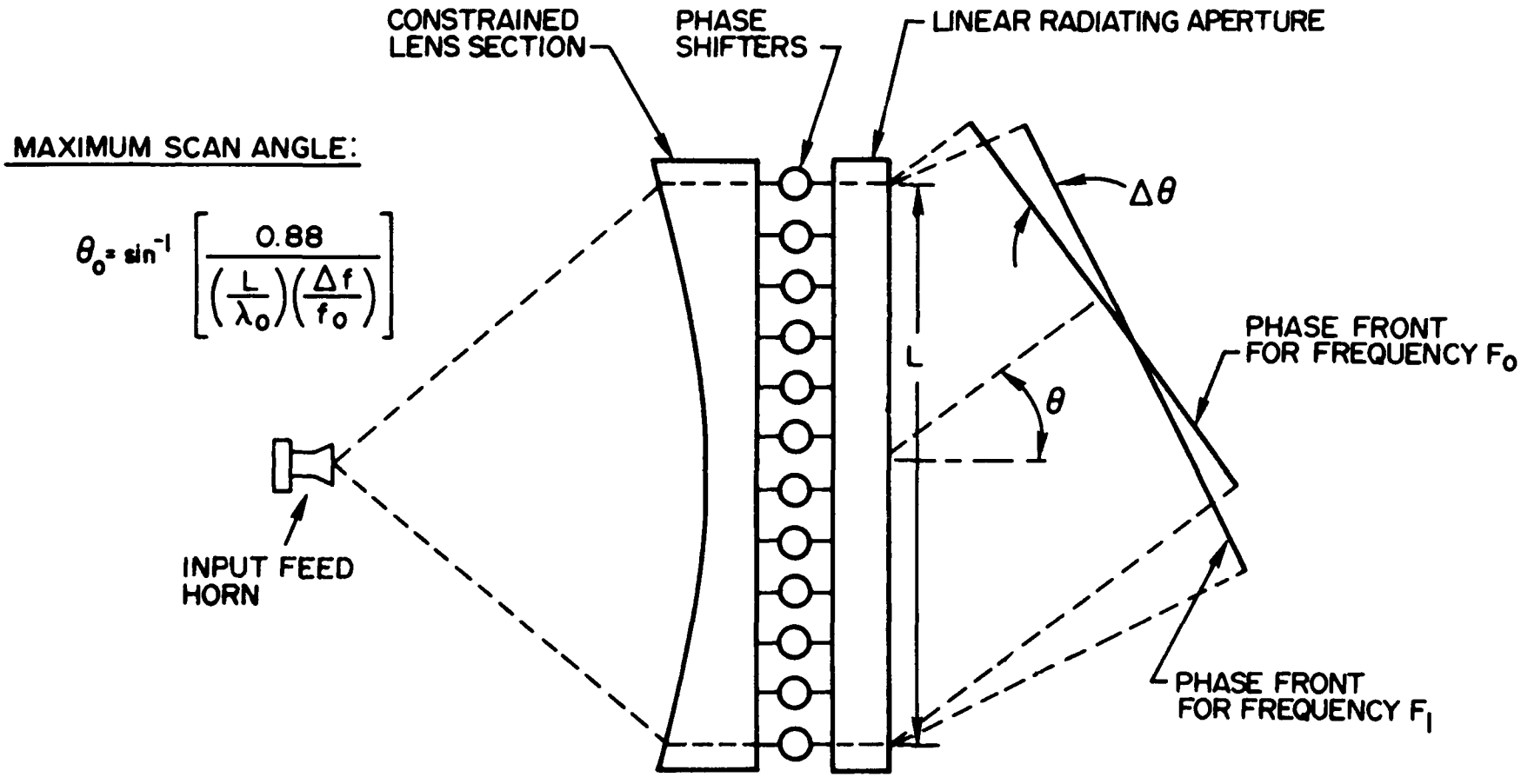

FIG. 1

BEAM STEERING IN A MULTI-FEED LENS

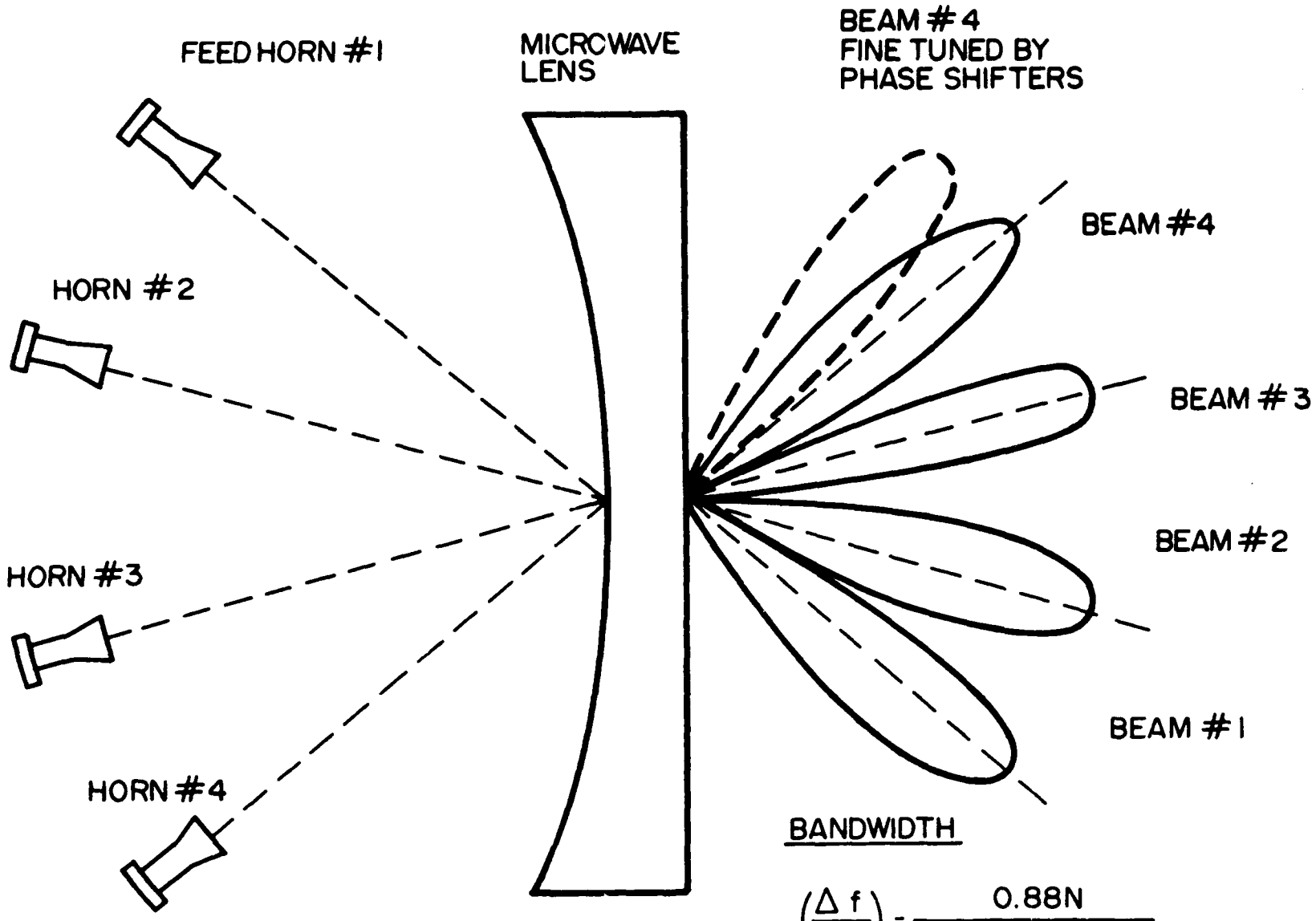

BANDWIDTH

$$\left(\frac{\Delta f}{f_0}\right) = \frac{0.88N}{(L/\lambda_0)(\sin\theta_0)}$$

N= NUMBER OF FEEDS

FIG. 2

3D CYLINDRICAL CONSTRAINED LENS

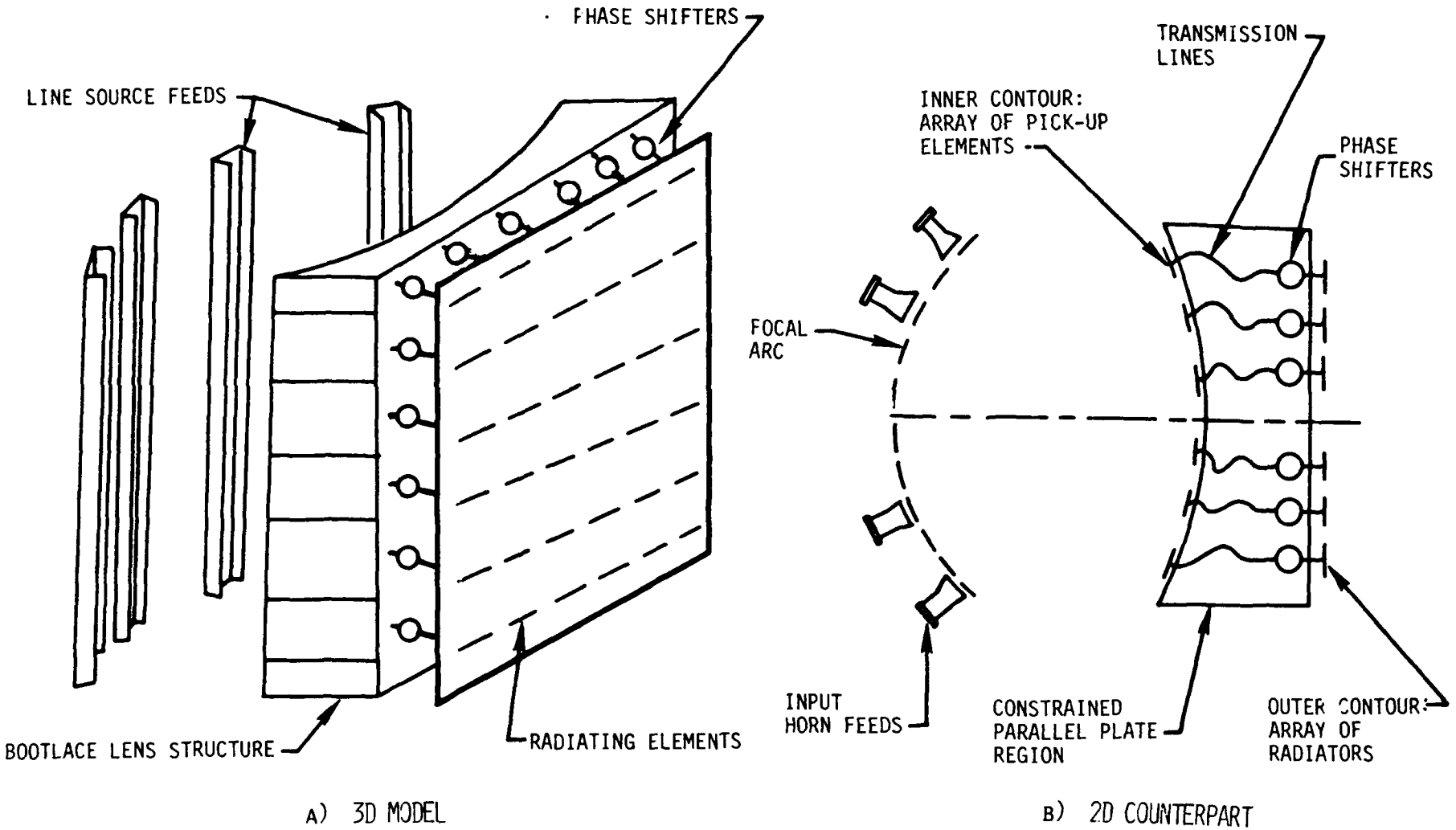

FIG. 3

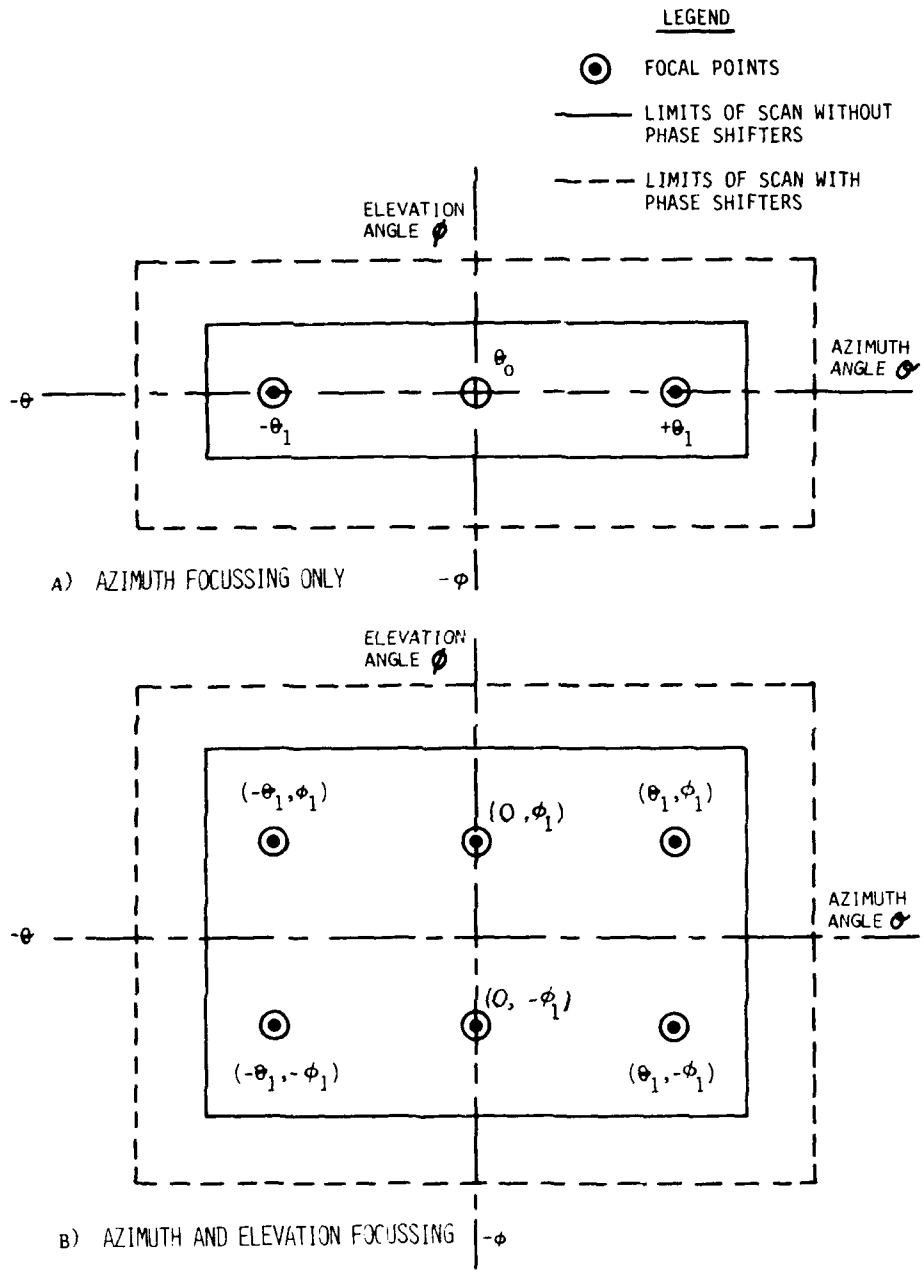

FOCUSSED BEAM LOCATIONS

FIG. 4

RAY DIAGRAM FOR 3D CYLINDRICAL LENS

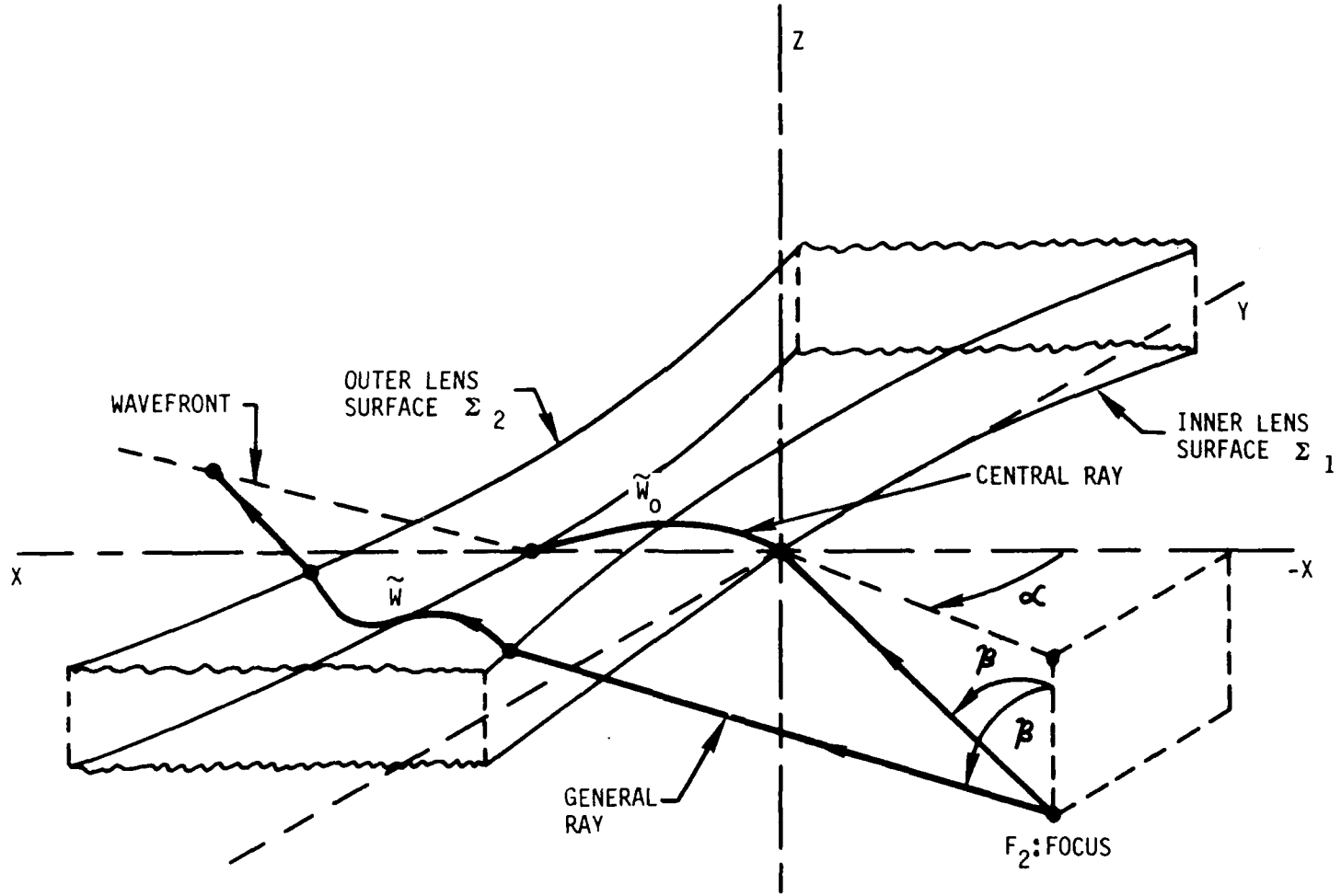

FIG. 5

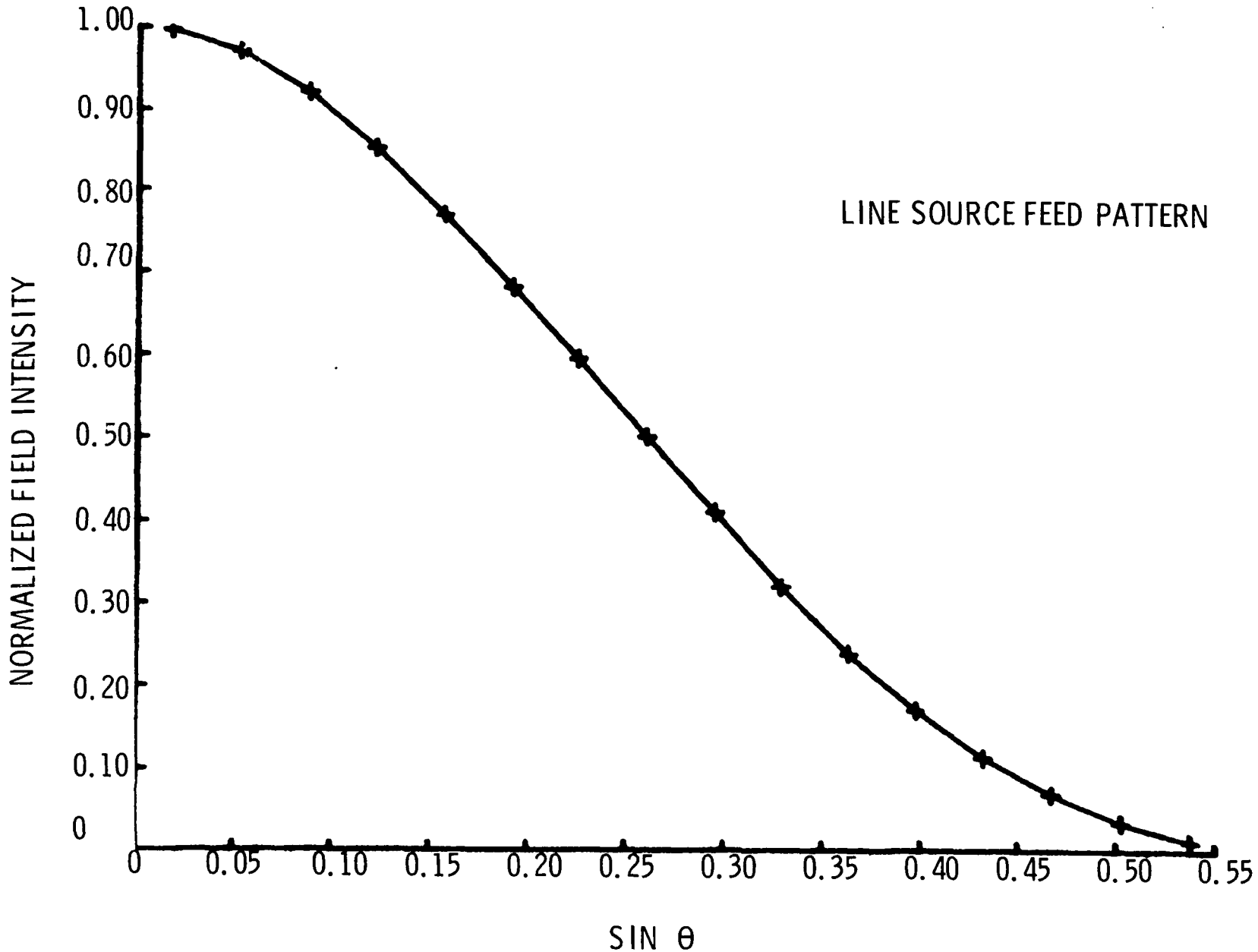
LINE SOURCE FEED PATTERN
NORMALIZED FIELD INTENSITY
1.00
0.90
0.80
0.70
0.60
0.50
0.40
0.30
0.20
0.10
0
0
0.05
0.10
0.15
0.20
0.25
0.30
0.35
0.40
0.45
0.50
0.55
SIN θ

FIG. 6

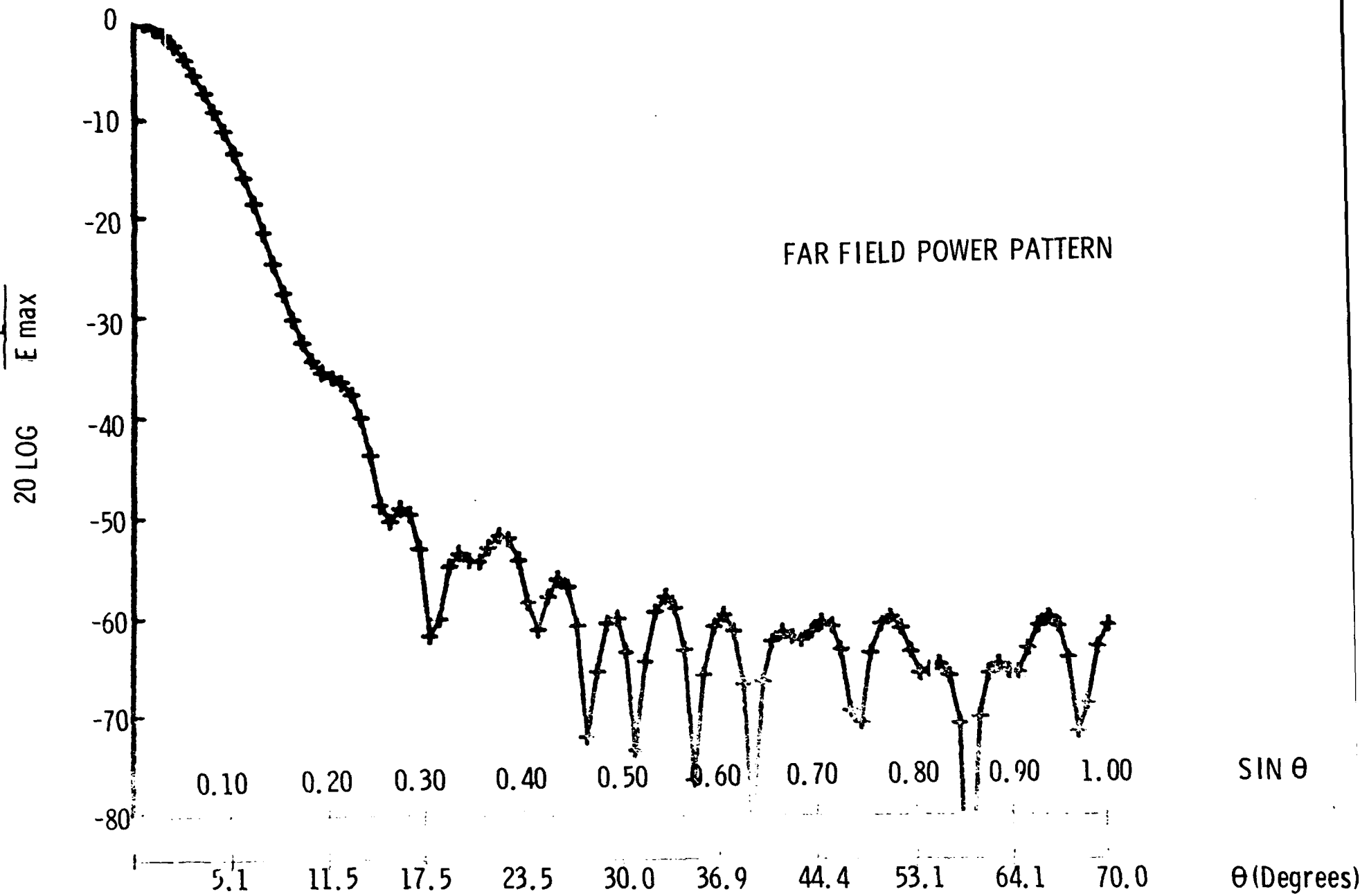
FAR FIELD POWER PATTERN
20 LOG E / E max
0
-10
-20
-30
-40
-50
-60
-70
-80
0.10
0.20
0.30
0.40
0.50
0.60
0.70
0.80
0.90
1.00
SIN θ
5.1
11.5
17.5
23.5
30.0
36.9
44.4
53.1
64.1
70.0
θ (Degrees)

FIG. 7

Hazeltine
Corporation
Greenlawn, N.Y. 11740 (516) 261-7000

INVESTIGATION OF METAL-GRID ANGULAR FILTERS

by
P. W. HANNAN
and
J. F. PEDERSEN

SUMMARY

An angular filter comprising several layers of crossed metal grids can provide rejection of waves at oblique incidence in any polarization, while passing waves at normal incidence. In practice, the amount of rejection provided by the filter should be limited by the tolerances that can be held during construction of the filter. Metal grids suitable for an angular filter have been tested in a new simulator that provides a range of incidence angles near grazing in the E plane.

SECTION I

INTRODUCTION

Angular filters comprising layers of dielectric have been synthesized and analyzed by Mailloux (Ref 1). Raytheon, under contract to RADC, has extended this synthesis and has tested an experimental model of a dielectric filter (Ref 2, 3).

Angular filters utilizing layers of metal grids have been proposed by Schell et al (Ref 4) and studied by Mailloux (Ref 5). Experiments with some metal-grid filters have been performed by Rope et al (Refs 6, 7). Mailloux and Franchi have analyzed and tested experimental models of metal-grid filters (Ref 8).

In comparison with dielectric filters, filters that use metal grids offer reduced weight and fabrication cost. Also, pure metal grids do not have the dielectric Brewster-angle effect that can cause a spurious passband for E-plane incidence. However, metal grids are generally supported by dielectric layers, so the question of spurious passbands still exists. There is also an important question of sensitivity to tolerances with either type of filter.

Under contract to RADC, Hazeltine is investigating the design of a metal-grid angular filter, with particular emphasis on the questions of spurious passbands and sensitivity to tolerances. Emphasis is also placed on a type of metal-grid configuration that is practical to construct in a large size filter, and is effective for any polarization. An experimental 5x5 foot X-band angular filter is presently being constructed.

In this paper, we report on some results of the first part of the investigation.

SECTION 2

THE METAL GRID ANGULAR FILTER

An angular filter is a device which passes or rejects an electromagnetic wave depending on the angle of incidence of this wave relative to the filter surface. A representative angular filter is indicated in Figure 1, in which waves incident at and near broadside (normal incidence) are passed by the filter but waves incident at angles further from broadside are rejected by the filter.

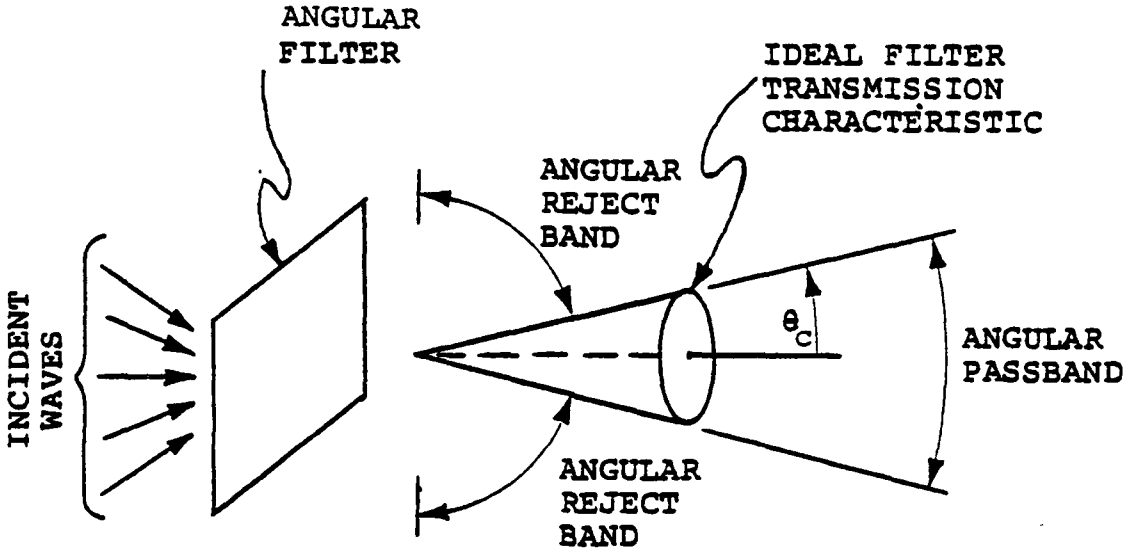

Figure 1. Angular Filter

Application of Angular Filter

If an angular filter is placed in front of a directive antenna, it can reduce those sidelobes of the directive antenna that correspond to waves that are incident in the angular reject band of the filter. The main lobe of the antenna corresponds to a wave that is incident in the angular passband of the antenna, and is not substantially affected by the filter. This case is indicated in Figure 2.

The antenna may have either a fixed main beam or a main beam that is scanning over a limited angular region. For a scanning beam antenna, the angular passband of the filter can encompass the scan region so that the main beam is always passed by potential grating lobes may be rejected. This application was considered by Mailloux (Ref 1). For a fixed-beam antenna such as the reflector antenna indicated in Figure 2, the filter can reduce the sidelobes caused by feed spillover, feed-support scattering, and reflector contour errors while retaining a strong main beam. The reflector antenna application is the one toward which this investigation is directed.

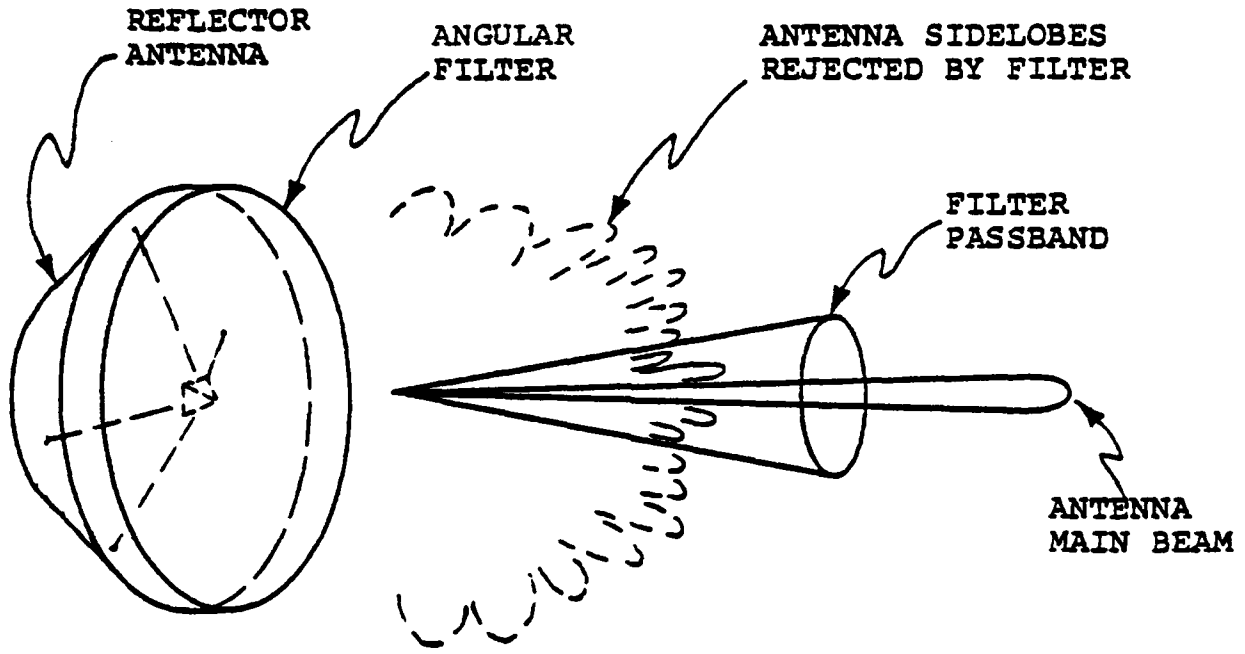

Figure 2. Application of Angular Filter to a Reflector Antenna

Approach for Angular Filter

There are various approaches that can achieve the angle-sensitive behavior needed for an angular filter. The approach considered in this investigation appears in Ref 4. This approach is reviewed here with the aid of Figure 3.

As indicated in the figure, the angular filter comprises a series of layers. Each layer acts essentially as a shunt susceptance to an incident plane wave. Between these susceptance layers are regions of essentially free space in which the plane wave travels in almost the same direction as its incidence direction.

In a transmission-line equivalent circuit of this angular filter the equivalent wavelength or "guide" wavelength (λ_g) is equal to the free-space wavelength divided by cos θ where θ is the angle of incidence. The phase shift between layers is therefore proportional to cos θ as well as to frequency. The nominal values for the susceptance layers and the phase shifts between layers can be specified so as to yield a conventional frequency filter. However, because the phase shifts between layers are proportional to cos θ as well as to frequency, the structure will also act as an angle-sensitive filter in which the term cos θ is the variable of significance. The net result is that the angular filter can be designed on the basis of a conventional frequency filter.

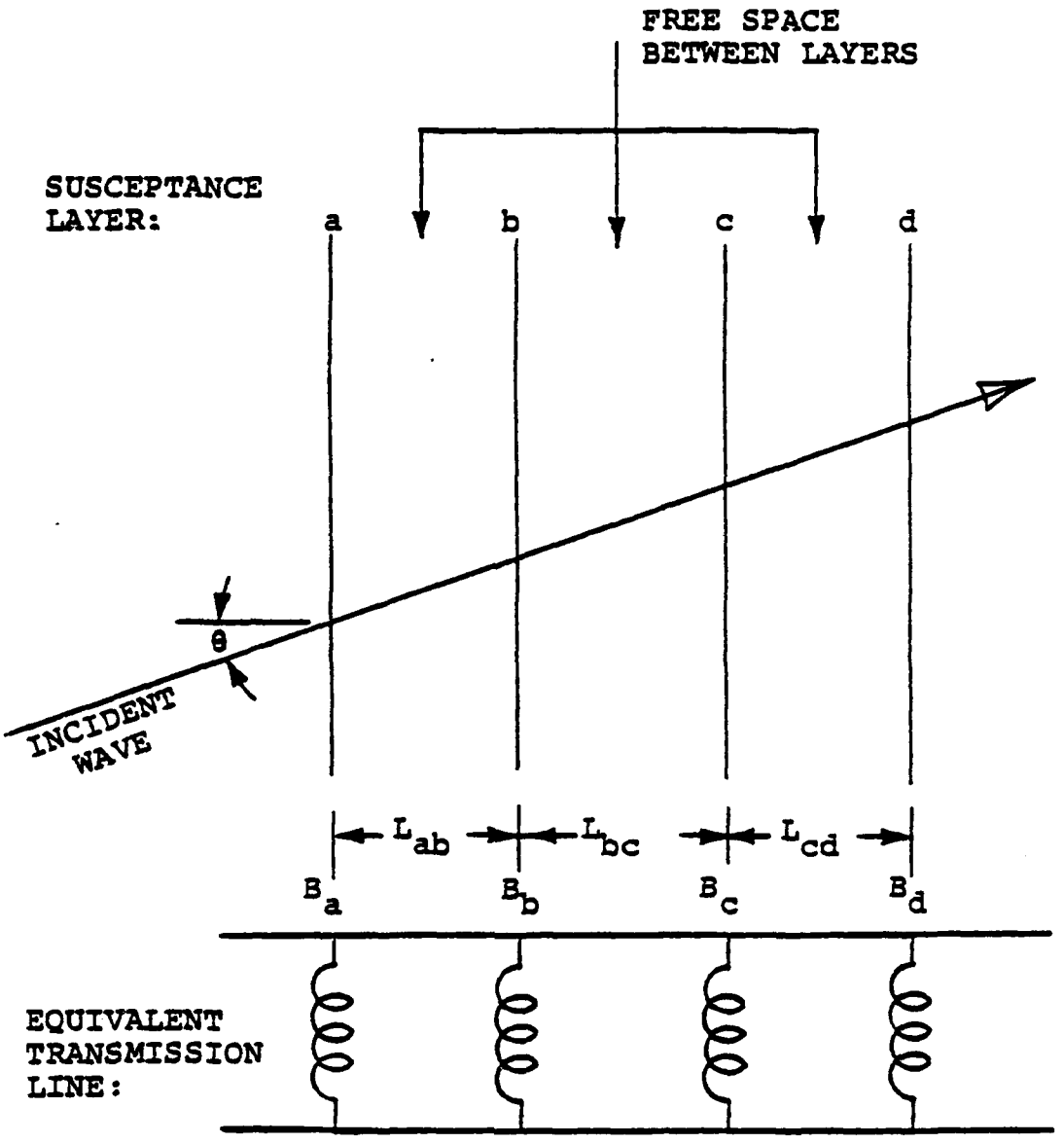

$$\text{EQUIVALENT WAVELENGTH} = \lambda_g = \frac{\lambda}{\cos\theta}$$

$$\text{EQUIVALENT PHASE SHIFT BETWEEN LAYERS} = \frac{2\pi L}{\lambda_g}$$

$$= \frac{2\pi L \cos\theta}{\lambda} = \frac{2\pi L}{c} f \cos\theta$$

Figure 3. Approach for Angular Filter

A choice exists as to where to locate the frequency passband on the curve of cos θ. The most generally useful choice is to center the frequency passband on θ = 0. This yields an angular filter with an angular passband nominally at broadside, and gives the widest frequency bandwidth of operation before a change in frequency causes the filter to reject a wave incident at broadside.

Frequency Bandwidth

The frequency bandwidth of operation of the type of angular filter described above can be estimated by consideration of the relation between cos θ and frequency. The resulting approximate formula for bandwidth is:

$$\frac{\Delta f}{f_m} = \frac{\sin^2\theta_c}{\cos\theta_c} \simeq \theta_c^2$$

$$\simeq \frac{1}{\pi} \times \text{passband solid angle}$$

$$\simeq 2 \times \frac{\text{passband solid angle}}{\text{hemisphere solid angle}}$$

where Δf is the full frequency band of operation, f_m is the mid frequency (geometric mean), and θ_c is the cutoff angle (edge of angular passband) of the angular filter at the mid frequency.

This simple formula gives the maximum possible bandwidth that could be obtained if the layer susceptances of the filter vary ideally with incidence angle and if the filter need only pass a wave at $\theta = 0$ (ie, the filter is used for a very narrow beam antenna). A similar formula appears in Ref 8. For a θ_c of 20° the bandwidth is about 12%, while for a θ_c of 10° the bandwidth is about 3%. It is evident that if the angular filter is to have a reasonably wide frequency band of operation, the filter should not be designed for a very narrow angular passband. It should be noted that a very narrow angular passband implies that substantial excess aperture may be needed (Ref 8), and this is also undesirable.

Figure 4 illustrates the relation between % frequency bandwidth and the ratio of passband solid angle to hemisphere solid angle at midband. With a 12% bandwidth the passband solid angle at midband is about 6% of the hemisphere solid angle, giving a reject band at midband having 94% of the hemisphere solid angle. If this filter provided adequate rejection throughout the reject band, then 94% of the antenna sidelobes in the forward hemisphere at midband would be filtered out. The sidelobes near the main beam would remain; these sidelobes are controllable only by the antenna itself. Of course, a practical angular filter does not have an abrupt cutoff at θ_c, nor does it necessarily have adequate rejection throughout the rest of its reject band; this is the main subject under investigation.

Choice of Basic Metal Grid

An inductive metal grid is preferred to a capacitive metal grid for the angular filter, because large susceptances can be obtained without difficult control of mechanical tolerances. Another choice is between a simple parallel grid and a crossed grid (two parallel grids crossed to each other). Although the crossed grid is more complex to construct, it is effective for any polarization of the incident wave. The crossed grid has been selected for this investigation.

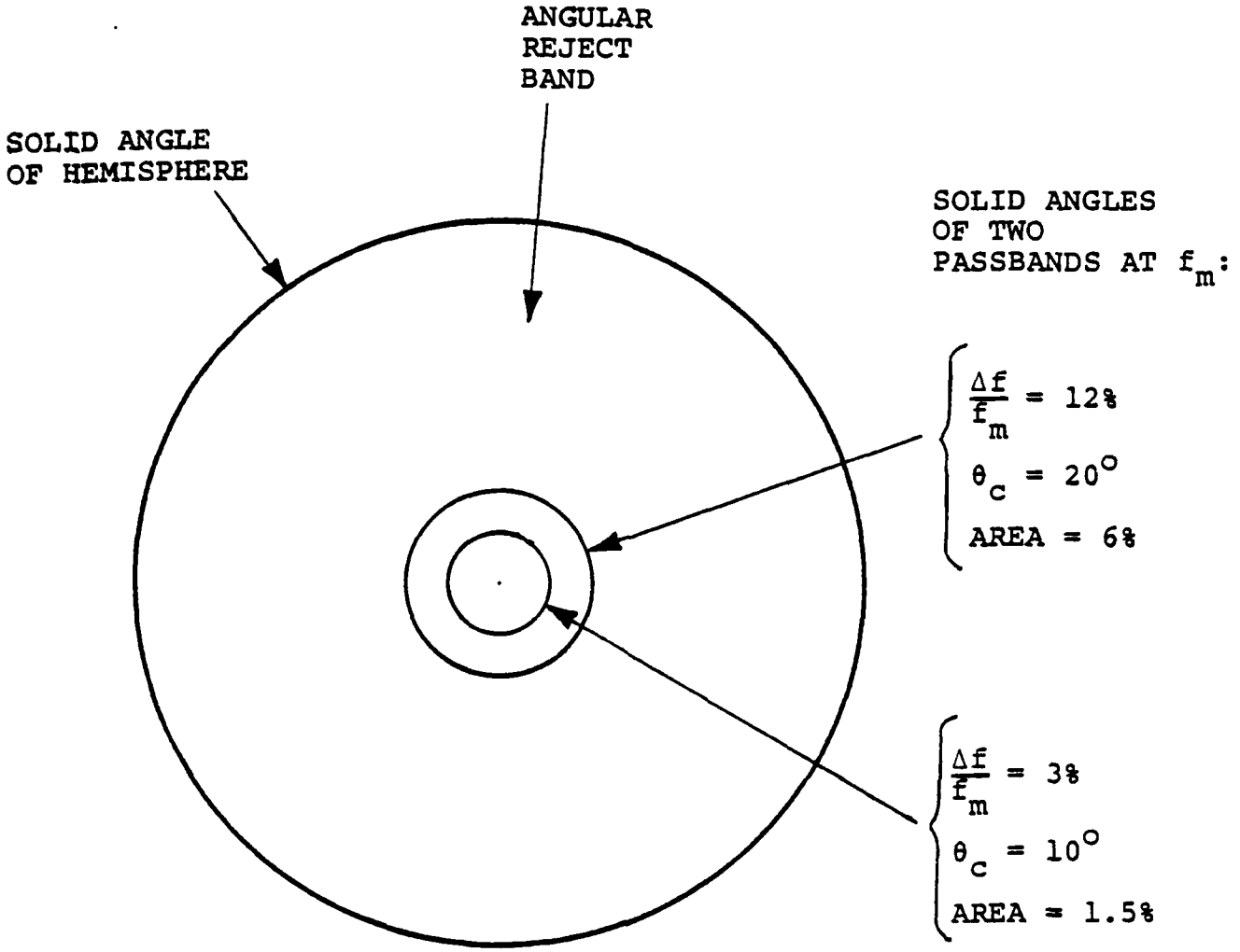

Figure 4. Examples of Relation Between Bandwidth and Passband Solid Angle

Susceptance of Crossed Metal Grids

The design and performance of a metal-grid angular filter is dependent on the susceptance behavior of the metal grids. A crossed grid of metal wires is shown in Figure 5. The angle of incidence θ and the orientation of the plane of incidence ϕ relative to the wires are indicated. The standard conventions for H-plane incidence and E-plane incidence are given. It is assumed that the grid is a square grid, that the spacing s is small compared to a wavelength, and that the diameter d of the wires is small compared to their spacing. It is also assumed that there is electrical contact between the two crossed sets of wires.

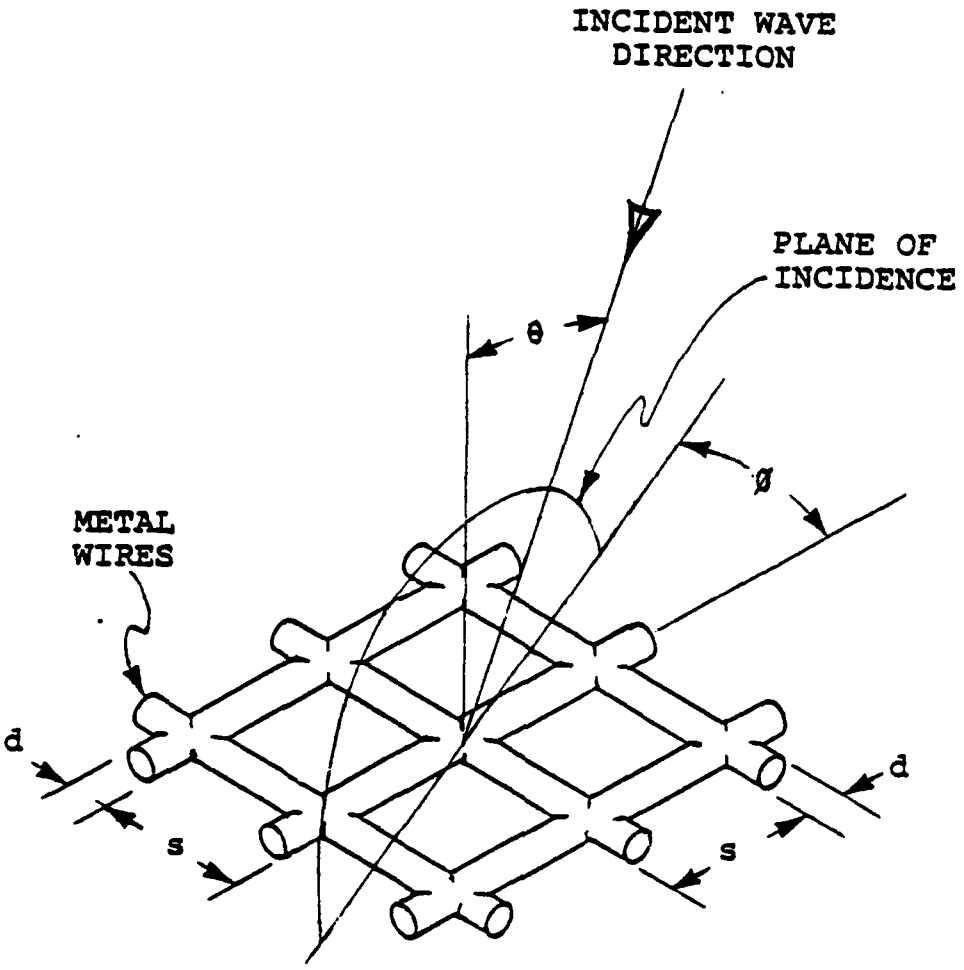

Figure 5. Geometry for Contacting Crossed Grid

At broadside incidence and for angles of incidence in the H-plane this crossed grid behaves approximately the same as a parallel wire grid in which all the wires are parallel to the incident electric field. MacFarlane (Ref 9) derived the inductive susceptance of a parallel grid of round wires for H-plane incidence. The approximate formula for inductive susceptance of the grid of wires for H-plane incidence is:

$$B_H \simeq - \frac{\lambda}{s \cos\theta \ln\left(\frac{s}{\pi d}\right)}$$

An interesting feature of this formula for B_H is the exact 1/cos θ variation of susceptance. This results in an angular filter that for H-plane incidence corresponds exactly to a frequency filter using shunt inductances in a transmission line. The design formulas given in Matthaei, Young, and Jones (Ref 10), for example, will yield a Chebyshev response in which cos θ replaces frequency as the variable of interest. This is the basis for the angular filter designs described in this paper.

For the E-plane of incidence a formula for the reflection coefficient of a contacting crossed grid of wires has been derived by Kontorovich et al (Ref 11) and Astrakhan (Ref 12). This relation, when converted to inductive susceptance, is:

$$B_E \approx - \frac{\lambda}{s \cos\theta \ln\left(\frac{s}{\pi d}\right)} \frac{\cos^2\theta}{1 - \frac{1}{2}\sin^2\theta}$$

The first term is the same as the H-plane formula. The second term is an angle-dependent term which has the effect of maintaining the susceptance nearly constant from 0° to 45° (fourth-order variation with θ), and then reducing the susceptance to zero at 90°.

Figure 6 shows an example of the transmission through one crossed metal grid vs. θ, for H-plane and E-plane incidence. The H-plane variation is desirable for an angular filter because it will provide greater rejection at large angles of incidence. The E-plane variation is not desirable because the filter rejection will become small near 90° where substantial rejection may be desired. Furthermore, with a small B_E near 90°, the filter may be susceptable to spurious passbands caused by other structures such as dielectric supporting materials.

The susceptance formulas given above are employed in the computations of angular filter performance given in the following section. The effects of practical modifications to the metal grids, such as non-contacting junctions between the crossed grids and the effect of dielectric supporting structure, are addressed in a later section.

SECTION 3

ANGULAR FILTER DESIGN ANALYSIS

It is the objective of this analysis to examine the basic tradeoffs between the filter parameters of passband width, passband ripple, number of poles, and the related qualities such as rejection capability and sensitivity to tolerances. For this purpose, only the essential elements of the filter (the susceptances and the lengths) are considered, without the perturbing effect of the dielectric materials that would be needed in a self-supporting construction. A basic factor that limits the performance available from the angular filter is the sensitivity to tolerances, as will be discussed.

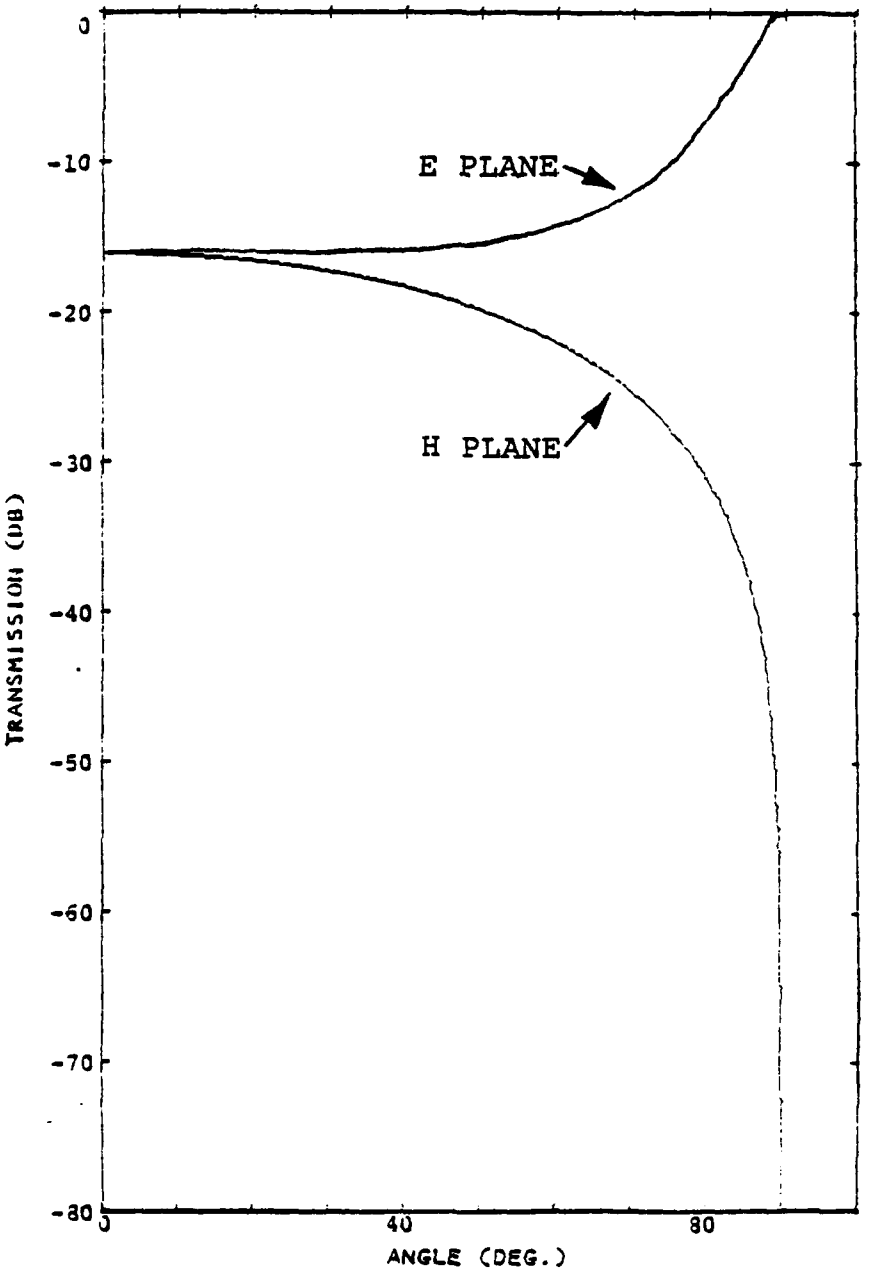

Figure 6. Transmission of One Metal Grid

Basic Filter Design

The design of the angular filter follows conventional frequency filter methods, which are well-documented in the literature (Ref 10). The narrowband design technique of Ref 10 is used since it is straightforward and is adequate for the major purposes of this study. A Chebyshev equal-ripple type has been selected by reason of its characteristic sharp cutoff beyond the passband. For any desired combination of passband width, number of poles, and passband ripple, the filter element values can be determined. For speed and accuracy, a computer

provides the nominal filter element values, ie, the various lengths and susceptances in each filter. Figure 7 shows the three types of filters that have been analyzed.

Nominal element values have been obtained for a number of 2-, 3-, and 5-pole filters of various passband widths and ripple values. The passband widths are grouped in three representative values within a ±10° to ±20° range, and passband ripple values range upward and downward from a typical value of .01 dB transmission loss. Table 1 lists the

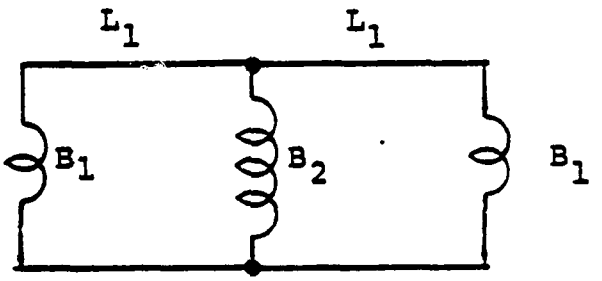

(a) Two-pole filter

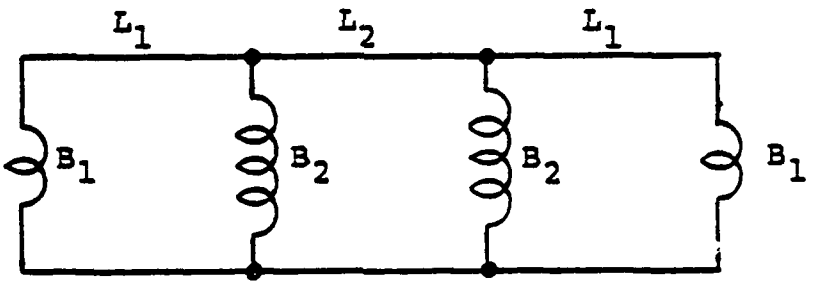

(b) Three-pole filter

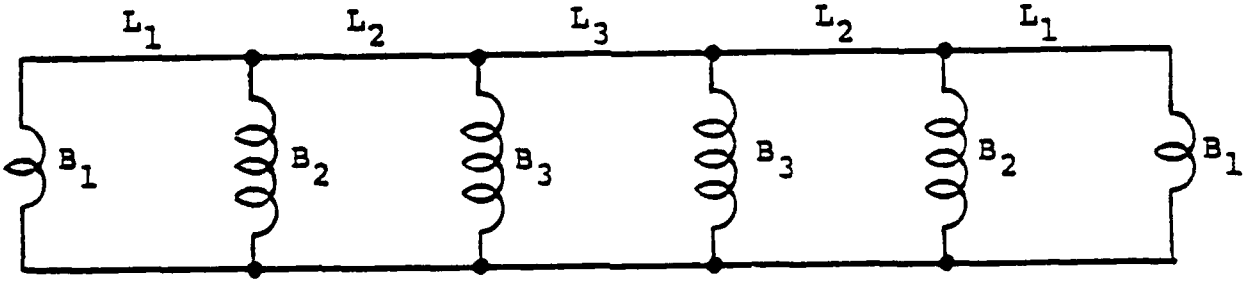

(c) Five-pole filter

Figure 7. Filter Elements for 2-, 3-, and 5-Pole Filters

various designs, and identifies each with a code indicating the design values. The letters A, B, and C denote passband widths of ±11.5, ±14 or ±18 degrees; the first number indicates the number of poles and the second number counts the number of zeros in the ripple dB value.

TABLE 1

FILTER IDENTIFICATION CODE

Filter Code	Passband Width (deg)	Quantity of Poles	Ripple (db)
A20	±11.5	2	.1
A21	±11.5	2	.01
A22	±11.5	2	.001
B20	±14.0	2	.1
B21	±14.0	2	.01
B22	±14.0	2	.001
C20	±18.0	2	.1
C21	±18.0	2	.01
C22	±18.0	2	.001
A31	±11.5	3	.01
A32	±11.5	3	.001
B31	±14.0	3	.01
B32	±14.0	3	.001
C31	±18.0	3	.01
C32	±18.0	3	.001
A51	±11.5	5	.01
A52	±11.5	5	.001
A54	±11.5	5	.00001
A56	±11.5	5	.0000001
B51	±14.0	5	.01
B52	±14.0	5	.001
B54	±14.0	5	.00001
B56	±14.0	5	.0000001
C51	±18.0	5	.01
C52	±18.0	5	.001
C54	±18.0	5	.00001
C56	±18.0	5	.0000001

Nominal Filter Performance

For each of the selected filter designs, performance with nominal element values has been computed and plotted. The plots include transmission loss, reflection coefficient, and insertion phase as a function of incidence angle in both the H-plane and E-plane. An example of the plots of transmission loss is shown in Figure 8. This particular filter has a nominal passband ripple of 0.001 dB and a nominal passband width (at the 0.001 dB point) of $\theta_c = \pm 14°$. Actually, because the filter

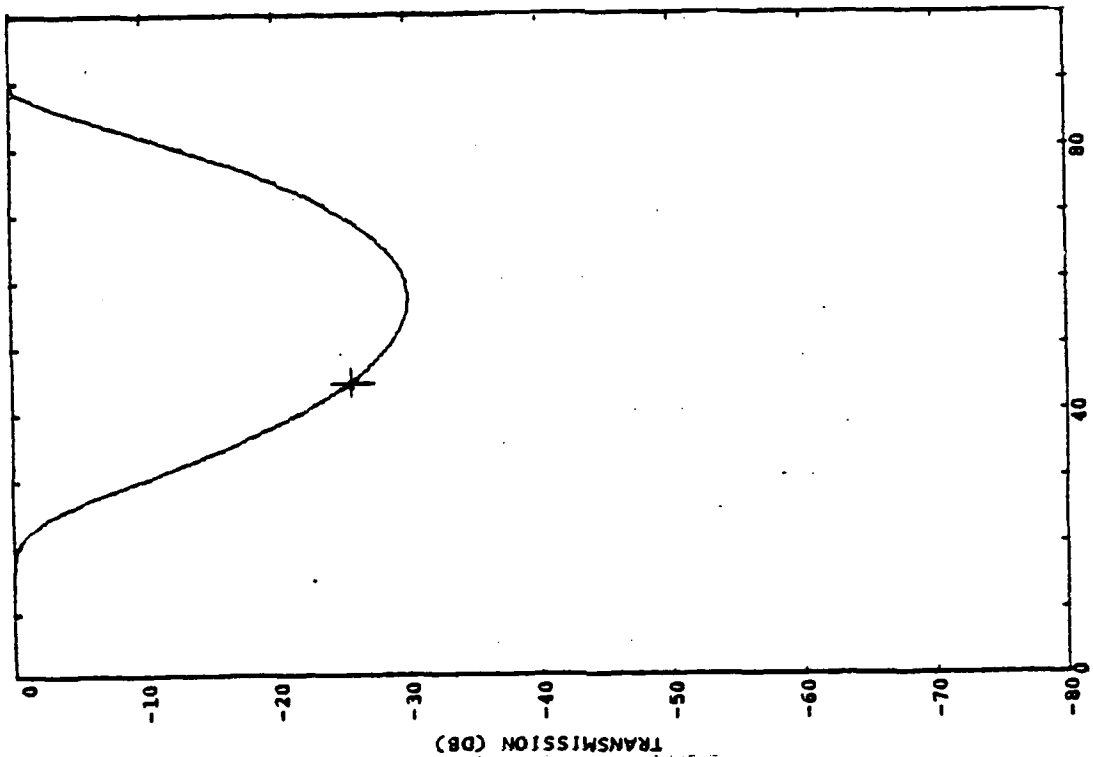

(b) E Plane

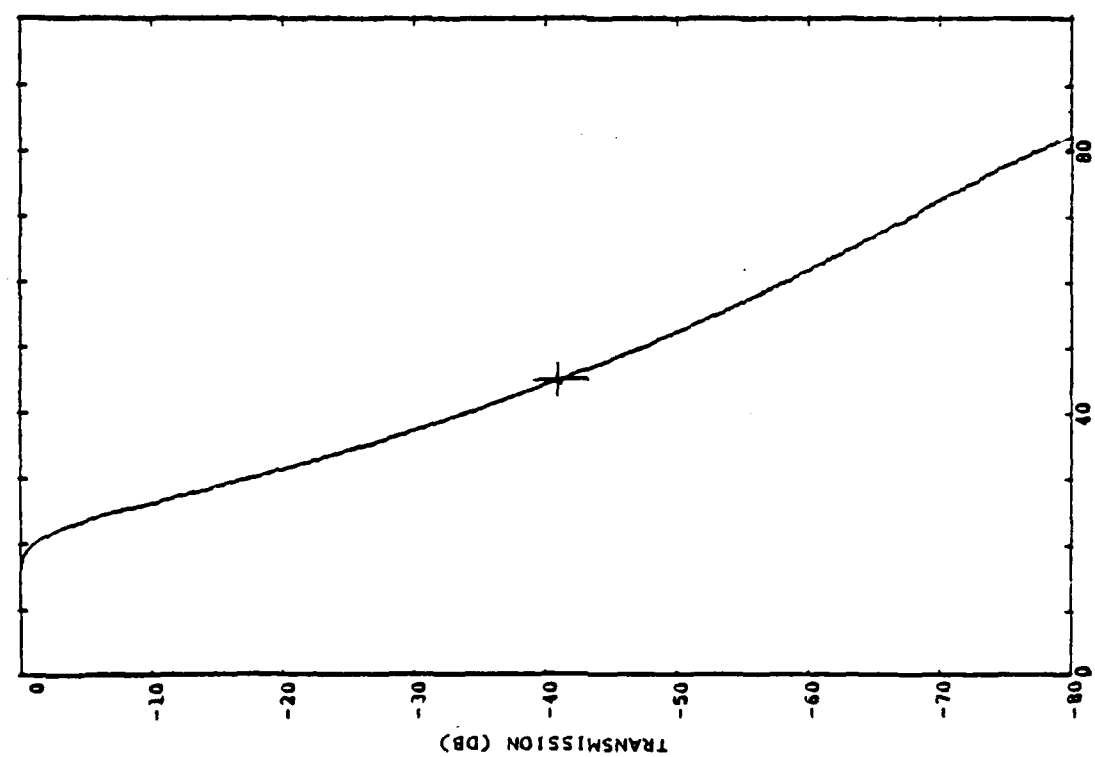

(a) H Plane

Figure 8. Transmission, Filter B32, H- and E-Planes

cutoff characteristic is gradual, a substantial value of rejection is obtained only beyond about 25°. As expected, the rejection is greater in the H-plane than in the E-plane, particularly near $\theta = 90°$.

In order to compare the various filters in Table 1, a single evaluation quantity is desirable. In this study we have arbitrarily selected the dB rejection at $\theta = 45°$ in the H-plane as the standard of comparison. This quantity can perhaps be regarded as the "strength" of the angular filter.

Figure 9 shows the rejection at $\theta = 45°H$ for the various filters. Several basic relationships are apparent in this plot. Rejection decreases with increased passband width for any given number of poles and ripple level. Rejection increases with an increase in ripple value, for any given number of poles and passband width. Rejection also increases with an increase in the number of poles for any given passband width and ripple level. In general, there are many combinations of passband width, number of poles and ripple level that can give a particular nominal value of rejection.

An interesting correlation is shown in Figure 10, relating the sum of all the susceptive (B) elements of a filter to its rejection at 45°H. For a given quantity of poles, a single curve relates the rejection to the total B, regardless of passband width or ripple level. More poles tend to give greater rejection for a given total B, particularly for filters with large rejection.

Filter Tolerances

In theory, it is possible to obtain very large values of rejection outside of the passband while retaining a negligible loss within the passband. Since the inductive susceptance of metal grids can be made very large simply by using small values of s/λ, a large value of rejection outside the passband would seem to be feasible. However, the effect of filter tolerances must be considered before any conclusion is reached.

When an angular filter is placed on the aperture of an antenna, it is intended to pass the main-beam energy without any distortion. However if the filter introduces a substantial variation of either transmission amplitude or transmission phase across the aperture, then it can create sidelobes. Also, if the filter reflects substantial main-beam energy, there may be interaction between the filter and the antenna that creates sidelobes. These sidelobes may be particularly harmful if they occur within the filter passband.

The angular filters shown in Figures 3 and 7 comprise a series of resonators. The resonant frequency of each resonator is determined primarily by the length L between adjacent metal-grid layers. If any L deviates from its nominal value, then there will be a deviation of transmission phase through the filter at broadside incidence. There will also be some reflection of a wave at broadside incidence.

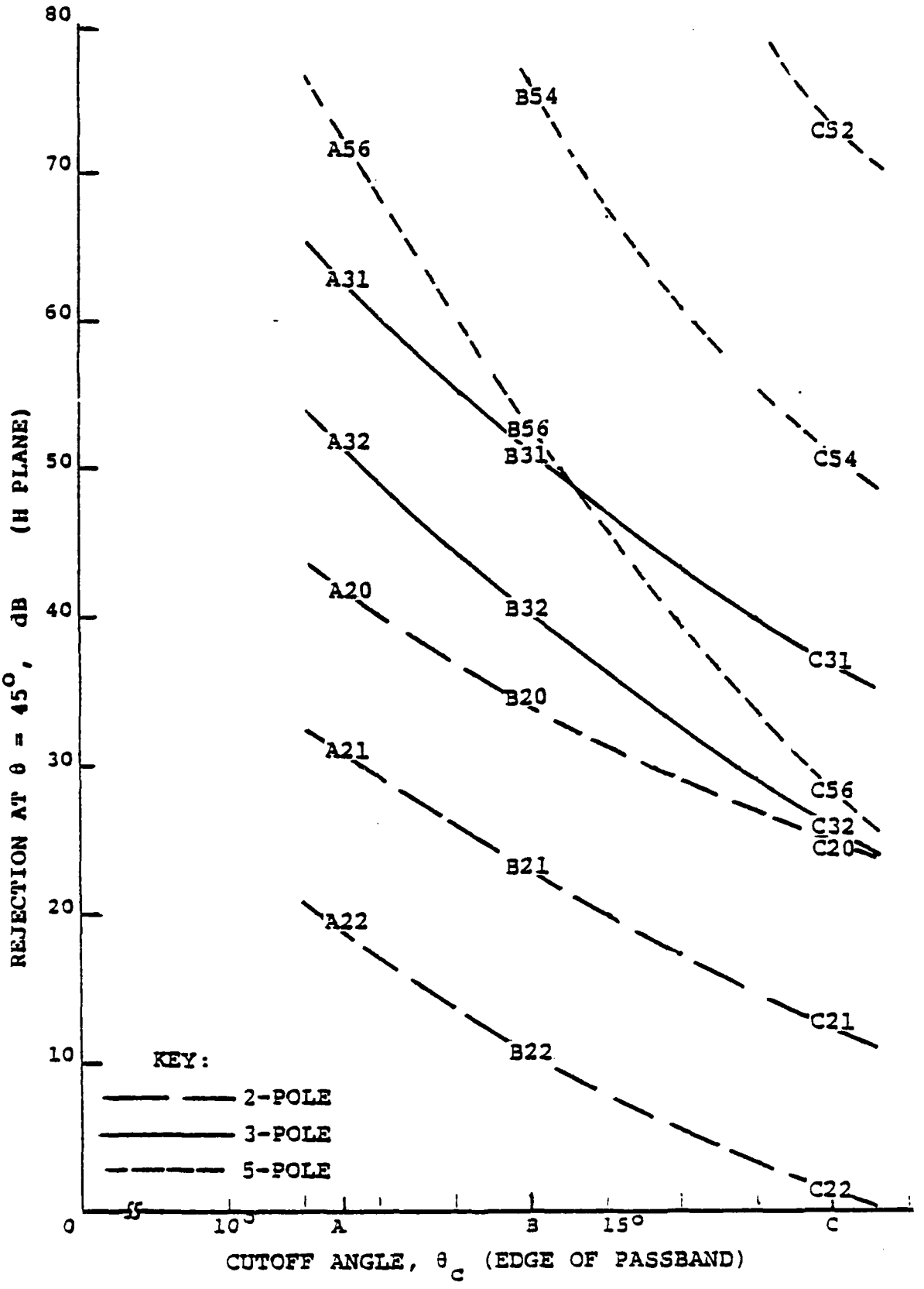

Figure 9. Rejection for Filters with Various Parameters

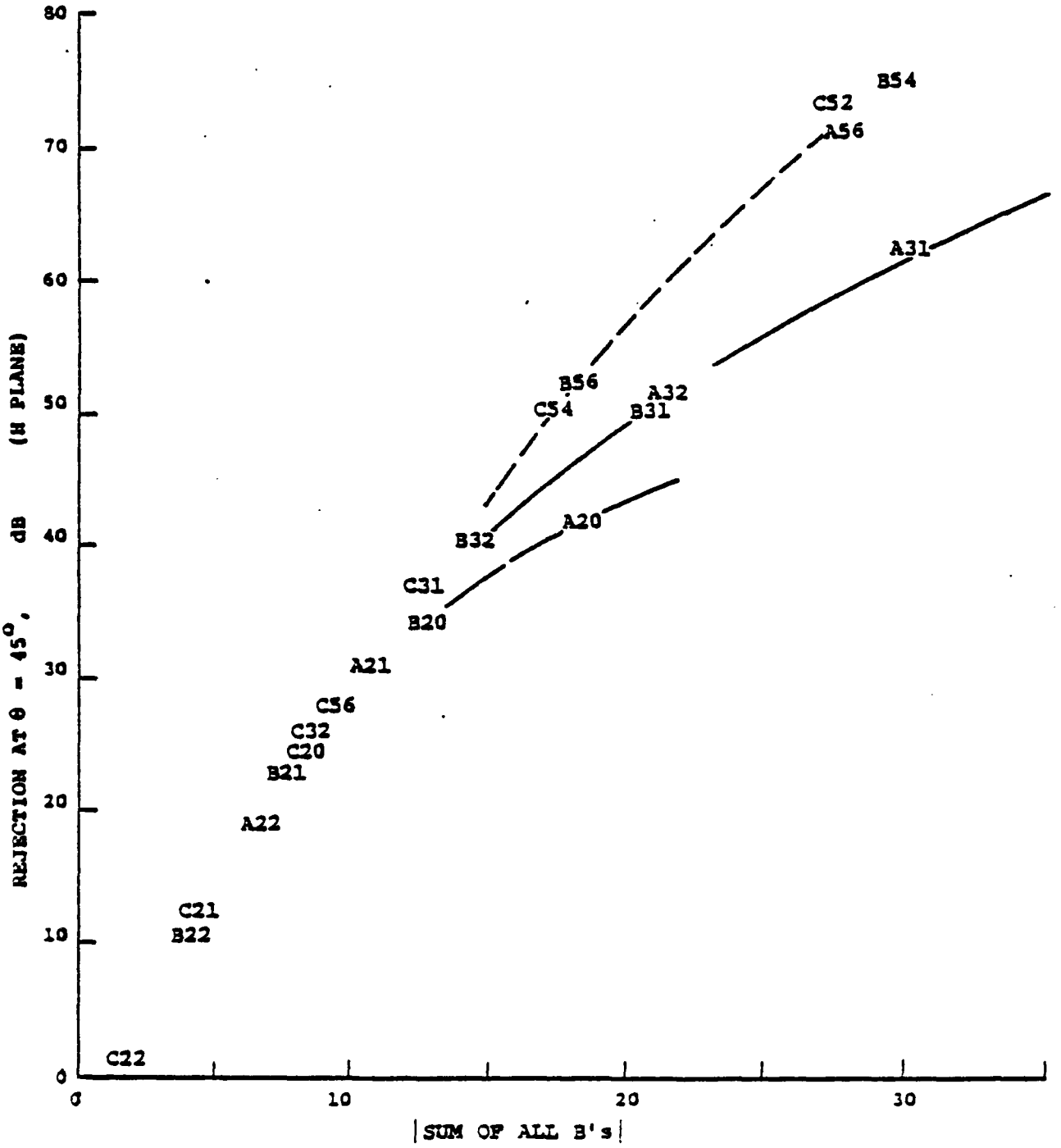

Figure 10. Rejection vs. Susceptance Sum for Various Filters

The magnitudes of these performance errors depend not only on the amounts of the errors in L, but also on the Q of each resonator. With high Q, a small error in L can cause large performance errors. High-Q resonators correspond to large susceptance values, which correspond to large values of filter rejection in its reject band. Thus, a filter that gives a larger rejection should be more sensitive to tolerance errors.

The sensitivity to various tolerance errors has been computed for various filters. An example is given in Figure 11. The vertical coordinate in this figure is the % tolerance on the central L of a filter that will cause an insertion phase error ($\Delta\phi_i$) of 5°, which is arbitrarily assumed to be just tolerable. The horizontal coordinate is the filter rejection at 45° in the H-plane. As expected, there is a clear trend of tighter tolerances required for greater filter rejection. It is also seen that more poles can permit a looser tolerance, but more poles require a more complex filter construction with more tolerances that must be controlled.

The tolerances considered in Figure 11 are given on a percentage basis. However, the actual construction of an angular filter would be likely to employ core material such as honeycomb as the principal means for controlling the length dimensions, and these materials typically can be made with length tolerances that are specified directly rather than as a percent of their length. For example, assume that a 0.010 inch tolerance on L is available, independent of the actual length. For an L of about $\lambda/2$, this corresponds to about 1.8% at 10 GHz and to about 0.6% at 3 GHz. As a result, a filter that gives no more than the assumed allowable 5° insertion phase error can be designed to provide considerably greater rejection at 3 GHz than at 10 GHz.

Figure 12 shows curves of the rejection at 45°H that is allowable vs. the frequency of operation of a 3-pole angular filter, assuming particular values for the center-length tolerance in inches, and using certain values of allowable insertion phase error ($\Delta\Phi_i$) as the basis. For a 0.010 inch tolerance on the center length and a 5° allowable $\Delta\Phi_i$, the allowable rejection at 45° is about 31 dB at 10 GHz and about 57 dB at 3 GHz.

The curves of Figure 12 are for a 3-pole filter. For a greater number of poles, the effect of frequency of operation is still greater. It is interesting to note that over the range of values plotted in Figure 12, the curves of dB rejection vs. log frequency are substantially linear and parallel. Over this range a 3-pole angular filter at 45°H yields about 15 dB less allowable rejection per octave of frequency.

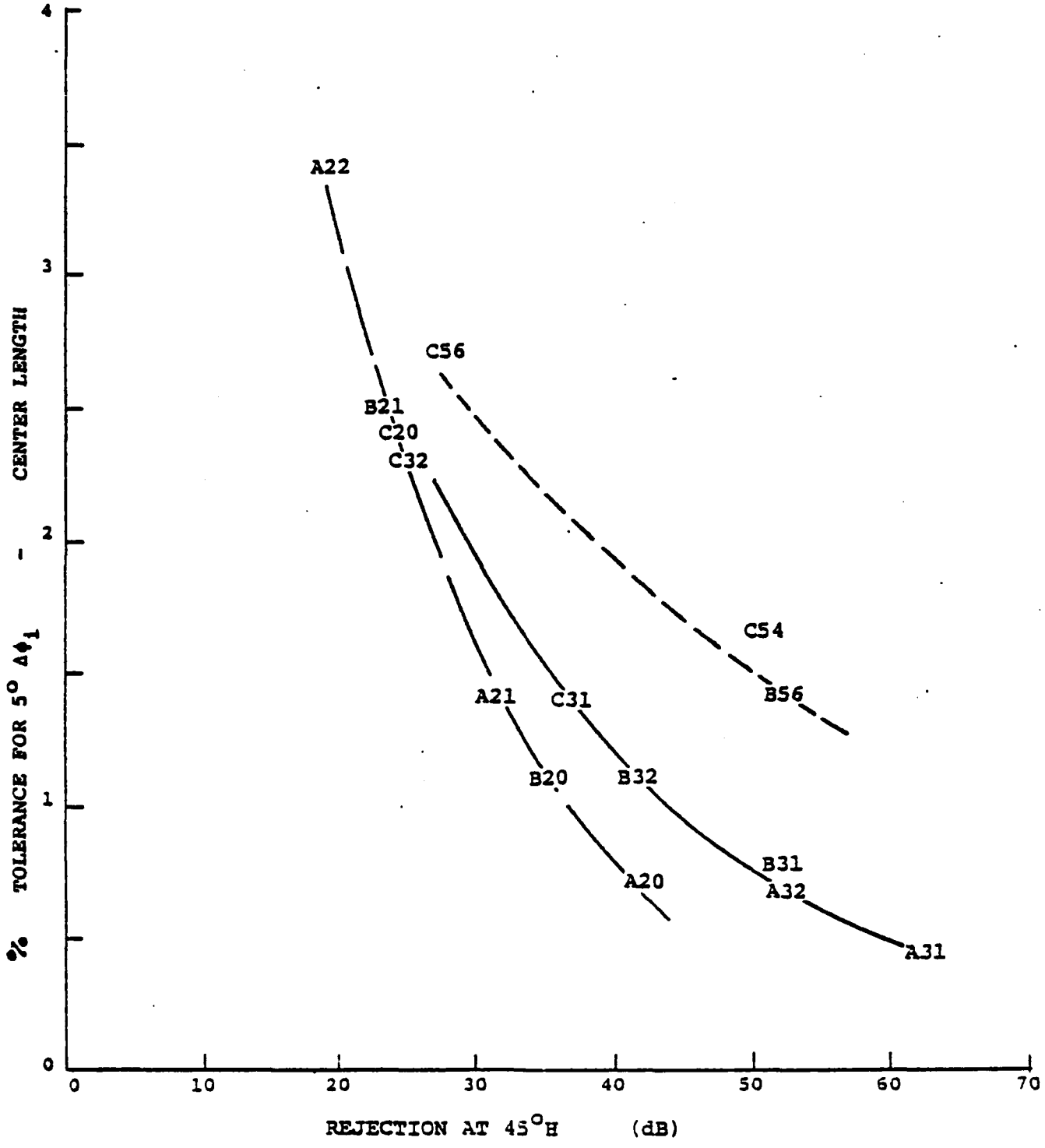

Figure 11. Tolerance on Center Length vs. Rejection for 5° $\Delta\phi_i$ Allowable

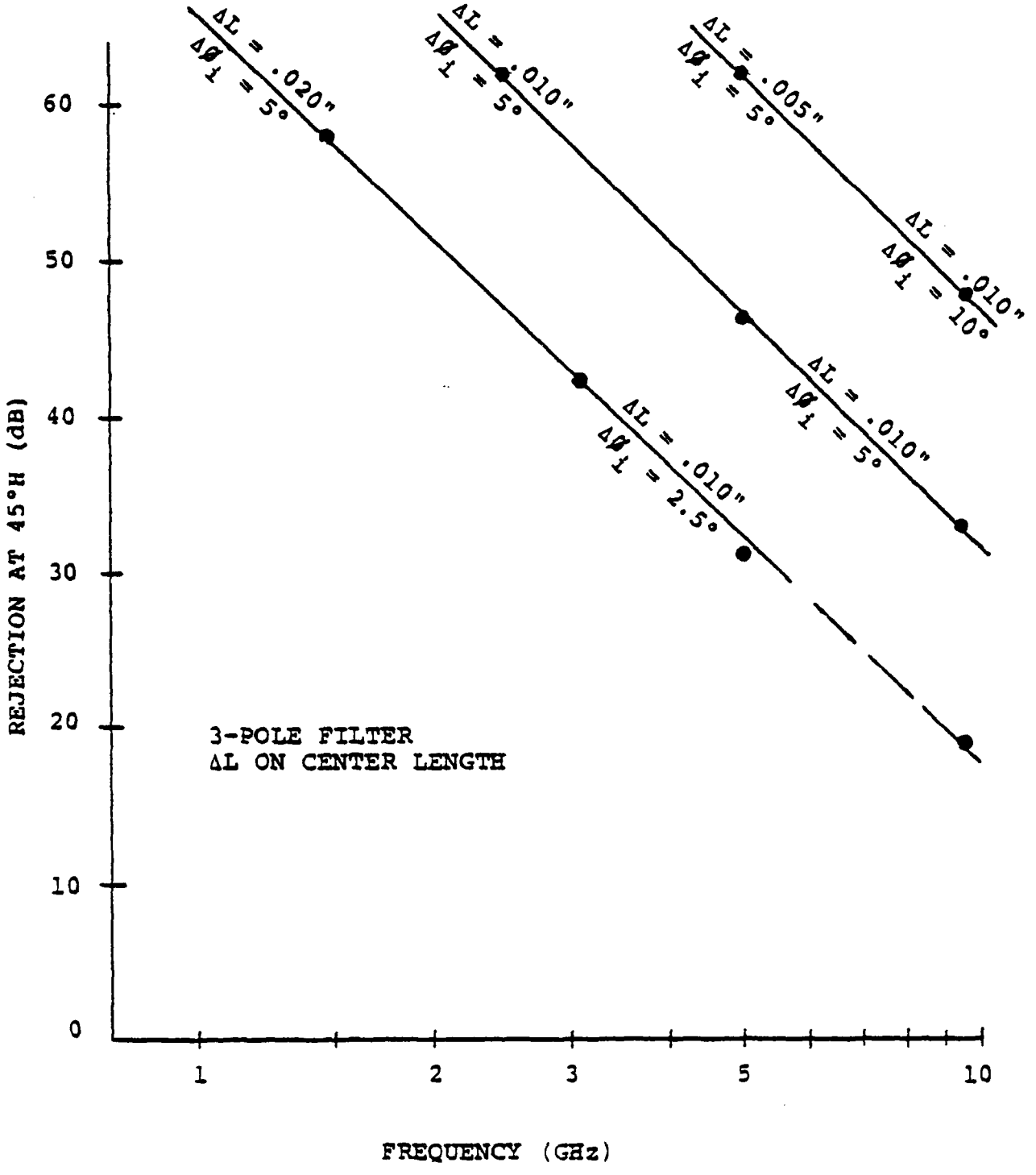

Figure 12. Allowable Rejection vs. Frequency

SECTION 4

TESTS OF A PRACTICAL METAL GRID SUPPORTED BY DIELECTRIC

In a practical angular filter the metal grid would need to be supported by dielectric. Figure 13 shows a dielectric support structure in which the metal grids are supported by thin dielectric skins, and the separation between metal-grid layers is obtained by a low-k dielectric core material such as dielectric honeycomb or foam. If one assumes that the inductive susceptance of the metal grid vs. incidence angle is unaffected by the dielectric, then it is a straightforward matter to include the dielectric structure in the computation of angular filter performance. However, this assumption is not a safe one to make for the metal grids with dielectric skins in the E-plane of incidence.

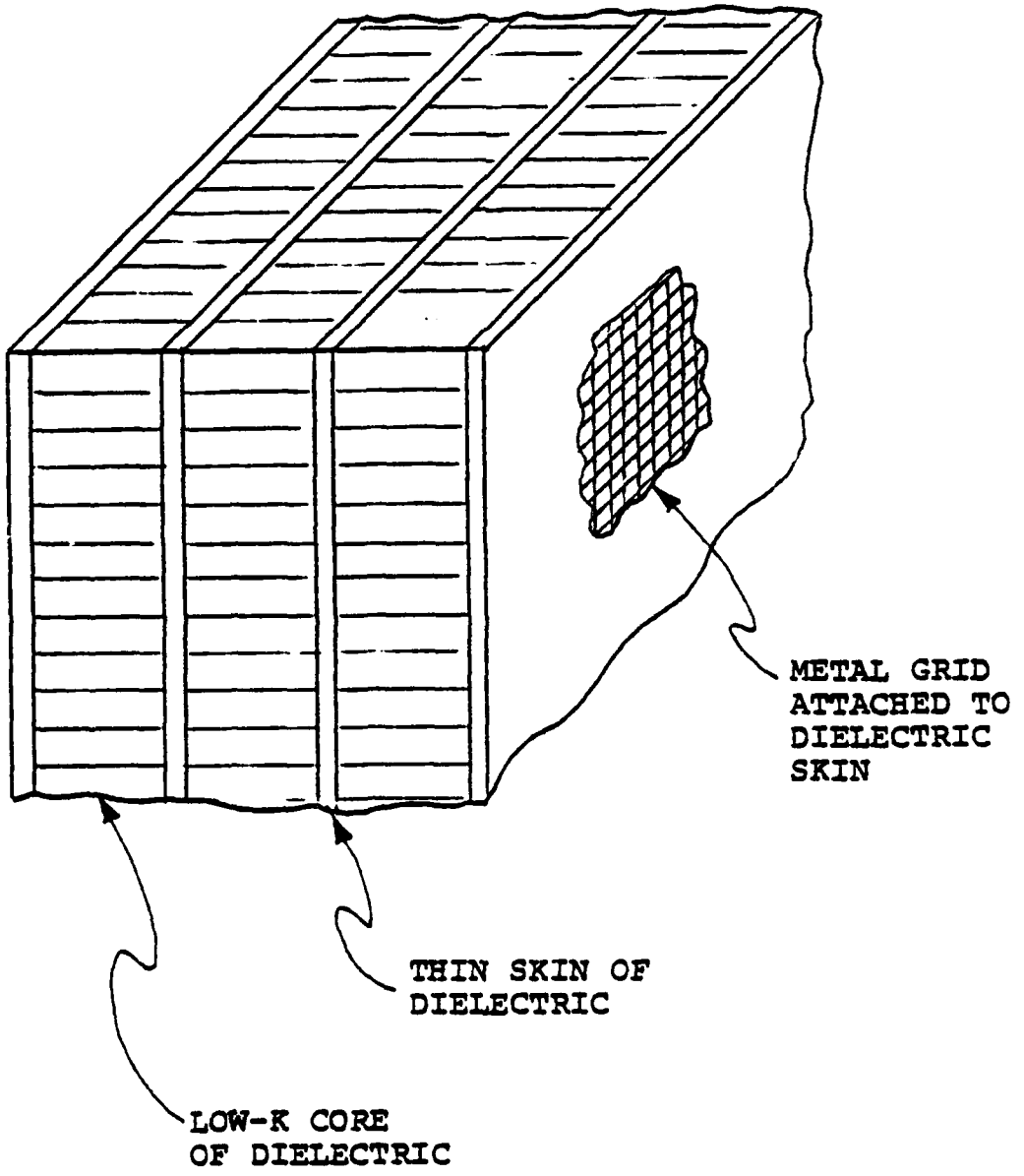

Figure 13. Dielectric Support Structure for Metal Grids in an Angular Filter

The crossed metal grid of wires that was shown in Figure 5 has electrical contact at all the intersections. However, this is expensive to construct. Alternate forms of contacting crossed metal grids, such as printed strips or holes in metal sheets, have practical size limitations if contact is to be reliably and economically obtained throughout the structure. A crossed grid configuration that is economical and that has no clear size limitation is the non-contacting or insulated grid of wires shown in Figure 14. This grid is embedded in a dielectric skin for support and also to insure that accidental contact does not occur.

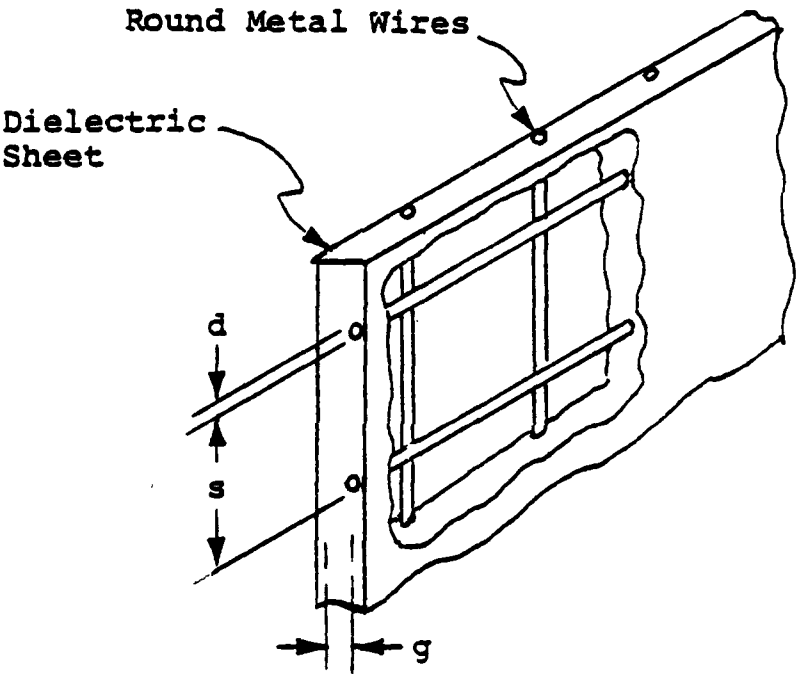

Figure 14. Insulated Crossed Grid of Metal Wires

The insulated crossed grid of metal wires has a less simple dependence of susceptance on incidence angle in the E-plane than does the contacting crossed grid (Ref 11, 12). The presence of the dielectric skin adds a further uncertainity, and introduces the possibility that the metal-grid susceptance may be considerably less than hoped for at large angles of incidence in the E-plane. Conceivably, the susceptance might approach zero at some angle, yielding a spurious passband.

A test was desired that would accurately measure the transmission through a metal grid over a range of incidence angles near grazing incidence in the E-plane. Since several grid and dielectric configurations were to be measured, a test that required only a small sample of the grid was needed. An infinite-array simulator (Ref 13, 14, 15) using waveguide operating near cutoff was developed for this purpose.

The Near-Grazing Simulator

For E-plane incidence, the simulator uses the TM-11 mode in square waveguide. The size of the waveguide in which the grid sample is mounted is only 1.005 times the cutoff dimension at the lowest frequency of operation, giving an angle of incidence only 6° from grazing incidence. Operating at higher frequencies permits a range of incidence angles further from grazing to be covered.

Figure 15 shows a diagram of this near-grazing-incidence simulator. On each side of the grid sample is a long taper (five feet at 5 GHz) to match the almost cutoff sample waveguide into the other components. A pair of tuners minimizes the residual mismatch in the system. Figure 16 is a photograph of the near-grazing simulator.

Tests of Metal-Grid Samples

A number of metal-grid samples were measured in the simulator. Figure 17 shows one such sample comprising a crossed grid of wires having an air gap between the two crossed sets. Figure 18 shows data points for the measured transmission through this grid from 60° to 84° incidence in the E-plane. Also shown is a curve calculated from the simple susceptance formula given earlier for a contacting crossed grid. It is seen that similar trends exist for the measured data and the calculated curve, but somewhat less rejection is obtained from the measurement.

To simulate the dielectric skin in which the wires of an actual angular filter might be embedded, a casting resin with a k of about 3.5 was poured into the crossed wire grid sample where it solidified and formed a sheet about 1/10 inch thick. The measured data points are shown in Figure 19 for this case. Also shown is a calculated curve that is based on the assumption that the wire grid susceptance is not affected by the dielectric. The clear displacement between the data and the curve indicates that the assumption of no interaction is not an accurate one in the E-plane of incidence.

Figure 20 shows a comparison of the measured data points for the crossed wire grid sample with and without the dielectric. At angles of incidence very close to grazing, the effect of the dielectric is to increase the rejection provided by the wire grid. This is a result of the large reflection that occurs with any dielectric sheet at angles very close to grazing. At lesser angles the dielectric causes a major decrease of the rejection. This decrease can significantly reduce the effectiveness of a metal-grid angular filter in the E-plane of incidence, where the rejection is already weaker than in the H-plane.

Although addition of dielectric skins to the crossed metal grid reduces its rejection in the E-plane of incidence, there was no evidence of a reduction to zero. It is therefore expected that an angular filter constructed of crossed wire metal grids supported by a small amount of dielectric will not have spurious passbands.

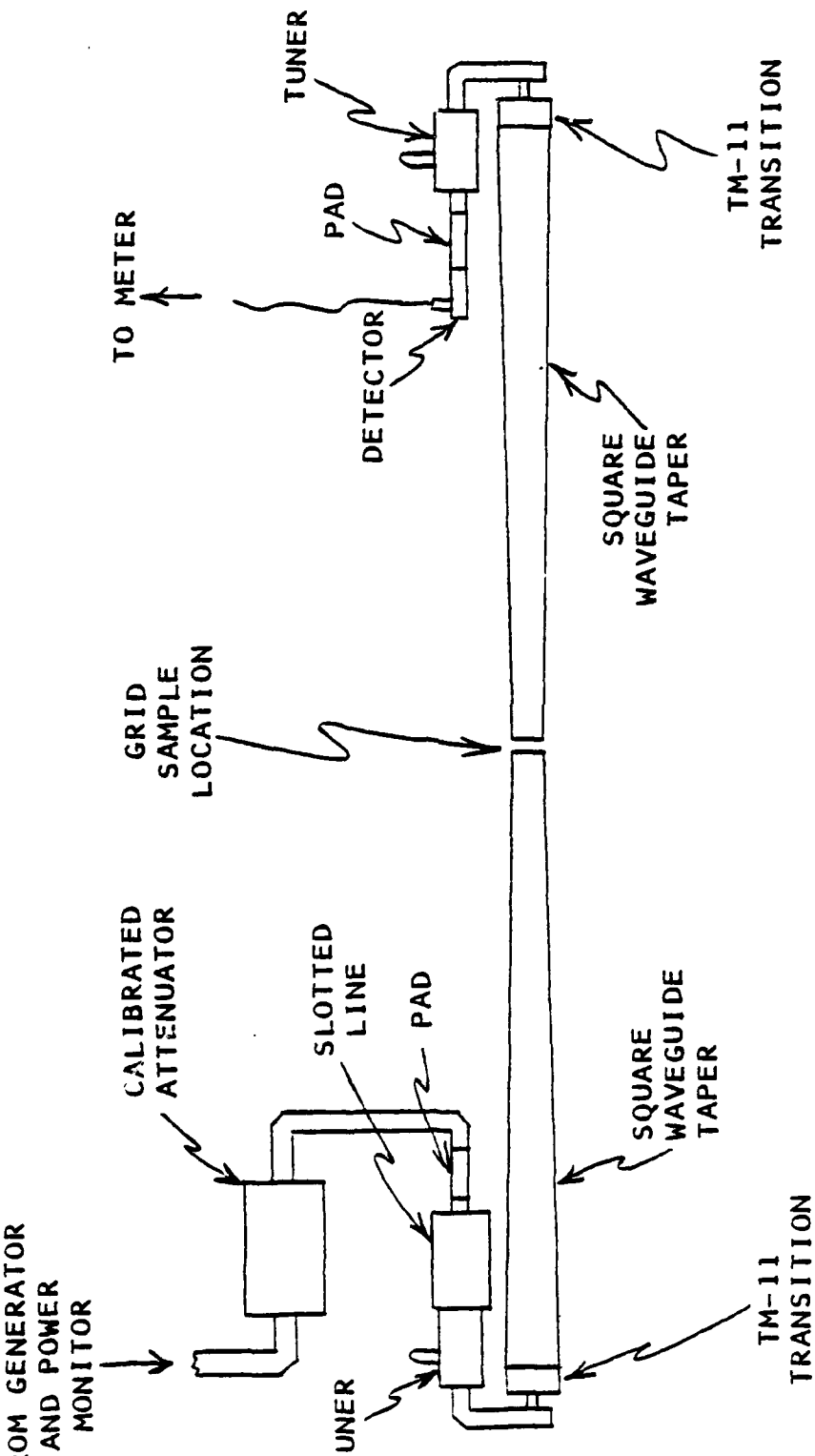

Figure 15. Diagram of Near-Grazing Simulator

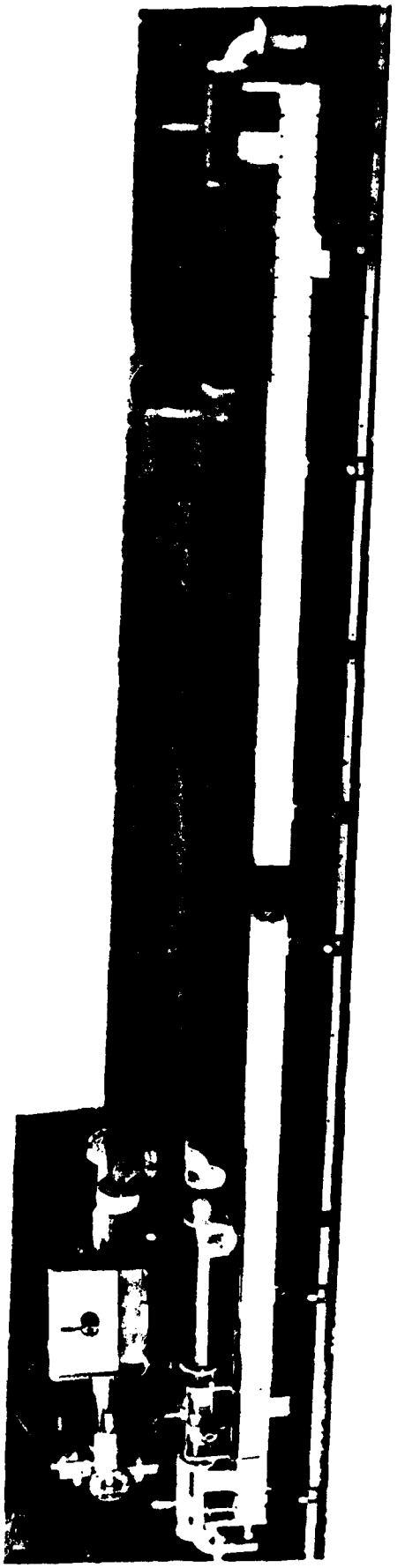

Figure 16. Near-Grazing Simulator

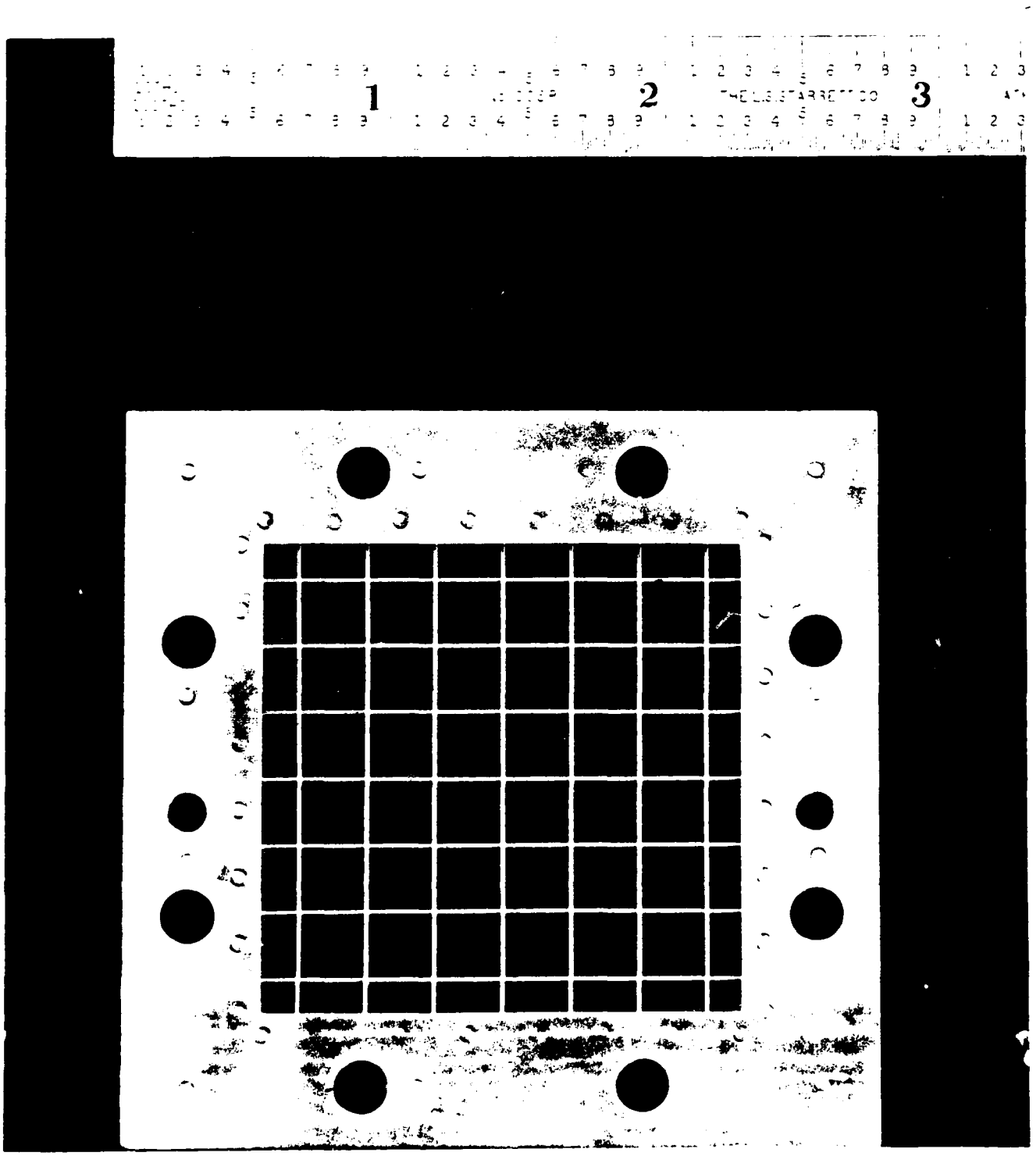

Figure 17. An Insulated Crossed Wire Sample for Near-Grazing Simulator

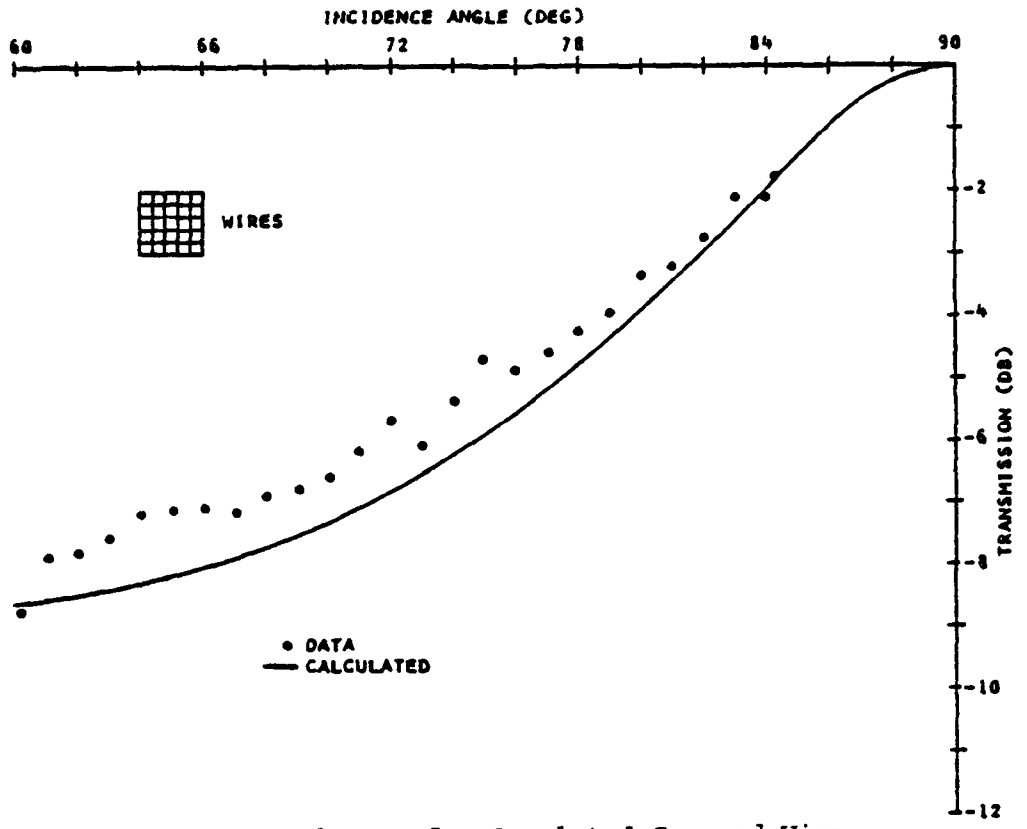

Figure 18. Measured Data for Insulated Crossed Wire Sample Near Grazing

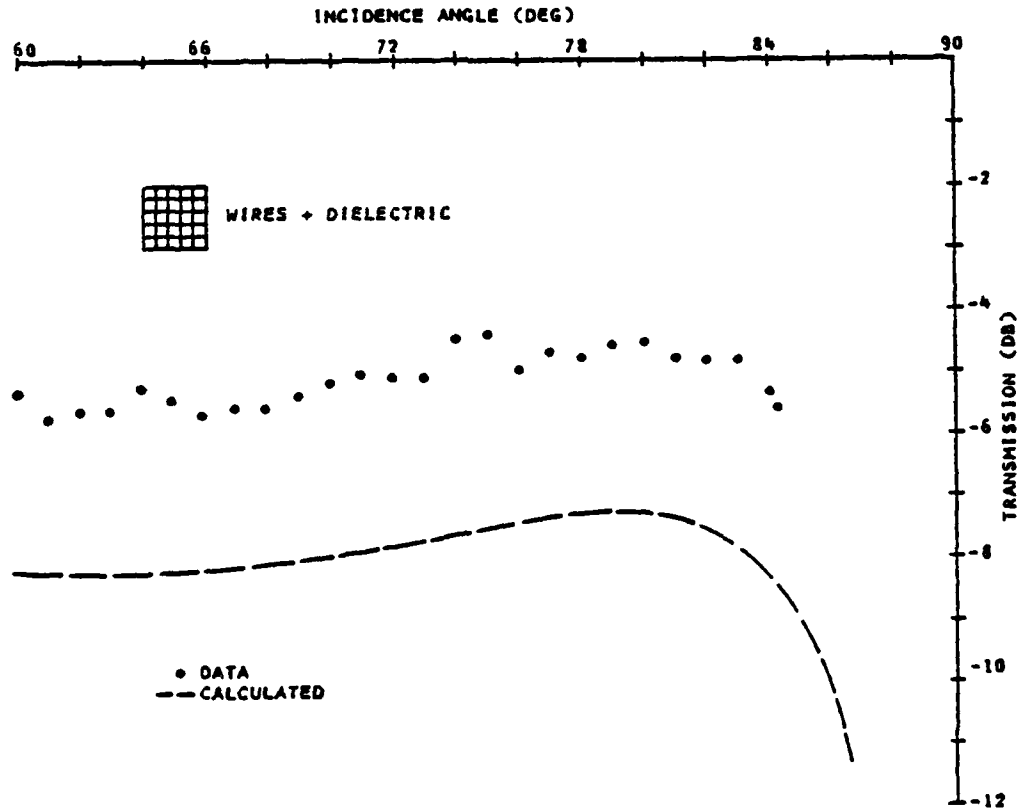

Figure 19. Measured Data for Insulated Crossed Wires with Dielectric Near Grazing

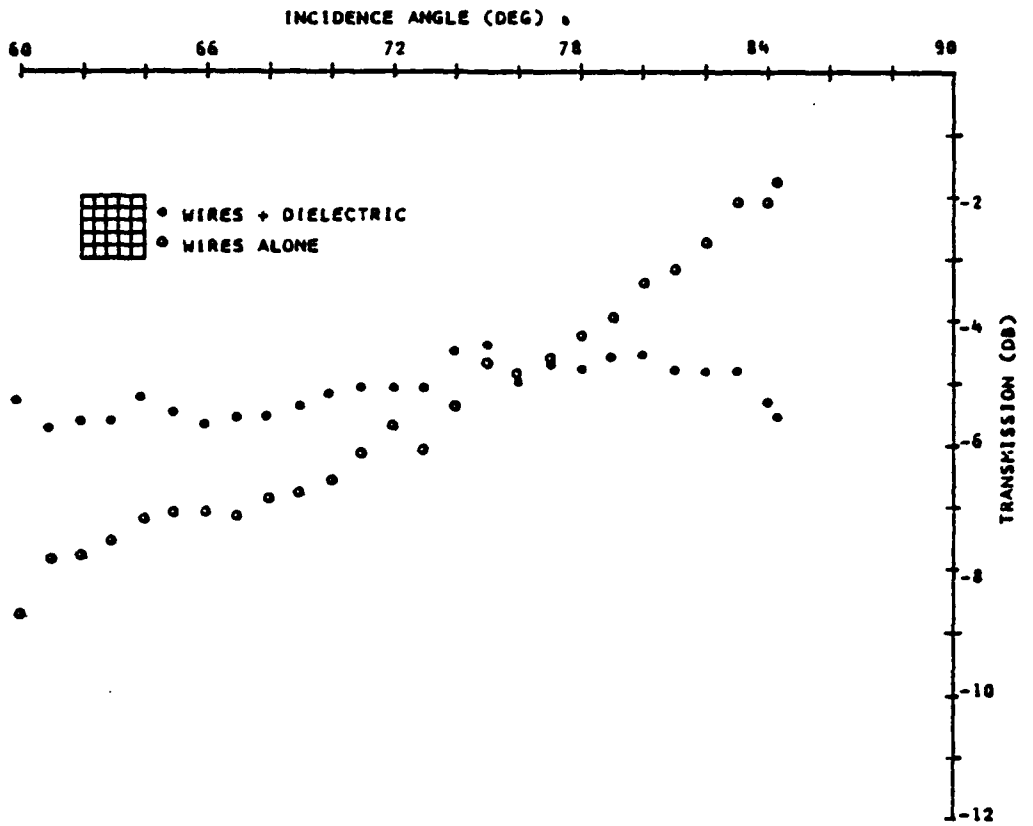

Figure 20. Data Comparison for Wires with and without Dielectric Near Grazing

SECTION 5

CONCLUSIONS

An angular filter comprising several layers of crossed metal grids can provide rejection of waves at oblique incidence in any polarization, while passing waves at normal incidence. The frequency bandwidth of operation is related to the passband size. In practice, the amount of rejection provided by the filter should be limited by the tolerances that can be held during construction of the filter. This limitation is typically less stringent at lower frequencies.

A simulator comprising a waveguide operating near cutoff in the TM-11 mode provides a useful tool for measuring the behavior of metal grids and their dielectric supports near grazing incidence in the E-plane. Measurements in such a simulator showed the reduced rejection of a crossed metal grid at large angles of incidence in the E-plane, and a further reduction caused by addition of dielectric supporting material. No evidence of a spurious passband was found.

A metal grid comprising crossed sets of wires insulated from each other avoids the problems of electrical contact while allowing the construction of a large size angular filter that is effective for any polarization.

SECTION 6

ACKNOWLEDGEMENT

This work has been supported by Rome Air Development Center under Contract F19628-78-C-0152, and is described in more detail in Ref 16. Appreciation is expressed to the project monitor, Dr. Peter R. Franchi.

SECTION 7

REFERENCES

(1) R. J. Mailloux, "Synthesis of Spatial Filters with Chebyshev Characteristics", IEEE Trans. Antennas and Propagation, pp. 174-181; March, 1976.

(2) J. H. Pozgay, S. Zamoscianyk, L. R. Lewis, "Synthesis of Plane Stratified Dielectric Slab Spatial Filters Using Numerical Optimization Techniques", Final Technical Report RADC-TR-76-408 by Raytheon Co., December, 1976.

(3) J. H. Pozgay, "Dielectric Spatial Filter Experimental Study", Final Technical Report RADC-TR-78-248 by Raytheon Co., November, 1978.

(4) A. C. Schell et al, "Metallic Grating Spatial Filter for Directional Beamforming Antenna" AD-D002-623; April, 1976.

(5) R. J. Mailloux, "Studies of Metallic Grid Spatial Filters", IEEE AP-S Int. Symp. Digest, p. 551; 1977.

(6) E. L. Rope, G. Tricoles, O-C. Yue, "Metallic Angular Filters for Array Economy", IEEE AP-S Int. Symp. Digest, pp. 155-157; 1976.

(7) E. L. Rope, G. Tricoles, "An Angle Filter Containing Three Periodically Perforated Metallic Layers", IEEE AP-S Int. Symp. Digest, pp. 818-820; 1979.

(8) R. J. Mailloux and P. R. Franchi, "Metal Grid Angular Filters for Sidelobe Suppression", RADC-TR-79-10; January 1979.

(9) G. G. MacFarlane, "Surface Impedance of an Infinite Parallel-Wire Grid at Oblique Angles of Incidence", JIEE, Vol. 93, Pt. 3A, pp. 1523-1527; 1946.

(10) G. L. Matthaei, L. Young, E. M. T. Jones, "Microwave Filters", Impedance-Matching Networks, and Coupling Structures", McGraw-Hill, pp. 85-101, 450-452; 1964.

(11) M. I., Kontorovich, V. Yu. Pretun'kin, N. A. Yesepkina, M. I. Astrakhan, "The Coefficient of Reflection of a Plane Electromagnetic Wave from a Plane Wire Mesh", Radio Engineering and Electronic Physics (USSR), Vol. 7, No. 2, pp. 222-231; February, 1962.

(12) M. I. Astrakhan, "Reflecting and Screening Properties of Plane Wire Grids", Radio Engineering (USSR), Vol. 23, No. 1, pp. 76-83; 1968.

(13) P. W. Hannan and M. A. Balfour, "Simulation of a Phased Array in Waveguide", IEEE Trans. AP, pp. 342-353; May, 1965.

(14) P. W. Hannan, "Discovery of an Array Surface Wave in a Simulator", IEEE Trans., AP, pp. 574-576; July, 1967.

(15) H. A. Wheeler, "Survey of the Simulator Technique for Designing a Radiating Element in a Phased Array", Phased Array Antenna Symposium, Artech House, pp. 132-148; 1970.

(16) P. W. Hannan and P. L. Burgmyer, "Metal-Grid Spatial Filter Studies", Interim Technical Report RADC-TR- by Hazeltine Corp.; August 1979.

LENS EFFECT IN DIELECTRIC RADOMES*

M. S. Sheshadri, S. W. Lee and R. Mittra
University of Illinois

1. INTRODUCTION

Presently available techniques ([1], [2]) for the design of dielectric radomes are based on a variety of approximate analyses, all of which ignore the fact that the radome is curved - the radome being treated as though it is locally a slab. This approximation, though useful in many cases, fails when the electromagnetic transmission is through the tip region of a radome, where the curvature is usually large.

In this paper we present an analysis based on geometrical optics in which the rays are traced through the radome, taking into account the surface curvature of the radome. Patterns calculated for paraboloidal radomes of different types show some interesting phenomena. The field which is transmitted through the tip region is highly sensitive to the curvatures of the inner and outer surfaces. For a given curvature of the inner surface, the curvature of the outer surface can be varied to obtain either a dip or a peak, in the axial direction of the far field zone. Such a lens effect predicted by the ray technique is also confirmed by using the conventional aperture integration method.

*This work was supported by Grant No. N00019-79-0281 of Naval Air Systems Command, Dept. of the Navy, Washington, D.C. 20361.

2. DESCRIPTION OF PROBLEM

The geometry of the radome problem under consideration is sketched in Figure 1. A point source at P_0 produces a spherical wave which goes through a curved dielectric shell with nonuniform thickness. Ray techniques are used to determine the field at point P_3 on a given surface outside the shell. First, let us describe the various elements involved in the problem.

Coordinate Systems and Time Convention. The main coordinate system is the rectangular system $(\hat{x},\hat{y},\hat{z})$, whose origin is chosen at the source point P_0 and the z-coordinate is in the direction of the beam maximum of the antenna. Other coordinate systems at points P_1, P_2 and P_3 along the ray are defined later. The field is time-harmonic with the time factor $\exp(+j\omega t)$ which is suppressed throughout.

Source. We assume that the source has a well-defined "phase center" at point P_0, the origin of the coordinate system $(\hat{x},\hat{y},\hat{z})$, and radiates a spherical wave denoted by $(\vec{E}^i,\vec{H}^i)$. If the antenna is an array of point sources, it is necessary to consider each element in the array separately and superimpose their final fields at the observation points.

Dielectric radome. The radome is a dielectric shell with nonuniform thickness of relative dielectric constant $\varepsilon_r = \varepsilon/\varepsilon_0$ or refraction index $n = \sqrt{\varepsilon_r}$, and is bounded by the inner and outer surfaces Σ_1 and Σ_2, respectively. The inner surface Σ_1 (near the source) is described by the equation:

$$z = f_1(x,y) \quad , \quad \text{for } a_1 < x < b_1 \text{ and } c_1 < y < d_1 \ . \tag{2.1}$$

The outer surface Σ_2 is given by the equation:

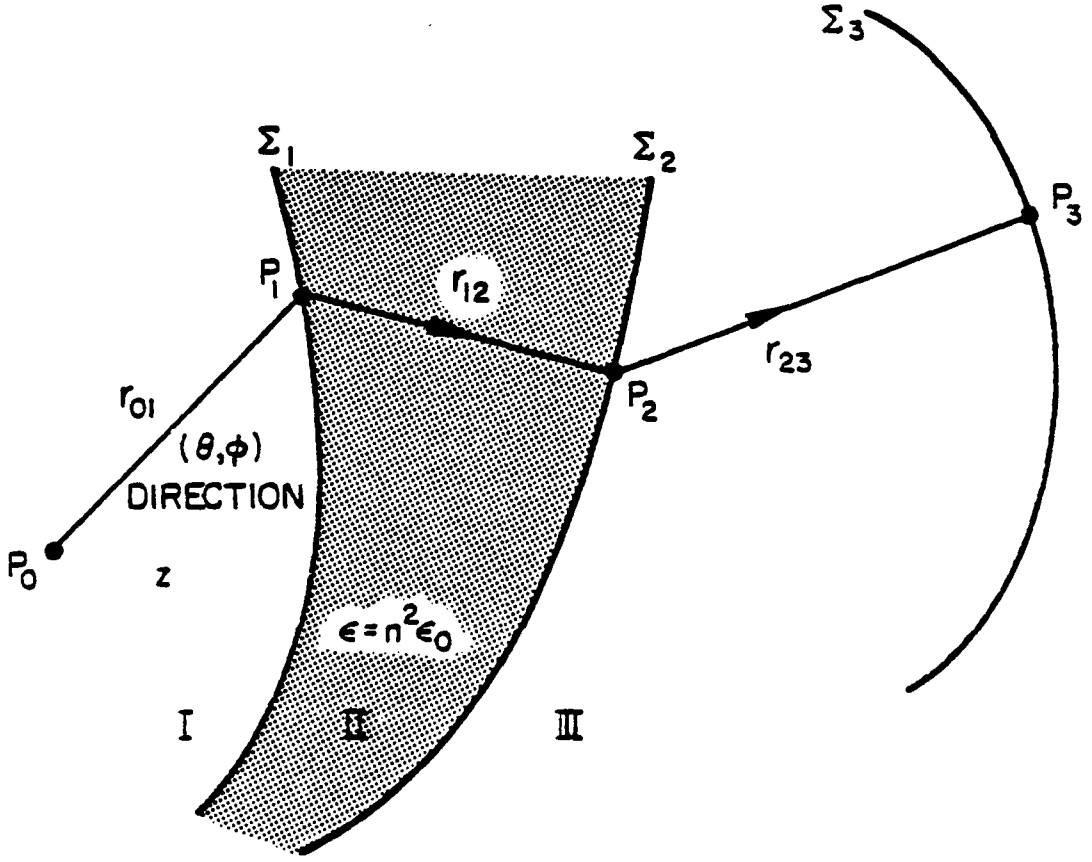

Figure 1. Transmission through a dielectric shell due to incidence from a point source at P_0.

$$z = f_2(x,y) \quad , \quad \text{for } a_2 < x < b_2 \text{ and } c_2 < y < d_2 \quad . \tag{2.2}$$

Observation points. Observation point P_3 is located on a prespecified surface Σ_3, which can be either one of the following two types:

(i) Spherical Σ_3 with center at P_0 and an infinitely large radius. In this case, P_3 is in the far field, and the field at P_3 calculated by the ray technique is the final result.

(ii) Planar Σ_3 which is just outside the radome and normal to the z-axis. In this case, we have to integrate the field on Σ_3 to obtain the far field.

In later calculations, we use mostly the spherical Σ_3 in (i).

3. GEOMETRICAL OPTICS FIELD

For a given incident field $(\vec{E}^i, \vec{H}^i)$ generated by the source at point P_0 (Fig. 1), the asymptotic solution of the field at point P_3 is determined using geometrical optics [3], [4]. The method of solution is described below.

Consider a ray in direction (θ,ϕ) extending from the source point P_0 to the point P_1 on Σ_1. The source region (Region I) is homogeneous and isotropic; hence, the ray is a straight line along the unit vector $\hat{r}_{01}$. First, the distance r_{01} is found and the coordinates of point P_1 are determined. Then the unit vector $\hat{N}_1$ normal to the surface Σ_1 at point P_1 is found (Figure 2). The plane of vectors $\hat{r}_{01}$ and $\hat{N}_1$ establishes the incident plane. The angle between these two vectors is the incident angle α_1^i. Using Snell's law, the refraction angle α_1^t is obtained, which establishes the direction of the transmitted wave, $\hat{r}_{12}$, in Region II (dielectric). The ray in Region II is a straight line along the unit

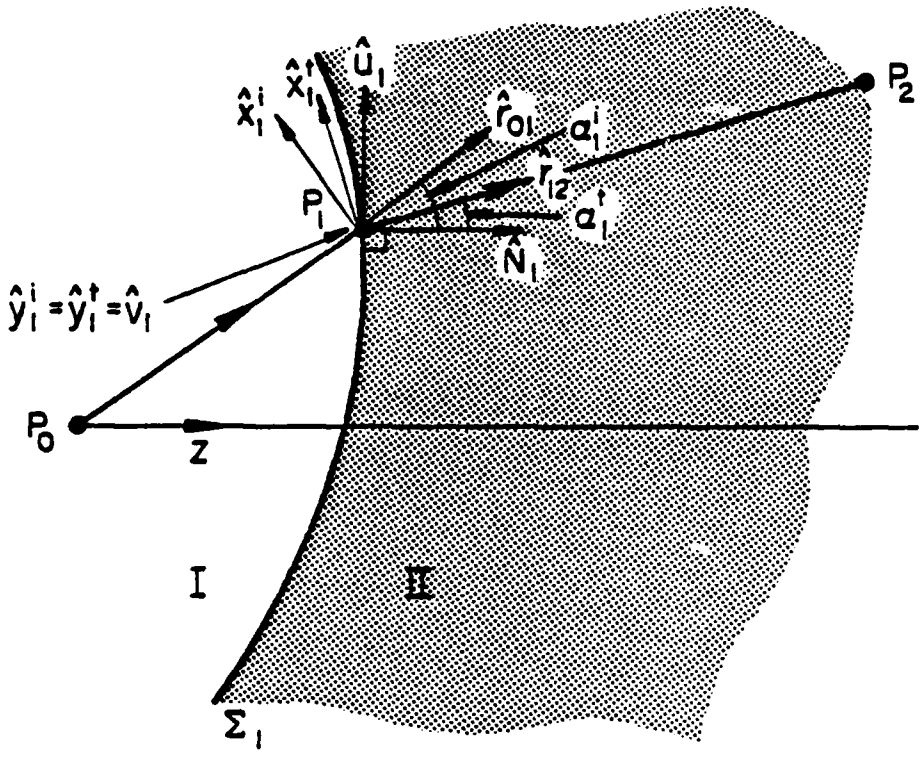

Figure 2. Coordinate systems for refraction at surface Σ_1.

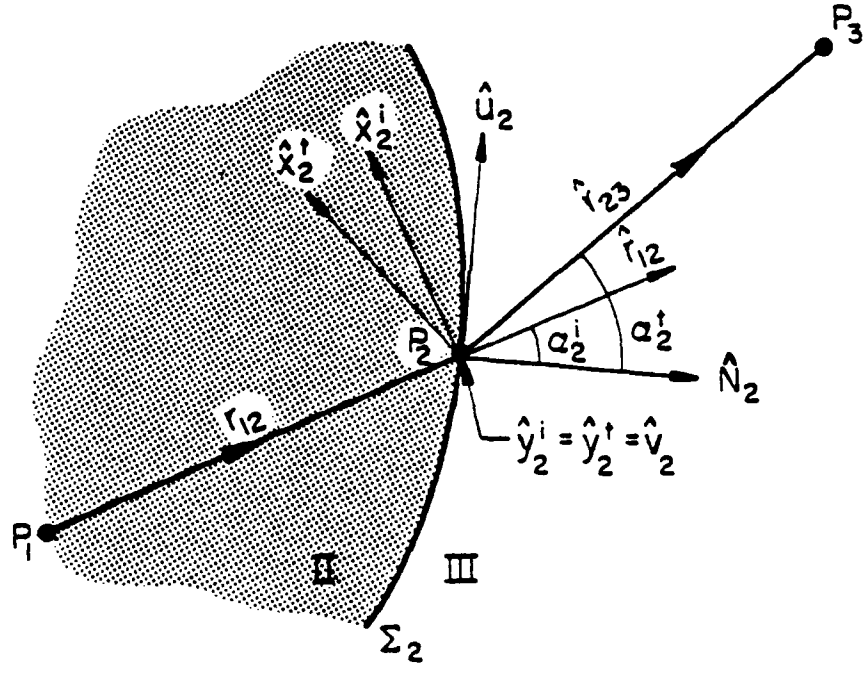

Figure 3. Coordinate systems for refraction at surface Σ_2.

vector $\hat{r}_{12}$. Three coordinate systems $(\hat{x}_1^i, \hat{y}_1^i, \hat{r}_{01})$, $(\hat{u}_1, \hat{v}_1, \hat{N}_1)$, and $(\hat{x}_1^t, \hat{y}_1^t, \hat{r}_{12})$, with common origin at point P_1, are then established. They belong to the incident ray, the surface Σ_1, and the transmitted ray, respectively.

The incident field $(\vec{E}_1^i, \vec{H}_1^i)$ is split into a normally polarized field $(\vec{E}_1^{in}, \vec{H}_1^{ip})$, (E-vector normal to the incident plane at P_1) and a parallel polarized field $(\vec{E}_1^{ip}, \vec{H}_1^{in})$. The transmitted field at point P_1 is obtained as follows:

$$\vec{E}_1^{tn} = t_1^n \vec{E}_1^{in} \quad , \quad \vec{H}_1^{tp} = Y \hat{r}_{12} \times \vec{E}_1^{tn}$$

$$\vec{H}_1^{tn} = t_1^p \vec{H}_1^{in} \quad , \quad \vec{E}_1^{tp} = Z \vec{H}_1^{tn} \times \hat{r}_{12} \tag{3.1}$$

in which t_1^n and t_1^p are transmission coefficients for the normal and parallel polarized fields, respectively,

$$t_1^n = \frac{2}{1 + \nu_{n1}} \quad , \quad \nu_{n1} = \frac{Y \cos \alpha_1^t}{Y_0 \cos \alpha_1^i} = n \frac{\cos \alpha_1^t}{\cos \alpha_1^i}$$

$$t_1^p = \frac{2}{1 + \nu_{p1}} \quad , \quad \nu_{p1} = \frac{Z \cos \alpha_1^t}{Z_0 \cos \alpha_1^i} = \frac{1}{n} \frac{\cos \alpha_1^t}{\cos \alpha_1^i} \tag{3.2}$$

$$Y_0 = \frac{1}{Z_0} = \sqrt{\frac{\varepsilon_0}{\mu_0}} = \frac{1}{120\pi} \quad , \quad Y = \frac{1}{z} = \sqrt{\frac{\varepsilon}{\mu_0}} = nY_0 \quad , \quad n = \sqrt{\frac{\varepsilon}{\varepsilon_0}} = \sqrt{\varepsilon_r} \ .$$

Note that the subscript 1, in $\vec{H}_1^{tn}$ for example, signifies the field evaluated at point 1.

The transmitted field at P_1 is incident on Σ_2 at point P_2. Coordinates of this point can be found from the knowledge of the coordinates of point P_1 and the transmitted ray direction $\hat{r}_{12}$. The field values, in

going from P_1 to P_2, undergo some change which is dependent on the divergence of the ray. Thus, we have

$$\vec{E}_2^i = (DF_{12})\, e^{-jkr_{12}}\, \vec{E}_1^t \tag{3.3}$$

in which $k = nk_0$ is the wave number in the dielectric and DF_{12} is the divergence factor for the pencil of rays travelling from P_1 to P_2 in the dielectric. It is given by

$$DF_{12} = (1 + q_1^{II} r_{12})^{-1/2} (1 + q_2^{II} r_{12})^{-1/2} \tag{3.4}$$

in which q_1^{II} and q_2^{II} are the principal curvatures (inverse of the radii of curvature) for the ray pencil in Region II. They are found from the curvature matrix of the transmitted ray at point P_1. The matrix itself is found from a formula involving the curvature matrix of the incident ray and that of the surface Σ_1 at point P_1. The curvature matrix of the transmitted ray pencil at point P_1 is also used to find the curvature matrix of the ray at point P_2 incident upon the surface Σ_2.

Having the field incident upon Σ_2 at point P_2, the ray direction $\hat{r}_{12}$, and its curvature matrix, we can proceed, in a manner similar to the transmission through Σ_1, to find the field transmitted through Σ_2 at P_2 (Figure 3). Thus, a unit vector $\hat{N}_2$, normal to Σ_2 is obtained, and together with $\hat{r}_{12}$ defines the incidence plane at point P_2. The incidence angle α_2^i ($\cos \alpha_2^i = \hat{N}_2 \cdot \hat{r}_{12}$) is then calculated. Again, Snell's law is invoked to find the refraction angle α_2^t at P_2. This angle specifies the ray direction $\hat{r}_{23}$ in Region III (outside the radome). Three coordinate systems $(\hat{x}_2^i, \hat{y}_2^i, \hat{r}_{12})$, $(\hat{u}_2, \hat{v}_2, \hat{N}_2)$ and $(\hat{x}_2^t, \hat{y}_2^t, \hat{r}_{23})$ with common origin at point P_2 are then introduced.

The field $(\vec{E}_2^i, \vec{H}_2^i)$ incident upon Σ_2 at P_2 is resolved into parallel and normally polarized fields, from which the transmitted fields are found as follows:

$$\vec{E}_2^{tn} = t_2^n \vec{E}_2^{in} \quad , \quad \vec{H}_2^{tp} = Y_0 \hat{r}_{23} \times \vec{E}_2^{tn}$$

$$\vec{H}_2^{tn} = t_2^p \vec{H}_2^{in} \quad , \quad \vec{E}_2^{tp} = Z_0 \vec{H}_2^{tn} \times \hat{r}_{23} \tag{3.5}$$

in which

$$t_2^n = \frac{2}{1 + \nu_{n2}} \quad , \quad \nu_{n2} = \frac{1}{n} \frac{\cos \alpha_2^t}{\cos \alpha_2^i}$$

$$t_2^p = \frac{2}{1 + \nu_{p2}} \quad , \quad \nu_{p2} = n \frac{\cos \alpha_2^t}{\cos \alpha_2^i} \quad . \tag{3.6}$$

The field at observation point P_3 is then found from the transmitted field at P_2, such that,

$$\vec{E}_3 = (DF_{23})\, e^{-jk_0 r_{23}} \vec{E}_2^t \quad , \tag{3.7a}$$

in which

$$DF_{23} = (1 + q_1^{III} r_{23})^{-1/2} (1 + q_2^{III} r_{23})^{-1/2} \quad , \tag{3.7b}$$

and q_1^{III} and q_2^{III} are the principal curvatures of the ray pencil in Region III. They are obtained from the curvature matrix of the transmitted ray at point P_2. This matrix is obtained from a formula already mentioned in connection with transmission through Σ_1. For a typical factor in Eqs. (3.4) and (3.7b), the following square root convention is used:

$$f = 1/\sqrt{1 + qr} = \begin{cases} +|f|, \text{ if } f \text{ is real} \\ \\ +j|f|, \text{ if } f \text{ is imaginary} \end{cases} . \qquad (3.8)$$

It should be mentioned here that we have ignored multiple reflections in the dielectric radome throughout our analysis.

Details of Analysis.

Coordinates of the first refraction point, P_1. For a given ray from the source P_0, the coordinates of P_1, the intersection of the rectilinear ray with the interface Σ_1, are given by

$$\begin{aligned} x_1 &= r_{01} \sin\theta \cos\phi \\ y_1 &= r_{01} \sin\theta \sin\phi \quad ; \quad r_{01} = (x_1^2 + y_1^2 + z_1^2)^{1/2} \\ z_1 &= r_{01} \cos\theta \end{aligned} \qquad (3.9)$$

in which θ and ϕ specify the ray direction in the spherical coordinate system with origin at P_0. Since point P_1 is on the surface $\Sigma_1(z = f_1(x,y))$, we can write

$$r_{01} \cos\theta = f_1(r_{01} \sin\theta \cos\phi \quad , \quad r_{01} \sin\theta \sin\phi) . \qquad (3.10)$$

For given θ and ϕ, this nonlinear equation must be solved for r_{01}. Once r_{01} is known, (x_1,y_1,z_1) are found from (3.9) and the unit vector $\hat{r}_{01}$ is

$$\hat{r}_{01} = \frac{x_1\hat{x} + y_1\hat{y} + z_1\hat{z}}{r_{01}} . \qquad (3.11)$$

Coordinate systems at point P_1. The unit vector $\hat{N}_1$, normal to the surface Σ_1 at point P_1, is

$$\hat{N}_1 = \left.\frac{\nabla g_1(x,y,z)}{|\nabla g_1(x,y,z)|}\right|_{P_1}, \quad g_1(x,y,z) = z - f_1(x,y), \quad \nabla = \frac{\partial}{\partial x}\hat{x} + \frac{\partial}{\partial y}\hat{y} + \frac{\partial}{\partial z}\hat{z}$$

$$\text{or } \hat{N}_1 = \frac{1}{\Delta_1}(\hat{z} - f_{1x}\hat{x} - f_{1y}\hat{y}) \tag{3.12}$$

in which

$$f_{1x} = \left.\frac{\partial f_1}{\partial x}\right|_{x_1} \quad f_{1y} = \left.\frac{\partial f_1}{\partial y}\right|_{y_1}, \quad \Delta_1 = (1 + f_{1x}^2 + f_{1y}^2)^{1/2} . \tag{3.13}$$

(Notice that the direction of $\hat{N}_1$ is chosen pointing away from the source.) Vectors $\hat{r}_{01}$ and $\hat{N}_1$ specify the incident plane at point P_1. The coordinate systems $(\hat{x}_1^i, \hat{y}_1^i, \hat{r}_{01})$, $(\hat{x}_1^t, \hat{y}_1^t, \hat{r}_{12})$ and $(\hat{u}_1, \hat{v}_1, \hat{N}_1)$ at point P_1 for the incident ray, the transmitted ray and the surface Σ_1, respectively, are chosen such that all three have one common coordinate perpendicular to the incident plane, that is, $\hat{v}_1 = \hat{y}_1^i = \hat{y}_1^t$ (Figure 2). Notice that, in general, the coordinate systems could be chosen arbitrarily. However, the choice made here offers some simplification in the calculation of curvature matrices, as is shown later. Thus,

$$\hat{v}_1 = \hat{y}_1^i = \hat{y}_1^t = \frac{\hat{N}_1 \times \hat{r}_{01}}{|\hat{N}_1 \times \hat{r}_{01}|} = \frac{1}{L_1}[-(y_1 + z_1 f_{1y})\hat{x} + (x_1 + z_1 f_{1x})\hat{y} \tag{3.14}$$

$$+ (x_1 f_{1y} - y_1 f_{1x})\hat{z}]$$

in which x_1, y_1, and z_1 are given in (3.9) and

$$L_1 = [(y_1 + z_1 f_{1y})^2 + (x_1 + z_1 f_{1x})^2 + (x_1 f_{1y} - y_1 f_{1x})^2]^{1/2} . \tag{3.15}$$

Then $\hat{u}_1$ and $\hat{x}_1^i$ are specified as

$$\hat{u}_1 = \hat{v}_1 \times \hat{N}_1 = \frac{1}{\Delta_1 L_1} \{[x_1(1 + f_{1y}^2) + f_{1x}(z_1 - y_1 f_{1y})]\hat{x} + [y_1(1 + f_{1x}^2)$$

$$+ f_{1y}(z_1 - x_1 f_{1x})]\hat{y} + [y_1 f_{1y} + x_1 f_{1x} + z_1(f_{1x}^2 + f_{1y}^2)]\hat{z}\} \qquad (3.16)$$

and

$$\hat{x}_1^i = \hat{y}_1^i \times \hat{r}_{01} = \frac{1}{r_{01} L_1} \{[x_1(z_1 - y_1 f_{1y}) + f_{1x}(y_1^2 + z_1^2)]\hat{x} + [y_1(z_1 - x_1 f_{1x})$$

$$+ f_{1y}(x_1^2 + z_1^2)]\hat{y} - [z_1(y_1 f_{1y} + x_1 f_{1x}) + (x_1^2 + y_1^2)]\hat{z}\} \qquad (3.17)$$

in which Δ_1 and L_1 are given in (3.13) and (3.15), respectively. Notice that both $\hat{u}_1$ and $\hat{x}_1^i$ are in the plane of incidence.

In order to specify the coordinate system for the transmitted ray at point P_1, the transmission direction $\hat{r}_{12}$ is first obtained. To this end, the incidence and refraction angles need be found. Incidence angle α_1^i is such that

$$\cos \alpha_1^i = \hat{N}_1 \cdot \hat{r}_{01} = \frac{z_1 - x_1 f_{1x} - y_1 f_{1y}}{\Delta_1 r_{01}} \quad . \qquad (3.18)$$

Snell's law is then applied, to find the refraction or transmission angle α_1^t such that

$$\sin \alpha_1^t = n^{-1} \sin \alpha_1^i = n^{-1}(1 - \cos^2 \alpha_1^i)^{1/2} \quad . \qquad (3.19)$$

Now $\hat{r}_{12}$, like $\hat{r}_{01}$, is in the plane of incidence and can be written as

$$\hat{r}_{12} = (\hat{r}_{12} \cdot \hat{u}_1)\hat{u}_1 + (\hat{r}_{12} \cdot \hat{N}_1)\hat{N}_1 = \sin \alpha_1^t \hat{u}_1 + \cos \alpha_1^t \hat{N}_1 \quad . \qquad (3.20)$$

Notice that due to the particular choice of $\hat{v}_1$ and $\hat{u}_1$, as given in (3.14) and (3.16), α_1^i and α_1^t are always less than $\pi/2$; hence, their sines and cosines are always positive real numbers (for lossless dielectric) and

no sign ambiguity exists. Once $\hat{r}_{12}$ and $\hat{y}_1^t$ are properly defined (in (3.14) and (3.20)), the third coordinate direction for the transmitted ray $\hat{x}_1^t$ is found from

$$\hat{x}_1^t = \hat{y}_1^t \times \hat{r}_{12} = \hat{v}_1 \times (\sin \alpha_1^t \hat{u}_1 + \cos \alpha_1^t \hat{N}_1) = \cos \alpha_1^t \hat{u}_1 - \sin \alpha_1^t \hat{N}_1. \quad (3.21)$$

Curvature matrix of the incident field at P_1. Since the source produces a spherical field, its curvature matrix in any orthonormal coordinate system at point P_1 (here $\hat{x}_1^i$ and $\hat{y}_1^i$) perpendicular to the ray propagation direction $\hat{r}_{01}$ is given by [3], [4],

$$Q_1^i = \begin{bmatrix} 1/r_{01} & 0 \\ 0 & 1/r_{01} \end{bmatrix} = \frac{1}{r_{01}} U \quad (3.22)$$

in which r_{01} is the radius of the spherical wavefront at point P_1, and U denotes a unit matrix.

Curvature matrix of the surface Σ_1. It can be easily shown that the derivatives of vector $\vec{r}_{01} \equiv \vec{r}_1$ (starting at the origin P_0 and ending at a point such as P_1 on Σ_1) with respect to two independent parameters x_1 and y_1 on the surface Σ_1, as given below,

$$\vec{r}_{1x} = \frac{\partial \vec{r}_1}{\partial x_1} = \frac{\partial x_1}{\partial x_1} \hat{x} + \frac{\partial y_1}{\partial x_1} \hat{y} + \frac{\partial z_1}{\partial x_1} \hat{z} = \hat{x} + f_{1x} \hat{z} \quad ,$$

$$\vec{r}_{1y} = \frac{\partial \vec{r}_1}{\partial y_1} = \frac{\partial x_1}{\partial y_1} \hat{x} + \frac{\partial y_1}{\partial y_1} \hat{y} + \frac{\partial z_1}{\partial y_1} \hat{z} = \hat{y} + f_{1y} \hat{z} \quad , \quad (3.23)$$

with $z_1 = f_1(x_1, y_1)$, $f_{1x} = \frac{\partial f_1}{\partial x_1}$, $f_{1y} = \frac{\partial f_1}{\partial y_1}$,

lie in the tangent plane to the surface at point P_1. It can also be easily shown that the derivatives of the unit vector $\hat{N}_1$ normal to Σ_1 at

P_1, with respect to x_1 and y_1, also lie in the same tangent plane and are given by

$$\hat{N}_{1x} = \frac{\partial \hat{N}_1}{\partial x_1} = \frac{1}{\Delta_1}(-f_{1xx}\hat{x} - f_{1yx}\hat{y}) + \frac{-f_{1x}f_{1xx} - f_{1y}f_{1yx}}{\Delta_1^2}\hat{N}_1$$

$$\hat{N}_{1y} = \frac{\partial \hat{N}_1}{\partial y_1} = \frac{1}{\Delta_1}(-f_{1xy}\hat{x} - f_{1yy}\hat{y}) + \frac{-f_{1x}f_{1xy} - f_{1y}f_{1yy}}{\Delta_1^2}\hat{N}_1 \qquad (3.24)$$

in which $\hat{N}_1$ is given in (3.12) as $\hat{N}_1 = \frac{1}{\Delta_1}(\hat{z} - f_{1x}\hat{x} - f_{1y}\hat{y})$.

The latter two vectors can be written in terms of the previous two vectors defined in (3.23) as,

$$\begin{bmatrix} \hat{N}_{1x} \\ \hat{N}_{1y} \end{bmatrix} = Q^{\Sigma_1}_{\vec{r}_{1x}\vec{r}_{1y}} \cdot \begin{bmatrix} \hat{r}_{1x} \\ \hat{r}_{1y} \end{bmatrix} .$$

The matrix $Q^{\Sigma_1}_{\vec{r}_{1x}\vec{r}_{1y}}$ is the curvature matrix of the surface in coordinates $\vec{r}_{1x}$ and $\vec{r}_{1y}$ and can be shown [3], [4] to be

$$Q^{\Sigma_1}_{\vec{r}_{1x}\vec{r}_{1y}} = \begin{bmatrix} \hat{N}_{1x}\cdot\hat{r}_{1x} & \hat{N}_{1x}\cdot\hat{r}_{1y} \\ \hat{N}_{1y}\cdot\hat{r}_{1x} & \hat{N}_{1y}\cdot\hat{r}_{1y} \end{bmatrix} \cdot \begin{bmatrix} \vec{r}_{1x}\cdot\vec{r}_{1x} & \vec{r}_{1x}\cdot\vec{r}_{1y} \\ \vec{r}_{1y}\cdot\vec{r}_{1x} & \vec{r}_{1y}\cdot\vec{r}_{1y} \end{bmatrix}^{-1}$$

$$= \frac{1}{\Delta_1^2}\begin{bmatrix} e_1G_1 - f_1F_1 & f_1E_1 - e_1F_1 \\ f_1G_1 - g_1F_1 & g_1E_1 - f_1F_1 \end{bmatrix} \qquad (3.25)$$

in which

$$E_1 = 1 + f_{1x}^2 \quad f_1 = f_{1x}f_{1y} \quad G_1 = 1 + f_{1y}^2$$

$$e_1 = -\frac{f_{1xx}}{\Delta_1} \quad f_1 = \frac{-f_{1xy}}{\Delta_1} \quad g_1 = \frac{-f_{1yy}}{\Delta_1} \quad .$$

The curvature matrix of the surface Σ_1 at point P_1, defined in the coordinate system $(\hat{u}_1,\hat{v}_1)$, is obtained from the one given in (3.25) as follows:

$$Q^{\Sigma_1}_{\hat{u}_1,\hat{v}_1} = (A_1)^{-1}\, Q^1_{\vec{r}_{1x}\vec{r}_{1y}}\, A_1 \tag{3.26}$$

in which matrix A_1 is given by

$$A_1 = \begin{bmatrix} \vec{r}_{1x}\cdot\hat{u}_1 & \vec{r}_{1x}\cdot\hat{v}_1 \\ \vec{r}_{1y}\cdot\hat{u}_1 & \vec{r}_{1y}\cdot\hat{v}_1 \end{bmatrix} .$$

Curvature matrix of the transmitted field at P_1. Now with the incident ray curvature matrix and the surface curvature matrix known, we proceed to find the transmitted ray curvature matrix Q_1^t. It is obtained from the following equation [4]

$$k(\Theta_1^t)^T Q_1^t \Theta_1^t = k_0(\Theta_1^i)^T Q_1^i \Theta_1^i + h_1 Q^{\Sigma_1} \quad , \quad h_1 = k\cos\alpha_1^t - k_0\cos\alpha_1^i \ . \tag{3.27}$$

Here Q^{Σ_1}, Q_1^i, and Q_1^t are defined in the $(\hat{u}_1,\hat{v}_1)$, $(\hat{x}_1^i,\hat{y}_1^i)$ and $(\hat{x}_1^t,\hat{y}_1^t)$ coordinate systems, respectively. Θ_1^i and Θ_1^t are matrices which relate the incident and transmitted ray coordinates to the coordinates of the surface Σ_1, and for these coordinate systems, as defined in Figures 2 and 3, they are given by

$$\Theta_1^i = \begin{bmatrix} \hat{x}_1^i\cdot\hat{u}_1 & \hat{x}_1^i\cdot\hat{v}_1 \\ \hat{y}_1^i\cdot\hat{u}_1 & \hat{y}_1^i\cdot\hat{v}_1 \end{bmatrix} = \begin{bmatrix} \cos\alpha_1^i & 0 \\ 0 & 1 \end{bmatrix}$$

$$\Theta_1^t = \begin{bmatrix} \hat{x}_1^t\cdot\hat{u}_1 & \hat{x}_1^t\cdot\hat{v}_1 \\ \hat{y}_1^t\cdot\hat{u}_1 & \hat{y}_1^t\cdot\hat{v}_1 \end{bmatrix} = \begin{bmatrix} \cos\alpha_1^t & 0 \\ 0 & 1 \end{bmatrix} . \tag{3.28}$$

Notice that due to the particular choice of coordinate systems the transpose, Θ^T, and the inverse, Θ^{-1}, of these matrices are easily found. Then, from (3.27)

$$Q_1^t = (\Theta_1^t)^{-1}[n^{-1}\Theta_1^i Q_1^i \Theta_1^i + (\cos \alpha_1^t - n^{-1} \cos \alpha_1^i)\, Q^{\Sigma_1}](\Theta_1^t)^{-1} \ . \qquad (3.29)$$

Again, it should be noted that this Q_1^t is valid in the $(\hat{x}_1^t, \hat{y}_1^t, \hat{r}_{12})$ coordinate system.

Divergence factor in the dielectric. At this point we can find DF_{12}, the divergence factor for the ray pencil in going from point P_1 to point P_2, as given in (3.4) and repeated here for convenience (see also, (3.8)):

$$DF_{12} = (1 + q_1 r_{12})^{-1/2} \ (1 + Q_2 r_{12})^{-1/2}$$

in which q_1 and q_2 are the principal curvatures (inverse of the radii of curvature) for the ray pencil in the dielectric (Region II) and are found from the following equation

$$q^2 - \text{trace}\ (Q_1^t)q + \det\ (Q_1^t) = 0 \quad , \quad Q_1^t = \begin{bmatrix} q_{11} & q_{12} \\ q_{21} & q_{22} \end{bmatrix}$$

or

$$q^2 - (q_{11} + q_{22})q + (q_{11}q_{22} - q_{12}q_{21}) = 0 \qquad (3.30)$$

$$q_1, q_2 = \tfrac{1}{2}\{(q_{11} + q_{22}) \pm [(Q_{11} + q_{22})^2 - 4(q_{11}q_{22} - q_{12}q_{21})]^{1/2}\} \ .$$

The divergence factor DF_{23} is found in a similar manner.

We now summarize the results obtained so far. The point source at P_0 (Figure 1) radiates a spherical wave described by

$$\vec{E}^i(r,\theta,\phi) = \frac{e^{-jk_0 r}}{(r/\lambda_0)} (P(\theta,\phi)\hat{\theta} + Q(\theta,\phi)\hat{\phi}),$$

$$= \frac{e^{-jk_0 r}}{(r/\lambda_0)} [(P\cos\phi\cos\theta - Q\sin\phi)\hat{x} + (P\sin\phi\cos\theta + Q\cos\phi)\hat{y} - P\sin\theta\hat{z}] \tag{3.31a}$$

$$\vec{H}^i = Y_0 \hat{r} \times \vec{E}^i \tag{3.31b}$$

where (r,θ,ϕ) are spherical coordinates with origin at P_0. The pattern functions $P(\theta,\phi)$ and $Q(\theta,\phi)$ in (3.31) are given. At point P_1 (Figure 2), we decompose the field into two components in the directions of $(\hat{x}_1^i, \hat{y}_1^i)$, i.e.,

$$\vec{E}_1^i = \vec{E}^i(r_1,\theta_1,\phi_1) = (\vec{E}_1^i \cdot \hat{x}_1^i)\hat{x}_1^i + (\vec{E}_1^i \cdot \hat{y}_1^i)\hat{y}_1^i \quad , \quad \vec{H}_1^i = Y_0 \hat{r}_{01} \times \vec{E}_1^i . \tag{3.32}$$

At the observation point P_3, we express the field as follows

$$\vec{E}_3^t = (\vec{E}_3^t \cdot \hat{x}_2^t + (\vec{E}_3^t \cdot \hat{y}_2^t)\hat{y}_2^t \quad , \quad \vec{H}_3^t = Y_0 \hat{r}_{23} \times \vec{E}_3^t \quad . \tag{3.33}$$

The two components of $\vec{E}_3$ in (3.33) are found from the matrix equation

$$\begin{bmatrix} \vec{E}_3^t \cdot \hat{x}_2^t \\ \vec{E}_3^t \cdot \hat{y}_2^t \end{bmatrix} = (DF_{12})(DF_{23}) e^{-jk_0(nr_{12}+r_{23})} \begin{bmatrix} t_1^p t_2^p (\hat{x}_2^i \cdot \hat{x}_1^t) & nt_1^n t_2^p (\hat{x}_2^i \cdot \hat{y}_1^t) \\ n^{-1} t_1^p t_2^n (\hat{y}_2^i \cdot \hat{x}_1^t) & t_1^n t_2^n (\hat{y}_2^i \cdot \hat{y}_1^t) \end{bmatrix} \begin{bmatrix} \hat{E}_1^i \cdot \hat{x}_1^i \\ \hat{E}_1^i \cdot \hat{y}_1^i \end{bmatrix} \tag{3.34a}$$

or more compactly,

$$\vec{E}_3 = (DF)\, e^{-jk_0(nr_{12} + r_{23})} \overline{\overline{T}}\, \vec{E}_1 . \tag{3.34b}$$

In (3.34), n is the refraction index of the dielectric, k_0 is the free-space wave number and t_1^n, t_1^p, t_2^n, t_2^p are the normal and parallel transmission coefficients at points P_1 and P_2, respectively, as given in (3.2) and (3.6). The two divergence factors are given in (3.4) and

(3.7b). Their calculations constitute the major effort of the present solution.

4. THE LENS EFFECT

As given in (3.31), the incident field $\vec{E}^i$ from the point source is characterized by two pattern functions P and Q. For the present computations, we assume that the point source is y-polarized. Then it follows that

$$P(\theta,\phi) = V_E(\theta) \sin \phi \tag{4.1a}$$

$$Q(\theta,\phi) = V_H(\theta) \cos \phi \tag{4.1b}$$

where $V_E(\theta)$ and $V_H(\theta)$ are, respectively, the E and H plane patterns, and they assume the form

$$V_E(\theta) = (\cos \theta)^m \quad , \quad V_H(\theta) = (\cos \theta)^n \quad . \tag{4.2}$$

In particular, for m = 1 and n = 0, the incident field is identical to the far field of a y-directed electric dipole. In the E-plane ($\phi = 90°$), the incident field in (3.31) becomes

$$\vec{E}^i(r,\theta,\phi = 90°) = \frac{e^{-jk_0 r}}{(r/\lambda_0)} [\hat{\theta} \cos \theta] \quad . \tag{4.3}$$

The total transmitted field through the radome in the E-plane is given by

$$\vec{E}^t(r,\theta,\phi = 90°) \sim \frac{e^{-jk_0 r}}{(r/\lambda_0)} [\hat{\theta} P(\theta)] \quad , \; r \to \infty \; . \tag{4.4}$$

In the following, we present results of $P(\theta)$ for various radomes.

We have studied a total of 8 radomes. Detailed results are presented in a technical report [5]. Among them, two types of paraboloidal radomes are of special interest presently. In both types, the inner surface is described by

$$\left(\frac{z}{\lambda_0}\right) = 50 - \frac{1}{8\lambda_0^2}\,(x^2 + y^2) \quad . \tag{4.5}$$

The outer surface for the first type is

$$\left(\frac{z}{\lambda_0}\right) = 50.5 - \frac{1}{9\lambda_0^2}\,(x^2 + y^2) \quad , \tag{4.6}$$

so that the thickness of the radome increases toward its base (Figure 4). The outer surface for the second type is

$$\left(\frac{z}{\lambda_0}\right) = 50.5 - \frac{1}{8.321\lambda_0^2}\,(x^2 + y^2) \quad , \tag{4.7}$$

so that the radome thickness is nearly uniform (Figure 5). For the incident field in (4.3), the E-plane pattern $|P(\theta)|$ for radomes E and F is presented in Figures 6 and 7.

It is particularly interesting to note that, for the field on the z-axis, there is a striking difference between radome E and radome F, namely, there is a dip in Figure 6 for radome E, whereas there is a peak in Figure 7 for radome F. This is so, despite the fact that, near the tip, radomes E and F are quite similar as may be seen from the expanded graph in Figure 8. The reason for such an anomalous behavior is explained below.

Let us consider the special case of transmission in the tip region of the symmetrical radomes under discussion.

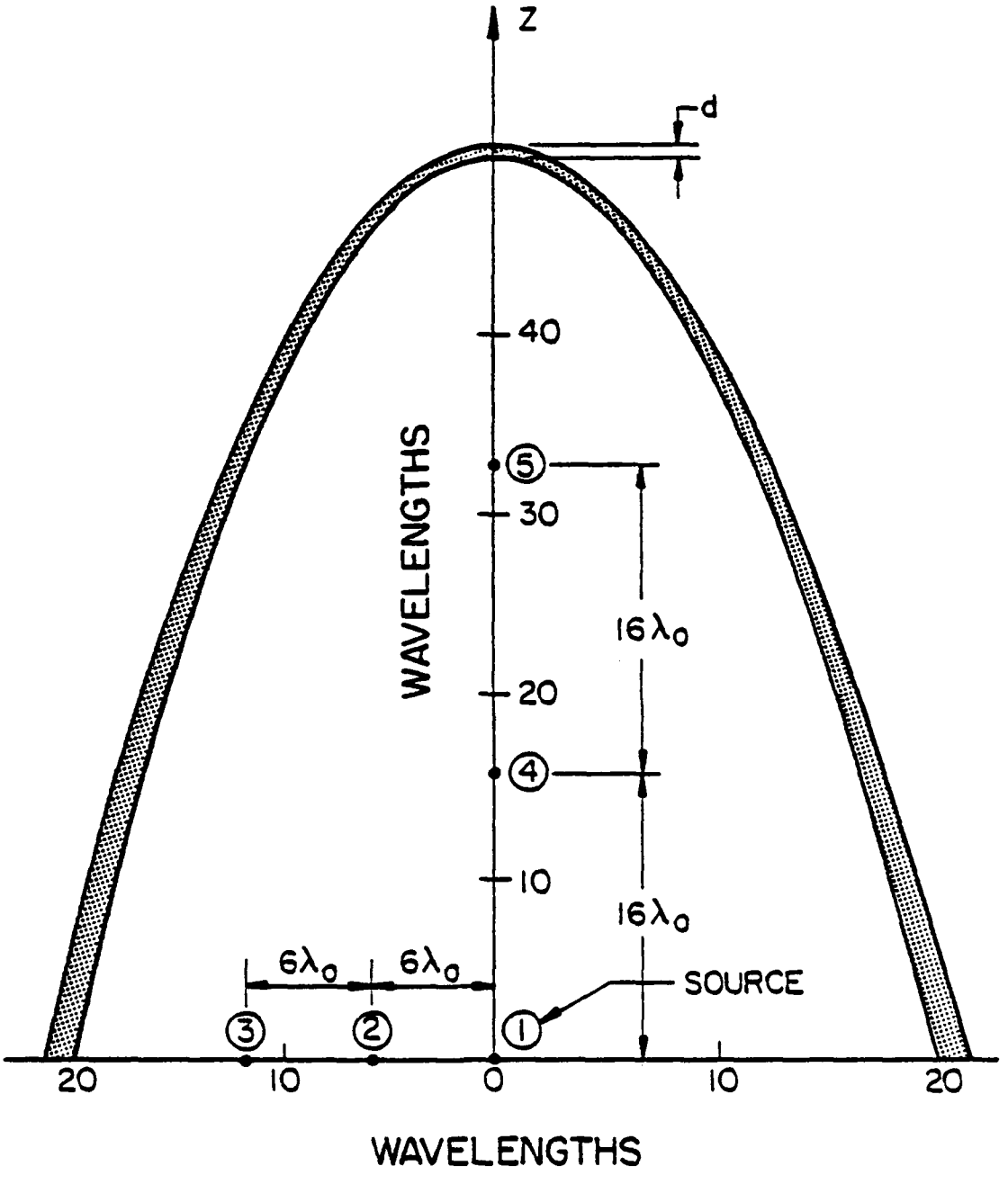

Figure 4. Paraboloidal radomes E and H described by Eqs. 4.5 and 4.6.

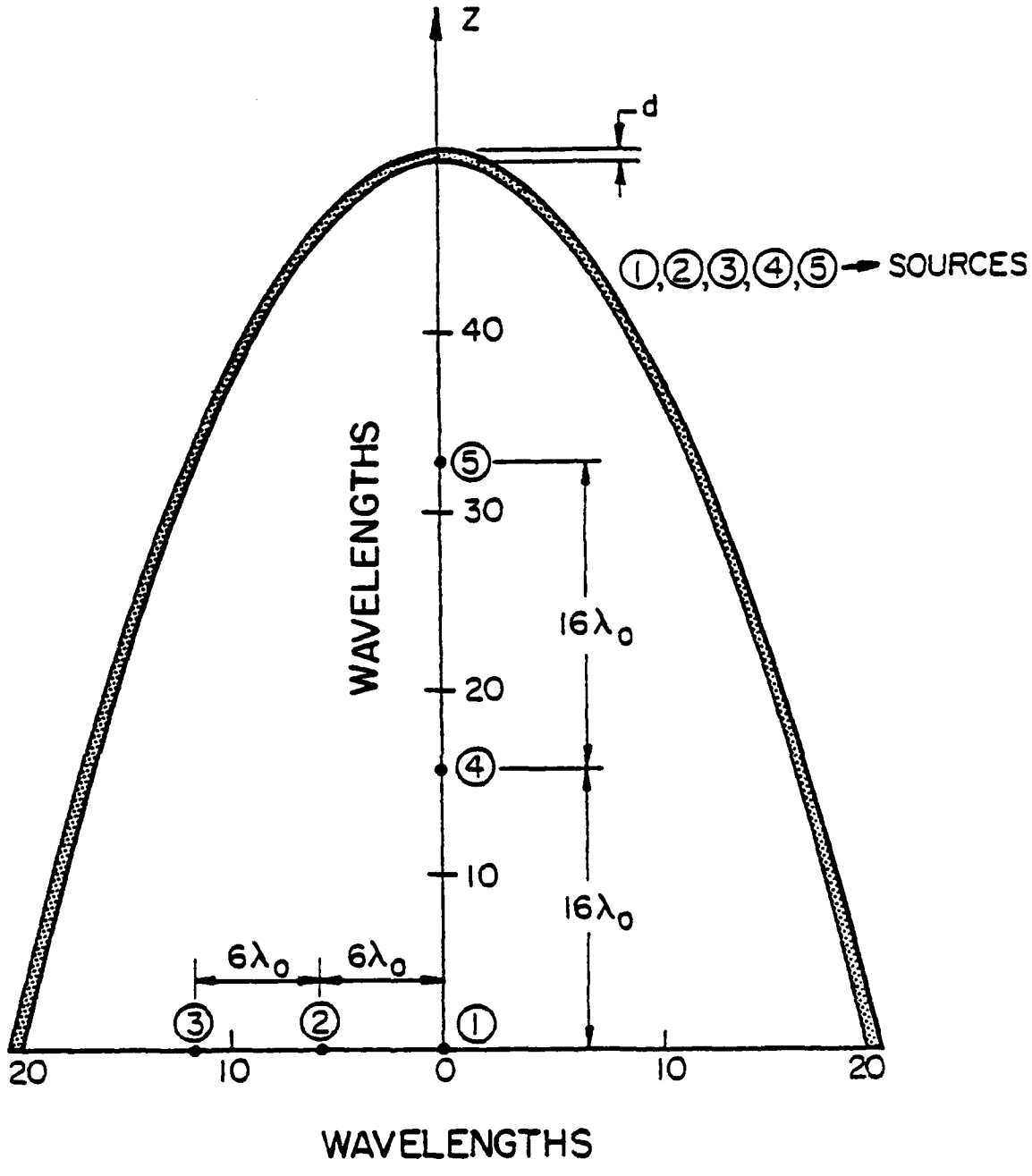

Figure 5. Paraboloidal radomes F and G described by Eqs. 4.5 and 4.7.

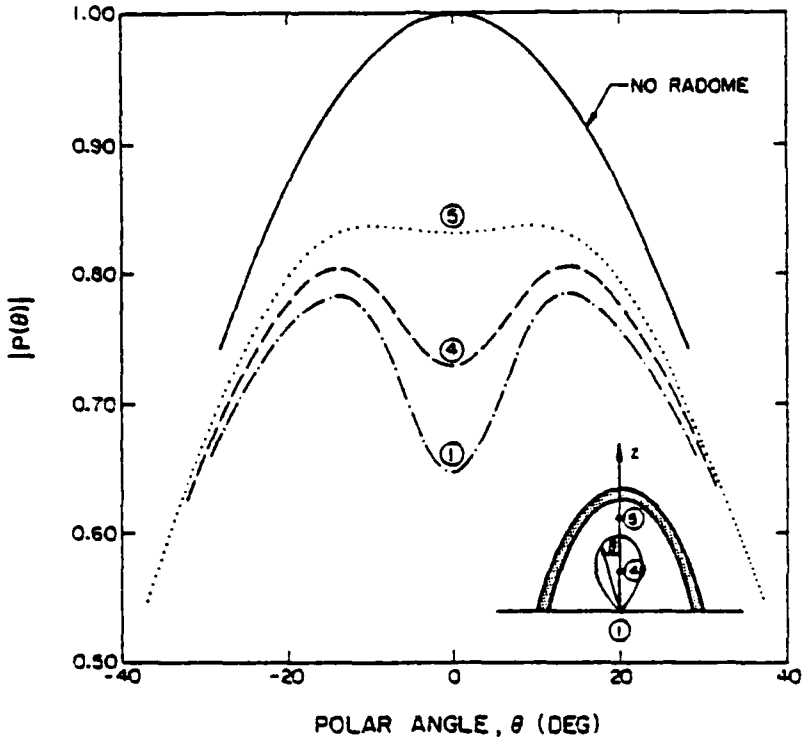

Figure 6. E-plane radiation pattern through radome E (ε_r = 2.5, d = $\lambda_0/2$).

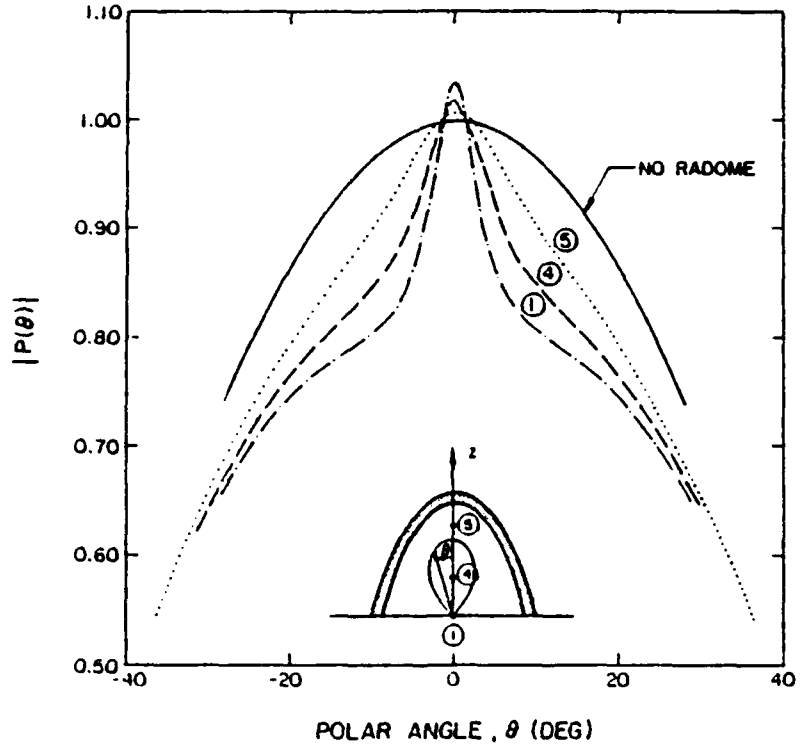

Figure 7. E-plane radiation pattern through radome F (ε_r = 2.5, d = $\lambda_0/2$).

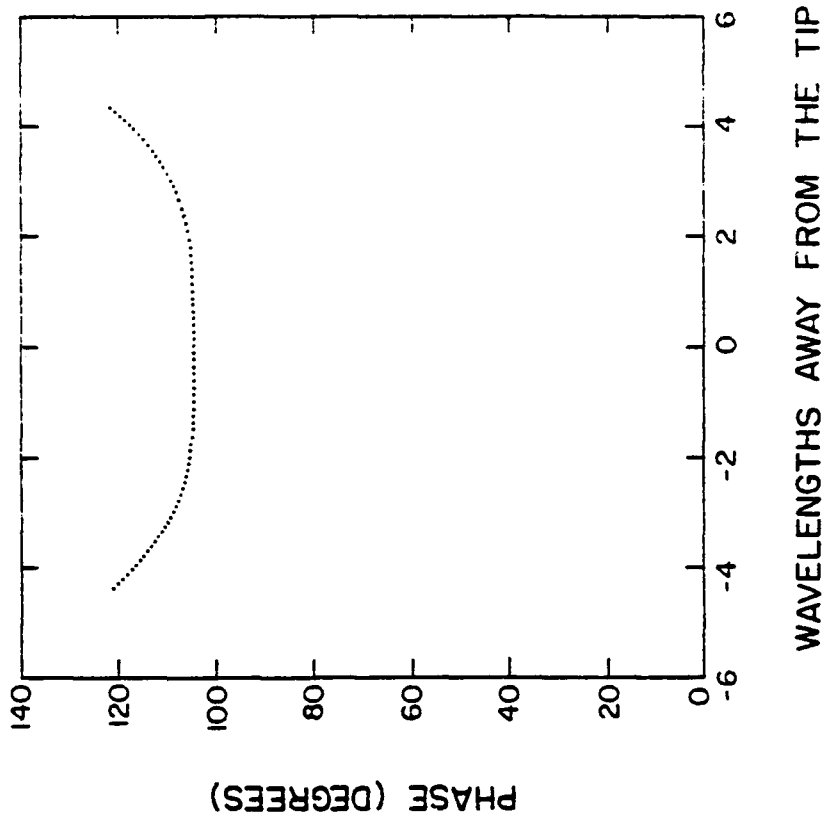

Figure 9. Phase distribution for critical R_2 case, on a plane normal to z-axis just outside the radome.

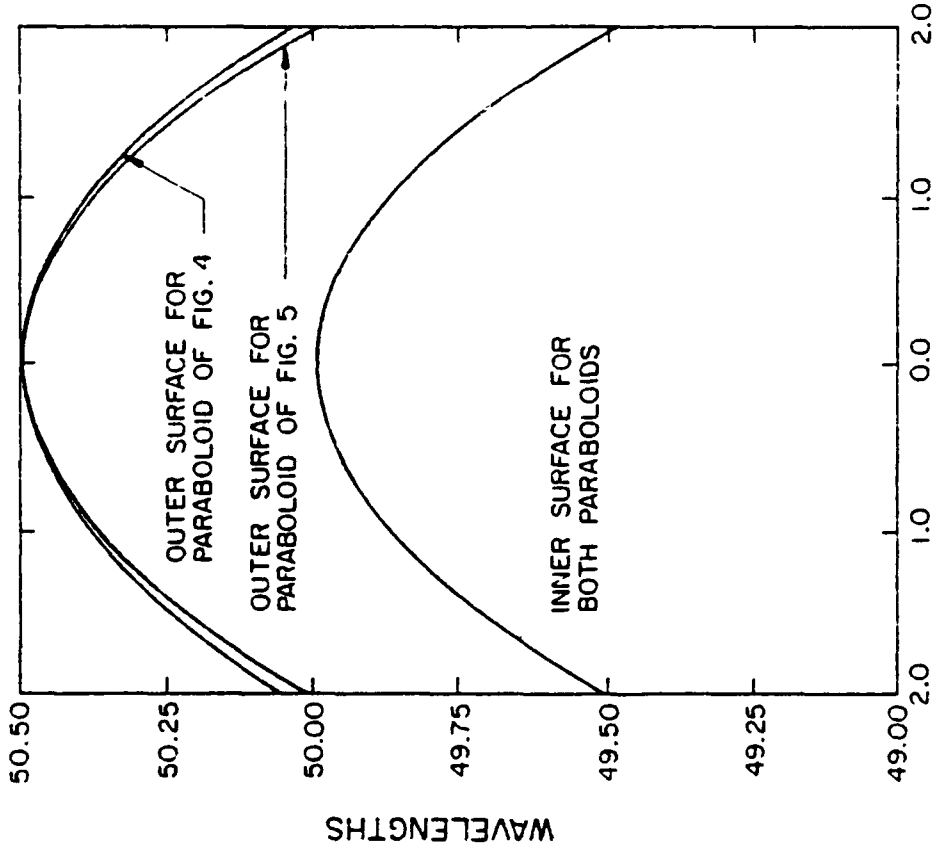

Figure 8. Expanded views of the paraboloids of Figures 4 and 5 around the tips.

For this case,

$$r_{23} \to \infty \quad \text{and} \quad \alpha_1^i = 0 \quad .$$

The total divergence, defined by

$$TD = (DF_{12} \quad DF_{23}) \frac{r_{23}}{r_{01}}$$

reduces to

$$TD = \left\{1 + (n - 1) \frac{r_{01}}{R_1 R_2} d \left[\frac{R_2 - R_1}{d} - 1 + \frac{1}{n}\left(1 - \frac{R_1}{r_{01}}\right)\right]\right\}^{-1} \tag{4.8}$$

where R_1 and R_2 are the radii of curvature of the inner and outer surfaces along the z axis and d is the radome thickness in this direction. It can be shown that if R_2 satisfies the relation

$$R_2 = \frac{(n - 1) r_{01} R_1}{R_1 + (n - 1) r_{01}} + \left(\frac{n - 1}{n}\right) d \quad , \tag{4.9}$$

TD in (4.8) becomes infinite. This means that the rays in the pencil near the axis emerging from the radome are parallel so that they focus at the far-field point. Figure 9 shows the phase distribution for this case on a plane normal to the z-axis just outside the radome. Note the constant phase in the tip region which indicates that the rays are parallel.

The geometrical parameters of radomes E and F on the z-axis are listed in Table I.

TABLE I

FIELD ON z-AXIS

Radome	R_1/λ_0	R_2/λ_0	r_{01}/λ	$\lvert P(\theta) \rvert$
E	4	4.500	50	0.647
F		4.161		1.036

Note that, while R_1 is the same for both radomes, R_2 does vary slightly (about 8%). According to (4.9), the critical value of R_2 for source position 1 ($r_{01} = 50\ \lambda_0$) is

$$\text{Critical } R_2 = 3.7\ \lambda_0 \quad . \tag{4.10}$$

At this critical R_2, the divergence factor DF and, therefore, field $\vec{E}_3$ in (3.34) as predicted by the present geometrical optics theory becomes infinite. In Figure 10, we plot the ratio of the field with and without the radome for three values of r_{01}. The solid curve in Figure 10 corresponds to the case discussed in Table I. For both radomes E and F, their values of R_2 are close to the critical value $R_2 = 3.7\ \lambda$ and, consequently, the fields on the z-axis are quite sensitive to R_2. For radome E, the pattern function $|P|$ has the value 0.647 (dip), whereas that of radome E, has the value 1.036 (peak).

This lens effect was also confirmed by the aperture integration technique in which the rays were traced to a plane normal to the z-axis just outside the radome and the field on this plane was integrated to obtain the far-field pattern.

Figure 11 shows the patterns obtained both with the direct ray method and through integration for a radome in which the focusing action can be very clearly observed. The outer surface of this radome was generated from the equation.

$$\left[\frac{z}{\lambda_0}\right] = 50.5 - \frac{1}{7.921\ \lambda_0^2}\ (x^2 + y^2) \tag{4.11}$$

and the inner surface was the same as in (4.5). It may be observed that the axial field strength obtained through direct ray tracing is much larger than that obtained by integration. This is because geometrical

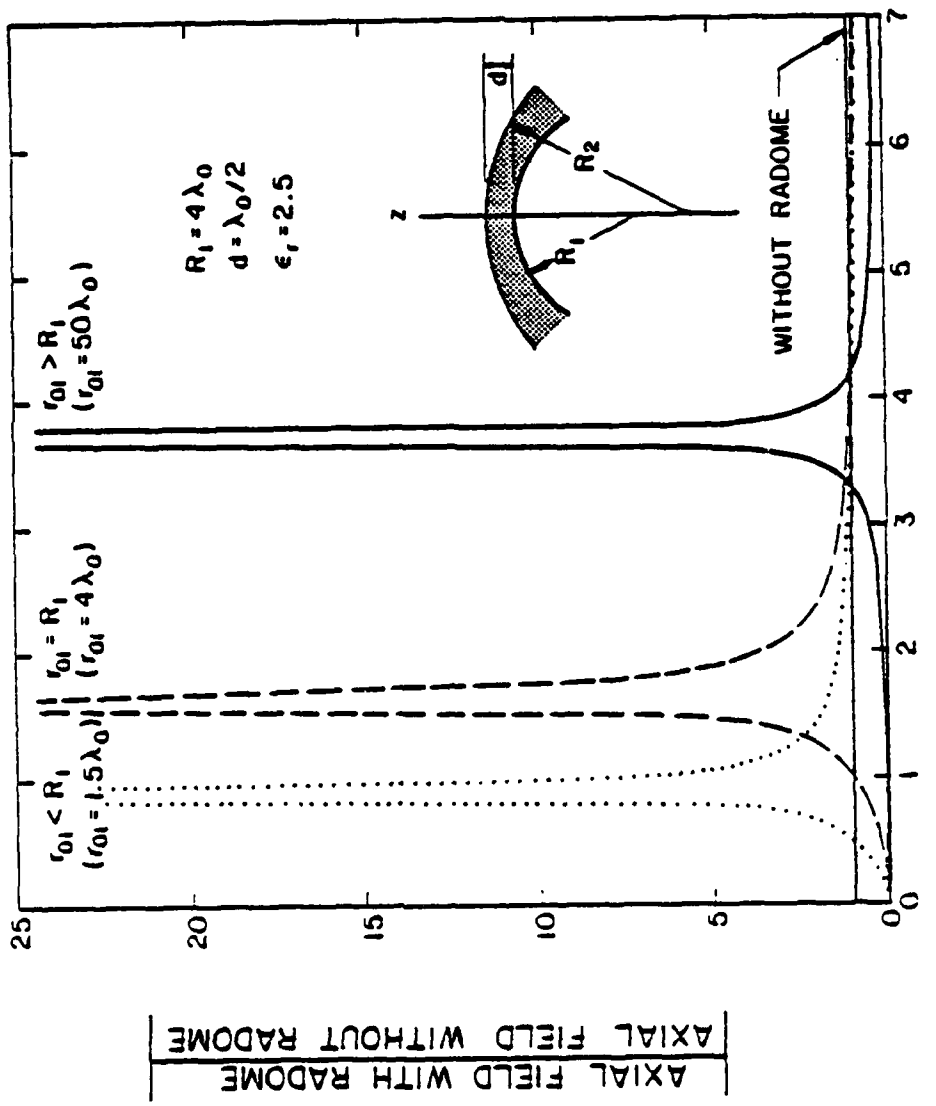

Figure 10. Variation of axial field strength with R_2, for a paraboloid with the source on z-axis.

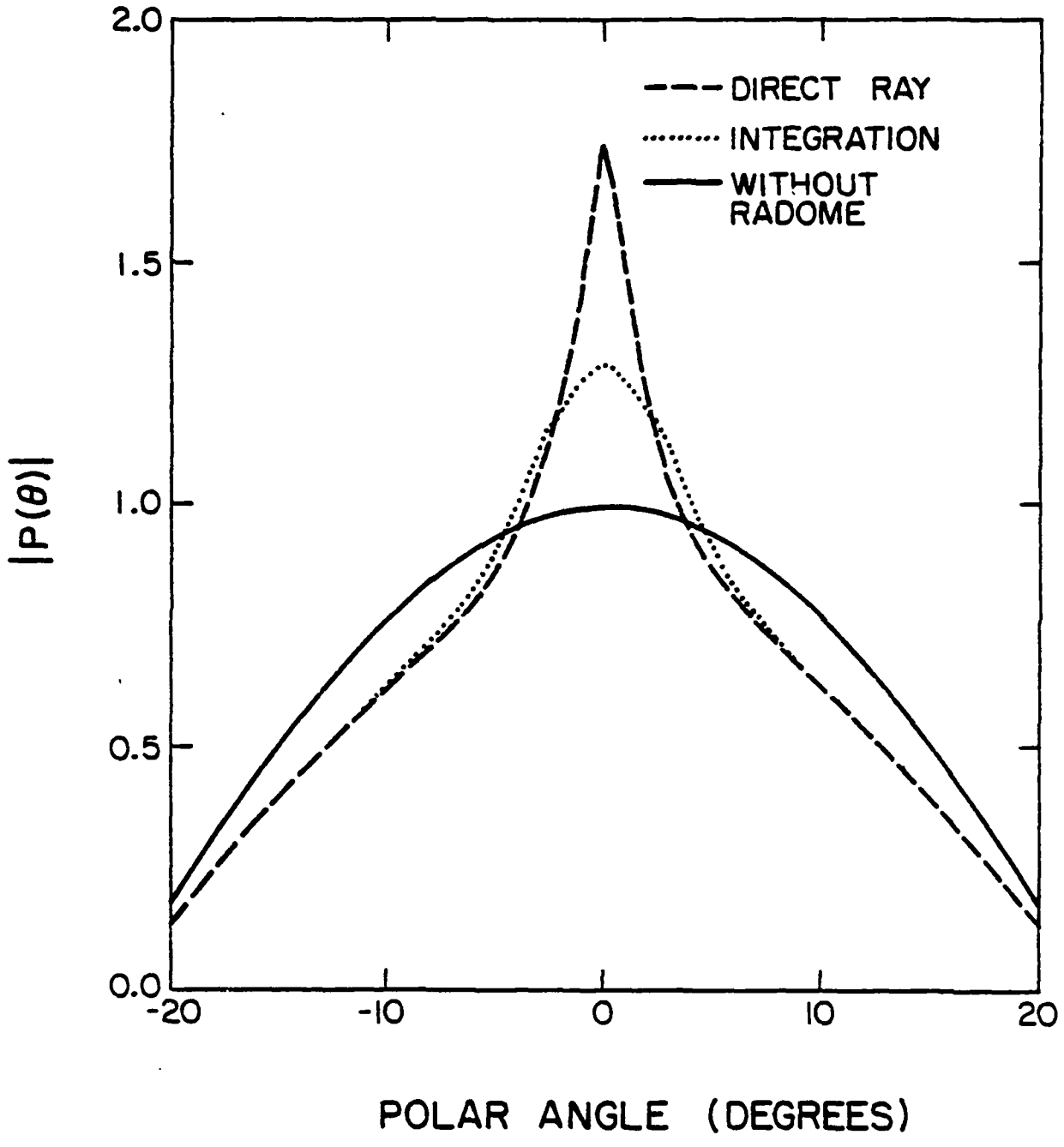

Figure 11. E-plane radiation pattern for the radome specified by Eqs. (4.5) and (4.11) ($\varepsilon_r = 2.5$; $d = \lambda_0/2$).

optics becomes less and less accurate as the rays in a pencil tend to become more and more parallel. In fact, a study of a number of radomes showed that both methods give nearly the same result until one approaches a total divergence factor of about 0.5 (the total divergence factor is defined here by $\left(r_{23} \cdot DF_{12} \cdot DF_{23}\right)_{r_{23} = \infty}$. Figure 12 shows this result.

REFERENCES

[1] D. T. Paris, "Computer aided radome analysis," IEEE Trans. Antennas Propagat., vol. AP-18, pp. 7-15, 1970.

[2] D. C. F. Wu and R. C. Rudduck, "Plane wave spectrum - surface integration technique for radome analysis," IEEE Trans. Antennas Propagat., vol. AP-22, pp. 497-500, 1974.

[3] S. W. Lee, "Geometrical theory of diffraction in electromagnetics, Vol. 1: Geometrical optics," Tech. Rept. 78-2, Electromagnetics Lab., Univ. of Ill., Urbana, IL, 1978.

[4] G. A. Deschamps, "Ray techniques in electromagnetics," Proc. IEEE, vol. 60, pp. 1022-1035, 1972.

[5] S. W. Lee, V. Jamnejad, M. S. Sheshadri, and R. Mittra, "Analysis of antenna radomes by ray techniques," Tech. Rept., Electromagnetics Laboratory, Univ. of Ill., Urbana, IL, May 1980.

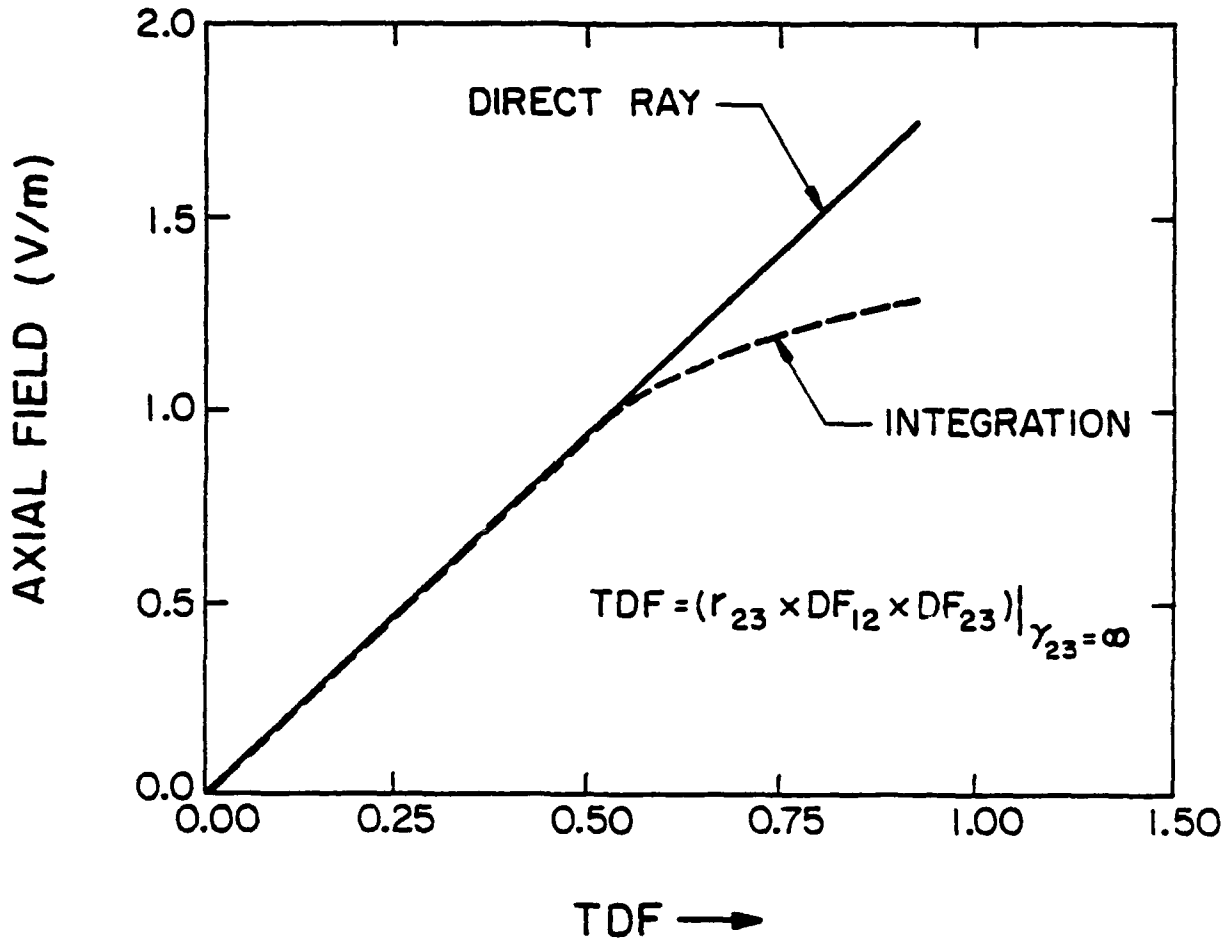

Figure 12. Comparison of integrated and direct ray axial fields for varying values of total divergence factor (ε_r = 2.5).

A HYBRID METHOD OF MOMENTS - GTD TECHNIQUE FOR COMPUTING ELECTROMAGNETIC COUPLING BETWEEN TWO MONOPOLE ANTENNAS ON A LARGE CYLINDRICAL SURFACE

Steven A. Davidson
Aeronautical Systems Division
Wright-Patterson AFB, Ohio

and

Dr. Gary A. Thiele
School of Engineering
University of Dayton, Dayton, Ohio

ABSTRACT

The problem of analyzing the electromagnetic interference (EMI) between two electronic systems when their antennas are located on or near large scattering objects is a difficult one. In recent years, the geometrical theory of diffraction (GTD) has been useful in treating scattering problems which are large in terms of the wavelength while the moment method (MM) has been useful in treating antenna problems which are not large in terms of the wavelength.

The hybrid technique presented in this paper is a method for solving electromagnetic problems in which an antenna or other discontinuity is located on or near a conducting body, such as antennas on aircraft or ships. The technique solves these kinds of problems by properly analyzing the interaction between the antenna or scatterer and the conducting body. The hybrid technique accomplishes this by casting the antenna structure in a moment method format and then modifying that format to account for the effects of the conducting body via the geometrical theory of diffraction. The technique extends the moment method to handle many problems that cannot be solved by GTD or the moment method alone.

In general, arbitrary radiators located on or near canonical shapes or combinations thereof can be solved using the hybrid technique. Electromagnetic parameters which the hybrid technique can solve for include the near and far fields, current distributions, impedances, and scattering data. In this paper, a transmitting and receiving monopole antenna, located on the surface of a perfectly-conducting circular cylinder, are analyzed to determine the amount of radiated power which arrives at the receiving antenna, after accounting for the reflection and curved surface diffraction effects of the conducting cylinder.

The purpose of this paper is to present the technique and to demonstrate some of its facility and its accuracy, as evidenced by the close agreement of its results to the results of an electromagnetic computer analysis program currently used by the United States Air Force (USAF) in solving similar problems. This computer program is known as the Intrasystem Electromagnetic Compatibility Analysis Program (IEMCAP). Using both computer programs, antennas are modeled as one-quarter wavelength monopoles and are positioned on conducting circular cylinders with radii ranging from one to 150 wavelengths and the power coupling between the antennas is computed by both computer codes. The near-perfect agreement in the results of these radically different analysis codes implies that their solutions, in general, are correct.

I. INTRODUCTION

The purpose of this paper is two fold. First, the idea of a hybrid technique of combining the method of moments with GTD is extended to account for the mutual coupling between two monopole antennas on a large circular cylinder by means of curved surface wave diffraction. Second, the results of this technique are compared to those of an analysis program used by the United States Air Force which predicts electromagnetic coupling between aircraft antennas. The close agreement between the results of these two different analysis techniques serves to validate both computer programs.

The basic hybrid technique used in this paper was first described in the literature by Thiele and Newhouse [1]. There, the technique was applied to antennas on and near finite planar surfaces. Wedge diffraction theory was combined with the method of moments to account for the finite planar surfaces. Ekelman[2], building on this previous work, developed a hybrid technique for combining the moment method treatment of wire antennas with the GTD to account for reflection of electromagnetic energy from the curved surface of an infinitely long cylinder as well as diffraction from the ends of a finite cylinder. In the present paper, curved surface diffraction theory is used to extend a method of moments thin-wire analyses program to account for the propagation of electromagnetic energy around the curved surface of an infinitely long cylinder.

II. METHOD OF MOMENTS

The method of moments is a procedure for reducing an integral equation of the form

$$\int_{\text{over structure}} I(z')K(z,z')dz' = E^{i}(z) \qquad (1)$$

to a system of simultaneous linear algebraic equations in terms of the unknown current I(z'). It can be used to determine the current distribution on an antenna, based on the physical properties of the antenna, its configuration, and even possible environmental influences such as the presence of a nearby conducting surface. Thus the traditional problem in antenna theory of deriving the form of the current distribution on an antenna is solved automatically. Once the current is known, radiation patterns and impedance can be determined in a straightforward manner.

The specific computer code used for the moment method portion of the analysis is based on the thin-wire program written by Richmond [3]. It requires that all antennas and scatterers consist of thin wires or a grid of thin wires. This constraint allows one to make use of Pocklington's integral equation to describe the relationship between an electric field incident on the surface of a wire and the resulting surface current induced on the wire. Details of the derivation of the Pocklington integral equation are given by Stutzman and Thiele [4].

III. GEOMETRIC THEORY OF DIFFRACTION - APPLICATION FOR A SMOOTH CONVEX SURFACE

The purpose of this section is to introduce a high frequency method, the geometrical theory of diffraction (GTD), which is applicable to curved bodies that are electrically large. This section will then discuss the use of GTD to determine the propagation of electromagnetic energy over the curved surface of a circular cylinder.

GTD views the propagation of electromagnetic energy as rays (analogous to rays of light) which are subject to scattering and diffraction from specific parts of a body such as flat surfaces, curved surfaces, or sharp edges. Unlike the method of moments, GTD only requires detailed information about the interacting body at points of reflection and diffraction. Thus, unlike the method of moments, the complexity and magnitude of the analysis does not increase as the electrical size of the interacting body increases. However, GTD relies on the use of more assumptions than the method of moments; primarily, the ray-like behavior of electromagnetic energy, which tends to render this method invalid at very low frequencies.

In conventional GTD analysis, the total field exterior to a curved surface will consist of incident, reflected, and diffracted rays which may be divided into five separate regions as shown in Fig. 1 [5]. The shaded Region II in the vicinity of the shadow boundary is a transition region which divides the lit zone from the shadow zone. Very close to the surface, Region II

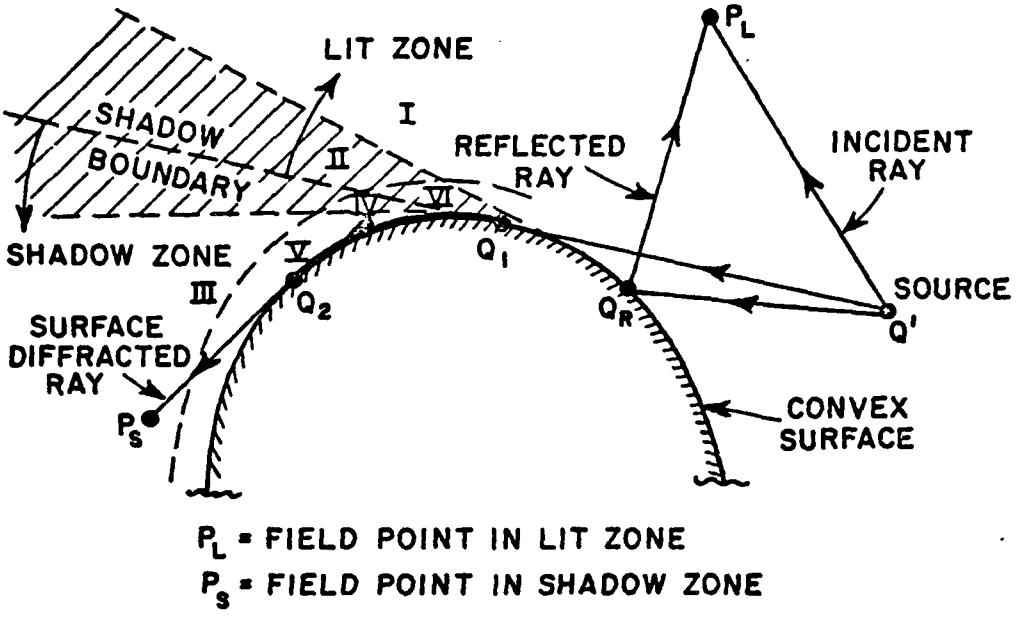

Fig. 1. The Rays and Regions Associated with Scattering by a Smooth Convex Cylinder

is subdivided into Regions IV and VI in the shadow and lit zone respectively. Region V is a subdivision of Region III which is in the immediate vicinity of the surface. More specifically, Regions IV and V are close to the portion of the surface which is a caustic of the surface diffracted rays; whereas, Region II is in the vicinity of the point of grazing incidence (Q_1) which is a caustic of the reflected ray. Regions IV, V and VI are therefore commonly referred to as the caustic or surface boundary layer regions. The curved surface diffraction hybrid analysis developed in this paper will be exclusively for this surface boundary layer.

The theory and equations which describe electromagnetic behavior in the surface boundary layer of an arbitrary, perfectly-conducting convex surface are explained by Pathak and Wang [6]. For the sake of brevity, this section will simply present the equations used to predict the electric field strength in the surface boundary layer from an infinitesimal electric current (or current moment) which is also located within the surface boundary layer. According to Eq. 31 in Ref. 6, the electric field strength from a source at point P' which is observed at point P (see Fig. 2) is given by the following expression:

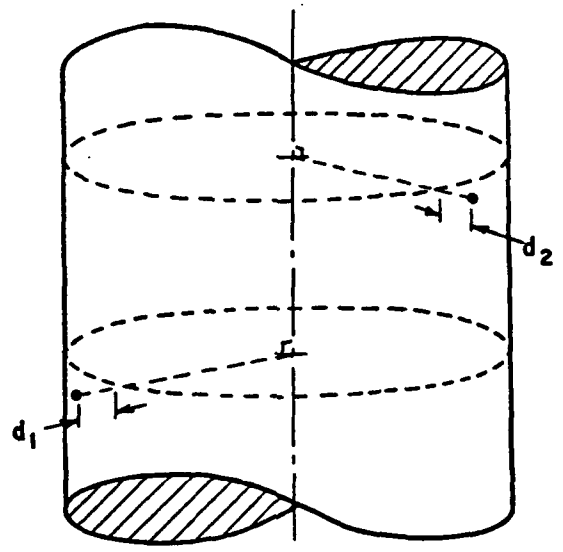

(a) SIDE VIEW

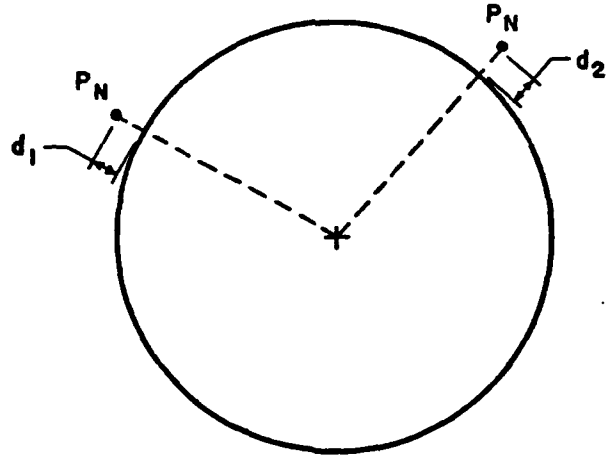

(b) END VIEW

Fig. 2. Circular Cylinder Geometry

$$\bar{E}_n^{\,e}(P) = z_o^2 DG(k_s)\bar{p}_e \cdot \hat{n}' \hat{n}$$

$$\left(\left\{F_n(\xi,y_1,y_2) - \frac{j}{k_s} F_h(\xi,y_1,y_2) + \left(\frac{j}{k_s}\right)^2 F_s(\xi,y_1,y_2)\right\} + T_o^{\,2} \frac{j}{k_s}\left\{F_s(\xi,y_1,y_2) - F_h(\xi,y_1,y_2)\right\}\right) \qquad (2)$$

where

z_o = impedance of the medium = $\eta = \sqrt{\mu/\epsilon}$

k = wavenumber of the medium = $2\pi/\lambda = \omega\sqrt{\mu\epsilon}$

s = length of the surface ray geodesic path from P' to P

ρ_g = radius curvature of surface along the ray = $a/\sin^2\delta$

δ = angle of path with respect to the cylinder axis

a = cylinder radius

$G(k_s) = \dfrac{ke^{-jks}}{j2\pi s z_o}$

$\xi = \dfrac{ms}{\rho_g}$

$m = \left(\dfrac{k\rho_g}{2}\right)^{1/3}$

$y_1 = m^{-1}kd_1$

$y_2 = m^{-1}kd_2$

d_1 = height of source point, P', above cylinder surface

d_2 = height of observation point, P, above cylinder surface

T_o = torsion factor = cos δ for a circular cylinder

D = spatial factor = 1 for a circular cylinder

$F_h(\xi,y_1,y_2)$ = "hard" type surface Fock function

$F_s(\xi,y_1,y_2)$ = "soft" type surface Fock function

p_e = strength of a current moment source at P'

n' = unit outward normal vector at source point P'

$\hat{n}$ = unit outward normal vector at observation point P

For $\xi \neq 0$, the Fock function may be approximated by a Taylor series expansion as follows:

$$F_h(\xi,y_1,y_2) = v(\xi) - \frac{j}{4}\,\xi^{-1}v_1(\xi)[y_1^2 + y_2^2] \tag{3}$$

$$F_s(\xi,y_1,y_2) = u(\xi) + \frac{j}{2}[u'(\xi) - \frac{3}{2}\,\xi^{-1}u(\xi)][y_1^2 + y_2^2] \tag{4}$$

According to Pathak and Wang [6], when ξ is large, say $\xi > .6$, a rapidly converging residue series representation for the Fock functions may be utilized. If, on the other hand, ξ is a small positive number less than or equal to .6, one may employ a small argument asymptotic expansion for the Fock functions.

At first glance, the mathematics for computing the observed electric field strength may appear to be a bit overwhelming. However, by confining the convex surface to that of a circular cylinder, the electric field strength of Eq. 2 becomes only a function of the location of the source and observation points P' and P; the location, orientation, and radius of the circular cylinder; and the magnitude and direction of the current moment at point P', $\bar{p}_e$, respectively.

IV. THE HYBRID TECHNIQUE

The hybrid technique seeks to combine the moment method with GTD in an optimum manner so as to yield an analysis procedure for antennas near large electrical bodies which is both efficient and accurate, relying on a minimum number of assumptions.

The basic technique to be described in this paper was first presented in the literature by Thiele and Newhouse [1]. The approach is to first model the wire antennas using the moment method and then modify the generalized impedance matrix to account for the effects of nearby conducting bodies via GTD. This differs from other hybrid approaches which use the moment method to extend GTD [7].

The basic moment method equation for wires

$$\int_{-L/2}^{L/2} I(z')K(z_m,z')dz' = -E_z^i(z_m) \tag{5}$$

predicts the electric field strength E_z^i at point z_m which is due to the current function I(z') over a wire of length L. Thru the use of expansion functions, F_n, the wire can be divided into N segments so that the fields at z_m can be written as:

$$\sum_{n=1}^{N} I_n \int_{\Delta z_n} F_n K(z_m,z_n')dz' = - E_z^i(z_m) \tag{6}$$

Applying a weighting function, W_m, to Eq. 6 in order to satisfy the boundary conditions in an average sense over the length of the wire results in:

$$\int_{-L/2}^{L/2} W_m \sum_{n=1}^{N} I_n \int_{\Delta z_m} F_n K(z_m,z')dz'dz = \int_{-L/2}^{L/2} W_m \cdot -E_z^i(z_m)dz \tag{7}$$

Interchanging the order of integration and summation:

$$\sum_{n=1}^{N} I_n \int_{-L/2}^{L/2} W_m \int_{\Delta z_m} F_n K(z_m,z')dz'dz = \int_{-L/2}^{L/2} W_m \cdot -E_z^i(z_m)dz \tag{8}$$

Following the notation used by Thiele and Newhouse, Eq. 8 can be expressed as:

$$\sum_{n=1}^{N} I_n < W_m, L(J_n) > = < W_m, -E_z^i(z_m) > \tag{9}$$

where $L(J_n)$ represents a linear operator which relates the surface expansion currents to the field at point m. Specifically, it can be thought of as the magnitude of the field at point m due to a unit test current at point n. For wires in free space with no other conducting bodies nearby,

$$L(J_n) = \int_{\Delta z_m} F_n K(z_m,z')dz' \tag{10}$$

Eq. 9 can be rewritten as:

$$\sum_{n=1}^{N} I_n Z_{mn} = V_m \tag{11}$$

where

$$Z_{mn} = <W_m, L(J_n)> \tag{12}$$

$$V_m = <W_m, -E_z^i(z_m)> \tag{13}$$

Since the linear operator, L, relates the expansion currents J_n to their electric fields, E, Eq. 12 could be expressed as:

$$Z_{mn} = <W_m, (\underline{a}E)> \tag{14}$$

where $\underline{a}$ is a complex scalar. If conducting bodies are in the vicinity of the wire antennas, Eq. 12 can be rewritten as

$$Z_{mn}' = \langle W_m, L'(J_n) \rangle \tag{15}$$

or

$$Z_{mn}' = \langle W_m, \underline{a}E_1 + \underline{b}E_2 \rangle \tag{16}$$

where

E_1 = field arriving at observation point m directly from J_n

E_2 = field arriving at observation point indirectly from J_n due to reflection or diffraction from a conducting body

$\underline{a}$ = complex scalar for E_1

$\underline{b}$ = complex scalar for E_2

Using properties of linear functions:

$$Z_{mn}' = \langle W_m, aE_1 \rangle + \langle W_m, bE_2 \rangle \tag{17}$$

$$Z_{mn}' = Z_{mn} + Z_{mn}^g \tag{18}$$

where

Z_{mn} = the "direct impedance" matrix term which relates the field at segment m that arrives directly, to the current on segment n

Z_{mn}^g = the "delta impedance" matrix term which relates the field at segment m that arrives indirectly, due to diffraction or reflection, to the current on segment n

Z_{mn}' = the net impedance matrix term.

The hybrid moment method procedure can thus be summarized by the following steps

1. Completely describe the geometry of the problem; location and size of all wire segments and any conducting bodies in the vicinity.

2. Determine the net impedance matrix terms, Z_{mn}':

   a. Determine the average field at segment m, if any, which arrives directly from a test current of one amp at segment n, (Z_{mn}).

   b. Determine the field at segment n, if any, which arrives indirectly, due to reflection by a conducting body, from a test current of one amp at segment n, (Z_{mn}^r).

   c. Determine the field at segment n, if any, which arrives indirectly, due to diffraction by a conducting body, from a test current of one amp at segment n, (Z_{mn}^d).

d. For each pair of wire segments n and m, sum the direct and delta impedance matrix terms to obtain the net impedance matrix term for that wire segment pair.

3. Define a field source which will generate an incident, average field, V_m, directly on each segment m. (For transmitting and receiving wire antenna problems, source field $[V_m]$ would be non-zero only for the transmitting antenna segments.)

4. Solve the matrix equation $[I_n] = [Z_{mn}]^{-1}[V_m]$ to obtain the current for every segment of all the wire antennas.

5. Use standard, simple electromagnetic relationships to determine such parameters as the antenna input impedance, radiated power, antenna efficiency, field patterns, mutual coupling between two wire antennas, etc., based on the now known current distribution on the wire antennas.

In this work we used Richmond's thin wire moment method program [8], which uses a piecewise sinusoidal expansion of the current in a Galerkin formulation of the moment method. The GTD for curved surfaces was then built into this program to implement the hybrid technique.

V. COMPARISON OF RESULTS WITH AN ALTERNATIVE ANALYSIS PROGRAM

This section will discuss an alternative electromagnetic analysis program which is promoted by the United States Air Force (USAF) and will show how well the results of the USAF analysis program agree with the hybrid method of moments (MOM) program for a variety of cylinder radii and relative antenna locations.

The Intrasystem Electromagnetic Compatibility Analysis Program (IEMCAP) is a USA Standard FORTRAN program for computer-aided implementation of electromagnetic compatibility (EMC) at all stages of an Air Force system's cycle, applicable to aircraft, space/missile, and ground-based systems [9].

The antenna-to-antenna coupling model, one of the many coupling modes between equipment subsystems which IEMCAP can analyze, is basically a geometric optics (GO) program which determines the severity of interference that a transmitting antenna may unintentionally produce in other antenna receiving systems on the same aircraft due to such phenomena as the generation of higher order harmonics. To use the antenna-to-antenna portion of IEMCAP, one begins by modeling the aircraft as a

conducting cylinder with a cone attached at one end. Wings, modeled as infinitely-thin flat plates, can be attached to the sides of the cylinder. Next, antennas are described by their gain patterns, supplied by the user. Up to three different quantized levels of antenna gain may be specified for the spherical sectors which enclose the antenna. The antennas are then positioned and oriented at their respective locations on the cylinder that represents the aircraft fuselage. The power, frequency range, signal modulation characteristics, and relative harmonic levels of transmitters are enumerated by the user as well as the antennas to which the transmitters are connected. Similarly, the power sensitivity threshold, frequency range, and out-of-band rejection of the receivers, as well as their antennas, are specified by the User. IEMCAP will then determine the magnitude of power delivered to a specific receiving antenna from one of the transmitting antennas, based on the relative position of the antennas on the modeled aircraft, the appropriate gains of the antennas, and the frequency of transmission. The magnitude of the received power is then compared to the receiver's power sensitivity for that frequency and if it exceeds that sensitivity, a potential electromagnetic inference (EMI) problem is predicted by IEMCAP.

In determining the magnitude of the power coupled to the receiving antenna, IEMCAP takes into consideration the distance between the antennas (free-space loss), diffraction around the fuselage (fuselage shading factor), and any diffraction off the edge of the wing which may lie in the direct path between the two antennas (wind diffraction factor). These three factors, all in units of decibels, are added together algebraically with the antenna gains (also in decibels) to arrive at the power coupling factor between the two antennas for a given frequency.

The fuselage shading factor used by IEMCAP is based on work by Hasserjian and Ishimaru [10]. In their analysis, a function is derived which relates the propagation around an infinite conducting cylinder to that over a flat plane. This function is approximated by IEMCAP as follows [11]:

$$SF_c = \frac{-A}{(\eta A + \xi)} \tag{19}$$

where

$$A = \rho_f \Theta_s^2 \sqrt{\frac{2\pi}{\lambda D_c}} \tag{20}$$

$$\eta = \begin{cases} 5.478 \times 10^{3} & \text{for } A < 26 \\ 3.340 \times 10^{-3} & \text{for } A \geq 26 \end{cases}$$

$$\xi = \begin{cases} .5083 \text{ for } A < 26 \\ .5621 \text{ for } A \geq 26 \end{cases}$$

and

SF_c = fuselage (cylindrical) shading factor (dB)

ρ_f = radius of cylinder (meters)

θ_s = angle around cylinder of propagation path (radians)

λ = wavelength (meters)

D_c = distance of the cylindrical segment of propagation path

It is possible to compare the performance of hybrid moment method against that of IEMCAP in computing cylindrical diffraction loss. As part of the standard output, IEMCAP will print the transfer loss between two antennas in units of decibels (dB). The corresponding number can also be obtained from the hybrid moment method program.

The next step was to choose an antenna configuration for both programs. For the first configuration, a transmitting monopole antenna was fixed on the surface of a circular cylinder while the receiving monopole antenna was positioned in the plane of the transmitting antenna perpendicular to the cylinder axis, at various angular separations from the transmitting antenna as shown in Fig. 3. The radius of the cylinder was initially chosen to be ten wavelengths. This corresponds to the fuselage of a cargo aircraft such as a C-141 or a C-5A at around one gigahertz (GHz), close to the frequencies used by airborne military navigation equipment.

Fig. 4 illustrates the excellent agreement between these two radically different approaches for calculating the power coupling factor between two antennas due to cylindrical surface diffraction. Here, values were computed at ten degree intervals. The only significant difference in results between the two methods is when the two antennas are separated by large angles. At these angular separations, both the short and long path diffracted field contributions are similar in magnitude at the receiving antenna. However the difference in the phase angle of the arriving fields results in a reinforcement or cancellation effect. By plotting only the values between 160 and 180 degrees, this phenomenon can be more clearly seen as Fig. 5 shows. The MOM code data in Fig. 5 is very similar to a standing wave pattern on a lossy transmission line in the vicinity of a discontinuity. The distance between null points is one-half wavelength. One observes that very close to 180 degrees, the total power received by the second antenna can vary

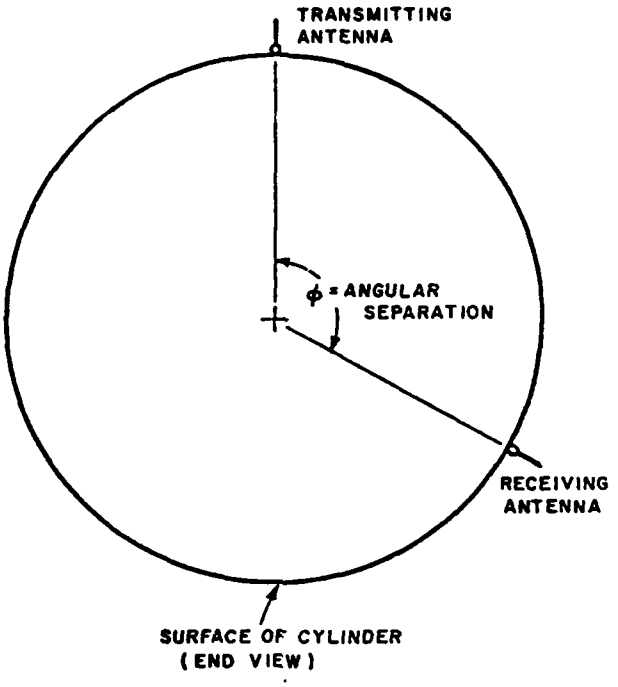

Fig. 3. Monopole Antennas on a Circular Cylinder

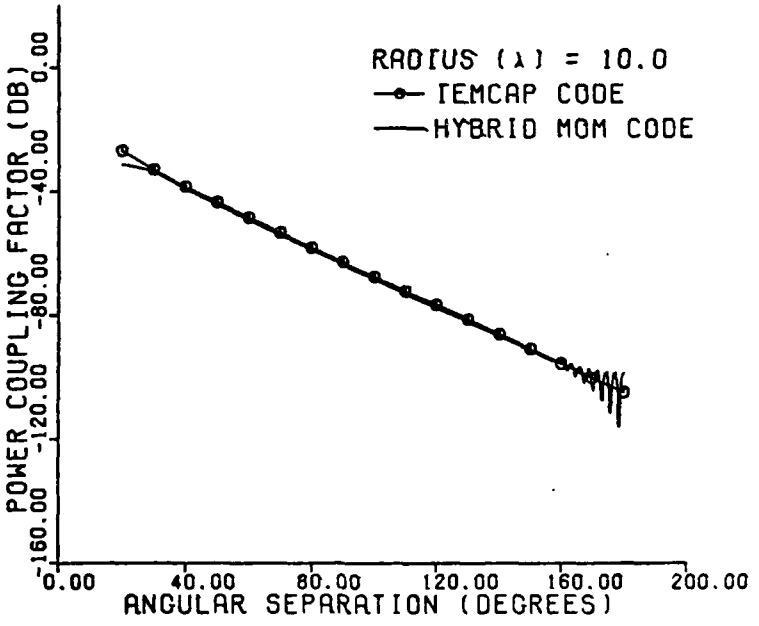

Fig. 4. Power Coupling Factor Between Two 1/4 Wavelength Monopoles on a Cylinder of Radius 10 Wavelengths

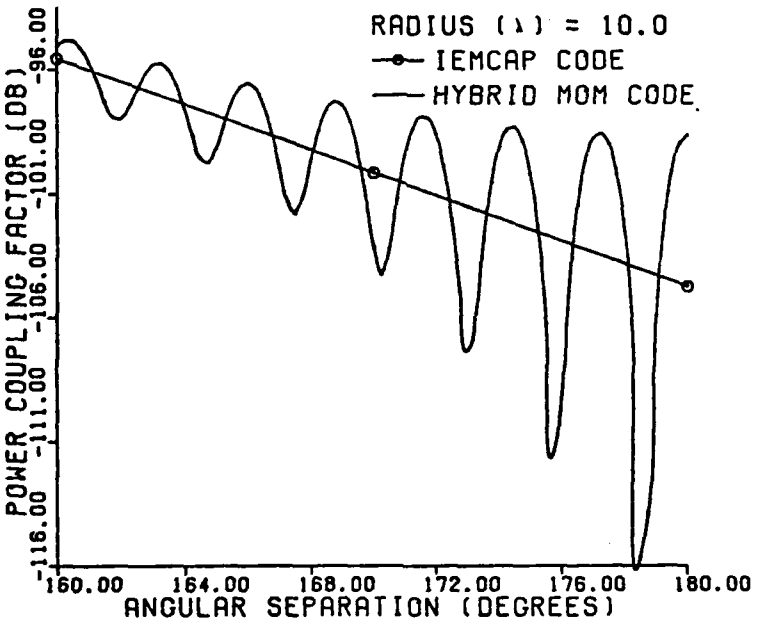

Fig. 5. Power Coupling Factor Between Two 1/4 Wavelength Monopoles on a Cylinder of Radiuw 10 Wavelengths for Angular Separations Between 160 and 180 Degrees

by almost as much as 20 decibels for a displacement of one-quarter wavelength!

Next, the radius of the cylinder was varied. As an upper limit, a cylindrical radius of 150 wavelengths was selected. This corresponds to the fuselage of a C-5A cargo aircraft (30 foot diameter) at a frequency of approximately 10 GHz which is near the operating frequencies of airborne radar, precision approach systems, and electronic warfare (EW) equipment. Fig. 6 shows very close agreement between the two approaches for all angular separations less than 130 degrees. As in Fig. 4, the MOM data oscillates for angular separations larger than 160 degrees. However, since the separation between the nulls is less than .2 degrees, these oscillations appear as a shaded area.

Further results show that the two programs generally yield the same answers for smaller cylinders with a 5, 3, or even 1 wavelength radius. A 3 wavelength result is shown in Fig. 7. Again, there is some deviation for very large angular separations due to the constructive/destructive reinforcement discussed previously. There is also somewhat of a deviation for very small angular separations. This is most likely due to the geometry

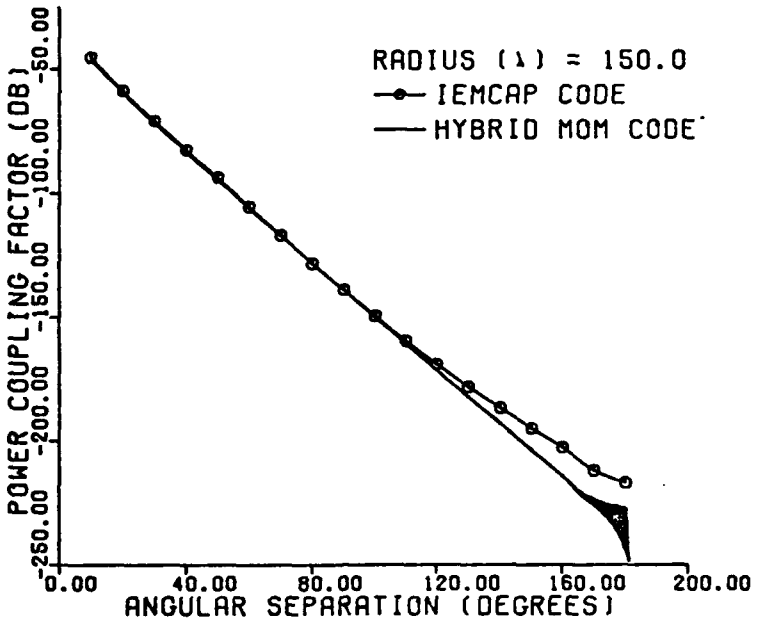

Fig. 6. Power Coupling Factor Between Two 1/4 Wavelength Monopoles on a Cylinder of Radius 150 Wavelengths

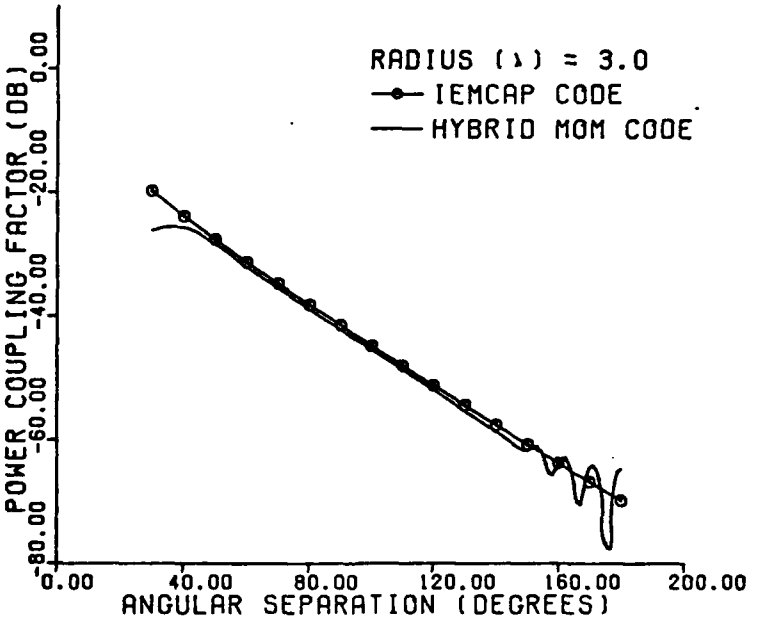

Fig. 7. Power Coupling Factor Between Two 1/4 Wavelength Monopoles on a Cylinder of Radius 3 Wavelengths

situation of the antennas and cylinder used by the hybrid MOM code. For these small angles, the electric field is no longer propagating through the surface boundary layer region described in Chapter III. Rather, source points on the transmitting antenna, as well as the observation points on the receiving antenna, may more properly be considered as points well off the cylinder surface, especially for the antenna segments farthest away from the cylinder surface. Therefore, a different set of surface diffraction equations should be used which permits the source and/or observation point to be outside the surface boundary layer [6].

VI. CONCLUSIONS

Based on comparisons made in this paper between the MOM code and the IEMCAP code in their ability to determine the loss in transmitted power due to cylindrical surface diffraction, several conclusions may be drawn. For intermediate angular separations (60 to 120 degrees), the deviation in results between the two codes is less than one decibel. This is a strong indication that both results are correct. For larger angular separations (120^{o} to 180^{o}) deviation between the codes can be explained by the reinforcement/cancellation effects due to phase information which is accounted for by the MOM code but not by IEMCAP. Yet the IEMCAP code values do agree with the average values of the standing-wave type patterns of the MOM code results. Thus, the MOM code results appear to be correct for cylindrical surface diffraction involving large angles. In addition, there is also good agreement between the two codes for cases of linear displacement along the axis of the cylinder where torsion is introduced into the path between the transmitting and receiving antennas.

However, deviation between results of the two codes is more severe for small angular separations (less than 60 degrees) between one-quarter wavelength monopoles on small cylinders with radii on the order of one wavelength. There is also a disturbing amount of disparity between the results of the MOM and IEMCAP codes when a longer five-eights wavelength monopole is used. It appears that the MOM code fails (gracefully) when source points are much more than one-quarter wavelength above the cylinder surface or when very little of the propagation path between the antennas resides in the surface boundary region, as for small angular separations on small radii cylinders. To reduce the effect of these problems, equations which account for curved surface diffraction from source and observation points outside the surface boundary layer, such as described by Pathak, Burnside, and Marhefka [5], should be considered.

REFERENCES

1. G. A. Thiele and T. H. Newhouse, "A Hybrid Technique for Combining Moment Methods with the Beometrical Theory of Diffraction," IEEE Trans. on Antennas and Propagation, Vol. AP-23, No. 1, Jan. 1975.

2. Ernest P. Ekelman, Jr., "A Hybrid Technique for Combining the Moment Method Treatment of Wire Antennas with GTD for Curved Surfaces," Report 710816-1, July 1978, ElectroScience Laboratory, Department of Electrical Engineering, The Ohio State University; prepared under Contract N00014-78-C-0049 for the Office of Naval Research, Arlington, VA.

3. J. A. Richmond, "Computer Program for Thin-Wire Structures in a Homogeneous Conducting Medium," NTIS, Springfield, VA 22131, NASA Contractor Report CR-2399, July 1973.

4. W. L. Stutzman and G. A. Thiele, Antenna Theory and Design, John Wiley and Sons, New York, 1980 (in press).

5. P. N. Pathak, W. P. Burnside, and R. J. Marhefka, "A Uniform GTD Analysis of the Scattering of Electromagnetic Waves by a Smooth Convex Surface," Report 784583-4, June 1978, ElectroScience Laboratory, Department of Electrical Engineering, The Ohio State University; prepared for the Naval Air Development Center.

6. P. H. Pathak and N. N. Wang, "An Analysis of the Mutual Coupling Between Antennas on a Smooth Convex Surface," Report 784583-7, Oct. 1978, ElectroScience Laboratory, Department of Electrical Engineering, The Ohio State University; prepared for the Naval Air Development Center.

7. W. D. Burnside, C. L. Yu, and R. J. Marhefka, "A Technique to Combine the Geometrical Theory of Diffraction and the Moment Method," IEEE Trans. on Antennas and Propagation, Vol. AP-23, July 1975, pp. 551-558.

8. J. H. Richmond, "Computer Program for Thin-Wire Structures in a Homogeneous Conducting Medium," Short Course on Application of GTD and Numerical Techniques to the Analysis of Electromagnetic and Acoustic Radiation and Scattering (Text Draft), The Ohio State University, Department of Electrical Engineering, Sept. 1975.

9. J. L. Bogdanor, R. A. Rearlman, and M. D. Siegel, "Intrasystem Electromagnetic Compatibility Analysis Program, Vol. I, User's Manual Usage Section," National Technical Information Service, U.S. Department of Commerce, Springfield, VA, NTIS No. AD-A008-527, Dec. 1974.

10. G. Hasserjian and A. Ishimaru, "Excitation of a Conducting Cylindrical Surface of Large Radius of Curvature," IRE Transactions on Antennas and Propagation, May 1962, pp. 264-273.

11. J. L. Bogdanor, R. A. Pearlman, and M. D. Siegel, "Intrasystem Electromagnetic Compatibility Analysis Program, Vol. I, User's Manual Engineering Section," National Technical Information Service, U.S. Department of Commerce, Springfield, VA, NTIS No. AD-A008-526, Dec. 1974.

12. Steven A. Davidson, "A Hybrid Method of Moments - GTD Technique for Computing Electromagnetic Coupling Between Two Monopole Antennas on a Large Cylindrical Surface," Master's Thesis, The Ohio State University, Columbus, OH, Mar. 1980.

BROADBAND CONICAL SPIRAL ANTENNA RCS PREDICTION USING THIN-WIRE APPROXIMATION

BY

M. S. Sohel, PH.D., P.E.
Engineering Specialist
General Dynamics
Fort Worth, Texas 76101

COMPENDIUM

A broadband conical spiral antenna was modeled by a thin-wire approximation and the method-of-moments technique was applied to predict the antenna RCS. The thin wire was divided into a maximum of 200 segments and the analytical RCS data were obtained by using Cyber-172 computer. Then an equiangular conical spiral antenna was designed, fabricated, and tested for electrical performance. The RCS of this antenna was recorded for two linear polarizations at 2.3, 8.4, and 16 GHz frequencies. It is concluded that the predicted RCS data agree with the measured RCS within 2-6 dB. The results of this study will be of paramount technical assistance to engineers who are concerned with not only the antenna performance but the antenna RCS as well.

INTRODUCTION:

Broadband conical spiral antennas are widely used for active and passive electronic countermeasure and direction-finding systems on aircrafts, missiles, and satellites; and from an RCS standpoint, serve an excellent replacement for their counter-part flat spiral antennas. Thus, it is necessary to develop theoretical techniques that would aid in predicting the RCS of such antennas. Because of the broad bandwidth, there are many complexities involved in properly modeling this antenna; however, recent availability of high-speed digital computers has made it somewhat possible to apply method-of-moments techniques to estimate the RCS.

In this paper, the conical spiral antenna is modeled as a thin-wire antenna, and the method-of-moments technique is applied to calculate the antenna RCS. The measured electrical performance of the antenna is given and the experimental RCS data are compared with the theoretical RCS data.

CONICAL SPIRAL ANTENNA DESCRIPTION:

An equiangular conical spiral antenna with its design parameters ($\vartheta, \alpha, \delta$, D, and d) described in the spherical coordinate system is shown below.

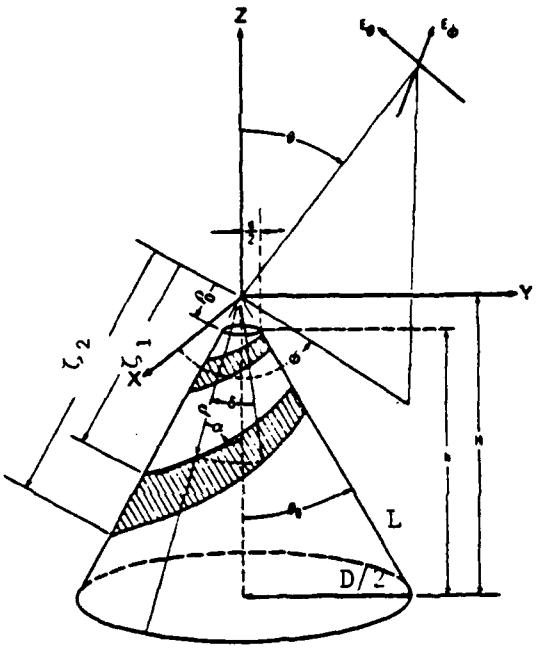

The outer edges of the spiral arm are defined by:

$$\zeta_1 = \zeta_0 \exp(b\phi) \qquad (1)$$

$$\zeta_2 = \zeta_0 \exp(b\phi - b\delta) \qquad (2)$$

where, $b = \sin\theta_o / \tan\alpha$

A rotation of both curves by 180 degrees over this body of revolution will give the second arm of this antenna.

It may be noticed that "θ_o", the cone half-angle, controls the front-to-back ratio of the antenna radiation and the space available for antenna installation; parameters "D" and "d", base and apex diameters, determine the lower and the upper frequency of operation; "α ", the spiral-rate angle, yields the beamwidth; and "δ ", the arm-width, optimizes the antenna impedance.

THIN-WIRE MODELING:

The conical equiangular spiral antenna may be designed by selecting a very narrow armwidth; i.e., $\delta = 0$. This antenna may be constructed with a thin metallic wire, instead of a wide metallic strip. A sketch of this antenna is shown below:

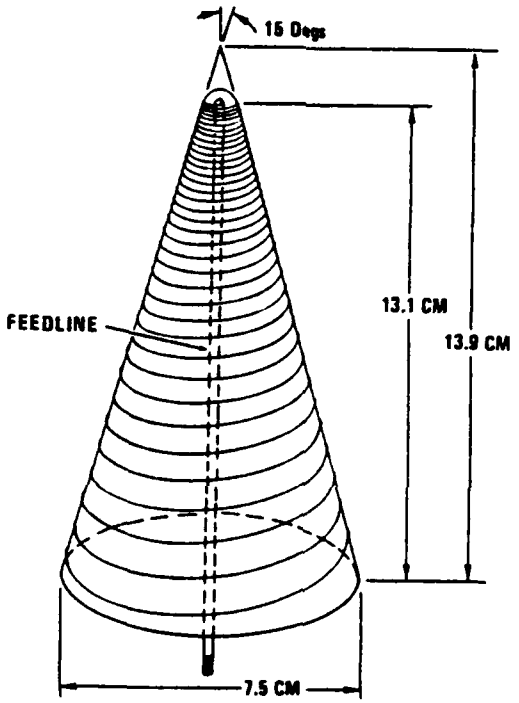

In order to apply the method-of-moments technique, the following approximations were made: (1) the current was assumed to flow only in the direction of the wire axis, (2) the current and charge densities were approximated by current "I" and charge "q" on the wire axis; and (4) the boundary conditions were applied only to the axial component of electric field intensity, E, at the wire axis. The resulting equations may be written as:

$$-E_i = -j\omega A_\ell \frac{\partial \Phi}{\partial \ell} \tag{3}$$

$$A_\ell = \mu \int_\ell I(\ell) \frac{e^{-jkR}}{4\pi R} d\ell \tag{4}$$

$$\phi = \frac{1}{\varepsilon} \int_\ell \sigma(\ell) \frac{e^{-jkR}}{4\pi R} d\ell \tag{5}$$

$$\sigma = \frac{-1}{j\omega} \frac{dI(\ell)}{d\ell} \tag{6}$$

Where,

E_i = Incidence Electric Field

A = Vector Potential

ϕ = Scalar Potential

R = Observation Point Distance

σ = Current Density

ℓ = Wire Length

μ = Permeability

ε = Permittivity

Then, based on ~~pulse basis point-matching~~ Richmond's piecewise sinusoidal approximation, the antenna spiral arms were divided into "N" segments, see Figure 1, and the antenna RCS calculations were made by the method-of-moments technique by programming it on Cyber-172 computer. Due to the computer memory limitations, the number of segments were restricted to 200. The analytical data so obtained is shown in Figures 4 through 6.

are length all equal

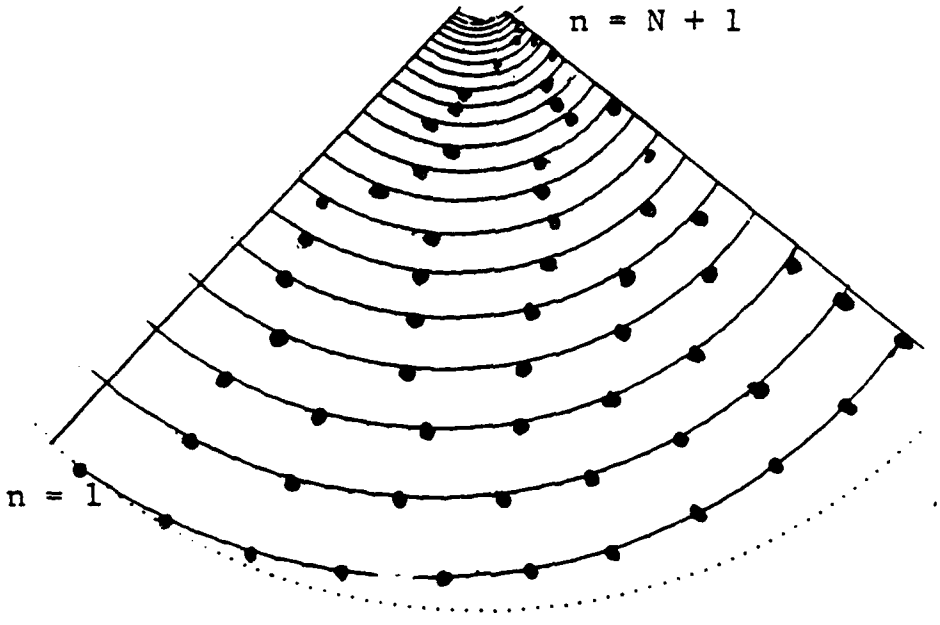

FIGURE 1 CONICAL SPIRAL ANTENNA SEGMENTS

ANTENNA DESIGN, FABRICATION, AND TESTING:

Based on the above thin-wire modeling technique, an equiangular conical spiral antenna was designed by selecting the following design parameters for the expected antenna performance given below:

Design Parameters		Expected Antenna Performance	
θ_o	= 15 degrees	Frequency Band	2-18 GHz
α	= 85 degrees	3-dB Beamwidth	85 degrees
δ	= small (thin wire)	Polarization	Circular
H	= 13.9 cms	Axial Ratio	1.5 dB
h	= 13.1 cms	Front-to-Back Ratio	9 dB
D	= 7.5 cms	VSWR (Connector)	2:1
d	= .214 cms	Impedance (Ant. Terminals)	250 Ohms
B	= non-metallic base	Average Gain	2 dBil

The equation describing the spiral arm of the antenna may be written as:

$$\zeta = \zeta_0 \exp\ (\sin\theta o/\tan\alpha) \qquad (7)$$

This equation was programmed on HP-9845 computer and its projection on a two-dimensional plane of a circle was plotted. The radius of this circle is given by the maximum radius of the spiral arm. A sector with circumference πD was cut out of this circle and rolled to form a cone. The angle of this sector is given by $\pi D/L$, where L is the hypotenuse of the cone. Next, a solid wooden cone was constructed and a thin polypropylene dielectric flat sheet was heated on a low flame and then stretched on this cone. After it cooled off, the dielectric material cone was removed and a computer plotted paper cone was inserted in it and glued. Lines describing the spiral arm were quite visible. The dielectric cone was sprayed with rubber cement and then a thin pliant copper wire was wrapped around the cone. The second arm was formed by rotating it by 180 degrees.

The antenna was tuned and balanced by a tapered line technique. The tapered end of the coax was used to feed the antenna at the apex and its other end was connected to a 50-ohm load through a TNC connector. This antenna is shown in Figure 2.

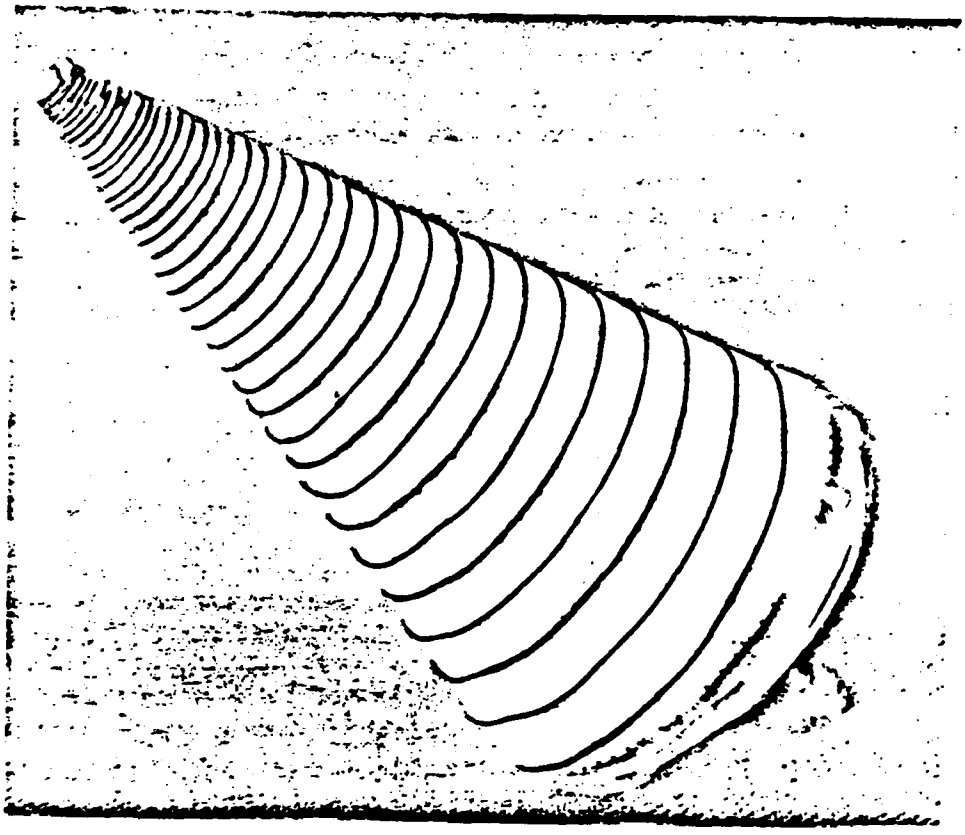

FIGURE 2 FABRICATED CONICAL SPIRAL ANTENNA

All the electrical performance data; i.e., radiation patterns, gain, axial ratio, and VSWR, were recorded at the General Dynamics Antenna Range and are summarized in Table 1.

TABLE 1 ELECTRICAL PERFORMANCE DATA OF THE SPIRAL ANTENNA

FREQUENCY (GHz)	VSWR	PEAK GAIN (DBiL)	3-dB BEAMWIDTH (DEGS)	AXIAL RATIO (dB)
2	1.8	0	90	1
7	2.2	2	70	3.5
16	1.9	3	95	2

RCS MEASUREMENTS:

Long pulse RCS testing was conducted at the Electronics Division of General Dynamics Radar Range. The test set-up, shown in Figure 3, was located in a tapered anechoic chamber, which is 46 meters long and 8-meter square at the large end. The background clutter signal was measured at 3, 5, 10, 16, and 35 GHz frequencies; it was below 41 dB below a square meter. The received power levels were digitized by the ratiometer and then transmitted to a computer for processing and for preparation of graphs and tables. The RCS of the test antenna was measured at 2.3, 8.4, and 16 GHz for horizontal and vertical polarizations. The data was recorded in analog and digital forms. The digitized data recorded at intervals of 1/10 of one degree in elevation angles were processed on a computer to generate the median RCS plots. The experimental RCS data so obtained is shown in Figures 4 through 6.

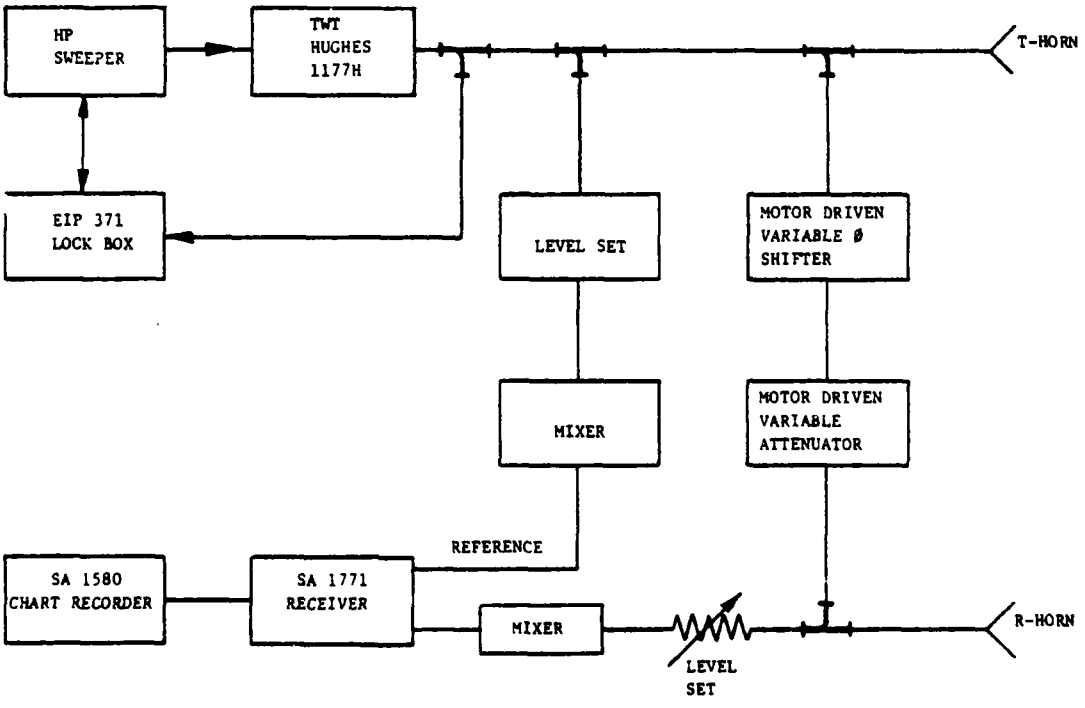

FIGURE 3 CW RCS MEASUREMENT SYSTEM BLOCK DIAGRAM

COMPARISON BETWEEN THE MEASURED RCS AND THE PREDICTED RCS DATA:

The antenna RCS data predicted by the method-of-moments technique and obtained by experimental measurements are shown in Figure 4 through 6 for two polarizations at three frequencies (2.3, 8.4, and 16 GHz).

A comparison of this data shows that the predicted RCS compares within 2-6 dB with the measured RCS for vertical and horizontal polarizations at 2.3, 8.4 and 16 GHz frequencies, except for horizontal polarization at 2.3 GHz where the agreement is not very good. Some mix up in the experimental measurement is suspected in this case. The accuracy of this technique can be enhanced further by increasing the number of segments of the wire and by taking into account the antenna-mode RCS contributions as well.

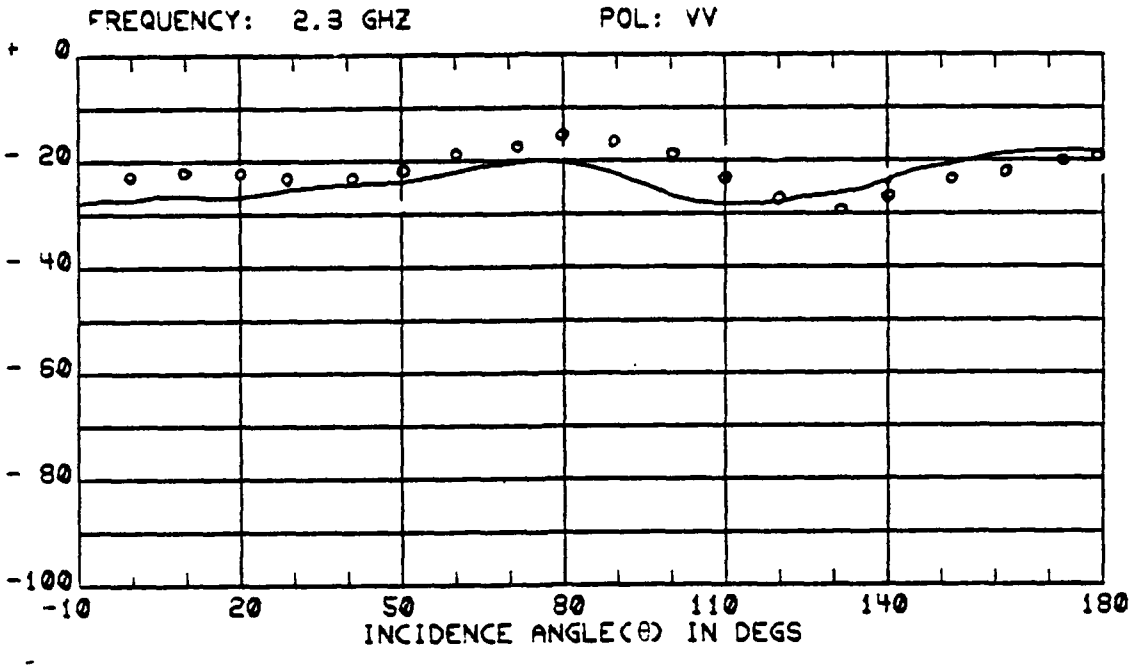

(a)

LEGEND:

_____ EXPERIMENT

o o o o THEORY

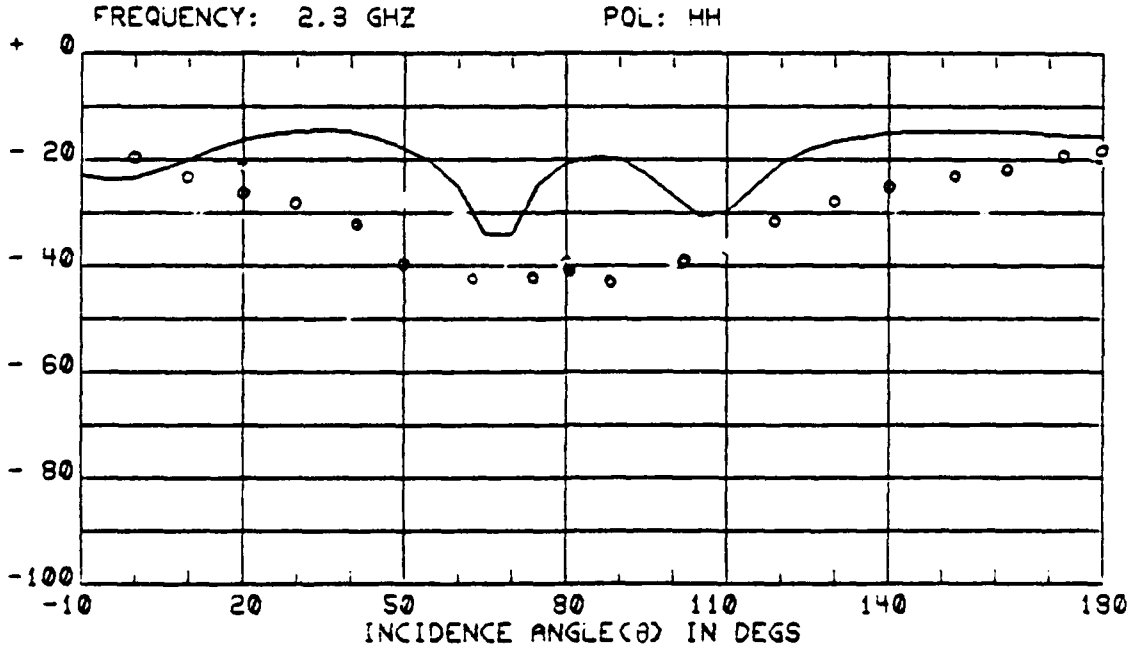

(b)

FIGURE 4 THEORETICAL AND EXPERIMENTAL RCS DATA AT 2.3 GHz

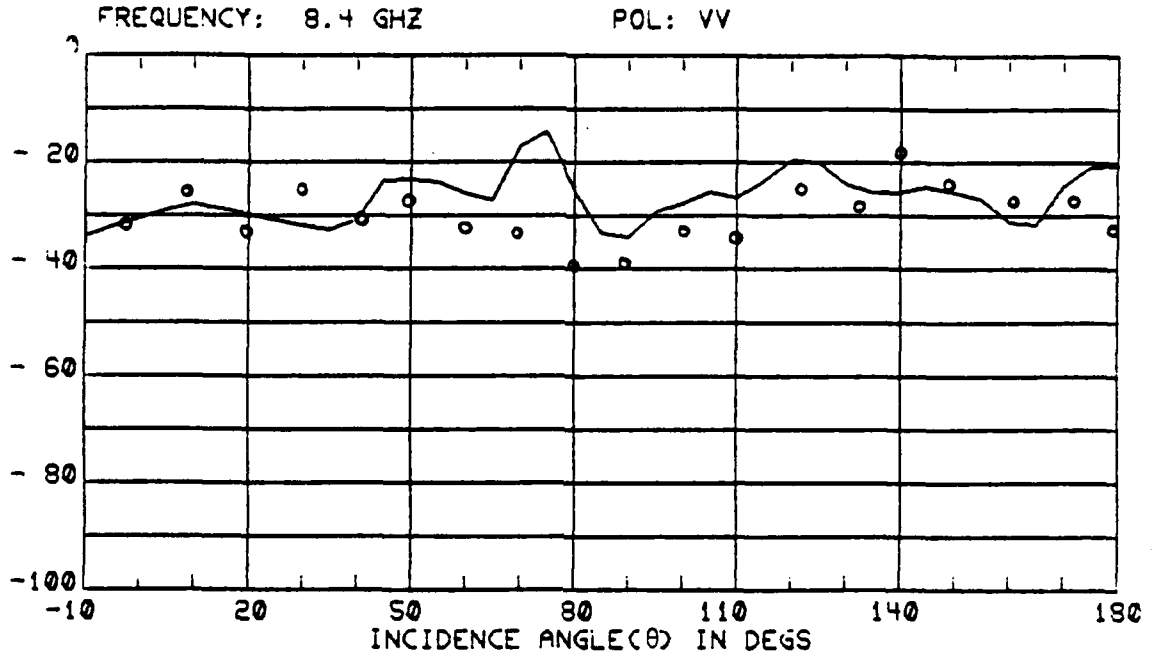

(a)

LEGEND:

_____ EXPERIMENT

o o o o o THEORY

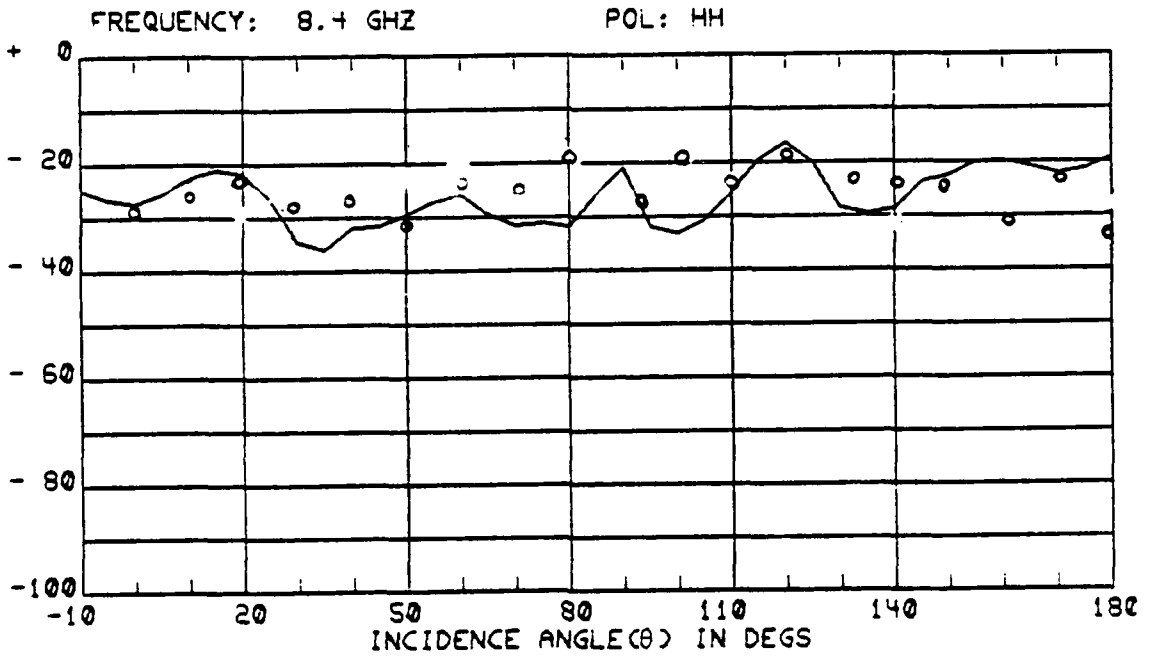

(b)

FIGURE 5 THEORETICAL AND EXPERIMENTAL RCS DATA AT 8.4 GHz

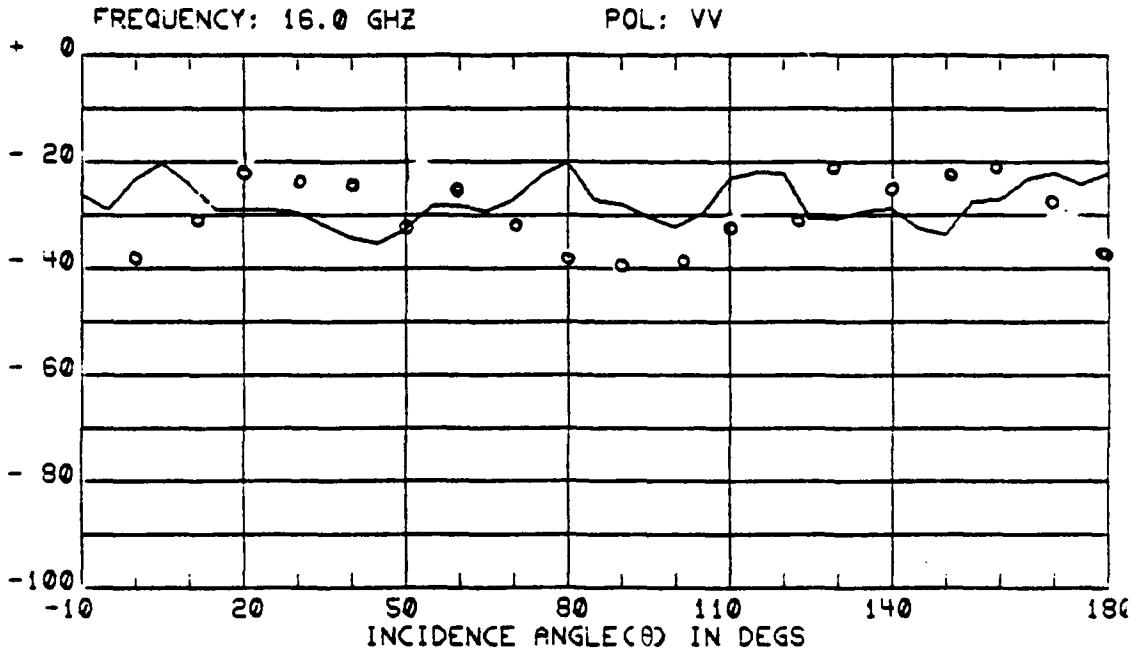

(a)

LEGEND:

_____ EXPERIMENT

o o o o THEORY

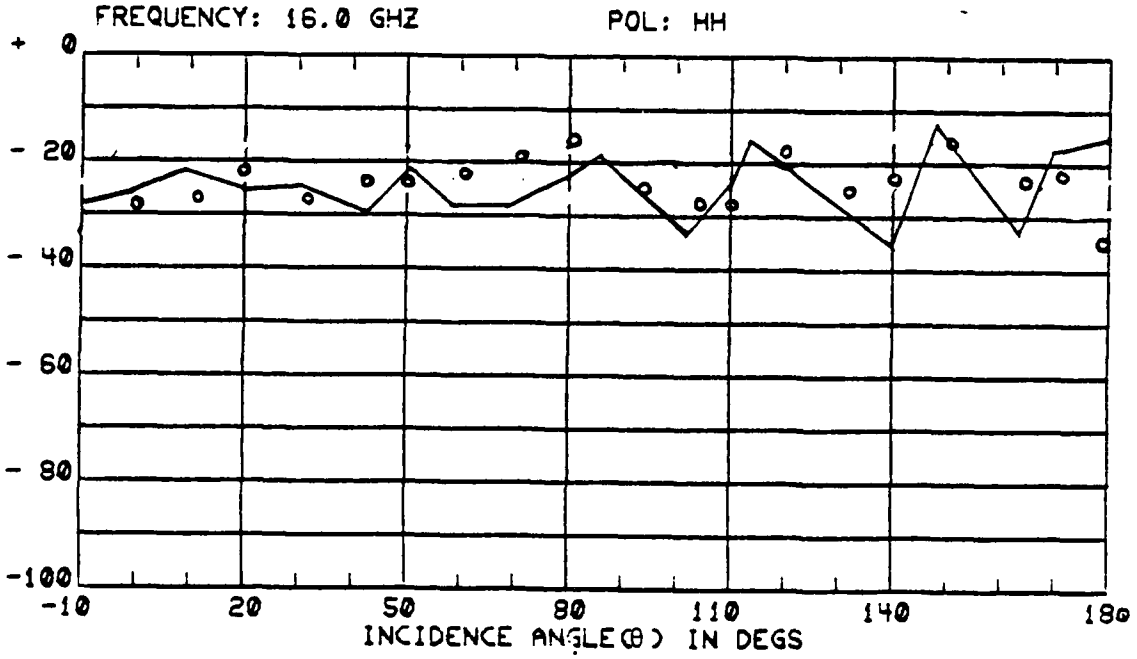

(b)

FIGURE 6 THEORETICAL AND EXPERIMENTAL RCS DATA

CONCLUSION:

The RCS of a broadband conical spiral antenna was predicted by modeling the antenna with a thin-wire and by applying the method-of-moments technique. The antenna RCS data were recorded at 2.3, 8.4, and 16 GHz frequencies. It is concluded the predicted RCS and the measured RCS agree within 2-6 dB. This comparison is good and the accuracy of this technique can further be embellished by increasing the number of segments of the antenna wire or by using sinusoidal base Glerikin functions for current distribution on the segments.

REFERENCES

H. H. Chao and B. J. Strait, "Computer Programs for Radiation and Scattering by Arbitrary Configurations of Bent Wires", TR No. 7, Air Force Cambridge Research Labs, Bedford, Mass., pp. 95, Sept. 1970.

J. D. Dyson, "The Undirectional Equiangular Spiral Antennas", IRE Transaction on Antennas and Propagations, pp. 32-334, Oct. 1959.

J. D. Dyson and P. E. Mayes, "New Circularly-Polarized, Frequency Independent Antenna with Conical Beam or Omnidirectional Patterns", IRE Transaction on Antennas and Propagation, pp. 334-342, July 1961.

C. S. Liang and Y. T. Lo, "A Multiple-Field Study for the Multiarm Log-Spiral Antennas", IEEE Transaction on Antennas and Propagation, pp. 656-684, Nov. 1968.

K. K. Mei, "On the Integral Equation of Thin-Wire Antennas", IRE Transactions on Antennas and Propagation, pp. 374-378, May 1965.

J. H. Richmond, "Method-of-Moments Technique - Personal Communication", The Ohio State University, July 1979.

J. H. Richmond, "A Wire-Grid Model for Scattering by Conducting Bodies", IEEE Transactions on Antennas and Propagation, pp. 782-786, Nov. 1966.

G. T. Ruck and et. al., "Radar Cross Section Handbook", Vols. I and II, Plenum Press, New York, 1970.

M. S. Sohel, "Antenna-Mode RCS Estimation of a TACAN Antenna", Presented at the 1979 URSI Symposium, Boulder, Colorado, Nov. 1979.

Y. S. Yeh and K. K. Mei, "Theory of Conical Equiangular-Spiral Antenans Part I - Numerical Technique", IRE Transactions on Antennas and Propagation, pp. 634-639, Sept. 1967.

W. L. Curtis, "Spiral Antennas", IRE Transactions on Antennas and Propagation, pp. 288-306, May 1960.

80-0640

A LOW SIDELOBE SHAPED BEAM SYNTHESIS PROCEDURE

K.G. Ramsey

September 24-26, 1980

Prepared for

1980 ANTENNA APPLICATIONS SYMPOSIUM
University of Illinois
Urbana, Illionis

By

WESTINGHOUSE ELECTRIC CORPORATION
Systems Development Division
Baltimore, Maryland 21203

A Low Sidelobe Shaped Beam Synthesis Procedure

ABSTRACT

A computed-aided design procedure for synthesizing shaped beam antenna patterns with very low sidelobes for linear arrays is described herein. The synthesis procedure is effected by the systematic location of array factor zeros within "the pattern visible region" to obtain the desired pattern shape and sidelobe level control.

The synthesis procedure is initiated by choosing a line source Taylor pattern with a sufficiently low sidelobe level and then computing and storing the associated array factor zeros. The desired (specified) shape beam pattern and the initial (Taylor) pattern are then computed and plotted on the same scale with the aid of a high-speed graphics plotting terminal.

The initial pattern zeros, in the regions where the shaped beam is desired, are then modified by moving them off the Z-plane real axis one at a time until a reasonable first approximation to the desired shaped beam pattern is obtained. Successive iterations, wherein the pattern zeros in question are readjusted, are made until the realized and desired patterns are sufficiently well matched within the shaped beam region. The pattern matching in the shaped beam region, via specific zero location off the Z-plane real axis, is found to have little effect on sidelobe levels outside the shaped beam region.

The corresponding aperture distribution is then found by taking the discrete fourier transform of the realized pattern function.

This paper describes the synthesis procedure in detail and shows the results of synthesizing a CSC^2 type pattern via the aforementioned procedure.

INTRODUCTION

It is often desirable, for a system point of view, to provide an antenna pattern which, in at least one plane, has a shaped beam response (see figure 1). Furthermore, it is frequently desirable to maintain low sidelobe levels in the areas outside the shaped beam region of the pattern. (See figure 1 again.)

The synthesis procedure described herein provides a systematic method of closely approximating a specified shaped beam pattern with a uniformly spaced linear array of discrete radiators while maintaining arbitrarily low sidelobe levels outside the shaped beam region. The idea for the development of this specific synthesis procedure arose from discussions in which the author has has with H. R. McComas, of Westinghouse, concerning pattern synthesis techniques.

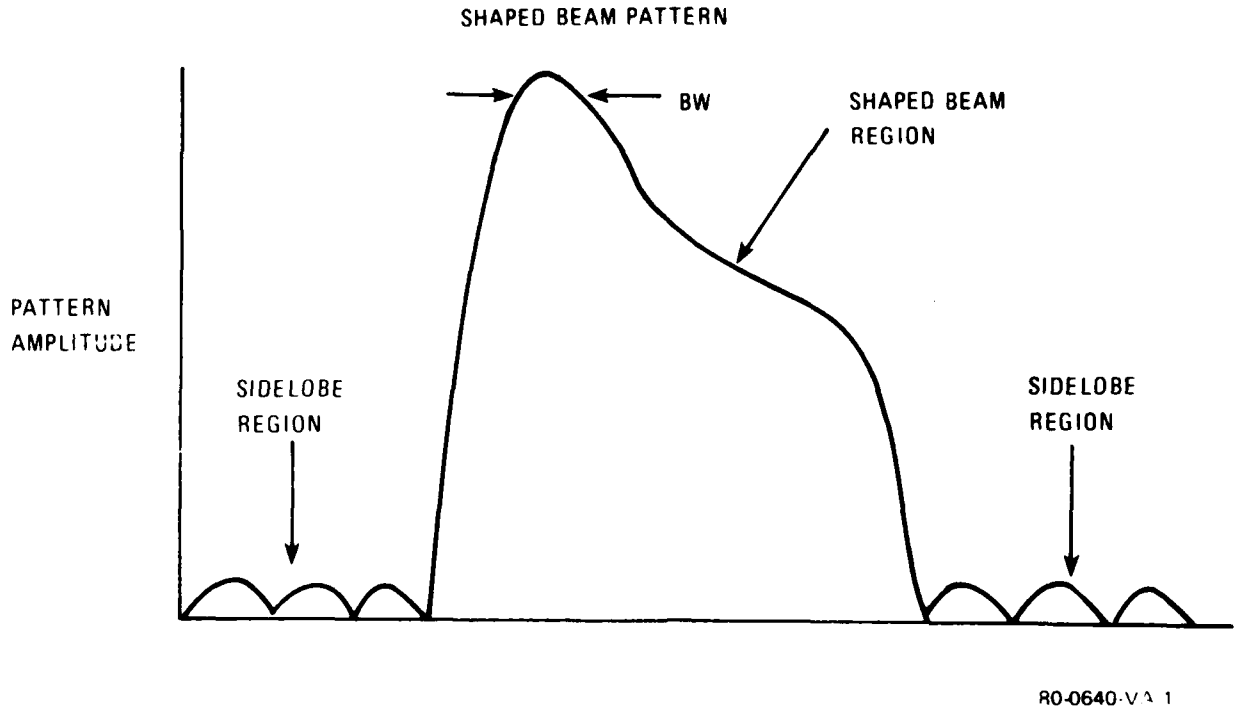

Figure 1. Shaped Beam Pattern

SYNTHESIS PROCEDURE

Hyneman and Johnson[1] have employed a shaped beam synthesis procedure wherein a set of Taylor line source pattern zeros are selected as a starting basis, and in which controlled displacement of the initial pattern function zeros is employed to effect a shaped beam pattern with approximately equal percentage ripple. The procedure described below uses a similar approach except that certain preselected pattern function zeros are modified one at a time using a video graphics display to monitor intermediate results during the procedure which is an iterative one.

It is well known that the far field pattern of a linear array of N isotropic radiators can be expressed as:

$$f(z) = a_1 + a_2 z + a_3 z^2 + \ldots\ldots + a_N z^{N-1} \tag{1}$$

where a_n is a complex voltage weighting coefficient at the nth element (see figure 2) and where:

$$z = e^{j\psi}$$

$$\psi = \frac{2\pi s}{\lambda} \sin\theta \tag{2}$$

λ = free space wavelength

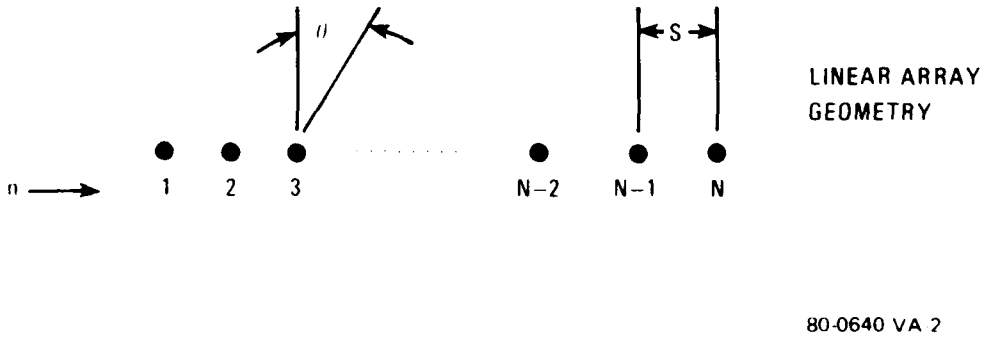

Figure 2. Linear Array Geometry

[1]R.F. Hyneman and R.M. Johnson, "A technique for the synthesis of shaped-beam radiation patterns with approximately equal-percentage ripple," IEEE Trans Antennas and Propagation, Vol. AP-15, pp. 736-743, November 1967

The N element linear array pattern can also be expressed as:

$$f(z) = a_N \prod_{n=1}^{N-1} (z - z_n) \tag{3}$$

where z_n is the nth pattern function zero as shown in figure 3.

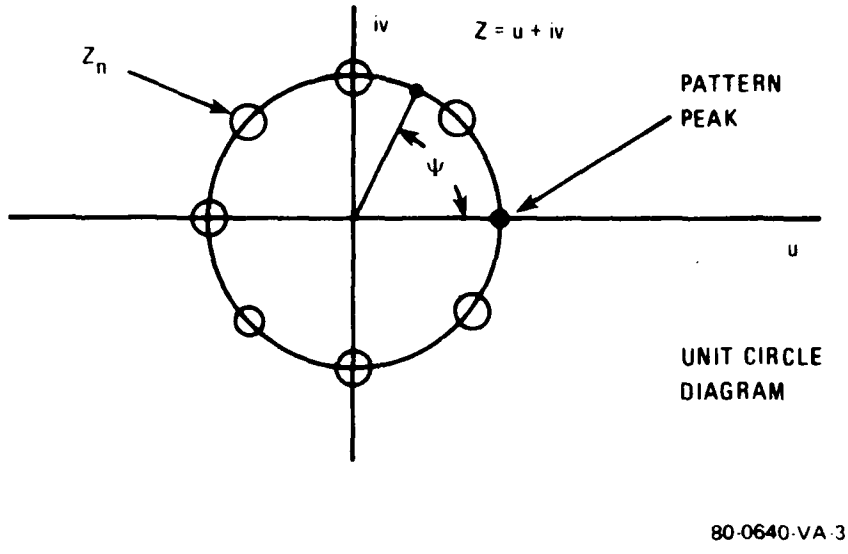

Figure 3. Unit Circle Diagram

$f(z) = a_N \prod_{n=1}^{N-1} (z - z_n)$ can be interpreted geometrically as the product of the N−1 vectors formed by rays extending to the variable point z on the unit circle of figure 3 from each of the zero locations of the pattern function (see figure 4).

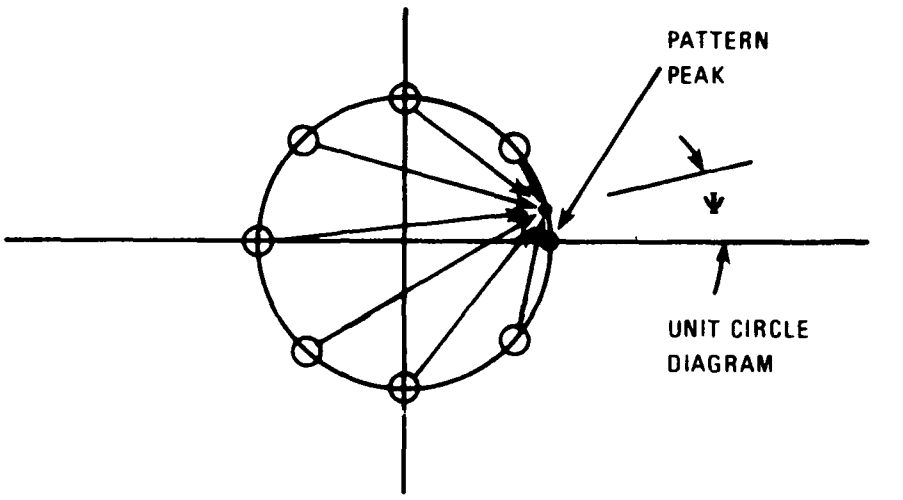

Figure 4. Unit Circle Diagram

The synthesis procedure outlined herein is implemented by first selecting the design sidelobe level, e.g. −40 dB, and positioning the pattern function zeros to the locations for a 40 dB Taylor pattern with large $\overline{n}$. The Taylor pattern zero locations are given by:

$$\psi_n = \pm \frac{360^\circ}{N} \sigma (A^2 + (n - \tfrac{1}{2})^2)^{1/2} \quad 1 \leq n < \overline{n} \tag{4a}$$

$$\psi_n = \pm \frac{360^\circ}{N} \qquad \overline{n} \leq n \tag{4b}$$

$$z_n = \cos \psi_n + j \sin \psi_n \tag{5}$$

$$\sigma = \frac{\overline{n}}{(A^2 + (\overline{n} - \tfrac{1}{2})^2)^{1/2}} \tag{6}$$

$$\overline{n} \leq N/2 \tag{7}$$

Large $\overline{n}$ is chosen as the starting point above because of the poor close in sidelobe response obtained with small $\overline{n}$ when the design sidelobe level is chosen to be −40 dB or less.

Choosing the zero locations of equations (5) results in the pattern shown in figure 5.

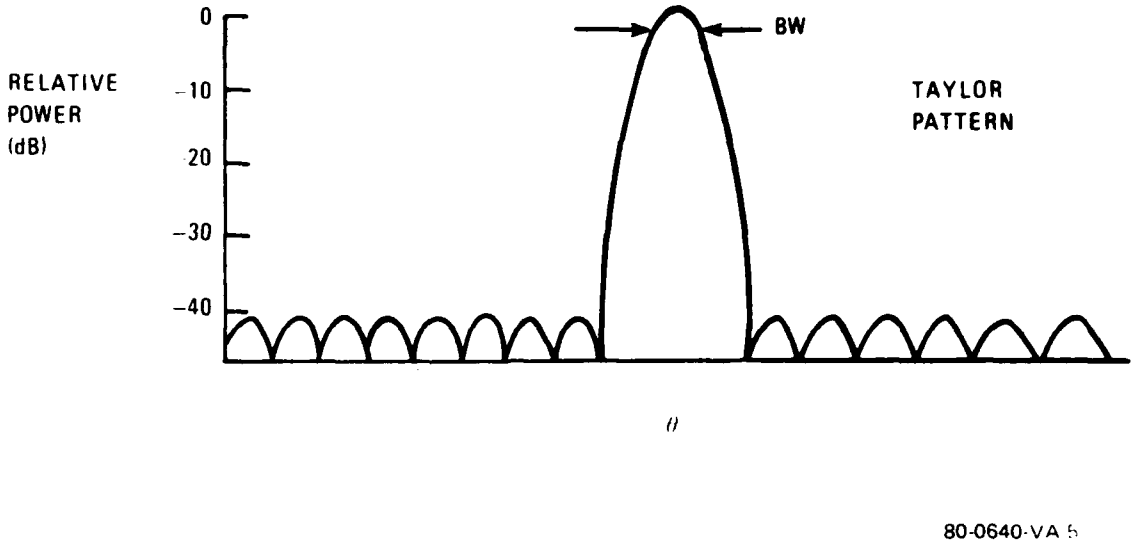

Figure 5. Taylor Pattern

At this point, it is necessary to adjust the number of elements N or the spacing between elements S to match the beamwidth parameter, BW, of the patterns in figures 1 and 5. In addition, the beam pointing angles of the two patterns must be matched by rotating the ensemble of Taylor zeros, ψ_n, in equation (4) by an appropriate amount ψ_o around the unit circle of figure 3.

where:

$$\psi_o = \frac{2\pi s}{\lambda} \sin \theta_o \tag{8}$$

θ_o = The beam pointing angle of the desired shaped beam pattern

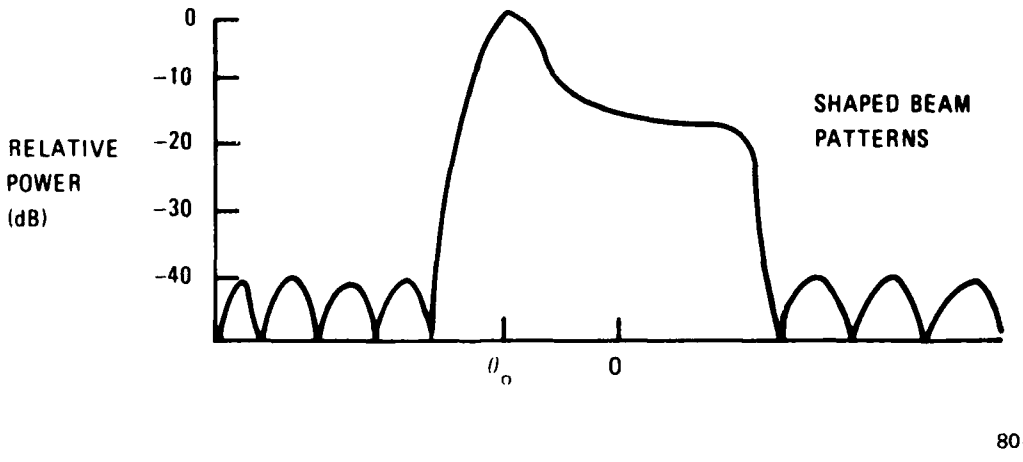

Figure 6. Shaped Beam Pattern

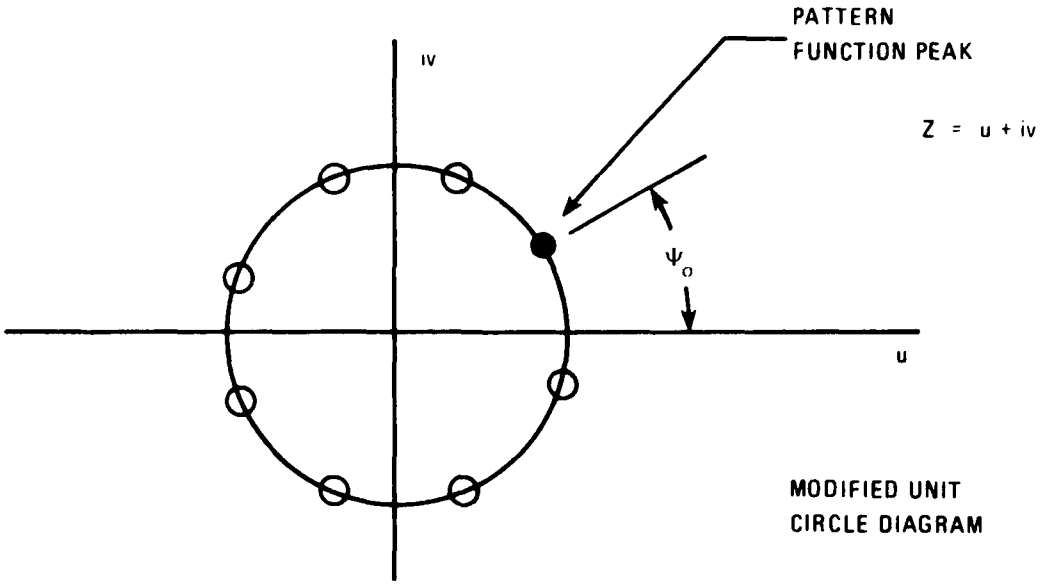

Figure 7. Modified Unit Circle Diagram

Figure 8 shows the Taylor pattern and the desired shaped beam pattern prior to the next step in the synthesis procedure.

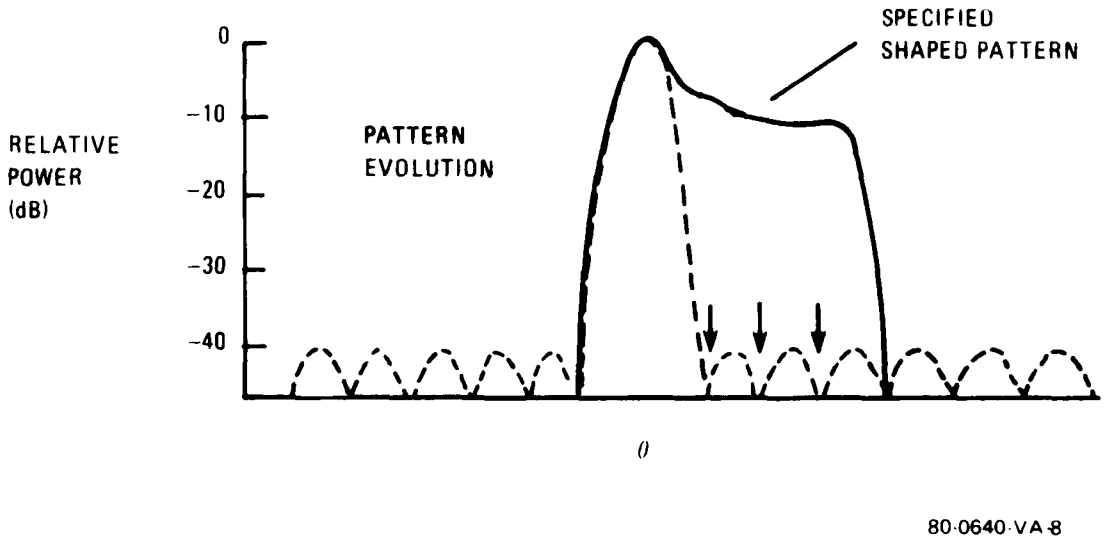

Figure 8. Pattern Evolution

The next step in the synthesis procedure is to move the Taylor pattern zeros, indicated by arrows in figure 8, off the unit circle (see figure 9) in order to warp the Taylor pattern in such a way as to match the specified shaped beam pattern.

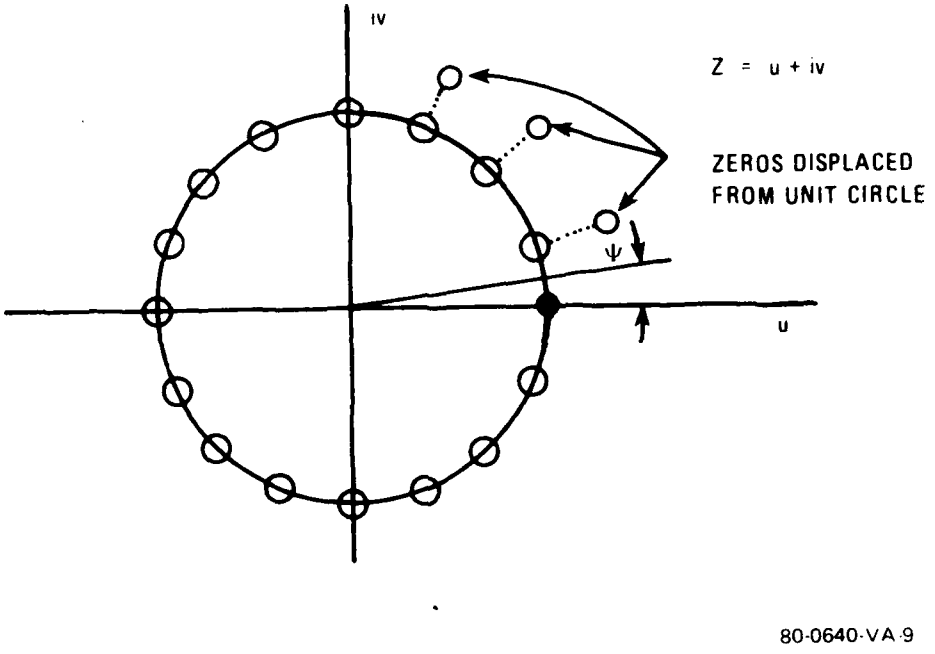

Figure 9. Unit Circle Diagram

This is done, one zero at a time, starting with the first zero on the right side of the Taylor pattern main beam (see figure 8). This sequential zero relocation process is iterated until the desired shaped beam pattern is approximated with sufficient accuracy. The relocation of zeros off the unit circle, for beam shaping purposes, is effected by multiplying the appropriate zeros z_n by real scale factors $\neq 1$.

During the synthesis procedure described above, it is necessary to monitor interim steps in the pattern approximating process. This was done by plotting pattern samples from each interim approximating pattern on a Tektronix Video Graphics Display Unit (see figure 10) and basing new zero relocation input data on the results of the previous approximation.

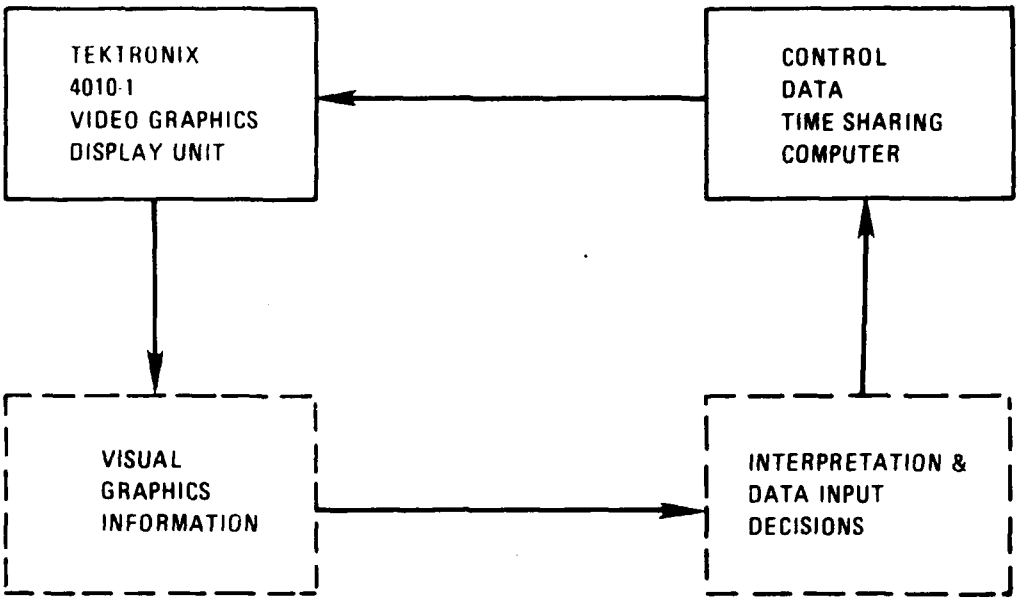

Figure 10. Interactive Graphics Block Diagram

Figure 11 shows a (dotted) specified and superimposed realized pattern obtained via the synthesis technique discussed above. A 46 dB Taylor pattern with large $\bar{n}$ was chosen as the starting point for the synthesis. Figure 12 shows the same pair of patterns with a different ordinate so that pattern matching in the shaped beam region can be more accurately assessed. The zeros which were moved off the unit circle to create the shaped region were done so by multiplying them by a real number greater than 1.

The last step in the synthesis procedure is the determination of the aperture distribution which produces the final approximating pattern. This may be easily accomplished in several ways with the aid of a large digital computer.

A fast fourier transform subroutine can be used to obtain the required aperture distribution by computing the discrete fourier transform of appropriate data samples of the pattern function given equation (3). The required aperture distribution may also be found by taking the final values z_n and expanding equation (3) into the form of equation (1). Dan Davis of Westinghouse has provided the author with a subroutine for computing the values a_n of equation (1) starting with equation (3).

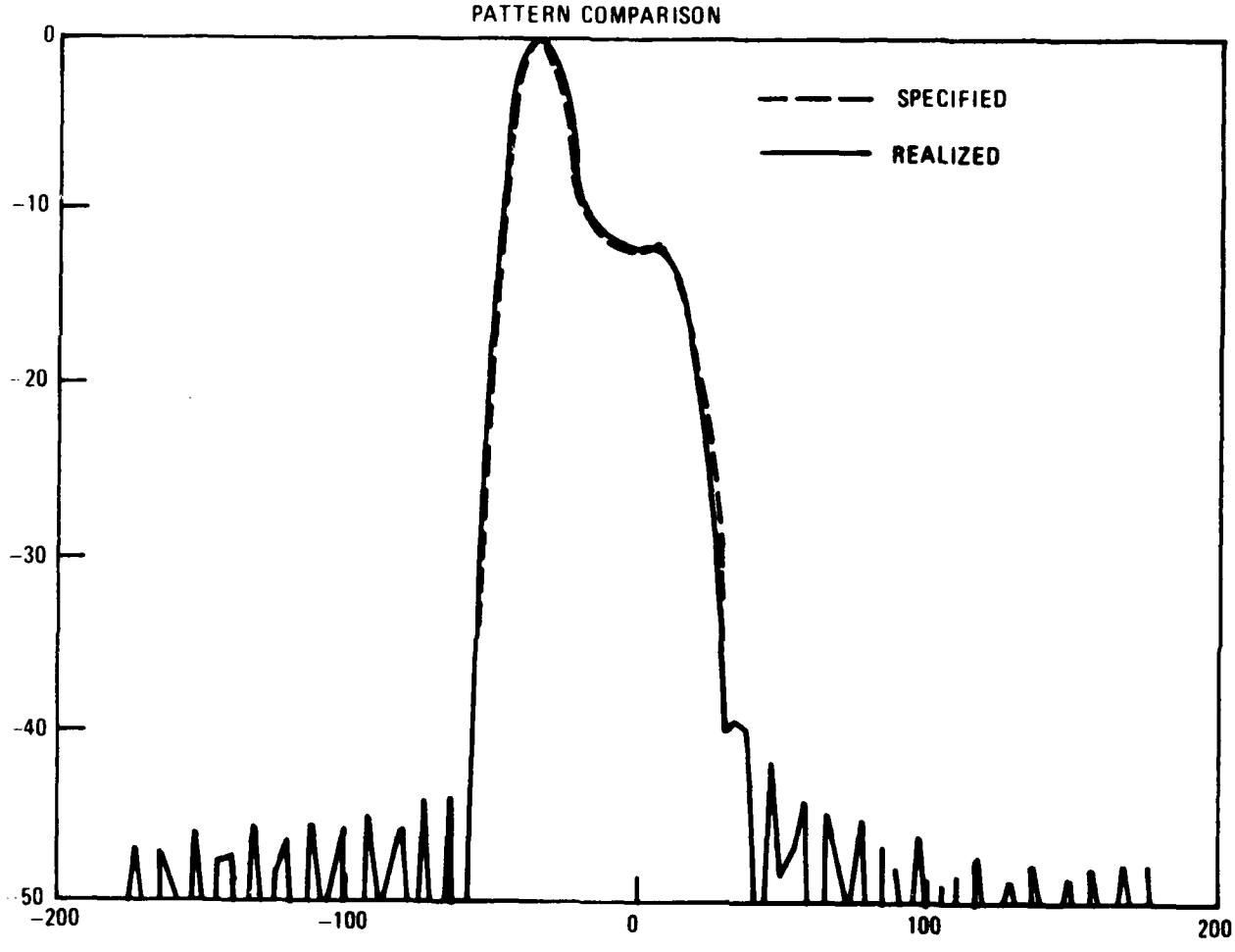

Figure 11. Pattern Comparison

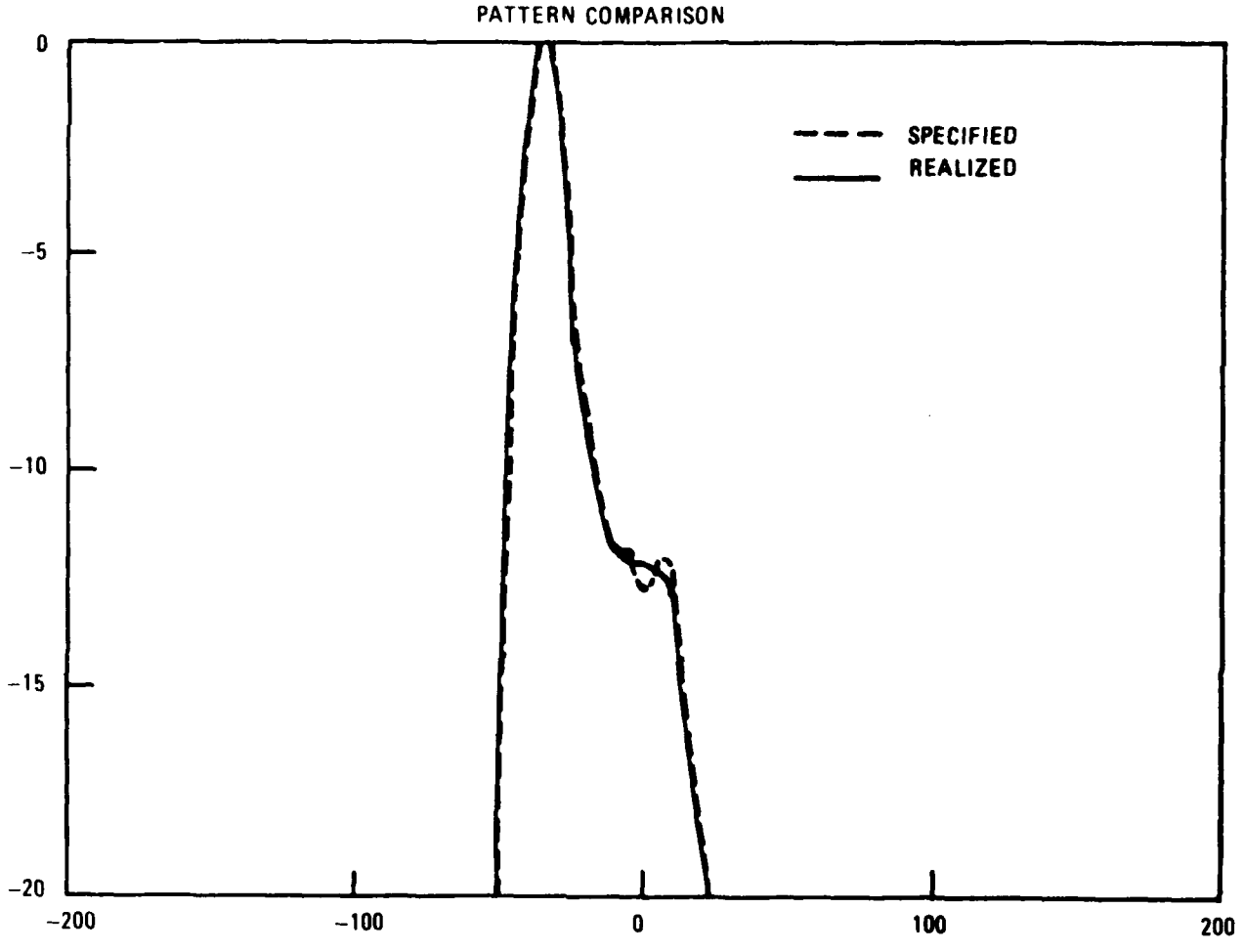

Figure 12. Pattern Comparison

SUMMARY

Described herein is a pattern synthesis procedure which comprises the systematic location of pattern function zeros in such a way as to produce a desired linear array antenna pattern within very close tolerances. The foregoing procedure which consists of the determination of a suitable approximation to a desired pattern and the associated complex aperture distribution is easily implemented with the aid of a digital computer.

DEVELOPMENT OF A 150-WATT PULSED S-BAND TRIPLER SOURCE

by

H.K. Hom and R.I. Wolfson
ITT Gilfillan, Van Nuys, California 91409

ABSTRACT

While recent technological advances in silicon bipolar transistors have produced impressive results at L-band, these devices have not met expectations in output power, gain, and efficiency at higher frequencies. An attractive alternative for the solid-state generation of microwave power is the use of a high-performance L-band transistor amplifier that drives a diode frequency multiplier. This paper describes the development and experimental results of a 150-watt pulsed tripler source designed to operate from 3.1 to 3.6 GHz with an overall dc-to-RF efficiency of 25 percent.

Section 1

INTRODUCTION

Modular all-solid-state transmitters offer significant life cycle cost (LCC) and operational advantages over tube counterparts in military radar systems. A modular configuration is particularly attractive for evolving systems, for as higher-power devices become available, they can readily be incorporated without major restructuring of existing architecture.

With L-band solid-state technology firmly established, it was natural that increased development effort should be directed toward all-solid-state S- and C-band systems. The U.S. Army Electronics Command (ECOM) sponsored contracts DAAB07-77-C-2731 to Microwave Semiconductor Corporation (MSC) and TRW Semiconductors to develop a 65-watt peak, 3.1 to 3.5 GHz silicon bipolar transistor with a 15 percent duty cycle and a 100-microsecond pulse length. By the end of 1978, the best results obtained were about 18 watts peak in prototype devices. This was increased to 50 watts peak over a limited frequency band in 1979. While these devices are usable for initial development of S-band power modules, a high-performance 100-watt peak transistor would be desirable for production hardware. Experience has shown that as higher-power devices become available, solid-state transmitters become more efficient, reliable, and cost effective.

Recent industry projections[1], shown in Figure 1, indicate that an 80- to 100-watt device for operation over 3.1 to 3.6 GHz will not be available until the 1985 time frame. Consequently, ITT Gilfillan has decided to develop an alternative source for the interim that uses a X3 diode frequency multiplier driven by a high-performance L-band transistor amplifier. The measured output power of an existing L-band transistor, and the projected output power of the tripler source for three assumed values of multiplier conversion efficiency, are also shown in Figure 1. Even for the worst case, the tripler source would result in higher power levels than 1985 projections for the S-band bipolar transistors.

[1] C.P. Snapp, "Bipolars Quietly Dominate," Microwave System News, November 1979, pg 49.

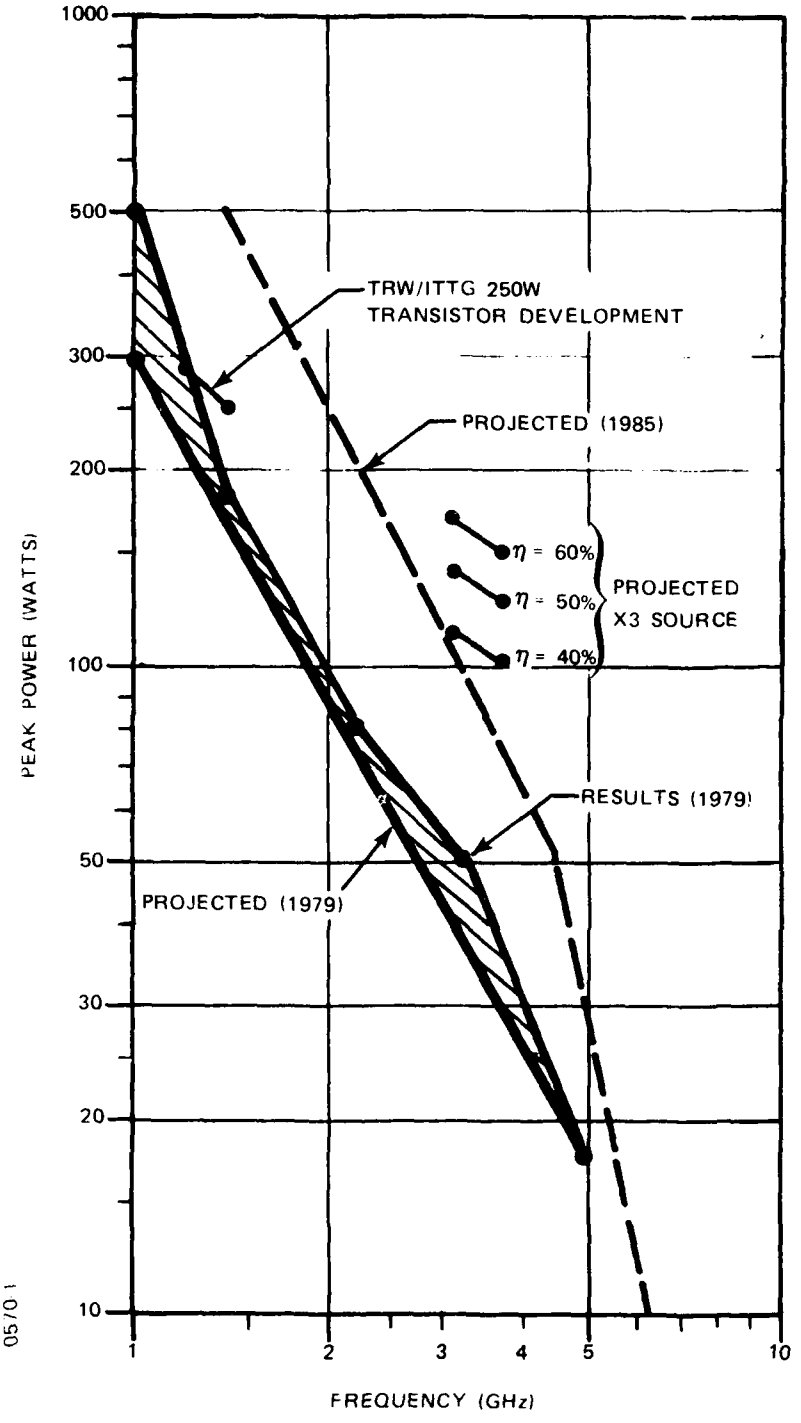

Figure 1. Peak-power output of silicon bipolar transistors and X3 source

Section 2

CIRCUIT DESIGN

A simplified block diagram of the 150-watt pulsed S-band tripler source is shown in Figure 2. An L-band transistor amplifier, which provides a peak output power of 250 watts minimum over the 1.033 to 1.200 GHz frequency band, drives the bimode varactor diode thorugh the input low-pass filter and matching network. The filter presents an open circuit to the diode junction at the second and all higher-order harmonic frequencies, thereby preventing loss back through the input. The matching networks are quarter-wave transformers that match the real part of the dynamic impedance of the diode to the 50-ohm characteristic impedance of the line. Line lengths between the diode and the two filters are chosen to cancel the capacitive reactance of the diode. The second-harmonic resonator presents a broadband, low-impedance path around the diode to idle the second-harmonic current, which is required for highly-efficient generation of the desired third-harmonic output frequency. The bias network establishes the operating point for the diode, and isolates the dc bias voltage from the RF circuitry. The output bandpass filter presents an open circuit to the diode junction at the fundamental frequency, and allows output power only at the desired third-harmonic frequency.

The L-band transistor amplifier and the tripler circuit are shown in Figures 3 and 4, respectively. Circuit development was done using 0.050-inch thick ceramic filled teflon-glass dielectric material in a combination of microstrip and balanced stripline. This configuration facilitates breadboarding, and results in a final unit with the optimum tradeoff between electrical and mechanical performance, size and weight, reliability, and cost.

Selection of the best diode for the tripler involves a tradeoff of many diode parameters, of which the most important are breakdown voltage, junction capacitance, snap time, and thermal resistance. Evaluation of candidate diodes for this application, which are listed in Table I, has not yet been completed.

Table I. Candidate Diodes for Tripler

Model Number	Minimum Breakdown (volts)	Junction Capacitance (pF)	Lifetime (nsec)	Maximum Snap Time (psec)	Thermal Resistance (°C/W)	Tripler Efficiency (%)
MA 44010	120	2.0	240	220	7.0	65
MA 44052	120	1.6-3.0	80-240	220	7.5	6.0
MO 6501X	220	1.76	200	60	--	--

0570-3

The diode is shunt mounted in microstrip to an aluminum baseplate that serves both as RF ground and as heatsink for good heat dissipation.

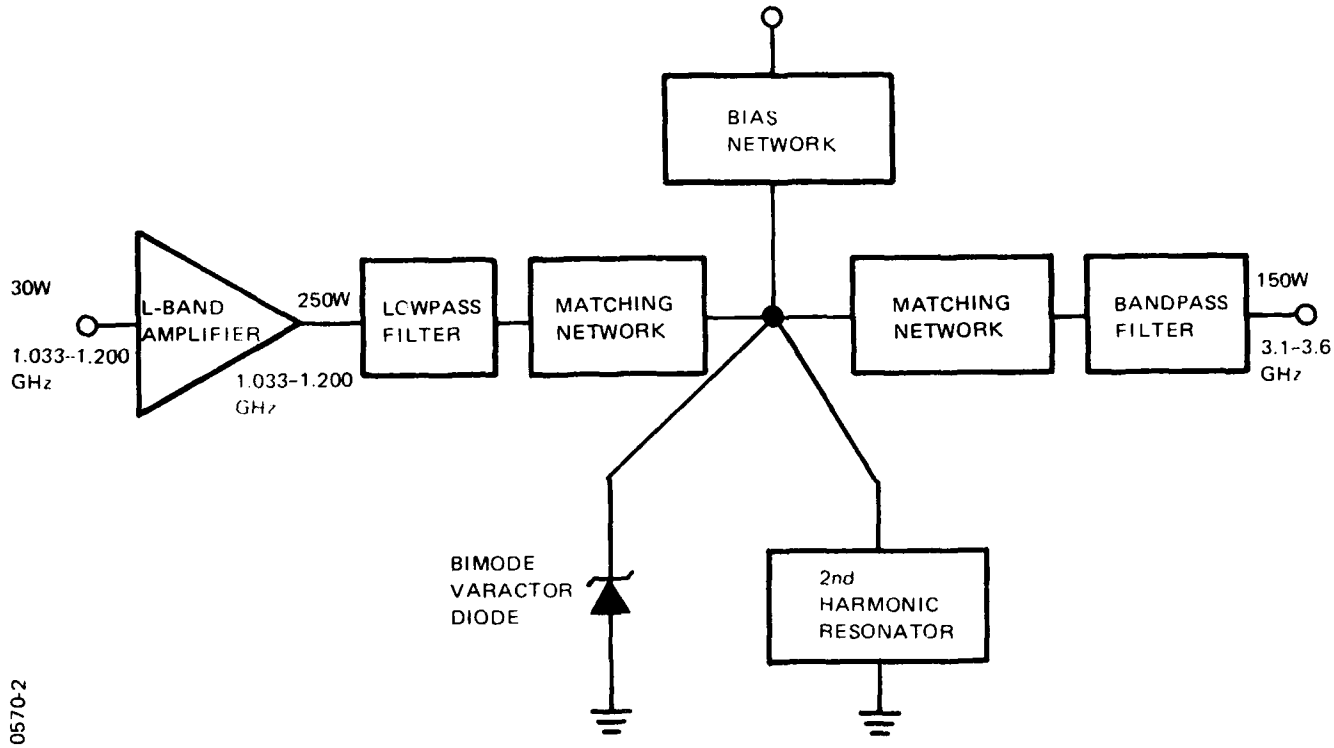

Figure 2. Block diagram of 150-watt pulsed S-band tripler source

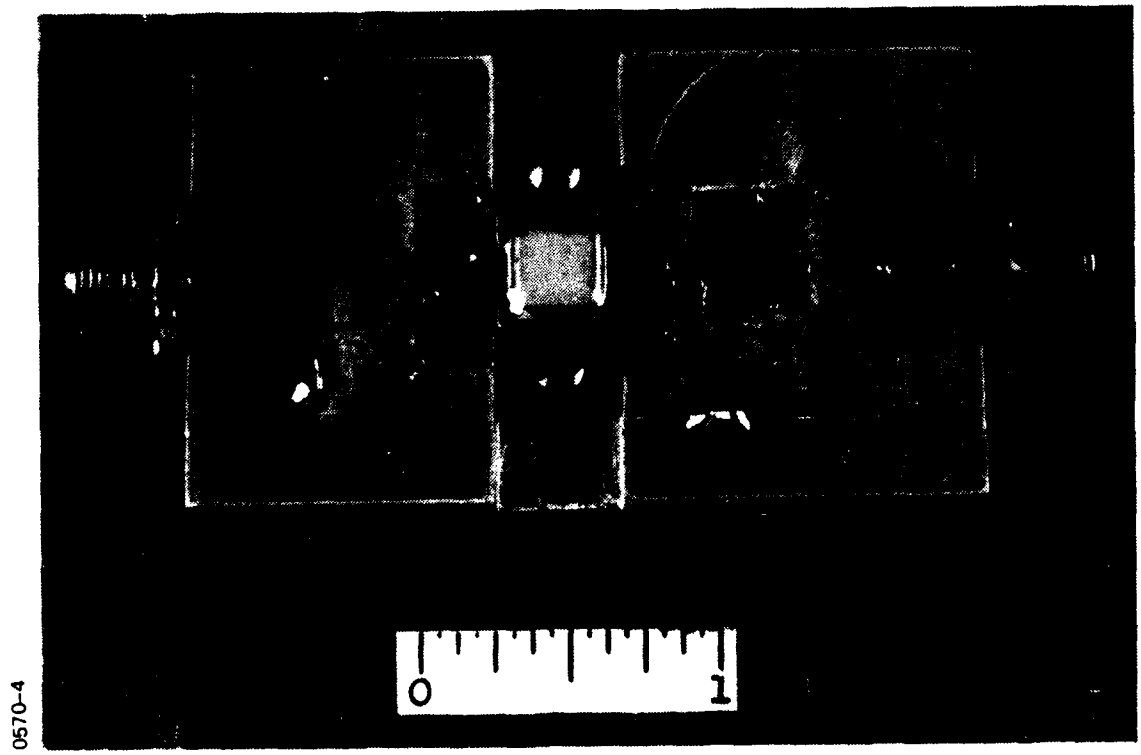

Figure 3. L-band transistor amplifier

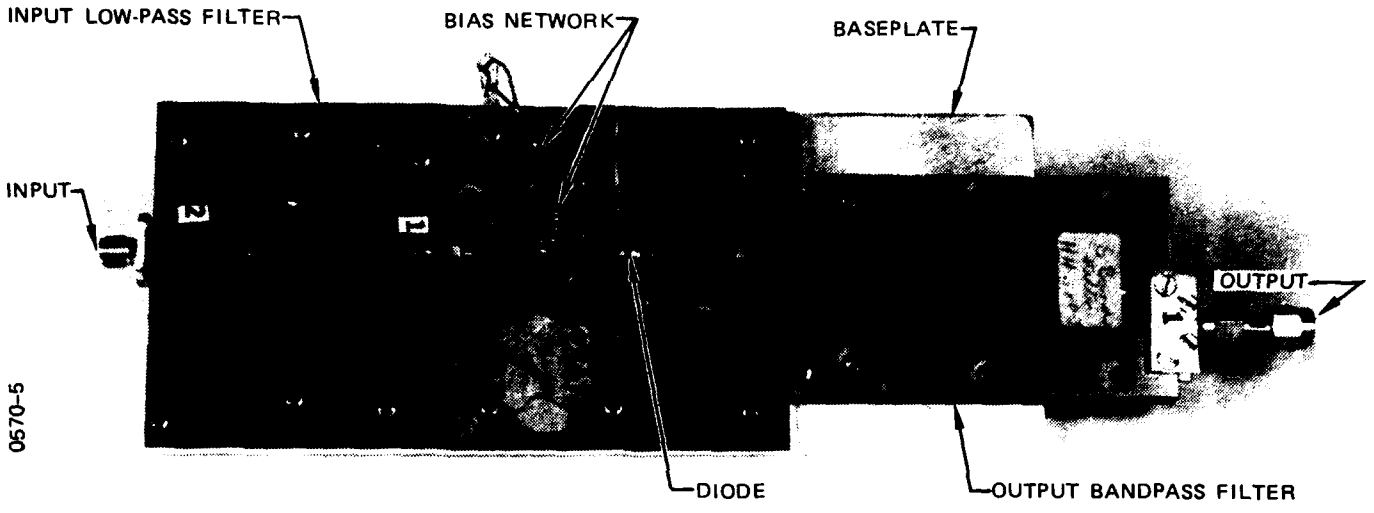

Figure 4. Frequency tripler circuit

Section III

EXPERIMENTAL RESULTS

At the time this paper was written, development of the tripler circuit was incomplete. Evaluation, selection, characterization, and matching of the diode in the circuit remains to be done.

Fabrication and test of the input low-pass filter, a two-section, constant-K, m-derived end section design, are complete. Swept-frequency insertion loss is shown in Figure 5. The insertion loss is less than 0.2 dB over the input drive frequency range 1.033 to 1.200, and greater than 45 dB at the idler and output frequencies.

The output bandpass filter has also been completed. This circuit was built in balanced stripline in order to obtain the high Q's necessary to relize low pass-band insertion loss and high out-of-band rejection. A three-section, maximally-flat design was used. Swept-frequency insertion loss is shown in Figure 6. The insertion loss is less than 0.8 dB over the output frequency range of 3.1 to 3.6 GHz, and greater than 20 dB and 40 dB at the idler and input frequencies, respectively.

Although the optimum diode for this application has not yet been selected, a preliminary test of the circuit was made with an L-band diode that was on hand. This device has a very high breakdown voltage and very low thermal resistance, but is otherwise unsuitable because of high junction capacitance and excessively long snap time. In spite of these drawbacks, five percent conversion efficiency of the tripler circuit was obtained over the 3.1 to 3.6 GHz band.

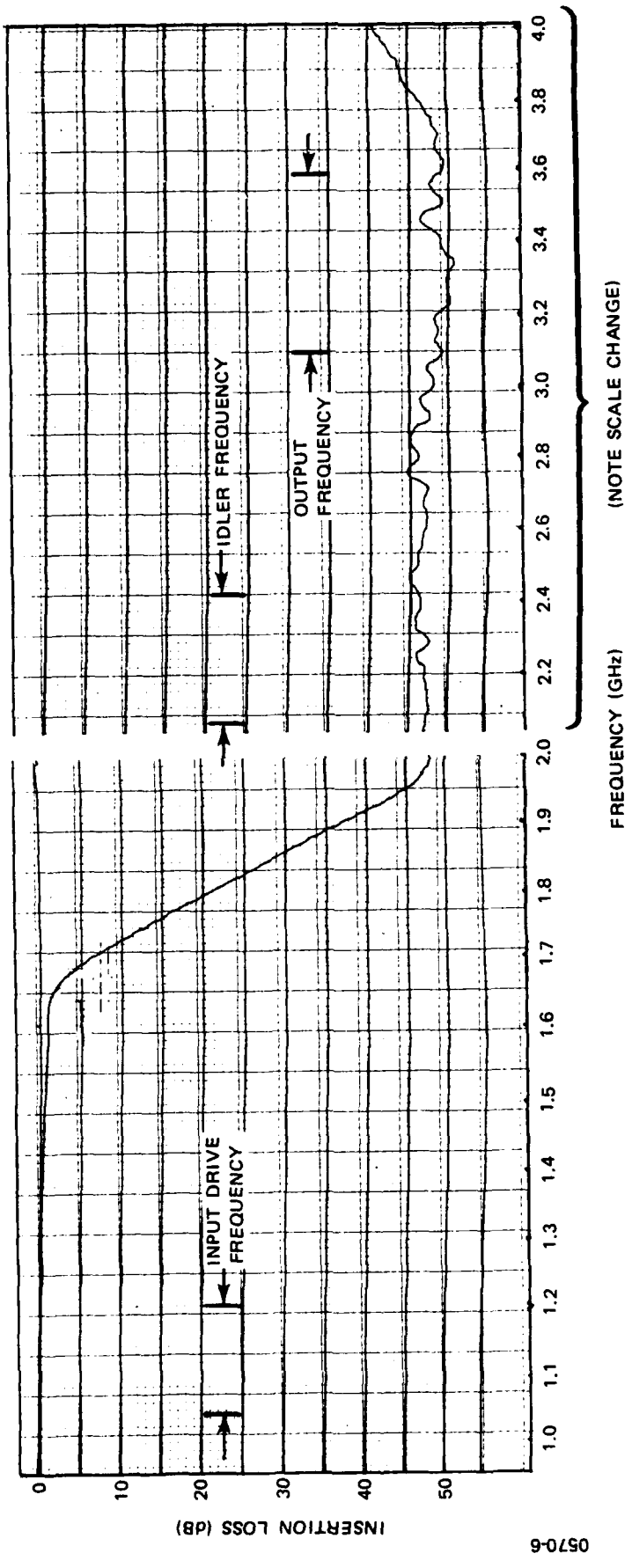

Figure 5. Swept-frequency insertion loss of input low-pass filter

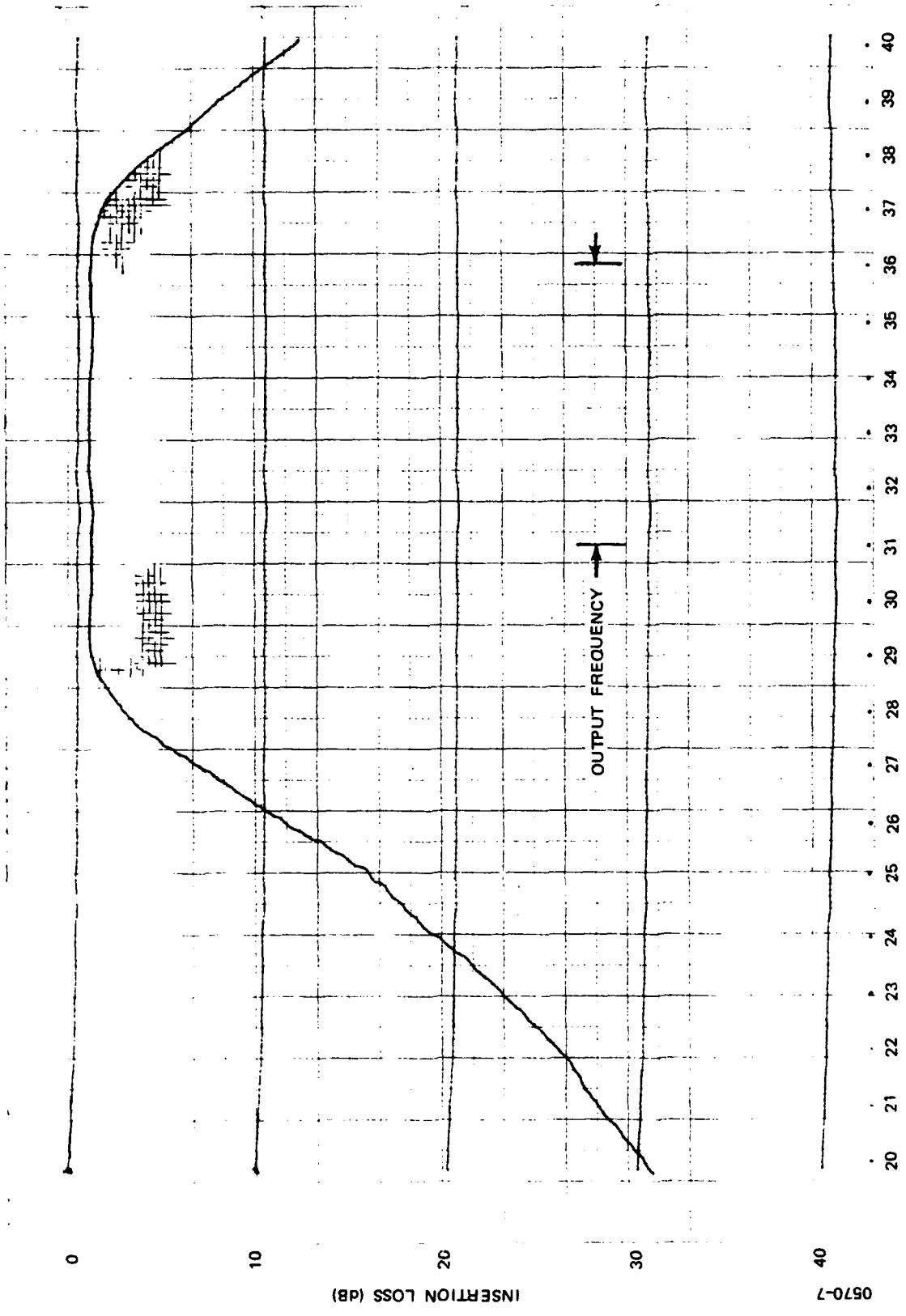

Figure 6. Swept-frequency insertion loss of output bandpass filter

Section IV

SUMMARY AND CONCLUSIONS

It has been shown from measured data on a high-performance L-band power transistor and from manufacturer's data of bimode varactors that a 150-watt pulsed S-band tripler source is practical. A 250-watt peak L-band amplifier has been breadboarded and tested. The tripler circuit has been built, and awaits final evaluation of several candidate diodes to select the best device for the application. The circuit will then be optimized for the chosen diode.

When completed, the transistor amplifier and tripler should provide 150 watts of pulsed RF power from 3.1 to 3.6 GHz with an overall dc-to-RF efficiency of 25 percent. Even for the worst-case performance based on diode parameters, the X3 source will result in higher power levels than 1985 projections for S-band bipolar transistors.

RANGE DISTANCE REQUIREMENTS FOR MEASURING LOW AND ULTRALOW SIDELOBE ANTENNA PATTERNS

P.S. Hacker and H.E. Schrank

Westinghouse Electric Corporation,
Baltimore, Maryland

ABSTRACT

This paper considers the effects of quadratic phase errors due to finite length pattern ranges on the measurement of low and ultralow sidelobe antennas. The well-known $2D^2/\lambda$ rule-of-thumb distance is shown to be adequate only for measuring patterns having moderately low sidelobes (i.e. down to about -30 dB). This distance is shown to be inadequate for measuring low (-30 to -40 dB) and ultralow (below -40 dB) sidelobe patterns if the near-in sidelobes are to be preserved within reasonable errors (e.g. less than 1 dB). A relationship between first sidelobe errors and range distances is derived from calculated patterns for a number of amplitude distributions with various quadratic phase errors. This relationship is plotted in terms of the change (error) in the highest sidelobe versus range distances in multiples of D^2/λ on log-log paper. This plot clearly shows the range distances required for various low sidelobe patterns and measurement tolerances. A corresponding plot of main lobe gain errors versus finite range distances is also presented.

The results show that the effects of quadratic phase error on near-in pattern sidelobes diminishes rapidly with angular distance from the main beam. Thus for a given range length ND^2/λ, the errors on the second and third sidelobes are significantly less than the error on the first sidelobe. This means that for many low and ultralow sidelobe antennas, practical range distances (such as $2D^2/\lambda$) can still be used to measure wide angle sidelobe levels accurately at the expense of "losing" the first one or two sidelobes.

INTRODUCTION

The question of what length pattern range is required to measure far-field patterns is not new and even some of the

earliest references[1,2,3,4] indicate that range length requirements depend on the sidelobe level of the antenna being tested and the desired accuracy in the pattern structure. For many years the $2D^2/\lambda$ distance with its maximum quadratic phase error of 22.5° (see table 1) at the edge of the antenna aperture served as an adequate "rule of thumb" criterion. However, in the mid-1960's a breakthrough in antenna sidelobe suppression techniques took place at Westinghouse, and it became necessary to measure antenna patterns with ultralow sidelobe levels. A re-examination of the effects of quadratic phase errors was made by Hacker[5] in 1967, using the analytical approach of Silver[1] with a Hamming pattern (cosine-squared on a -22 dB pedestal amplitude distribution) as a convenient math model. The results (which are summarized in Appendix A) showed that several multiples of the $2D^2/\lambda$ distance are necessary to accurately measure the first two or three near-in sidelobes on a Hamming-like pattern; at shorter ranges these near-in sidelobes merge with the main beam and appear as "shoulders."

TABLE 1

EQUIVALENT EXPRESSIONS FOR
QUADRATIC PHASE ERROR

	MAX PHASE ERROR AT EDGE OF APERTURE		
RANGE DISTANCE	RADIANS	DEGREES	WAVELENGTH
Infinite	0	0	0
$32\ D^2/\lambda$	$\pi/128$	1.406	$\lambda/256$
$16\ D^2/\lambda$	$\pi/64$	2.813	$\lambda/128$
$8\ D^2/\lambda$	$\pi/32$	5.625	$\lambda/64$
$4\ D^2/\lambda$	$\pi/16$	11.250	$\lambda/32$
$2\ D^2/\lambda$	$\pi/8$	22.500	$\lambda/16$
D^2/λ	$\pi/4$	45.000	$\lambda/8$
$0.5\ D^2/\lambda$	$\pi/2$	90.000	$\lambda/4$
$0.25\ D^2/\lambda$	π	180.000	$\lambda/2$

The purpose of this paper is to assemble some "classical" reference information with some recently calculated low* and ultralow** sidelobe patters to show the effects of various amounts of quadratic phase error on the patterns, both qualitatively and quantitatively. Also, some interesting and (hopefully) useful summary information will be presented, including the unusual behavior of the unique Hamming pattern which exhibits slightly improved maximum sidelobe levels with increasing quadratic phase error! To the authors' knowledge, this has not been presented anywhere so far, nor do any other known patterns remain impervious to reduced range distances.

In addition to showing the effects of quadratic phase errors on sidelobe levels, a by-product of the computed data is the relation between peak mainlobe directive gain and those same phase errors. In this respect the Hamming pattern behaves quite normally, but the cosine pattern seems to behave slightly different from all the others studied.

All the data presented and discussed is for one-dimensional linear-aperture antennas.

REVIEW OF SELECTED REFERENCES

One of the most educational and useful antenna papers ever published is K. Milne's on marine radar "aerials".[3] In it, Milne presents many computed and plotted patterns, some of which are reproduced here. Figures 1, 2, and 3 show very clearly how the same quadratic phase errors ($\beta = \pi/2$, and $\beta = \pi/4$) result in increasing distortions for the -13 dB pattern (figure 1), the -23 dB pattern (figure 2), and the -32 dB pattern (figure 3). Another pair of well-presented graphs are shown in figure 4, which summarizes the behavior of a complete family of patterns, namely the cosine-on-a-pedestal group. Superimposed on the abscissa, which is the phase error in degrees, are corresponding

---

* low sidelobes are defined here as ranging from -30 to -40 dB

** ultralow sidelobes are defined as those below -40 dB

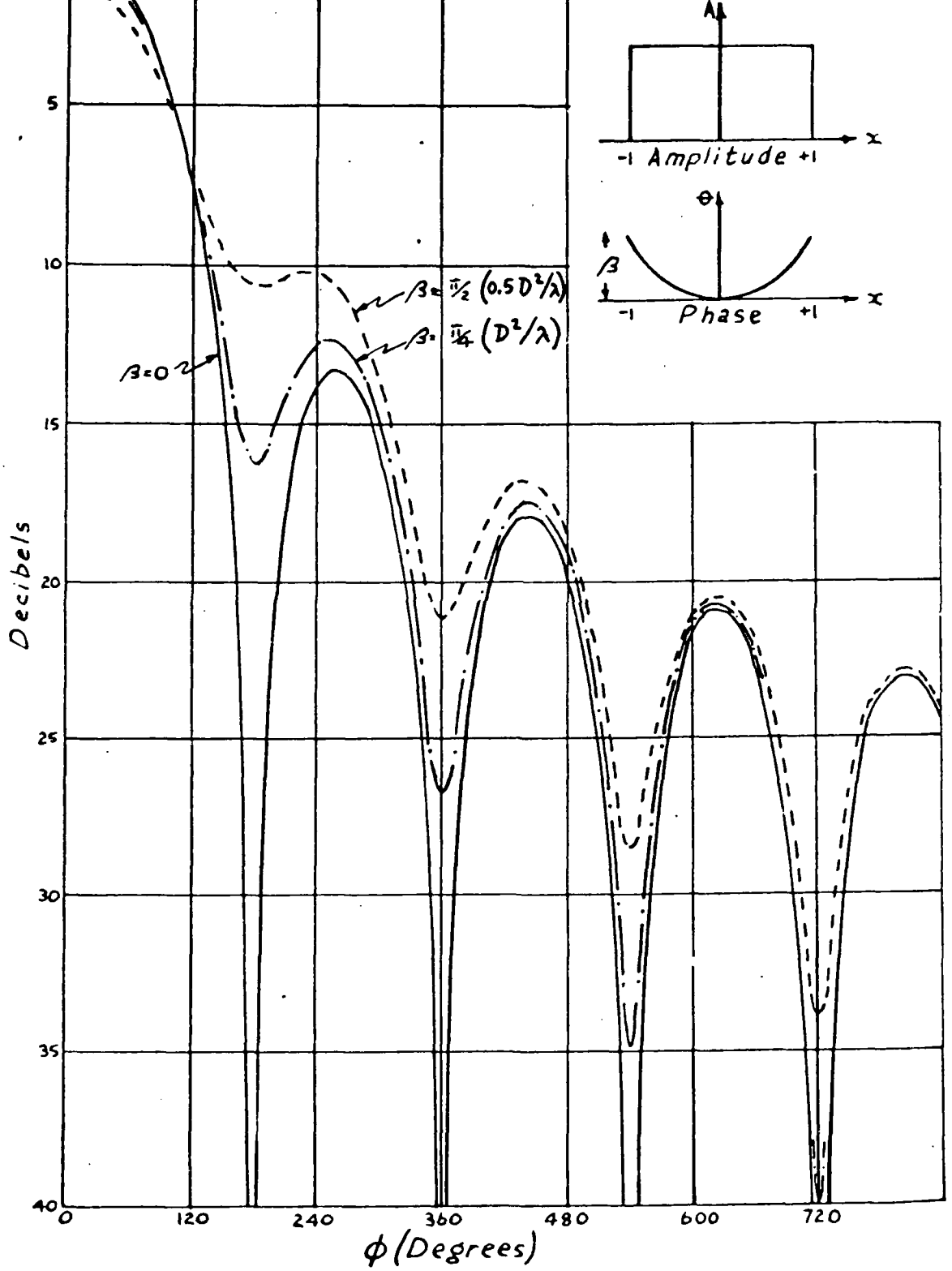

Figure 1. Quadratic Phase Errors With Uniform Amplitude

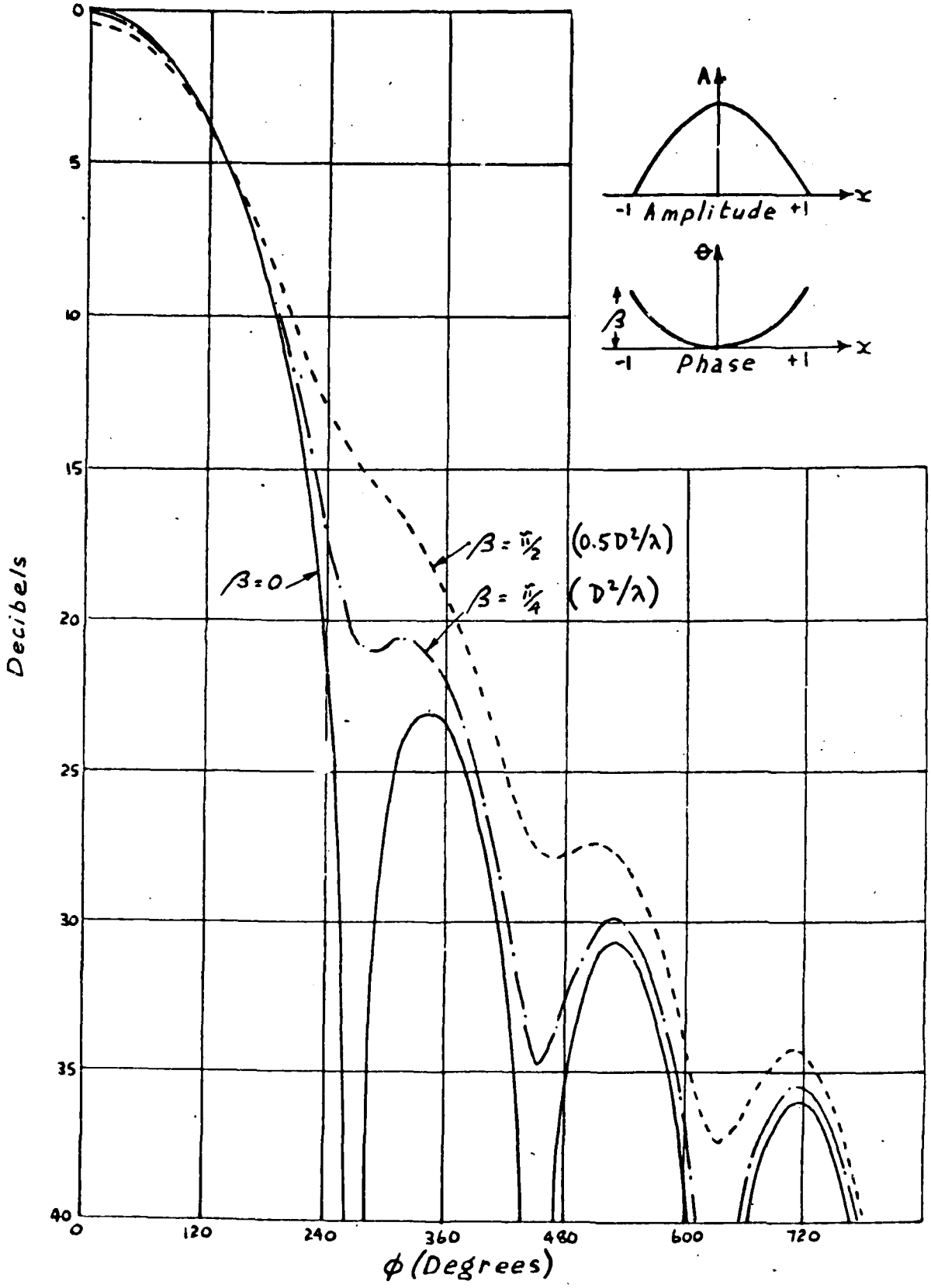

Figure 2. Quadratic Phase Errors With Tapered (Cosine) Amplitude

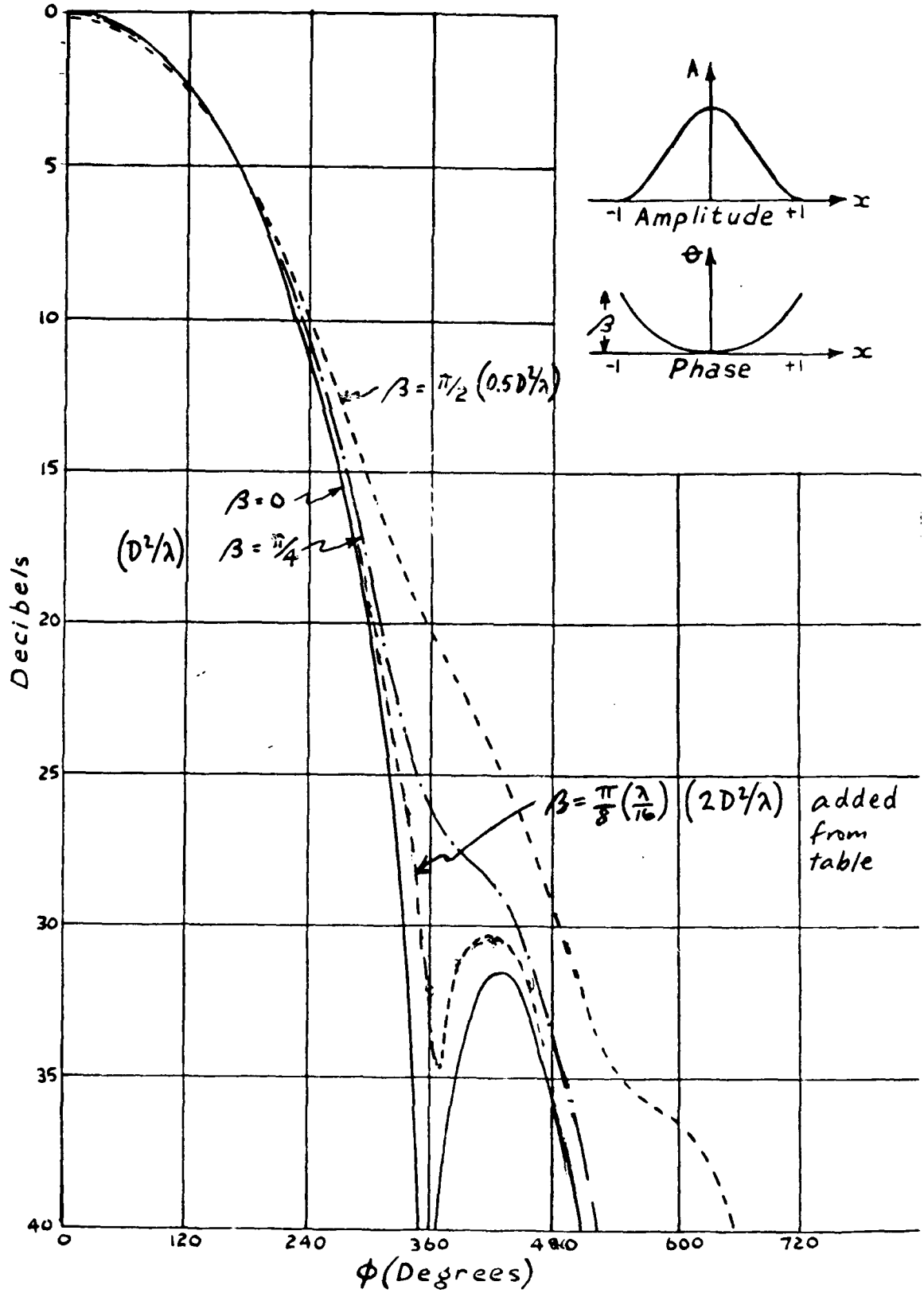

Figure 3. Quadratic Phase Errors With Tapered (Cosine - Squared) Amplitude

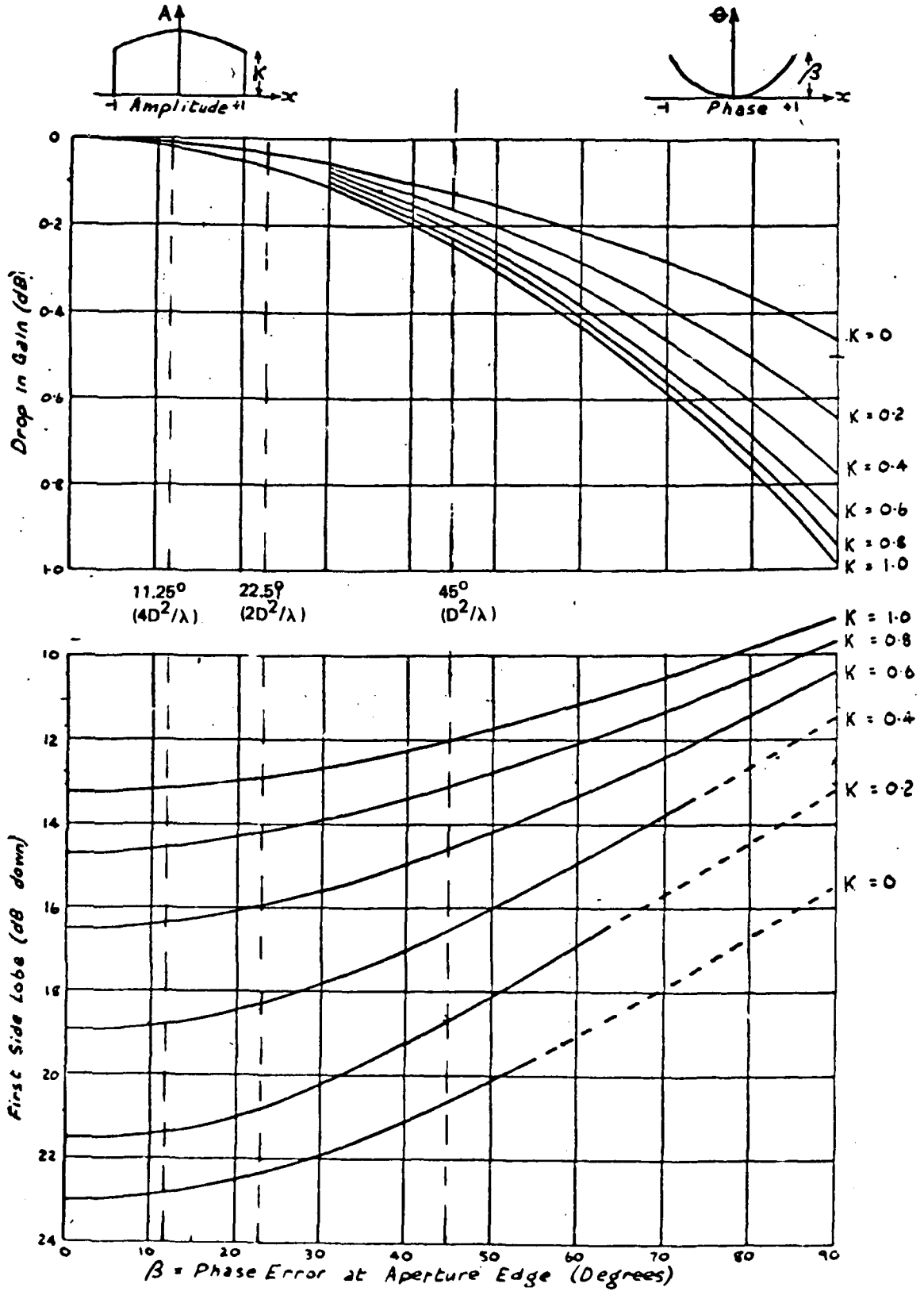

Figure 4. Effects of Quadratic Phase Error on Tapered Amplitude
K + (1 - K) Cos (π - X/2)

range distances expressed in multiples of D^2/λ. The first sidelobe levels shown at the ordinate ($\beta = 0$) can be checked with J. Ramsey's[6] figure 7.

Similar figures are found in many other references, of which Hollis[7] et al is an example, and his figure 14.3 shows a -30 dB Taylor pattern at three range distances. The same figure is also presented in IEEE Standard 149-1979[8] as figure 3, page 21. The information presented in these and similar references is helpful, but is generally limited to two or three sidelobes and one or two phase error conditions. Furthermore, none of them deal with sidelobe levels near or below -40 dB.

SOME LOW AND ULTRALOW SIDELOBE PATTERNS

To investigate the effects of quadratic phase errors on lower sidelobe patterns, computations were made on the following distributions (in addition to a uniform distribution as a control case):

1. Cosine-Squared
2. Hamming
3. Modified Taylor (-50 dB first SL, -60 dB rest)
4. Chebyschev (-40 dB)
5. Chebyschev (-60 dB)

The results of these computations are plotted as shown in figures 5 through 9, for various quadratic phase errors expressed in terms of multiples of D^2/λ.

Peak values of the first six sidelobes were also derived from the computations, and the values for the highest sidelobe in each case are given in table 2. Note that two numbers are given for each entry: the upper one is the change in sidelobe level relative to the renormalized peak in each case, while the lower number (in parentheses) is the change relative to the absolute original sidelobe levels. They differ (in dB) by the change in main lobe directivity caused by the quadratic phase errors.

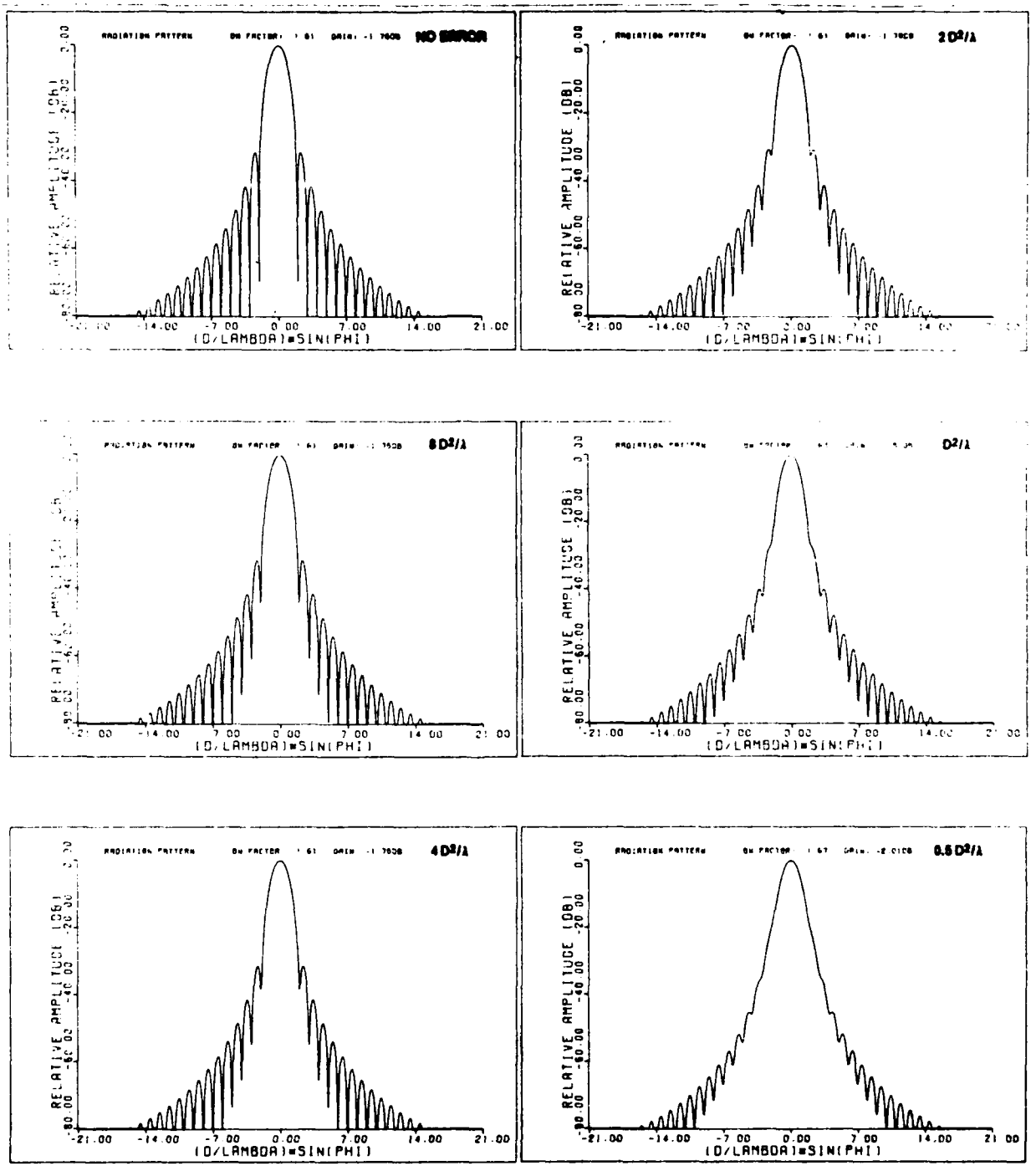

Figure 5. Cosine - Squared Patterns (Note Patterns Are Renormalized for Each Range Distance)

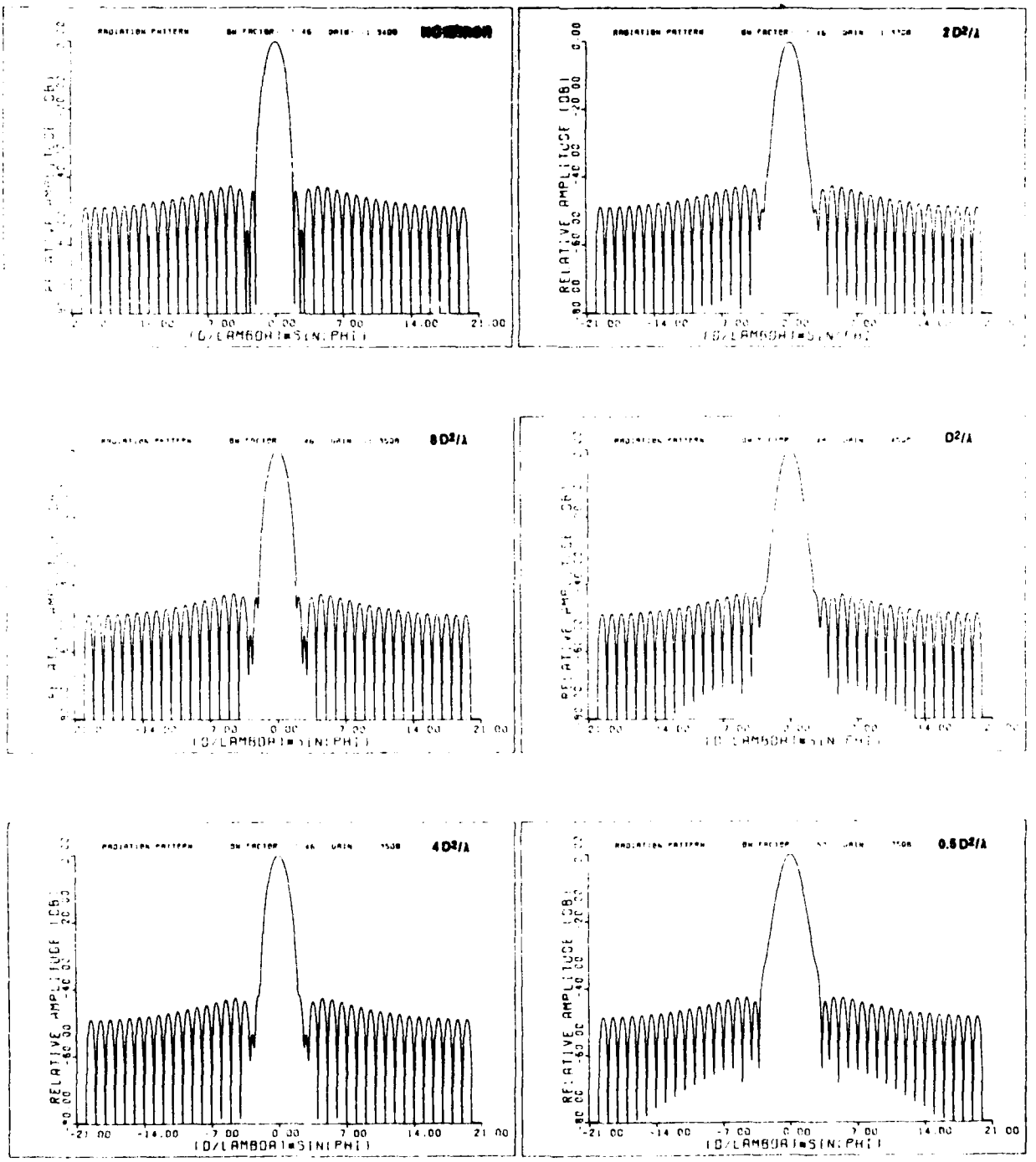

Figure 6. Hamming Patterns

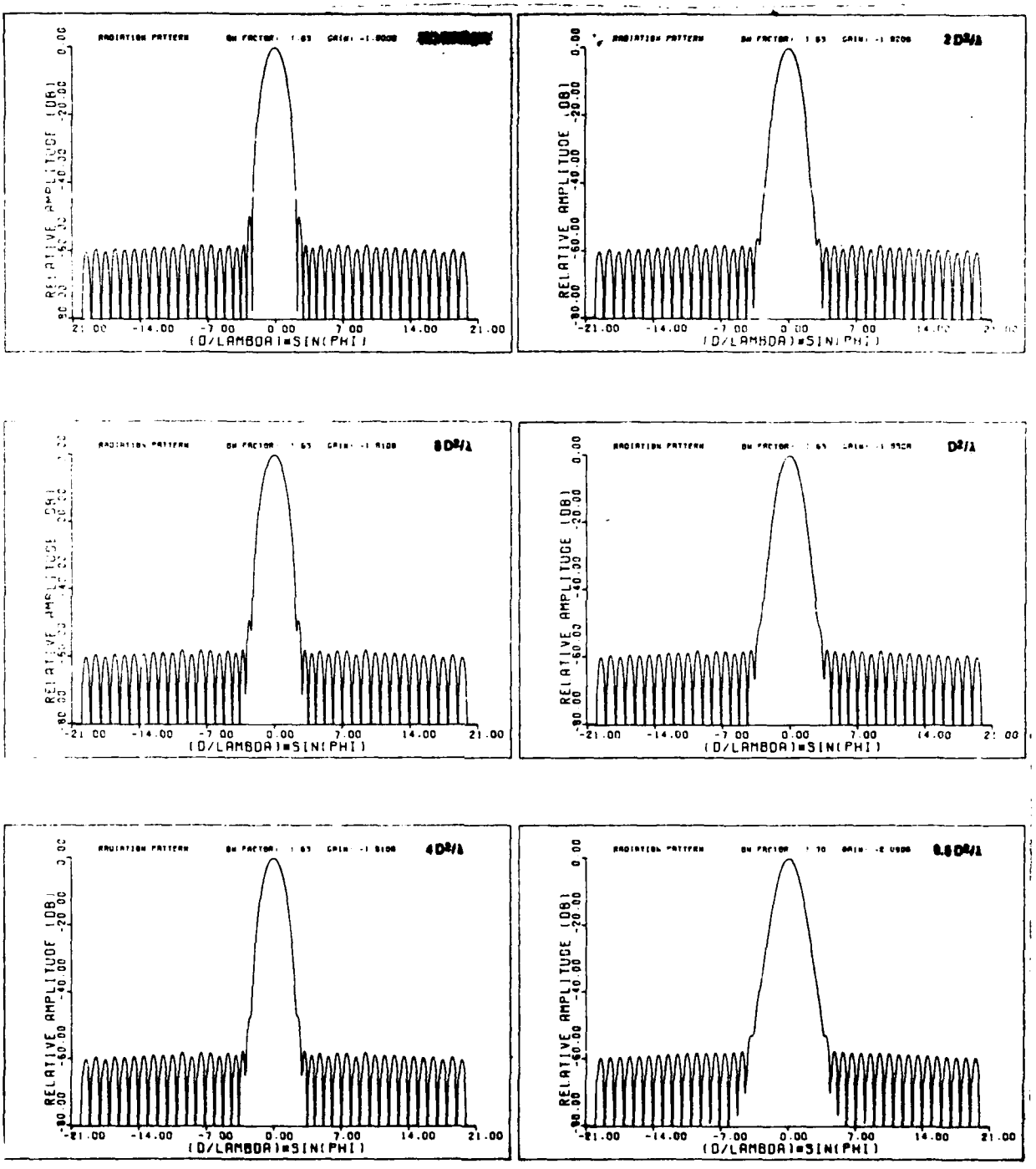

Figure 7. Modified Taylor Patterns

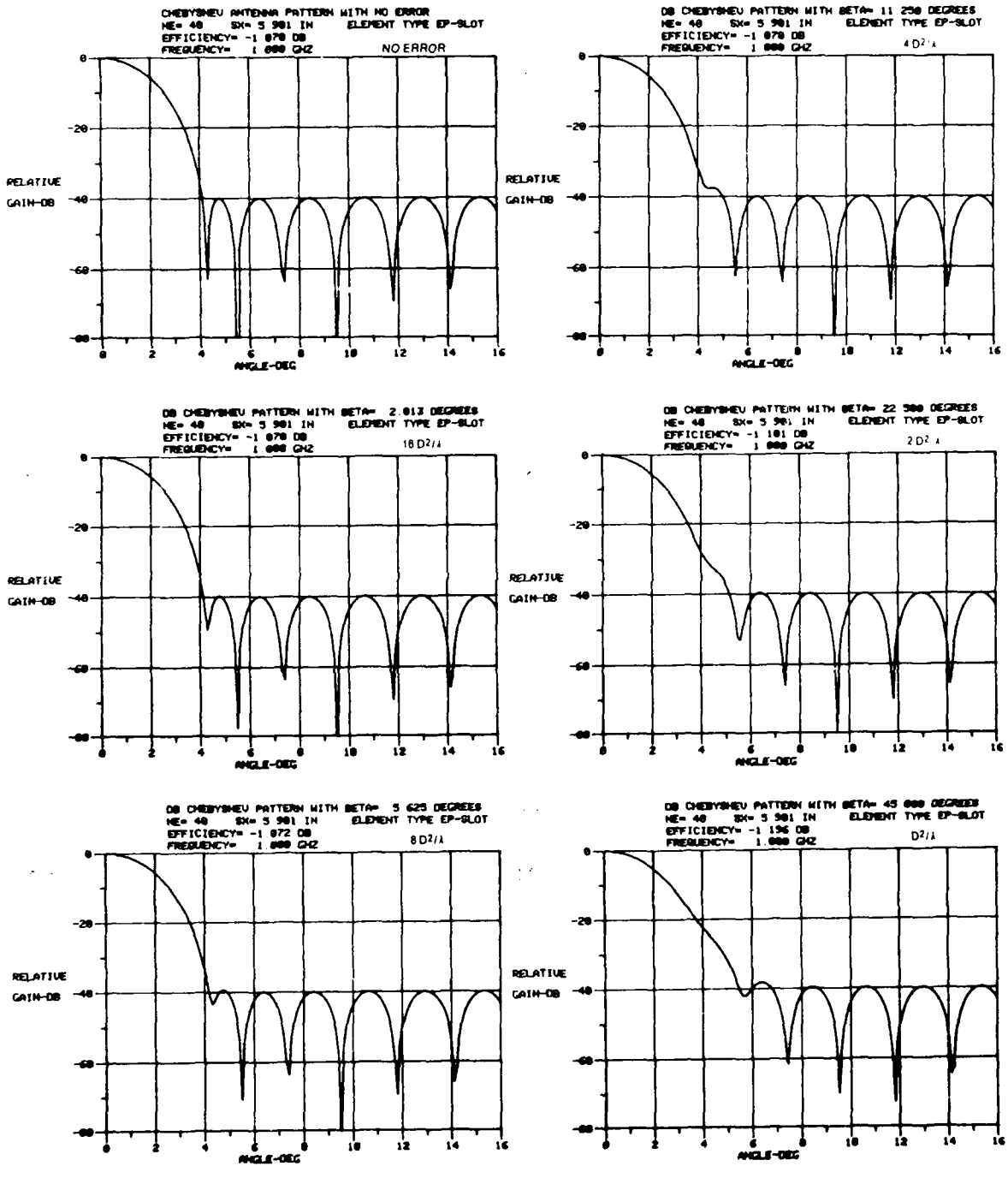

Figure 8. Chebyschev (-40 dB) Patterns

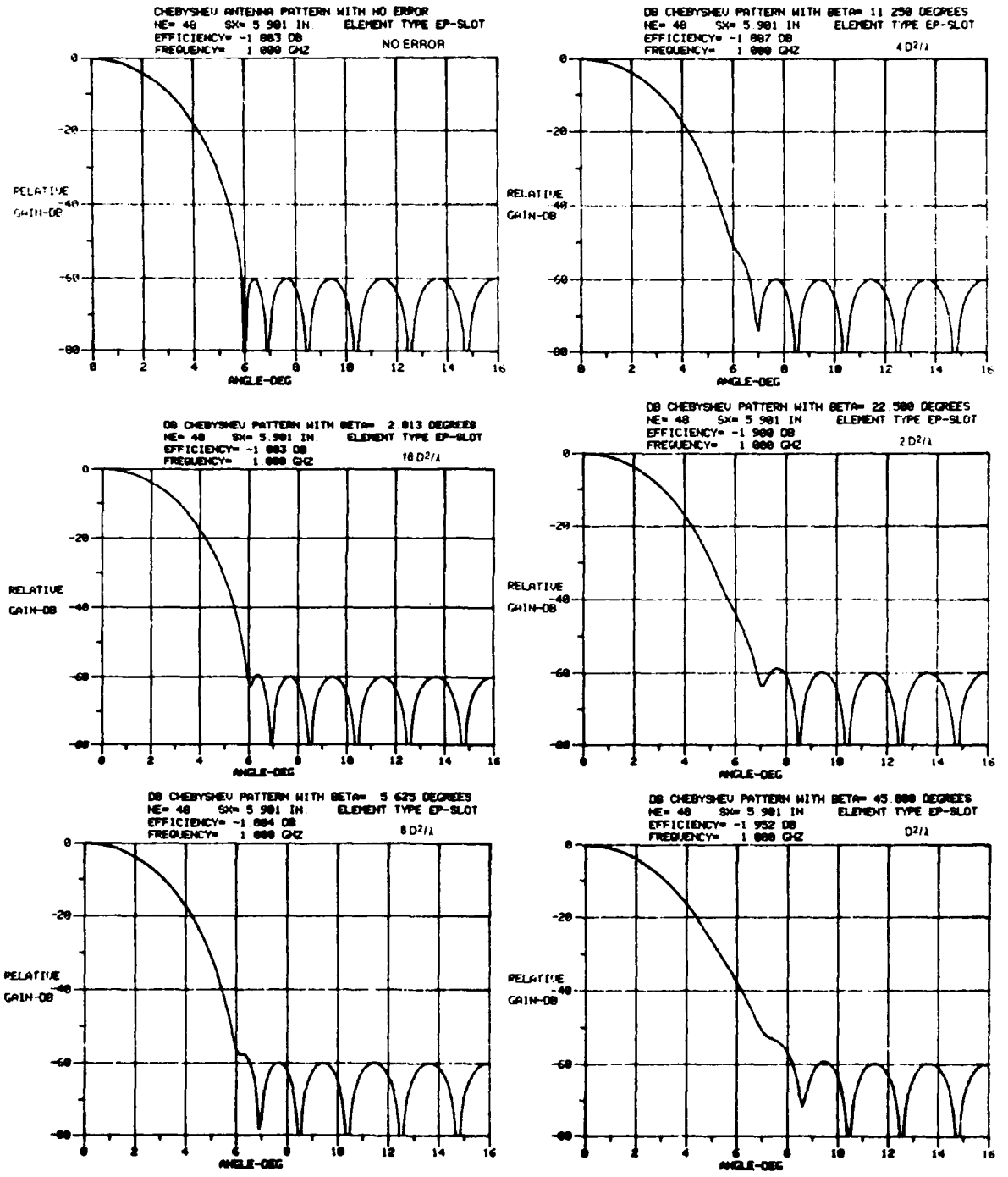

Figure 9. Chebyschev (-60 dB) Patterns

TABLE 2

CHANGES IN HIGHEST SIDELOBE LEVEL
DUE TO QUADRATIC PHASE ERROR

	Max. Sidelobe Level	dB Rise in SL Due to Quadratic Phase Errors Rel. to New Peak/(Absolute = Rel. to Original Level) $16\,D^2/\lambda$	$8\,D^2/\lambda$	$4\,D^2/\lambda$	$2\,D^2/\lambda$	D^2/λ	$0.5\,D^2/\lambda$
Uniform	-13.24	–	.02 (.02)	.08 (.07)	.32 (.26)	1.22 (.98)	4.21 (3.25)
Cosine	23.2	–	–	–	.74 (.68)	2.68 (2.53)	7.70 (7.24)
$(\text{Cosine})^2$	-31.47	–	.06 (.06)	.24 (.24)	.96 (.94)	– –	– –
Hamming	-42.42 **		0 (*.01)	0 (*.01)	*.01 (*.04)	*.03 (*.14)	*.14 (*.55)
Mod Taylor	-49.67	–	.57 (.56)	S			
40 Cheby.	40.01	.14 (.14)	.58 (.58)	2.37 (2.36)	S		
60 Cheby.	-60.02	.55 (.55)	S				

NOTES: ** Fourth Sidelobe from main lobe (all others are first SL)
* Sidelobe level reduced (all others are increased)
S Sidelobe merged into shoulder on main lobe.

80-0810-T-2

Note the amazing results for the Hamming pattern, where the absolute level of the maximum sidelobe is improving slightly as range distance gets shorter. This is contrary to all other patterns.

SUMMARY AND CONCLUSIONS

The data contained in the above figures and table can be plotted in several ways, but the most unifying and introspective way was found to be a log-log plot of absolute change in sidelobe level versus range distance in multiples of D^2/λ, as shown in figure 10. This plot reveals that all pattern sidelobes (including the Hamming) vary with range distance along almost straight lines, and that the various lines are not exactly but very nearly parallel. From this plot we can determine at a glance how long a measuring range is necessary for any specified accuracy (change) in sidelobe level, depending on the type of pattern being used. For example, if we wish to measure a cosine-squared pattern with

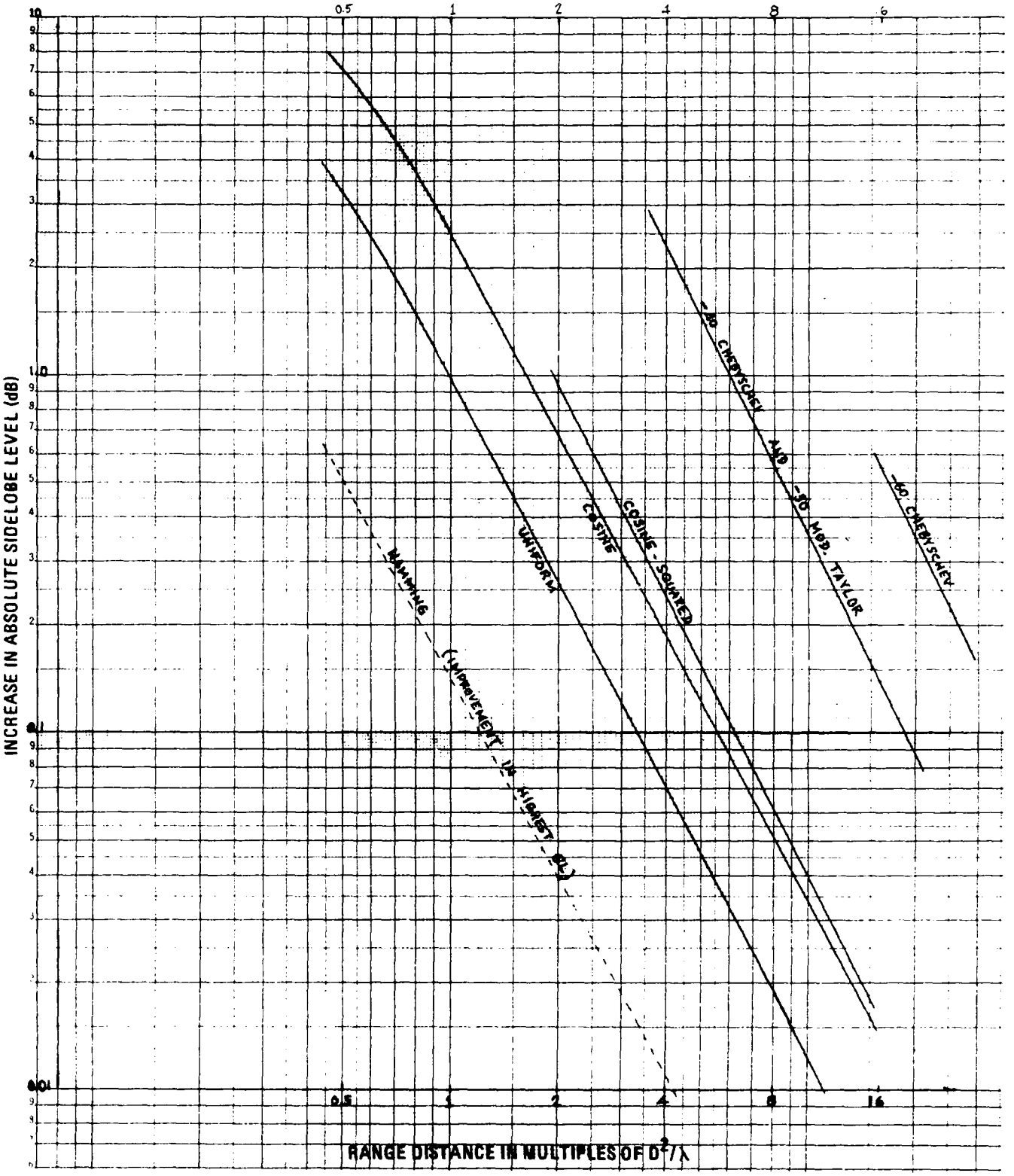

Figure 10. Change in Absolute Sidelobe Level Due to Quadratic Phase Error

no more than 0.5 dB error in its first sidelobe level, we must operate at about 2.8 D^2/λ (or more).

Plotting the reduction in main lobe directivity gain against range distance again shows very nearly straight-line behavior when plotted on log-log scales as in figure 11. Note that the lines are not parallel, but their slopes are reasonably alike, with the exception of the cosine pattern, which is the least sensitive in terms of gain reduction versus decreasing distance. The data is also tabulated in table 3 on figure 11.

The conclusions that can be reached from this brief study are that ultralow sidelobe antennas do require much greater than $2D^2/\lambda$ distances if the near-in sidelobes must be kept from merging with the main lobe, but, if measurements are made at distances near $2D^2/\lambda$, only the first one or two sidelobes are "lost," while the rest are affected negligibly.

ACKNOWLEDGEMENTS

The authors would like to acknowledge the siginficant contributions made toward this paper by Westinghouse colleagues Ed Frost, Dan Davis, and Kurt Ramsey who gave much-appreciated assistance in the pattern computations and the plotting arrangements.

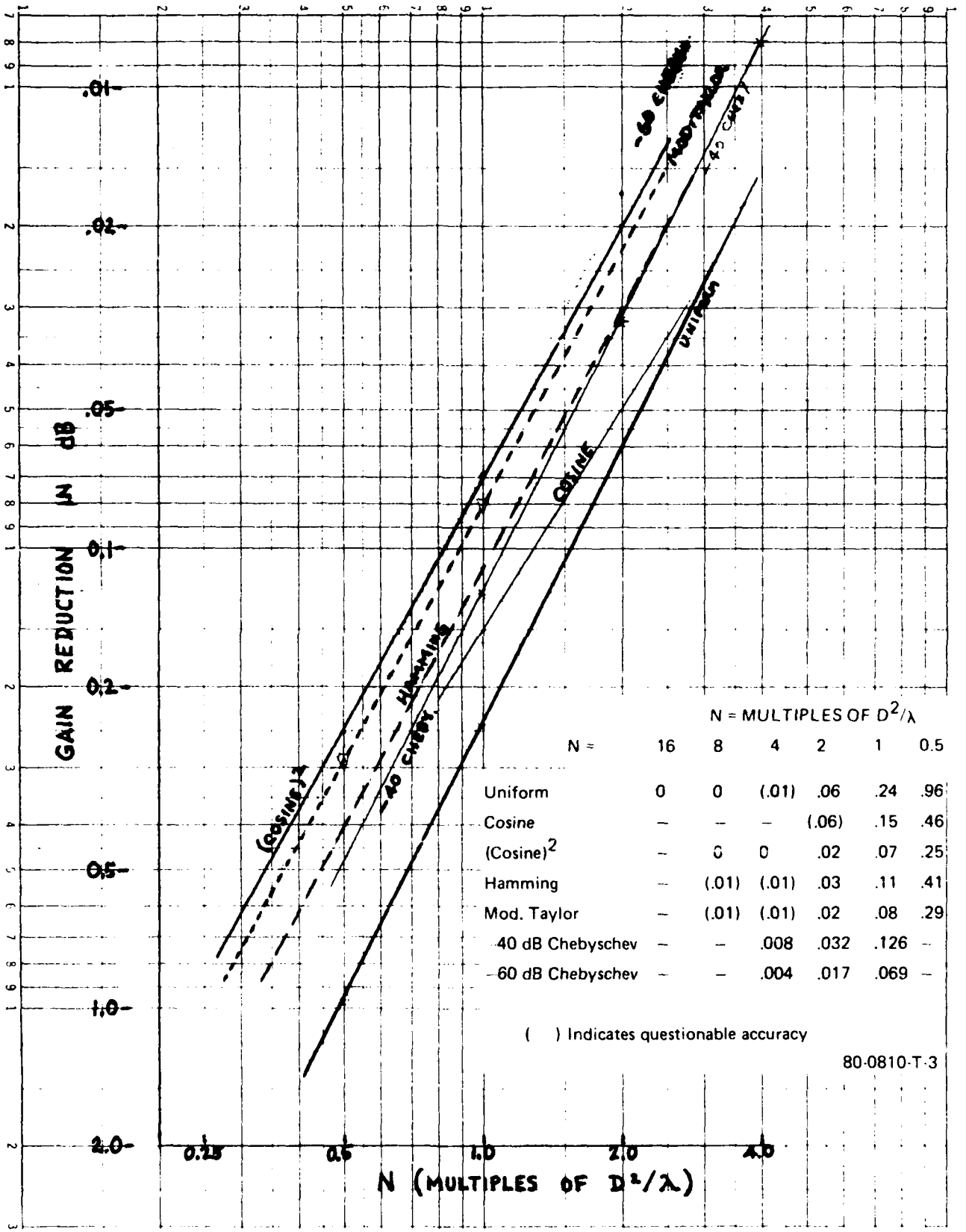

N =	16	8	4	2	1	0.5
Uniform	0	0	(.01)	.06	.24	.96
Cosine	–	–	–	(.06)	.15	.46
$(Cosine)^2$	–	0	0	.02	.07	.25
Hamming	–	(.01)	(.01)	.03	.11	.41
Mod. Taylor	–	(.01)	(.01)	.02	.08	.29
40 dB Chebyschev	–	–	.008	.032	.126	–
60 dB Chebyschev	–	–	.004	.017	.069	–

Figure 11. Directive Gain Reduction at Various Range Distances

APPENDIX A

EFFECTS OF FINITE LENGTH ANTENNA RANGE ON MEASUREMENTS OF LOW SIDELOBE ANTENNAS

A.1 INTRODUCTION

For many years it has been common practice to make the approximation that the field strength pattern of an antenna is essentially unchanged from a distance of $2D^2/\lambda$ to infinity, where D is the maximum antenna dimension, and λ is the wavelength. At a range length of $2D^2/\lambda$ there is a differential path length between rays to the antenna center relative to the edge of $\lambda/16$ or $\pi/8$ radians, which is indicative of the curvature or sphericity of the wavefront at the antenna when used as a receiver. The effect of this phase curvature upon the measured gain of a uniformly illuminated antenna is that the measured gain is 99 percent of the true gain. If the range length is reduced to D^2/λ the measured gain in only 94 percent of the true gain.

In view of these considerations $2D^2/\lambda$ (or even D^2/λ) has been deemed adequate for pattern measurements of all types of antenna. It is the purpose of this appendix to show the inadequacies of these considerations for antennas where all of the sidelobe structure may be significantly below -30 dB with respect to the main beam.

A.2 QUADRATIC PHASE ERROR

The curvature of the phase front at the aperture of an antenna under test on a range of finite length is such that the phase differential increases as the square of the distance from the center of the aperture. It is a simple geometric exercise to show that the maximum value of this phase error is:

$$B = \frac{\pi D^2}{4\lambda R} \qquad (1)$$

As is shown on pages 188-189 of "Microwave Antenna Theory and

Design" edited by S. Silver[1], the radiation pattern in field strength units as a function of β is:

$$g(x) = K \sum_{m=0}^{\infty} \frac{j^m \beta^m}{m!} \frac{d^{2m}}{dx^{2m}} \left[g_o(x) \right] \qquad (2)$$

where x is a variable proportional to the sine of the angle measured from the normal to the antenna aperture (a line source is assumed for purposes of this discussion), $g_o(x)$ is the radiation pattern at infinity, and K is a constant of proportionality.

Equation (2) is usually approximated by the first two terms yielding:

$$g(x) \approx K \left[g_o(x) + j \beta g_o''(x) \right] \quad . \qquad (3)$$

When β is small and/or the sidelobes close to the main beam are no lower than 20-25 dB relative to the peak, this expression is adequate and predicts minor variations in the pattern.

It will now be shown that for antennas with very low sidelobes the $2D^2/\lambda$ criterion is not adequate, and that higher order derivatives are required than used in equation (3) for accurate predictions to be obtained, particularly for the angular region close to the main beam.

A.3 LOW SIDELOBE APERTURE DISTRIBUTIONS

Aperture distributions used for most low sidelobe antenna applications can be characterized by amplitude functions represented by a cosine series. Thus, for a one-dimensional aperture:

$$f(z) = \sum_{o}^{N} A_n \cos \left(2n\pi Z / Z_{max} \right) \qquad (4)$$

where the aperture extends between $\pm Z_{max}$. Such a truncated series can represent any realizable symmetrical aperture function which has a constant phase (real functions).

The voltage pattern of these distributions at infinite range is found by taking the Fourier Transform of (4). This can be shown to yield a function expressed as:

$$g_o(x) = \sum_{n=-\infty}^{\infty} B_n \sin P(x+n)/P(x+n) \qquad (5)$$

where $B_n = B_{-n}$ (real), $P = 2\pi z_{max}/\lambda$, λ is the wavelength, and θ is the angle relative to broadside ($x=\sin\theta$).

This infinite set of sin u/u functions is complete and orthogonal for an aperture of extent $2z_{max}$. For most low sidelobe distributions the B_n coefficients are significant only for $|n| \leq 2$ and in many cases $|n| \leq 1$. For example, when n is restricted to -1, 0, 1, all of the cosine-squared-on-a-pedestal functions are included. When the Taylor functions are expanded in these terms, the B_n for $|n| < 2$ are very small, well below normally achievable tolerance levels.

The effects of finite range lengths will be analyzed, first for patterns which can be decomposed into the summation of three orthogonal and adjacent sin u/u beams, and then the analysis will be extended to include five such beams. The results will be indicative of the effects for all low sidelobe distributions using amplitude only as the aperture control variable.

Consider the function:

$$\begin{aligned} g_o(u) &= \sin u/u + C \sin(u+\pi)/(u+\pi) \\ &\quad + C \sin(u-\pi)/(u-\pi) \qquad (6) \\ &= \sin u/u - C \sin(u+\pi)/(u+\pi) - C \sin(u-\pi)/(u-\pi) \end{aligned}$$

Figure A-1 shows the pattern function plotted in decibels for C = 0.426 which is the constant for the very low sidelobe Hamming function. Note that except for the main beam and the first two sidelobes, nulls are evenly spaced at integral multiples of π. The maximum sidelobe level is about -42 dB relative to the main beam peak.

A.3.1 EFFECTS OF QUADRATIC PHASE ERROR

In order to show the effects of quadratic phase errors on patterns represented by equation (6), equation (3) will first be

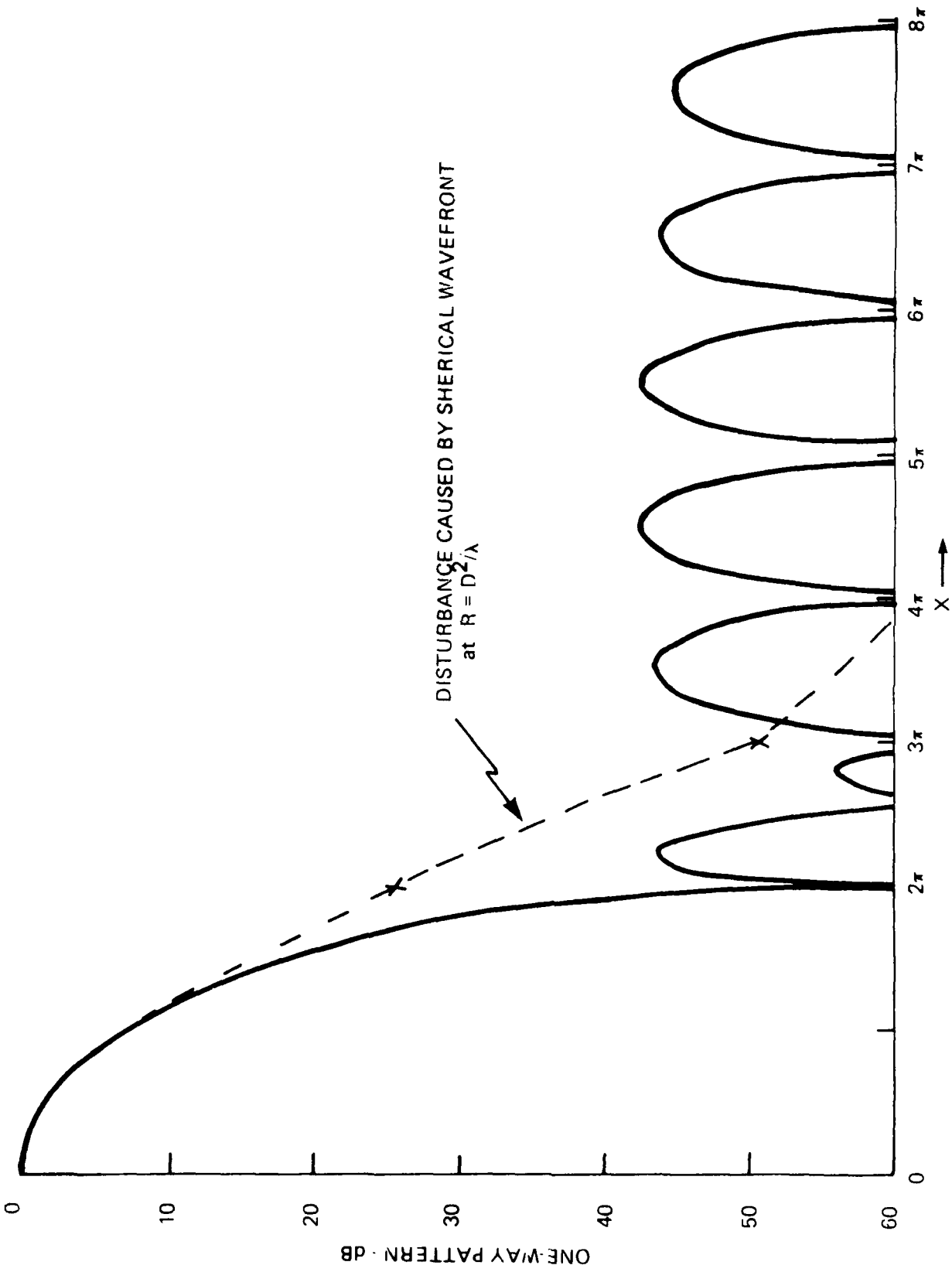

Figure A-1. Hamming Function Pattern

used, followed by an analysis which includes the next terms in the series expansion of equation (2):

$$g_o''(u) = \frac{-u^2 \sin u - 2u\cos u + 2\sin u}{u^3} + \frac{C\left[(u+\pi)^2 \sin u + 2(u+\pi)\cos u - 2\sin u\right]}{(u+\pi)^3} + \frac{C\left[(u-\pi)^2 \sin u + 2(u-\pi)\cos u - 2\sin u\right]}{(u-\pi)^3} \qquad (7)$$

When this function is compared to the unperturbed pattern of equation (6) the following can be noted:

1. The first term of each term of (7) is a sin u/u term which matches (6) and therefore does not change the relative level of radiation anywhere.

2. The third term of each major term of (7) is a sin u/u^3 term which will have the same null structure as (6). These terms will alter the amplitudes of the sidelobes close to the main beam but will have little effect further out due to the $1/u^3$ dependence.

3. The second term of each major term of (7) is a cos u/u^2 term which has no effect at angles of sidelobe peaks (for $u \geq 3\pi$), but which has maximum effect at the nulls ($u = n\pi$, with $n \geq 2$) of the pattern of (6).

Evaluating (7) at integral multiples of π greater than or equal to 2, we have:

$$g_o''(n\pi) = -\frac{2}{(n\pi)^2} + \frac{2C}{[(n+1)\pi]^2} + \frac{2C}{[(n-1)\pi]^2} \quad ; \qquad (8)$$

this has been evaluated for D^2/λ or $\beta = \pi/4$ for C = 0.426. The results are tabulated on the following page.

n	Level below main beam peak
2	−29 dB
3	−49 dB
4	−72 dB
5	<−70 dB
6	<−70 dB

Because β is inversely proportional to range these results decrease by 6 dB per "octave" increase in range.

Referring to figure A-1 it is obvious that even at $2D^2/\lambda$ it will be impossible to determine the level of the first three sidelobes. In fact, until the range is lengthened to at least $8D^2/\lambda$ it is impossible to measure these lobes.

To further emphasize the point, measurements taken on antennas with the Hamming distribution (C = 0.426) have shown that the first two sidelobes cannot be measured at ranges of 20 to 40 D^2/λ. In many respects then, it is just as good to work at D^2/λ or $2D^2/\lambda$ as it is at such greater ranges.

A fairly obvious question which could arise is whether the disturbances in the pattern just discussed are due to over-truncation of the series of equation (2). Accordingly the series was evaluated taking into account the next term:

$$g(x) \approx g_o(x) + j\beta g_o''(x) - \frac{\beta^2}{2} g_o''''(x) \qquad (9)$$

In order to use (9) the fourth derivative of sin u/u must be found for each of the terms of (6). This differentiation yields

$$\frac{d^4}{d^4}\left(\frac{\sin u}{u}\right) = \frac{24 \sin u}{u^5} - \frac{24 \cos u}{u^4} - \frac{12 \sin u}{u^3} + \frac{4 \cos u}{u^2} + \frac{\sin u}{u} \qquad (10)$$

Once again the terms involving sin u/u, sin u/u^3, and sin u/u^5 only perturb the pattern at its peaks in between values of x of integral multiples of π. The cosine terms represent the severe disburbances in the null regions. When these are evaluated for $n \geq 2$ at D^2/λ or $\beta = \pi/4$ we have

n	Level below main beam peak
2	−26.3 dB
3	−55.6 dB
4	<−70.0 dB
5	<−70.0 dB
6	<−70.0 dB

Referring to equation (9) it is interesting to note that the high level due to the fourth derivative at n = 2 is in phase quadrature with the contribution from the second derivative so that cancellation cannot occur.

It is also important to point out that the fourth derivative contributions are proportional to β^2 and therefore decrease at 12 dB per "octave" in range. In other words, the forth derivative contributions will be unimportant at $x = 2\pi$ at ranges of $4D^2/\lambda$ even though the second derivative terms would still be at the -41 dB level.

If two more symmetrical sin u/u functions are added (i.e., five total components) then equation (6) becomes:

$$g_o(u) = \sin u/u + C_1 \sin (u\pm\pi)/(u\pm\pi) + C_2 \sin (u\pm 2\pi)/(u\pm 2\pi)$$
$$= \sin u/u - C_1 \sin u/(u\pm\pi) + C_2 \sin u/(u\pm 2\pi) \qquad (11)$$

The second derivative then becomes:

$$g_o''(u) = -\frac{u^2 \sin u - 2u \cos u + 2\sin u}{u^3}$$
$$+ \frac{C_1\left[(u+\pi)^2 \sin u + 2(u+\pi)\cos u - 2\sin u\right]}{(u+\pi)^3}$$

$$+\frac{C_1\left[(u-\pi)^2\sin u + 2(u-\pi)\cos u - 2\sin u\right]}{(u-\pi)^2}$$

$$-\frac{C_2\left[(u+2\pi)^2\sin u + 2(u+2\pi)\cos u - 2\sin u\right]}{(u+2\pi)^3} \qquad (12)$$

$$-\frac{C_2\left[(u-2\pi)^2\sin u + 2(u-2\pi)\cos u - 2\sin u\right]}{(u-2\pi)^3}$$

Proceeding with this analysis it can be shown that the results are not significantly affected by the additional higher order terms.

A.4 CONCLUSIONS

The foregoing analysis indicates that accurate determination of sidelobe levels close to the main beam are nearly impossible to obtain with an antenna range of practical length. However, in many applications where low sidelobes are required (pulse doppler radar, radio astronomy etc.), the average level of radiation outside the main beam is of more importance than the levels of individual lobes. For these applications the loss of information on two or three lobes close to the main beam can be tolerated and ranges between one and two D^2/λ are adequate.

REFERENCES

1. S. Silver, "Microwave Antenna Theory and Design," McGraw Hill, 1949.

2. Cutler, King, and Kock, "Microwave Antenna Measurements," Proc. IRE, Dec. 1947.

3. Milne, K. "The Effects of Phase Error on Simple Aperture Illuminations," Proc. of Conference on Centimetric Aerials..., London, June 1950.

4. Rhodes, D.R. "On Minimum Range for Radiation Patterns," Proc. IRE, Sept. 1954.

5. Hacker, P.S. "Effects of Finite Length Antenna Ranges on Measurements of Low Sidelobe Antennas," Internal Memo., Westinghouse, May 23, 1967 (see Appendix A).

6. Ramsey, J. "Lambda Functions Describe Antenna/Diffraction Patterns," Microwaves, June 1967.

7. Hollis, Lyon, and Clayton, "Microwave Antenna Measurements," Scientific Atlanta, 1970.

8. Test Procedures for Antennas, IEEE Standard 149-1979, Wiley, 1979.

AN INTERFACE BETWEEN ANECHOIC CHAMBER AND COMPUTER

By

Randy C. Willers

This project was funded by the Andrew Corporation of Orland Park, Illinois.

The author is currently with Eagle Signal of Davenport, Iowa.

ABSTRACT

The design of a data acquisition system for an anechoic chamber is discussed. By use of a minicomputer and commercially available parts, a system can be built to provide storage of radiation and phase pattern data. Such a system is flexable in its handling of data and can be easily programmed to display and analyze recorded patterns. It is primarily intended for users who currently have an anechoic chamber with a receiver and pattern recorders.

AN INTERFACE BETWEEN ANECHOIC CHAMBER AND COMPUTER

I. INTRODUCTION

The recording and analysis of antennas under test requires the handling of large amounts of data. This process can be greatly simplified and accelerated by digitizing and storing test data on a computer. The project undertaken was to find a means of collecting and saving data on a suitable medium while an antenna was being tested in an anechoic chamber. After the data was taken, it could be analyzed and antenna performance parameters computed. By feeding information directly into a computer, analysis could be done quickly and efficiently, saving many man-hours in the process.

The data being taken showed two relationships, the antenna radiation pattern and phase pattern. The radiation pattern depicts the received signal amplitude and the phase pattern relates the phase of the received signal with respect to the transmitted signal, both as a function of the azumith.

The parameters which were computed from this data included antenna gain, beam efficiency, aperture efficiency, and half-power beam width. The data and calculated

parameters provided a basis to assess new antenna designs and design changes.

In order to record the radiation pattern, the main beam must be accurately measured. In the extreme case of high gain antennas, the main beam could be a lobe which is only 0.3° wide, which may be further reduced to 0.1° in future designs. In order to measure data over these angles, angle resolution of up to 0.01° was desired. This meant that 16 bits of resolution would be needed over the 360° range of the azumith.

For amplitude readings over a 40 dB range, the patterns were to have an accuracy of 0.05 dB. The phase was to be accurate to $.5^{\circ}$ or less over the 360° range. In digitized form, both amplitude and phase could be digitized to 10 bits to maintain the desired precision.

The system was broken into two parts. The first part was the hardware design of the system. The interface between the test equipment at the anechoic chamber and the minicomputer had to be designed, with commercially available components to be used as much as possible. This allowed for maximum reliability and ease of serviceability. The second part of the system design was the writing of the software. Computer programs had to be written to gather data, display it in a convenient fashion, and calculate antenna performance parameters.

II. HARDWARE DESIGN

A. Overview

The system hardware was broken into three areas. The first part consisted of the intruments at the anechoic chamber which provided the azimuth, amplitude and phase information. The azimuth was provided by a synchro transmitter which gave synchro information on the antenna angle. This information is contained in three AC voltage signals commanly labeled S1, S2, and S3. The azimuth is determined by a phase relationship between these signals and a reference voltage. The amplitude signal was found at the output of a Scientific Atlanta 1554-2 crystal bolometer amplifier. This amplifier would vary the gain of the signal from the Scientific Atlanta 1750 receiver which was used at the anechoic chamber. The phase signal came from a Scientific Atlanta 1556 DC chopper amplifier, which varied the gain of the phase signal from the 1750 receiver.

The second part of the hardware consisted of the Chamber Interface Unit. It would contain the circuitry needed to convert the information from the chamber test equipment into a form meaningful to the controlling mini-computer.

The last section of the hardware was the LSI-11 MINC (Multiple INstrument Computer). This is a mini-

computer manufactured by the Digital Equipment Corporation. It contained a KD11-HA processor with 64 kilobytes of semiconductor memory. The MINC also had an RX02 disk drive system, with a maximum storage area of one megabyte. The MINC contained a digital input and an analog-to-digital converter which were used in the system.

B. Chamber Interface Unit

The Chamber Interface Unit was divided into two main sections, the angle interface, and the amplitude and phase interface.

The angle interface provides the MINC with the azimuth of the antenna being tested. It converts the signals from the synchro transmitter in the chamber to a digital form which goes to the MINC digital input. The angle interface consisted of three subsections; the synchro-to-digital converter, the buffer latches, and control circuitry.

The synchro-to-digital converter is a monolithic device. It is a tracking converter which continually converts the signals from the synchro transmitter in the chamber into a 16 bit binary word at TTL logic levels. The converter is a model 168H102 and is manufactured by Control Sciences, Inc.

The buffer latches provided line driving capability for transmitting the data to the MINC. The control

circuitry provided a means of handshaking between the MINC and the Chamber Interface Unit.

The amplitude and phase interface of the unit converts the information on the signal strength and phase to a DC level which becomes the input to the MINC analog-to-digital converter. The interface consists of two similar halves, one for the amplitude signal and the other for the phase. The input signals to the interface come from the high signal outputs of the appropriate Scientific Atlanta amplifier. The input signals are one kilohertz sine waves whose amplitudes vary linearly with the signal strength or phase. Each half consists of three subsections; an input buffer, and AC-to-DC converter, and a low pass filter.

The input buffer is used to buffer the interface unit from the high output impedance of the Scientific Atlanta amplifiers. The AC-to-DC converter is a monolithic device (model AD536AJH) manufactured by Analog Devices, Inc. It converts the one kilohertz signal into a DC voltage which is equivalent to the RMS value of the input. The low pass filter removed any one kilohertz ripple left from the AC-to-DC converter.

III. SOFTWARE DESIGN

A. Overview

The computer programs written for the interface system

were done in FORTRAN. Extensive use was made of the software libraries that were provided by the Digital Equipment Corporation. These libraries consisted of the system library to support FORTRAN functions, the the MINC library which supported the digital input and the analog-to-digital converters in the MINC. There were three major programs written for the system.

B. Program PATTRN

Program PATTRN is the program used to record data and store it on disk while the antenna is being tested. It performed the following functions.

1. Recorded the general information that is specific to the antenna being tested. This is provided by the operator and is used to identify the antenna with the patterns stored on the disk.
2. Recorded the raw data while taking a pattern.
3. Printed antenna and pattern information on the terminal for identification.
4. Calibrates the gain of the crystal-bolometer amplifier and/or the DC chopper amplifier to the inputs of the MINC.
5. Adjusts the pattern data set so a desired peak or null can be set to the zero degree angle. This compensates for the difference between the antenna orientation and the synchro information.

C. Program DRAW

Program DRAW displayed the antenna radiation and phase patterns on the MINC terminal. It was used for the following purposes.

1. Displayed an entire radiation pattern, as recorded, on the MINC terminal.
2. Allowed the user to overlay two selected patterns. This provided a comparison of the two patterns to spot differences.
3. Displayed an enlarged view of a radiation or phase pattern.

D. Program ANALZE

Program ANALZE calculated certain function on the antenna pattern data stored on disk. For any given pattern, the user can choose to calculate one of the following.

1. The gain of a radiation pattern.
2. The beam efficiency for an angle given by the user.
3. The aperture efficiency of a horn.

IV. CONCLUSION

A. Results

The construction of the Chamber Interface Unit was finished in March of 1980. It was installed at that time and is currently in use. Though not all of the software

had been implemented and debugged at that time, radiation and phase patterns had been taken by the system and accurately displayed on the MINC terminal. Installation of the system took eleven weeks at a cost of approximately $26,000. This included the purchase price of the MINC.

B. Improvements

While the designed system performed adequately, there was one point where it varied from the original specifications. The desired accuracy of the amplitude measurement was to be 0.05 dB over the 40 dB range. The actual input signal used to determine the amplitude is linear, so the quantizing error of the analog-to-digital converter increased exponentially through the range of the input signal. This meant the signal at -40 dB had a quantizing error of +0.5 dB.

Improvements in the software could also be made. The programs stored all data in semiconductor memory when recording a pattern. For extremely large amounts of data, the system should have some direct memory access capabilities which could transfer data to disk simultaneously with the recording of a pattern.

V. REFERENCES

Conversion Products Catalog, Analog Devices, Inc., Norwood, Mass., 1977.

Cress, Paul, et. al; Fortran IV with Watfor and Watfiv, Prentice-Hall, Inc., Englewood Cliffs, N.J., 1970.

Daryanani, Gobind; Principles of Active Network Synthesis and Design, John Wiley and Sons, New York, 1976.

Data Acquisition Products Catalog, Analog Devices, Inc., Norwood, Mass., 1978.

Dobkin, Robert C.; "True RMS Detector", Linear Brief 25, Linear Applications, Volume 2, National Semiconductor Corporation, Santa Clara, California, 1973.

Hayes, John P.; Computer Architecture and Organization, McGraw-Hill, New York, 1978.

Linear Integrated Circuits, Semiconductor Data Library, Motorola, Inc., 1976.

MINC-11; A closer look at the MINC system, Digital Equipment Corporation, Maynard, Mass., 1979.

MINC-11, Introduction to MINC, Digital Equipment Corporation, Maynard, Mass., 1979.

Morris, Noel M.; Electronics for Works Electricians, McGraw-Hill, London, 1976.

Phase Amplitude Receivers, Series 1750 Instruction Manual, Scientific Atlanta, Inc., Atlanta, Georgia, 1975.

Rectangular Pattern Recorders, Series 1520 Instruction Manual, Scientific Atlanta, Inc., Atlanta, Georgia, 1976.

Smith, Ralph J.; Circuits, Devices, and Systems, John Wiley and Sons, New York, 1976.

Synchro Conversion Handbook, ILC Data Device Corporation, Bohemia, N.Y., 1974.

The TTL Data Book for Design Engineers, Texas Instruments, Inc., 1076.

Log 0569

*EXPERIMENTAL RESULTS OF A COMMUTATING FEED FOR CIRCULAR ARRAYS**

R.I. Wolfson, C.F. Cho and G.G. Charlton

ITT Gilfillan, Van Nuys, California

*The work described herein was supported by the United States Air Force, Electronic Systems Division, Hanscom AFB, through Contract No. F19628-79-C-0034 and under the direction of Mr. Walter Rotman and Lt. Gregory Cruz.

ABSTRACT

The development and final test results of an experimental commutating feed are described. Two key technological developments were accomplished: noncontacting magnetic loop couplers which allow low-loss transfer of RF energy with the precise control of amplitude and phase needed to realize low sidelobe levels; and the implementation of a large-scale, rotating stripline distribution network used to feed a 90-degree sector of a circular array antenna. Although the experimental model was not completly optimized, test results indicate that the design is capable of achieving an input VSWR of 1.2:1, insertion loss of 1.5 dB, and sidelobe levels below -30 dB over the operating band of 1.2 to 1.4 GHz. Excellent performance is also obtained over the extended frequency band, 1.0 to 1.5 GHz, which includes the IFF band.

EXPERIMENTAL RESULTS OF A COMMUTATING FEED FOR CIRCULAR ARRAYS

Introduction and Background

One of several antenna concepts being considered for systems such as the Unattended Radar (UAR) is a circular array, shown in Figure 1. The principal motivations for such an approach over a conventional rotating antenna are reduced drive power, improved reliability, and availability of simplified maintenance. Over the past decade, numerous purely electronic scan concepts for circular arrays have been developed. All of these approaches have been plagued by high loss and poor reliability due to the large number of components in series, and poor sidelobe performance due to large amplitude and phase errors.

To address these problems, the Department of the Air Force, Electronic Systems Division, funded ITT Gilfillan to develop, construct and evaluate a commutating feed assembly for steering the beam of a circular array. Details of the development of this device have already been presented presented,[1] and final test results are described herein.

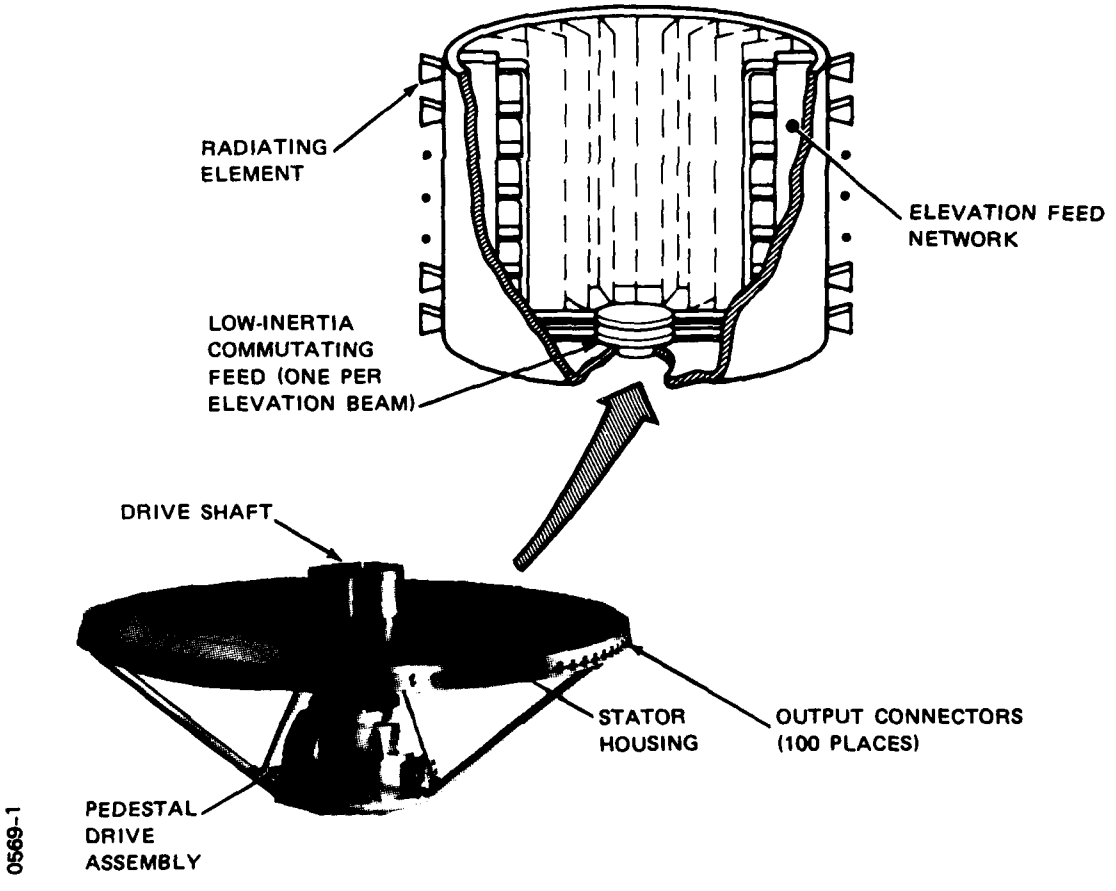

Figure 1. Circular array antenna with low-inertia commutating feed

Table I presents a summary of the requirements for the commutating feed assembly.

Table I. Commutating Feed Assembly Requirements

Frequency Band	1.2 to 1.4 GHz
Number of Output Ports	100
Number of Excited Ports	26
Excited Sector	90°
Array Diameter	180 inches
Aperture Illumination	Consistent with -20 dB sidelobes
VSWR	
Input	1.3:1 maximum
Output Ports	1.3:1 maximum
Insertion Loss	1.0 dB maximum
Power Capacity	
Peak	10 kW
Average	500W
Rotation Rate	15 rpm
Drive Power	50W maximum
Environment	-35°F to +100°F minimum (as encountered in Arctic)
Reliability	Consistent with Unattended Radar operation
Stacking	2 or more Commutators
Growth	200 Outputs
	69 Excited

0569-2

A simplified block diagram of the commutator is shown in Figure 2. The annular rotary coupler is a special design that provides two equal-amplitude, in-phase RF output signals.

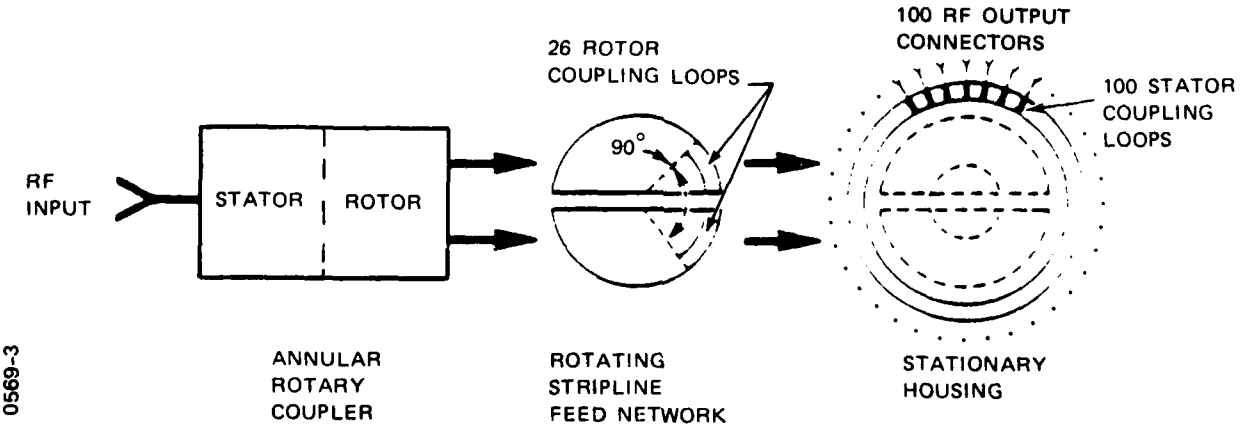

0569-3

Figure 2. Block diagram of commutating feed assembly

Assembly of Commutating Feed

The stripline feed network shown in Figures 3 and 4, consists of a center-fed array of directional couplers, delay lines for phase compensation, phase trimmers, and printed circuit rotor coupling loops. The design illumination selected for the 13-element series feed is a -29 dB, $\bar{N} = 4$ Taylor distribution.

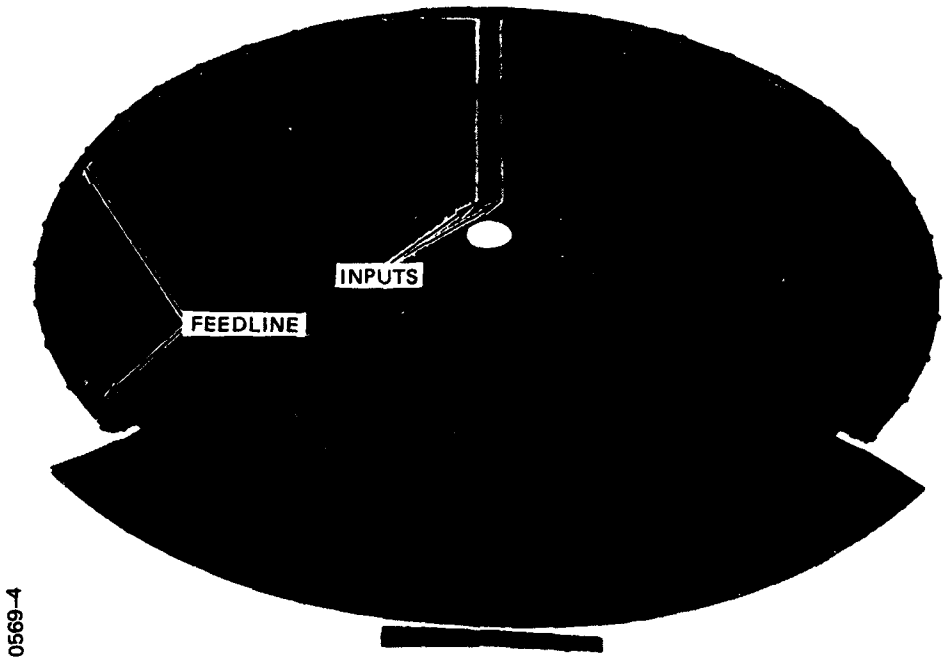

Figure 3. Stripline feed network circuit board, input side

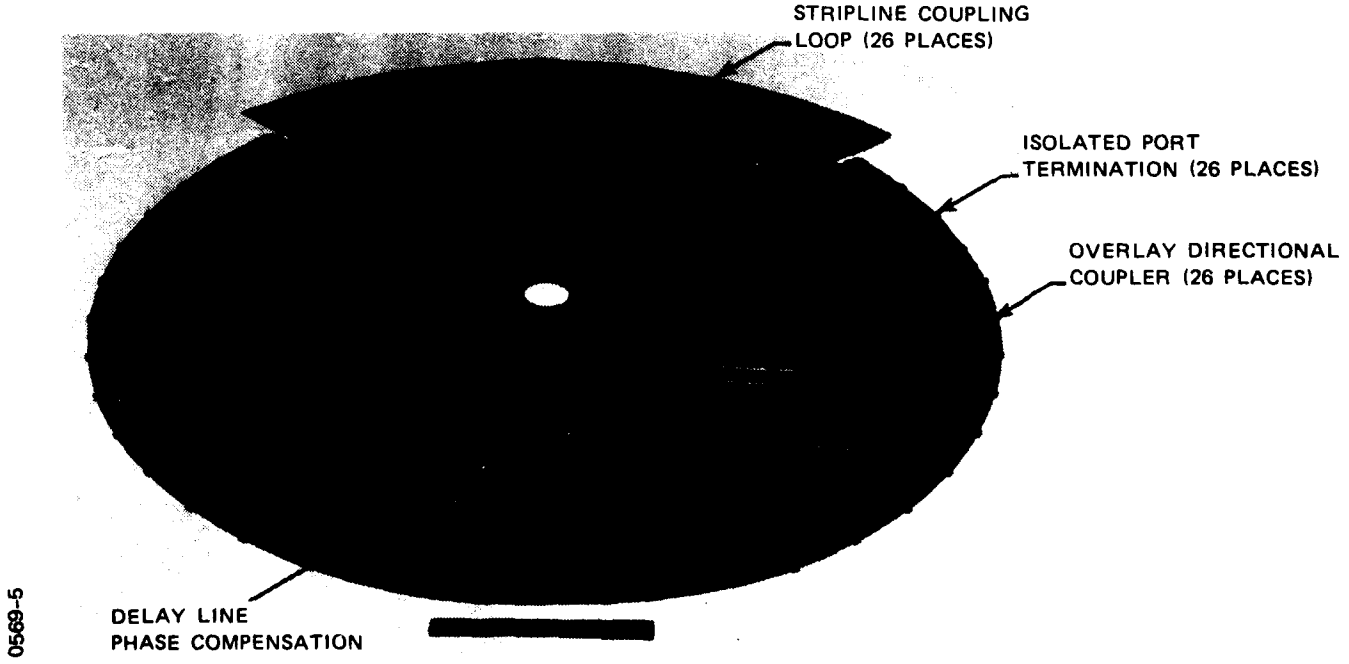

Figure 4. Stripline feed network circuit board, coupled side

The stationary housing, shown in Figure 5, includes the support structure, pedestal drive assembly, bearings, RF chokes, stator coupling loops, and output connectors.

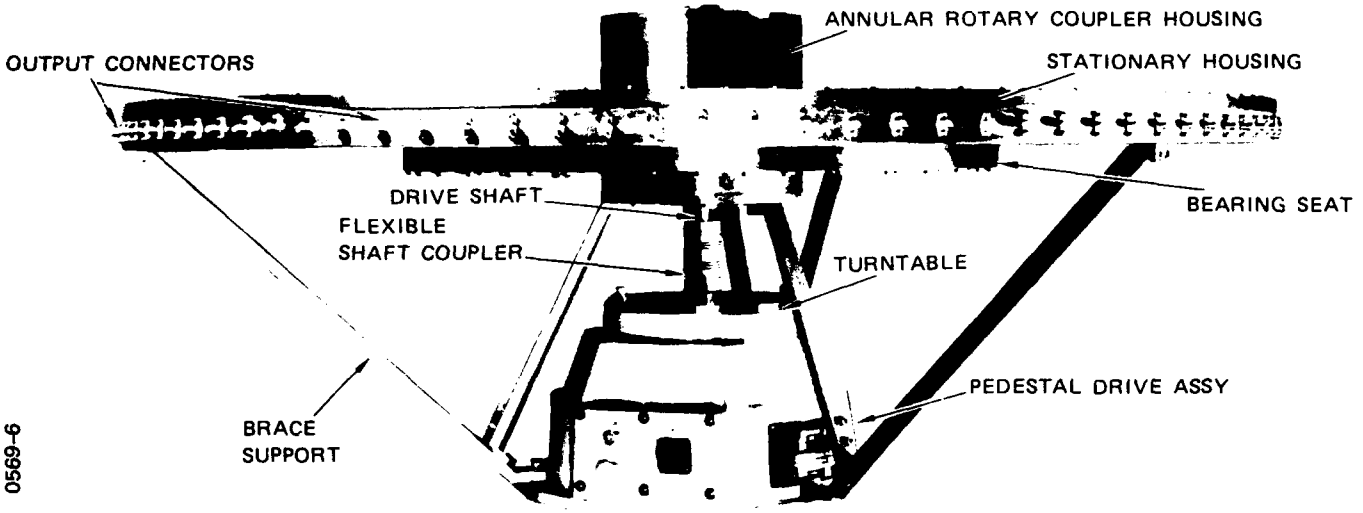

Figure 5. Stationary housing and assembled commutating feed

A key technological development of the program consists of noncontacting magnetic loop couplers, which allow low-loss transfer of RF energy with the precise control of amplitude and phase needed to realize low sidelobe levels. The loop coupling region of the commutating feed is shown in the perspective drawing, Figure 6.

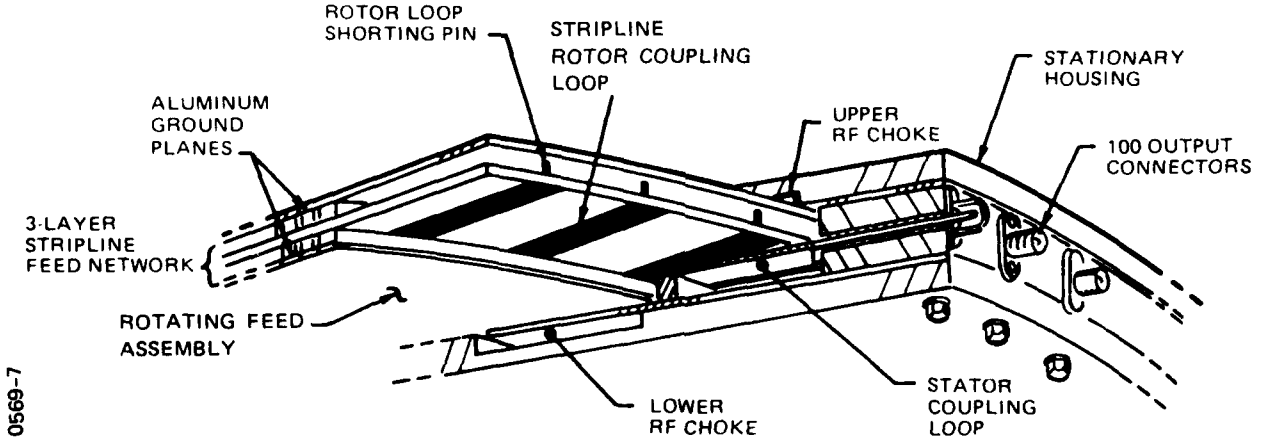

Figure 6. Loop coupling region

The rotating stripline feed assembly is shown in Figure 7. The 90-degree annular sector on the right, which extends beyond the ground plane, contains the 26 stripline rotor coupling loops. The other annular sector provides dynamic balance to avoid excessive vibration as the assembly rotates.

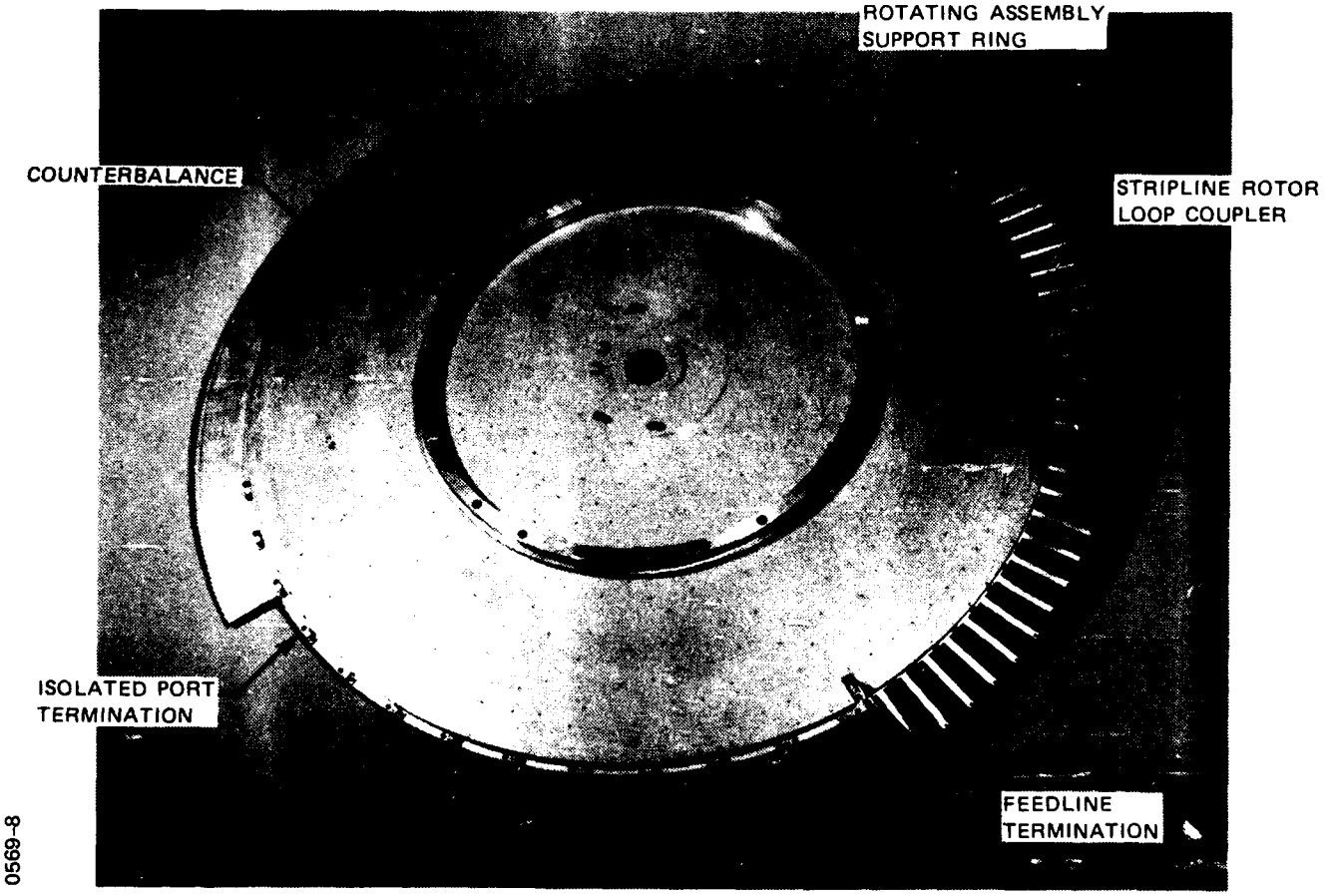

Figure 7. Rotating stripline feed assembly

The lower housing assembly, which contains an 18-inch bearing, the lower annular RF choke, and 100 stator loop couplers, is shown in Figure 8.

Test Results of Experimental Commutator Model

The input VSWR of the experimental commutator model, measured at the input to the annular rotary coupler, is shown in Figure 9. Typically, the input VSWR is less than 1.15:1 over 25 percent of the band, less than 1.5:1 over 65 percent of the band, and less than 1.8:1 overall. Although the annular rotary coupler, the stripline feed network, the loop-coupling region, and the stator loops had been carefully matched in the various breadboard test fixtures, no attempts were made to improve the overall input VSWR of the completed final assembly. It is felt that if this additional matching were incorporated, the goal of 1.3:1 could be realized over the entire band.

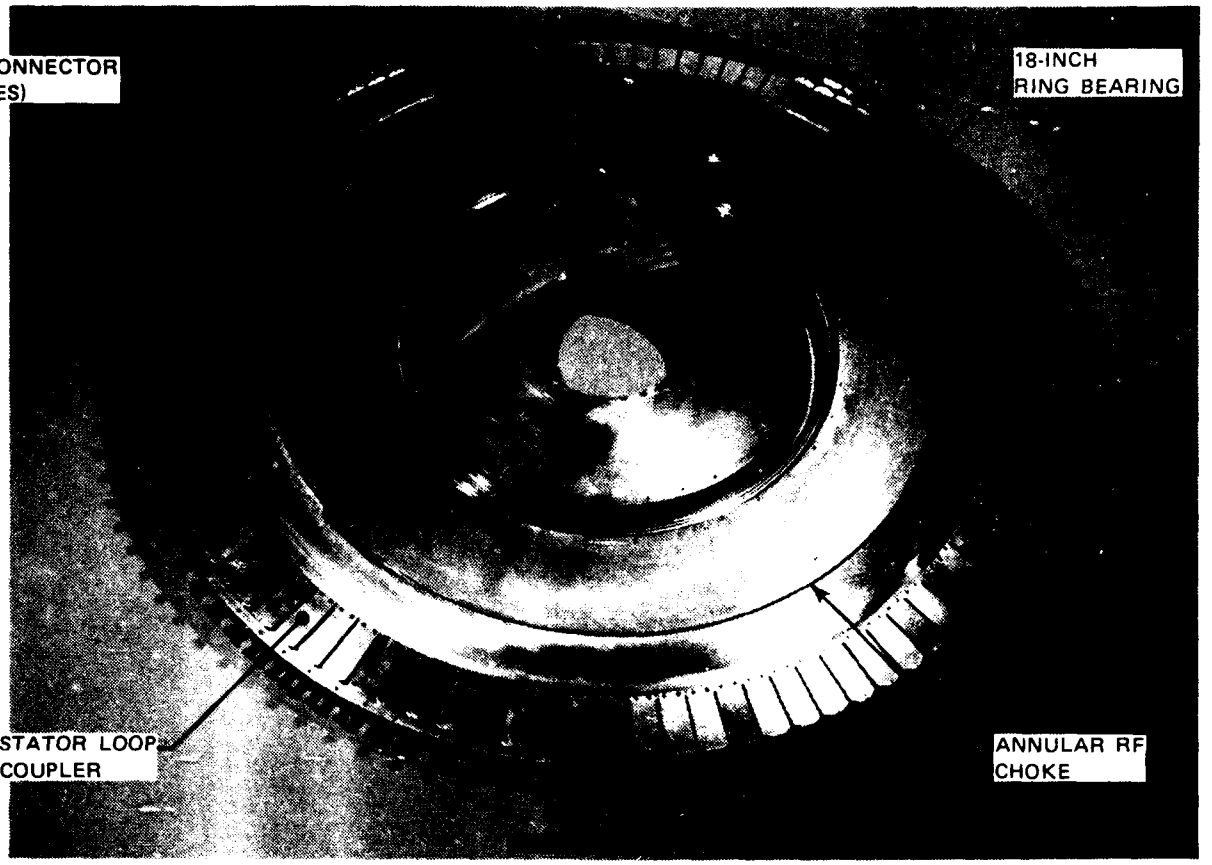

0569-9

Figure 8. Lower housing assembly

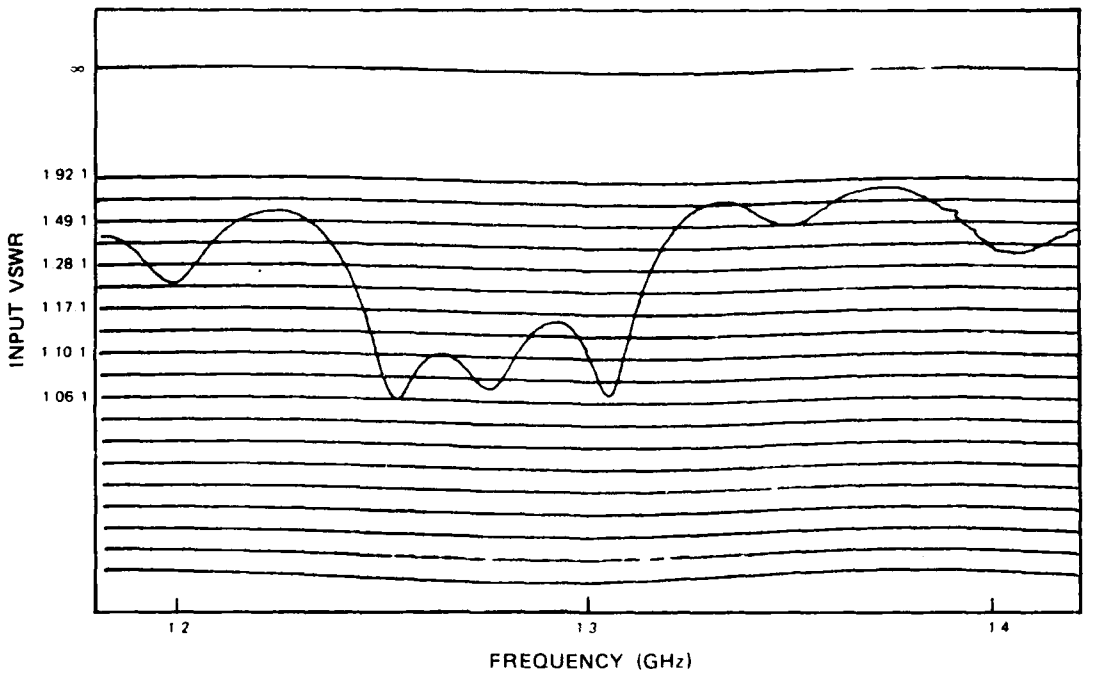

0569-10

Figure 9. Input VSWR of experimental commutator model

The coupled amplitude and phase excitation at 26 adjacent output ports in the illuminated 90-degree sector was measured with the rotor loops located directly over the stator loops. The swept-frequency amplitude, shown in Figure 10 for one-half of the symmetrical feed network, illustrates the broadband nature of the stripline circuitry and loop couplers.

Coupled amplitude, measured at 1.2, 1.3 and 1.4 GHz, is shown in Figure 11 along with the ideal design illumination for a lossless network. The data in each case have been normalized to the peak value, which occurs at one of the center elements, number 13 or 14. Note that elements 24 through 26 do not appear to be functioning properly. The probable cause is poor RF grounding at the ends of rotor loops 24 through 26 due to loose # 2-56 shorting screws threadedd into the stripline ground plane. The problem was not corrected, as disassembly of the commutating feed assembly would be required, and furthermore, these edge elements do not greatly affect the overall performance of the unit.

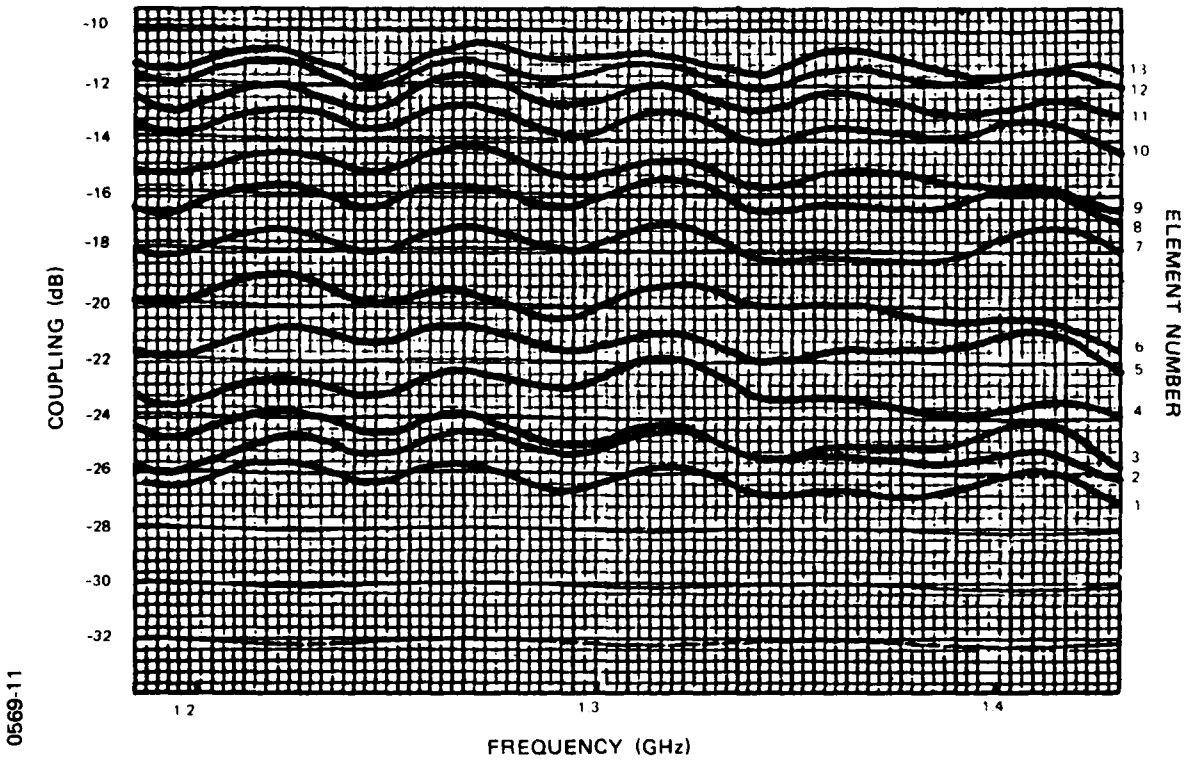

Figure 10. Coupling to output ports 1 through 13 versus frequency

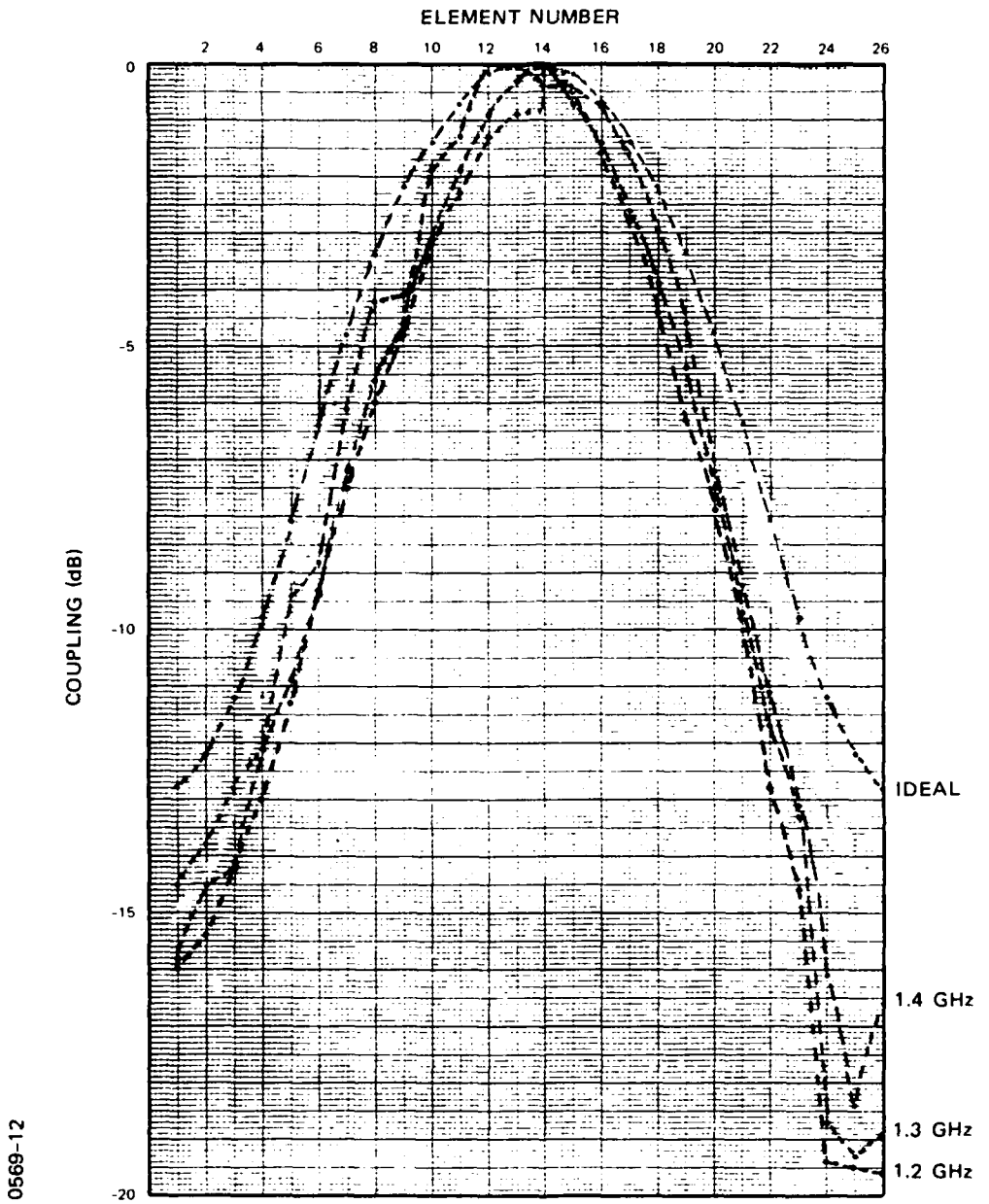

Figure 11. Coupling versus element number at 1.2, 1.3 and 1.4 GHz

Phase error, which is defined as the difference between the measured value and the ideal design value, and is referenced to the phase at element number 1, is shown in Figure 12 for 1.2, 1.3, and 1.4 GHz. Phase trimmers for each element, which are located within the stripline feed assembly, were adjusted for minimum phase error at midband, 1.3 GHz. Larger phase errors arise at the band edges because the frequency dependence of the phase trimmers is not the same as that of the various element pathlengths.

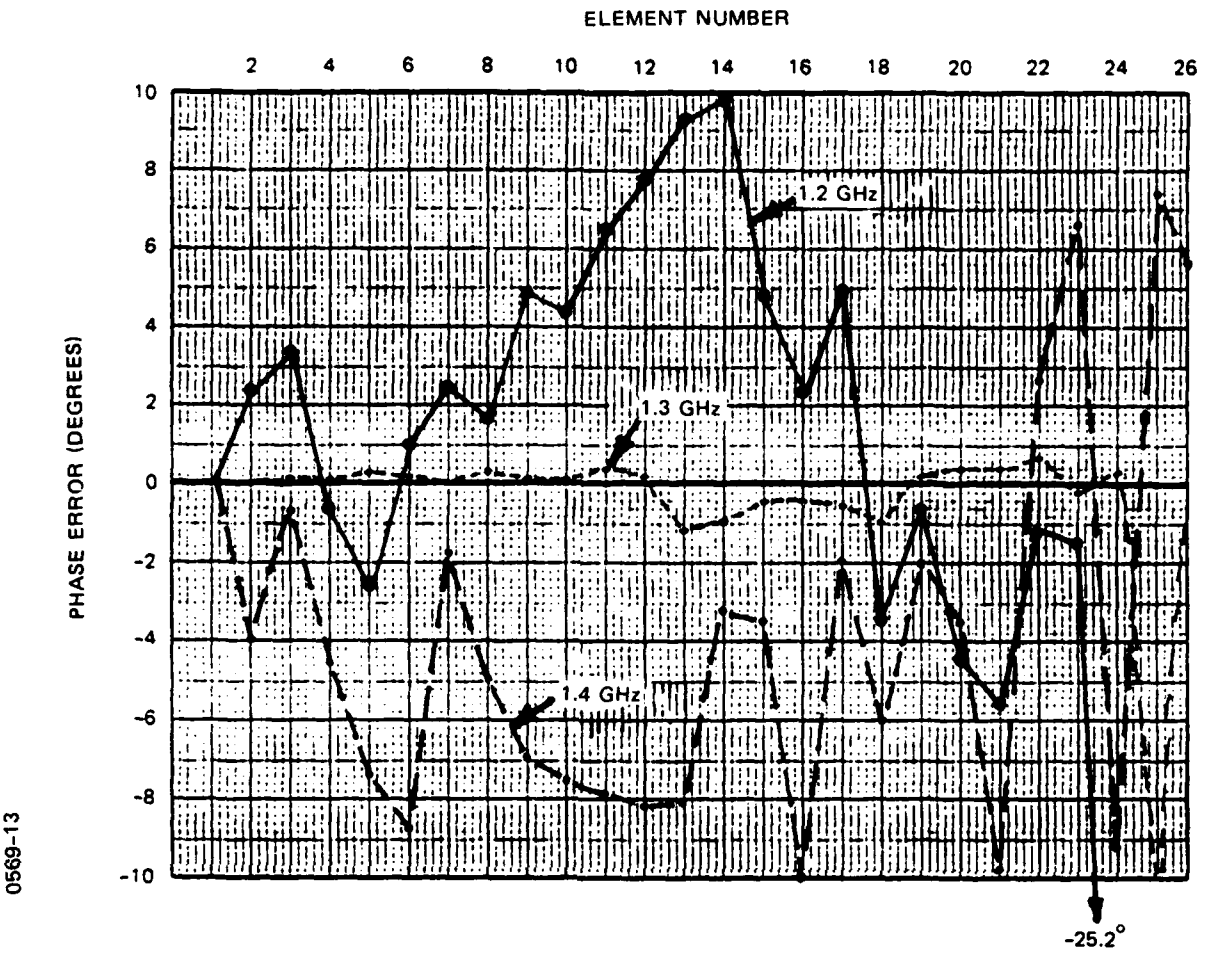

Figure 12. Phase error versus element number

Insertion loss of the commutator is determined by measuring amplitude and phase at 26 output ports within the 90-degree excited sector, and computing the far-field vector sum. The results are given in Table II.

Table II. Insertion Loss of Experimental Commutator Model

Frequency (GHz)	Insertion Loss (dB)
1.2	1.58
1.3	1.41
1.4	1.84

0569-14

The higher insertion loss at 1.4 GHz is due primarily to the annular rotary coupler, which was originally designed for operation in the 0.96 to 1.215 GHz band.

Azimuth patterns were computed for a 180-inch diameter circular array of 100 uniformly-spaced elements. Although the feed network was designed to be phase compensated at an elevation scan angle of 15 degrees, these patterns assume zero elevation scan, which represents a slightly worse situation in terms of sidelobe levels and beamwidth.

Figures 13 through 15 show patterns computed at 1.2, 1.3, and 1.4 GHz, using the amplitude and phase data of Figures 11 and 12. The reference lines represent the sidelobe specification limit, -20 dB, and the sidelobe design limit that would be realized with ideal excitation, -30 dB. Table III summarizes the results of these pattern computations.

Table III. Results of Pattern Computations

Frequency (GHz)	1.2	1.3	1.4
Highest Sidelobe (dB)	-28.4	-26.6	-28.4
Aperture Efficiency (dB)			
Theoretical	- 1.25	- 1.27	- 1.28
Measured	- 1.84	- 1.69	- 1.59
Dissipation Loss (dB)	- 1.58	- 1.41	- 1.84

0569-15

Although the experimental commutator model is not required to operate over the IFF frequency band, 1.03 GHz, measurements were made at 1.03 GHz in order to demonstrate the extremely wideband performance of the device. The pattern shown in Figure 16 was computed using amplitude and phase data measured for one-half of the feed network, and assuming symmetrical excitation.

The measured values of insertion loss, VSWR, and amplitude and phase distribution were taken with rotor loops centered directly above stator loops. Additional data were taken[2] to show the effects of rotation of the commutator on these parameters. Two distinct sources of variation can be identified. The first is associated with mechanical differences amongst the 100 stator loops. As rotation occurs, any given rotor loop couples in sequence to each of the stator loops, and any irregularities appear as amplitude and phase variations. Thus, these excitation errors are essentially a measure of the precision with which the commutator has been constructed. The rms variations of these parameters for the experimental model are 0.28 dB and 2.18 degrees, respectively. During normal operation of the commutating feed, smaller errors would be expected because of the averaging effect of multiple coupling from all 26 rotor loops.

The second source of variation arises because adjacent rotor loops, which have dissimilar amplitude and phase excitations, couple in changing proportion as they move in the vicinity of the stator loops. The effect is most noticeable when the rotor loops are positioned above the gaps between stator loops. The magnitude and slope of the variations can be minimized over an appreciable percentage of rotational angle by using narrow rotor loops and much wider stator loops.

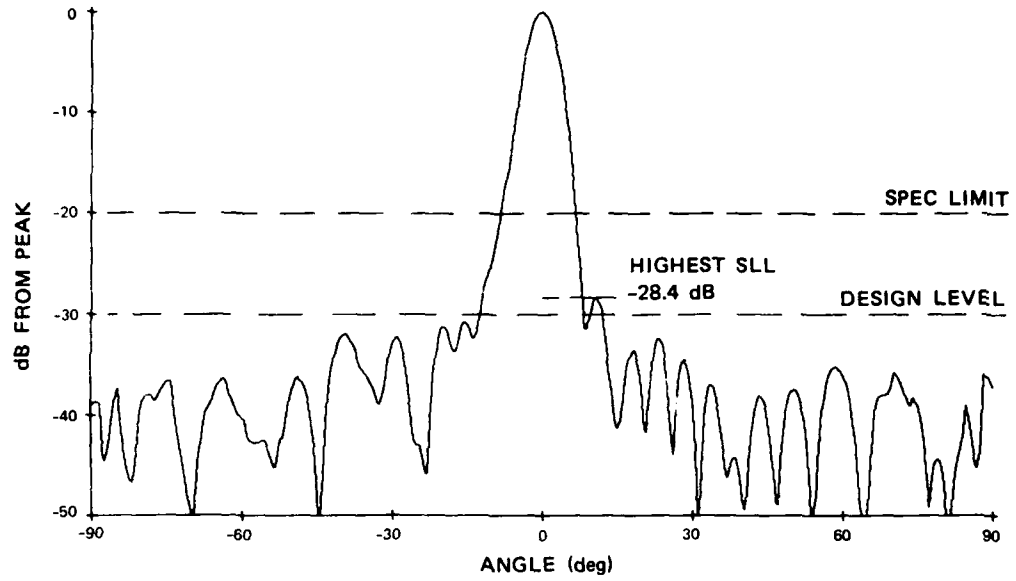

Figure 13. Computed azimuth pattern of experimental commutator model at 1.2 GHz

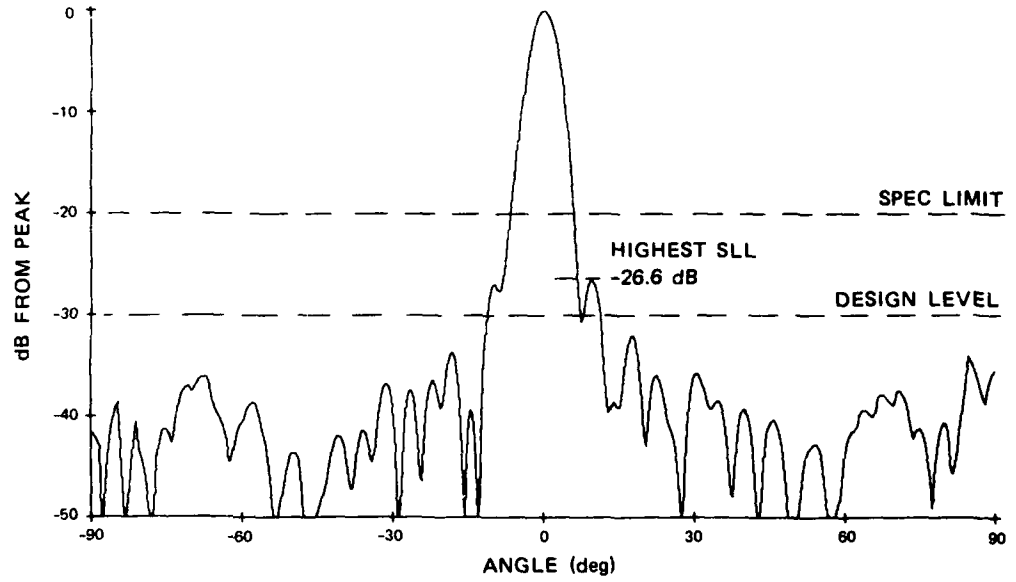

Figure 14. Computed azimuth pattern of experimental commutator model at 1.3 GHz

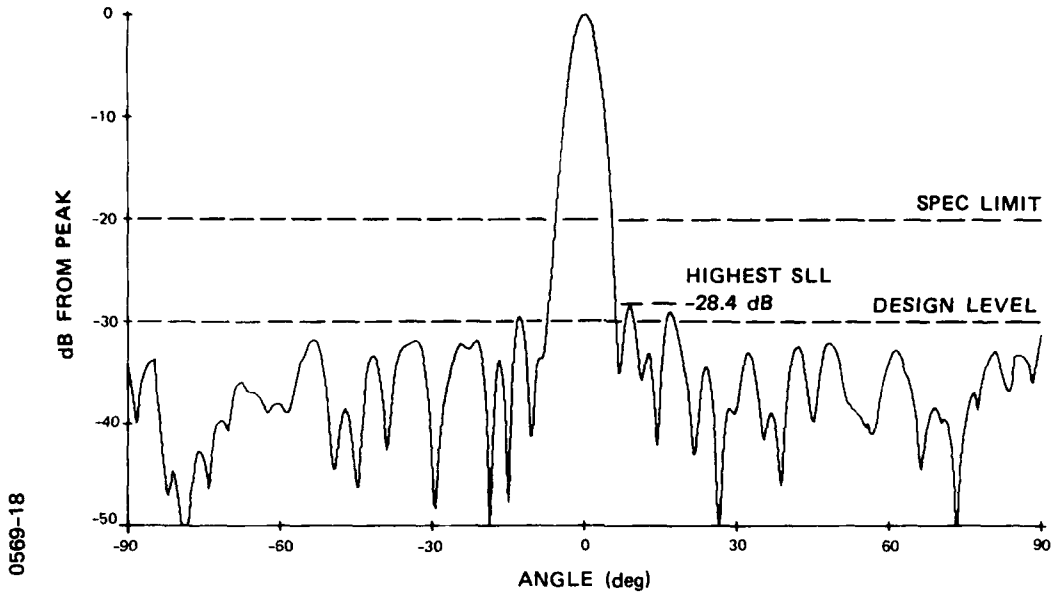

Figure 15. Computed azimuth pattern of experimental commutator model at 1.4 GHz

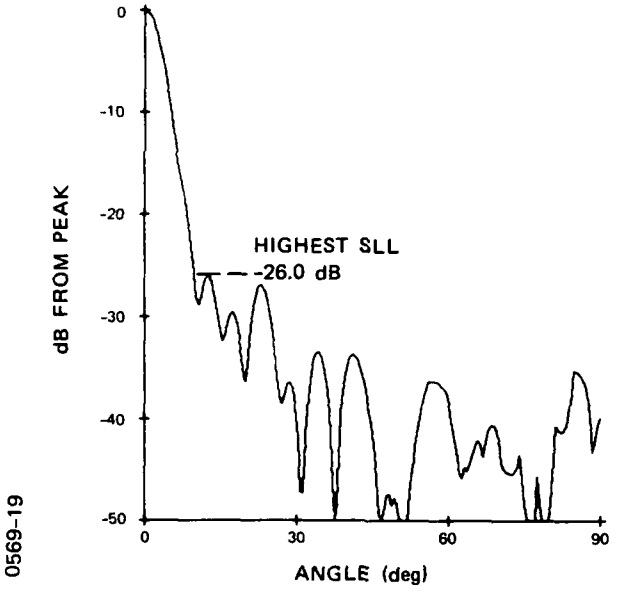

Figure 16. Computed azimuth pattern at 1.03 GHz

In the experimental commutator model, the rotor loops are 0.25-inch wide, and the stator loops are approximately 1.00-inch wide separated by 0.10-inch gaps. Patterns computed from amplitude and phase data taken at various rotational angles show that even when the rotor loops are in the gap position, excellent patterns are obtained, although insertion loss increases about 0.5 dB due to the larger mismatches of the coupling loops. If this condition is undesirable from a systems standpoint, it can be avoided by transmitting and receiving only during the 80 percent of the time when the rotor loops and stator loops overlap.

Summary and Conclusions

The development of the experimental commutator model has clearly demonstrated the viability of this approach for low-cost azimuth steering the beam of a circular array. Excellent electrical performance is obtained, with improvements in reliability, maintenance and life-cycle cost compared to alternative approaches.

REFERENCES

[1] R.I. Wolfson and C.F. Cho, "A Low-Inertia Commutating Feed for Circular Arrays," Symposium on Antenna Applications, (Allerton), 1979.

[2] R.I. Wolfson, "Commutating Feed Assembly," Final Report 0510, ITT Gilfillan, March 1980, prepared under Air Force Contract F19628-79-C-0034, pp 112, 116-122, 127-132.